VENTILATION PATHWAYS IN THE TROPICAL ATLANTIC AND PACIFIC OCEANS WITH A FOCUS ON THE OXYGEN MINIMUM ZONES:

DEVELOPMENT AND APPLICATION OF A NESTED HIGH-RESOLUTION GLOBAL MODEL SYSTEM

Dissertation
zur Erlangung des Doktorgrades
der Mathematisch-Naturwissenschaftlichen Fakultät
der Christian-Albrechts-Universität zu Kiel

vorgelegt von

Franziska Ulrike Schwarzkopf

Kiel, 2016

GEOMAR
Helmholtz-Zentrum für Ozeanforschung Kiel

Referent: Prof. Dr. Claus W. Böning

Koreferent: Prof. Dr. Peter Brandt

Tag der mündlichen Prüfung: 08.06.2016

Zum Druck genehmigt: 08.06.2016

gez. Prof. Dr. Wolfgang J. Duschl, Dekan

Zusammenfassung

In den östlichen Teilen des tropischen Atlantiks und Pazifiks befinden sich Sauerstoffminimumzonen (SMZ), die sich dort auf Grund eines Zusammenspiels schwacher physikalischer Belüftung und hoher biologischer Produktivität bilden. In diesen Zonen wurde über die letzten Jahrzehnte eine Abnahme der ohnehin niedrigen Sauerstoffkonzentrationen beobachtet. Wie sich die SMZ unter veränderten Klimabedingungen verhalten ist bisher unklar; Zukunftsprojektionen zeigen unterschiedliche Reaktionen der SMZ von einer verstärkten Abnahme bis hin zu einer Zunahme der Sauerstoffkonzentrationen. Es ist jedoch klar, dass die SMZ komplexen biogeochemischen und physikalischen Prozessen unterliegen, deren Verständnis notwenig ist, um verlässliche Prognosen über Änderungen geben zu können. In dieser Arbeit werden die physikalischen Aspekte der Ventilation der SMZ mithilfe eines genesteten hochauflösenden Ozeanmodellsystems analysiert.

Dieses Modellsystem basiert auf dem Modellcode von NEMO unter Verwendung von AGRIF. In den relevanten Regionen, dem tropischen Atlantik und dem tropischen Pazifik, wurde jeweils ein sogenanntes Nest mit einer horizontalen Auflösung von 0,1° entwickelt, das in eine globale Modellkonfiguration mit einer horizontalen Auflösung von 0,5° eingebettet ist. Simulationen, in denen atmosphärische Randbedingungen von 1948 bis 2009 zum Antrieb der verschiedenen Modellkonfigurationen genutzt werden, bilden die Grundlage für die vorliegende Analyse der physikalischen Ventilation der SMZ. Die in den genesteten Modellkonfigurationen simulierte Zirkulation kommt in vielen Aspekten der beobachteten sehr nahe und stellt eine deutliche Verbesserung im Vergleich zur grobaufgelösten Simulation dar.

Das Hauptaugenmerk der Analysen liegt auf den Ursprungsregionen und dem Alter des Wassers in den SMZ sowie auf den Pfaden, die dieses Wasser zurücklegt, bevor es in die SMZ gelangt. Zwei Methoden werden verwendet: eine Lagrangesche Rückverfolgung von Partikeln, welche sich zu einer bestimmten Zeit in den SMZ befinden, und eine Verfolgung von Oberflächenwasser mithilfe zweier sogenannter “Tracer”, einem Farbstofftracer, welcher die Konzentration eines an der Oberfläche gesättigten Stoffes simuliert, und einem Alterstracer, der die Zeit angibt, die seit dem letzten Kontakt eines Wasserpaketes mit der Oberfläche vergangen ist. Die beiden Methoden beleuchten einerseits das Ende und andererseits den Anfang der Ventilationspfade in die SMZ und können teilweise zu einem vollständigen Pfad zusammengeführt werden.

Als Ursprungsregionen des Wassers in den SMZ im Atlantik und Pazifik stellen sich die subtropischen Becken der jeweiligen Ozeane heraus, mit einem größeren Beitrag aus dem Süden als aus dem Norden. Konvektionsgebiete in der Weddellsee und für die SMZ im Atlantik zusätzlich im Nordatlantik tragen ebenso zur Ventilation bei. Die Hauptpfade des Wassers, das in die SMZ gelangt, führen aus den Subtropen über die Westränder der Becken in die äquatorialen Stromsysteme und in diesen südlich beziehungsweise nördlich des Äquators nach Osten. Für die südliche der SMZ im Pazifik stellt sich zusätzlich ein flacher Pfad dar, der direkt aus dem tropischen Ostpazifik kommt.

Abstract

The Oxygen Minimum Zones (OMZs) in the eastern parts of the tropical Atlantic and Pacific Oceans occur in the upwelling regions where high biological productivity comes along with circulation conditions causing low oxygen levels. During the last decades an expansion and strengthening of these regions has been observed. The cause of the decrease in oxygen and a possible continuation under global warming conditions is under debate. There is, however, agreement that it is based on a complex interplay between diverse biogeochemical and physical processes, acting on different spatial and temporal scales. To investigate the causes of these trends, the mechanisms of OMZ ventilation need to be understood first. This study examines the physical aspects of the ventilation, using a set of high resolution nested ocean models.

Based on the Nucleus for European Modelling of the Ocean code, eddying models with 0.1° horizontal resolution of the tropical Atlantic (TRATL01) and the tropical Pacific Ocean (TROPAC01) are developed, that are embedded in global 0.5° configurations (ORCA05) via two-way nesting provided by Adaptive Grid Refinement in Fortran. The nesting approach allows to simulate relevant small scale processes in the regions of main interest while maintaining the global context. The analysis of the ventilation processes affecting the OMZs is based on hindcast experiments for the period from 1948 to 2009, forced with prescribed atmospheric conditions as given by the Coordinated Ocean Reference Experiment II forcing set. TRATL01 and TROPAC01 show a high fidelity in representing the circulation in the respective tropical ocean basins and better compare to observations than ORCA05.

The main goal of this study is to identify the pathways, source regions and age of the waters in the OMZs. To decipher these aspects, Lagrangian trajectory analyses in conjunction with passive tracer simulations reflecting a surface dye and an artificial age tracer are utilized. The tracers and trajectories implemented here give insights on both, the beginning and the end, of the path of a water parcel from the surface into the OMZs, respectively. They can occasionally be connected, providing the full path.

For both OMZs, either in the Atlantic or in the Pacific Ocean, the subtropics of the respective ocean basin are identified as the dominating source regions with a larger contribution from the South than from the North. Additionally, convection sites in the Weddell Sea and in the northern Atlantic are part of the source regions for waters ventilating the OMZs, where the latter region contributes only to the ventilation of the Atlantic OMZs. It is shown, that in both ocean basins the main supply route of well ventilated waters from the subtropics into the OMZs is via the western boundary and the alternating zonal current bands spanning the entire tropical region. Generally, the pathways as well as the source regions for the northern and southern OMZs within the respective ocean are very similar, except for the very last part of the paths, when waters cross the basin from the western boundary to the East on different sides of the equator. In the southern tropical Pacific Ocean, an additional shallow path occurs, directly connecting the eastern tropical Pacific with the southern OMZ.

Contents

1. Introduction

In this introductory chapter, the subject of the following study is set into its context within the climate system. The importance of the tropical Oxygen Minimum Zones and of the understanding of mechanisms affecting the evolution and changes of these zones is shown. The current state of knowledge is briefly depicted. Open questions that will be addressed in this study are derived and the methods used to assess those are introduced. The structure of the main part of this work is outlined at the end of this chapter.

Contents

In the corners at the bottom of the pages, flipbooks show 80 years of the paths of particles from the mixed layer into the northern (red) and southern (black) Oxygen Minimum Zones in the tropical Atlantic (odd pages) and Pacific (even pages) Oceans. The depth of the particles is given by the blue colourscale.
To see the particle move from the mixed layer into the OMZs in the Atlantic Ocean, use your left thumb, starting at the last page. For the pathways into the OMZs in the Pacific Ocean, use your right thumb, starting at the first page.

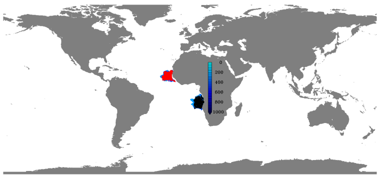

1.1. Ocean ventilation and Oxygen Minimum Zones

Ocean ventilation is a major process affecting marine life [e.g. Brewer and Peltzer (2009)] as well as the climate system [Bryan et al. (2006)]. Upper Ocean waters with properties determined by the atmospheric conditions above [Liss and Merlivat (1986); Phillips (1994)] are transported downward, renewing the interior and deep Ocean waters [Khatiwala et al. (2012)]. Oxygen, carbon dioxide (CO_2) and other soluble gases are carried with these waters and the ventilation therefore is of fundamental importance for their uptake and storage within the ocean. Ventilation timescales range from decades to centuries and millennia [England (1995); Haertel and Fedorov (2012); Holzer and Hall (2000)]. Depending on the different time scales the supply with these substances differs regionally, leading to diverse conditions with zones of high and low concentrations of the various substances. The partly long temporal scales make the ventilation a factor in building poorly oxygenated zones [Luyten et al. (1983)] and that remotely controls the climate.

The ventilation is responsible for the supply of the interior Ocean with nutrients and elements needed for biogeochemical cycles including oxygen and CO_2 and also plays a buffering role for the climate in storing green house gases for long times. The oceanic uptake of gases at the surface is mainly determined by the temperature in the surface waters and by partial pressue gradients between the atmosphere and the ocean, the so called solubility pump [Phillips (1994); Takahashi et al. (2002)]. Regions with lower temperatures show higher solubilities and are therefore more effective in drawing down atmospheric CO_2. The gas concentrations that are set at the surface are transported with the water parcel into the ocean. During its residence time below the surface, on its way through the interior ocean it is affected by biogeochemical processes, altering the concentrations of these gases and nutrients within the water through biological production and consumption or by other chemical transformations [e.g. Denman et al. (2007)]. In upwelling areas, where nurtrient rich waters reach the surface, CO_2 is outgassed to the atmosphere. Under global warming, the Ocean might regionally change its role from a CO_2 sink into a CO_2 source [Takahashi et al. (2012); Gruber et al. (2009)]. When a water parcel returns to the surface after up to hundreds or thousands of years and again interacts with the atmosphere, the concentrations and solubilities might then have changed. The gradient between the ocean and the future atmosphere could have reversed and a positive feedback might come into play, accelerating global warming [Cox et al. (2000); Sarmiento and Quéré (1996)].

Dissolved oceanic oxygen is determined by the same physical processes as CO_2, but in contrast it is not affected by changes in its atmospheric concentrations. Along the way of a water parcel through the ocean, oxygen concentrations are evolving due to physical (mixing) and biological (production and consumption) processes, even in abyssal layers [Craig (1971)]. Changes in the oxygen supply define and alter habitats of marine organisms that depend on the abundance of oxygen [e.g. Stramma et al. (2012)]. In poorly ventilated regions, the so called shadow zones [Luyten et al. (1983)], where ventilation timescales are extraordinarily long for intermediate depth ranges and the supply with oxygen is low, co-occurring with high biological productivity and therefore, high oxygen consumption, the Oxygen Minimum Zones (OMZs) are formed [Karstensen et al. (2008)]. These

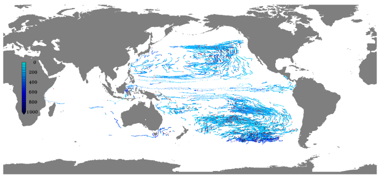

are located in the eastern tropical Atlantic and Pacific Ocean, being subject of the present study, as well as the northern Indian Ocean and the North Pacific.

Within the OMZs, chemical and biological processes differ from those in oxygenated waters [Helly and Levin (2004); Bopp et al. (2002)]. In these regions changes in oxygen can have important effects on the carbon cycle and thereby the CO_2 concentrations [Joos et al. (2003)] and on the nitrogen cycle in particular on the production of trace gases such as nitrous oxide [Elkins et al. (1978)]. Where oxygen is (almost) completely depleted, nitrate is used for remineralization instead [e.g. Ridder and England (2014)] producing nitrous oxide and molecular nitrogen within the denitrification chain [e.g. Paulmier and Ruiz-Pino (2009)]. Nitrous oxide with its high green house gas potential might, through outgassing, be of relevance for the climate [Gleßmer et al. (2011)] and has already been shown to increase [Arévalo-Martínez et al. (2015)]. Changes in the strength and extent of the poorly oxygenated waters are therefore affecting CO_2 and other green house gas concentrations, not only locally but, via the large scale circulation, also globally.

It is under debate, how ocean ventilation changes under global warming conditions. Keeling and Garcia (2002) expect, that ventilation and oxygen concentrations decrease while model results by Gnanadesikan et al. (2007) show that in poorly ventilated regions, oxygen concentrations might increase under global warming. Yamamoto et al. (2015) differentiate between centennial scale reduction in oxygen concentrations and a recovery of deep ocean oxygenation on millenial timescales, that later on lead to an increase in oxygen concentrations. In some low oxygen areas, including the southern Atlantic OMZ and at the boundary of the northern Atlantic OMZ as well as the southern Pacific OMZ, Oxygen concentrations have been observed to locally decrease within the period from 1960 to the mid 2000s [Stramma et al. (2008, 2010)]. To investigate the causes of these trends, mechanisms of OMZ ventilation need to be understood first.

The tropical Atlantic and Pacific Oceans are marked by the strong equatorial currents bordered by the poleward limbs of the subtropical gyres [Schott et al. (2004)]. In the eastern parts of these basins, where ventilation happens on long time scales, OMZs are located close to the coast north and south of the equator. The vertical location of these zones is at intermediate depth between ~300 m and ~700 m. In the Atlantic ocean, minimum oxygen values are higher than in the Pacific Ocean where strongest OMZs are located in the eastern tropics with large spatial extent and even anoxic conditions [e.g. Stramma et al. (2008)].

The oxygen budget within the OMZs is a complex and not yet fully understood interplay between different consumption and supply processes [Karstensen et al. (2008)]. Recently Brandt et al. (2015) gave a broad overview on processes affecting the formation of OMZs as well as mechanisms causing changes within the OMZs, with a focus on the eastern tropical north Atlantic and, to a minor extent, on the eastern tropical south Pacific. Oxygen consumption and supply oppose each other, leading to regionally varying oxygen concentrations, and imbalances between the two cause changes in these concentrations. They summarize, that oxygen consumption is to 80% balanced by the divergence

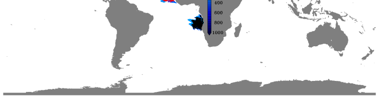

of meridional eddy and diapycnal fluxes. The remaining 20% can be ascribed to zonal advenction, that cannot be observationally quantified, and to the long-term tendency [Brandt et al. (2015)].

This budget has been observed exemplarily at 23° W, close to the western boundary of the OMZ in the north eastern tropical Atlantic by Hahn et al. (2014) building on Karstensen et al. (2008) and Fischer et al. (2013). They find that above the deep oxycline advective and zonal eddy processes dominate the supply part of the budget. For the vertical structure of the contributions they find, that in the upper part of the OMZ depth range these factors vanish and below the OMZ core their contribution again grows to values comparable to the meridional eddy and diapycnal supply. Most studies analyzing the advective part of the ventilation process focus on the equatorial currents, that indeed advect oxygen rich waters from the western parts of the basins towards the east [e.g. Brandt et al. (2010)]. However, a connection from the equatorial region into the OMZs, that are located several degrees off the equator, is not shown.

During the revision of the present thesis, a study by Peña-Izquierdo et al. (2015) was published, which examines the pathways of water masses into the north eastern tropical Atlantic OMZ by analyzing a model at an eddy-permitting resolution using a Lagrangian approach. Among their findings, that are in good agreement with what is shown here, they exhibit the importance of northern, off-equatorial currents for the ventilation of this OMZ and that the connection between the OMZ and the equatorial region is weak.

The above mentioned studies mainly focus on the OMZ in the north eastern tropical Atlantic and the importance of the zonal equatorial circulation for transporting oxygen-rich waters to the vicinity of the OMZs. They furthermore point to the importance of meridional and diapycnal eddy-driven oxygen supply. The current knowledge about the advective, large scale ventilation processes and their importance for the OMZs, especially for those in the tropical Pacific, is limited. The differences and similarities in ventilation processes between the Pacific and Atlantic OMZs have not been covered to date. A comprehensive examination of the whole oxygen supply paths from the ventilation at the Ocean surface into the cores of the OMZs is missing. These factors leading to the following questions are subjet to the present study:

- Which currents and circulation features are contributing to the ventilation of the OMZs?
- Where are the source regions of waters entering the OMZs?
- What are the pathways and timescales, waters take to enter the OMZs?
- What are the similarities and where are the differences between the ventilation of the OMZs in the Atlantic and the Pacific Ocean?

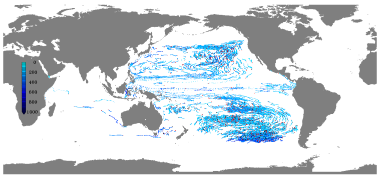

1.2. Need for an efficient model system

Observationally, ventilation can be investigated based on the classical water mass properties such as temperature and salinity [Johnson (2008); de Brauwere et al. (2007)] and on anthropogenic trace gases like Chloro Fluoro Carbons (CFCs) and their concentration in the ocean [e.g. Khatiwala et al. (2012)]. CFCs have been emitted into the atmosphere since the 1930s [McCulloch et al. (2003)] and their concentrations are well known [Walker et al. (2000)]. Since their release, these trace gases are also present in the ocean, where they are almost inert and therefore provide a measure for ocean ventilation, as their concentrations only change by advective and diffusive processes, along their way through the world ocean. CFC concentrations can be used as a measure for the age of the water, but only for waters subducted after the CFC introduction [Sonnerup (2001)]. Pathways can additionally be investigated based on drifter and float data [e.g. Carr and Rossby (2001); Grodsky and Carton (2002)], however, these observational attempts are restricted to the instrumental design by e.g. pre-defined drifting depths and limited to short time scales of only up to several years. On long time scales observational quantities, exhibiting ventilation pathways, especially into poorly ventilated regions like the OMZs are unavailable. Here, Ocean models come into play, providing the framework for analyses beyond observationally available temporal and spatial scales.

To get trustworthy results from analyses based on numerical ocean models, those should be able to realistically simulate the ocean with a variety of processes affecting the ventilation. Convection and subduction play a key role to bring surface waters into the interior ocean [Blanke et al. (2002)], distinct currents transport water masses and mesoscale features contribute to mixing processes [e.g. Chanut et al. (2008)]. Coarse models with horizontal grid sizes of $O(1)^\circ$ are able to simulate major features but do not resolve eddies [Houry et al. (1987)]. Although the effect of mesoscale processes is parameterized [e.g. Gent and McWilliams (1990)], these models miss the high spatial variability of the eddy field and its impact on the circulation. These models are mainly used for long integrations spanning centuries to millenia and for coupled ocean-atmosphere or earth system simulations and have been shown to fail in simulating the OMZs [e.g. Deutsch et al. (2011)]; the mesoscale is an important factor in simulating oxygen supply [Gnanadesikan et al. (2013)]. Models with higher ($O(0.1)^\circ$) resolutions are still too expensive to do such long integrations and are therefore mostly used for decadal scale simulations. One way to provide a multi-decadal time frame and still simulate mesoscale features is regional modelling at high resolution. The main disadvantage of regional models however, is the loss of feedbacks into the global context. The compromise between integration lengths, spatial coverage and model resolution used within this study is a nesting approach, where distinct regions are simulated at high resolution, embedded via two-way communication in a global model at intermediate resolution [Blayo and Debreu (2006)].

The nesting approach used here is provided by Adaptive Grid Refinement in Fortran (AGRIF) [Debreu et al. (2008)] and allows for flexible implementation of nested regions in different ways. One-way nesting only provides boundary conditions from the coarse model to the nested region whereas two-way nesting provides the possibility to feed back dynamical effects from the high resolution area to the rest of the global ocean during a side-by-side integration of the two. This approach

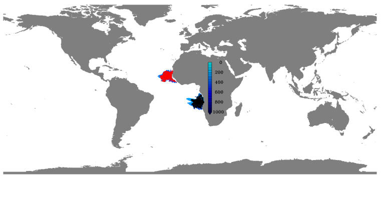

is well established in the field of high resolution ocean modelling and has been used for the investigation of a variety of subjects [e.g. Biastoch et al. (2008); Djath et al. (2014); Fischer et al. (2015)].

The models used within this study are based on the Nucleus for European Modelling of the Ocean (NEMO) code [Madec (2008)]. The configurations are a global configuration at 0.5° horizontal resolution (ORCA05) and two nested configurations with focus on the tropical Atlantic (TRATL01) and the tropical Pacific (TROPAC01) respectively, both at 0.1° horizontal resolution in the nested area, embedded in the global ORCA05 configuration. Hindcast and control experiments in all three configurations are performed, forced by atmospheric conditions for the period from 1948 to 2009 [Griffies et al. (2009)].

To follow waters from the surface into the interior ocean and the OMZs in these models, two different methods are applied. The purely advective ventilation is analyzed based on Lagrangian experiments and two passive tracers exhibit a combination of the advective and diffusive parts of the ventilation. Both of these methods are lacking any biochemical influence and hence provide a purely physical view on the ventilation. In the Lagrangian experiments particles that end up in the northern and southern OMZs in the tropical Atlantic and Pacific Ocean are traced backwards in time towards their source regions over a period of 80 years. The two passive tracers are an ideal age tracer, set to zero at the surface, growing with time elsewhere and a dye, saturated at the surface, spreading into the interior ocean [England (1995)] for a period of 140 years. All these experiments are performed in the global configuration ORCA05 and the nested configurations TRATL01 and TROPAC01 for the respective oceans.

From a process-oriented and methodological point of view, hereafter the following questions arise:

- What is the influence of mesoscale features on the ventilation paths?
- Which methods are suitable to analyze ventilation pathways?
- What can the applied tracers tell about the ventilation and oxygen concentrations?
- What can be gained by the combination of tracers and trajectories?

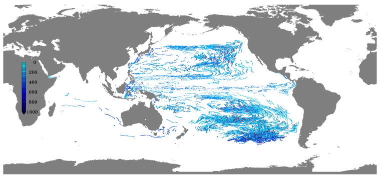

1.3. Structure of the study

The numerical ocean model framework used in this study is introduced in chapter 2. The nesting concept and the high resolution configurations focusing on the tropical Atlantic and Pacific Ocean that have been developed as part of this work are presented; caveats with these models are exhibited. The forcing strategy and the resulting experiments are introduced and the methods used to analyze ventilation processes, namely integrations of passive tracers and Lagrangian particle tracking, based on these experiments are explained.

A model assessment exhibiting the strengths and limitations of the models is given in chapter 3. The models are validated against observations with focus on sea level and the mean circulation and variability in the tropical Atlantic and Pacific Ocean. In the nested model of the tropical Atlantic Ocean a tracer release experiment, that has been done in the real ocean, is reproduced. Furthermore, a comparison between the nested, high resolution models and the global model at intermediate resolution is given to exhibit the gain from the newly developed configurations when simulating the tropical circulation. A digression to the influence of wind stress over the Pacific Ocean on Indian Ocean heat content and sea level variability on multi-decadal time scales is made to elucidate the ability of the models to reveal distinct mechanisms.

Chapter 4 provides insights on the global ventilation with focus on the OMZs in a 140 years time frame based on passive tracer integrations. The mean circulation in ORCA05 spreading these tracers is shown. The evolution of the two passive tracers and their distribution at the end of the integrations is analyzed and compared to those in the nested models. A comparison of the passive tracers to the observed spatial distribution of oxygen that additionally is subject to transformation by biogeochemical processes is made.

In chapters 5 and 6 the advective ventilation of the Atlantic and Pacific OMZs, respectively, is analyzed based on 80 years long Lagrangian backward integrations of particles released in the corresponding northern and southern OMZs. The mean circulation in the nested models is shown. Subduction areas, pathways and timescales on which water enters the OMZs are analyzed. Circulation features affecting the ventilation are identified and the influence of mesoscale features is assessed.

Chapter 7 summarizes the findings of this study and gives conclusions for the ventilation of the OMZs and suggestions for methodological aspects that arose during this study. A synthetic view on the tracer integrations and the Lagrangian experiments is given, identifying definite and potential pathways into the OMZs and source regions of waters entering these zones. A comparison between the ventilation of the Atlantic and Pacific OMZs is given. A brief outlook on methods that ideally would be used to examine the ventilation pathways in future experiments is closing this study.

The appendix A provides enlarged and additional figures, supporting the main part of this study.

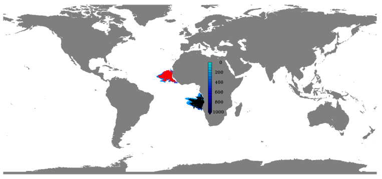

2. Models and methods

This chapter introduces the numerical models, parametrizations and the forcing data used in this study. Furthermore the tools and methods used to analyze the model output are described.

Contents

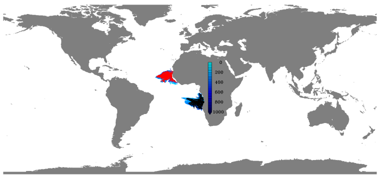

2.1. Model architecture

The model hierarchy developed and used in this study is based on the Nucleus for European Modelling of the Ocean (NEMO, section 2.1.1) version 3.1 code [Madec (2008)] in the Drakkar [Barnier et al. (2007)] configuration using an ORCA grid (section 2.1.2). All models are ocean-only models forced by prescribed atmospheric conditions given by the Co-ordinated Ocean Reference Experiments (CORE) version 2 (section 2.1.3) [Griffies et al. (2009)] and they are coupled to the Louvain-la-Neuve ice model (LIM2) [Fichefet and Maqueda (1997)]. The models mainly differ in horizontal resolutions from 0.5° to 0.1°, where the highest resolution is achieved regionally, using the two-way nesting approach realized by the Adaptive Grid Refinement In Fortran (AGRIF) [Debreu et al. (2008)] (section 2.1.4).

2.1.1. Model framework

The NEMO ocean engine provides a framework for diverse applications in oceanic sciences varying in temporal and spatial scales as well as specializations. The ocean circulation model can be used in global or regional configurations with or without coupling to other components like atmospheric or biogeochemical models. NEMO is a primitive equation ocean model derived from the Navier-Stokes equations, using the following assumptions [Stewart (2008)]:

1. Spherical earth: the planet earth is assumed to be an ideal sphere instead of an ellipsoid, where geopotential surfaces are perpendicular to the earth's radius; gravity is parallel to the radius.
2. Thin-shell: the depth of the ocean is assumed to be negligible small compared to the earth's radius.
3. Incompressibility: a water volume is constant and cannot be compressed; the divergence of the three-dimensional velocity field is zero; sound waves are excluded.
4. Boussinesq approximation: temporal density variations are small compared to mean density.
5. Hydrostatic approximation: horizontal flow dominates vertical acceleration; pressure gradient only depends on buoyancy and gravity.

The resulting equations are characterized by the prognostic variables temperature, salinity, the full three-dimensional velocity field and sea surface height [Madec (2008)] and discretized in finite differences on a staggered Arakawa-C grid (figure 2.1) [Mesinger and Arakawa (1976), Arakawa and Lamb (1977)]. The discretization on a staggered lattice should be preferred to avoid smoothing effects that destroy variability on grid scale. The C-grid seeks to minimize the amount of spatial averaging that is needed to calculate the advection of tracers and the horizontal pressure gradient. The only quantity that includes averaging is the Coriolis term as zonal and meridional velocities are located at different positions within the grid.

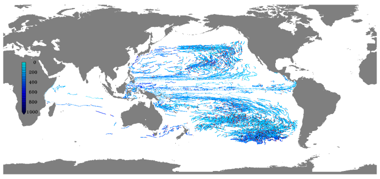

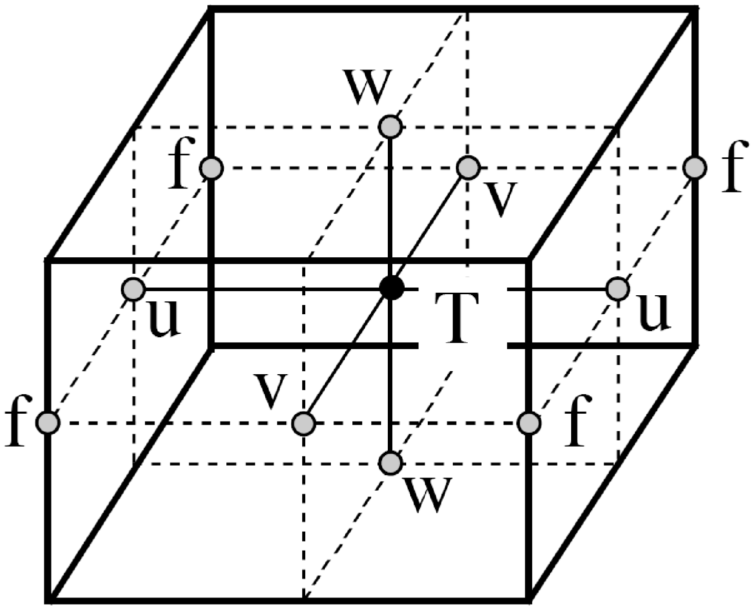

Figure 2.1.: Position of variables in an Arakawa-C grid: T indicates the position, where temperature and salinity (and their derivatives) as well as sea surface height are defined; u,v and w show the location of the three velocity components and f indicates where vorticity is defined. (Figure taken from Madec (2008), figure 3.1)

2.1.2. Global ocean model configuration

The global ORCA configuration developed within the European DRAKKAR collaboration [Barnier et al. (2007)] is the basis for all models used in this work. Its tri-polar, curvilinear horizontal grid allows to simulate the entire ocean without a singularity at the North Pole. This is achieved by replacing the North Pole by two poles, one located in Canada and the other in Russia (figure 2.2 a) while the South Pole does not differ from its geographical position, as it is on land anyway. In the Indian Ocean at 73° E, the first and the last grid points in zonal direction are located and connected using cyclic boundary conditions. In the vertical, the grid consists of 46 z-levels with increasing thickness ranging from 6 m at the surface to 250 m in the deepest layer. The uppermost 500 m of the water column are covered by 20 layers (figure 2.2 b). Partial cells [Pacanowski and Gnanadesikan (1998)] allow for a better representation of the topography: where necessary, the last cell above the bottom is only partially filled (figure 2.2 c). At least a portion of 25 meters of any cell within the water column has to be filled with ocean, therefore some cells do not fully represent the depth given by the model's bathymetry (first and sixth column in figure 2.2 c)

The surface is represented in a free linearized filtered sense following Roullet and Madec (2000). The free surface allows for external gravity waves, that would need a very short time step; with the

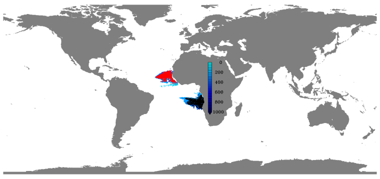

a) Horizontal grid

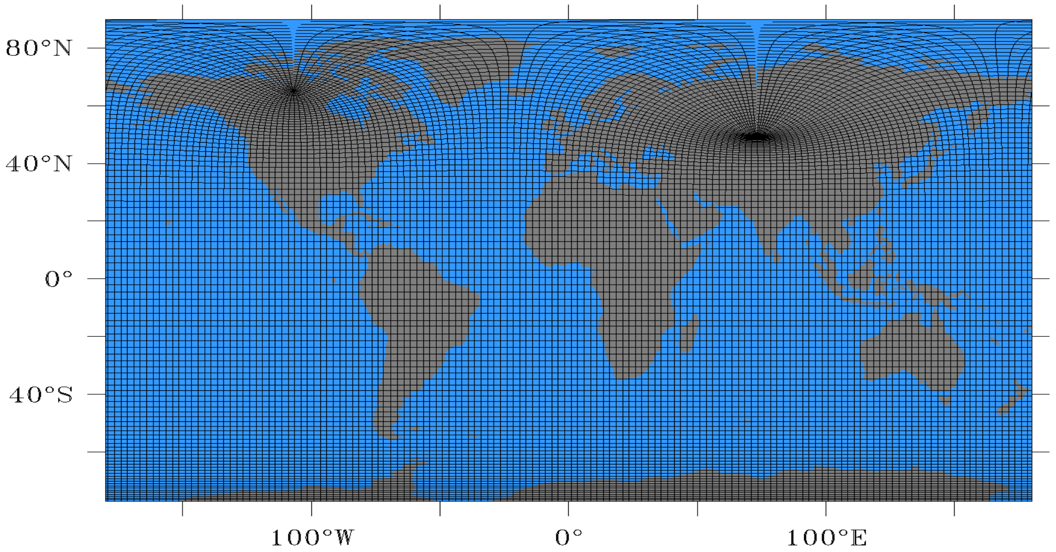

b) Vertical levels

c) Partial cells

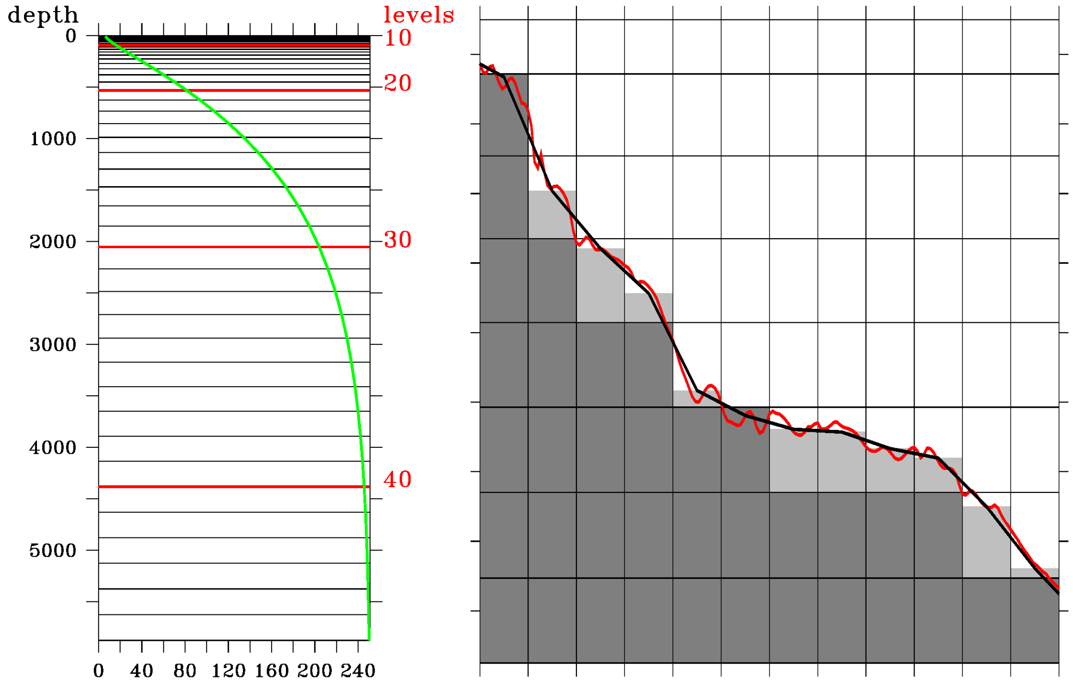

Figure 2.2.: Specifics of the ORCA grid: a) horizontal, tri-polar grid, every fifth grid line of an ORCA05 (0.5°) grid is plotted; b) vertical resolution, indicating the depth of the model layers (black lines) and their thickness (green curve) in meters, the red lines mark every tenth level; c) partial cells along the bottom: the section shows full cells (dark grey) and the partial cells (light grey) according to the model's bathymetry (black curve); the red curve depicts the topography as given by ETOPO2 [U.S. Department of Commerce and Atmospheric Administration (2006)].

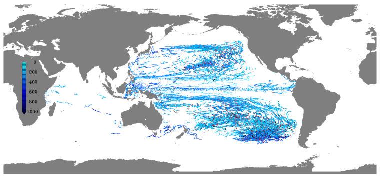

implicit free surface, used here, no explicit time stepping is needed but a solver is applied.

The vertical tracer and momentum diffusion is based on the turbulent kinetic energy (TKE) turbulent closure scheme [built on Bougeault and Lacarrere (1989) with modifications by Madec et al. (1998)]: statically instable density profiles are treated in a way that the terms for vertical eddy viscosity and diffusivity become large and stabilize the stratification [Madec (2008)]. The lateral momentum and tracer diffusion is along isopycnal slopes in longitudinal and latitudinal directions.

2.1.3. Atmospheric forcing

The initial conditions of the ocean models are no motion and climatological temperature and salinity distributions as given by the World Ocean Atlas 1998 climatology with improvements for the Arctic Ocean [Steele et al. (2001), based on Levitus et al. (1998)]. Beginning with this initial state, the models are integrated, forced with atmospheric boundary conditions given by the Co-ordinated Ocean Reference Experiments (CORE) [Griffies et al. (2009)] mainly built on NCEP/NCAR reanalysis products merged with satellite products. Bulk formulae, also provided by CORE, connect the atmospheric conditions with the ocean [Large and Yeager (2009)].

Due to varying coverage by observations, the periods of full interannual variability differ among the variables. Full, 62 year coverage is given for wind, air temperature and humidity, whereas the availability for precipitation and radiation is restricted to the last 31 years and 26 years at the end of the forcing period, respectively (see table 2.1). A mean annual cycle of monthly and daily data, respectively, is prescribed for the variables before the period in which interannual variation starts. The forcing fields are available on a 2° × 2° horizontal Mercator grid. Climatological river runoff is applied, representing the most important rivers, whereas coastal runoff is equally distributed around the continents. The forcing fields are provided at different frequencies, ranging from 6-hourly to monthly. Details on the prescribed fields are given in table 2.1.

Two different forcing strategies are applied, "interannual forcing" (IAF) and "normal year forcing" (NYF). A 62 year long interannually varying data set provides the basis for hindcast experiments, where the ocean's state during the forcing period is computed. Additionally, a climatological version, where a "normal year" is repeatedly applied is used to identify the model intrinsic variability and drift. The CORE normal year is an averaged year from almost the full forcing period (from 1948 to 2007) providing a smooth transition between December and January and keeping synoptic variability of a "moderate" year (1995) [Large and Yeager (2004)].

A conjunction of IA and NY forcing is used in a sensitivity study in the Indo-Pacific region where the impact of local versus remote winds on upper ocean heat content in the tropical Indian Ocean is investigated [Schwarzkopf and Böning (2011)] (see section 3.2).

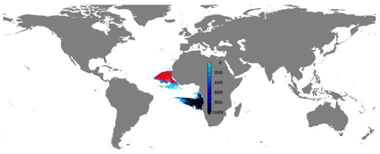

value	resolution	IA availability	interpolation
Zonal wind 10 m above the sea surface	6 hourly	1948 - 2009	bicubic
Meridional wind 10 m above the sea surface	6 hourly	1948 - 2009	bicubic
Air temperature 10 m above the sea surface	6 hourly	1948 - 2009	bicubic
Air specific humidity 10 m above the sea surface	6 hourly	1948 - 2009	bicubic
Downwelling short-wave radiation	daily	1984 - 2009	bilinear
Downwelling long-wave radiation	daily	1984 - 2009	bicubic
Rain	monthly	1979 - 2009	bilinear
Snow	monthly	1979 - 2009	bilinear

Table 2.1.: Forcing fields: the variables and their temporal resolution are given as well as the availability period of interannually varying fields and the applied interpolation method (see section 2.1.3, IOF).

Sea surface salinity restoring is used to partly balance drifts in the oceanic hydrography: the uppermost level (with a thickness of 6.4 m) of the ocean is (very weakly) relaxed towards the sea surface salinity given by the World Ocean Atlas 1998 [Levitus et al. (1998)] on a time scale of 1 year by changing fresh water fluxes accordingly. Details on the effect of different restoring strategies can be found in Behrens et al. (2013).

Interpolation on the fly

The $2^\circ \times 2^\circ$ forcing fields have to be applied to the underlying model grid. This could be done in two ways: interpolating the data “online” while the model is running (“on the fly”) or “offline” before the model starts. Doing the interpolation offline produces an enormous amount of data because every variable has to be interpolated onto every model grid used. More flexible concerning different model grids (see following sections) and with less memory requirements is the interpolation on the fly where only weights are needed to interpolate data from the original grid of the forcing onto the model grid. These weights are computed using the Spherical Coordinate Remapping and Interpolation Package (SCRIP, Jones (1998)): For every single grid cell of the model the weights contain information about the contribution of the adjacent points in the original data. Two methods, bilinear and bicubic interpolation, are implemented and two sets of weights are provided to the model and applied to the original forcing fields while the model is running. Whether bilinear or bicubic interpolation is used for the different forcing fields depends on their sign: bicubic interpolation can produce spurious negative values for quantities which are positive definite as, e.g., precipitation and shortwave radiation (compare to table 2.1).

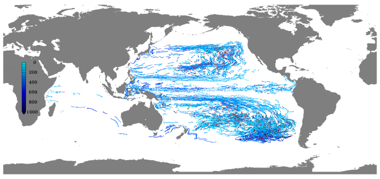

2.1.4. Regional grid refinement by two-way nesting

Given the need to resolve eddies which are responsible for mixing and complex current systems that contribute significantly to advective ventilation processes [e.g. Duteil et al. (2014)], high-resolution models are indispensable here. To achieve high resolution in crucial areas but not lose the global context, a two-way nesting approach provided by AGRIF is chosen, where the regions of high resolution are embedded into a coarser global ocean as rectangular "fixed grids" [Debreu (2006)]. For the experiments here, nests at 0.1° horizontal resolution are embedded into a global configuration with a horizontal resolution of 0.5° (ORCA05). The two components, "base" and "nest", of the model are integrated in parallel interchanging information between the two grids in both directions: the global base model not only provides boundary conditions for the nest but also receives feedback from it.

Figure 2.3 shows a schematic of the nesting process as described by Debreu et al. (2008): First, the base model (B) is integrated one time step with the length rdt ($B^n \rightarrow B^{n+1}$) forward. Based on the two solutions B^n and B^{n+1} the lateral boundary conditions (BC) for the nest (N) are spatially and temporally interpolated (BC^n_{int}). Using these BCs, the nest is integrated forward ρt time steps (length: rdt/ρt). The new conditions along the nest boundary (BC^{n+1}_{up}) is then used to update the base model that is then advanced by the next time step, repeating the described procedure. A frequency (bcl) is defined, at which the nest not only updates the base model along the nest boundary but also at every base model grid point within the nested domain (BC^{n+bcl}_{up}). (A note on the sensitivity of the choice of bcl is given in 2.1.6.)

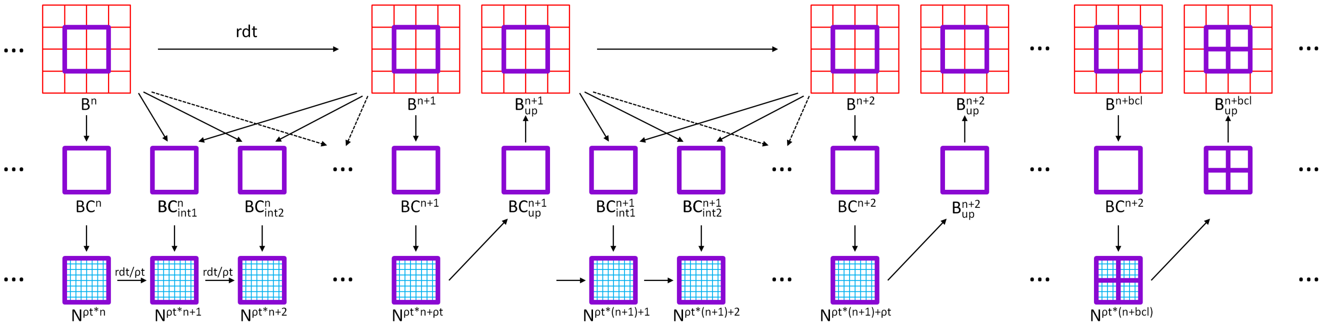

Figure 2.3.: Schematic view of the integration procedure with AGRIF. The red grid stands for the base model (B), the blue grid indicates the nest grid (N) and the purple box shows the boundaries of the nested region and its location in the base model. Along these grid lines, the lateral boundary conditions (BC) for the nest are provided from two consecutive time steps (n and n+1) in the base model by interpolation (tilted arrows; indicated as BC_{int}). The base model time step (rdt) is divided by the temporal refinement factor (ρt) to get the nest time step. At Every ρt nest time step, the base model is updated with the new boundary conditions from the nest ($BC^{\rho t(n+1)}_{up}$) and at every bcl (so called baroclinic update frequency) time step it receives an update along all grid points within the nested region (BC^{n+bcl}_{up}; purple lines).

The spatial refinement, for stability reasons requires a smaller time step. Although the CFL-criterion suggests a temporal refinement factor of five, here, test integrations show, that stability is still given

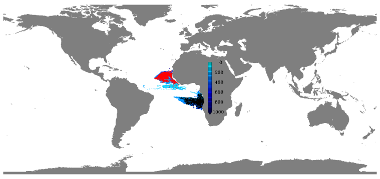

with a factor of four. Additional, horizontal diffusivity (aht0) and viscosity (ahm0) parameters that go into the applied Turbulent Closure Scheme [Madec (2008)] need to be adjusted. The values for the base model are taken from the reference ORCA05 simulations provided by the Drakkar group ($aht0 = 600\, m^2/s$ and $ahm0 = -12 \cdot 10^{11}\, m^4/s$) and for the nested regions they are adopted from Biastoch (2008) ($aht0 = 200\, m^2/s$ and $ahm0 = -2.125 \cdot 10^{10}\, m^4/s$).

To assure a smooth transition of signals from the nest into the base region, a "sponge layer" is applied along the boundaries of the nest. Small scale features moving undamped into the coarse region would cause instabilities or reflections at the boundaries. Therefore an additional viscosity term is applied on tracers and momentum in the first and last grid boxes within the nested domain. The coefficient used here is $2160\, m^2/s$.

Nest preparation

The "nesting tools" are Fortran95 based programs to interpolate between different grids [Lemarié (2006)]. Here, they are used to produce input data defining grids and bathymetry as well as interpolated restart and forcing fields for the nested region of the model.

The input data given to the nesting tools are the coordinates field from the base model including all horizontal grid information, bathymetry files from the base model and ETOPO2 [U.S. Department of Commerce and Atmospheric Administration (2006)] as well as data that need to be available on the nest's grid. Those data together with a namelist, describing the position and refinement factors as well as some characteristics of the nest and base model (e.g. partial cells) are used to create nest specific data to run the model.

In a first step a coordinates file for the nest, depending on it's position within the base model and the refinement factors is built, using fourth order polynomial interpolation. Three grid cells along the boundaries are coarse in the nest and used to connect to the base model. Based on this grid information and a high-resolution topography (ETOPO2, downloaded from http://www.ngdc.noaa.gov/mgg/fliers/06mgg01.html) the bathymetry of the nest is interpolated by median averaging all high-resolution grid points within one grid cell of the nest. The bathymetry is then connected to the one of the base model: using partial cells, it is ensured, whether the three coarse boundary grid cells are at the same level as the coarse bathymetry. Finally the bathymetry is smoothed to avoid too sharp gradients using a hanning filter. For the base model, an updated bathymetry is created to allow for two-way exchange between the grids, turning land points on the base model grid to ocean points if they include ocean in the nest bathymetry.

Initial conditions (temperature and salinity) as well as the runoff and sea surface salinity (used for restoring) fields are then interpolated from the coarse grid onto the nest via bicubic interpolation. (The nesting tools also provide the possibility to interpolate all the other forcing fields onto the nest

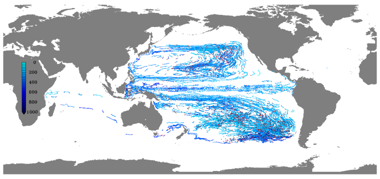

grid. This is not done in this study but “interpolation on the fly” (IOF, 2.1.3) is used.) Usually a nested run is started from a coarse model spin up (to save computation time), therefore also a corresponding restart needs to be interpolated bilinearly.

2.1.5. Model configurations and experiments

A series of high resolution nested models has been developed and is used in combination with a global model at intermediate resolution for different purposes throughout this study. All of the nested models have a horizontal resolution of 0.1° and are embedded in an ORCA05 configuration. All configurations are based on the ORCA grid as described in section 2.1.2. The specifics of the distinct configurations will be introduced in the following.

Configurations

The standard configuration here is an ORCA05 setup with 0.5° nominal horizontal resolution leading to a grid size of 55 km at the equator gradually decreasing to 20 km near the poles. This intermediate resolution model does not explicitly resolve eddies [Houry et al. (1987)], but their effective flattening of isopycnal surfaces is accounted for by a lateral eddy induced velocity parameterization (GM) [Gent and McWilliams (1990)].

Nested AGRIF configurations for the Tropical Atlantic (TRATL01) and Pacific (TROPAC01) at 0.1° resolution are developed and used in this study to investigate ventilation processes, affecting the oxygen minimum zones in the eastern parts of these ocean basins. In the Atlantic Ocean, the nest extends from 30° S to 30° N, spanning the basin from 70° W to the African continent at 18° E (figure 2.4 a). The nest in the Pacific Ocean spans the entire basin, between 49° S and 31° N including Australia and New Zealand, and reaches from the coast of South America (60° W) into the Indian Ocean up to 73° E (figure 2.4 b), where the cyclic folding line of the ORCA05 grid is located (crossing that line with a nest is technically not possible yet).

Additional configuration:

The Fukushima Daiichi nuclear power plants were destroyed by the magnitude 9.0 Tōhoku earthquake and subsequent Tsunami hitting the reactors in March 2011. In consequence, radioactive material was released into the environment. A large amount also entered the Ocean through rainfall and direct release of contaminated waters from the power plants into the Pacific Ocean off Fukushima. The spread of long living isotopes such as ^{137}Cesium over a decade has been addressed by model experiments using different horizontal resolutions, including a dedicated AGRIF configuration of the Northern Pacific Ocean, NPAC01. The results have been published in the open access journal “Environmental Research letters”, July 2012: Behrens et al. (2012).

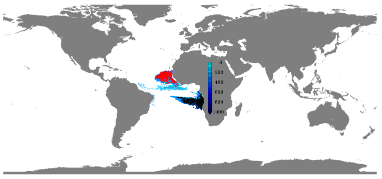

a) TRATL01

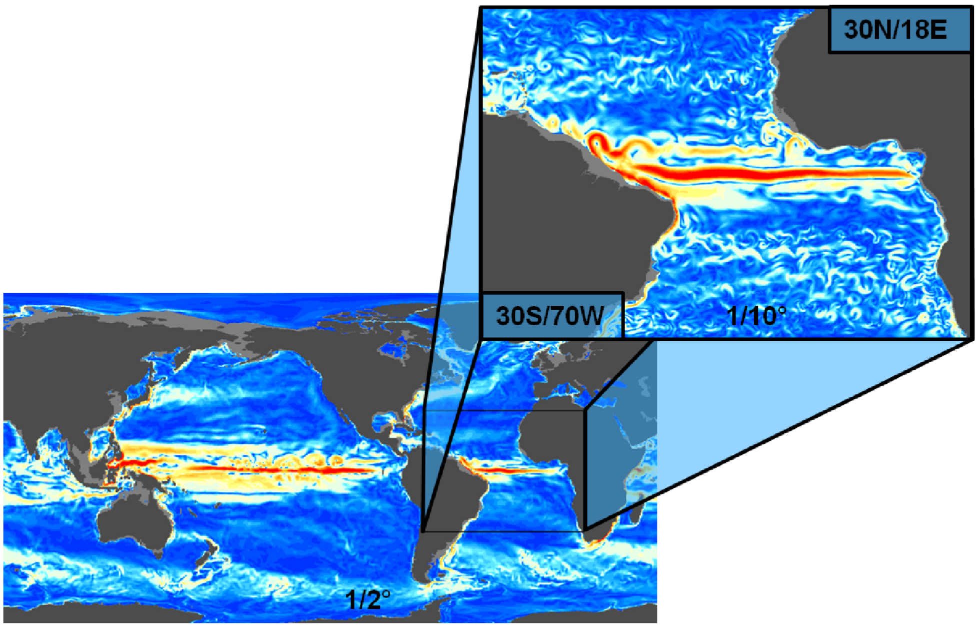

b) TROPAC01

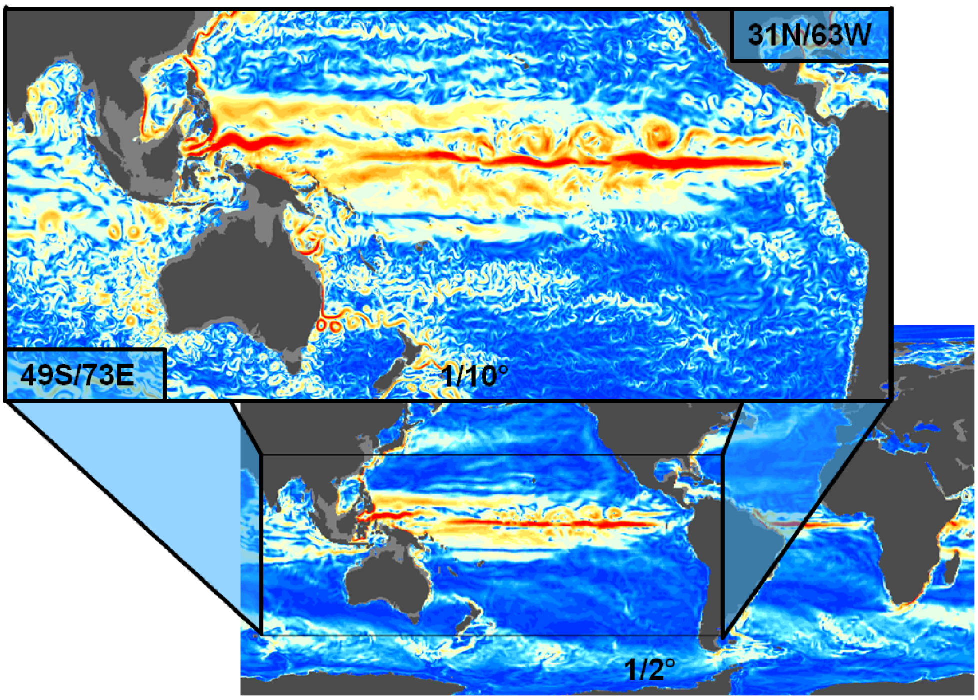

Figure 2.4.: Regional setup of TRATL01 and TROPAC01: Snapshot of speed at 100 m depth in the ORCA05 at 0.5° horizontal resolution (global fields) with embedded nests at 0.1° resolution in the tropical Atlantic from 70° W to 18° E and 30° S to 30° N (TRATL01, a) and in the tropical Pacific from from 73° E to 63° W and 49° S to 31° N (TROPAC01, b).

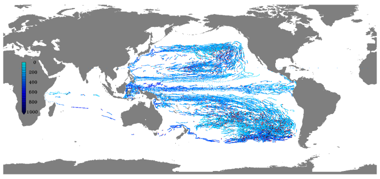

Behrens, E., F. U. Schwarzkopf, J. F. Lübbecke, and C. W. Böning (2012), Model simulations on the long-term dispersal of ^{137}*Cs released into the Pacific Ocean off Fukushima, Environ. Res. Lett. 7, 034004, doi:10.1088/1748-9326/7/3/034004.*

NPAC01 has a zonal extent from 100° E to 100° W and spans the North Pacific from 17° N to ~60° N (54° N to 66° N, depending on the longitudinal location due to the rectangular definition of the nested region on the curvilinear ORCA grid).

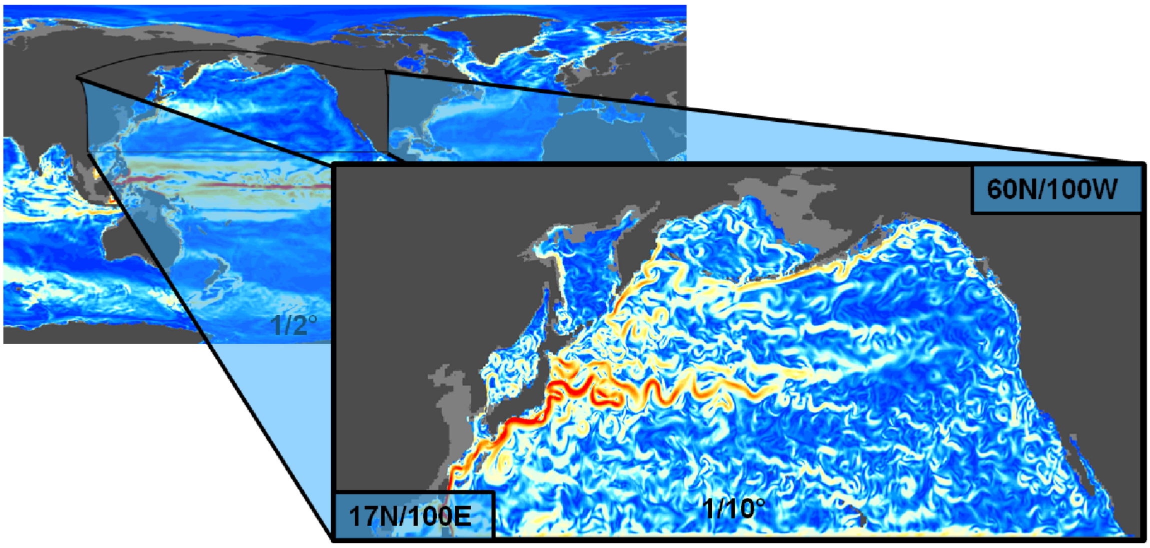

Figure 2.5.: Regional setup of NPAC01: Snapshot of speed at 100 m depth in the ORCA05 at 0.5° horizontal resolution (global fields) with an embedded nest at 0.1° resolution in the norther Pacific from 100° E to 100° W and from 17° N to ~60° N.

Experimental strategy

For each of the three configurations ORCA05, TRATL01 and TROPAC01, two main experiments were performed: an interannually forced hindcast experiment from 1948 to 2009 and a climatologically forced run, parallel to each of the hindcasts. The latter ones are used to identify model intrinsic variability and trends not caused by the forcing itself. Each of these experiments is preceded by the same 80 years long spin-up experiment in ORCA05 forced with the normal year forcing as provided by CORE-II (see section 2.1.3). The spin-up is used to overcome initial shocks and subsequent adjustment processes due to the initialization with an ocean at rest and climatological hydrography [Kantha and Clayson (2000)]. In the actual analyses of the nested configurations, the first O(10) years are neglected as well, taking into account additional adjustments, when switching to the higher resolution. This time appears to be appropriate in the tropical oceans, based on

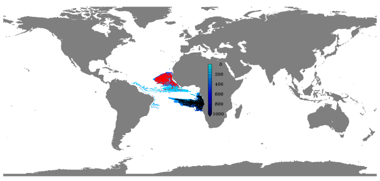

wave dynamics and from time series analyses, not shown here, that exhibit initial trends to vanish after the first ten years. The period of the climatologically forced run in ORCA05 is extended to 200 years. The integration strategy for the experiments used throughout this study is visualized in figure 2.6 and their names are given in table 2.2.

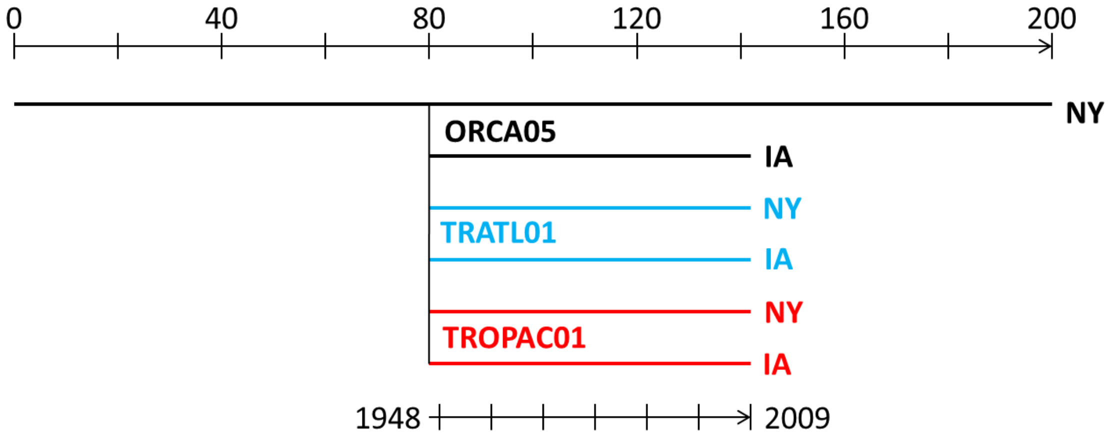

Figure 2.6.: Experimental integration strategy: the ocean state after 80 years of the 200 years long normal-year (NY) forced experiment in ORCA05 (ORCA05-NY) provides the initial conditions for NY experiments in TRATL01 (TRATL01-NY) and TROPAC01 (TROPAC01-NY) as well as interannually (IA) forced hindcast experiments from 1948 to 2009 in ORCA05 (ORCA05-IA), TRATL01 (TRATL01-IA) and TROPAC01 (TROPAC01-IA).

Configuration	Internal Name	Acronym	Initial conditions	Forcing
ORCA05	TRC001	ORCA05-NY	Levitus	NYF 200 yrs
ORCA05	TRC006	ORCA05-IA	ORCA05-NY year 80	IAF
TRATL01	TRC001	TRATL01-IA	ORCA05-NY year 80	IAF
TRATL01	TRC002	TRATL01-NY	ORCA05-NY year 80	NYF 62 yrs
TROPAC01	TRC001	TROPAC01-IA	ORCA05-NY year 80	IAF
TROPAC01	TRC002	TROPAC01-NY	ORCA05-NY year 80	NYF 62 yrs

Table 2.2.: Model Experiments in ORCA05, TRATL01 and TROPAC01: interannual forcing (IAF) covers the period 1948 to 2009 where the normal year forcing (NYF) can be applied for an arbitrary number of years, indicated in the forcing column.

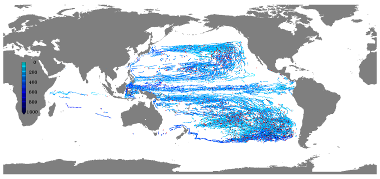

2.1.6. Caveats of the nested configurations

Output on base model grid

For the nested models, output is provided on both, the nest and the entire global base model grid. For the latter, the interpolation process of data from the nest to the base model grid during the model integration in conjunction with the time averaging during the output production can cause some subtle inconsistencies leading to unrealistically noisy structures. The problems are restricted to the model output (not affecting the integration process) and occur in different ways; two of them are described here exemplarily for the nested configuration in the Tropical Atlantic TRATL01:

1. Vertical velocities: to avoid discontinuities in the global model, horizontal velocities are interpolated from the nest grid onto the base model grid, and only afterwards, vertical velocities are computed, using the continuity equation. Very noisy, unrealistic fields of vertical velocities occur on the base model grid within the nested region (figure 2.7). A series of experiments differing in the frequency (bcl, see section 2.1.4) at which the base model is updated with the information from the nest, shows a reduction of the noise amplitudes when updating the base model more often and an increase when reducing the update frequency. This behaviour, however, only holds for regions with highest variability on grid scale.

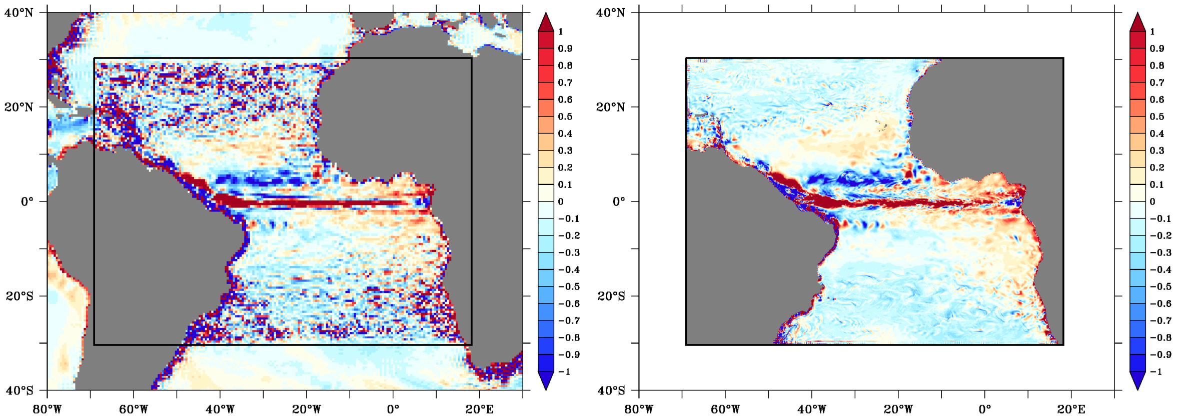
a) Base model grid

b) Nest grid

Figure 2.7.: Vertical velocity at 100 m depth [10^{-5} m/s] averaged from May to August in an arbitrarily chosen model year, here 2000, from a) the base model and b) the output on the nest grid.

2. Horizontal velocities and MOC: when computing the MOC by integrating meridional velocities, another noisy structure occurs in the base model within the nested region. The meridional velocity itself does not show this noise, but already shows strong alternating structures on grid scale. These are represented by smooth transitions from e.g. positive to negative values in the nest, where in the base model strong negative values are directly neighbouring strong positive values (figure 2.8). Only the integration of these structures leads to unacceptable noise in the MOC on the base model grid.

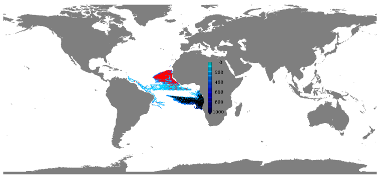

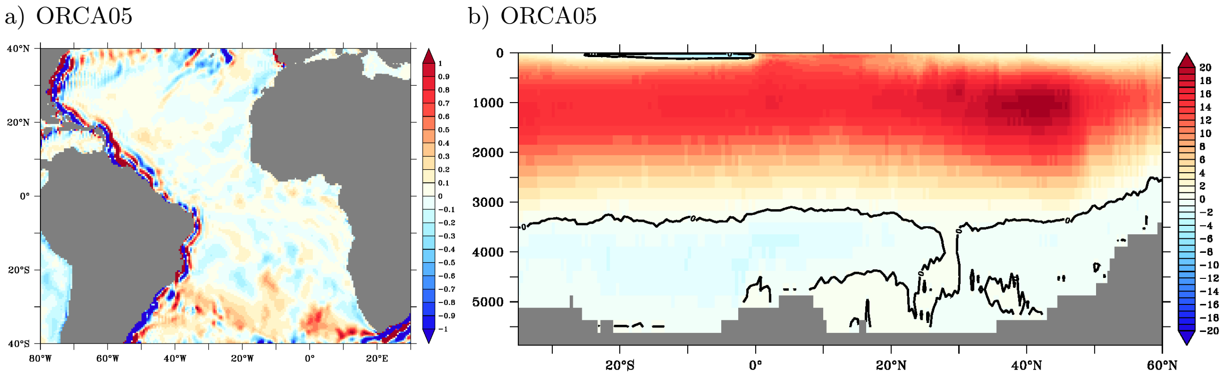
a) ORCA05

b) ORCA05

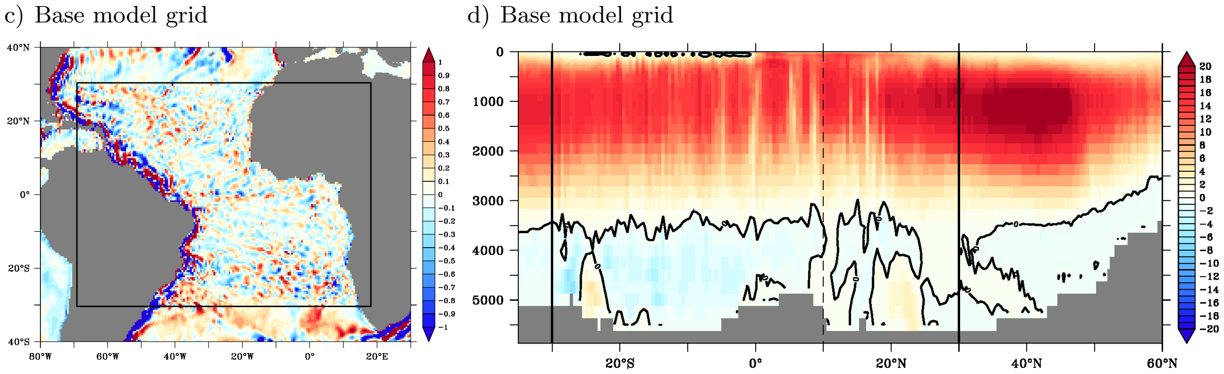
c) Base model grid

d) Base model grid

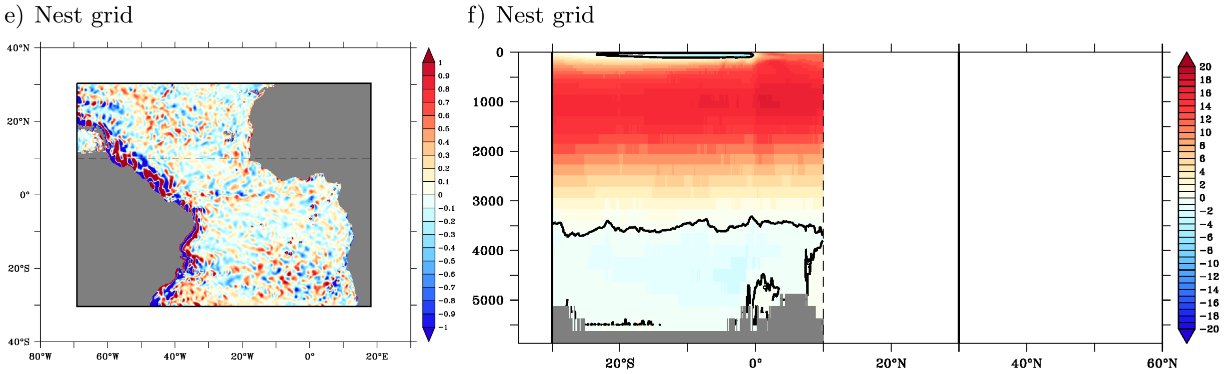
e) Nest grid

f) Nest grid

Figure 2.8.: Annual mean (year 2000) meridional velocity [cm/s] at 1000 m depth and MOC [Sv] from an un-nested global ORCA05 simulation a) and b)), the base model of TRATL01 c) and d)) and the nest of that model e) and f)) restricted to the region where the western and eastern boundaries in the nest are on land (between the southern boundary at 30° S and 10° N) and therefore allow for MOC computation. Bold lines in c) to f) mark the limits of the nested region and dashed lines mark the northern limit for MOC calculations in the nest.

To avoid physically unrealistic results due to these inconsistencies in the output fields, the analyses within nested regions will be restricted to the high resolution output of the nests throughout this study. Again, the described behaviour only occurs in the output fields and not during model integration.

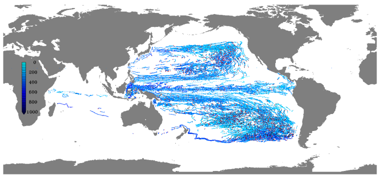

Instabilities in TROPAC01

In the interannually forced experiments in TROPAC01 (TROPAC01-IA), localized spots with unrealistically overshooting hydrographic values appear within the Philippine archipelago and at the north-east corner of Malaysia, most pronounced in the Maqueda Bay (Samar Island) and in the Sulu sea off coast of Sandakan (Malaysia) (figure 2.9 b shows the locations of most pronounced deviations). These unrealistic values of T and S are restricted to the surface in very confined regions and do not impact the velocity fields. Causes for this behaviour can be found in bathymetric inconsistencies between the base model and the nest, possibly in conjunction with lateral boundary conditions (see figure 2.9 a for details) and probably strong events in the forcing, as this only occurs in the interannually forced experiment and not in the climatological run. The coarseness of the base model does not allow to represent the coastlines as good as in the nest (figure 2.9 c). Additionally, some narrow bays (e.g. red boxes in figure 2.9 c; locations of overshoots) are represented by only one grid box, leading to problems with the lateral no-slip boundary condition. Whether the implementation of the GM parameterization in the base model that is not necessary in the nest plays a role here, is not further investigated.

The integration time step is chosen relatively long, partly based on considerations concerning the computational costs and might contribute to the issue described here. A reduction of the time step leads to a reduction of the occurrence of the overshoots but does not eliminate them completely. To keep an admittedly dissatisfying balance between the computational costs and the inconsistencies found in TROPAC01-IA the time step for this experiment is divided by a factor of two compared to all the other experiments used throughout this study.

Further investigation after the completion of the experiments in TROPAC01 exhibited a defect in the runoff field used for the nest integration: the applied interpolation method lead to negative values at some narrow bights, that, in later experiments were identified as major contributor causing the overshoots.

As the main focus that TROPAC01 is used for in this study concentrates on the eastern part of the nest and the signal described above does not propagate away from the Philippines, the results are not affected by these inconsistencies but their presence should be kept in mind.

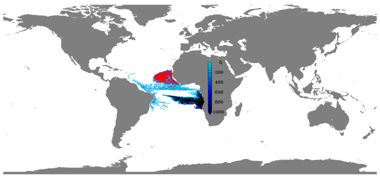

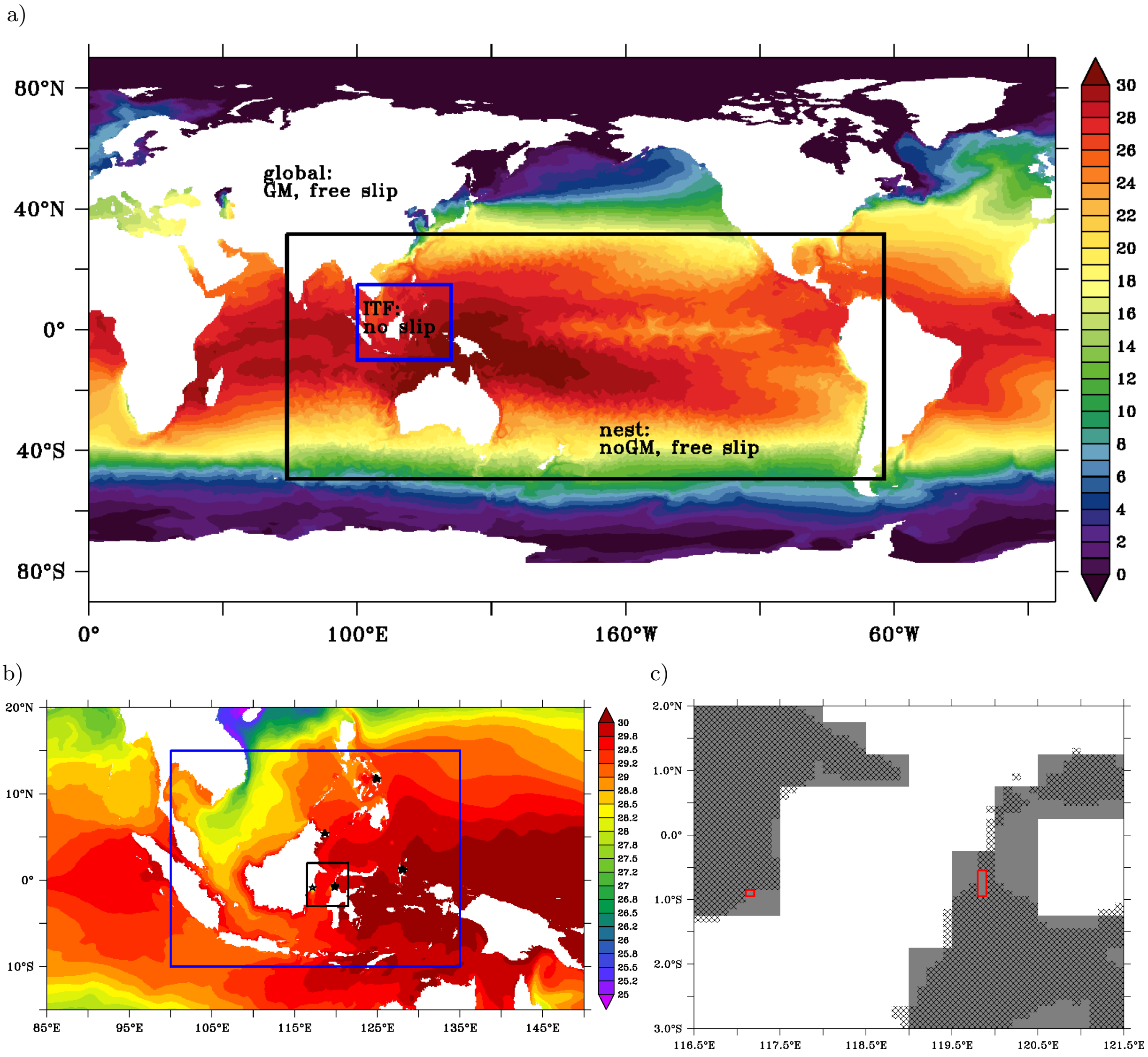

Figure 2.9.: Arbitrarily chosen SST snapshot in TROPAC01: shown in a) is the base model SST with the nest SST overlaid (black box) In the base model the GM parameterization is active to simulate the effect of non-resolved eddies acting to flatten isopycnal surfaces. Due to the higher resolution, this effect is explicitly resolved in the nest, where GM is deactivated. To improve the circulation through the maritime continent, the lateral boundary condition in this area is switched from "free slip", which is used everywhere else, to "no slip" (blue box). Within this region, in some bays, bathymetric inconsistencies appear, causing unrealistically high/low values of T and S (stars in b)). At these locations (black box in b); area shown in c)) inconsistencies between the nest and the base model bathymetry occur. c) shows the land mask of the base model (grey shading) and the nest (hatched area), indicating problematic bays by the red boxes.

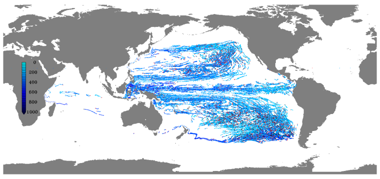

2.1.7. Passive tracers

The Tracer in the Ocean Paradigm (TOP) component in NEMO allows to introduce tracers following presrcibable behaviours. Customized sources minus sinks models are used here. Different passive tracers were introduced: first, an age tracer, that gives the time since the last surface contact and second, a surface concentration dye, both underlying solely advection and diffusion (see England (1995) for a detailed description of these two tracers). In addition, dedicated tracer release experiments were performed.

Age tracer

The tracer “AGE” is initialized with 0 everywhere and grows with time except for the surface, where it is held at 0. This formulation defines the time since a water parcel had the last surface contact as its “age”. In general, AGE is only meaningful in equilibrium, when the entire ocean is mixed and AGE does not change anymore. During transition from initialization to equilibrium, AGE changes (even in better ventilated regions) due to mixing processes with other e.g. deeper lying, less ventilated zones [England (1995)]. Although it needs several thousand years to reach such an equilibrium, the tracer AGE is only integrated for 142 years (80 years spin-up plus 62 years hindcast) here, owing to the amount of expensive computing time needed for the integration of such high-resolution models as TRATL01 and TROPAC01 (see section 2.2). The change of AGE over time within the regions of interest for the present study slows down significantly towards the end of these 142 years (figure 2.10 a), however it has to be kept in mind, that the presented AGE values, especially in the poorly ventilated regions, are too low compared to their real age.

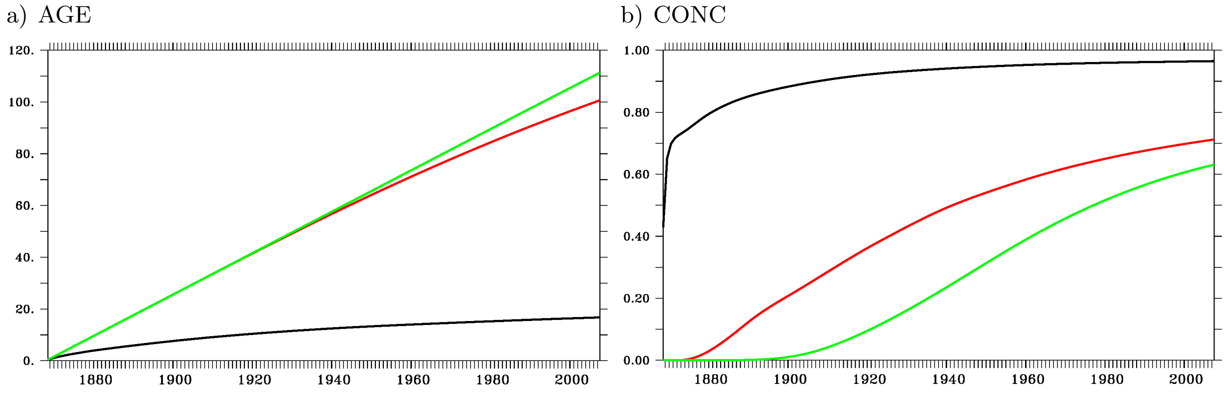
a) AGE

b) CONC

Figure 2.10.: Schematic evolution of AGE (a)) and CONC (b)) over 140 years of integration from zero-initialization at 100 m (black), 500 m (red) and 2000 m (green) depth. With increasing depth, AGE needs longer to slow down its growth and CONC needs longer to reach a saturated state

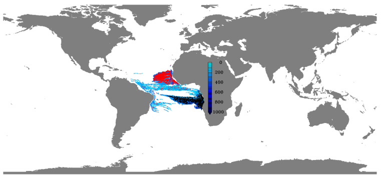

Surface concentration

The tracer "CONC" is initialized with 0 everywhere except for the surface, where it is set to and held at 1. This tracer depicts the concentration of a dye that is saturated at the surface and shows its pathways towards the interior ocean. In well ventilated regions, CONC increases rapidly to saturation. In regions where the ventilation is low, CONC increases slowly and only reaches saturation after a few thousand years, when the full ocean is ventilated (figure 2.10 b). CONC is a meaningful quantity already during its evolution and should tend to one in an equilibrated state.

Tracer release experiments

The third sort of tracer used in this study is a dye that can be applied in various ways to track the spreading of a substance injected into the ocean. The tracer is set to one (released) in a certain area for a limited time. Here, this is done to simulate the GUTRE experiment [Banyte et al. (2012)] (section 3.4) and to simulate the possible spread of radioactive contaminated waters released into the Pacific Ocean after the disaster in Fukushima in March 2011 [Behrens et al. (2012)].

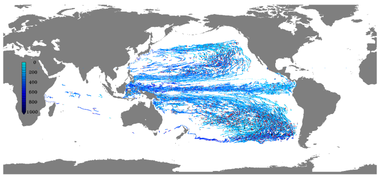

2.2. Note on computational requirements

The integration of models like the global high-resolution models developed and used within this study requires a large, high performance computer infrastructure. The models are integrated on two different types of computer architectures, scalar and vector machines. The scalar machines are used for massive parallel processing, where many central processing units (CPUs) are operating on a single operand each, whereas vector machines do the operation on a whole vector of operands at the same time with only a few CPUs.

The global ORCA05 simulations are partly performed at the computing centre at Kiel University on a NEC-SX8 and SX9 vector machine. Here, 4 CPUs are used to integrate an entire model year within approximately 5.5 hours on the SX8 and 3.5 hours on the SX9 respectively.

The nested experiments and the tracer experiments in ORCA05 are integrated at the North-German Supercomputing Alliance (HLRN) on a SGI Altix ICE with a scalar architecture. The parallelization in NEMO is done by area decomposition, i.e. the entire model domain is divided into rectangles of several degrees in latitude and longitude where each of them is integrated on one processor communicating with neighbouring regions via Message Passing Interface (MPI). The MPI processes are the bottle neck in scalability: at some point, the communication between the CPUs takes more time than the integration itself and an increase in the number of CPUs used for the integrations does not lead to a decrease in computing time anymore. This has been tested exemplary with TROPAC01 (figure 2.11). 512 CPUs turned out to provide the best balance between required computing resources (given in NPLs (“Norddeutsche Parallelrechner-Leistungseinheit”); proportional to the product of computing time and number of CPUs) and the real time needed to integrate a model year (blue stars).

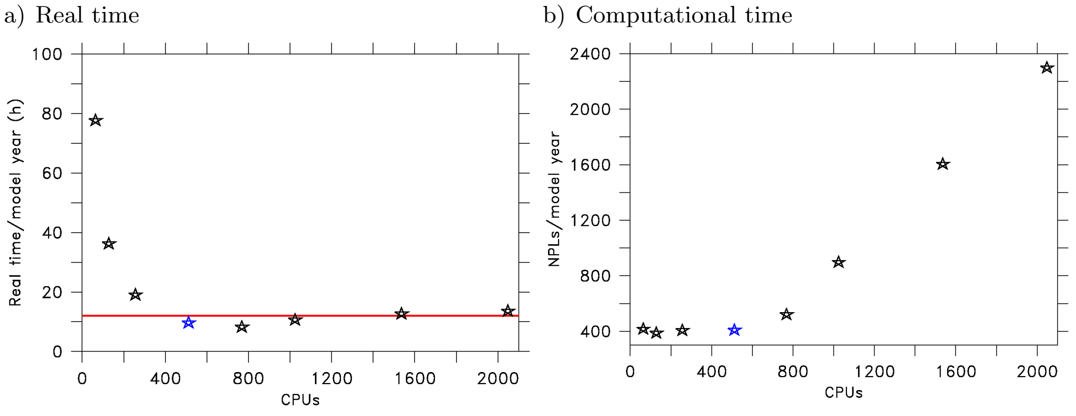
a) Real time

b) Computational time

Figure 2.11.: Scalability of TROPAC01: the real time needed to integrate one model year depending on the number of CPUs is given in a). The red line marks some kind of threshold for the shortest time reachable. b) shows the costs [NPLs/model year], clearly increasing with the number of CPUs. The blue stars mark the chosen 512 CPUs.

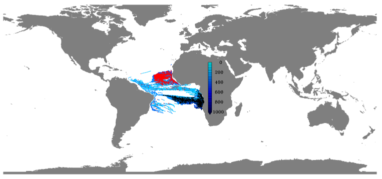

With the infrastructure described above, the time needed to integrate a model year in ORCA05 is about one hour. For the nests the time rapidly increases to about four hours for one model year of TRATL01 and almost twelve hours for a model year in TROPAC01. For the interannually forced TROPAC01-IA experiment, the time step had to be reduced due to instabilities (see section 2.1.6), leading to a doubling of integration time. The models are integrated year-wise, meaning the model needs to be restarted for every year, leading to waiting time between the integrations of two subsequent model years. All in all, a 62 years long hindcast in TRATL01 needs about a month, whereas for TROPAC01 this can take more than three months, depending on the availability of the computers.

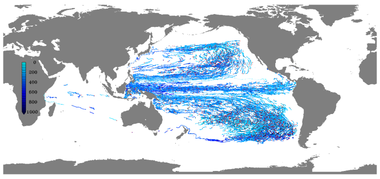

2.3. Analysis of Lagrangian particle spreading

ARIANE is an offline trajectory tool, used to do Lagrangian analyses based on velocity fields given as output from the models. Particles can either be seeded at distinct individually chosen locations or along sections corresponding to the velocities into a certain direction or at certain hydrographic conditions. The paths of the particles can then be integrated forward and backward to investigate their fate and origin, respectively. ARIANE also allows for the differentiation between the qualitative paths followed by the particles, and a quantitative measure of transports from one section to another. Some features of ARIANE are given here. A more complete description is provided as a tutorial by Blanke and Grima (2008).

2.3.1. Particle release

Particles (or water parcels) can be seeded in basically two different ways:

1. Seeding at exact locations and time: the locations of seeded particles (longitude, latitude, depth) and the point in time, when it is released can be determined directly.
2. Seeding along a section: a closed section (either by land or other sections) is defined along which particles are seeded according to the velocity field into a pre-defined direction. In this way, more particles are going along with stronger currents. Additionally, using this method, hydrographic conditions can be prescribed, that have to be fulfilled for the particle release, e.g. only water within a certain temperature range is tracked.

In this study the first strategy is used to seed particles within a box, independent from the current structure, as the velocity fields in the release areas are rather sluggish and circulation within the release area would not be taken into account by just releasing the particles along the boundaries of a box, as method two would do.

2.3.2. Qualitative and quantitative experiments

Two types of experiments can be performed using ARIANE:

1. Qualitative: a qualitative ARIANE experiment shows the way of particles, seeded at certain locations over the full period of integration. At every time step, the position of each particle is stored. Additionally, hydrographic properties along the particle tracks can be stored.
2. Quantitative: in a quantitative run, particles are seeded along a certain section (see section 2.3.1) and several other sections can be defined along which particles are collected. The way,

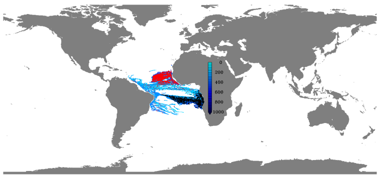

particles take from one to another section is not stored, but the number of particles, crossing each section as well as the time needed to get from the release position to the end section is stored. Additionally, each particle represents a transport value derived from the velocity field at its release location, so that in the end, transports between two sections can be determined.

Here, only qualitative experiments are used, as most of the measures provided by the quantitative method can be derived within the post-processing, except for the transport that is assigned to each water parcel.

2.3.3. Forward and backward integrations

The motion of the particles is integrated by deriving local streamlines for each time step, provided by the underlying velocity fields, and by moving the particles from their current position along those streamlines to their new location, one time step later. The integration then can be done in two ways:

1. Forward: forward integration shows the fate of particles by integrating them forward in time directly using the velocity output from the models. This is mainly used to examine, where waters (or particles in the water) released at a certain location end up under distinct conditions.

2. Backward: with the backward integration, the origin of particles found at a given location or within certain areas can be found by going backward in time. Technically, this is done by changing the sign of all velocities.

This study mainly uses backward integrations, to find the origin and pathways of water parcels that end up in certain areas.

2.3.4. Particle populations

Following a method developed and published by Gary et al. (2011) to qualitatively analyze the resulting trajectories, particle populations are derived. Therefore, a regular, three dimensional grid is defined and the particle occurrences within the individual boxes during the integration time are counted. The resulting populations provide an integrated measure for pathways and residence times of the traced particles.

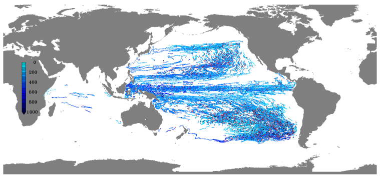

3. Assessment of spatio-temporal variability

To validate the models used in this study and to show their limitations, some data-model intercomparison is provided in this chapter. The global scale behaviour of the models will be assessed by analyzing sea surface height variability (section 3.1). By evaluating the Pacific influence on tropical Indian Ocean variability the possible benefits of numerical models in analyzing distinct mechanisms is shown (section 3.2). The main focus of the validation will be on the regions of major interest to this study loacted in the eastern tropical Atlantic (section 3.3) and Pacific (section 3.5) Oceans. A case-study on tracer spreading is presented to show the model behaviour compared to an in-situ experiment (section 3.4) and finally the effect of an incerased horizontal model resolutions will be considered (section 3.6).

Contents

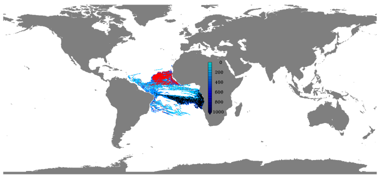

3.1. Sea surface height variability in the tropical oceans

Sea surface height (SSH) in the global ocean is determined by several hydrographic factors like density and heat content as well as the ocean dynamics as consequence of wind induced circulation [Gill and Niiler (1973)]. It therefore offers an integrative measure of the state of the ocean. Globally distributed, partially very long term record, tide gauge stations and satellite altimetry data (AVISO) since the early 1990s provide a large data base for validating the model's capability of simulating SSH variability and trends. Here, regional SSH anomalies representing the influence of ocean dynamics [Wunsch et al. (2007)] on the sea level are investigated comparing the detrended modelled SSH with both, satellite altimetry and tide gauge data.

3.1.1. Observational data sets

Tide gauges

Tide gauges are land based devices, continuously measuring the sea level at a fixed location. The measured sea levels are given relative to a mean state, therefore only sea level anomalies are analyzed. Stations around the world (figure 3.1) provide a large database of long term sea level records. The Permanent Service for Mean Sea Level (PSMSL) provides a collection of tide gauge data that are used here to compare modelled and measured sea level variability. This is achieved on a point-wise basis but over a long time, complementing and facilitating the global comparison with short-term satellite measurements (subsection 3.1.1, below). Only quality controlled data are used here [Holgate et al. (2013)].

Satellite altimetry data

Since 1993 several satellite missions measure sea level along their ground tracks using altimetry. The entire earth (except for the polar regions) is covered by individual tracks roughly every 9 days which are merged to 7-daily fields of sea surface height anomalies. The along track data are mapped onto a grid with 1/3° by 1/3° resolution. Sea level anomalies are computed using a time averaged reference sea level and are provided by Ssalto/Duacs and distributed by Aviso, with support from Cnes (http://www.aviso.altimetry.fr/ducas).

3.1.2. Sea surface height variability: model vs. observations

A comparison between tide gauge measurements, satellite altimetry and modelled SSH from an ORCA05 experiment is presented here, for the tropical Atlantic Ocean (figure 3.2), the tropical Pacific Ocean (figure 3.3) and the tropical Indian Ocean (figure 3.4).

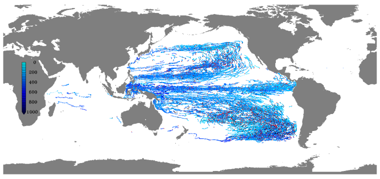

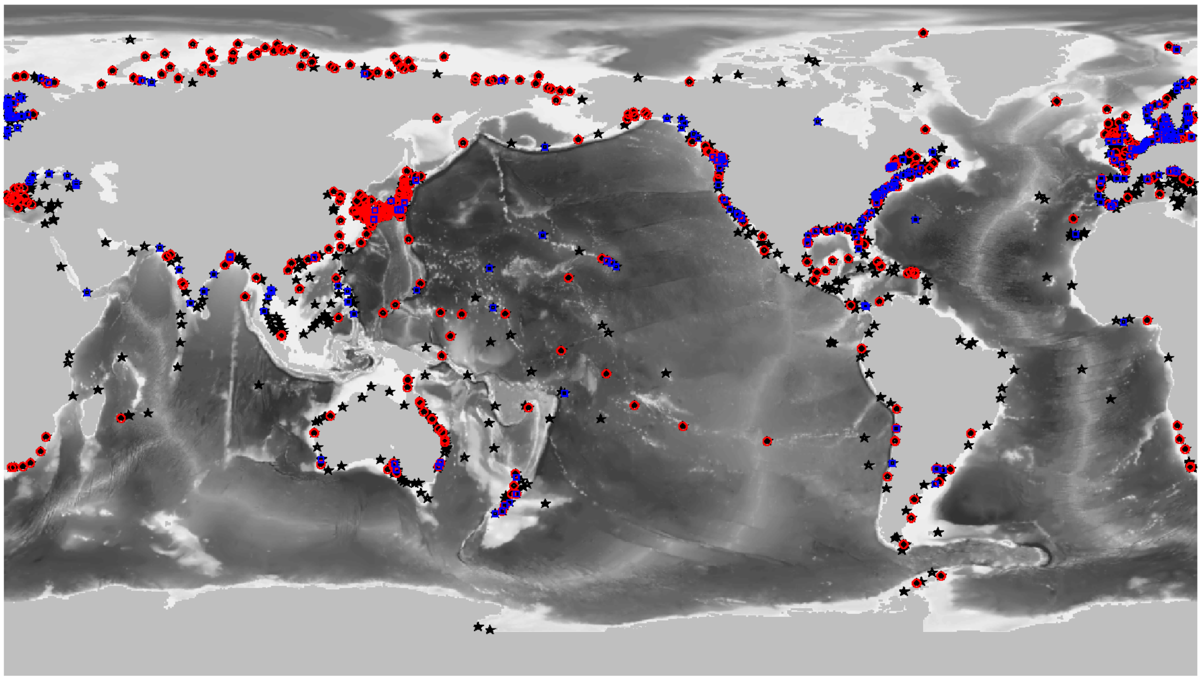

Figure 3.1.: The locations of the tide gauge stations are given by the black stars. Red circles mark the stations, with records longer than 30 years; blue squares stand for stations with records longer than 60 years.

Areas within the tropical oceans are selected based on the availability of tide gauge measurements, which unfortunately are rare in the regions of interest. Nevertheless, they will be used to investigate the model skill to reproduce local SSH variability. Especially in the tropical Atlantic Ocean (figure 3.2) tide gauge measurements are scarce in space and time. Although the boxes are chosen small (figure 3.2 upper panels), comparing tide gauge and modelled SSH variability within the selected boxes reveals a large discrepancy. The modelled SSH variability (blue curve), except for a minimum in the early 1960s, substantially differs from the SSH variability measured by the tide gauges (red curves). However, comparing the modelled SSH variability within the chosen boxes with AVISO data (green), shows an agreement on interannual time scales. This implies, that the available tide gauge measurements from this region only give insights for the locations of the gauges and are not representative for the surrounding area.

In the tropical Pacific Ocean, the availability of data is much better, mainly due to the presence of several tropical islands, which allow to investigate SSH anomalies not only along the continental coasts but also within the open ocean. Especially in the western part of the tropical Pacific Ocean, within the warm pool region, open ocean tide gauge stations are available. The spread of individual stations is given by the black curves in figure 3.3 a, which show at least one strongly deviating station. Modelled SSH anomaly within this box goes along very well with the averaged tide gauge time series (red curve) on interannual time scales. A negative linear trend in the modelled SSH causes some tilt of the curves against each other. The agreement between tide gauge (red) and satellite

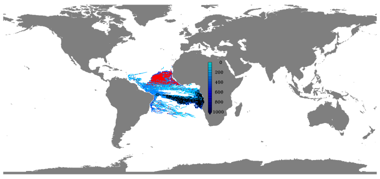

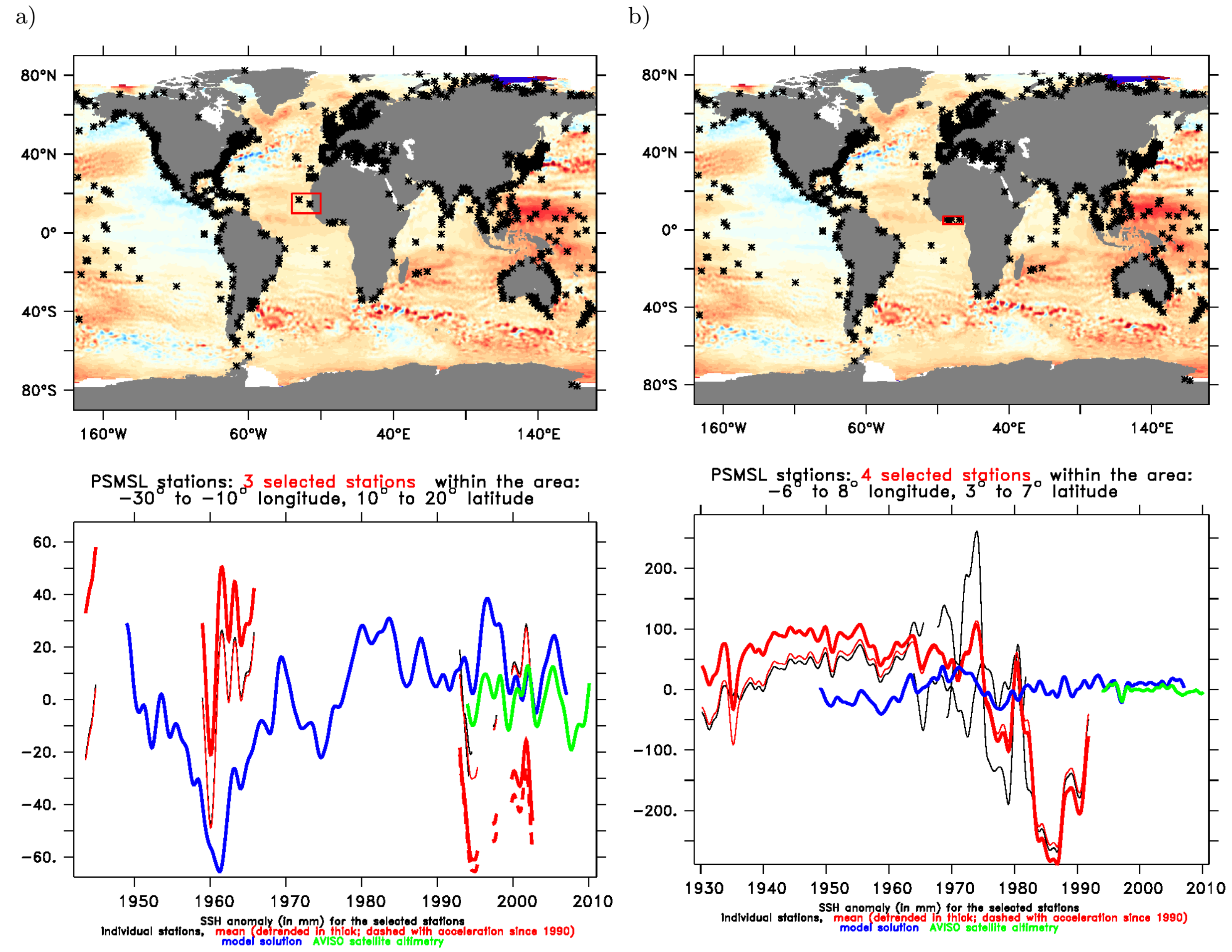

Figure 3.2.: Upper panel: linear trend pattern of SSH over the satellite period from 1993 to 2008 (shading; blueish areas indicate sea level fall, red regions correspond to sea level rise); the locations of all tide gauge stations are indicated by the black stars, the red box indicates the area for which SSH anomaly time series are given below. Lower panel: SSH anomaly time series [mm] from individual tide gauge stations (black curves) and an average of those stations (red thin) as well as a constantly (1.7 mm/yr) detrended time series (red thick) and an acceleratedly (2.6 mm/yr from 1990) detrended time series (red dashed). Modelled SSH anomaly within the marked box (blue) and SSH anomaly as measured by satellite altimetry (AVISO, green) are overlaid

altimetry data (green) confirms that the SSH anomaly within the chosen box is represented by the tide gauge measurements, emphasizing the capability of the model to simulate the SSH anomalies here. In the eastern tropical Pacific, although the number of tide gauge stations decreases significantly, the available stations are representative for the chosen box there (figure 3.3b). The comparison with AVISO and the model again shows an agreement of the interannual SSH variability.

In the tropical Indian Ocean, the tide gauge data are also quite scarce. Nevertheless, along the Australian West coast (figure 3.4 a), the three SSH anomaly time series agree very well. In the

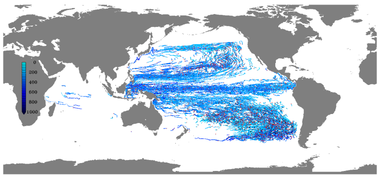

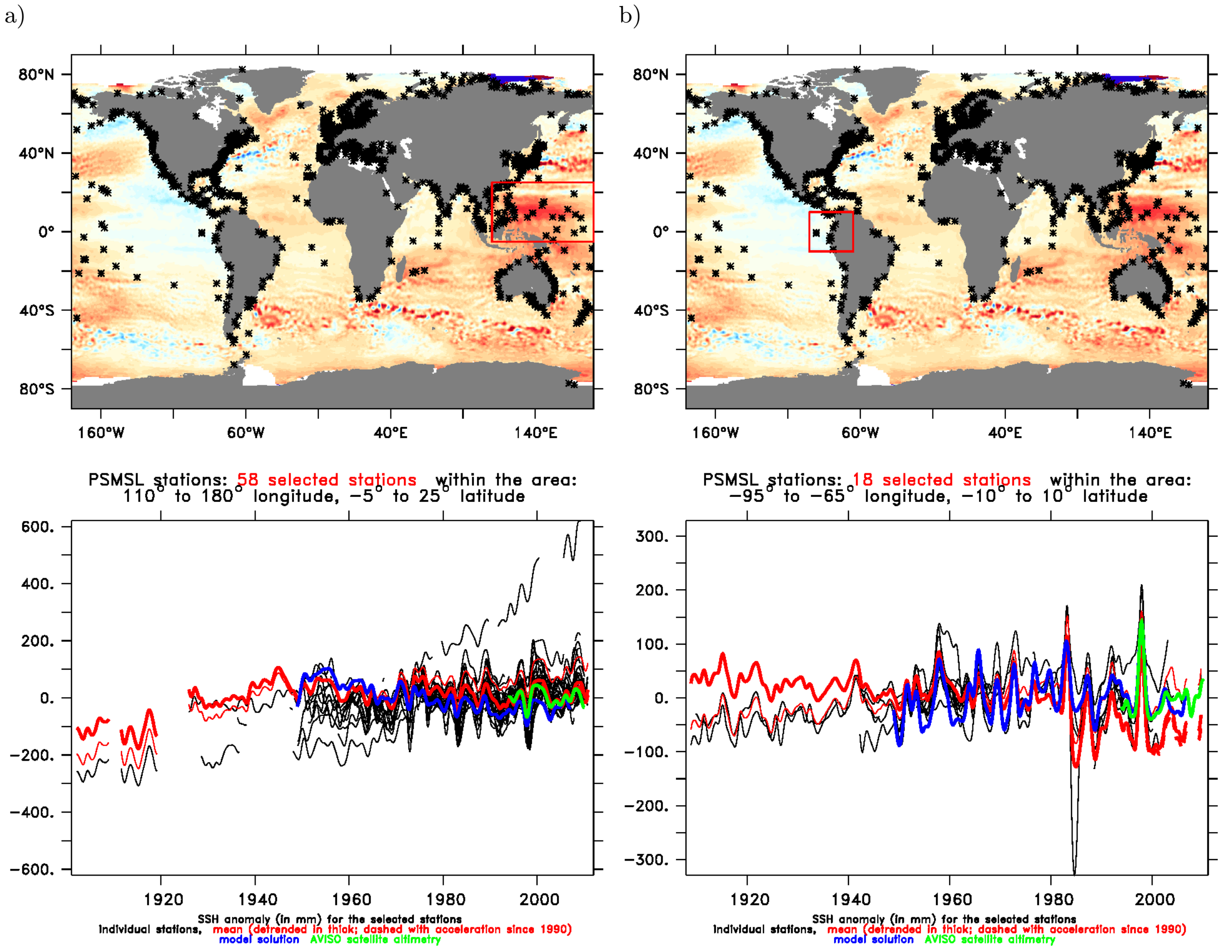

Figure 3.3.: See figure 3.2

western Indian Ocean (figure 3.4 b), at least the trend reverse around 2000 is depicted in all, tide gauge, satellite and modelled, SSH anomaly time series. On interannual to decadal time scales, for the tropical South Indian Ocean region, SSH variability and trends are discussed in section 3.2.

The comparison between in situ and remotely observed sea level variations and the modelled SSH exposes the capability of the model to reproduce interannual and decadal variability in the wind driven circulation, as reflected in this measure.

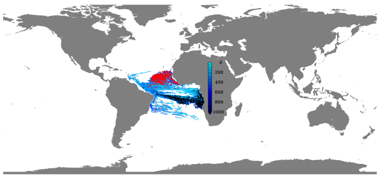

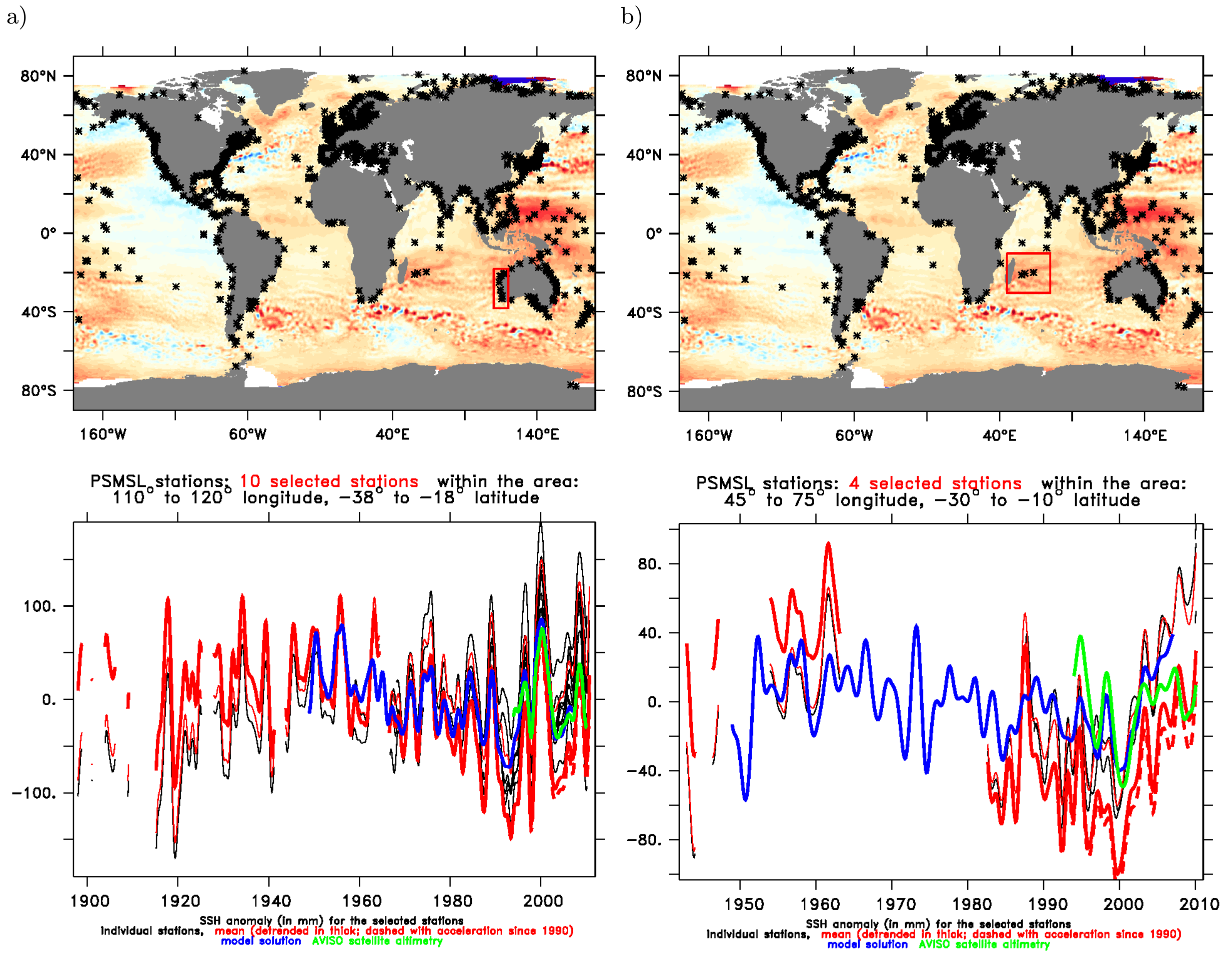

Figure 3.4.: See figure 3.2

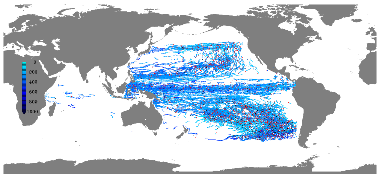

3.2. Sensitivity study in the Indo-Pacific

The ocean models employed in this study can be used to identify mechanisms and factors influencing distinct behaviours of the Ocean. This can be done in various ways, by isolating single factors influencing Ocean dynamics e.g. by artificially changing the forcing fields, applied to the model, by restricting interannual variability to only some parameters, keeping the others climatological or by artificially changing the model's bathymetry, e.g. by closing straits to only mention a few.

In this section, a study showing the results of such an isolation is presented. The topic, this study is dealing with, is the influence of wind forcing over the Pacific Ocean on tropical Indian Ocean heat content and sea level variability on decadal time scales. In the experiments used here, interannual forcing is restricted to single ocean basins to identify the forcing influences over different regions separately [Schwarzkopf and Böning (2011)]. The same set of experiments has been used to investigate the influence of forcing over the Pacific Ocean on the asymmetry of the Indian Ocean Dipole and therefore on seasonal time scales [Ummenhofer et al. (2013)]:

Ummenhofer, C. C., F. U. Schwarzkopf, G. Meyers, E. Behrens, A. Biastoch, and C. W. Böning (2013), Pacific Ocean Contribution to the Asymmetry in Eastern Indian Ocean Variability. J. Climate, 26, 11521171, doi: 10.1175/JCLI-D-11-00673.1

This section has been published in the American Geophysical Union Journal "Geophysical Research Letters":

Schwarzkopf, F. U., and C. W. Böning (2011), Contribution of Pacific wind stress to multi-decadal variations in upper-ocean heat content and sea level in the tropical south Indian Ocean, Geophys. Res. Lett., 38, L12602, doi:10.1029/2011GL047651.

3.2.1. Introduction

The global ocean is warming, and sea level is rising, in response to anthropogenic changes in surface heating [Domingues et al. (2008)]. Trends in upper ocean heat content during the past 50 years are, however, spatially highly inhomogeneous, reflecting strong effects of oceanic heat redistribution due to changes in ocean circulation [Doney et al. (2007)]. A prominent large-scale pattern of subsurface cooling from 1960 to 1999 around depths of 100-200 m has been observed in the tropical Indian Ocean (IO), associated with a shoaling of isopycnals along the thermocline ridge around 10° S [Han et al. (2006); Alory et al. (2007)]. Corresponding to the decrease in heat content in this zonal band, recent studies of ocean reanalysis products have identified a distinct pattern of multi-decadal sea level decrease during the late 20th century [Han et al. (2010); Timmermann et al. (2010)].

Understanding the causes of these regional trend patterns is of crucial importance for projections of future ocean and climate conditions. The inhomogeneous changes in IO upper ocean heat content and the associated spatial modulation in tropical sea surface warming [Trenary and Han (2008);

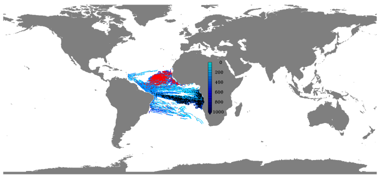

Alory and Meyers (2009)] are likely to influence natural modes of variability and to affect regional climate conditions in IO-rim countries [Ummenhofer et al. (2009); England et al. (2006)]. The corresponding sea level decrease in the south tropical IO more than offset the effect of global anthropogenic sea level rise during the last decades; however, projections of future trends, extremely important for various low-lying tropical islands and coastal areas are controversial, ranging from little or no rise [Han et al. (2010)] to an acceleration of the global mean rise in this area [Timmermann et al. (2010)].

Several mechanisms have been invoked to explain the subsurface cooling in the south tropical IO. Simulations with idealized 2-layer models [Han et al. (2006)] and an ocean general circulation model [Trenary and Han (2008)] attributed the shoaling of the thermocline to anomalous upward Ekman pumping velocities driven by wind stress changes over the IO. In contrast, Alory et al. (2007) proposed an oceanic teleconnection between the tropical Pacific and Indian Oceans via wave processes through the Indonesian Archipelago: noting that the IO cooling trend occurred along the off-equatorial Rossby wave pathway in the latitude range of the Indonesian Throughflow (ITF), they suggested an association with the observed multi-decadal weakening of the Pacific trade winds in the late twentieth century [Vecchi et al. (2006)], through a shoaling of the thermocline in the western tropical Pacific [Williams and Grottoli (2010)] and a weakening of the ITF [Wainwright et al. (2008)]. The significance of this oceanic teleconnection for decadal variability in the eastern subtropical IO has been documented in studies of the century-long sea level record at Fremantle, Western Australia [Feng et al. (2004)]. For the trends in the interior tropical IO, some indications for a Pacific contribution had been noted in earlier ocean models [Reason et al. (1996)] and in 20th century climate model experiments [Cai et al. (2008)], but its significance and spatio-temporal manifestation are much less clear. In this study the relative contribution of local (IO) vs. remote (Pacific) atmospheric forcing to the (multi-)decadal changes in the tropical IO heat content and sea level is investigated by a sequence of experiments with a global ocean general circulation model.

3.2.2. Model Experiments

The simulations build on various global implementations of the ocean/sea-ice numerical NEMO framework [Madec (2008)], developed in the European DRAKKAR collaboration [Barnier et al. (2007)]. The basic experiment (REF) is a 0.5°-grid hindcast simulation of the ocean's response to atmospheric forcing in 1958-2004 (preceded by a 20-year spin-up), given by the formulations and refined atmospheric reanalysis products developed by Large and Yeager (2004) that represent the basis of the Co-ordinated Ocean Reference Experiments (COREs) proposed by Griffies et al. (2009). A companion eddy-permitting version (REF025, using a 0.25°-grid) showed relatively minor effects of model resolution on the evolution of heat content and sea level in the Indo-Pacific. [Results from REF025 were therefore deferred to the supplementary material in the original article, but are shown inline here.] Details on all the model experiments are provided in Table 3.1.

The identification of the causes of IO decadal variability is aided by two experiments with artificial

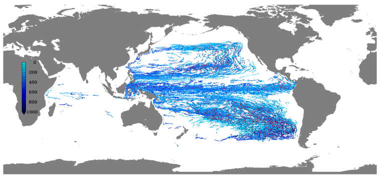

Name	Configuration	Experiment	Forcing	Period
spin-up	ORCA05	KAB107	interannual	20 years
CLIM	ORCA05	KAB108	climatological	47 years
REF	ORCA05	KAB109	interannual	1958-2004
PAC	ORCA05	KFS118	mixed (Figure 3.5a)	1958-2004
IND	ORCA05	KFS119	mixed (Figure 3.5b)	1958-2004
REF025	ORCA025	KAB001	interannual	1958-2004

Table 3.1.: The model experiments are integrated using NEMO v2.3 with the tripolar ORCA configuration in two different horizontal resolutions 0.5 degree and 0.25 degree, developed in the European DRAKKAR group. There are 46 vertical levels with thickness varying from 6 m at the surface to 250 m in the deep layers.

perturbations in the forcing (Figure 3.5). In PAC, the world ocean is subject to climatological, normal year forcing, except for the Pacific north of 50° S, where the same interannual forcing is used as in REF. In IND, interannual forcing is applied only to the IO north of 25° S. In order to separate atmospherically-forced ocean variability from spurious model drift, REF was complemented by a simulation (CLIM) over the same time span with climatological forcing everywhere; the trend of this experiment was subtracted from the interannually-forced cases prior to further analysis. For calculation of model sea surface height (SSH) fields, we followed previous studies [e.g. Wunsch et al. (2007)] and subtracted the time-varying global-mean SSH; the adjusted fields thus represent regional SSH anomalies due to ocean dynamics.

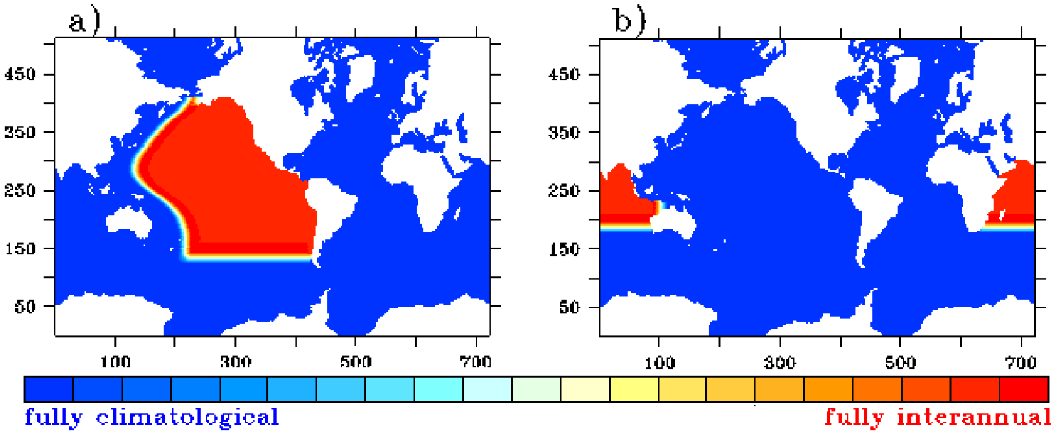

Figure 3.5.: Masks for mixed interannual/climatological forcing for PAC (a) and IND (b).

3.2.3. Interannual Variability and Multi-decadal Trend of Sea Level and Heat Content

A manifestation of upper ocean heat content variability in the tropical Indo-Pacific is given by the patterns of sea level change provided by satellite altimetry data since 1993 [Cazenave and Nerem (2004)]. During the second half of the 1990s, the southwestern Pacific and eastern IO exhibited the

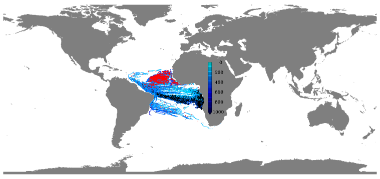

strongest sea level rise in the world ocean (Figure 3.6). The hindcast simulation REF (Figure 3.6a) reproduces the spatial pattern of the observed trend during this period (Figure 3.7a); it also captures the large-scale reversal in the decadal tendencies near the end of the 20th century noted by Lee and McPhaden (2008). Time series of SSH anomalies follow the altimeter records (Figure 3.6c-e) and emphasize the close correspondence between regional sea level and upper ocean heat content variability; they also reproduce the long term tide gauge record at Fremantle [cf. Feng et al. (2004)] (Figure 3.6f).

Although regional sea level is dominated by strong interannual-decadal variability (in some areas exceeding 10 cm in a few years) related to El Niño/Southern Oscillation (ENSO) [e.g. Behera and Yamagata (2010)], the model simulation also suggests a pronounced, basin-scale pattern of change on multi-decadal time scales (Figure 3.6b): sea level rose during 1960-1999 by 2-3 cm/decade in the subtropical South Pacific and by 1-2 cm/decade in the subtropical South IO; it fell in the western tropical Pacific (by up to 8 cm/decade), off western Australia and in the tropical IO, with the strongest decline in the IO occurring along 10° S (2-3 cm/decade). The spatial pattern and magnitude of the simulated trend in the tropical IO compare well with recent ocean reanalyses [Timmermann et al. (2010); Han et al. (2010)]. As discussed in these studies (and shown in Figure 3.6c-e), these sea level trends are associated with upper ocean warming (cooling) trends related to a deepening (shoaling) of the thermocline.

3.2.4. Causes of Sub-surface Cooling in the South Tropical Indian Ocean

The vertical structure of heating and cooling in the IO (Figure 3.8) can be compared with the linear trend of zonally-averaged temperature obtained from historical temperature profiles [cf. Alory et al. (2007)]. The overall pattern in REF (Figure 3.8a) matches the observed trend: a general surface warming, a wedge of deep warming penetrating to 800 m near 40° S-45° S, and a prominent subsurface cooling trend in the tropical thermocline, with strongest magnitude between 100 m and 300 m near 7° S-15° S. As in the observational analysis, the subsurface signals can be accounted for by a shift of isopycnals (Figure 3.9a and b): the deep warming to a southward expansion of the subtropical gyre and the tropical cooling to a shoaling of the thermocline.

The role of local atmospheric forcing (in the IO basin) versus remote forcing (in the Pacific) is addressed by the perturbation experiments PAC and IND (Figure3.8b and c). Whereas the surface warming is almost exclusively due to the local forcing, a significant part of the subsurface IO cooling was contributed by the Pacific (wind) forcing (Figure3.8b and e). The strongest cooling trend in PAC is found in the Indonesian Archipelago and off western Australia, from where a wedge with decreasing values extends west along the tropical south IO. While the remote forcing had a cooling effect all over the IO, the local forcing (Figure 3.8c and f) produced an alternating pattern of zonally-extended bands of warming and cooling in the IO thermocline; its contribution to the thermocline cooling was mainly confined to the western basin.

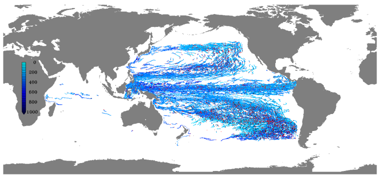

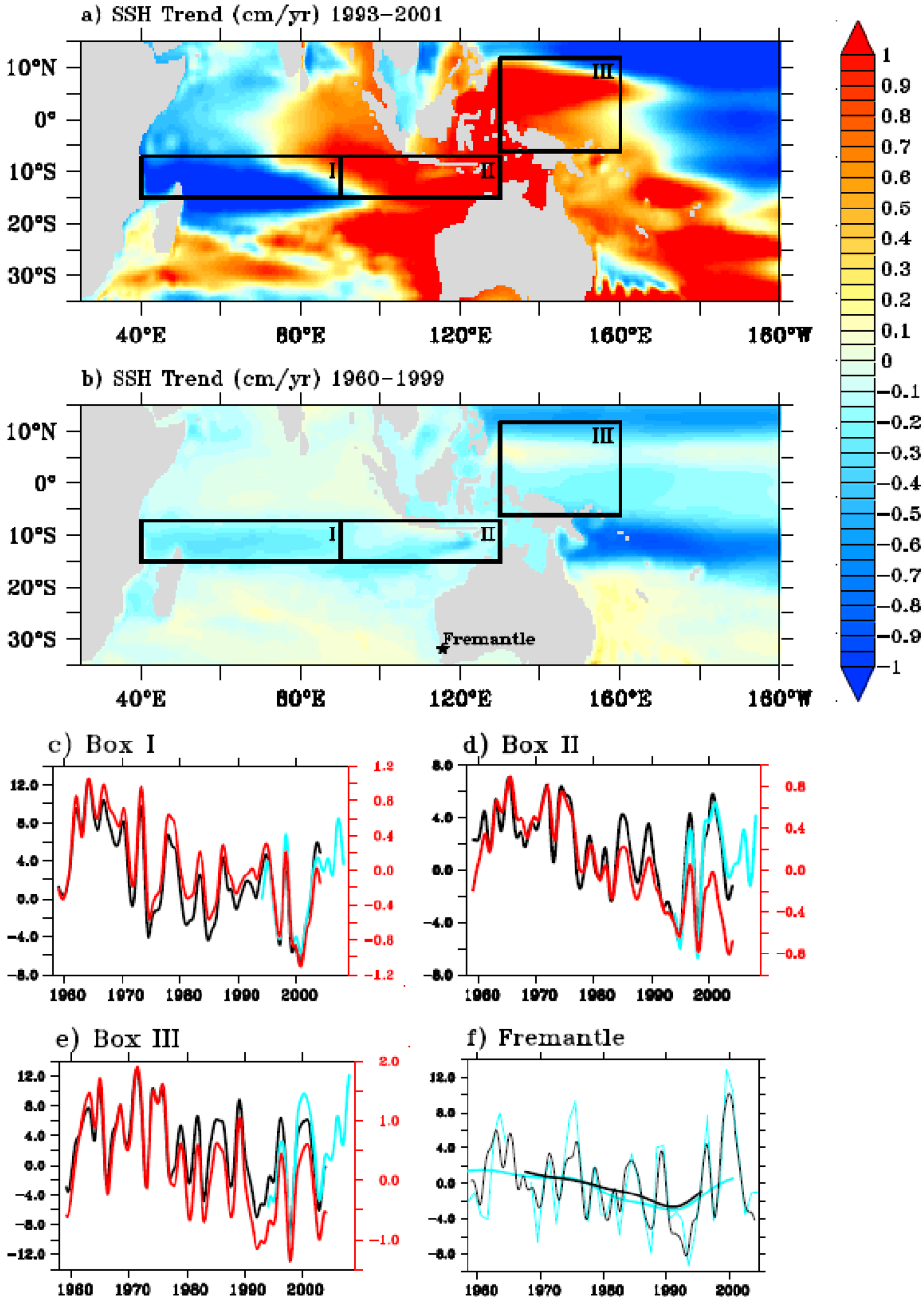

Figure 3.6.: Linear trend in SSH derived from REF in (cm/yr) for (a) 1993-2001, (b) 1960-1999. Time series for boxes (c) I, (d) II and (e) III of SSH anomalies (cm): REF (black), satellite altimetry (cyan); compared to 100-300 m heat content anomalies (GJ/m2) (red). Correlations between REF and altimetry are 0.94, 0.94 and 0.91 in box I, II and III. (f) Sea level anomalies at Fremantle: observed (cyan), REF (black); thin lines annual mean, thick lines low-pass (19-years) filtered values; correlations between REF and tide-gauge are 0.89 (0.98) for annual mean (filtered) time series.

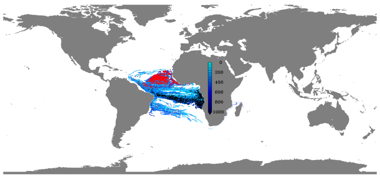

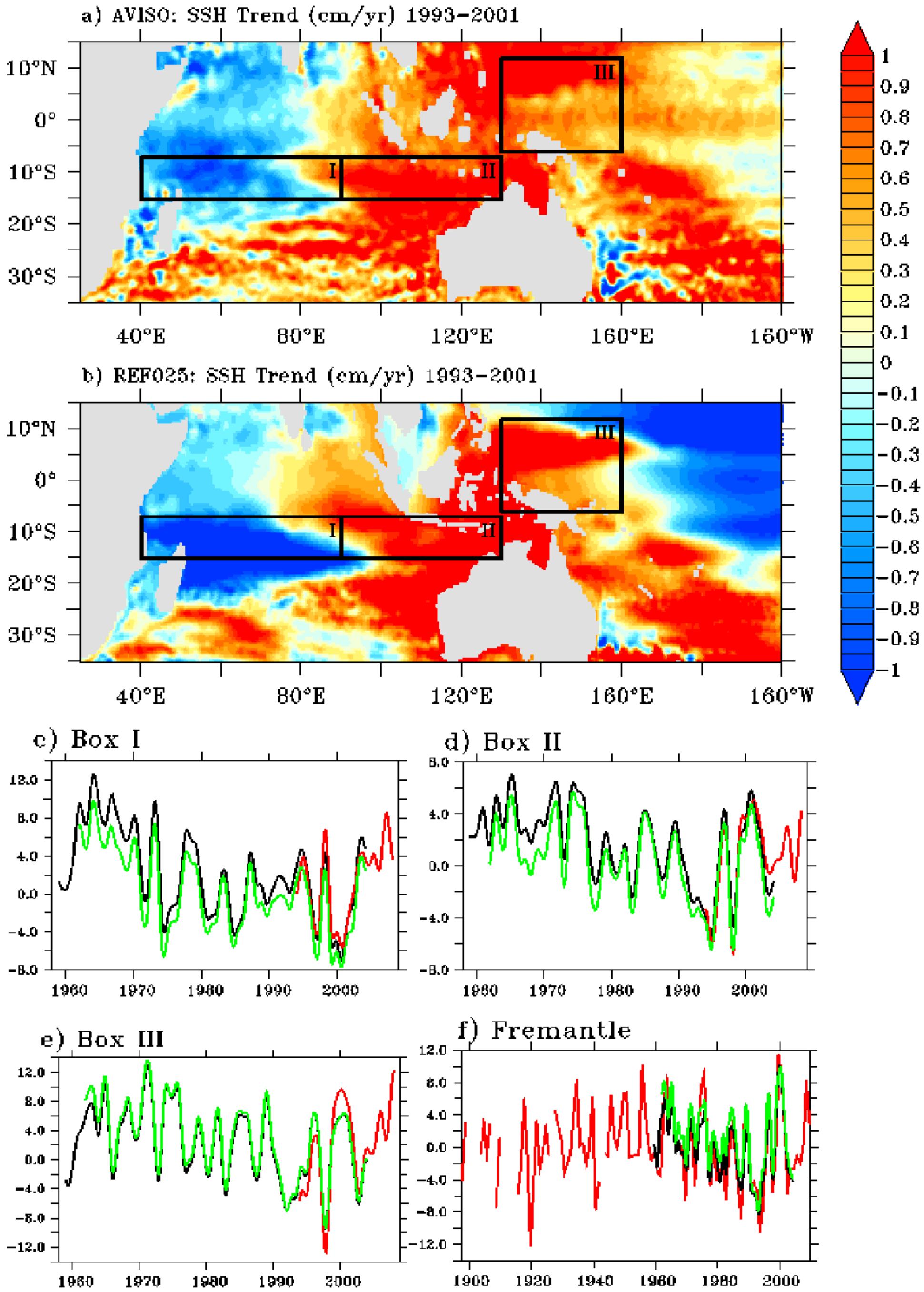

Figure 3.7.: Linear Trend in SSH from 1993 to 2001 derived from a) AVISO satellite altimetry data and b) REF025. The temporal SSH evolution of the two data sets (AVISO in red and REF025 in green) in comparison with the SSH from REF (in black) is shown in c) for box I, in d) for box II and in e) for box III; f) shows the observations at the Fremantle sea level station in red.

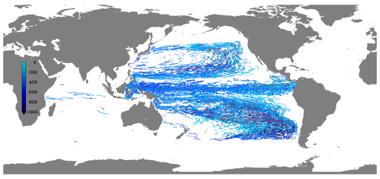

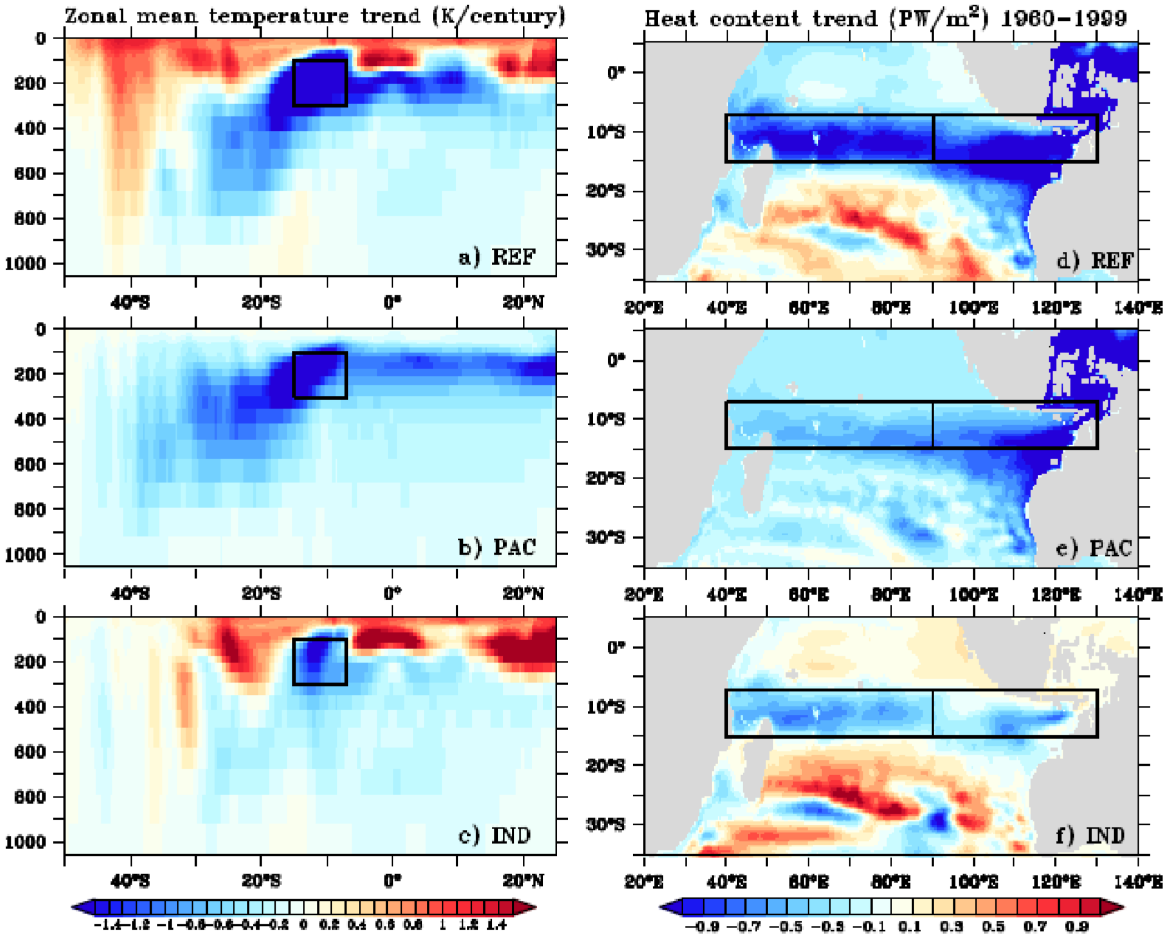

Figure 3.8.: Linear trends (1960-1999) of IO zonal mean temperature (in K/century) for (a) REF, (b) PAC and (c) IND; and of 100-300 m heat content (in PW/m2) for (d) REF, (e) PAC and (f) IND.

The local and remote contributions to the tropical IO trend are elucidated by time series of heat content anomalies (Figure 3.10). The net changes (as simulated in REF) can be understood as a linear superposition of the IO and Pacific forcing effects, i.e., by the sum of the changes simulated in IND and PAC (see Figure 3.11). Averaged over the whole zonal extent of the IO (Figure 3.10a), the linear trend between 7° S and 15° S for 1960-1999 is 0.29 °C/decade in REF, with a larger contribution from PAC (0.18 °C/decade) than from IND (0.10 °C/decade). The changes in the western basin (Figure 3.10b) are governed by stronger interannual variability, primarily due to IO forcing, with the multi-decadal trend as a relatively small residual; in contrast, the eastern basin is predominantly under the influence of the remote forcing (Figure 3.10c), contributing the bulk (75%) of the longer-term cooling. On decadal timescales (85-months filtered time series) the correlation between heat content anomalies in REF and PAC is 0.95 for the eastern box. The time series (especially in the eastern basin) indicate that the trend was not monotonous: the cooling began in the mid-1970s after a phase of decadal warming, and it ended in the 1990s (the latter termination standing out especially in PAC).

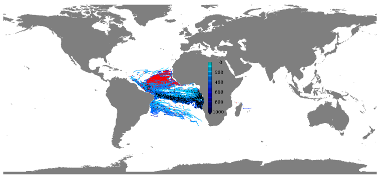

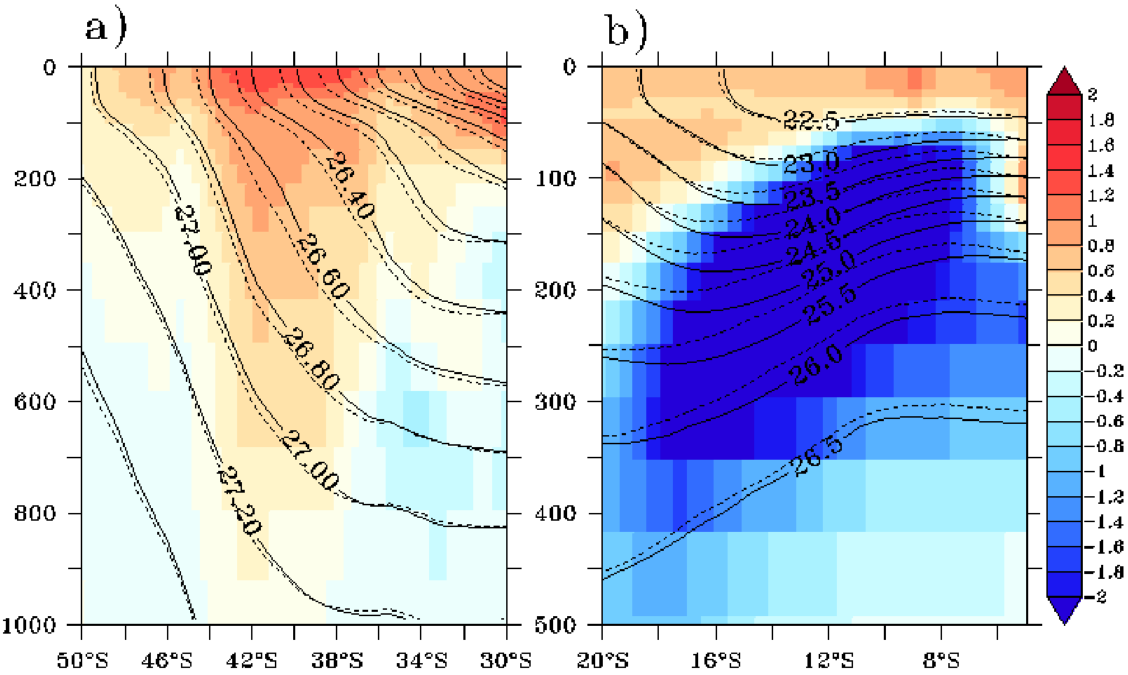

Figure 3.9.: Linear trend from 1993 to 2001 in zonal mean temperature in the IO for two distinct areas (see black boxes in Figure 3.13: a) Southern IO showing a pattern of deep reaching warming as observed in historic temperature profiles by Alory et al. (2007); b) southern tropical IO where the strongest subsurface cooling trend is found. The contours depict isopycnals for the 1960s (solid) and the 1990s (dashed), showing a southward shift in a) and a shoaling in b), as discussed in the observational study of Alory et al. (2007). As confirmed by additional sensitivity experiments (not shown here), the adiabatic trends in the IO thermocline are related to the wind-driven ocean circulation, while the warming at the surface reflects trends in the air-sea heat fluxes.

The spatio-temporal characteristics of the two forcing mechanisms are elucidated further by Hovmoeller diagrams (Figure 3.12) that allow an inspection of the connectivity of the heat content changes along the IO thermocline ridge with the variability in the tropical Pacific. In each of the experiments, the heat content variability appears as a manifestation of a Rossby wave signal: westward propagation of the anomalies in the IO latitude band is 13 cm/s, much higher than the mean speed of the South Equatorial Current (2-3 cm/s) in this area (see Figure 3.13). A similar westward progression is seen for the multi-decadal cooling trend during the 1970s to 1990s. Overall, the set of experiments suggests that both the interannual variability and the multi-decadal changes in the eastern portion of the tropical IO thermocline were predominantly caused by oceanic signals entering from the Pacific (Figure 3.12b), whereas the western basin (west of the Ninety-East-Ridge) was more strongly dominated by locally-forced interannual variability (Figure 3.12c); local and remote trend contributions there were of comparable magnitude.

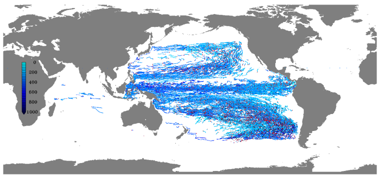

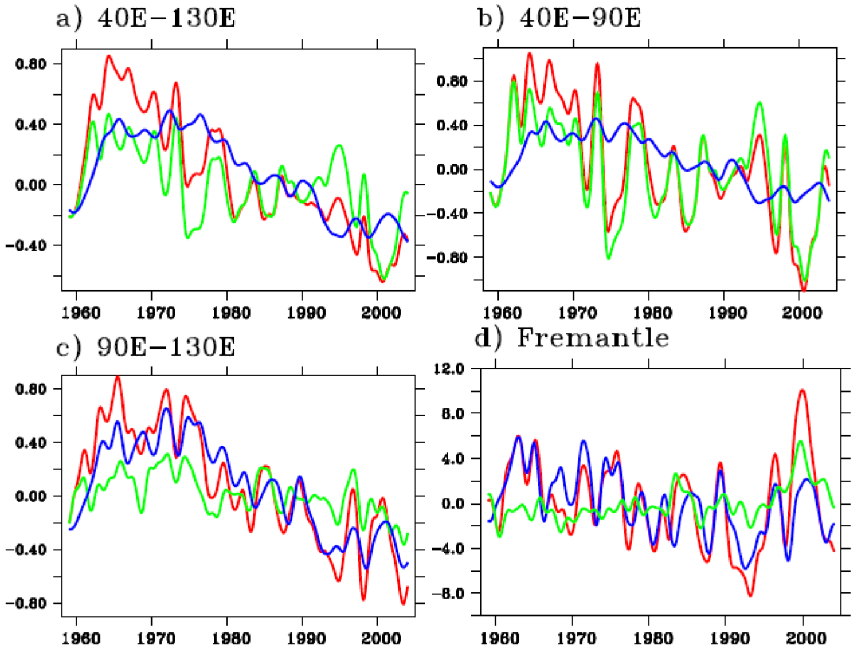

Figure 3.10.: Relative influence of Indian and Pacific forcing on IO changes: heat content anomaly (100-300 m) (GJ/m2) averaged over the boxes marked in Figure 3.8 for (a) whole IO extent, (b) western IO and (c) eastern IO; (d) sea level anomaly (cm) at Fremantle for REF (red), PAC (blue), IND (green).

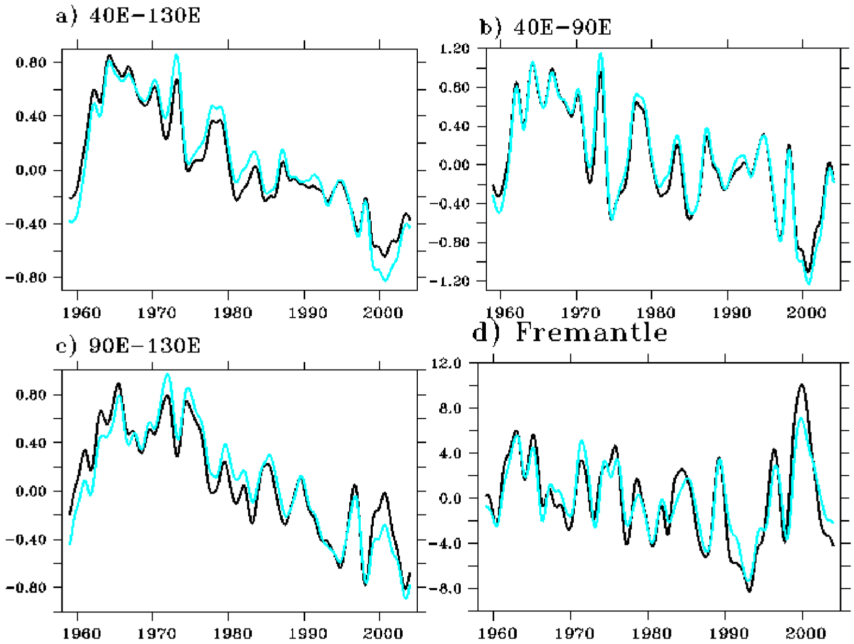

Figure 3.11.: Heat content anomaly (100-300m) from REF (black) and PAC+IND (cyan) in analogy to the three IO boxes shown in Figure 3.10 (a), b) and c)) and sea level at the Fremantle station d).

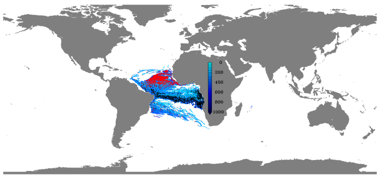

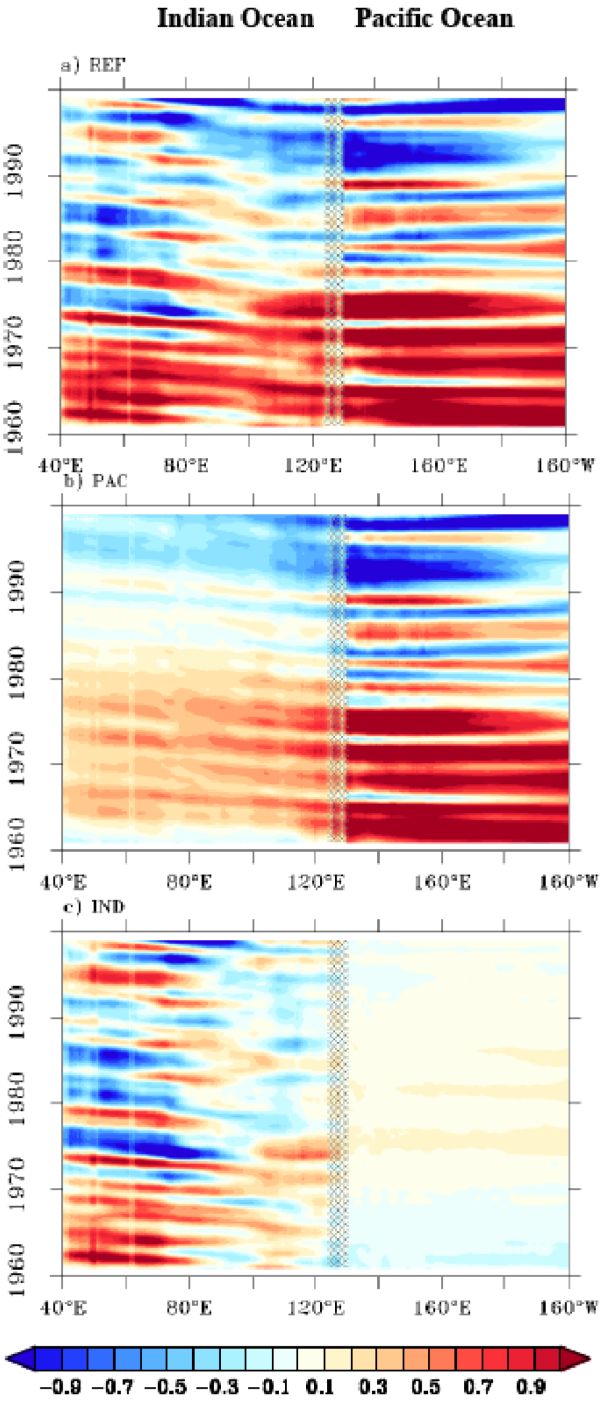

Figure 3.12.: Zonal propagation of heat content (100-300 m) anomalies (GJ/m2) averaged between 15° S-7° S in the Indian, and 6° S-12° N in the Pacific Ocean for (a) REF, (b) PAC and (c) IND. Hatched areas indicate the Indonesian Throughflow region.

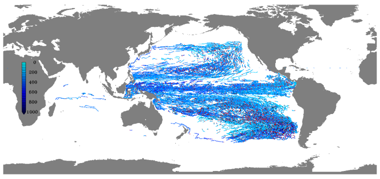

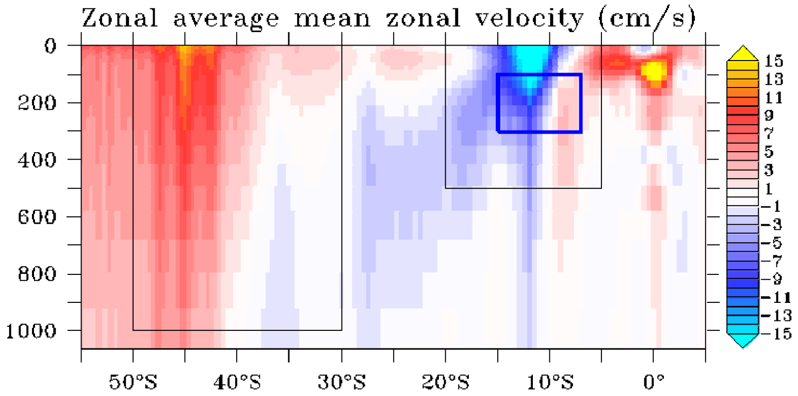

Figure 3.13.: Zonal average of the mean (1958 to 2004) zonal velocity in the IO. Mean speed of the South Equatorial Current (blue box) in the eastern part of the IO is 2-3 cm/s. The black boxes denote regions shown in Figure 3.9.

3.2.5. Concluding Discussion

The ocean hindcast simulation based on the CORE atmospheric forcing formulation is shown to capture the late 20th-century subsurface cooling in the south tropical IO [Han et al. (2006); Alory et al. (2007)] and its manifestation in sea level [Han et al. (2010); Timmermann et al. (2010)]. Aided by experiments with perturbations in the atmospheric forcing the simulations suggest:

1. The subsurface cooling and sea level fall occurred mainly between the mid-1970s and mid-1990s, bracketed by opposite tendencies before and after this period: an evolution consistent with the observed long-term sea level changes off western Australia and their interpretation as a footprint of multi-decadal climate variability in the tropical Pacific [Feng et al. (2004, 2011)].

2. Both IO and Pacific wind forcing contributed to the tropical IO changes: the IO forcing is the main cause of interannual variability in the western basin, whereas a large fraction of the multi-decadal variations is related to the winds over the Pacific Ocean.

3. The multi-decadal Pacific signal progresses westward in the IO with the same speed as the interannual (i.e., ENSO related) variability leaking in from the western tropical Pacific [e.g., Meyers (1996); Wijffels and Meyers (2004); Cai et al. (2005)], suggesting the importance of Rossby waves on both interannual and multi-decadal time scales.

The results have implications for the future evolution of the IO thermocline structure and sea level: in particular, a continuation of the late 20th-century trends could be expected, if the observed weakening of the Pacific trades [Vecchi et al. (2006)] and shoaling of the western equatorial Pacific thermocline [Williams and Grottoli (2010)] should continue in the 21st century as suggested by anthropogenic climate change simulations [Collins et al. (2010)].

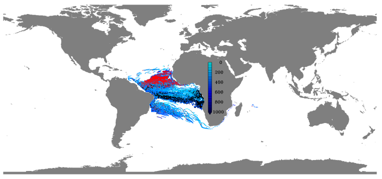

3.3. Zonal current bands in the tropical Atlantic Ocean at 23° W

Repeated ship sections in the tropical Atlantic Ocean provide a good coverage of the circulation around 23° W. Brandt et al. (2010) analyzed the relationship between zonal current bands and oxygen distribution in the eastern part of the tropical North Atlantic basin. The observed mean zonal velocity section and a sampling strategy, which takes into account the spatial and temporal coverage of the ship sections, are used here to assess the capability of the model to capture the mean flow structure in this region (section 3.3.1). Stationary mooring-based measurements along 23° W are used to test the model skill in reproducing the current variability (section 3.3.2). Improvements in modelling the zonal current structure due to increased horizontal model resolution are shown in section 3.6.

3.3.1. Mean spatial structure

Brandt et al. (2010) used observations from 22 different ship sections between 28.5° W and 23° W during the period 1999 to 2008 to estimate the mean zonal velocity. These sections not only vary in their zonal location but also differ in their meridional and vertical extent. Details on the sampling of the observational data are given in figure 3.14. The calculated mean zonal velocity between 28.5° W and 23° W as given in Brandt et al. (2010) (their figure 2a) is reproduced in figure 3.14a). The number of measurements at given latitudes and depths range from only six at the deep northern corner to up to 18 in the upper ocean right at the equator (figure 3.14b, top right). Overall, the number of measurements decreases away from the surface and the equator. The zonal position and the individual meridional (figure 3.14c) and vertical (figure 3.14d) extent of the different sections show the majority to be located at 23° W with a deviation west to 28.5° W. In figure 3.14e the time of the observations is given and figure 3.14f shows the monthly coverage, indicating a concentration of measurements towards the late 2000s and spring and summer seasons, with reduced sampling in autumn. The potential effect of this observational coverage in comparison to a time averaged section with equal weights in time and space is assessed here, based on the modelled velocity fields.

The mean zonal velocity calculated from TRATL01-IA by subsampling the data in the same way as the observations were taken, concerning time (here, one 5-day average at the given point in time is used), zonal location as well as meridional and vertical extent of the measurements (figure 3.15a), is compared to the 1999 to 2008 time averaged section along 23° W, which covers the meridional range from 6° S to 14° N from the surface, down to 1000 m depth (figure 3.15c). Additionally, the subsampled version, based on monthly mean data (b) and the full mean averaged over the zonal extent from 28.5° W to 23° W (d) are given. While the strong eastward currents (EUC, SEUC, NECC/NEUC) and the near surface westward currents (nSEC and sSEC) are robustly present in all calculations and represent the observations well, the model apparently fails to capture the weaker currents like the NICC, SICC or nNECC. Below the EUC where in the observations by Brandt et al. (2010) the westward EIC is located, the individual subsampled means also show westward velocities, while the full mean cases, exhibit eastward velocities. Overall, the strength of the currents reduces when

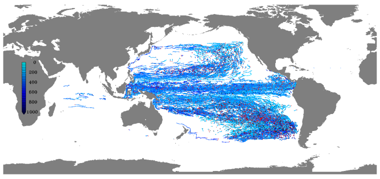

a) Averaged zonal velocity b) Data coverage

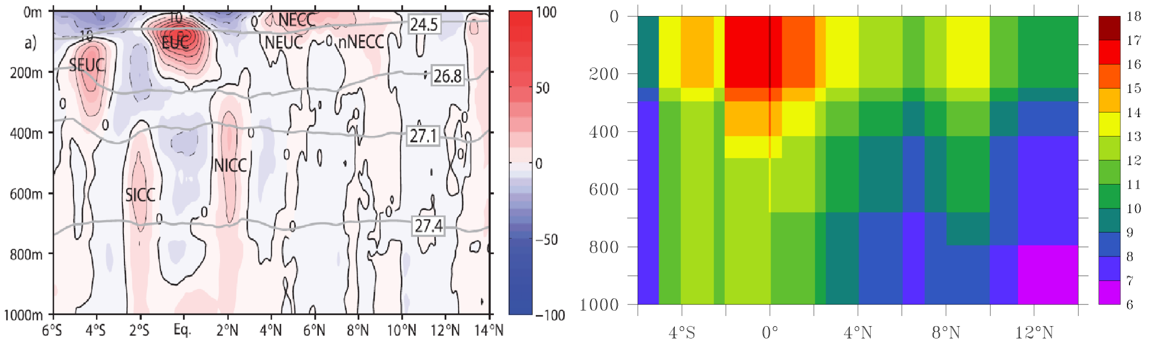

c) Latitudinal extent d) Vertical extent

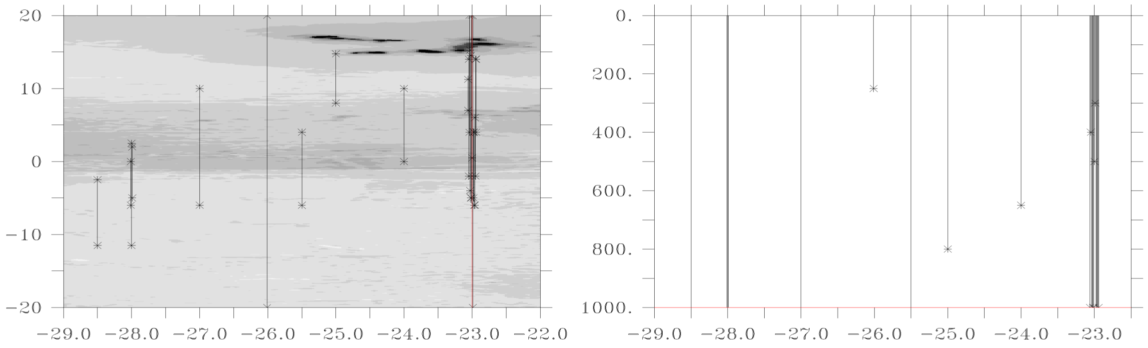

e) Temporal coverage

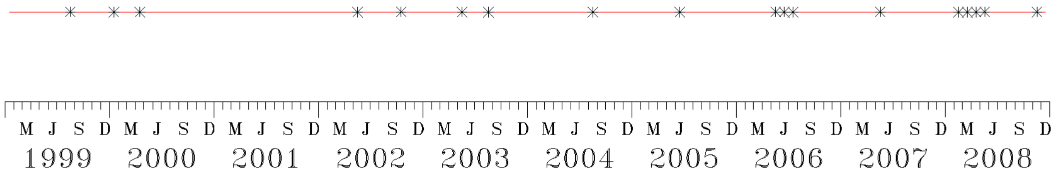

f) Seasonal distribution

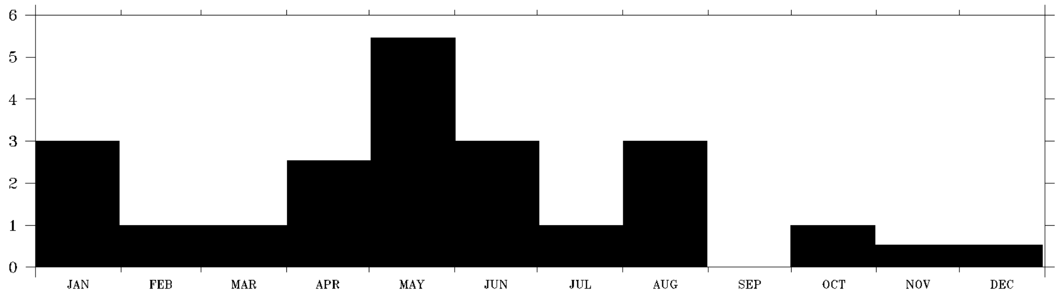

Figure 3.14.: a) Mean zonal velocity between 28.5° W and 23° W as given in Brandt et al. (2010) (their figure 2(a)) and the spatial and temporal data coverage b)- f) reproduced from the information in their table 1.

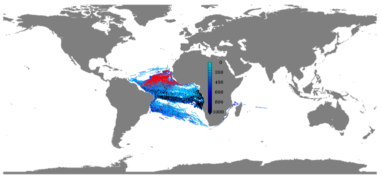

using the full averaging period compared to the subsampled cases, indicating fluctuations within the circulation. The alternating band-like structure of the vertically extended currents north of about 5° N is represented using all methods, although their exact meridional location and strength varies.

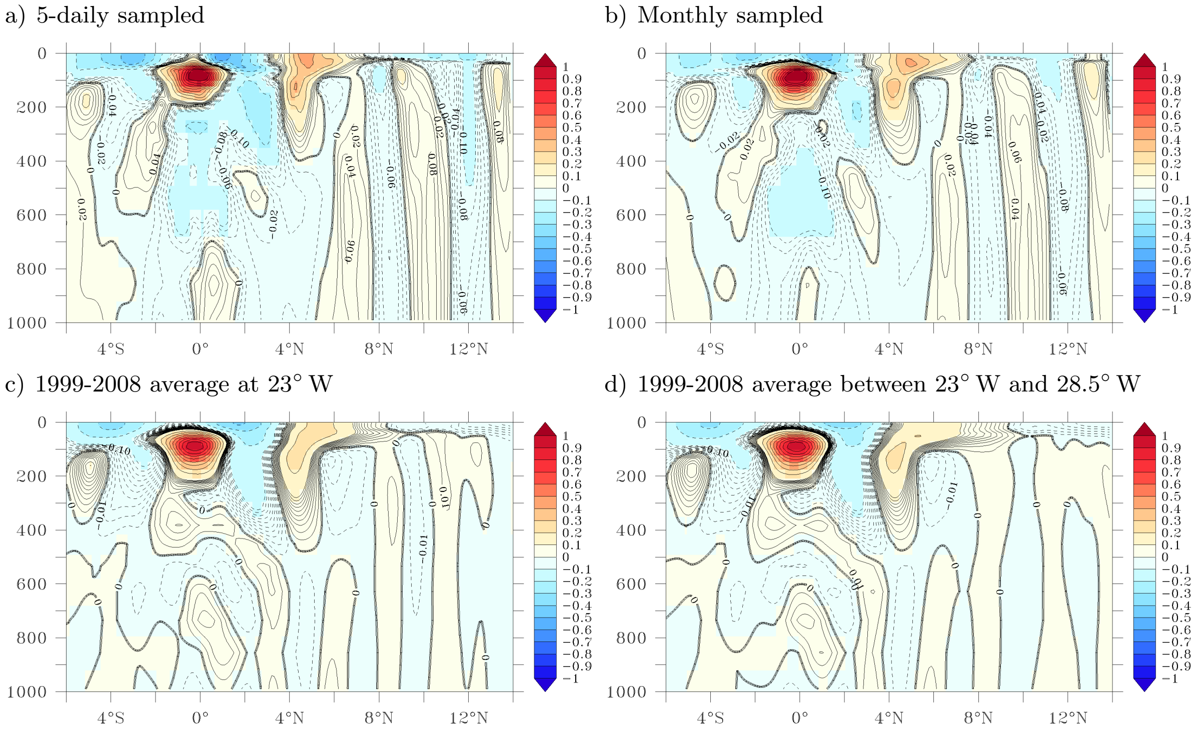
a) 5-daily sampled
b) Monthly sampled
c) 1999-2008 average at 23° W
d) 1999-2008 average between 23° W and 28.5° W

Figure 3.15.: Mean zonal velocity from TRATL01-IA sampled in space and time like the observations based on 5-daily averages a), based on monthly averages b), temporally averaged from 1999 to 2008 at 23° W c) and additionally averaged between at 28.5° W and 23° W d).

Not only the averaging period but also the temporal coverage is of importance as shown in figure 3.16 by comparing averages, subsampled like the observations, but shifted in time. A slight deviation of the chosen point in time by only taking the neighbouring 5-day averages, leads to differing current structures as depicted in figure 3.16a) and b). The overall structure remains the same but especially close to the equator, the current core of the NICC, in one case, can either be connected to an increasing deeper equatorial current or stays almost unchanged. An equivalent comparison based on monthly data with time shifts of one month forth and back (figure 3.16c and d), shows rather similar structures c) except for showing a stronger eastward equatorial current between 700 m and 1000 m, or, in the other case d) completely changes the equatorial pattern. A clear, deep reaching westward EIC below the EUC is simulated in the latter case and the NICC and SICC get their so called “tall jet“ shape as described by Ascani (2008) where the SICC also reaches up to the EUC. In this case, a shallow nNECC core evolves. Shifting the 5-daily data forth and back by one year e) and f) not only exposes the already mentioned variability of the currents in the vicinity of the equator, but also changes in sign for the tall jets north of 5° N that could also be interpreted as changes in their latitudinal positions. The shape of the NEUC/NECC system also changes. Even

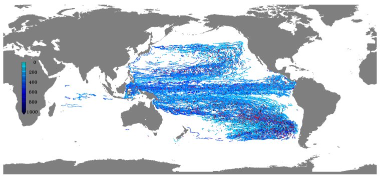

more variability of this kind can be seen when shifting the sampling period by five and ten years into the past (figure 3.16g and h) where now, additionally, the NEUC/NECC strength is lower, implying a strengthening of these currents over time.

To give a more quantitative measure for this sensitivity to the sampling, the standard deviation of the velocities on different scales is given in figure 3.17, where on the left hand side the absolute and on the right hand side the relative deviation to the mean velocity is shown. The absolute high frequency (5-daily (a) and monthly (c)) variability of the zonal velocities is highest at the equator, at the upper northern flank of the EUC and within the region where the NECC/NEUC occur. At lower frequency (interannual, (e)) the strongest standard deviation is found within the EUC and south of the NEUC/NECC. On the spatial scale from 28.5° W to 23° W (g) the variability is about twice as high as for the interannual time scale and the maxima are located just north of the cores of the EUC and NECC. Comparison of the variability to the absolute values of the mean velocities (right column) explains the behaviour shown in figure 3.15, where within the strongest currents, the relative variability is lowest for all subsampling examples. Except for these strong currents, the standard deviation is higher than the mean velocity (averaged from 1999 to 2008 and between 28.5° W to 23° W), indicated by the red colour in the high frequency cases (figures 3.17b and d). On interannual time scale (figure 3.17f), these currents become more robust, as well as some deeper velocity features, which still vary by about 30% of their mean velocity. The robustness of the velocities depending on their zonal sampling location is also restricted to the strong currents mentioned before (figure 3.17h).

An exact agreement between measured and modelled velocity cannot be expected because of the stochastic variability overlain on the forced variability and the mean flow. Nevertheless, the main features of the observed current structures are represented in the model, especially, when the influence of spatial and temporal subsampling is accounted for in the model average. In the remainder of this study, the time averaged velocity fields will be used, when talking about mean sections. The strong effect of the high-frequency variability (see section 3.3.2) emphasizes the importance of continuous velocity measurements for the estimation of ”mean“ current fields. From the investigations within this section, it appears that the ”true“ time mean velocity section might not be fully covered with the available observations, as given by on average two sections per year within the past decades.

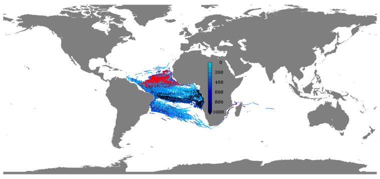

a) 5-day shift forward b) 5-day shift backward

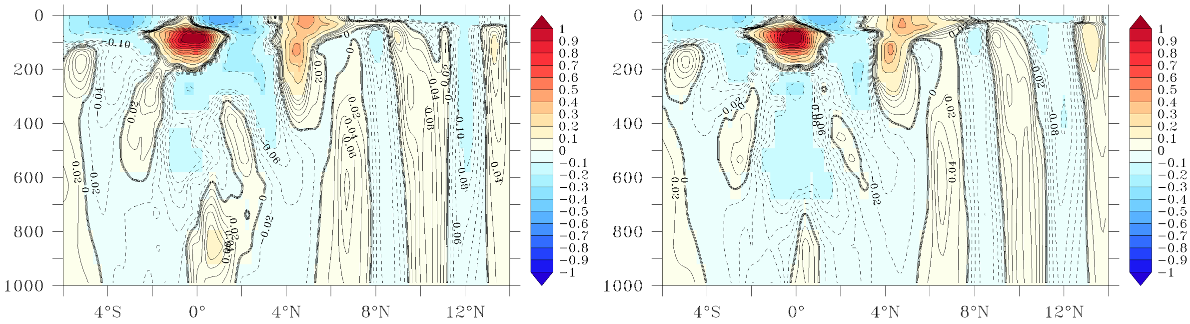

c) 1-month shift forward d) 1-month shift backward

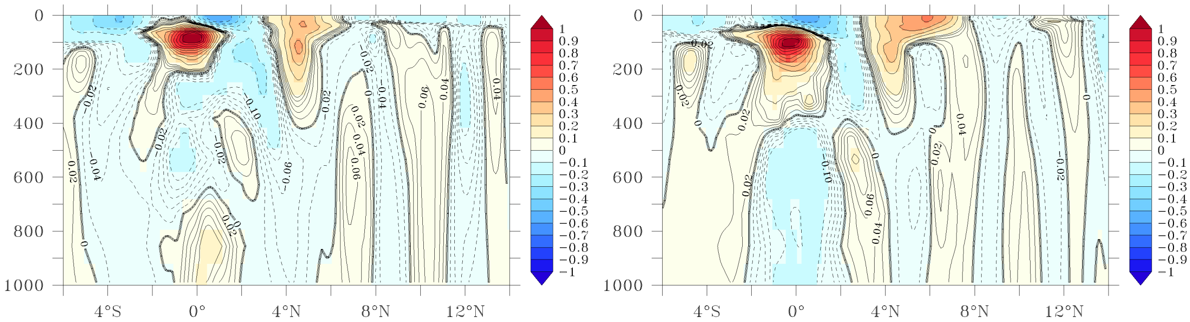

e) 1-year shift forward f) 1-year shift backward

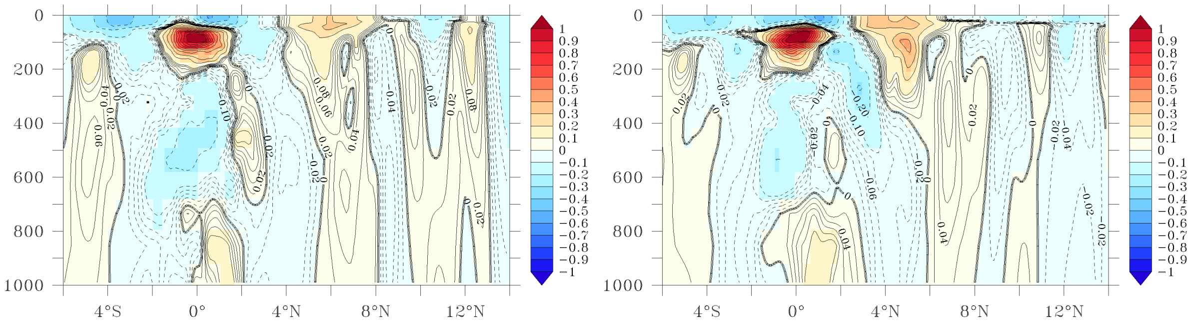

g) 5-year shift h) 10-year shift

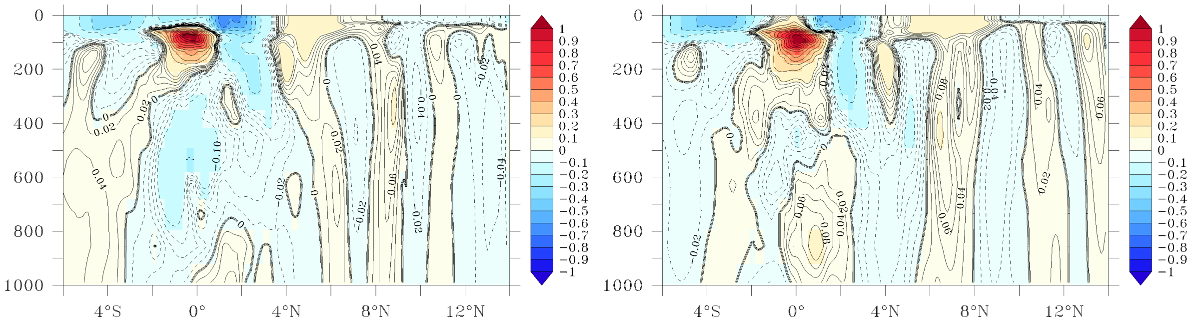

Figure 3.16.: Same as figure 3.15a) but with a shift in time of 5 days forward a), 5 days backward b), based on monthly data with a shift of one months forward, c) and one month backward d), based on 5 daily data shifted by one year forward e) and one year backward f) in time as well as for shifts of five years g) and ten years h).

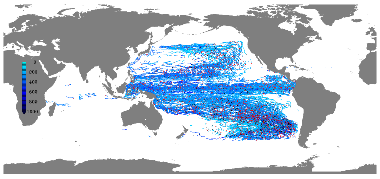

a) Absolute temporal 5-daily std b) Relative temporal 5-daily std

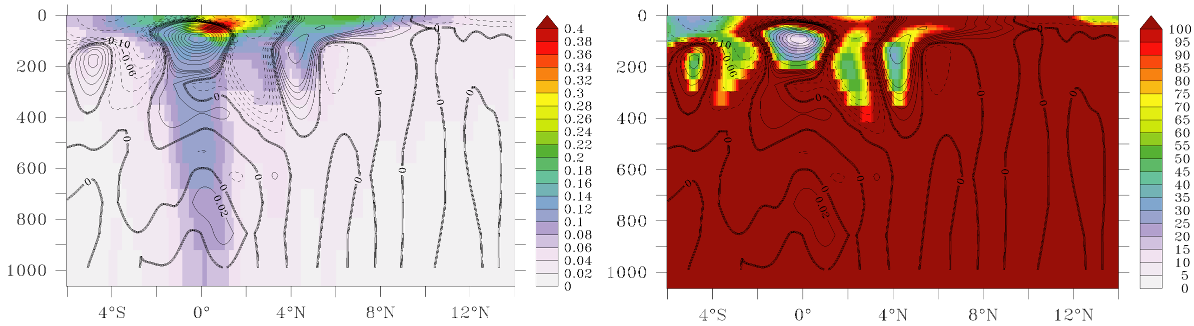

c) Absolute temporal monthly std d) Relative temporal monthly std

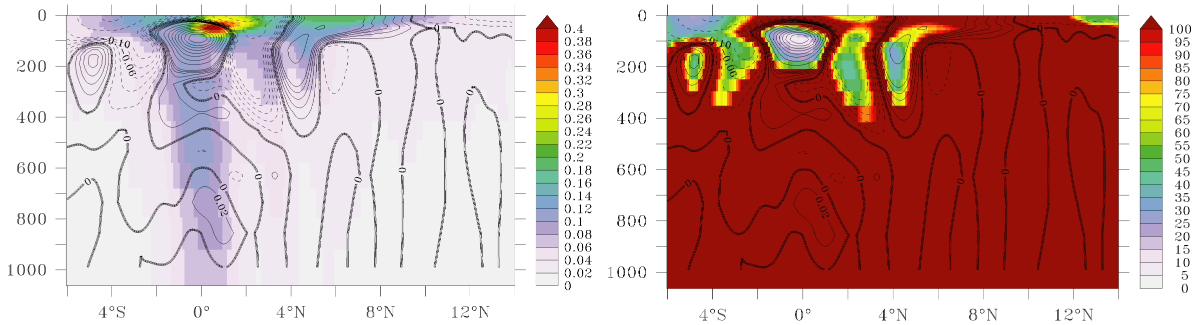

e) Absolute annual std f) Relative annual std

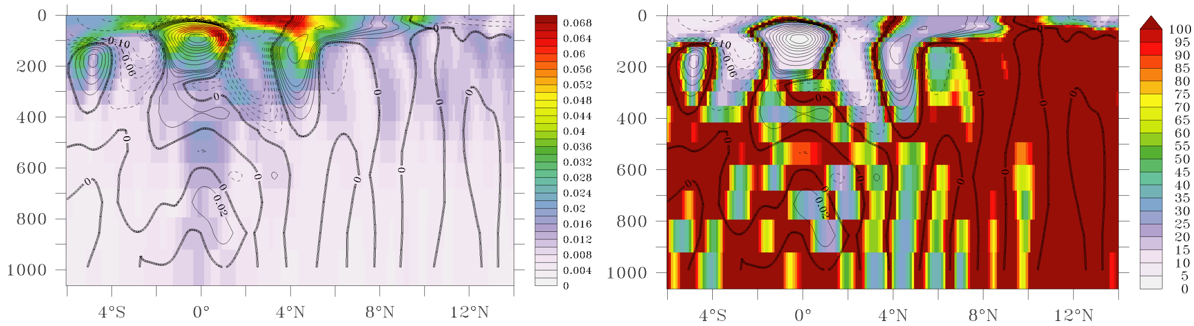

g) Absolute zonal std h) Relative zonal std

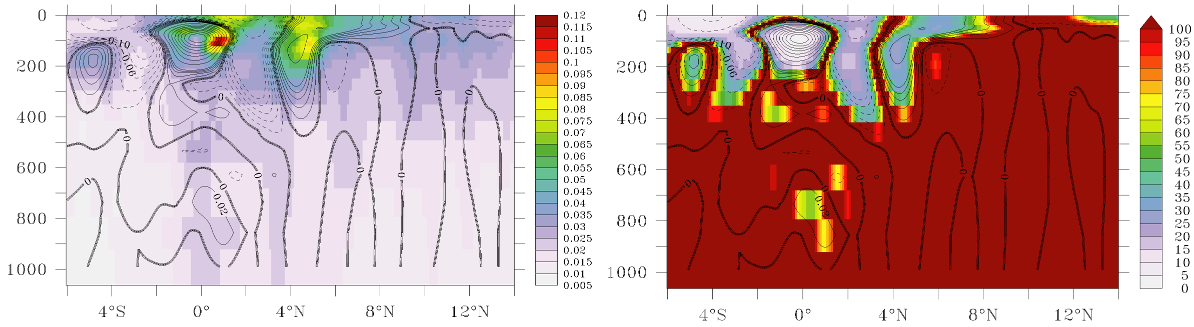

Figure 3.17.: Standard deviation (std) [m/s] in the zonal velocity fields at 23° W (left, note different scales) and normalized by the mean velocity (right, the colourscale gives the standard deviation as percentage of the mean velocity in the time period 1999 to 2008, averaged between 28.5° W and 23° W with red giving the regions where the standard deviation is higher than the mean velocity) at 5-daily (a and b), monthly (c and d), and annual (e and f) time scales as well as for the deviation in zonal direction between 28.5° W and 23° W (g and h).

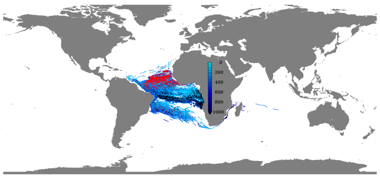

3.3.2. Temporal variability

The representation of the temporal variability in the velocity field is assessed by comparing modelled velocity time series to mooring data at 23° W (courtesy of Peter Brandt) right on the equator, at 2° N and 5° N at 400 m depth and additionally 1200 m depth for the mooring at 0° N. For the model, the depth levels closest to the observations are used (382 m and 1137 m respectively).

The observations on the equator at 400 m and 1200 m depth as well as the modelled velocities are both dominated by a seasonal cycle, that is generally well reproduced (figure 3.18). The amplitudes of variability in the observed velocities are captured in the model and at least the sign of the temporally averaged velocities agrees, although the mean flow in the model is weaker when compared to the observations. The seasonal cycle is less variable in the model than in the observations, where, for instance, it is not as distinct in 2006 for the 400 m case. The overlapping period of the time series at 1200 m depth is only about two years long (2006-2008), but shows a good agreement of model and observations. The black curves in the left column show the absolute velocities from TRATL01-IA. In the right column, the velocity anomalies are compared, where for the modelled data, additionally, the linear trend over the period 2003 to 2009 from TRATL01-NY is removed from the TRATL01-IA time series to eliminate a possible spurious model drift. Doing so shows an even better agreement between the observed and the modelled velocity time series at both depths, where in the “undetrended” case modelled and observed velocities slightly diverge with time for the timeseries at 400 m depth.

The observed zonal velocities at 400 m depth for the off-equatorial locations are compared to the modelled velocities in figure 3.19. Here, the congruence between model and observations is less pronounced than for the measurements right at the equator. At 5° N, the overlapping period between model results and the observations covers only less than two years. The modeled velocity shows a more distinct seasonal cycle and its variability is higher when compared to the observations. In 2010, when no modelled velocities are available, the variability of the observed velocity further decreases. The core of the NICC in the observations is located at 2° N in 400 m depth (see figure 3.14a) with overall eastward velocities. The mean current speed is 0.13 m/s with a standard deviation of 0.01 m/s. The modelled velocity at 2° N in 400 m depth is less variable and even shows a slightly westward mean flow, not showing a NICC-like behaviour there.

The model shows a more variable NICC than the observations, located farther north and deeper down at about 3° N below 500 m depth. This explains the discrepancy between the modelled and observed time series at the observed NICC location. However, the amplitudes of variability almost match. Additionally, a comparison with the modelled velocities in the center of the modelled NICC is done, showing slightly positive velocities (figure 3.20), but still weaker than in the observations. The anomalies show weaker amplitudes in the model, but a clear seasonal cycle, that is not present in the observations.

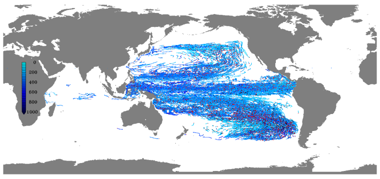

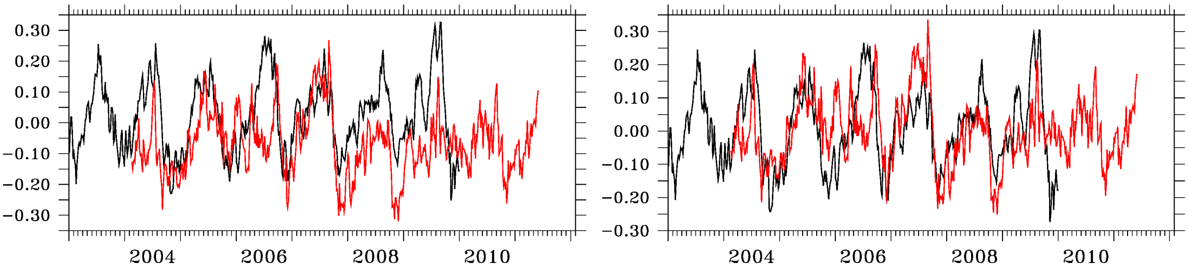
a) 0° N, 400 m
b) Anomaly: 0° N, 400 m

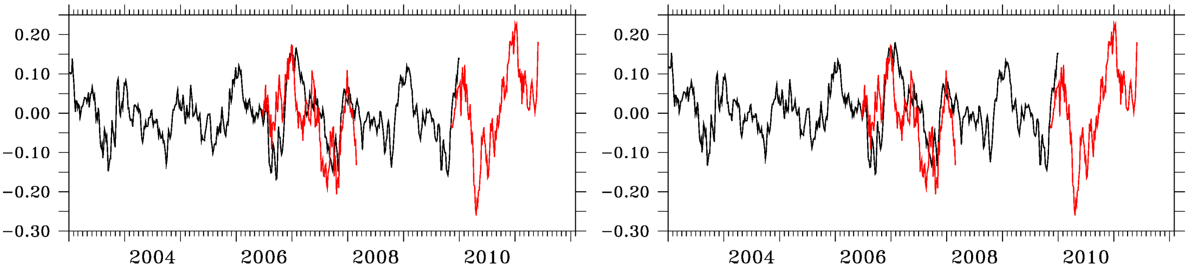
c) 0° N, 1200 m
d) Anomaly: 0° N, 1200 m

Figure 3.18.: Zonal velocity (left) and velocity anomalies (right) [m/s] from mooring measurements (red) and TRATL01 (black) at 23° W on the equator in 400 m depth (a and b) and 1200 m (1137 m) (c and d)

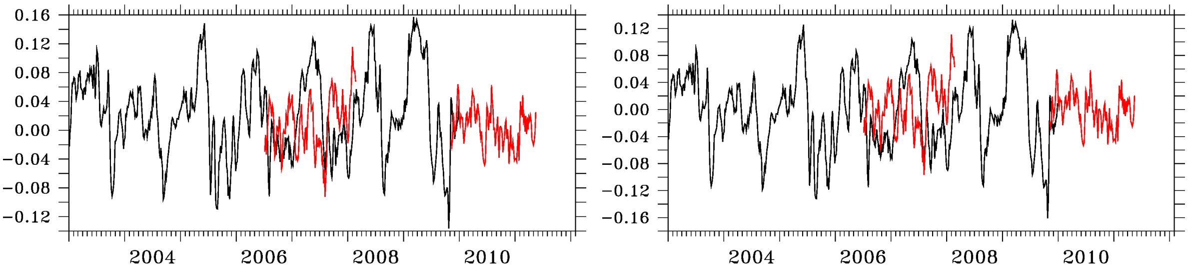
a) 5° N, 400 m
b) Anomaly: 5° N, 400 m

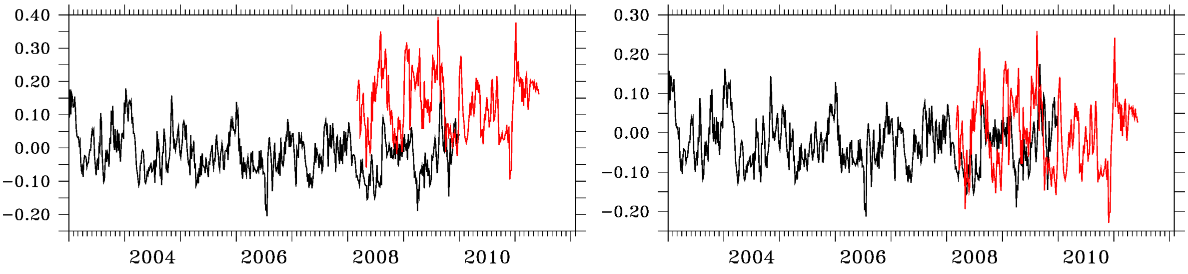
c) 2° N, 400 m
d) Anomaly: 2° N, 400 m

Figure 3.19.: Zonal velocity (left) and velocity anomalies (right) [m/s] from mooring measurements (red) and TRATL01 (black) at 23° W and 400 m depth for 5° N (a and b) and 2° N (c and d)

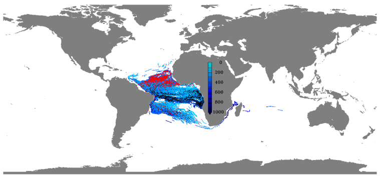

a) 2° N, 400 m

b) Anomaly: 2° N, 400 m

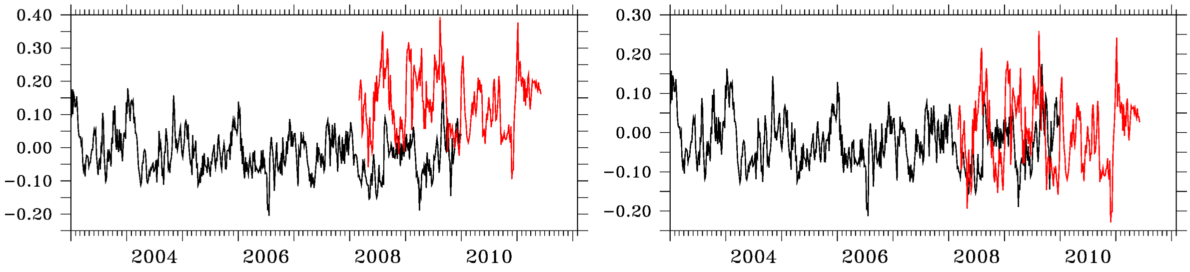

c) At modelled NICC max.

d) Anomaly: at modelled NICC max.

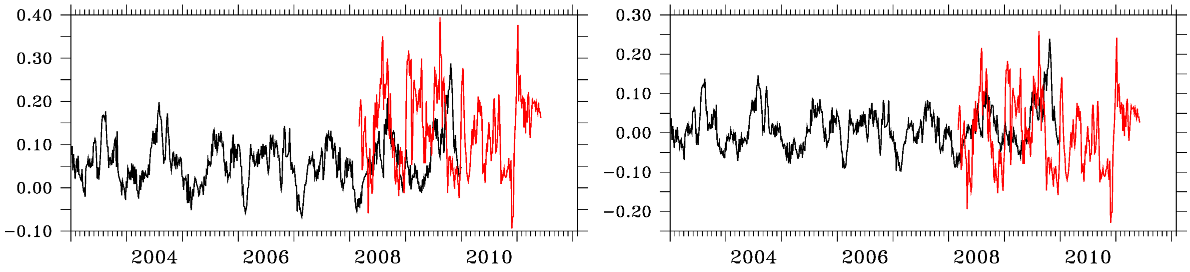

Figure 3.20.: Zonal velocity (left) and velocity anomalies (right) [m/s] from mooring measurements at 23° W at 2° N in 400 m (red) and TRATL01 (black) at the same location (a and b) and in the core of the NICC in TRATL01 (c and d)

Overall, the velocity timeseries right on the equator are reproduced in the model concerning seasonal cycle, mean flow and amplitudes of high-frequency variability, whereas some interannual variations are not captured i.e. the minimum in the observed zonal velocity at 400 m depth in 2006 is opposed by a maximum in the model. The off-equatorial velocity time series differ between observations and the model in their mean flow, although the range of variability and some features of the seasonal cycle are reproduced, even in the very short period of overlapping data.

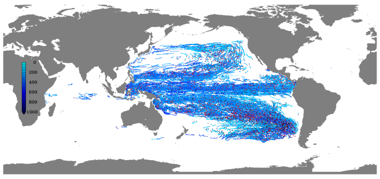

3.4. Regional tracer spreading

An observational attempt to measure diapycnal diffusivity was done during the Guinea Upwelling Tracer Release Experiment (GUTRE). A passive tracer (CF_3SF_5) was injected into the ocean at 23° W, 8° N on an isopycnal layer corresponding to $\sim$350 m depth, the upper rim of the OMZ, in 2008 [Banyte et al. (2012)]. Three cruises, dedicated to measure the temporal and spatial evolution of the tracer, were done 7, 20 and 30 months after the release. The diapycnal mixing coefficient was estimated to be of the order of $10^{-5}\, m^2/s$. Horizontal mixing showed a clear discrepancy between the meridional and zonal component, with the latter being roughly twice as large, depicted by a stronger tracer spreading in zonal direction as shown in their figure 4. The results from GUTRE are used here to asses the capability of the model to reproduce regional mixing characteristics.

Analogous to GUTRE, a numerical tracer release experiment was performed in TRATL01 (TRE001). A passive dye was injected into the ocean in the area 7.9° N to 8.4° N and 23.1° W to 22.8° W at 382 m depth (level 18) on January 1^{st} 1999. The time was chosen arbitrarily, as the corresponding time period to GUTRE was not covered by the forcing data. The tracer spreading after 7, 20 and 30 months is analyzed qualitatively (figure 3.22).

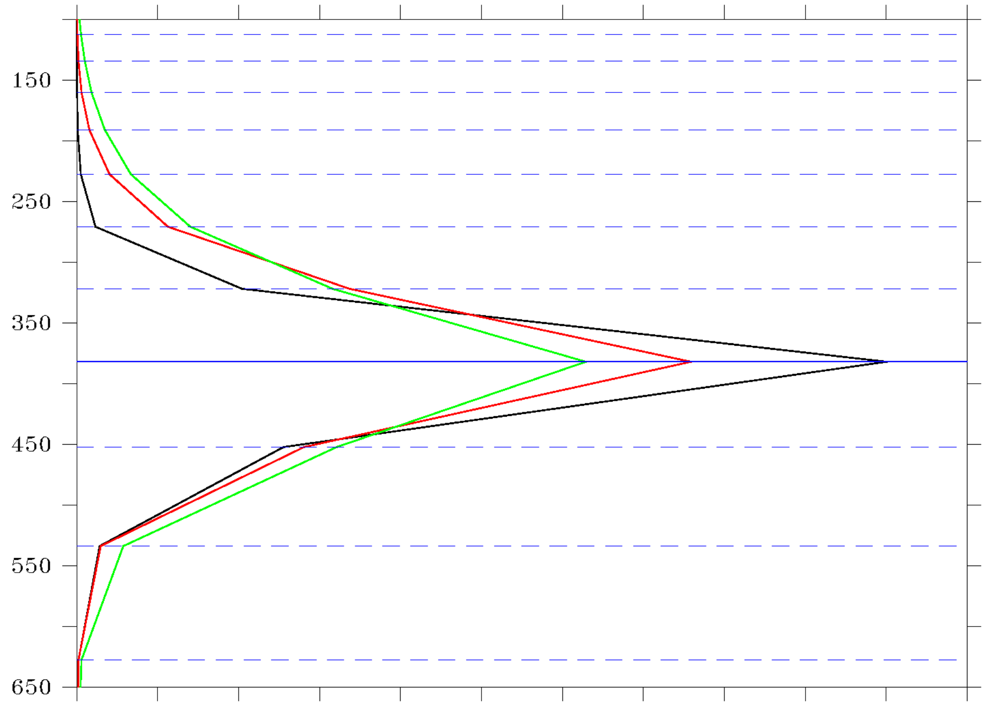

Figure 3.21.: Simulated vertical tracer spread, 7 (black), 20 (red) and 30 (green) months after release in the TRATL01 experiment TRE001. The blue lines depict the locations of the model's depth levels; the tracer was injected at the depth, given by the solid blue line.

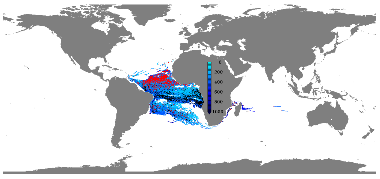

a) 7 months

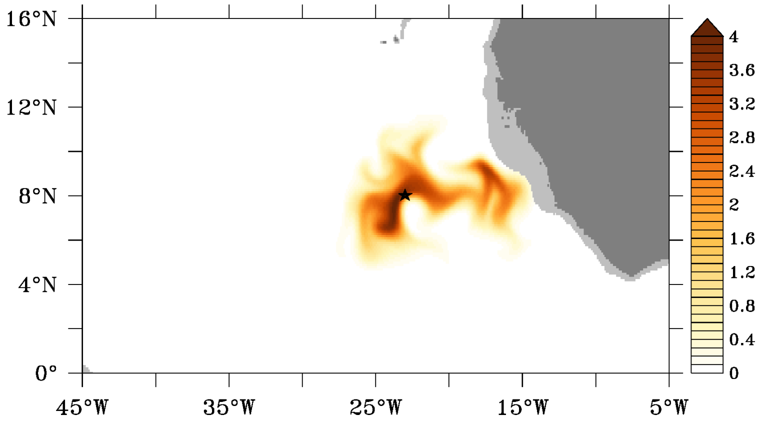

b) 20 months

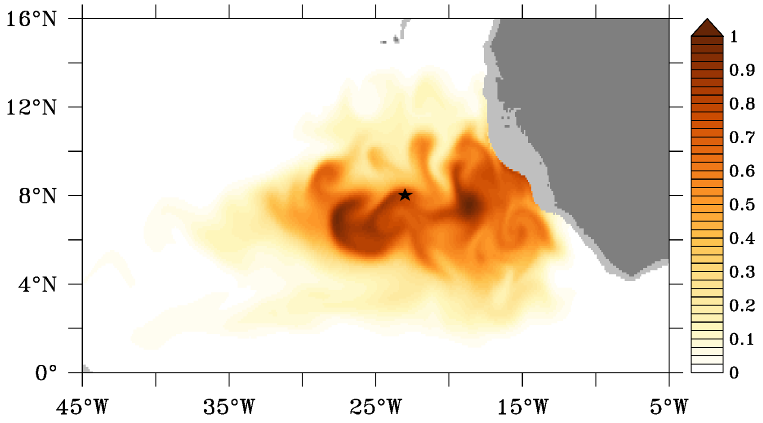

c) 30 months

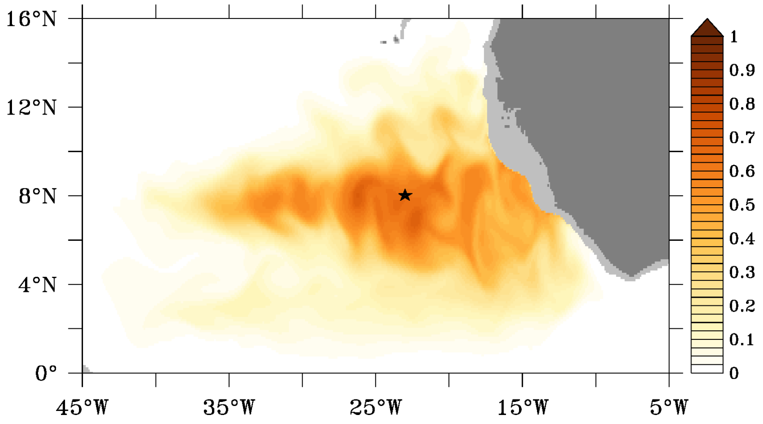

Figure 3.22.: Depth accumulated tracer distribution (arbitrary units) 7 a), 20 b) and 30 c) months after the release in TRATL01 (note the different scales for the first and the latter two distributions)

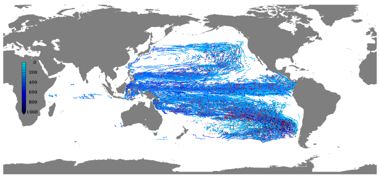

The vertical tracer displacement of O(10 m) relative to the release density layer as seen in the observations [Banyte et al. (2012)] cannot be resolved in the model as the layer thickness, where the tracer is injected is 70 m. A tendency to mix the tracer upward can be seen (figure 3.21), but the focus here is on the horizontal spreading.

In the modelled tracer distribution, zonal mixing also appears stronger than meridional mixing. The extent of the tracer patch, given as the distance between the first and last occurrences of tracer in zonal or meridional direction 7 months after its release is about 13° in longitude and 7° in latitude. After 20 as well as 30 months, the zonal extent is about 30°, whereas the meridional extent increases from about 13° after 20 months to 16° another 10 months later with overall decreased, smeared out concentration levels. This leads to a factor of about two between the zonal and meridional mixing confirming the findings from Banyte et al. (2012).

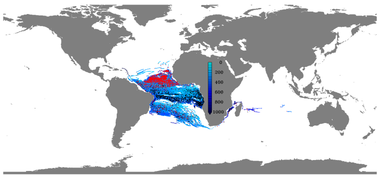

3.5. Current variability in the tropical south east Pacific Ocean

The circulation in the Tropical South East Pacific Ocean, where a very pronounced OMZ is located, was investigated by Czeschel et al. (2011). Observational glider data and shipboard ADCP sections were compared to simulated velocity fields from an assimilation model (SODA) [Carton and Giese (2008)] and TROPAC01 (see figure 3.23 for a reproduction of their figure 2b-d).

Czeschel, R., L. Stramma, F. U. Schwarzkopf, B. S. Giese, A. Funk, and J. Karstensen (2011), Middepth circulation of the eastern tropical South Pacific and its link to the oxygen minimum zone. J. Geophys. Res., 116, C01015, doi:10.1029/2010JC006565.

3.5.1. Zonal current structure

A shipboard ADCP section at ∼86° W was carried out in February 2009 and compared to simulated velocity fields from February 2002 by Czeschel et al. (2011) (figure 3.23). The choice of a different model year was dictated by the limitation of the model integration to the year 2007, at the time of the study; 2002 was chosen due to its comparable ENSO characteristics to those in 2009. Some observed current features could be reproduced with the models, whereas some could not be found within the model fields. Czeschel et al. (2011) attributed the mismatch between observed and modelled velocity fields to deficits in the models. Another factor that could contribute to the differences is a potential discrepancy between the years 2009 and 2002. The latter argument is investigated and supported here.

The experiment TROPAC01-IA_old, used in Czeschel et al. (2011) is an earlier version of TROPAC01-IA, where no eddy parameterization (GM, Gent and McWilliams (1990)) was used in the base model and the special treatment around the maritime continent (no-slip, see section 2.1.6) was not introduced yet. Another difference to TROPAC01-IA is the absence of an island in the Lombok strait that influenced the Indonesian Throughflow and was therefore added in the more recent version. The forcing period for TROPAC01-IA_old was restricted to the period 1948 to 2007 while it reaches the end of 2009 in TROPAC01-IA. TROPAC01-IA_old was initialized after an interannually forced spin-up in ORCA05 without GM for 25 years, whereas TROPAC01-IA follows a 80 years long climatological spinup in ORCA05 with GM. Here, a comparison between the old model results and the current structure in the new experiments in 2002 and additionally 2009 is presented (figure 3.24).

The change in the configuration between TROPAC01-IA_old and TROPAC01-IA does not affect the most prominent circulation features in the south eastern tropical Pacific Ocean: at ∼86° W in February 2002 both experiments (figure 3.24a and b) show a strong EUC (maximum velocity: ∼0.5 m/s in both experiments) at the equator with its core at about 70 m depth. Below the eastward flowing EUC, a deep reaching (600 m) westward velocity patch is simulated. Another eastward current is simulated between 4° S and 3° S at 100 m depth. These features are also present in the

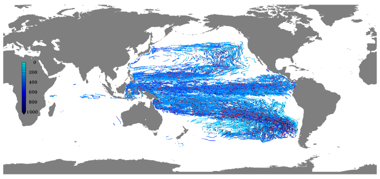

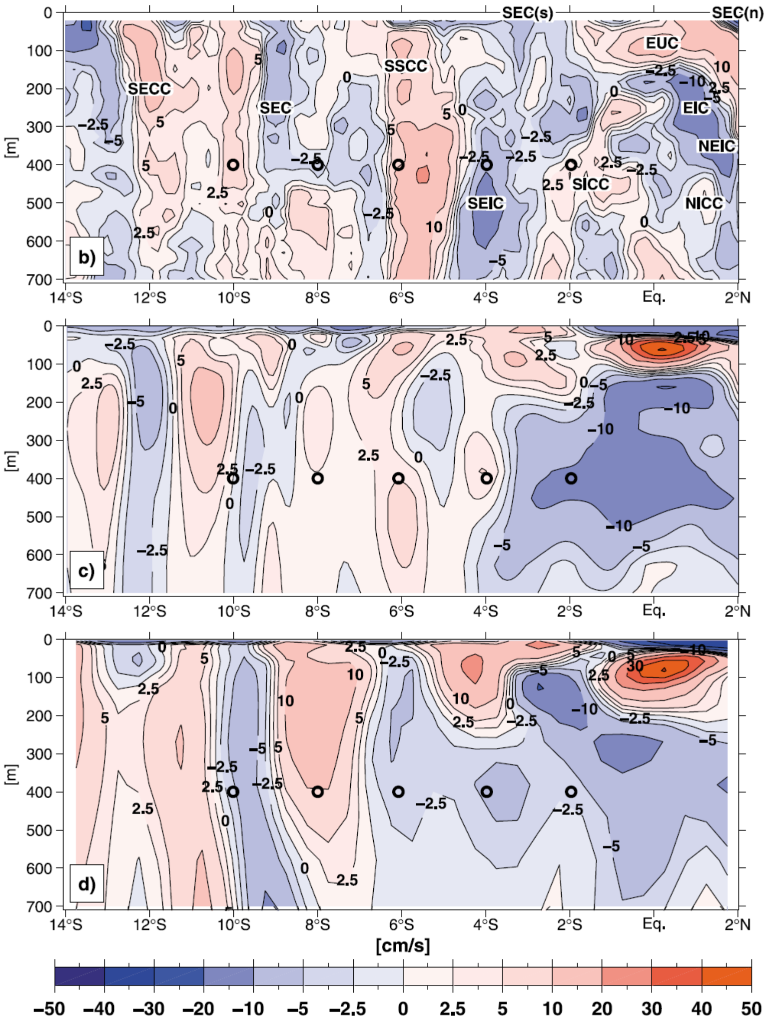

Figure 3.23.: Zonal velocity [cm/s] b) from ADCP measurements at 85°50'W in February 2009, c) velocity from TROPAC01 at 85°48'W in February 2002, and d) SODA model velocity distribution at 86° W in February 2002. The black circles at 400 m depth at 10° S, 8° S, 6° S, 4° S, and 2° S are the deployment locations of the floats. (Figure taken from Czeschel et al. (2011), figure 2 b-d; note that the discrepancy in longitude is due to the model grids.)

February 2002 data, given by the assimilation model SODA (figure 3.23d). The SSCC in both TROPAC01 experiments is located at about 6° S reaching from ~30 m down to more than 700 m depth. This current is shifted south in SODA. The zonal current bands south of ~8° S vary in their meridional position between both, TROPAC01-IA_old and TROPAC01-IA as well as TROPAC01 and SODA, suggesting a more sensitive and more variable current field there.

The comparison between TROPAC01-IA in February 2002 and 2009 (figures 3.24b and c) for the region north of 4° S shows two completely different patterns: in 2002 the strong EUC and the west-

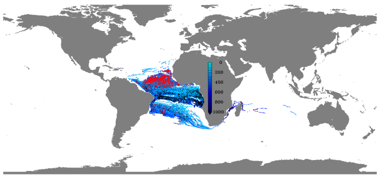

a) TROPAC01-IA_old 2002

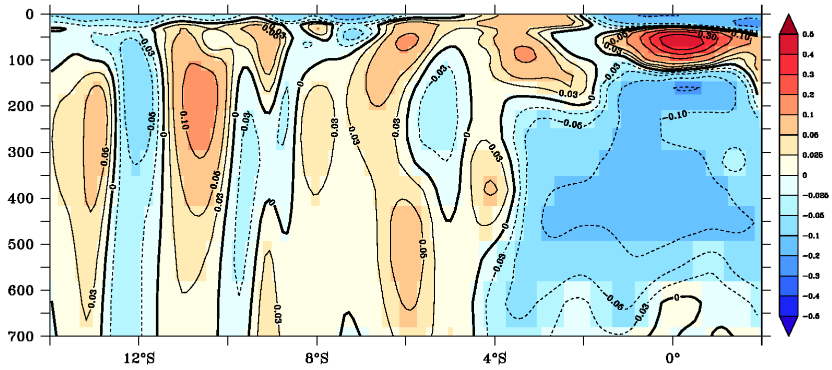

b) TROPAC01-IA 2002

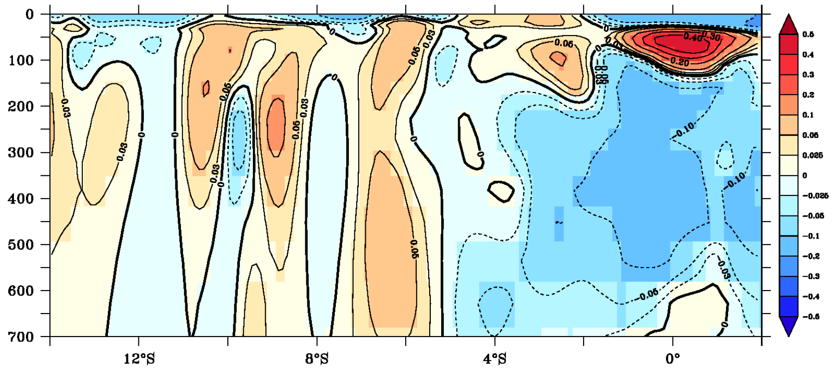

c) TROPAC01-IA 2009

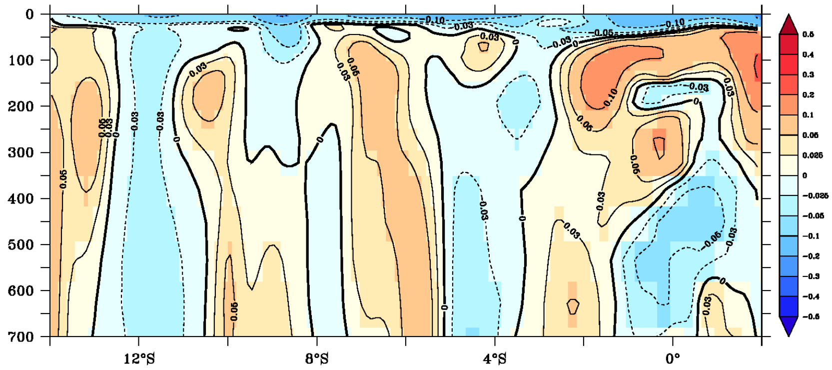

Figure 3.24.: Zonal velocity [m/s] at 85.83° W in February 2002 from TROPAC01-IA_old a), based on the same data as 3.23, c), from TROPAC01-IA b) and in February 2009 from TROPAC01-IA c)

ward velocity below dominated the structure, whereas the EUC in 2009 is much less pronounced and located off-equatorial (see figure 3.25 for more details on the EUC location). Below these currents, in the 2009 field, east- and westward flowing currents are simulated that can be identified as the EIC, the NEIC and the SICC and possibly the NICC. A comparison of this structure to the observed current field in February 2009 (figure 3.23b) shows a very good agreement in all mentioned

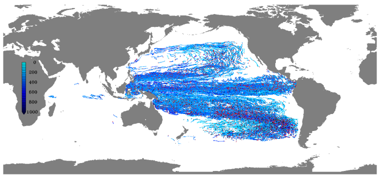

features, except for the NICC that is located further down the water column in TROPAC01-IA. The SSCC is similar between TROPAC01-IA_old and TROPAC01-IA and also reproduces very well the observations. The SEIC and SEC marked in figure 3.23b) can easily be identified now, being not as clear in the 2002 fields. The SECC is shifted south compared to the observations but still present in TROPAC01-IA.

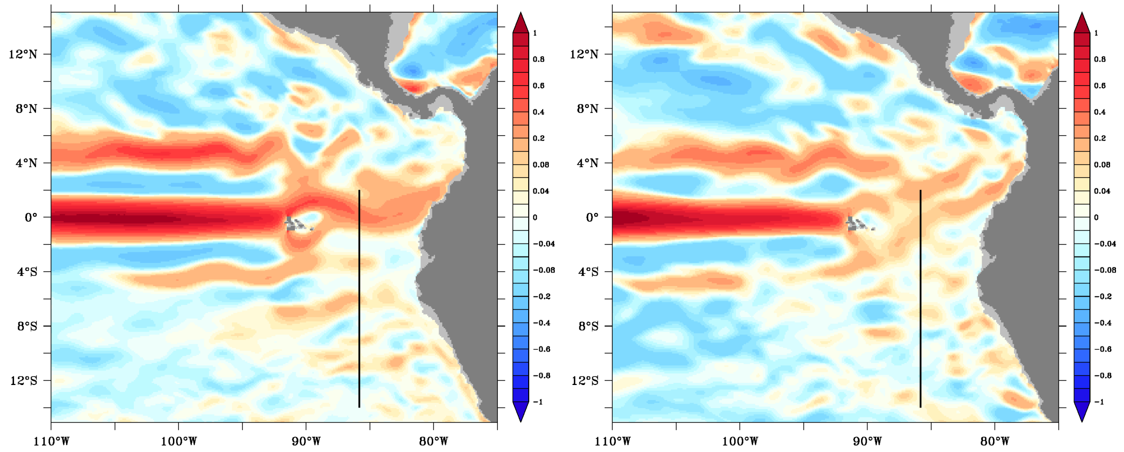
a) 2002, 50-100 m

b) 2009, 50-100 m

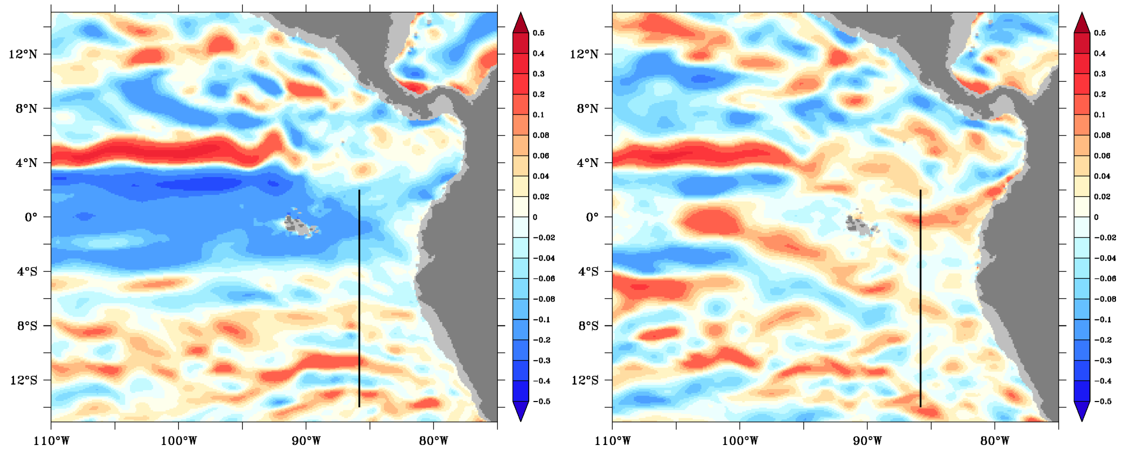
c) 2002, 250-300 m

d) 2009, 250-300 m

Figure 3.25.: Zonal velocity [m/s] averaged between 50 m and 100 m (top) depth and 250 m and 300 m (bottom) in February 2002 a) and c) and in February 2009 b) and d) from TROPAC01-IA. Black lines indicate the sections in figure 3.24.

In conclusion, TROPAC01 simulates a realistic zonal current field in the tropical south east Pacific Ocean in February 2009. In addition, the comparison between 2002 and 2009 depicts the high variability in the current field. Since SODA is an assimilation model and therefore includes observational data, the similarity between the 2002 field in TROPAC01 and SODA supports the usefulness of TROPAC01 for studies of variability, mechanisms and pathways in the eastern tropical Pacific.

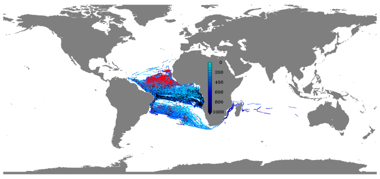

A further look into the horizontal current structure in TROPAC01-IA for February 2002 (TROPAC01-IA_old produces comparable current fields and is therefore not shown here) and 2009 confirms the important role of the Galapagos Islands on the circulation east of them as suggested by Eden and Timmermann (2004). The weak and off-equatorial located EUC along the section at ∼86° W can be explained by a bifurcation of the EUC when it impinges on the Galapagos islands (figure 3.25, top): The zonal current structure along the equator, west of the Galapagos islands shows a strong EUC and the well defined westward southern and northern SEC. When the EUC hits the Galapagos Islands, it bifurcates into a northern and a southern branch [Lukas (1986)] to pass around the islands and seems to eliminate the two SEC branches. In February 2002 (figure 3.25 a) the NECC and SECC get connected with the EUC after its bifurcation and vanish east of the Galapagos islands, where the two branches of the EUC reunify and build a rather strong EUC at ∼86° W (see figure 3.24 b). In February 2009 the EUC west of the Galapagos islands is weaker than in 2002 and more diffuse east of the islands. The current core, that is identified as the EUC in figure 3.23 a) appears to be a mixture between a part of the EUC and parts of the SECC, however it is hard to identify which current is seen in the section.

At depth, between 250 m and 300 m depth, the equatorial current structure in February 2002 differs fundamentally from the one in 2009 (compare figures 3.24b and c, as well as figures 3.25c and d). This discrepancy is not only restricted to the region east of the Galapagos islands but is already very pronounced to the west of the islands. In 2002 a swath of westward flowing water opposes the clearly defined nSEC and sSEC structure, interrupted by an eastward conjunction of the NICC and the SICC at the equator. The structure east of the Galapagos islands in 2002 reproduces the swath of westward currents whereas in 2009 the current structure is more variable and a clear identification of individual currents is problematic.

3.5.2. Variability in zonal currents

The two velocity sections shown above for the model years 2002 and 2009 represent two different snapshots of the current field. They point to a strong variability on different timescales, west and east of the Galapagos Islands, that is elucidated here (see figures 3.26 to 3.29).

West of the Galapagos Islands at 102° W, between 50 m and 100 m depth, where the EUC core is located in the eastern part of the Pacific Ocean, annually averaged zonal velocities show meridionally alternating eastward and westward currents (figure 3.26a). North of ∼2° S the most prominent current bands are the EUC at the equator, the nSEC centered at 2° N and the NECC between 4° N and 6° N. Their interannual variability is low and only marked by slight variations in the meridional extent and the exact location as well as the strength of their cores. South of 2° S the velocities change signs during the ten years but the absolute values are very small within this depth range.

Monthly averaged velocities (figure 3.26b) already show stronger variability. The EUC shows a sea-

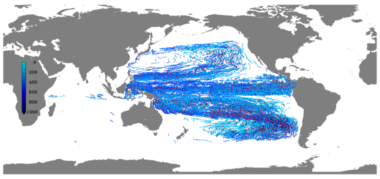

a) Annual

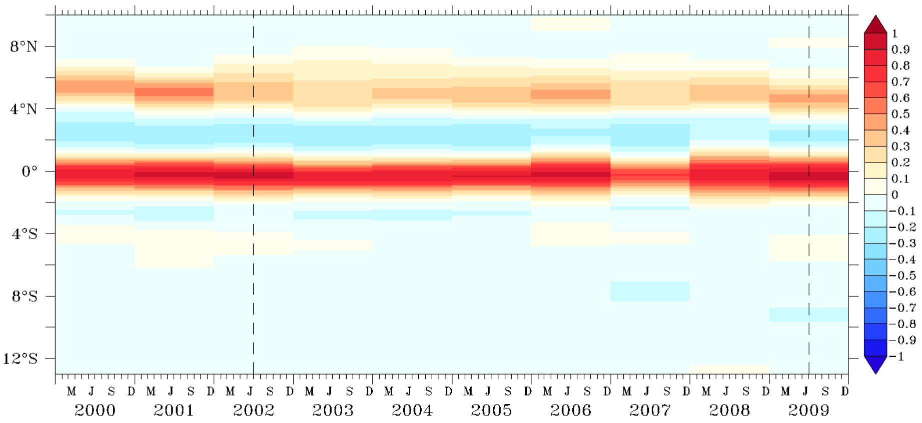

b) Monthly

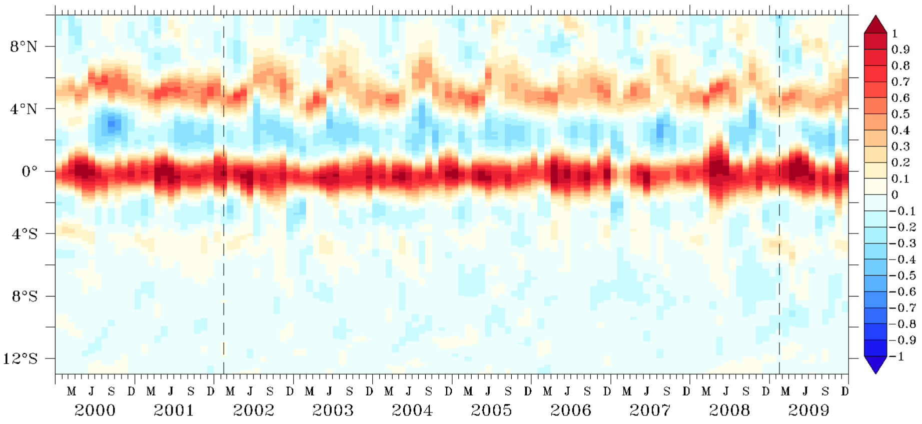

c) 5-daily

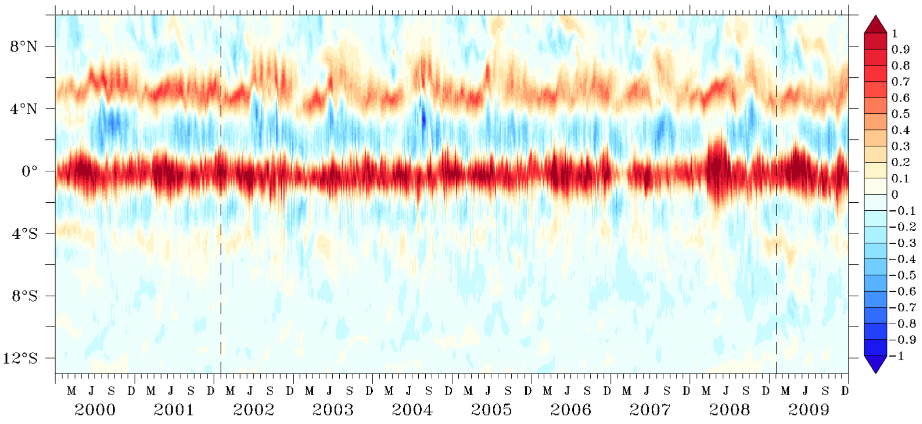

Figure 3.26.: Zonal velocity at 102° W averaged between 50 m and 100 m depth based on annual a), monthly b) and 5-daily c) averages. The dashed lines mark the points in time, discussed before.

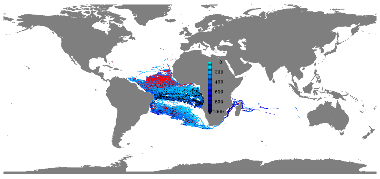

sonal cycle with highest velocities of more than 1 m/s in late spring and core velocities of ~0.6 m/s in winter along with variations in its width between 3° and 1.5°. The two most outstanding events during the ten year period from 2000 to 2009 are a rapid weakening in February 2007 which leads to the weakest EUC in this decade and a very strong and wide (more than 5°) EUC 15 months later in May 2008. The nSEC and the NECC show even stronger seasonal cycles when compared to the EUC. In the given depth range, the width of the nSEC is largest, when the EUC is narrowest and the location of the NECC, that keeps its width over time, is shifted farthest north. South of the equator, the sSEC is simulated as a weak westward current, that is however vanishing every few years, at least at the given depth range. This could mean, that the sSEC is shallower and not captured by the 50 m to 100 m depth range. South of the sSEC, at about 4° S, a band of dominating eastward velocities up to 0.3 m/s is simulated, whereas south of that band, mainly westward velocities are present.

The overall structure remains the same when going from monthly to 5-daily averaged velocities (figure 3.26c). However, the amplitudes and extreme positions and extensions of the currents are stronger and show additional variability on that timescale. For instance, the NECC that appears to be rather constant in the second half of 2002 in monthly averages, exhibits strong intramonthly fluctuations, that only become visible in the 5-daily averages; the EUC in the beginning of 2007 not only weakens but vanishes completely in at least one 5-day frame, whereas in 2008 its meridional extent reaches ~6° for a very short time.

East of the Galapagos Islands at 85.6° W the annually averaged zonal velocity between 50 m and 100 m depth shows overall weaker and less robust structures (figure 3.27a) when compared to the section west of the Galapagos Islands (figure 3.26a; note the different colour scales). The EUC is still depicted as a continuous band of eastward velocities, although its strength is very weak and varies between 0.1 m/s and 0.3 m/s. The NECC is depicted as a very weak band, and north of it overall westward velocities occur. Between the equator and 6° S overall eastward velocities are simulated, whereas south of 6° S velocities are westward, but again very weak and fluctuating around zero.

In the monthly averaged fields (figure 3.27b) a strong seasonal cycle appears within the EUC, when located at the equator, being strongest in late spring for the majority of the years analyzed here, whereas in the period 2003 to 2005 the velocities in the given depth range, right at the equator are westward. The amplitudes of the monthly averaged velocities are higher with more than 0.5 m/s in the EUC. Positive velocity signals propagate poleward to ~6° N and S from the equator, starting at the time when EUC velocities are highest. South of 6° S, the velocity field is very noisy and no identifiable, temporally persisting current band is present. North of the equator, at ~3° N seasonally re-occurring westward velocities are simulated and north of 6° N westward velocities dominate. On a 5-daily base (figure 3.27c), the overall structure again remains the same, although the higher frequency fluctuations show the same behaviour as for the section at 102° W.

At a deeper layer, between 250 m and 300 m depth, west of the Galapagos Islands at 102° W (figure

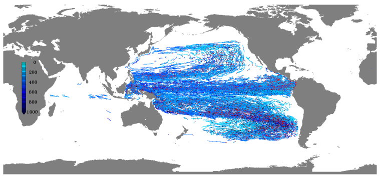

a) Annual

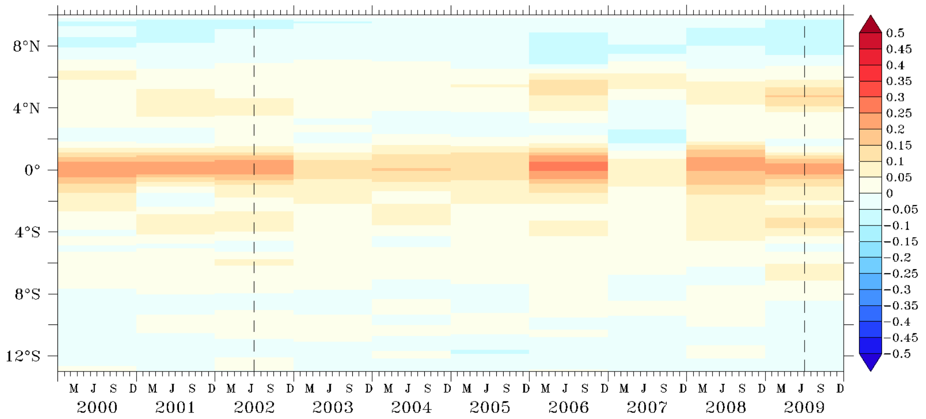

b) Monthly

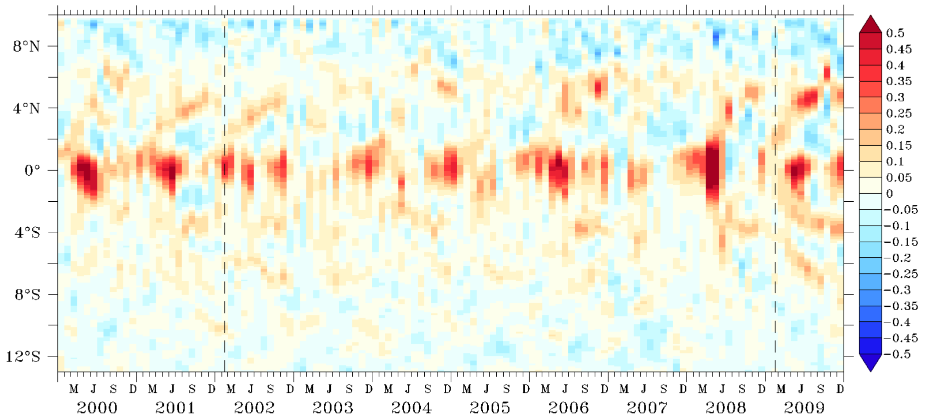

c) 5-daily

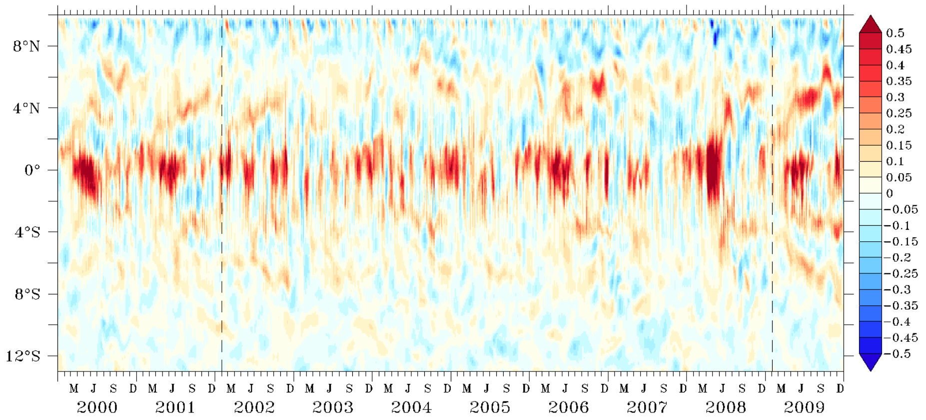

Figure 3.27.: Zonal velocity at 85.6° W averaged between 50 m and 100 m depth based on annual a), monthly b) and 5-daily c) averages. The dashed lines mark the points in time, discussed before. Note the different scales compared to figure 3.26.

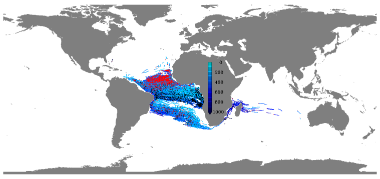

3.28) the strongest currents are the deep branch of the westward nSEC in conjunction with the NEIC at ∼3° N and the eastward Northern Subsurface Counter Current (NSCC) that might also include some deeper parts of the NECC between 4° N and 6° N. The rest of the current field is marked by weak, mainly eastward velocities south of 4° S, and weak westward bands between the equator and 4° S as well as north of 6° N.

The monthly averaged velocities still show the two rather homogenous velocity bands that dominated the annual mean field. Between 2° S and 2° N a temporally alternating velocity pattern occurs, that is not tied to a seasonal cycle. South of this band, westward velocities dominate over the ten years. North of 6° N and south of ∼4° S the velocity structure is very noisy with varying eastward and westward velocities. As for the shallower layers, the difference between the monthly and 5-daily averaged velocity fields is small in the overall current structure but still depicts fluctuations on timescales shorter than months.

At 86° W, east of the Galapagos Islands, in the annually averaged velocity field, no temporally constant or dominating structure is visible (figure 3.29a). Velocities are weak and change sign at any latitude during the ten years shown here. In the monthly averaged fields (figure 3.29b), velocity propagation from the equator poleward appear, when strong eastward or westward velocities occur at the equator. In a band south of 10° S signals that propagate equatorwards appear, whereas the rest of the section is marked by an unstructured velocity pattern. The pattern in the 5-daily averaged zonal velocities (figure 3.29c) remains similar to the one with monthly averages. However, even on that timescale strong fluctuations from one to the next data point with changing signs and significant amplitudes are visible.

The two points in time in 2002 and 2009, that were chosen to be compared to observations are marked as dashed lines in figures 3.26 to 3.29. The strong EIC at 85.6° W that is located at the equator in the 2002 snapshot is a very short-lived signal. A slight shift in time would have shown a different structure, for example only one time step before the chosen one, eastward velocities were simulated between 250 m and 300 m depth (figure 3.29). The EUC that appears to be strong and located directly on the equator in 2002 is also only a temporally short feature, that appeared right before the snapshot and vanishes two months later (figure 3.27), as in the opposite direction in 2009, where right at the equator a low EUC point in time was covered by the observations.

In the shallow layer, west of the Galapagos Islands at 102° W, the velocity signals are rather robust and a mean velocity structure might be covered by only a few measurements, whereas in the deeper layer, seasonal and higher frequency fluctuations already complicate the measurement of a mean zonal velocity field. The sampling requirements need to be even more stringent for both depth layers east of the Galapagos islands. Examining a temporally averaged velocity section seems to be meaningless here, as the fluctuations on all timescales are strong and also the spatial variability is masking any current because of the rather chaotic behaviour of the equatorial currents, after they impinge on the Galapagos Islands.

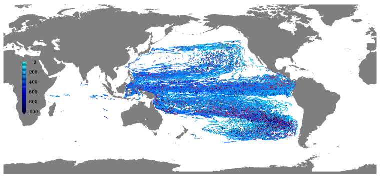

a) Annual

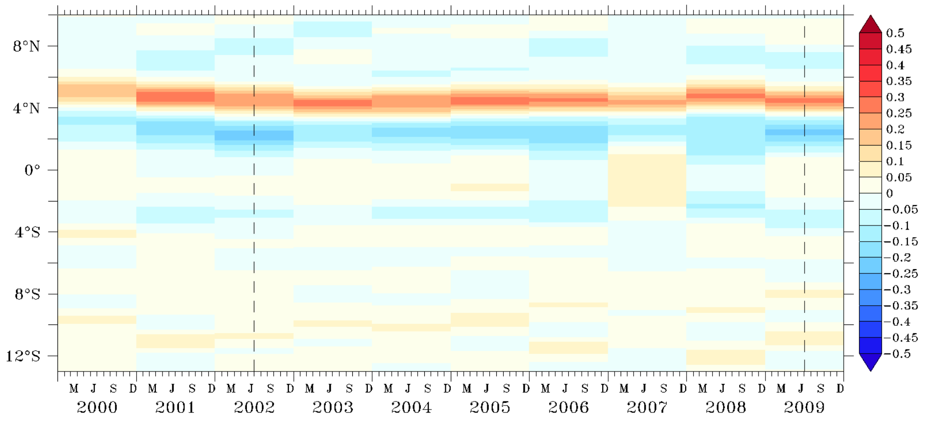

b) Monthly

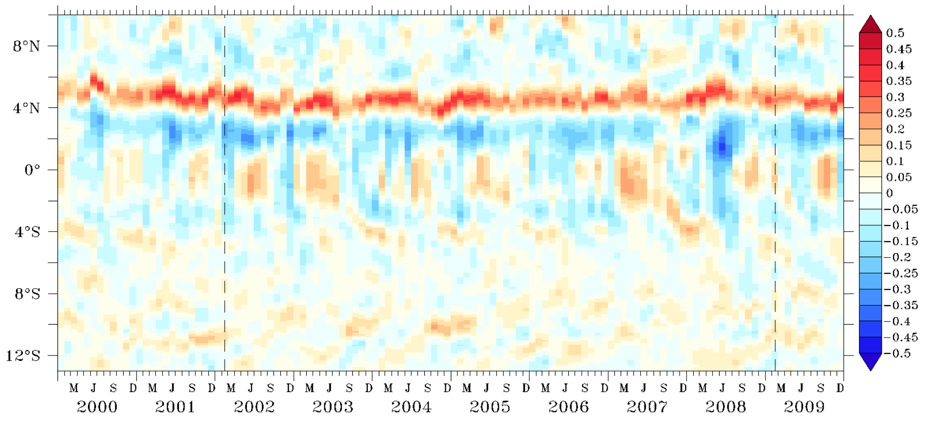

c) 5-daily

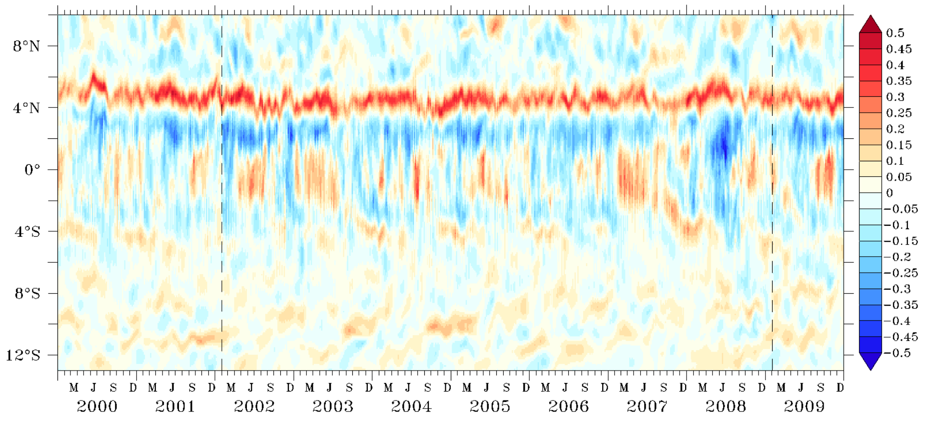

Figure 3.28.: Zonal velocity at 102° W averaged between 250 m and 300 m depth based on annual a), monthly b) and 5-daily c) averages. The dashed lines mark the points in time, discussed before.

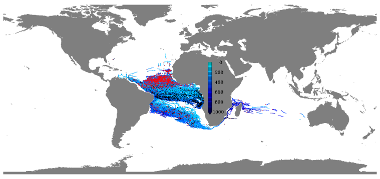

a) Annual

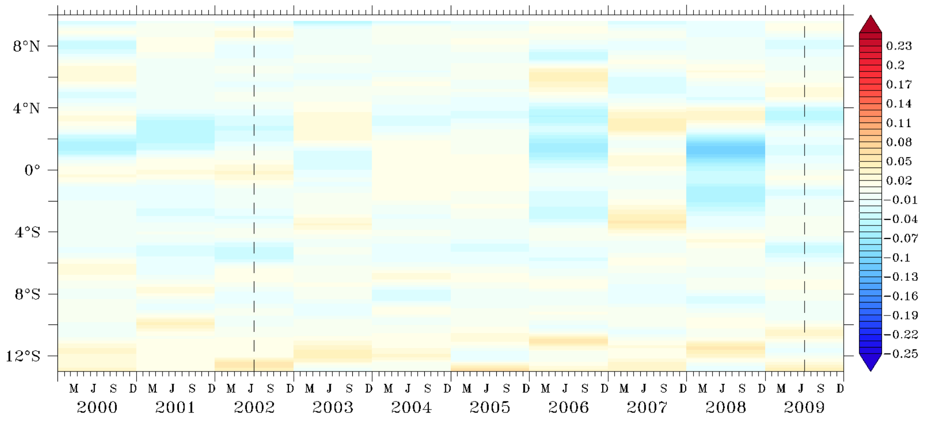

b) Monthly

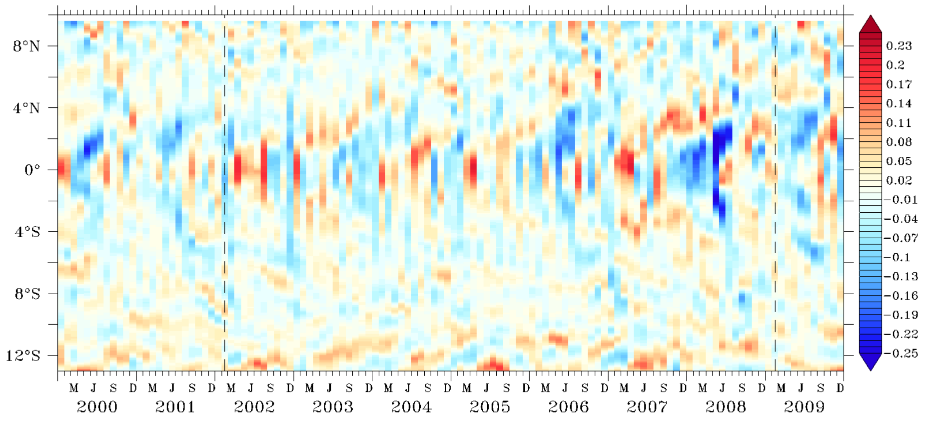

c) 5-daily

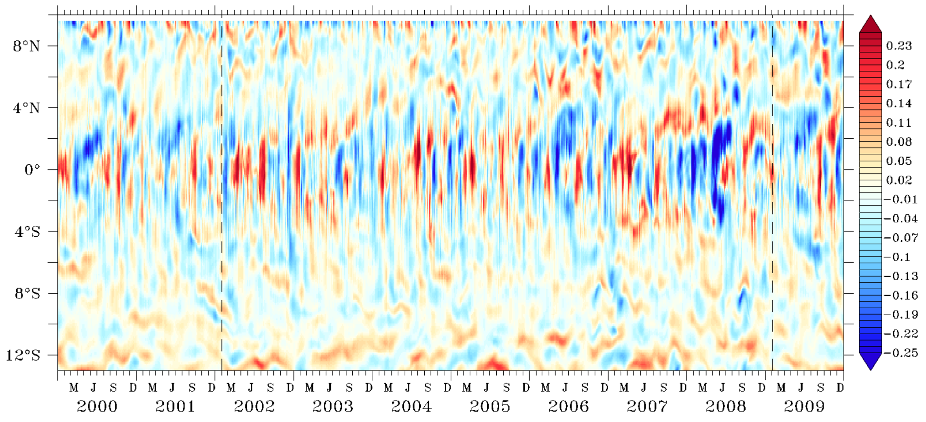

Figure 3.29.: Zonal velocity at 85.6° W averaged between 250 m and 300 m depth based on annual a), monthly b) and 5-daily c) averages. The dashed lines mark the points in time, discussed before. Note the different scales compared to figure 3.28.

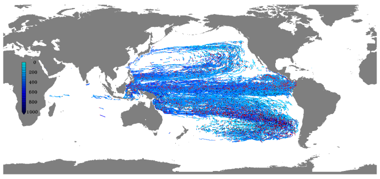

3.5.3. Sea surface height and meridional currents

A snapshot of the SSH anomaly from satellite altimetry on February 4^{th} is given in Czeschel et al. (2011), (their figure 1b) and reproduced here (figure 3.30a). A comparison with the modelled SSH at the same time (figure 3.30b) shows in general good agreement in SSH amplitudes and patterns. In a band from 5° N to ~4° S exclusively negative anomalies occur in both, observed and modelled SSH. South of this area, a tilted pattern of negative and positive SSH bands with superposed eddies is given in observational as well as modelled SSH, where in the latter, this banded structure reaches further north. The individual eddies visible in the modelled SSH pattern are not located at exactly the same positions as they occur in observations. Their locations, however, influence the velocity structure, which can contribute to the difference between observed and modelled zonal sections of the meridional velocity at the three different latitudes given by Czeschel et al. (2011) (see figure 3.31).

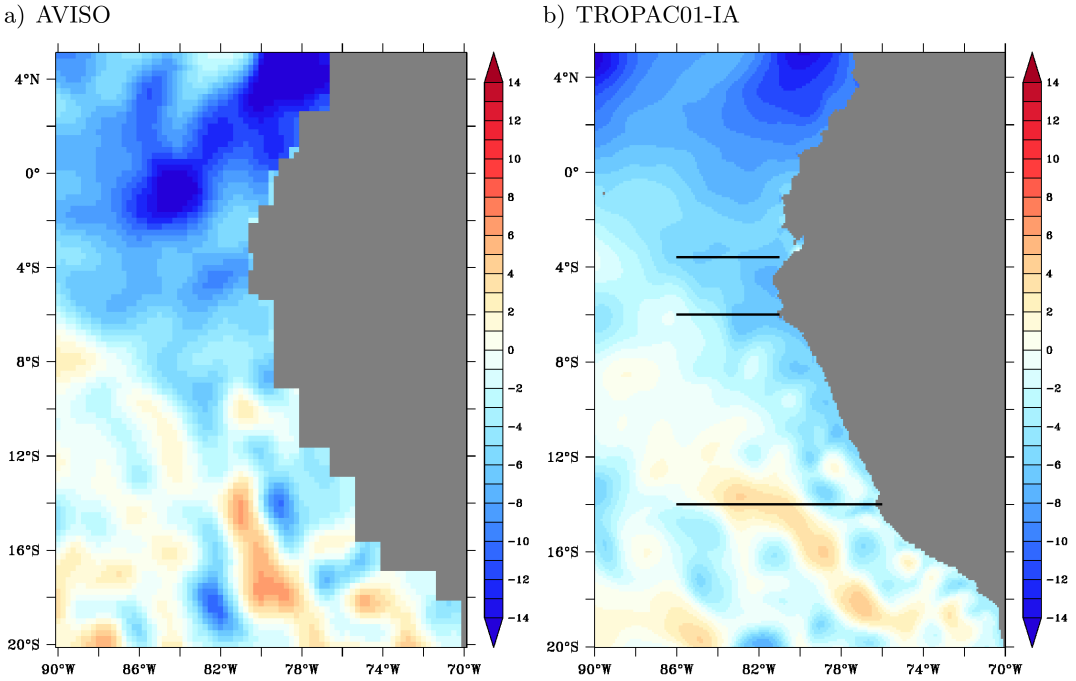
a) AVISO

b) TROPAC01-IA

Figure 3.30.: SSH anomaly (mean SSH in 2009 subtracted) [cm] on February 4^{th} from AVISO satellite altimetry a); compares to Czeschel et al. (2011), their figure 1 b) and TROPAC01-IA b). Black lines indicate the sections shown in figure 3.31.

The meridional velocities at ~3.6° S, 6° S and 14° S in late January/early February 2009 are depicted in figure 3.31 from observations (left, column taken from Czeschel et al. (2011), figure 3) and TRATL01-IA (right). The current bands in the model output seem to be overall zonally shifted compared to the observations. The northward Peru Coastal Current (PCoastalC) can hardly be seen at 6° S (but is present at the other two latitudes), whereas the southward Peru Chile Counter Current (PCCC) and Peru Under Current (PUC) are simulated at ~3.6° S and 6° S as well as the PCCC and the northward Peru Chile Current (also called Humboldt Current; HC/PCC) at 14° S.

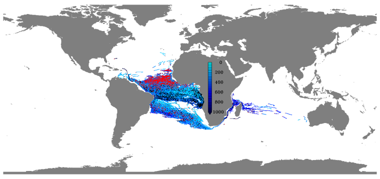

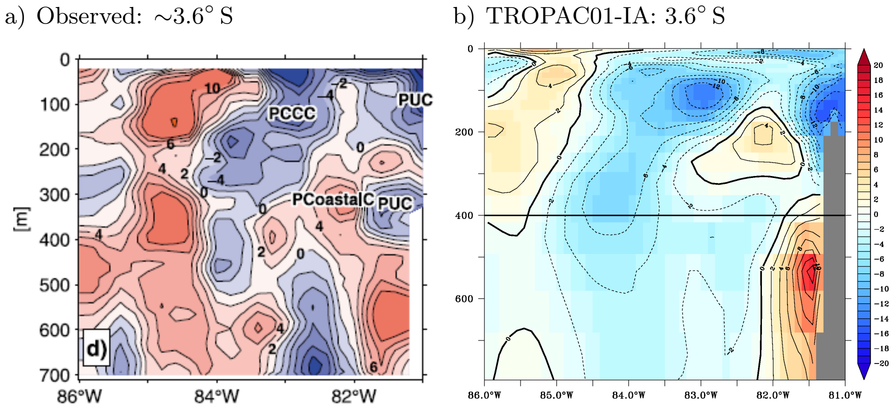

a) Observed: ~3.6° S

b) TROPAC01-IA: 3.6° S

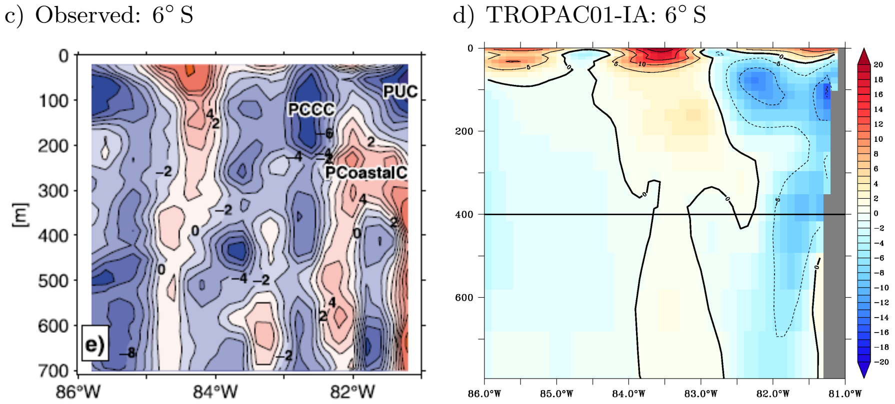

c) Observed: 6° S

d) TROPAC01-IA: 6° S

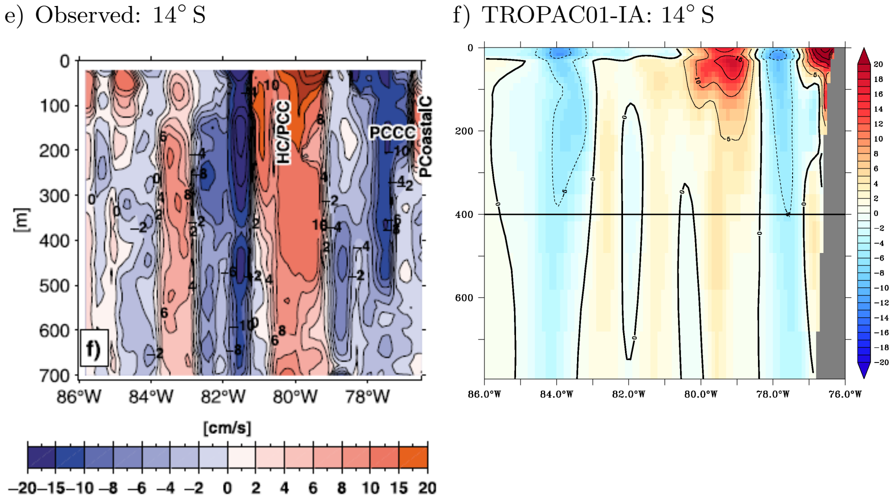

e) Observed: 14° S

f) TROPAC01-IA: 14° S

Figure 3.31.: Meridional velocity [cm/s] from observations (left figures taken from Czeschel et al. (2011), their figure 3) and TROPAC01-IA (right) at ~3.6° S a) and b) and 6° S c) and d) in early February 2009 and 14° S e) and f) in late January 2009. Sections are marked in figure 3.30b); note the different zonal extent in e) and f). Black lines indicate the depth for the Hovmoeller diagrams shown in figure 3.32.

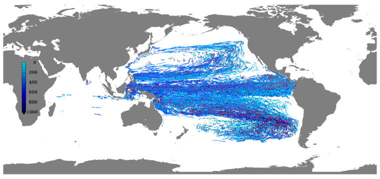

The temporal evolution of the velocity structure at 400 m depth shows a dominant westward propagation of the meridional currents (figure 3.32) partly representing the eddies depicted in the SSH anomaly pattern (figure 3.30b). At the northernmost section (figure 3.32 a), the propagation speed is faster than for the sections further south. Most signals evolve at the coast, propagate to the west and get superimposed by additional signals west of $\sim$84° W. At 6° S (figure 3.32 b) the propagation before April is not as clear but from June to October the current bands propagate straight to the west at a speed of $\sim$1.5°/month (corresponding to $\sim$6.4 cm/s), accelerating to $\sim$5°/month ($\sim$21.4 cm/s) towards the end of 2009. At 14° S the propagation east of 82° W is very homogenous throughout the entire year with a propagation speed of 1.5°/months ($\sim$6.7 cm/s). In the beginning of 2009 a southward current stays at 82° W for about five months before it aligns with the other current bands and propagates west. These propagating patterns explain, why the meridional current bands in the model are not exactly located at the same positions as in the snapshot of observations provided by Czeschel et al. (2011) (figure 3.31).

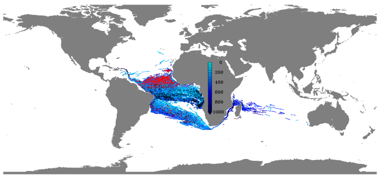

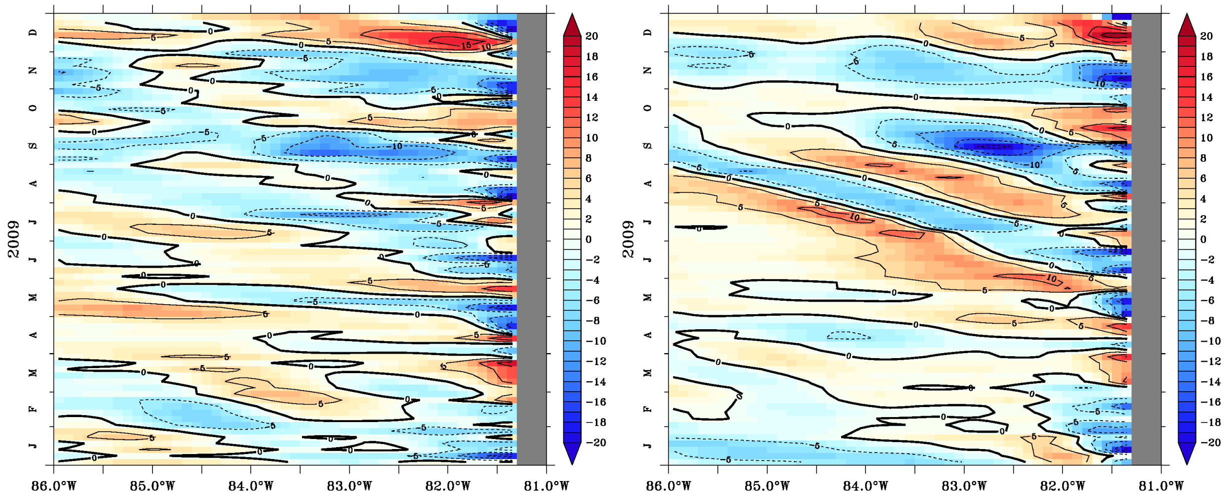
a) 3.6° S

b) 6° S

c) 14° S

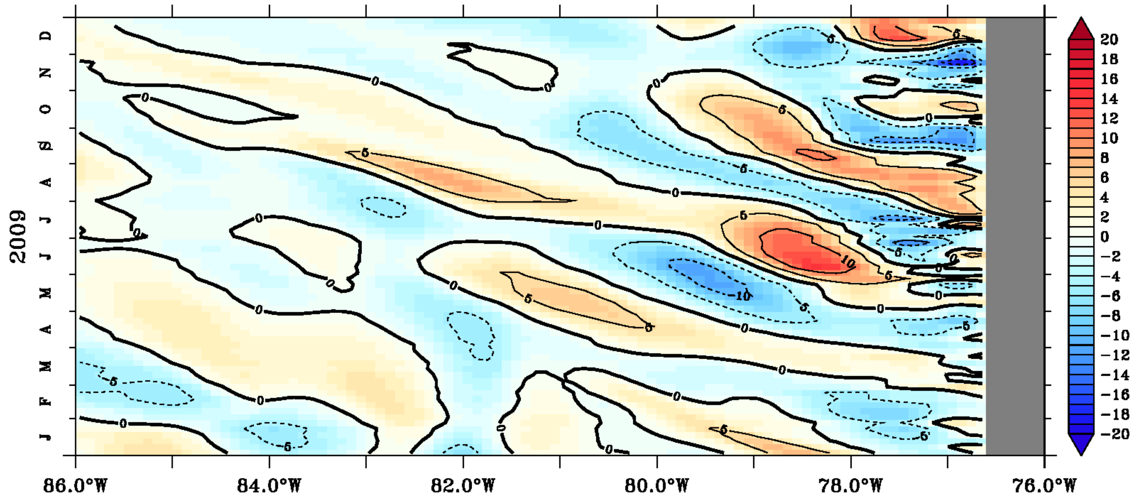

Figure 3.32.: Hovmoeller diagram of meridional velocities [cm/s] in 400 m depth at ~3.6° S a), 6° S b) and 14° S c) in 2009. Compare to figure 3.31.

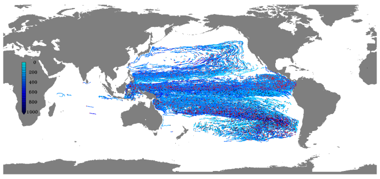

3.6. Benefits from increased horizontal resolution

To assess the influence of the model resolution on the current structures in the tropical oceans, some of the measures discussed for the nested models in the sections before are compared briefly to an ORCA05 simulation within this section.

3.6.1. Tropical Atlantic Ocean

The influence of the sampling method on the zonal current structure has been discussed in section 3.3.1; here, the change when going from the 0.5° simulation (ORCA05) to the 0.1° solution (TRATL01) is given.

a) ORCA05

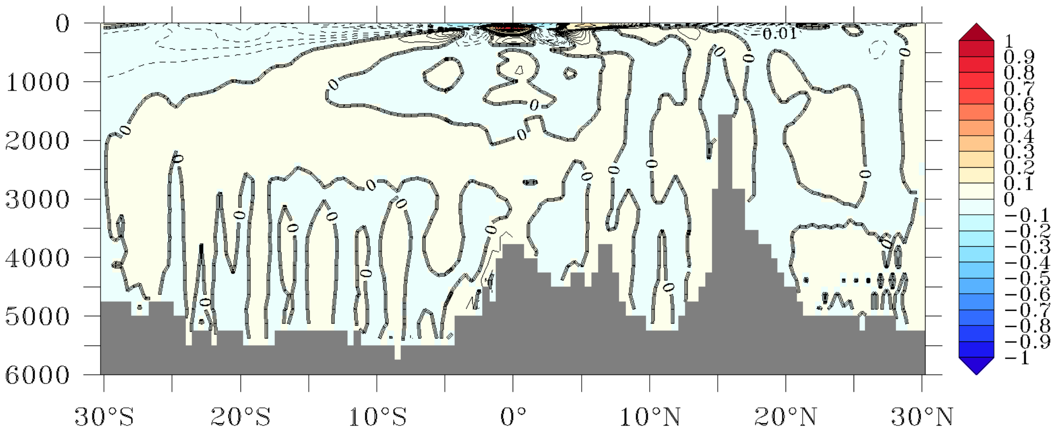

b) TRATL01

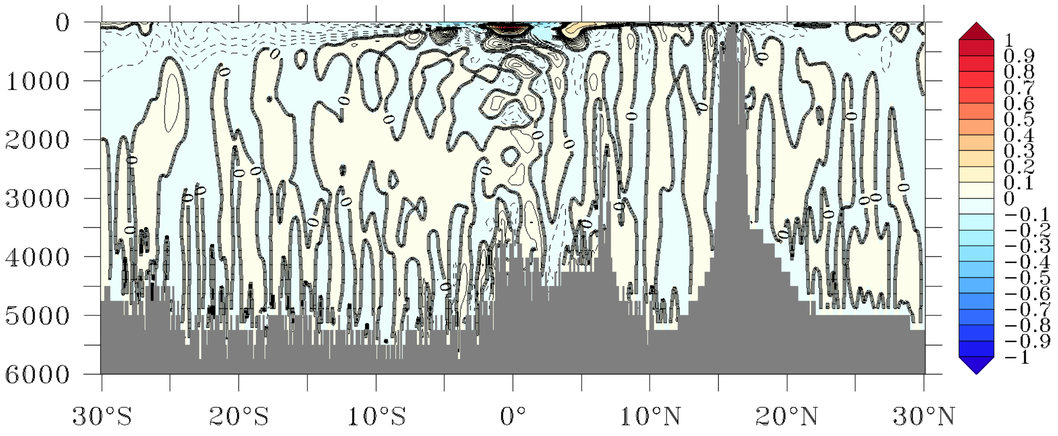

Figure 3.33.: Mean (1999 to 2008) zonal velocity [m/s] at 23° W in ORCA05 a) and TRATL01 b)

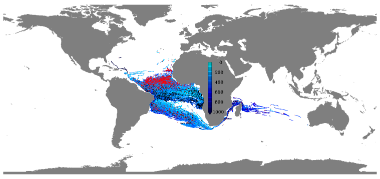

In the upper ~300 m of the water column, the zonal current structure at 23° W in ORCA05 and TRATL01 are very similar (figure 3.33), dominated by strong, alternating currents between ~6° S and 6° N, representing the eastward EUC, NECC and SEUC and the westward flowing sSEC and nSEC (see also figure 3.34). Poleward of this region and below this upper layer, the zonal velocities are smaller (~1 cm/s) in both simulations but have much more structure in TRATL01 compared to ORCA05 where wide swaths of westward and eastward velocities are simulated. TRATL01 shows strong band-like structures described before as tall jets. In ORCA05 these tall jets are restricted to the latitudinal band between 5° N and 15° N, where in the mean velocity fields from 1999 to 2008 two almost barotropic, eastward bands are simulated.

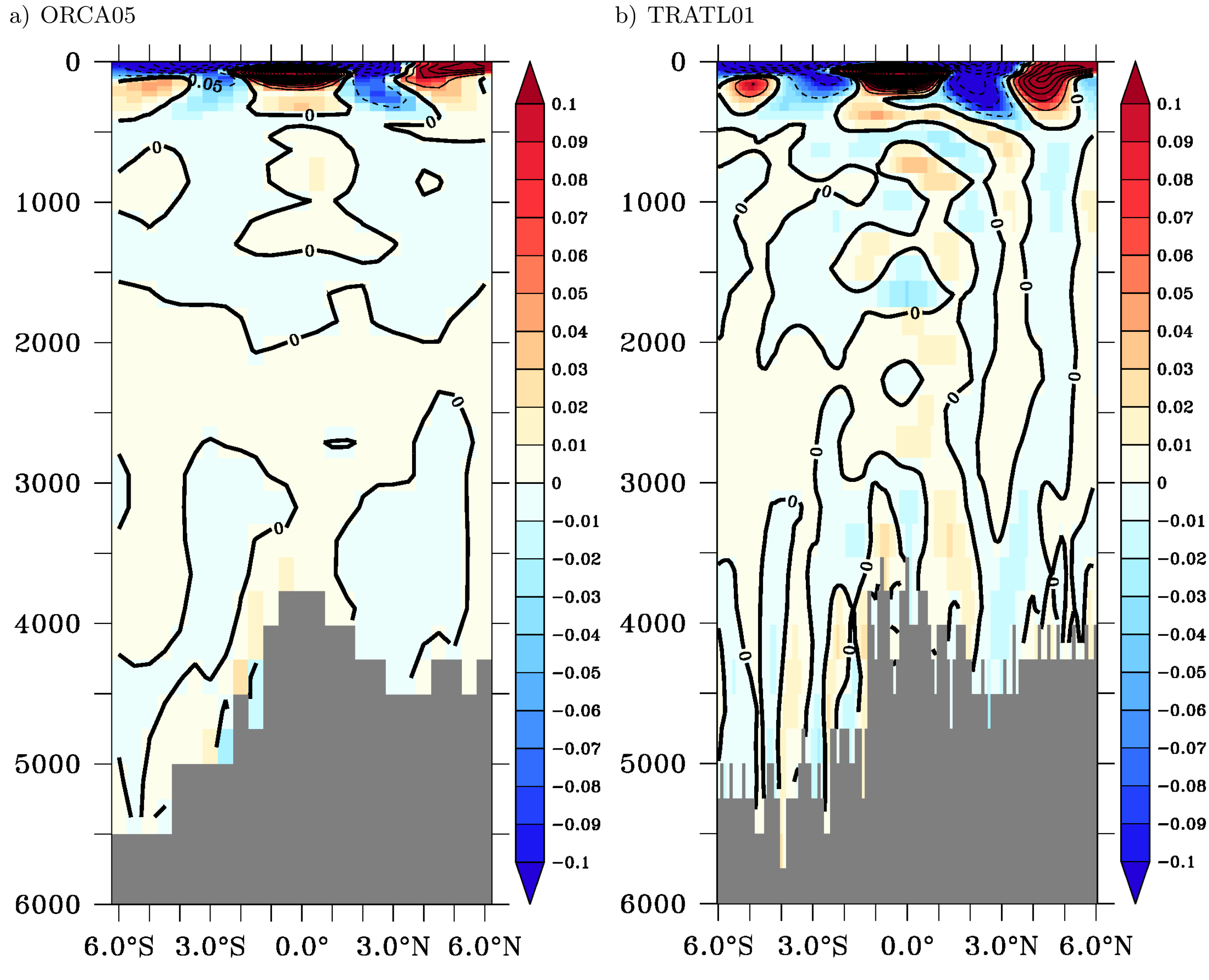

Figure 3.34.: Mean (1999 to 2008) zonal velocity [m/s] at 23° W in ORCA05 a) and TRATL01 b)

Focusing on the equatorial band between 6° S and 6° N (figure 3.34) indicates some tendency in TRATL01 to produce equatorial deep jet (EDJ) like structures, absent in ORCA05. These vertically alternating currents, that were shown to contribute to the ventilation of the eastern tropical

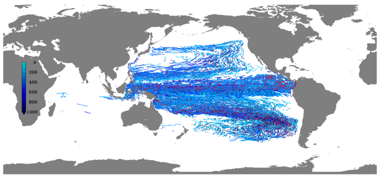

Atlantic [Brandt et al. (2012)] are simulated with core speeds of ~5 cm/s in TRATL01, comparable to the observations. The observed vertical propagation of the EDJs [Brandt et al. (2011, 2012)] is not represented in TRATL01, probably due to the coarse vertical resolution of the model.

The representation of the equatorial and off-equatorial zonal currents has an impact on the ventilation of the eastern tropical Atlantic and therefore the OMZs. The strongest current in this region is the EUC. Its zonal structure (figure 3.35), especially its eastward penetration, plays a major role in these ventilation processes [e.g. Duteil et al. (2014)]. TRATL01 shows a very strong, far east reaching EUC (figure 3.35b), whereas in ORCA05 the EUC is weaker, less deep and more concentrated towards the west. Similar resolution dependencies have been shown before [e.g. Hüttl and Böning (2006)]

a) ORCA05

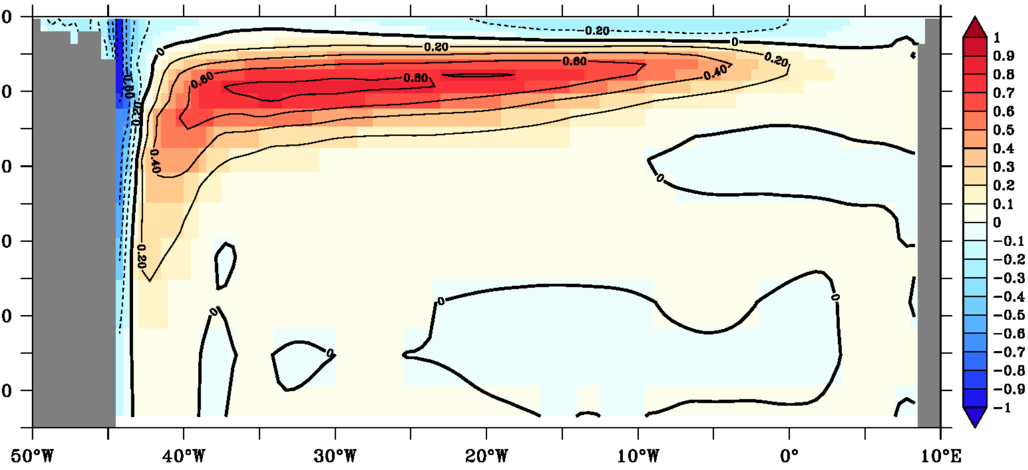

b) TRATL01

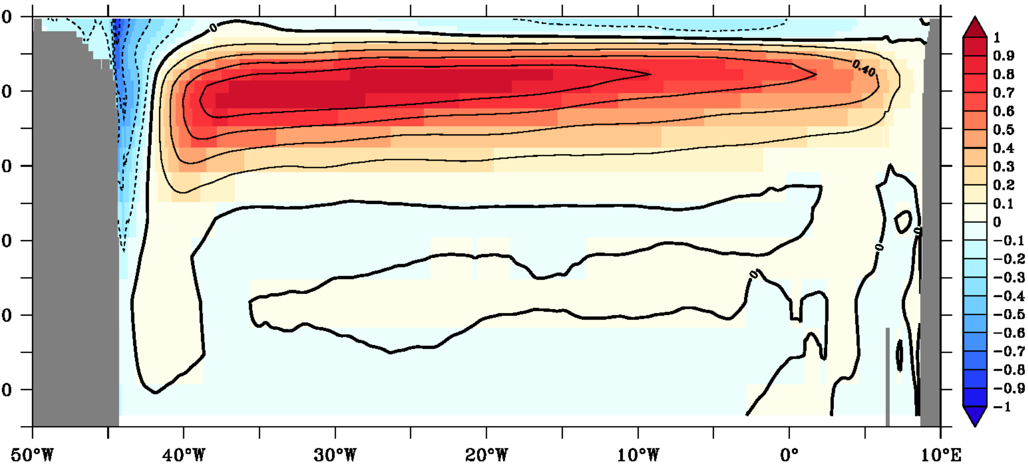

Figure 3.35.: Mean (2000 to 2009) zonal velocity [m/s] on the equator from ORCA05 a) and TRATL01 b)

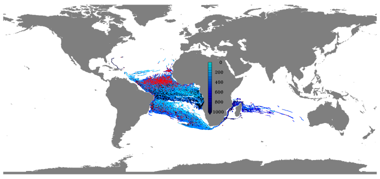

3.6.2. Tropical south east Pacific Ocean

A model-data inter-comparison of velocity snapshots in the eastern tropical Pacific Ocean (section 3.5) shows a good agreement between observed and modelled structures, when using the high resolution TROPAC01-IA simulation. Here, this high-resolution model is compared to an ORCA05 simulation. Zonal velocity snapshots at ~86° W in 2002 and 2009 depict the capability of the high-resolution model to produce the band-like structure of zonal currents as seen in observations (figure 3.36b and d). ORCA05 (figure 3.36a and c) does not show this structure. Here, the currents are overall weaker compared to TROPAC01. As in the Atlantic, the eastward penetration of the EUC is stronger in the high-resolution simulation, when compared to ORCA05. The EUC east of the Galapagos Islands, at ~86° W, for instance in February 2002, has a core velocity of ~0.2 m/s in ORCA05 while in TROPAC01 this velocity is higher than 0.5 m/s. The band-like structure in TROPAC01 is replaced by rather broad currents in ORCA05.

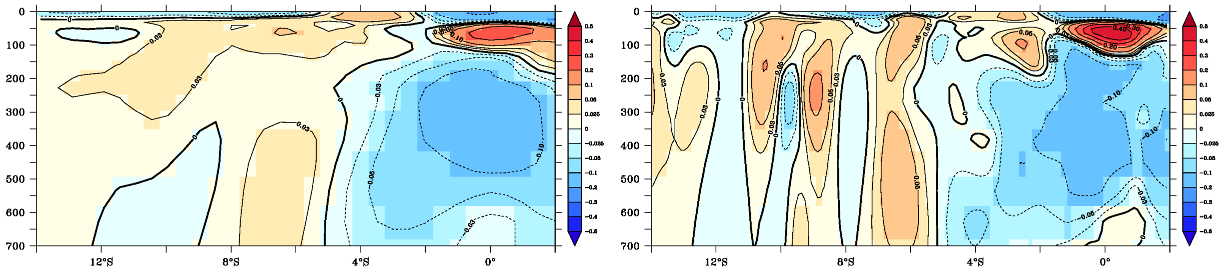

a) ORCA05, 2002 b) TROPAC01, 2002

c) ORCA05, 2009 d) TROPAC01, 2009

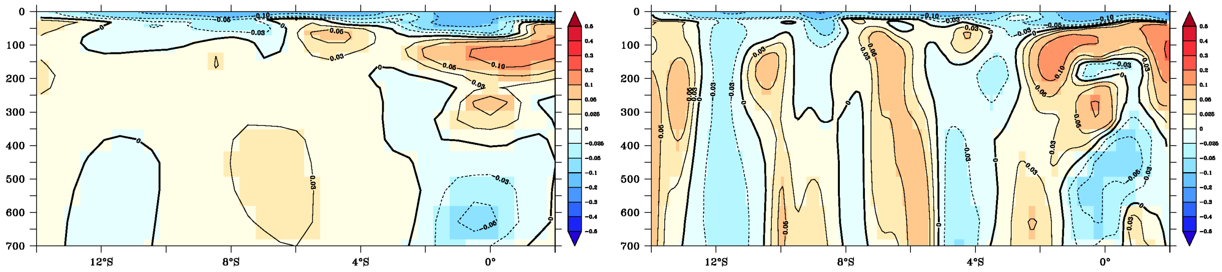

Figure 3.36.: Zonal velocity [m/s] at 85.83° W in February 2002 (top) and 2009 (bottom) from ORCA05 (left) and TROPAC01-IA (right)

It has also be shown (section 3.5), that the current structure changes a lot with time by comparing the velocity fields at two different times. The zonal velocity at ~86° W, especially close to the equator, shows a completely different structure in 2002 compared to 2009 (figure 3.36b and d). The remarkably strong westward current around the equator between 150 m and 600 m depth is depicted in both, the 0.1° and the 0.5° model experiments (figure 3.36a and b), as well as in SODA (see figure 3.23 and Czeschel et al. (2011)), although this feature appears to be weaker there. This implies, that the structure is forced by the prescribed atmospheric fields rather than being intrinsic chaotic variability.

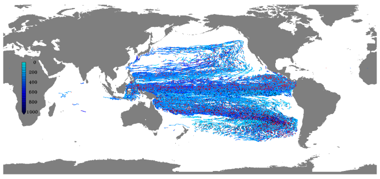

a) ORCA05, 3.6° S b) TROPAC01, 3.6° S

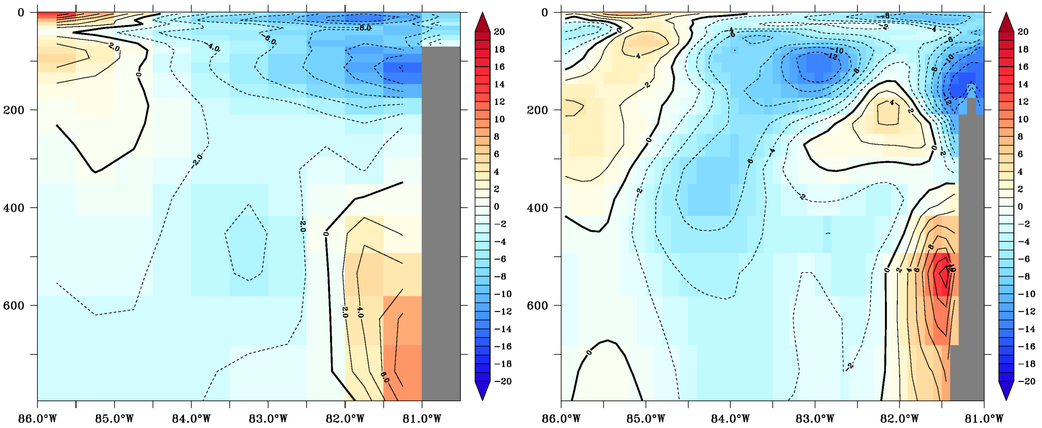

c) ORCA05, 6° S d) TROPAC01, 6° S

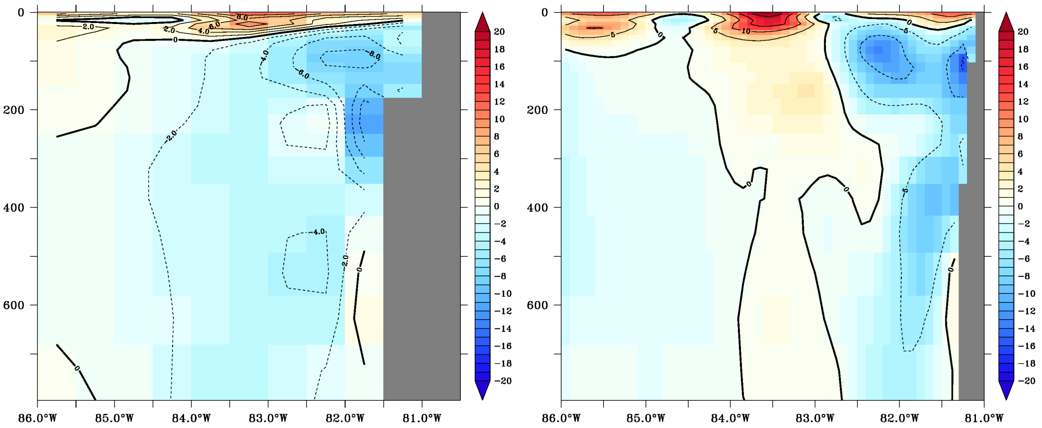

e) ORCA05, 14° S f) TROPAC01, 14° S

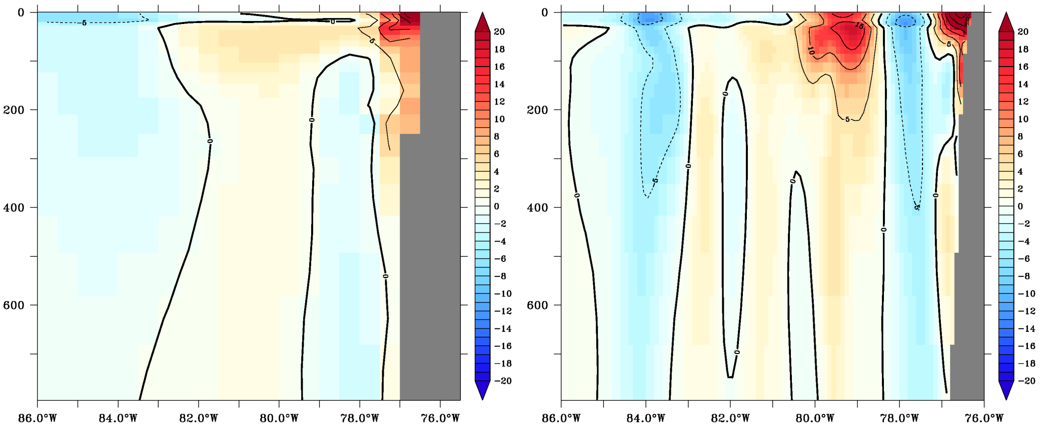

Figure 3.37.: Meridional velocity [cm/s] from ORCA05 (left) and TROPAC01-IA (right) at ∼3.6° S a) and b) and 6° S c) and d) in early February 2009 and 14° S e) and f) in late January 2009. Note the different zonal extent in e) and f).

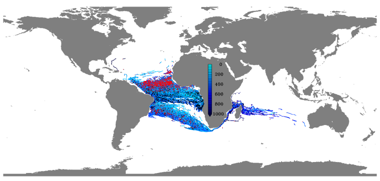

A comparison between the meridional velocity along the Peruvian coast at 3.6° S, 6° S and 14° S (figure 3.37) in ORCA05 and TROPAC01 is not as clear as for the zonal velocity. At 3.6° S (figure 3.37a and b) most features that appear in TROPAC01 are also present in ORCA05 although with different strength and not exactly located at the same positions. In the two sections further south, the current structures close to the coast are similar in both simulations, whereas the current bands depicted off-coast in TROPAC01 are either at different locations (14° S, figure 3.37c and d) or absent (6° S, figure 3.37e and f) in ORCA05. Compared to the zonal velocities, these meridional currents are weaker and show a zonally propagating behaviour (see figure 3.32). This could contribute to the mismatch between the current locations in TROPAC01 and ORCA05, where eddies are parameterized and therefore do not mask, alter or influence the mean currents.

In an 0.5° resolution bathymetry, the Galapagos Islands are non-existent. Due to their importance for the circulation east of them [e.g. Eden and Timmermann (2004)], some artificial tuning of the ORCA05 bathymetry has been done to provide a barrier for the zonal currents, represented by three land grid cells (figure 3.38).

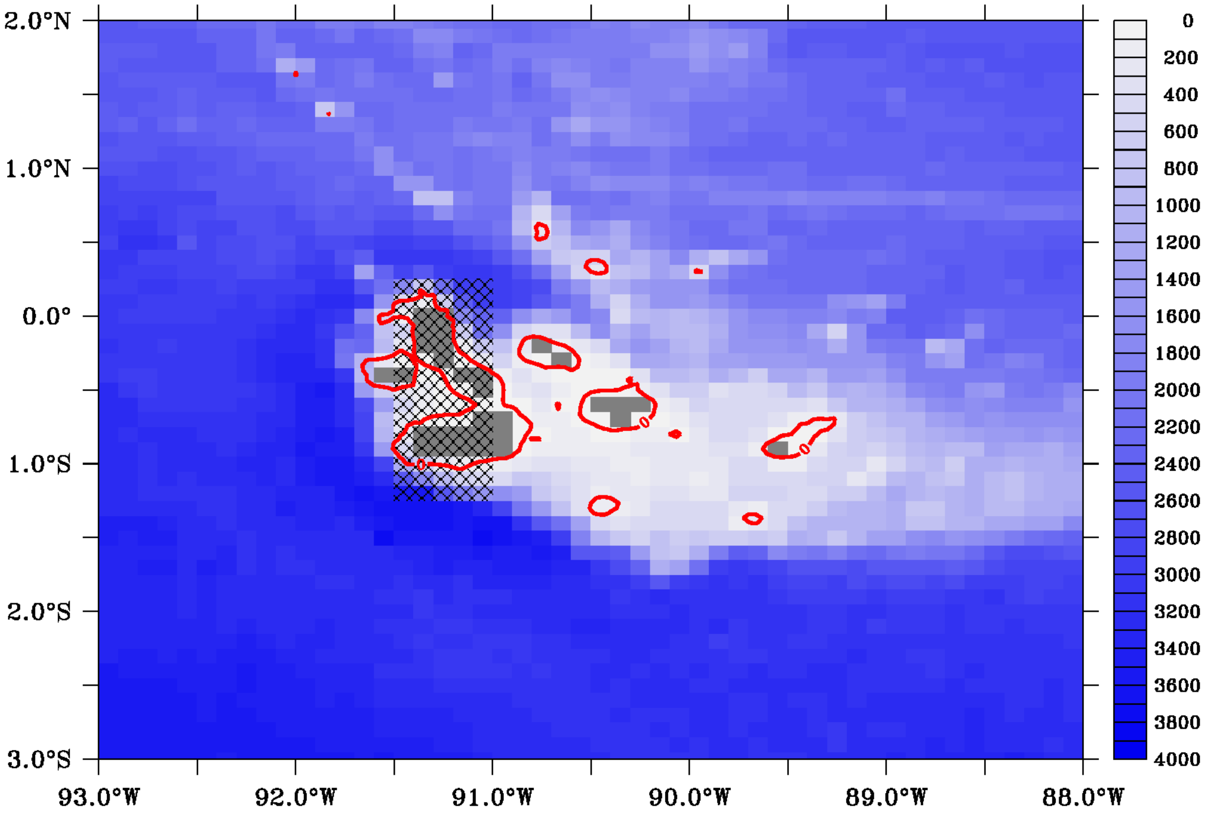

Figure 3.38.: Representation of the Galapagos Islands in TROPAC01 and ORCA05. Shaded is the TROPAC01 bathymetry; grey indicates land in TROPAC01, the cross-hatched area (representing three grid cells) is land in ORCA05; red contour gives the zero-line in ETOPO2.

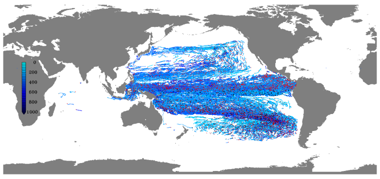

The effect of the introduction of this artificial barrier in ORCA05 is evident in the horizontal structure of the major zonal velocity bands in the eastern tropical Pacific Ocean when comparing to TROPAC01 (figure 3.39). All strong (velocities higher than 1cm/s) currents are represented in ORCA05 although they are weaker in the coarser case than in TROPAC01 and do show rather straight characteristics instead of meandering behaviours. The introduction of land points at the location of the Galapagos Islands in ORCA05 can hence be considered successful.

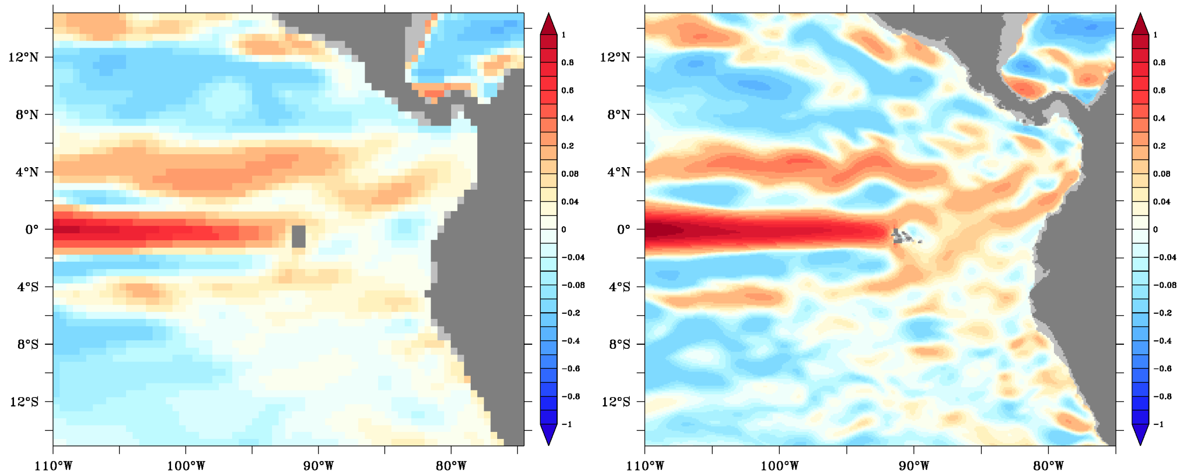
a) ORCA05, 50-100 m

b) TROPAC01, 50-100 m

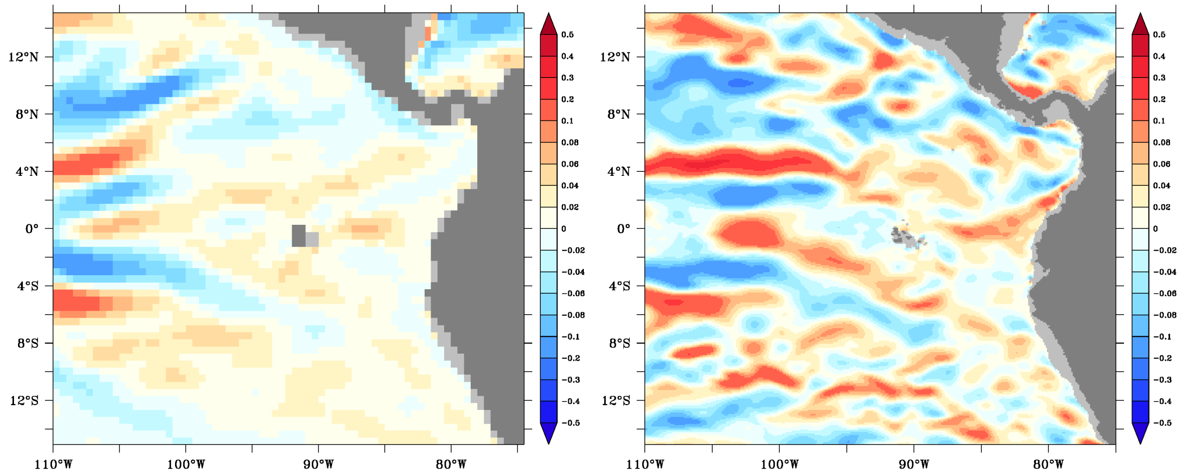
c) ORCA05, 250-300 m

d) TROPAC01, 250-300 m

Figure 3.39.: Zonal velocity [m/s] averaged between 50 m and 100 m (top) depth and 250 m and 300 m (bottom) in February 2009 from ORCA05 a) and c) and TROPAC01-IA b) and d).

4. Global ventilation processes

In this chapter, an overview of the mean circulation in the upper 1000 m of the water column derived from the ORCA05-IA simulation is given (section 4.1) to provide a framework for the interpretation of the tracer experiments described in section 4.2 as well as for the Lagrangian experiments discussed in chapters 5 and 6. The temporal evolution of the two passive tracers CONC and AGE and their meaning in the simulation of ventilation processes affecting the OMZs are described in a global context based on ORCA05-NY. The final tracer distribution is shown, focusing on the eastern tropical Atlantic and Pacific Oceans to illustrate the impact of the higher model resolution on the tracer structure (section 4.3.2).

Contents

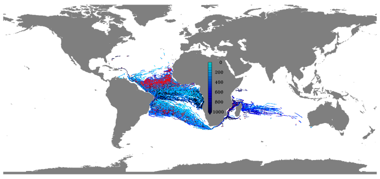

4.1. Mean circulation in ORCA05

The global barotropic streamfunction as derived from ORCA05-IA (figure 4.1) gives an integrated view on the ocean circulation. The most prominent feature is the Antarctic Circumpolar Current (ACC) [Nowlin Jr. and Klinck (1986)] in the Southern Ocean. North of the ACC, the so called supergyre [Ridgway and Dunn (2007)] is located, connecting the anticyclonic southern subtropical gyres of all three Ocean basins from the eastern Pacific via the Indian Ocean throughout the western Atlantic. The tropical Oceans are marked by the meridionally rather narrow tropical gyres, flanked by the northern subtropical gyres in all three basins. The tropical and subtropical gyres are closed by marked western boundary currents [Stommel (1948); Munk (1950)]. The subpolar gyres in the North Atlantic and Pacific Ocean close the list of the most prominent large scale circulation features.

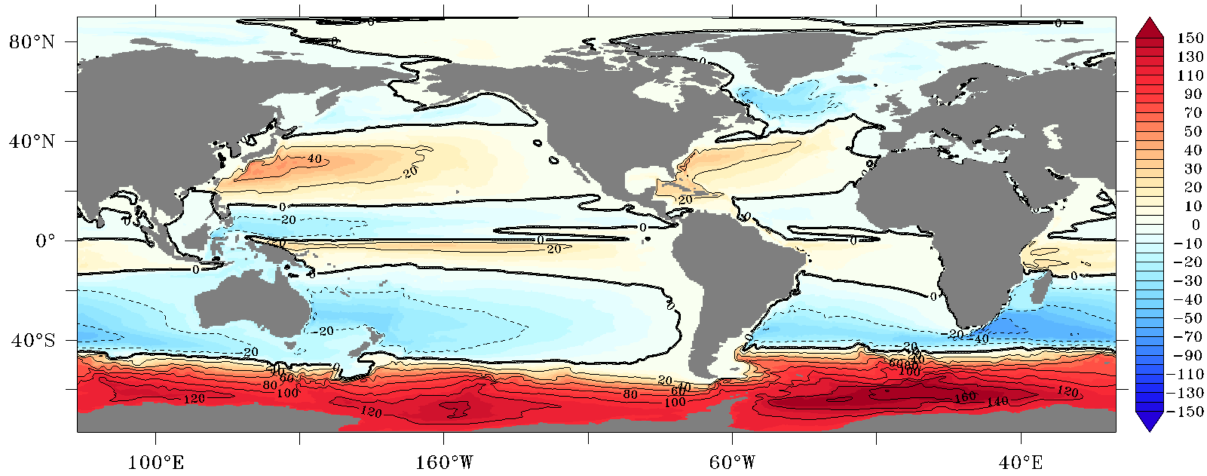

Figure 4.1.: Ten year averaged (2000 to 2009) barotropic streamfunction (Sv).

The vertical structure of these circulation features is briefly described by means of horizontal maps of temporally averaged velocity fields at different depths (figures 4.2 and 4.3) and will be analyzed in detail for the tropical Atlantic and Pacific Oceans based on the nested simulations in sections 5.1 and 6.1. At the surface (figure 4.2 a), the directly wind driven circulation is depicted, with the dominating South Equatorial Current (SEC) alongside the equator forced by the trade winds [Schott et al. (2004)] and some features of the ACC driven by the westerlies. Convergences at the western boundaries of the Ocean basins result in poleward coastal currents as well as the currents through the Indonesian passages. Below the uppermost layer, at 100 m depth (figure 4.2 b) the coastal currents prevail and the ACC features compare well to those at the surface. The most prominent currents here are the Equatorial Under Currents (EUCs) in all three basins [e.g. Metcalf and Stalcup (1967), Blanke and Raynaud (1997)] and overall off-equatorial zonal bands that evolve in the Pacific Ocean and to a weaker extent in the Atlantic. In the Indian Ocean a current evolving at the Indonesian Outflow crosses the basin westward at ∼15° S [Schott et al. (2009)].

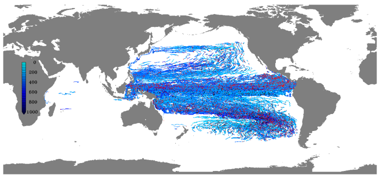

a) Surface

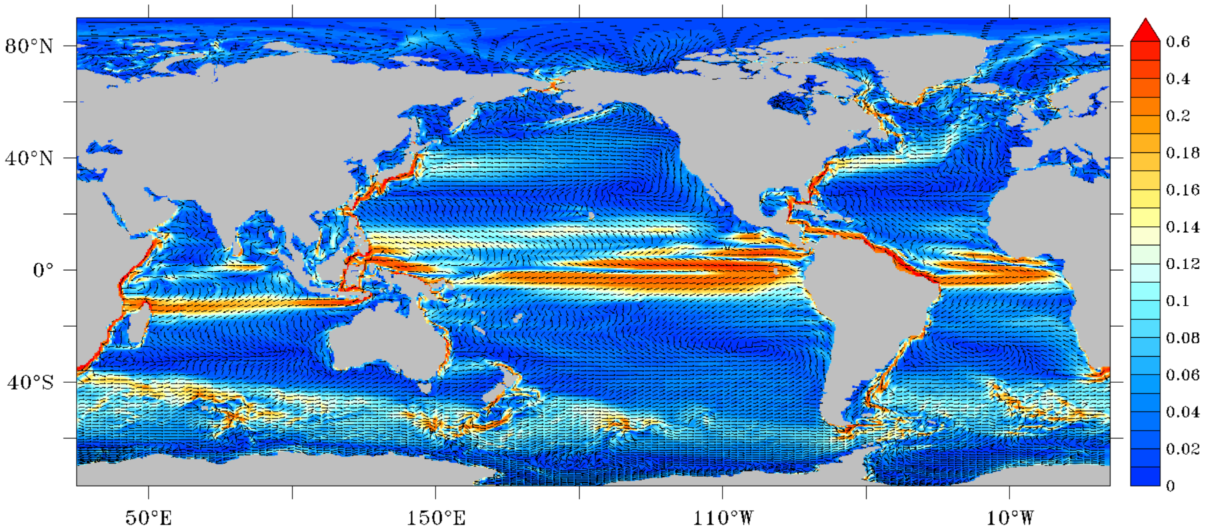

b) 100 m depth

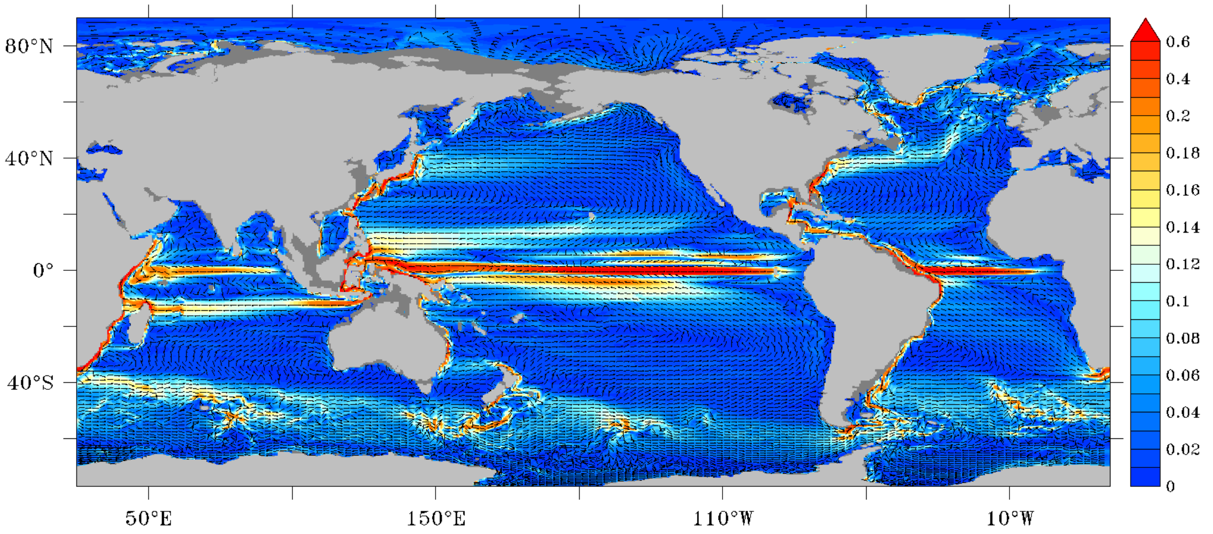

Figure 4.2.: Ten year averaged (2000 to 2009) circulation in ORCA05 at the surface a) and at 100 m depth b): shaded is speed [m/s] with vectors marking the flow direction overlaid. Note the non-linear scale.

In a mid-depth range, at 600 m (figure 4.3 a) the ACC is the dominant current. Zonal structures in the tropical Indian and Pacific Oceans are still present, although focused on the western parts of the basins while in the Atlantic basin the entire tropical Ocean, except for the western boundary, is marked by only very slow velocities. The Northern and Southern Equatorial currents (NEC and SEC) move waters westwards and towards the equator in all three basins. The lower limbs of the North Atlantic Current (NAC) [Krauss (1986)] and the Kuroshio extension [Qiu (2002)] are visible as well as the Agulhas Current [Lutjeharms (2006)] feeding into the Atlantic SEC. At 1000 m depth

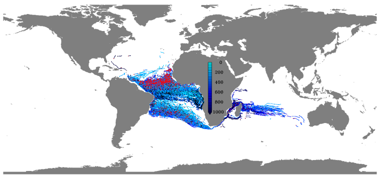

(figure 4.3 b) the ACC and the currents are along the western boundaries of the basins as well as the SECs and the NECs are clearly visible. In the Atlantic basin no noteworthy currents in the tropical Oceans are simulated whereas an equatorial current confined to the western part of the Pacific basin and a zonal band located at the Indonesian outflow, zonally crossing the Indian Ocean, are present [Ollitrault and Colin de Verdière (2014)].

a) 600 m depth

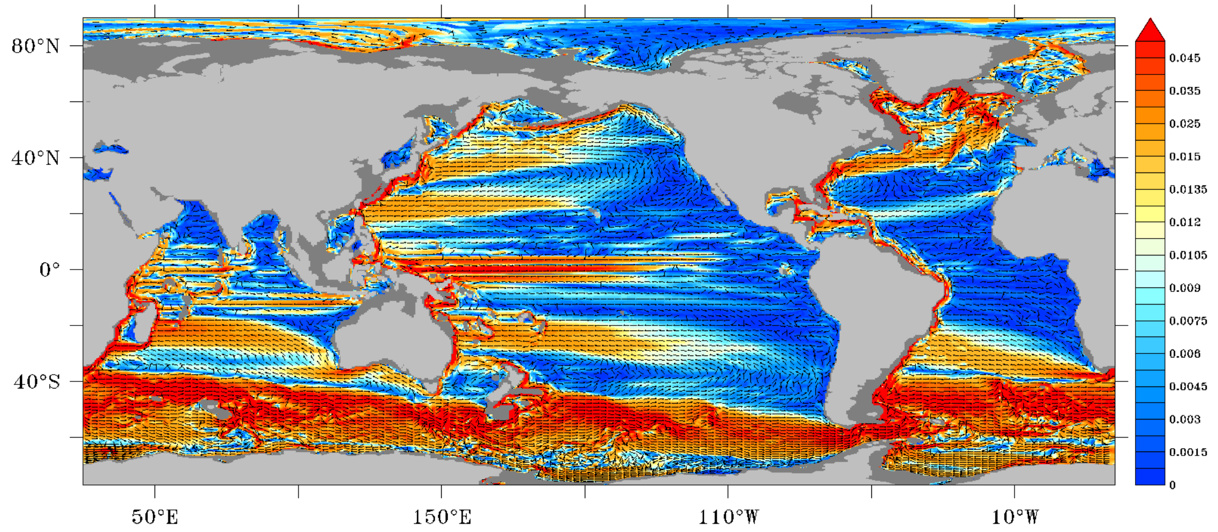

b) 1000 m depth

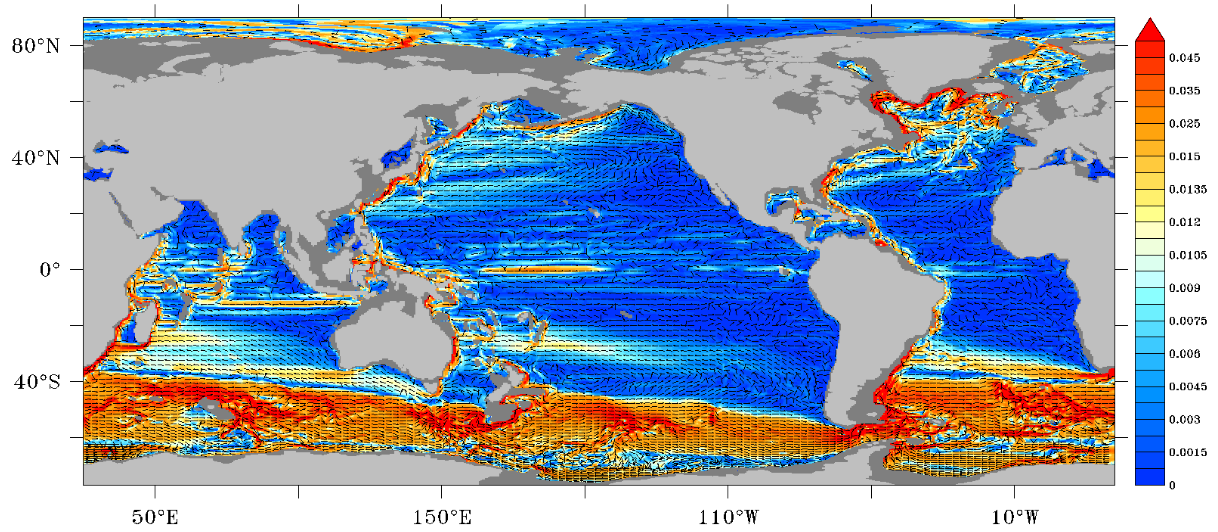

Figure 4.3.: Ten year averaged (2000 to 2009) circulation in ORCA05 at 600 m depth a) and 1000 m depth b): shaded is speed [m/s] with vectors marking the flow direction overlaid. Note the non-linear scale.

This velocity field in its temporally varying form is responsible for the advective part of the spreading of the two passive tracers CONC and AGE, that is discussed in the following section.

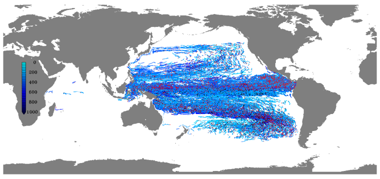

4.2. Passive tracers in ORCA05

Ideally the spreading of the two tracers AGE and CONC (see subsection 2.1.7 for details) would be analyzed in the high resolution models TRATL01 and TROPAC01 to identify pathways of the tracers, especially in the CONC fields. The tracers in TRATL01 and TROPAC01 are initialized using the final distribution of an 80 years long spin-up in ORCA05 and therefore, gradients in the two fields are already reduced in a way that the ventilation pathways are hard to identify in the high-resolution models. Due to the differences in the representation of the circulation and the diffusivity in the nested models and ORCA05 it can be expected that pathways of tracers, initialized in TRATL01 and TROPAC01 would differ from those simulated in ORCA05. The former are, however not available here and the initial tracer evolution has to be analyzed using the tracer fields from the coarser ORCA05-NY simulation.

4.2.1. Surface concentration dye (CONC)

The evolution of the tracer CONC, that can be understood as a dye, that is saturated at the surface, re-filling from an infinite source, spreading into the Ocean, in ORCA05-NY at 300 m depth first shows tracer entrainment in the convection areas [Killworth (1983)] in the North Atlantic Ocean as well as in the Indian and Pacific sector of the Southern Ocean (figure 4.4) .

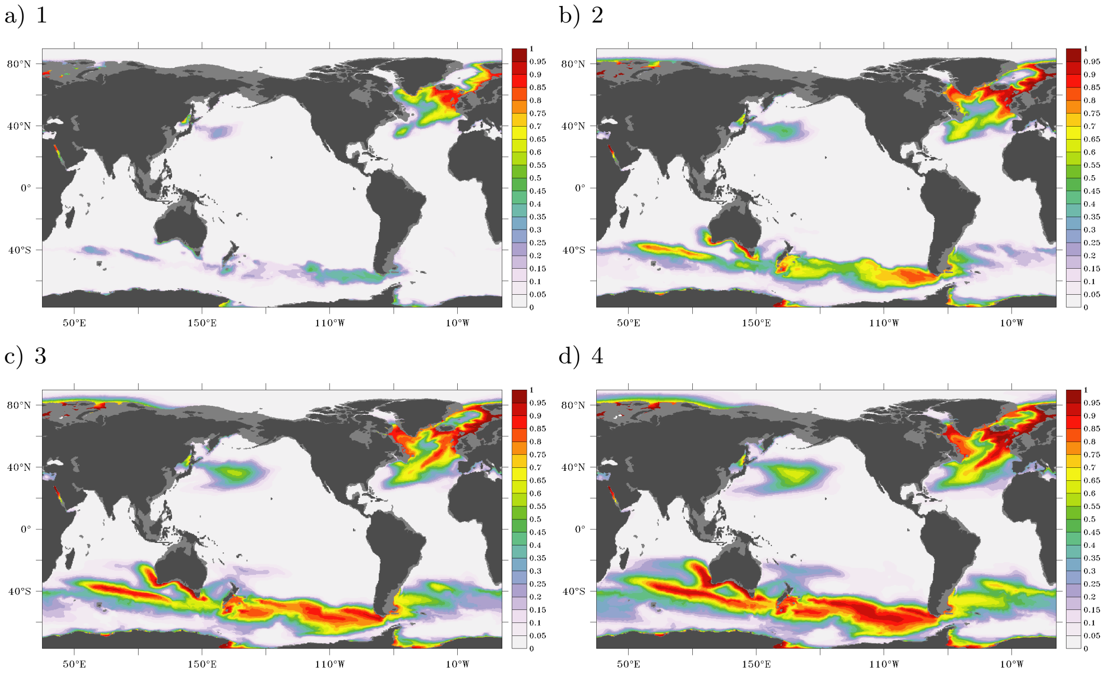

Figure 4.4.: CONC at 300 m depth as an annual average after 1 a), 2 b), 3 c) and 4 years d) integration in ORCA05.

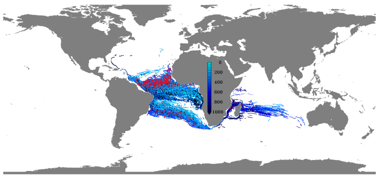

In the second year, the Ross and Weddell Sea show significant tracer values and a patch in the Kuroshio extension area develops. After four years, tracer at 300 m depth also occurs in the Atlantic sector of the Southern Ocean, and then slowly starts to invade all three basins from the South.

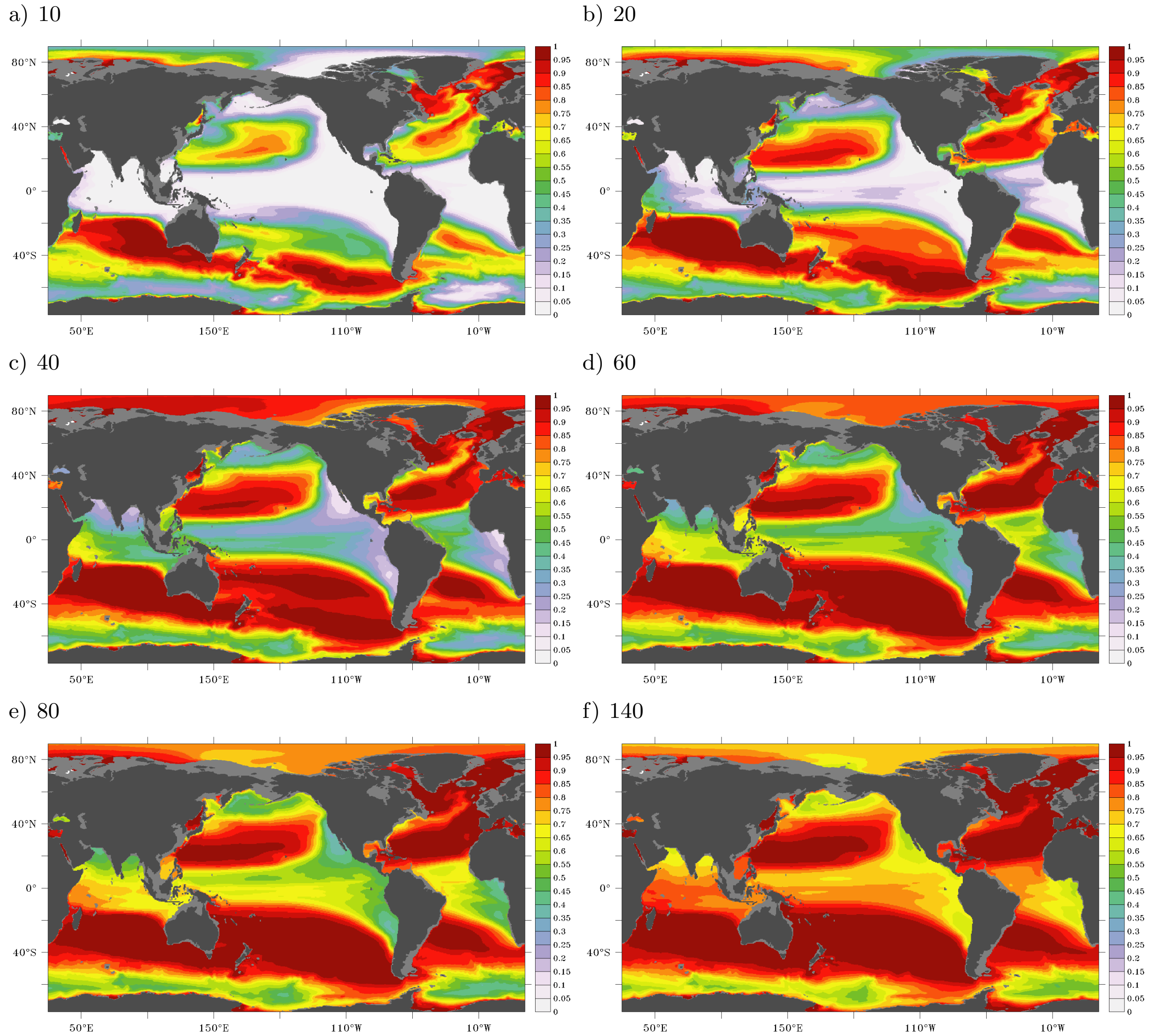
a) 10 b) 20 c) 40 d) 60 e) 80 f) 140

Figure 4.5.: CONC at 300 m depth as an annual average after 10 a), 20 b), 40 c), 60 d), 80 e), and 140 years f) integration in ORCA05.

In the following two decades, tracer levels overall grow with time and the zones where significant tracer values occur expand. After 20 years of integration, the outer structure of the poorly ventilated regions, the shadow zones [Luyten et al. (1983)], in the Atlantic and Pacific Ocean are represented by the CONC field (figure 4.5b)). From then on, at this intermediate depth mainly the levels increase until they saturate at 1, without significant changes in the shape of the tracer distribution, except

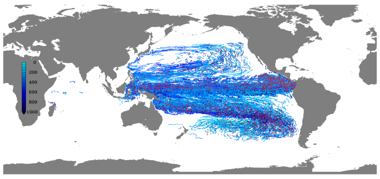

for the areas with lowest CONC values that shrink but only slowly gain tracer. After 80 years, wide areas in the subtropical oceans, as well as almost the entire North Atlantic and the Arctic Ocean are already saturated at 300 m depth. However, this only holds for the relatively shallow layer shown here.

The vertical structure of the tracer evolution in the Atlantic (figure 4.6) and Pacific (figure 4.7) Ocean, in a basin wide zonally averaged sense, exhibits the most prominent differences in the ventilation of the two Oceans. In the North Atlantic, convection in the northeastern part [Marshall and Schott (1999)], rapidly brings tracer from the surface to deeper layers. Already after ten years, the 0.5 isoline in CONC reaches 1500 m north of 45° N. In the South, the entrainment is slower, located in two areas, the Weddell Sea and around 50° S. Here, the tracer reaches the seafloor in significant amounts within ~100 years. The tracer enters the subtropical and tropical Atlantic from the North, layered between 1500 m and 2500 m depth. After 140 years the tracer distribution exhibits a zone of low values in the depth range from 500 m to 1500 m depth between 30° S and 20° N whereas CONC values above and below are higher. The shape of CONC distribution and its evolution in time is in good agreement with what is known from the global meridional overturning circulation [e.g. Marshall and Speer (2012); Kuhlbrodt et al. (2007)] and mirrors the spread of water masses formed at high latitudes [e.g. Lynn and Reid (1968); Gordon (2001)].

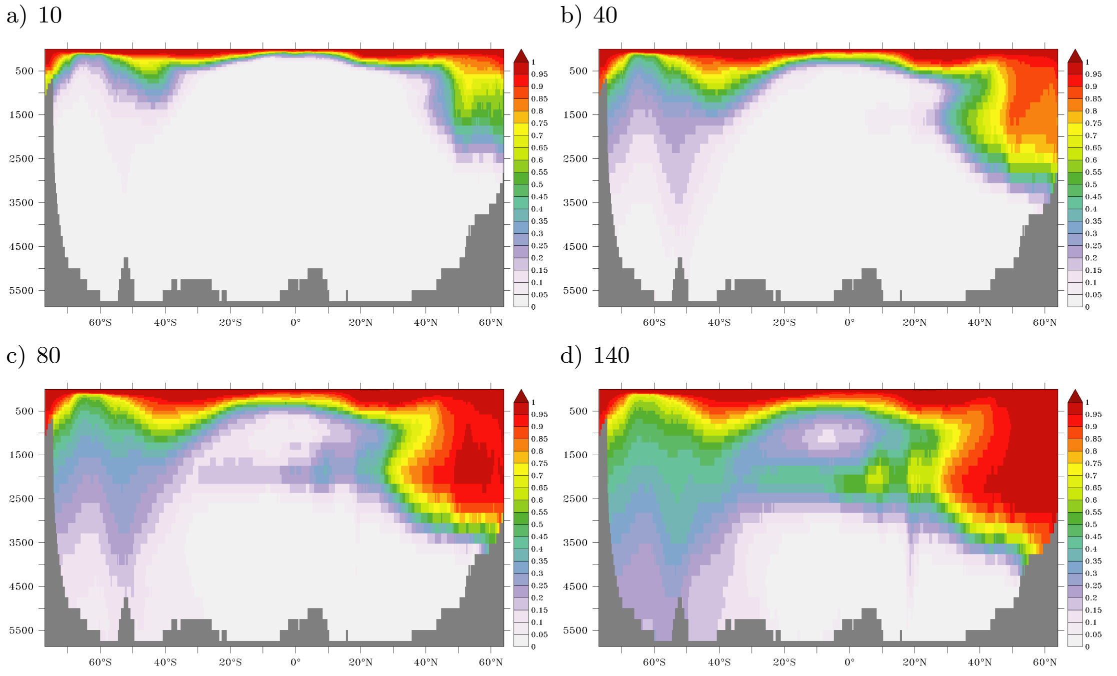

Figure 4.6.: CONC zonally averaged over the Atlantic basin as an annual average after 10 a), 40 b), 80 c), and 140 years d) integration in ORCA05.

In the Pacific Ocean, deep convection only happens in the South [Marshall and Schott (1999)] (see

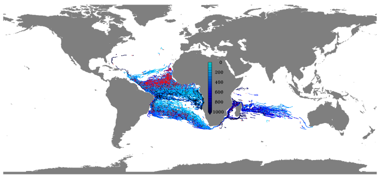

figure 4.7). The tracer entrainment into the inner basin is therefore limited to that single source. After 40 years, the tracer starts to enter the southern subtropics along the seafloor in very low concentrations. Even after 140 years of integration CONC values below 1000 m depth and north of 30° S are almost negligible. In both basins and the rest of the global ocean, besides the deep convection, CONC values additionally increase with time from the surface downwards due to mixing processes.

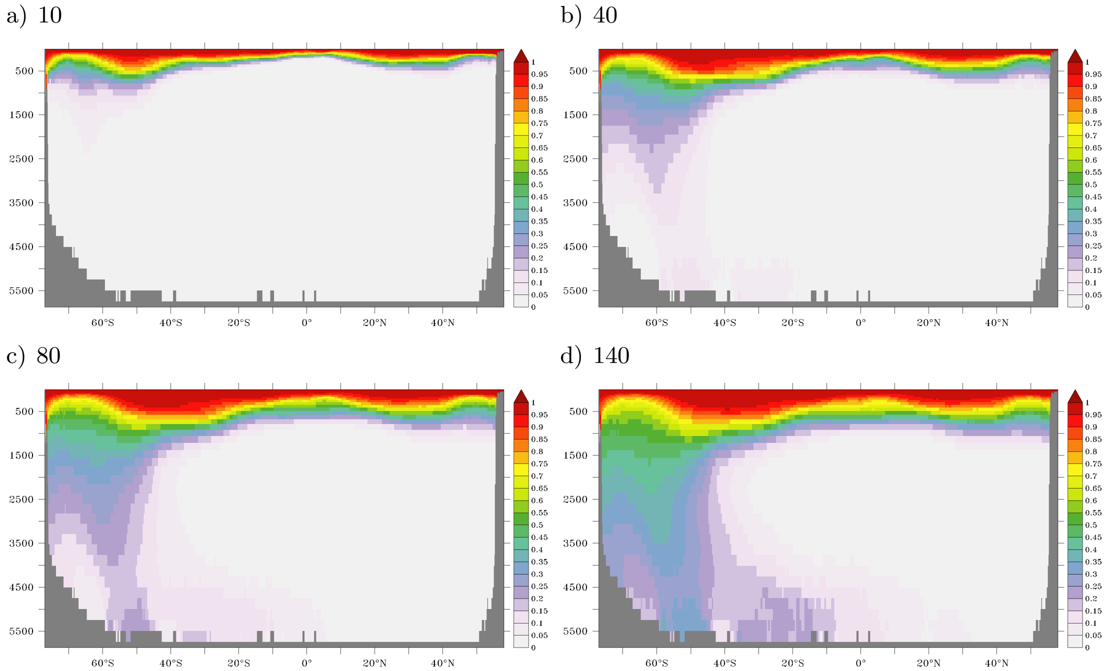
a) 10 b) 40 c) 80 d) 140

Figure 4.7.: CONC zonally averaged over the Pacific basin as an annual average after 10 a), 40 b), 80 c) and 140 years d) integration in ORCA05.

4.2.2. Time since the last surface contact (AGE)

The main difference in the concepts behind the tracers CONC and AGE is, that while CONC only has an infinite source at the surface and reaches saturation (CONC = 1) everywhere, completely losing any structure if the integration time is long enough, AGE has a “sink” at the surface and a constant source everywhere else. For AGE, this leads to an equilibrium state showing the three-dimensional age structure of the Ocean after an integration, that is long enough to completely ventilate the global ocean, which takes several thousand years [England (1995)]. To illustrate the evolution of the tracer AGE, the fields shown here are normalized by the maximum AGE at the corresponding point in time. In contrast to CONC, high AGE values mark poorly ventilated regions. Note, that therefore the colourscale is inversed for the AGE illustration to facilitate the comparison between the patterns (not the values) of the two passive tracers.

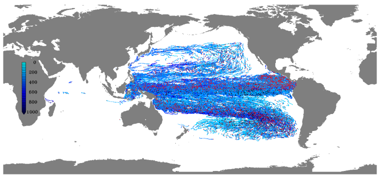

AGE at 300 m depth within the first four years of the integration in ORCA05-NY (figure 4.8) shows a similar (in inverse sense), although less pronounced, structure like CONC (compare to figure 4.4) in the North Atlantic and in the Indian and Pacific sector of the Southern Ocean. In the North Pacific and the South Atlantic, AGE only shows very weak signals in the first years of the integration, with spatially very confined patches of low values when compared to their surroundings. The convection areas along the Antarctic continent are also only marked by weak signals.

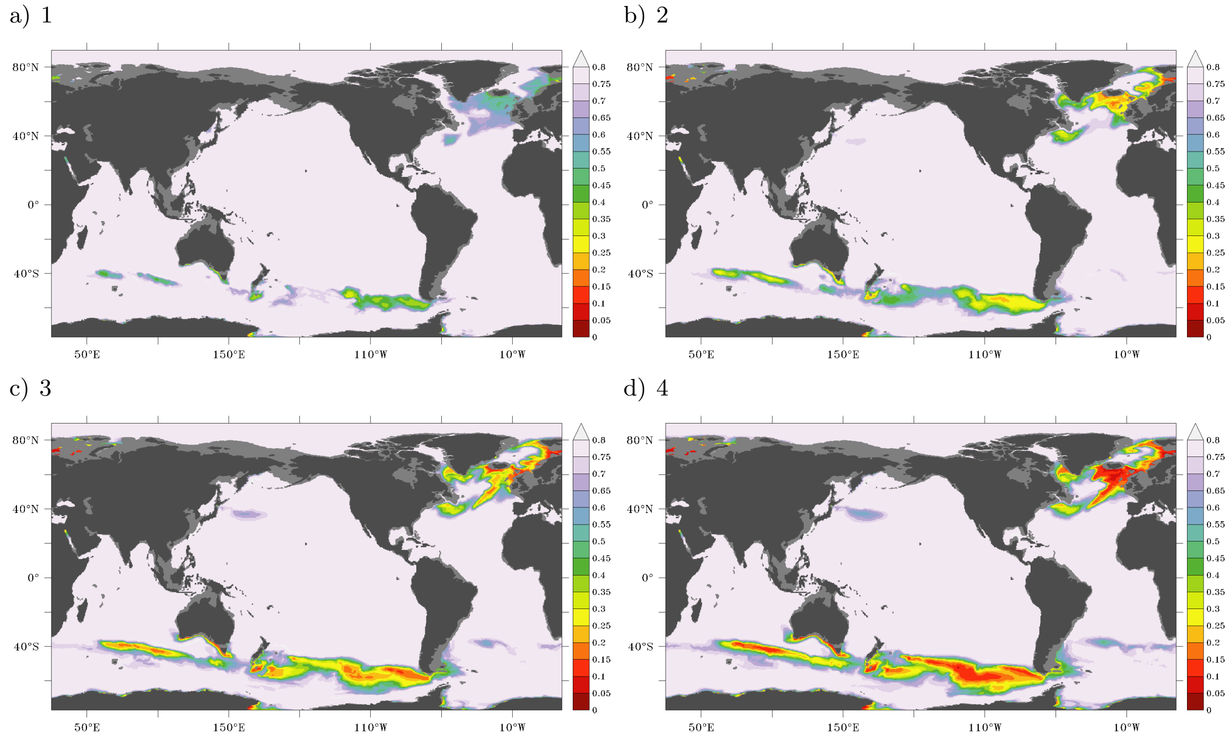
a) 1 b) 2 c) 3 d) 4

Figure 4.8.: Relative AGE at 300 m depth as an annual average after 1 a), 2 b), 3 c) and 4 years d) integration in ORCA05.

Even after ten years of integration, the low AGE signals in the North Pacific and the South Atlantic are still weak, and only slowly evolve during the following two decades (figure 4.9). In the meantime, the marked low AGE areas in the southern parts of the Indian and Pacific Oceans as well as the North Atlantic start to strengthen and expand, as well as the convection areas in the Weddell [Fahrbach et al. (1995)] and Ross Seas. After 80 years of integration areas of high AGE values begin to demarcate in the tropical Pacific and Atlantic Oceans as well as the North Pacific and the northern Indian Ocean. These zones persist throughout the rest of the integration period, as well as the low AGE areas, that also keep their structures. After 140 years, the full integration period, the AGE pattern at 300 m depth still exhibits all the above mentioned features that can no longer be identified as clearly in the CONC fields after such a long integration.

The vertical structure of AGE, zonally averaged over the Atlantic (figure 4.10) and Pacific (figure

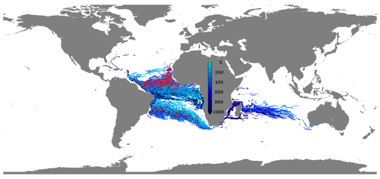

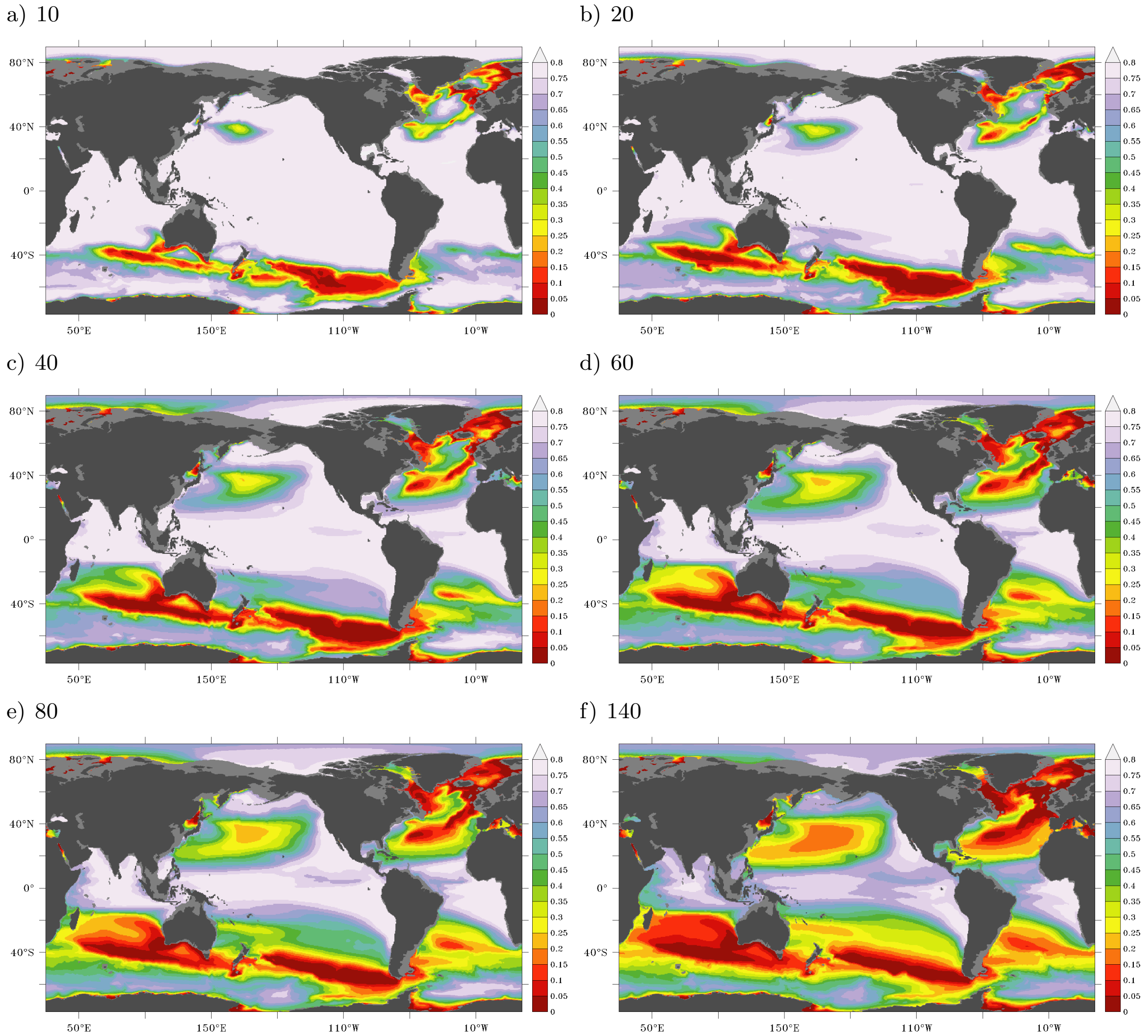
a) 10 b) 20 c) 40 d) 60 e) 80 f) 140

Figure 4.9.: Relative AGE at 300 m depth as an annual average after 10 a), 20 b), 40 c), 60 d), 80 e) and 140 years f) integration in ORCA05.

4.11) Ocean, however, sheds a different light onto the AGE tracer in comparison to CONC. Here, in AGE, the mid-depth convection in the North Atlantic appears to be slower and weaker when compared to the CONC fields and the convection in the Southern Ocean, even after 140 years of integration only shows an entrainment down to 2500 m depth. The pattern of minimum CONC values at mid-depth in the tropical Atlantic is absent in the AGE distribution.

In the Pacific Ocean, the zonally averaged AGE pattern also shows only very weak entrainment after 140 years of integration reaching no deeper than 2000 m depth. Here, no further vertical structure evolves within the integration period.

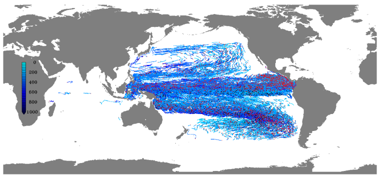

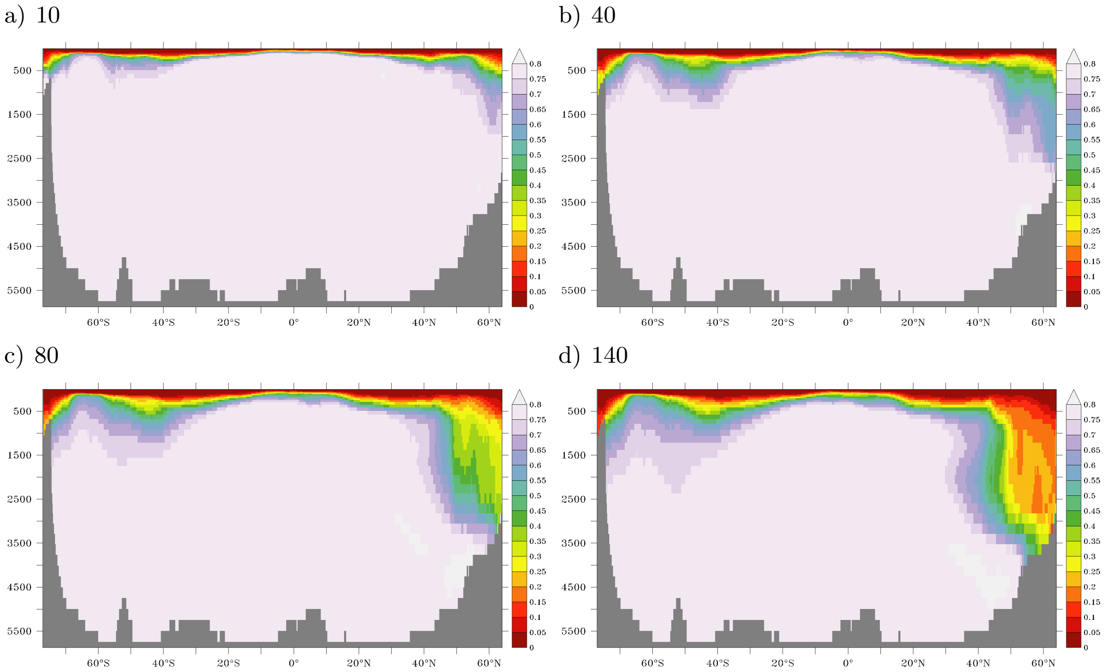
a) 10
b) 40
c) 80
d) 140

Figure 4.10.: Relative AGE zonally averaged over the Atlantic basin as an annual average after 10 a), 40 b), 80 c), and 140 years d) integration in ORCA05.

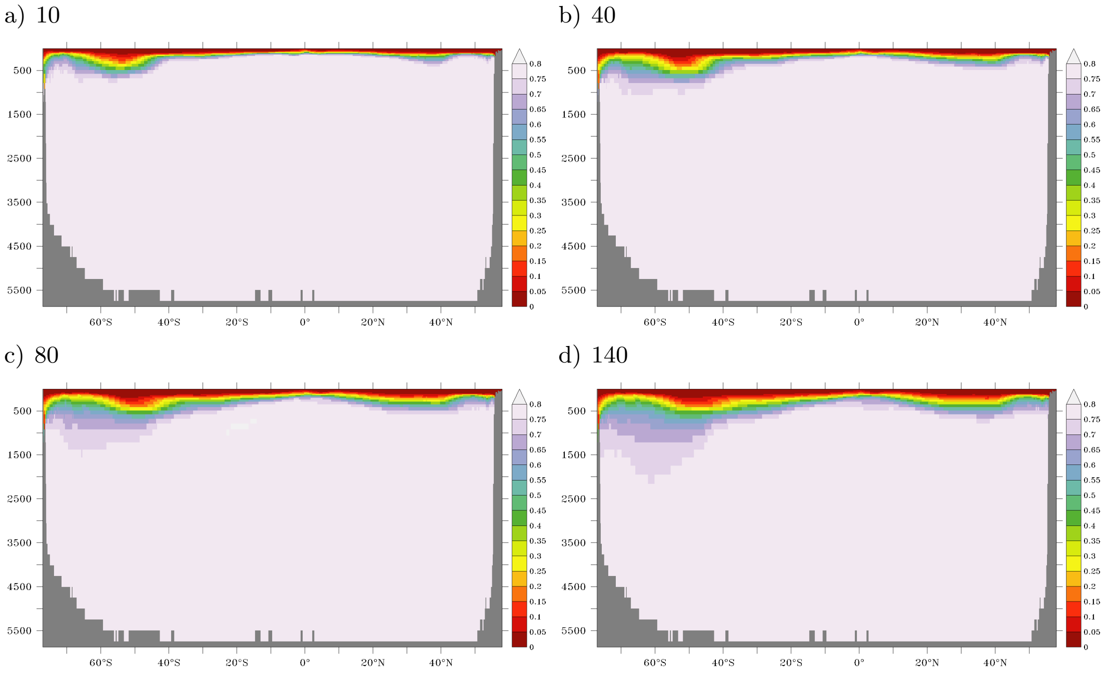
a) 10
b) 40
c) 80
d) 140

Figure 4.11.: Relative AGE zonally averaged over the Pacific basin as an annual average after 10 a), 40 b), 80 c), and 140 years d) integration in ORCA05.

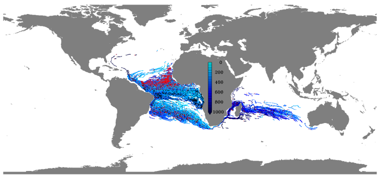

4.2.3. Comparison with the observed oxygen distribution

The horizontal structure of CONC at 300 m depth after 20 years of integration (figure 4.5b) shows strong similarities to the structure in the mean oxygen concentration at 300 m depth as given by the World Ocean Atlas [Garcia et al. (2006)] (figure 4.12a). Comparing the observed oxygen concentrations and CONC at later points in time within the integration leads to less agreement between the two fields. This is because CONC increases with time, lacking any consumption and therefore finally approaching saturation everywhere. The gradients in CONC reduce and the structures that clearly mark the poorly ventilated areas blur during the integration time, at least at this depth.

a) 300 m depth

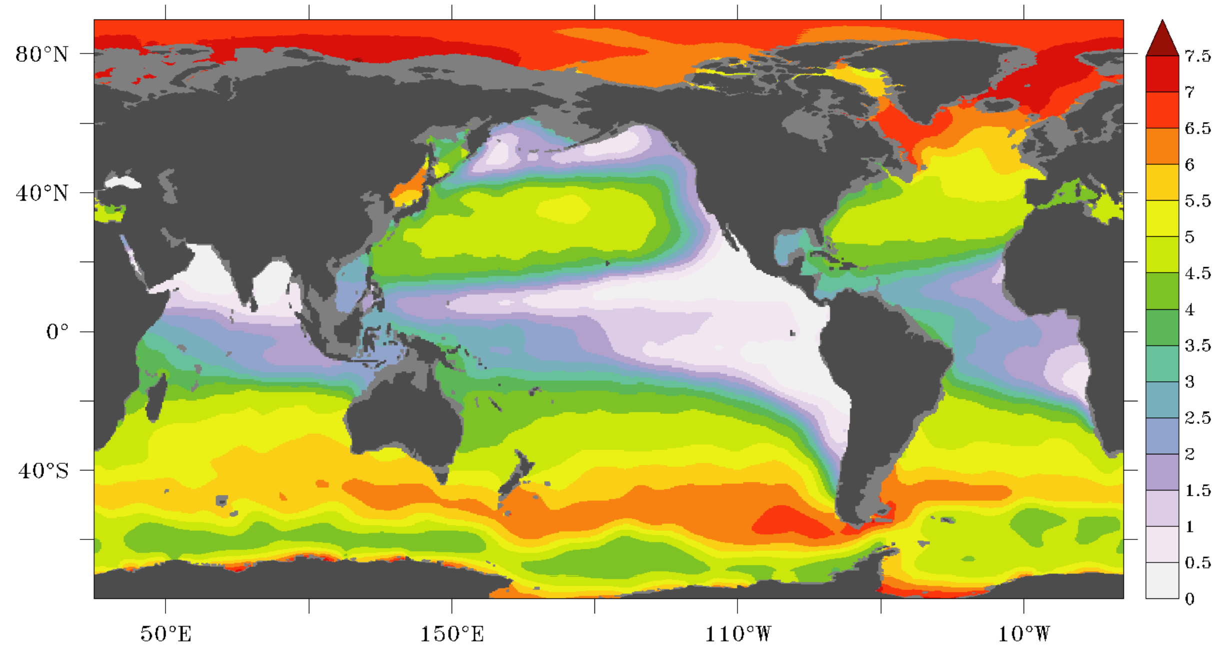

b) Pacific basin

c) Atlantic basin

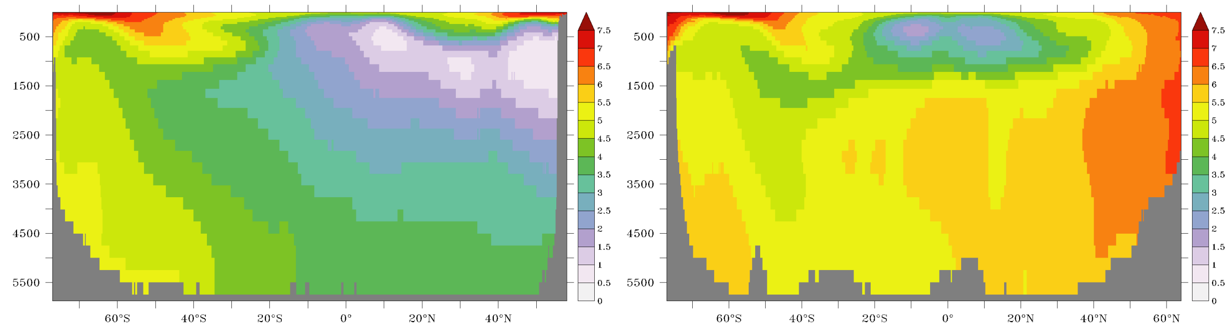

Figure 4.12.: Mean oxygen concentration (ml/l) from the World Ocean Atlas 2005, regridded onto the ORCA05 grid at 300 m depth a), zonally averaged over the Pacific basin b) and the Atlantic basin c).

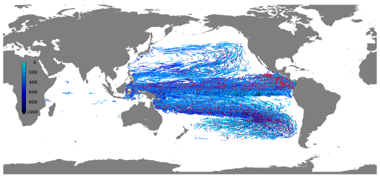

The zonally averaged fields, however, show that for deeper layers, the meridional and vertical structure in CONC and the observed oxygen fields (figure 4.12b and c) differ substantially, even after 80 years of integration (figures 4.6c) and 4.7c). In the Pacific Ocean the oxygen field exhibits a wide area of very low oxygen concentrations in a layer between ∼300 m and 1500 m depth, north of 10° S, that vertically expands towards the north. In the southernmost part, due to deep convention, oxygen concentrations are relatively high throughout the water column, layering oxygen richer waters along the seafloor beneath low oxygenated waters above [Gordon (2001), Talley et al. (2011)]. A similar, but less pronounced structure in CONC begins to evolve only at the end of the entire integration period of 140 years used within this study (figure 4.7d).

The zonally averaged mean oxygen distribution in the Atlantic Ocean (figure 4.12c) exhibits two areas of lowest oxygen concentrations with their cores located at ∼10° N and S at 400 m depth surrounded by a wider area of low concentrations. High oxygen values are observed in the North Atlantic throughout the entire water column, expanding with decreasing values towards the south. In the southernmost part enhanced oxygen concentrations are also present due to the deep convection [Gordon (2001); Talley et al. (2011)]. The comparison of this observed pattern with CONC in the Atlantic Ocean after 140 years of integration (figure 4.6d) shows, that the high oxygen values in the deep ocean are not reflected in the CONC field but very weak concentrations are simulated. This is most probable due to the limited integration period; the Ocean has not had enough time to be filled up with the tracer. However, the area with low CONC values between 20° S and 20° N is located within the area of relatively low oxygen concentrations, although deeper and without showing the two distinct cores. The high oxygen concentrations in the North Atlantic as well as the corresponding weaker signal in the South are represented by the strong CONC entrainment in the North and less pronounced from the South.

The horizontal oxygen structure at 300 m depth is reproduced quite well by the tracer AGE from the 80th year of the integration onwards. Here, the structures do not vanish with longer integration, as they do in the CONC fields. The vertical patterns however, even after 140 years of integration do not show a similarity, as strong as CONC does, with the observed oxygen field. The contrast between the vertical distribution of CONC and AGE is due to the ubiquitous source of the tracer AGE acting on all subsurface waters, masking the gradient between the young, convected waters and the surrounding.

The above presented evolution and distribution in the two introduced passive tracers exhibit a combination of CONC for the shorter and AGE for the longer time scales (relative to the ventilation time scales) to be most suitable to investigate the ventilation with a view on the global oxygen distribution. AGE at the end of the integration exhibits the long persistent features of the oxygen distribution, at least at intermediate depth, where the integration time is of the same order as the ventilation time. CONC contributes to the understanding of the beginning of the ventilation paths.

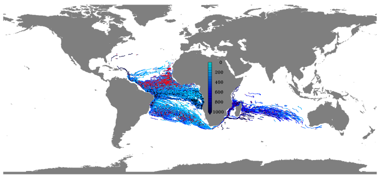

4.3. Tracers in the nested models

The CONC and AGE fields in ORCA05-NY after 80 years of integration (see figures 4.5e, 4.6c and 4.7c as well as 4.9e, 4.10c and 4.11c) are used to initialize the nested configurations TRATL01 and TROPAC01. The above described evolution of the CONC and AGE tracers within this period has the following implications for the nested tracer simulations: In the depth range of the OMZs, already with the initialization the CONC field is too blurred to clearly identify the potential effect of the narrow equatorial currents in the tracer distribution; the strong horizontal gradients in CONC, that depict those pathways have almost vanished by that time. The AGE field in that depth range, however, seems to be in a good state to initialize the nested models, but for deeper layers, it is too young to capture the real pattern in the age of the waters [England (1995)].

The initialization of TRATL01 and TROPAC01 with those tracer fields is an admittedly bad compromise between the behaviour of the two different tracers and the computational resources needed to either integrate the AGE tracer longer before initializing the nested configurations or the initialization of CONC within the nested configurations, starting at zero everywhere in the TRATL01 and TROPAC01. The spin-up in ORCA05, for AGE leads to slightly better starting conditions than a setup, starting with zero AGE in the nested configurations, but for CONC, the starting distribution suffers from all the weaknesses of the coarse ORCA05 simulation, such as non-represented currents (see section 3.6).

Hence, investigating the temporal evolution of the tracers in the nested models can only give very limited insight into the ventilation of the OMZs. Therefore only the final tracer distributions are considered here.

4.3.1. Comparison of tracers in ORCA05 and the nested models

The overall pattern in the CONC and AGE fields from ORCA05 compared to the barotropic streamfunction shows a general agreement between areas of high CONC and low AGE values with anticyclonic gyres; poorly ventilated regions are co-located with cyclonic patterns (figures 4.13 and 4.14) [Williams and Follows (2003)]. Along the northern part of the ACC, low AGE and high CONC values are present, consistent with Southern Ocean ventilation processes [Sallée et al. (2010)], flanked by pronounced high AGE and low CONC values in the South. In the Atlantic and the Pacific Ocean, the northern flank of the southern hemisphere subtropical gyres and the southern flank of the northern hemisphere subtropical gyres are broadly consistent with the outer limits of the poorly ventilated tropical areas. The cyclonic subpolar gyre in the Pacific Ocean is marked by poorly ventilated waters, whereas in contrast to this rule, the occurrence of deep convection in the subpolar gyre of the North Atlantic [Pickart et al. (2008)] leads to well ventilated waters there.

In comparison to the global 0.5° simulation, the tracer fields in both nested 0.1° simulations show

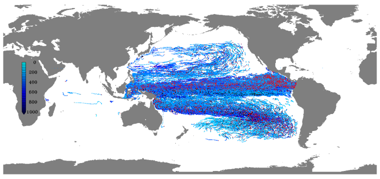

a) ORCA05

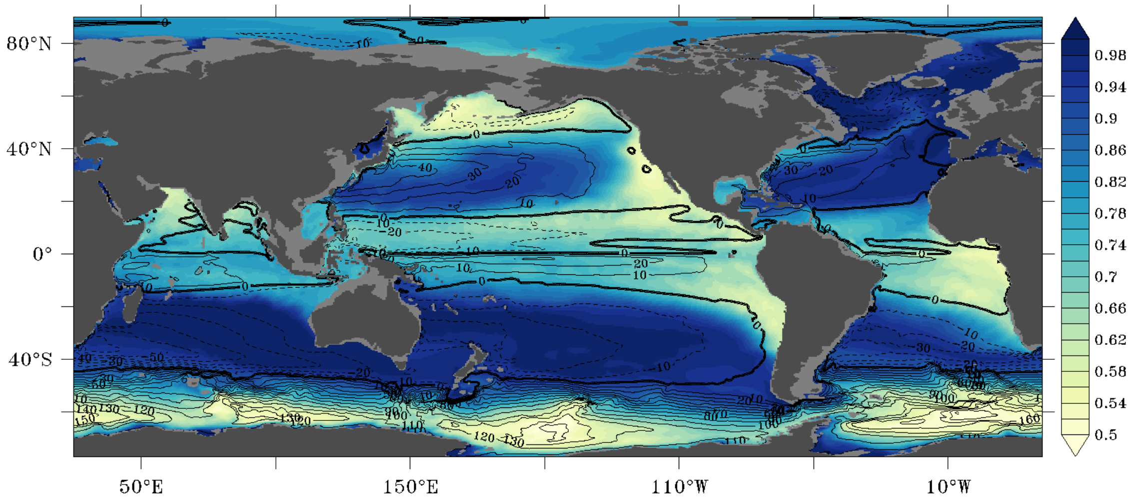

b) TROPAC01

c) TRATL01

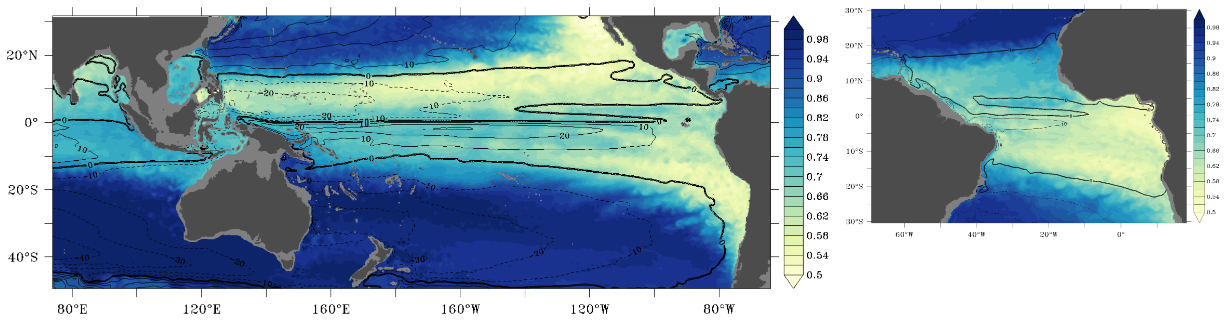

Figure 4.13.: Snapshot (5-day average) of the tracer CONC after 140 years of integration at 400 m depth in ORCA05 a), TROPAC01 b) and TRATL01 c). The ten year averaged (2000 to 2009) barotropic streamfunction (Sv) from ORCA05 is overlaid in all panels.

mesoscale features. The well defined outer limits of the poorly ventilated areas in the Pacific Ocean, as given by steep gradients in CONC and AGE, are broken up in TROPAC01 (figure 4.13b). Along the curved gradient between the subtropical gyres and the meridionally widening tropical zones of poorly ventilated areas east of them, plumes of alternating higher and lower CONC values occur in TROPAC01. A band of low CONC along the South American coast reaches south to more than 40° S in TROPAC01 that is missing in ORCA05, where a meridional gradient at ~35° S is simulated instead. The region with lowest CONC in the southern as well as in the northern part of the eastern tropical and subtropical Pacific Ocean is more structured in TROPAC01 than in ORCA05, depicting areas of even lower CONC values in the high-resolution model when compared to the coarser one. In a ~10° wide zonal band around the equator, higher concentrations enter the eastern part of the basin from the South, showing stronger gradients with its surrounding in TROPAC01 than in ORCA05. Along ~10° N, a band of low CONC spans the entire basin, with lower values in TROPAC01 than in ORCA05.

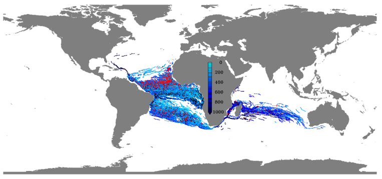

a) ORCA05

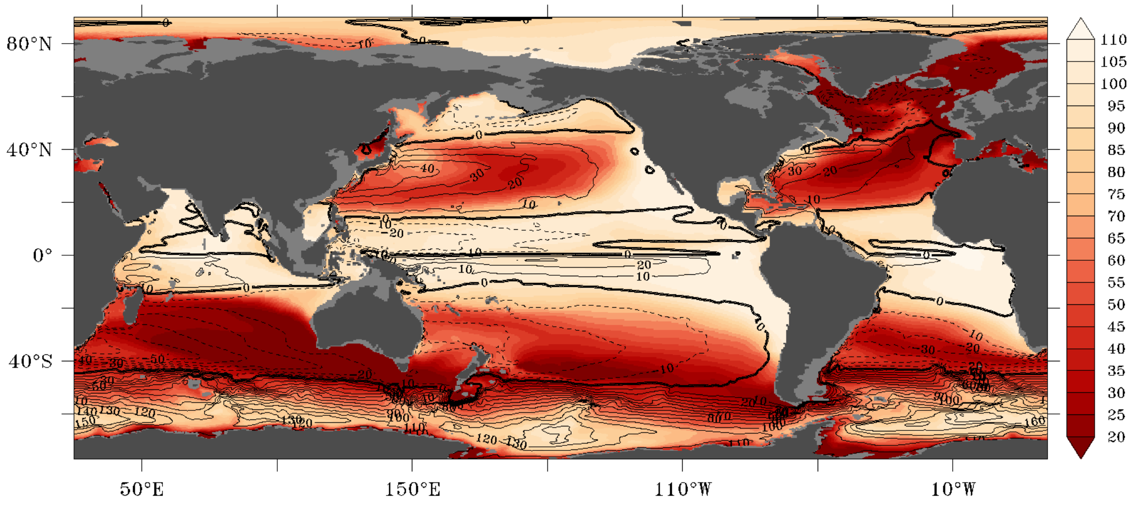

b) TROPAC01 c) TRATL01

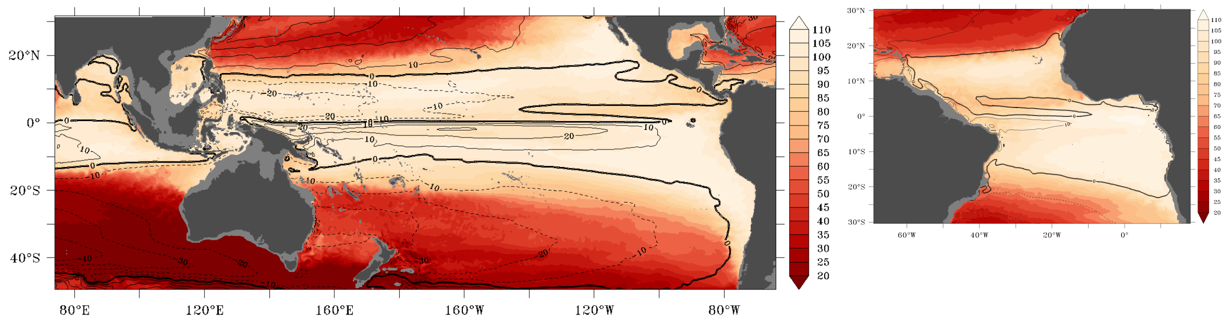

Figure 4.14.: Snapshot (5-day average) of the tracer AGE after 140 years of integration at 400 m depth in ORCA05 a), TROPAC01 b) and TRATL01 c). The ten year averaged (2000 to 2009) barotropic streamfunction (Sv) from ORCA05 is overlaid in all panels.

In the AGE distributions (figure 4.14), the comparison between TROPAC01 and ORCA05 is similar to the one in CONC with AGE showing weaker gradients in TROPAC01 and mesoscale structures, that ORCA05 is lacking, however, the imprint of the higher resolution in the fields is less pronounced than in CONC. Where in CONC, some of the poorly ventilated areas show lower values in TROPAC01 than in ORCA05, in AGE they also shows lower values in the nested model, with the opposite meaning, namely better ventilation in TROPAC01 when compared to ORCA05.

In the Atlantic Ocean, the comparison between the nested and the global 0.5° simulation shows, besides the resolved mesoscale in TRATL01 very similar patterns. The main differences are smeared out gradients along the outer limits of the poorly ventilated regions and tongues of higher concentrations entering the easternmost part of the OMZs. The mesoscale features are marked by eddying structures and plumes of higher concentrations entering the low CONC area as well as plumes of lower concentrations penetrating into the areas of higher CONC. Higher CONC values compared

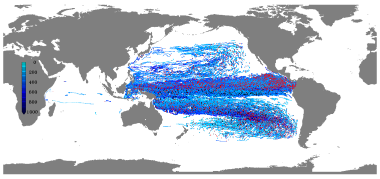

to the surrounding are found where the SEUC enters the eastern part of the basin in TRATL01, missing in ORCA05. Higher CONC values in the easternmost part of the northern tropical Atlantic Ocean and along 4° N, co-located with the NEUC are found in TRATL01, with the latter being absent in ORCA05. The importance of the NEUC and SEUC for bringing better ventilated waters towards the eastern part of the basin has been pointed out by Duteil et al. (2014). In AGE, the signature of the NEUC is also only present in TRATL01 and within the poorly ventilated areas, the overall age is lower in TRATL01 than in ORCA05.

4.3.2. Tracer distribution in and around the OMZs

Low CONC and high AGE values mark the regions where the connection to surface layers is weak and slow and that are therefore poorly ventilated. The areas of lowest CONC and highest AGE are not restricted to the observed OMZs, that are not strictly defined [Karstensen et al. (2008)], but incorporate them as well as the zones, that are defined as nOMZ and sOMZ within this study (red and green boxes in figures 4.15 and 4.17). These regions have a large lateral extent in the northern and southern tropical Atlantic at the end of the integration period of 140 years (80 years spin-up plus 60 years hindcast).

TRATL01

North of the equator at 400 m depth, highest AGE is simulated away from the coast in a zonal band centered at ∼15° N reaching from 40° W to 20° W (figure 4.15a). The patch with lowest CONC has the same meridional location but is shifted towards the west (figure 4.15a), possibly implying a weak, direct ventilation from above in the east. For instance, the patch of lower AGE at the African coast at 6° N can be attributed to direct ventilation from above (see figure 5.4 for vertical velocities). A zonal band with elevated CONC and lower AGE values is co-located with the NEUC at ∼4° N. Highest AGE values are 100 years and lowest CONC values are 0.6.

South of the equator, low CONC and high AGE at 400 m depth are simulated in a wide area, that is separated into a northern and a southern part by the South Equatorial Counter Current (SECC) [Molinari (1982)], transporting better ventilated waters from the western boundary towards the eastern part of the basin. The separation into two areas appears to be different in AGE and CONC, while the low AGE tongue is located at ∼5° S, the high CONC tongue is located further south and tilted, between 5° S in the western part of the basin to 13° S, in the east. These signatures are stronger when compared to the northern part of the Atlantic Ocean with maximal AGE higher than 110 years and minimal CONC values of 0.5. The difference in absolute CONC and AGE values between the northern and southern parts of the eastern tropical Atlantic is in agreement with the observed oxygen fields, that show a more pronounced minimum in the South when compared to the North [e.g. Karstensen et al. (2008)].

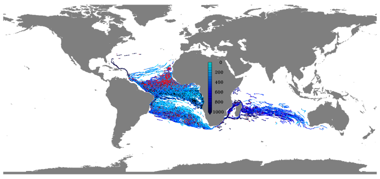

a) AGE

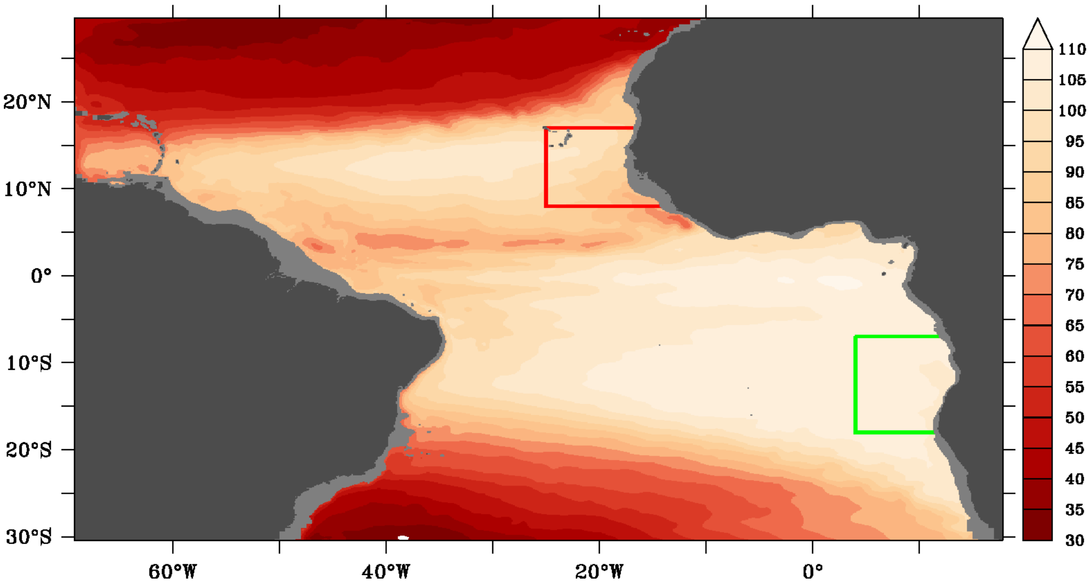

b) CONC

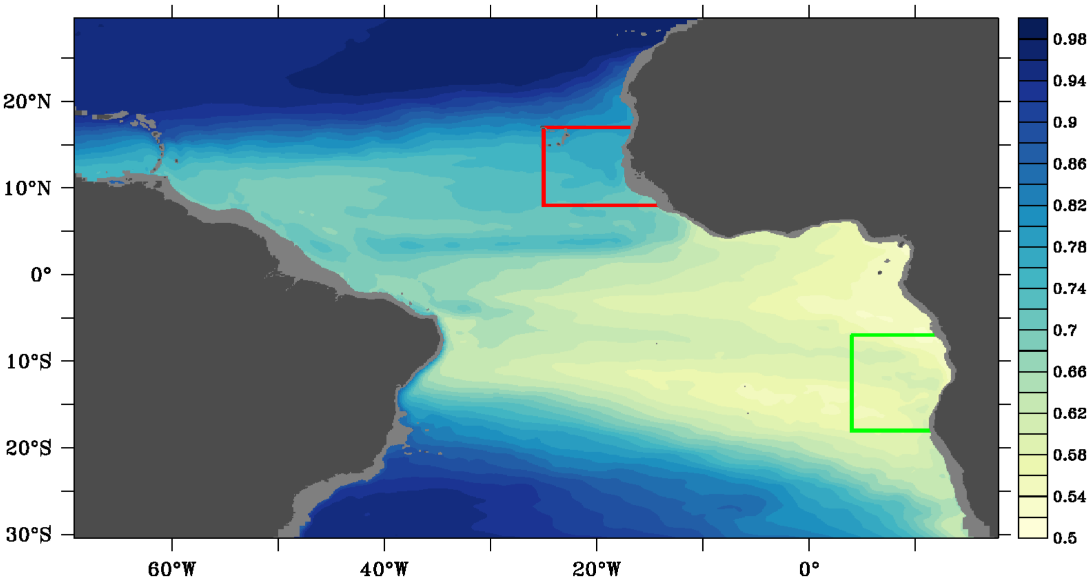

Figure 4.15.: Tracer AGE a) and CONC b) as annual average in the 140th year of the integration at 400 m depth.

One possible factor contributing to the difference between the OMZs' strengths, as also represented in the CONC and AGE fields, is the direct advective ventilation from above, that is only possible with waters, that are layered below ~150 m depth. See section 5.1.1 for details on the local, vertical processes. This direct path is stronger in the nOMZ when compared to the sOMZ.

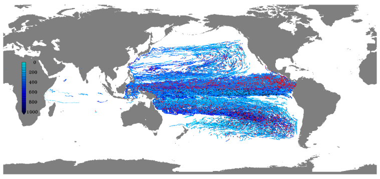

Sections through the nOMZ at 20° W and the sOMZ at 7° E (figure 4.16) show domed isosurfaces in both tracers spanning the meridional extent of the OMZs. In CONC, the poleward boundary of the OMZs are co-located with the area, where the gradient towards higher CONC values starts. At 20° W two cores of lower AGE and slightly higher CONC values compared to the surrounding waters occur down to ~300 m depth at 3° N and 11° N indicating two current bands that transport younger waters towards the nOMZ. In the vicinity of 23° W these bands are observed to carry elevated oxygen values on short time scales [Brandt et al. (2008)] as well as in a temporal mean sense [Brandt et al. (2010)]. At 7° E, higher CONC values (compared to the surrounding) are located down to ~400 m depth between 12° S and 8° S, that can also be seen in observations as slightly elevated oxygen concentrations in a climatological field as shown by Duteil et al. (2014) and more pronounced in a section in March 1995 [reproduced by Karstensen et al. (2008); their figure 3] along 5° E, with only a very weak signature in AGE. Again, the absolute values are lower in CONC and higher in AGE along the section through the sOMZ when compared to the nOMZ.

a) AGE at 20° W

b) CONC at 20° W

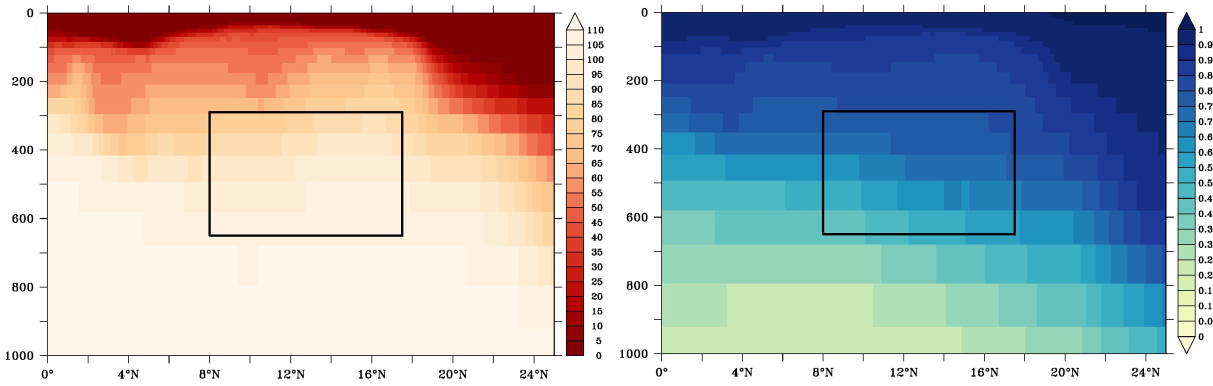

c) AGE at 7° E

d) CONC at 7° E

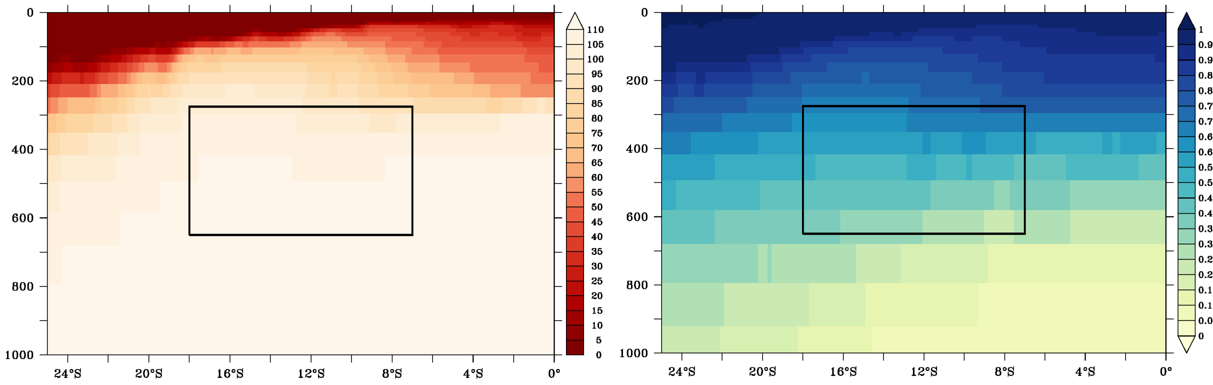

Figure 4.16.: Tracer AGE (a and c) and CONC (b and d) after 140 years of integration (annual average) along 20° W (a and b) and 7° E (c and d).

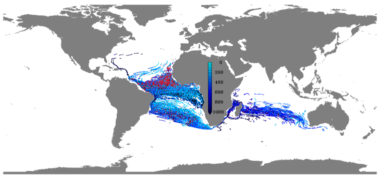

TROPAC01

In the northern tropical Pacific, highest AGE values (figure 4.17a) with more than 105 years after 140 years integration are simulated between 15° N and 25° N along the American coast extending towards ∼125° W and are consequently located further north when compared to the observed OMZ in the northern tropical Pacific Ocean (compare to figure 4.12a) as well as the region defined as nOMZ in this study (red box). An additional patch of AGE values above 105 years is located in the centre of the basin at 15° N.

a) AGE

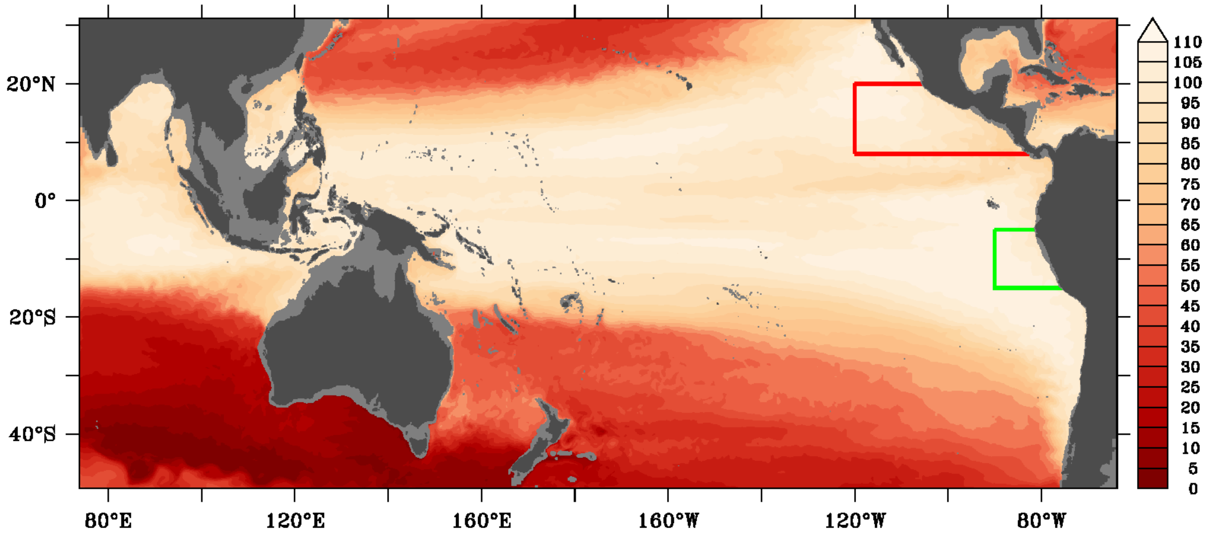

b) CONC

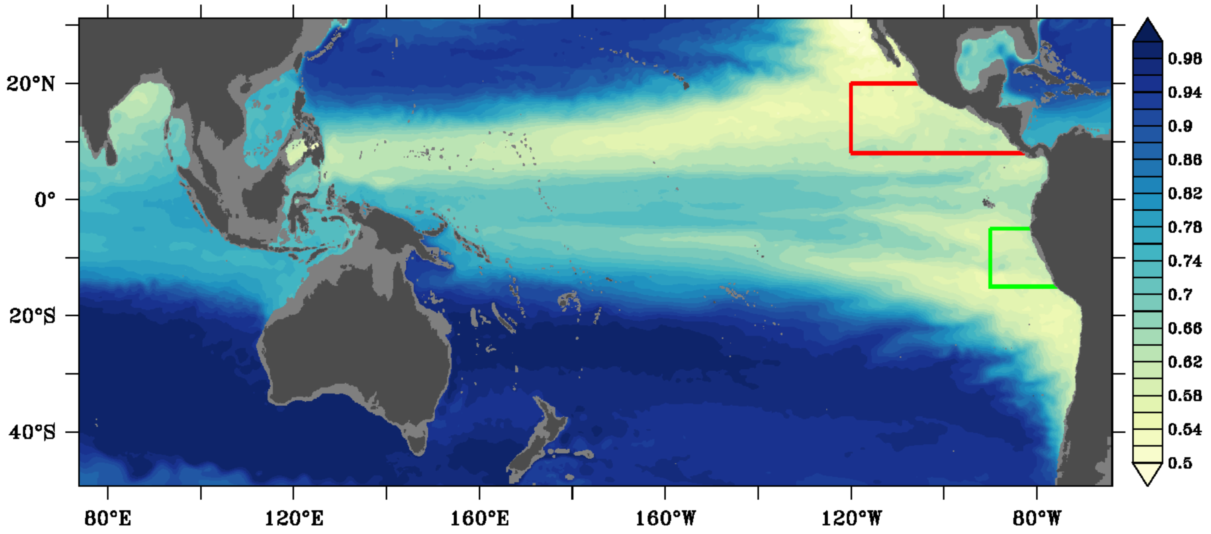

Figure 4.17.: Tracer AGE a) and CONC b) as annual average in the 140th year of the integration at 400 m depth.

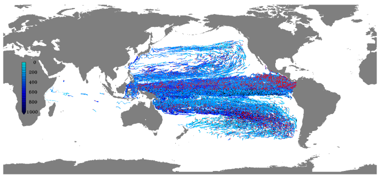

In CONC (figure 4.17b), this patch in the centre of the basin is less pronounced and the overall structure is more homogenous with lowest values below 0.55 in a ∼5° wide band from 18° N at 120° W to 8° N near the dateline. A patch of even lower CONC values is simulated along the American coast north of 25° N. A tongue of low CONC values, that is not mirrored in high AGE values is simulated at 3° N in the eastern part of the basin. The discrepancy in the location of the observed oxygen minima and the modelled AGE maxima and CONC minima can be attributed to model restrictions like the limited integration period, or the complete lack of biological processes. Longer integration would, by mixing with older waters from below, increase AGE values [England (1995)]. As the age of waters is a purely physical measure, in areas, like the OMZs, where strong biological consumption occurs [Löscher et al. (2015)], low oxygen levels can coincide with relatively young waters.

In the southern tropical Pacific, highest AGE values are simulated along the American coast from slightly north of the equator to 25° S in two tongues centered at 10° S reaching into the basin to 130° W and at ∼3° S reaching west to 110° W. The area defined as sOMZ is located where the two tongues are connected. Similar to the northern part, a patch of high AGE is located in the centre of the basin, here at 7° S. This is also given in the CONC structure, where lowest values co-occur with highest AGE values.

A section along 110° W (figure 4.18a and b), cutting through the nOMZ shows a domed shape of AGE and CONC spanning the nOMZ. The apex is located at ∼14° N in both, AGE and CONC. At 4° N AGE shows lower values while CONC shows elevated values, reaching down to ∼500 m depth, marking the NSCC, transporting better ventilated waters from the western part of the basin towards the east.

AGE and CONC along a section through the sOMZ at 85° W (figure 4.18c and d) also exhibit doming isosurfaces. Following the 85 years in AGE or 0.8 in CONC isosurfaces, the apex is located at ∼ 14° S. However, equatorward from 13° S in AGE and 12° S in CONC the gradients between ∼100 m and 350 m depth weaken, showing relatively low AGE (60 years) and high CONC values (0.9) up to 80 m depth at 6° S. For both sections, the CONC and AGE distributions are in agreement with what is observed in the oxygen fields [Fiedler and Talley (2006)].

The two passive tracers AGE and CONC are an integral measure for the contact between the surface and the interior ocean including advective and diffusive processes and therefore give insights on the ventilation. It has been shown above, that the tracer fields at the end of the model simulations are capable of broadly representing the observed oxygen distributions in the depth layer of the OMZs in the tropical Atlantic and, with some more limitations, in the tropical Pacific Ocean. To complement these tracer experiments, the origin of waters within the northern and southern OMZs in the tropical Atlantic and Pacific Oceans are investigated using a Lagrangian approach in the following two chapters.

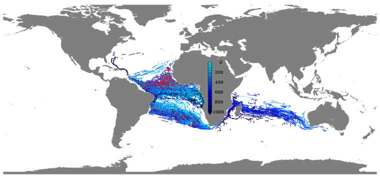

a) AGE at 110° W b) CONC at 110° W

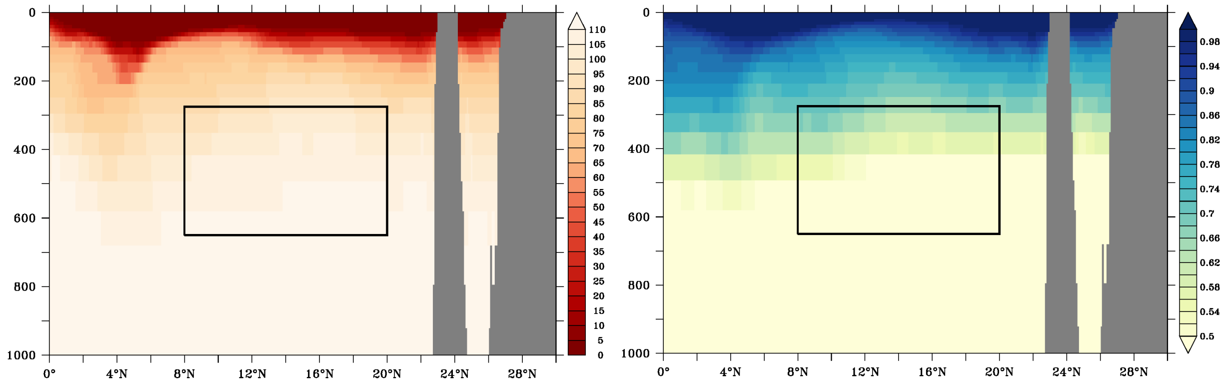

c) AGE at 85° W d) CONC at 85° W

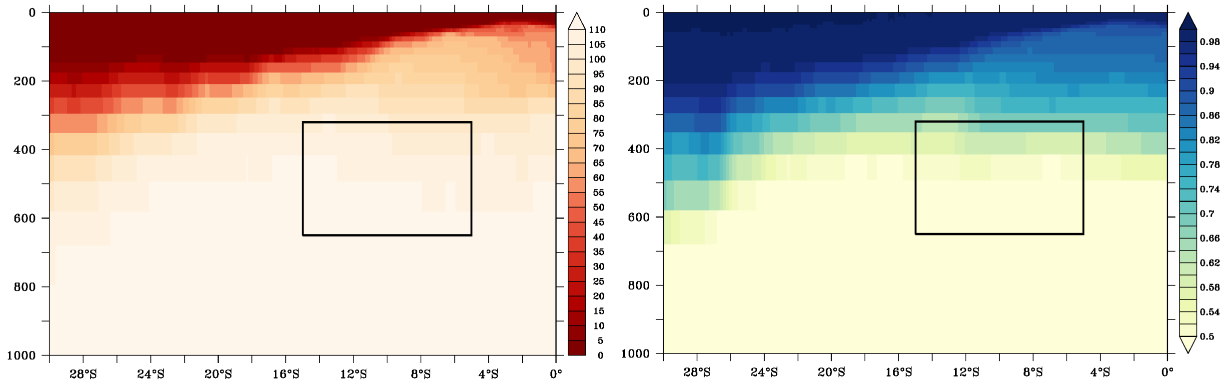

Figure 4.18.: Tracer AGE (a and c) and CONC (b and d) after 140 years of integration (annual average) along 110° W (a and b) and 85° W (c and d).

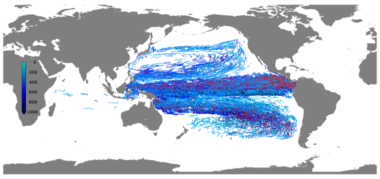

5. Ventilation of the eastern tropical Atlantic

As shown in chapter 4, poorly ventilated regions are located in the eastern tropical Atlantic Ocean, at mid-depth in the northern and southern parts of the Ocean basin, including the northern and southern Oxygen Minimum Zones (nOMZ and sOMZ). The physical transport processes affecting these zones are described, assessed and discussed within this chapter. Lagrangian experiments based on the temporally varying three dimensional velocity fields in TRATL01-IA and ORCA05-IA are performed in which the source regions and pathways of particles ending up in the OMZs are investigated. The passive tracers evaluated above, exhibit the zones, where the connection to surface waters is weak, whereas the trajectories explicitly focus on the paths that provide this albeit weak connection. Thereby the two methods yield insight on two different ends of the same path.

Contents

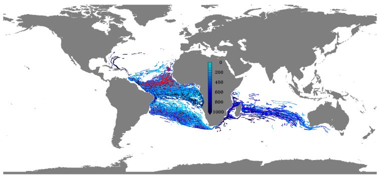

5.1. Mean circulation in the eastern tropical Atlantic

In the tropical and subtropical Atlantic Ocean, the mean circulation is marked by a strong zonal equatorial current system, a pronounced current band along the South American Coast and the anticyclonic circulation of the subtropical gyres. Stramma and Schott (1999) provide a schematic overview of the currents in different depth ranges in this area. Here, a ten year average (2000 to 2009) of the velocity field as simulated in TRATL01 is given in figure 5.1 for different depth levels within the upper 2000 m of the water column. Note that these figures are duplicated and the circulation at additional depths are shown in the appendix in enlarged versions (figures A.1 to A.18), juxtaposing the TRATL01 and ORCA05 circulations.

The surface circulation is dominated by the westward flowing South Equatorial Current (SEC) with its amplified northern (nSEC) and central (cSEC) branches embracing the equator, forced by the northeast and southeast trade winds [Talley et al. (2011)]. The southern (sSEC) branch is located further off-equatorial and characterized by a wider, slower flow. The SEC feeds into the poleward North Brazil (NBC) and Guiana Currents to the north and the Brazil Current (BC) to the south along the South American coast. East of 30° W, between 3° N and 6° N, the North Equatorial Counter Current (NECC) flows eastward with a slight southerly component. Along the African coast, the Angola and Benguela Currents are dominating the flow field. In the northern part, the North Equatorial Current (NEC) flows westward. See Schott et al. (2004) for a schematic of these currents and details on their generation.

Below the surface at 25 m depth, the uppermost edge of the Equatorial Under Current (EUC) becomes visible, located directly on the equator, flowing eastward [Stramma and Schott (1999); Brandt et al. (2014)]. Going further down to 50 m, 100 m or even 200 m depth, the EUC becomes the most prominent current structure in the tropical Atlantic Ocean with a mean speed of more than 1 m/s. Below 200 m depth, the nSEC and cSEC slowly vanish while the South Equatorial Undercurrent (SEUC) develops at about 5° S and the North Equatorial Undercurrent (NEUC) appears at 5° N as lower flank of the NECC [Schott et al. (2002)]. Off the equator, the mainly westward flow field, that had a poleward component near the surface, changed to a westward flow with an equator-ward component down here. Along the Brazilian coast, the NBC core shifts south and is sometimes referred to as North Brazil Under Current (NBUC). The NBC flowing north-westward along the coast [da Silveira et al. (1994)] turns south-east feeding into the EUC and even in an averaged velocity field, shows ring structures, the so called North Brazil Rings [Garraffo et al. (2003)], at their preferred locations. The pronounced currents along the African coast are no longer present at these depths.

At about 300 m depth, right at the equator, the Equatorial Intermediate Current (EIC) evolves in the western part of the basin, with westward velocities below the EUC [e.g. Brandt et al. (2012)]. This current is only a weak feature in a long term mean in TRATL01 but becomes seasonally very pronounced with its maximum in boreal autumn. Proceeding further down, alternating eastward and westward current structures mark the mean circulation on the equator. Below 300 m depth,

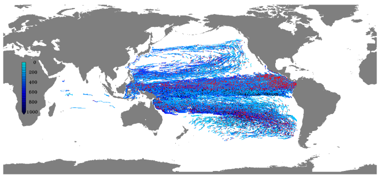

a) Surface b) 50 m depth

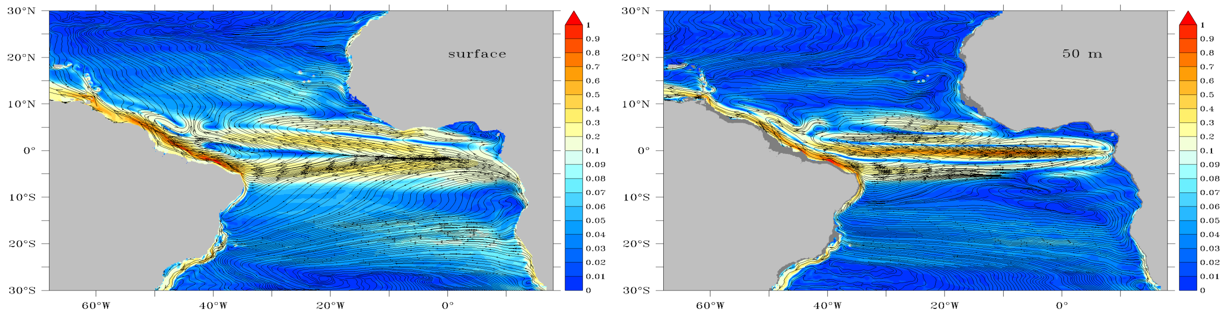

c) 100 m depth d) 200 m depth

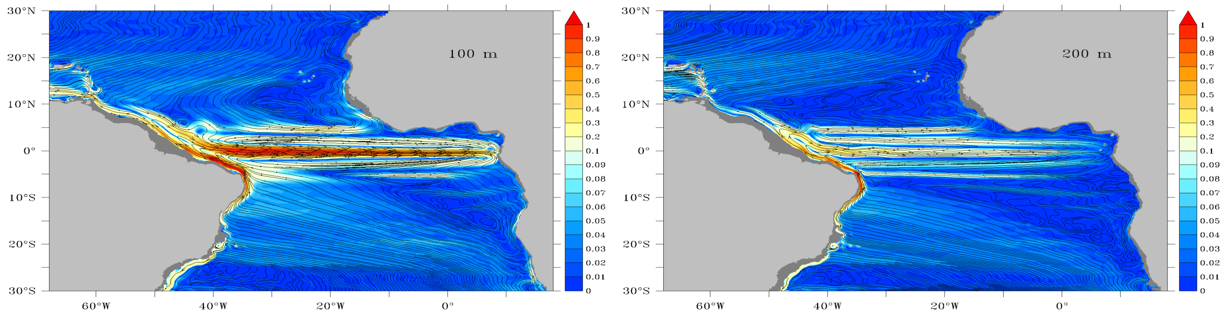

e) 300 m depth f) 500 m depth

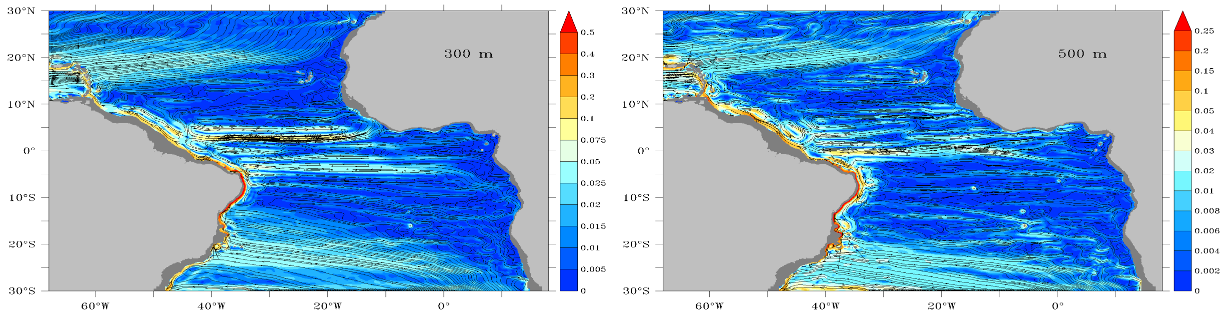

g) 1000 m depth h) 1500 m depth

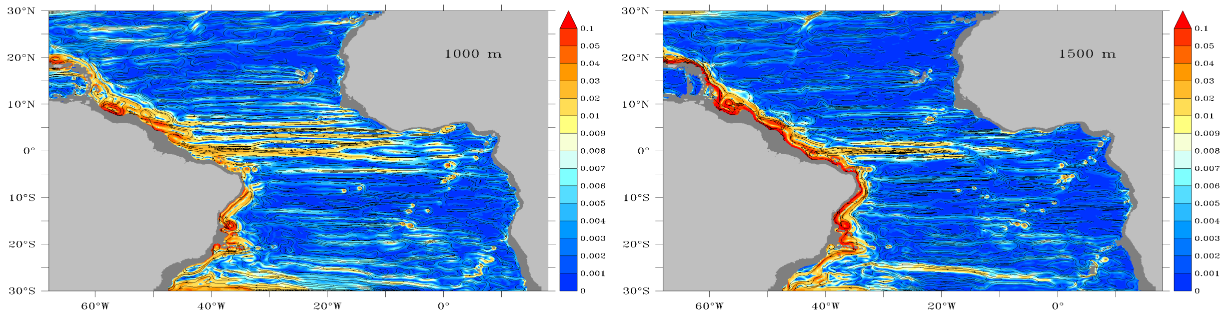

Figure 5.1.: Ten year averaged (2000 to 2009) circulation at different depths in TRATL01: shaded is speed [m/s] with streamlines overlaid. Note the different scales. See Appendix for enlarged versions.

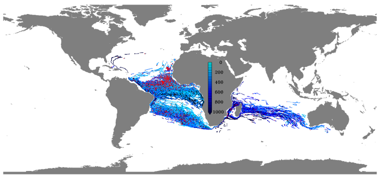

the dominance of zonal structures persists throughout the uppermost 2000 m of the water column in the entire tropical Atlantic basin, most pronounced in a ∼15° wide band around the equator. These deep band like structures have previously been described based on different types of float measurements [Ollitrault et al. (2006), Rosell-Fieschi et al. (2015)].

The comparison of the mean circulation in TRATL01 and ORCA05 shows weaker and less focused zonal currents in the coarser model. TRATL01 shows higher fidelity and better compares to observations than the ORCA05 representation (see also chapter 3):

At the surface, the mean current structure depicts the same features in ORCA05 as in TRATL01 (see figures A.1 to A.18 in the appendix) with only some weak, smaller scale structures towards the northern and southern boundary of the nested region are missing in ORCA05. This high similarity is due to the fact that the surface currents are mainly wind driven [Sverdrup (1947); Munk (1950)] and both models are subject to the same forcing. Already at 25 m and more pronounced at 50 m depth, the two current fields start to deviate from each other. The most prominent difference is the deeper and weaker EUC in ORCA05 as well as its missing connection to the nSEC and sSEC via the easternmost extension of the EUC. Therefore, those two current bands are in general very weak below the surface and missing in the eastern part of the Atlantic in the ORCA05 simulation. At 100 m depth, the core depth of the EUC, the restriction of this current band to the east (see figure 3.35) makes the most prominent difference between the two representations. Below these uppermost layers, the zonal current system, that is represented in TRATL01 is only very weak in ORCA05. At the depth range between ∼300 m and 700 m there are still many current features with velocities in the order of cm/s, that are not present in ORCA05. Below ∼500 m depth, except for the NBC, the SEC and the NEC, no mentionable currents are simulated in ORCA05 within the nested region of TRATL01.

Two prominent areas, where only very low velocities co-occur with the locations of the northern and southern OMZs in the eastern part of the basin are characterized by flow speeds below 5 cm/s (see figure 5.2). Here, the circulation is sluggish throughout the entire water column, except for the coastal currents near the surface. Within this study, the northern and southern Oxygen Minimum Zone (nOMZ and sOMZ) in the tropical Atlantic Ocean are defined as the regions between the African coast and ∼10° off coast, in a ∼10° wide, off equatorial band at mid-depth range (see boxes in figure 5.2 and table 5.1) These two zones are subject to closer investigation within this chapter.

OMZ	Longitude	Latitude	Depth
Atlantic nOMZ	25° W to African coast	8° N to 17.5° N	290 m to 650 m
Atlantic sOMZ	4° E to African coast	18° S to 7° S	275 m to 650 m

Table 5.1.: OMZ definitions

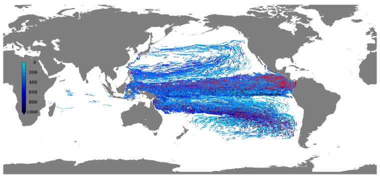

a) TRATL01

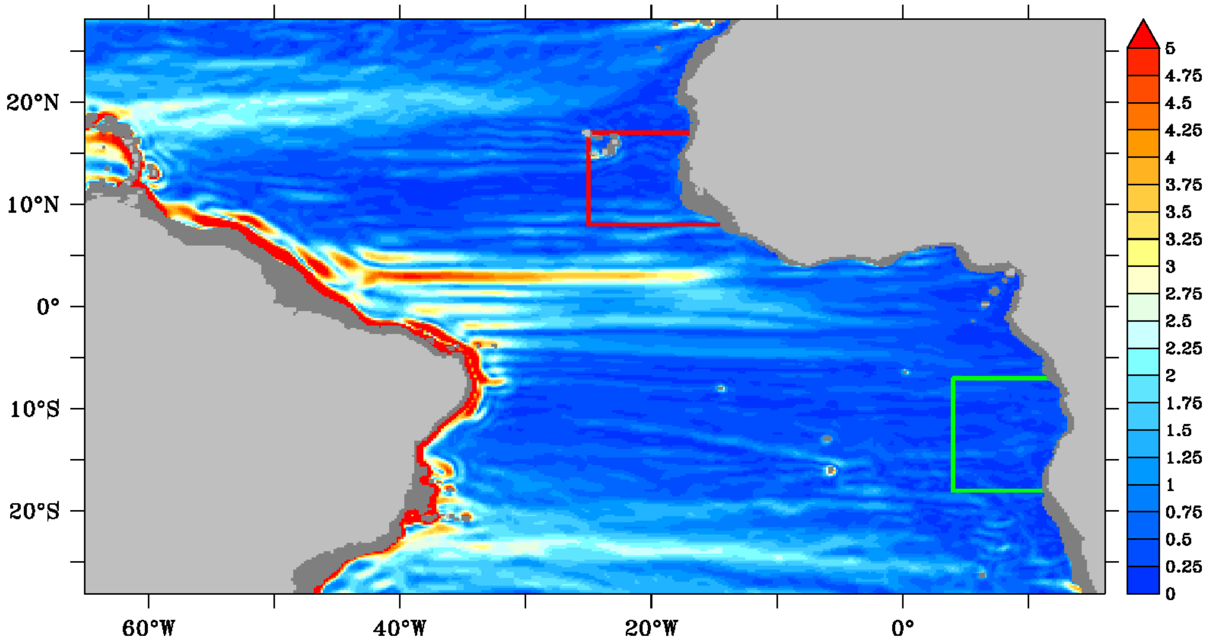

b) ORCA05

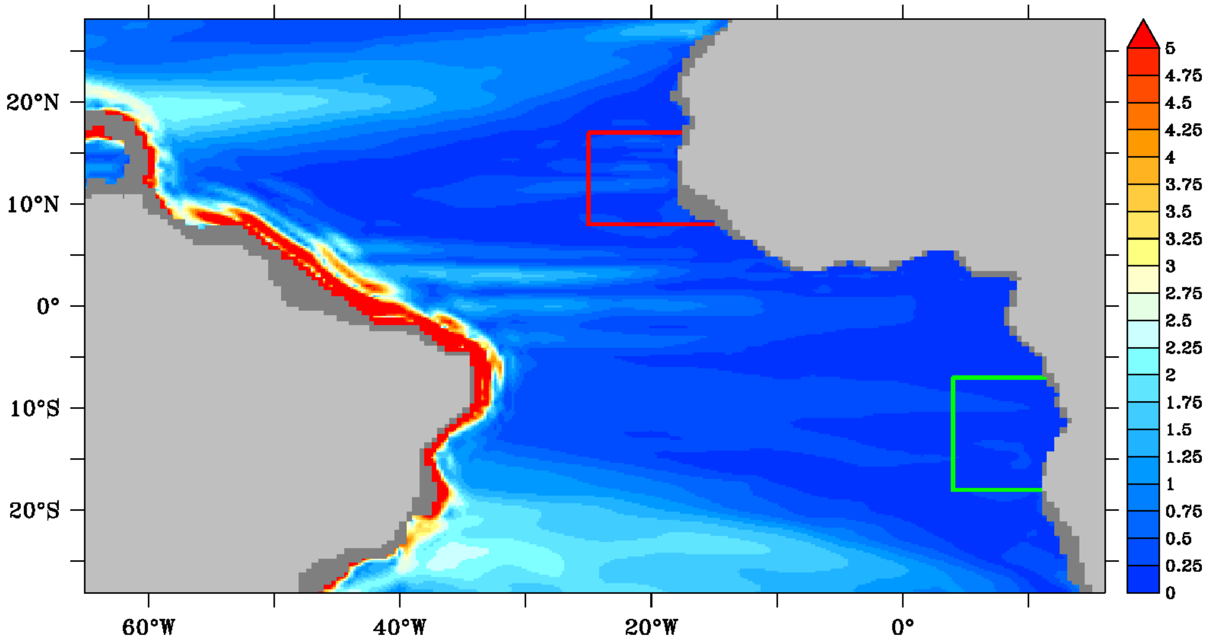

Figure 5.2.: Averaged (2000 to 2009) speed [cm/s] in the OMZ depth layer between 300 m and 650 m in TRATL01 a) and ORCA05 b). The boxes indicate the regions referred to as nOMZ (red) and sOMZ (green)

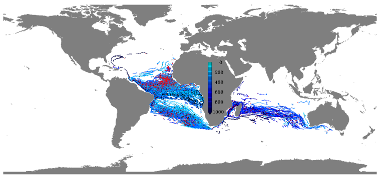

5.1.1. Vertical velocities in TRATL01

The above described horizontal circulation in the different depth layers is connected by vertical motion, computationally, as a result of the continuity of the three dimensional velocity field [Madec (2008)]. Temporally averaged (ten year mean) profiles (figure 5.3) and maps (figures 5.4 and 5.5) of vertical velocities in and close to the OMZs provide insight into the net effect of vertical motion not only on the trajectories in the following Lagrangian experiments but also the supply of the OMZs with waters from above and below [Löscher et al. (2015)].

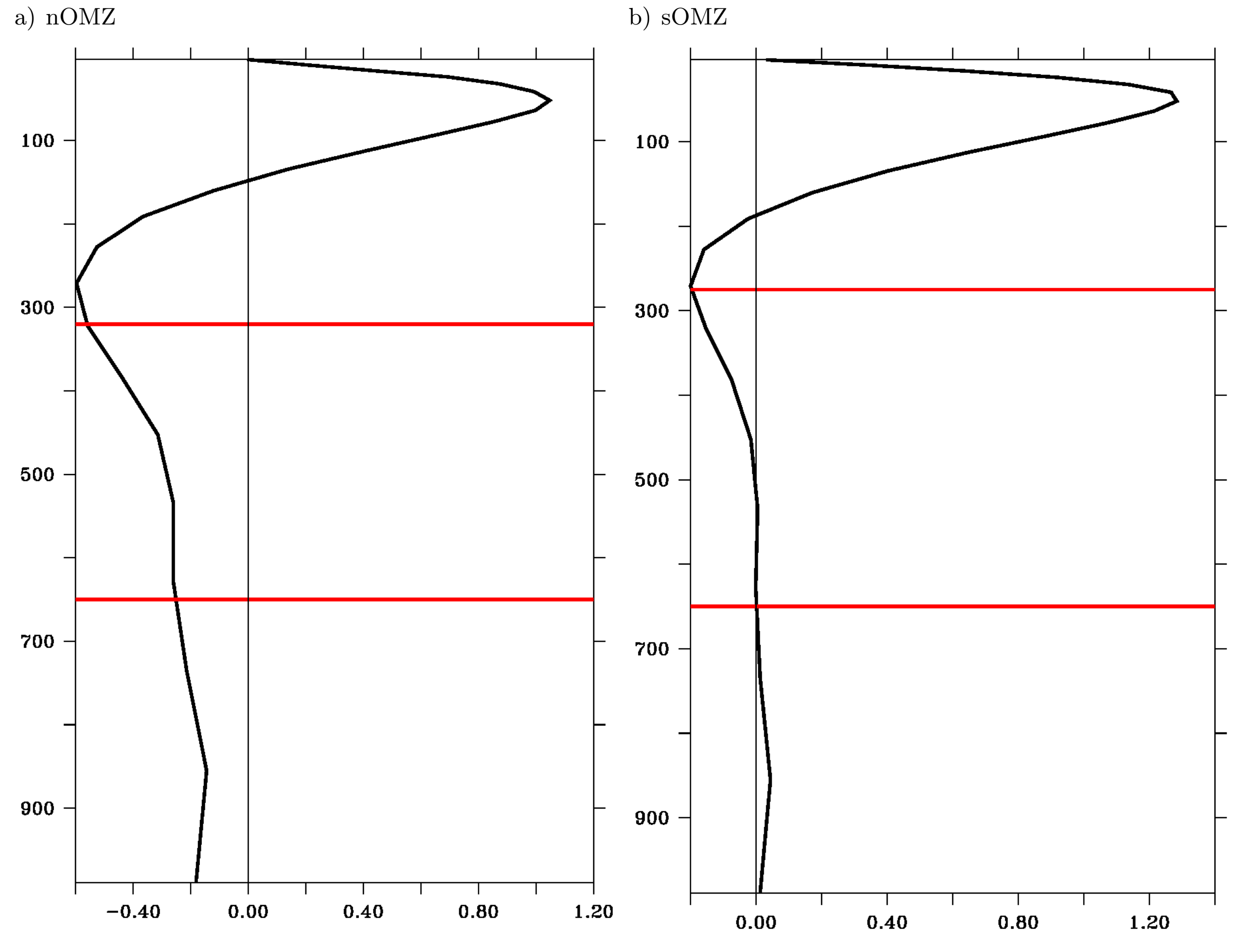

Figure 5.3.: Ten year mean vertical velocity (10^{-6} m/s) profile in TRATL01 horizontally averaged over the nOMZ a) and sOMZ b). The red lines indicate the upper and lower limits of the OMZs respectively.

Profiles of vertical velocities averaged over the horizontal extent of the OMZs (figure 5.3) show upwelling (positive vertical velocities) in the upper 125 m and 150 m depth for the nOMZ and sOMZ areas, respectively [Capone and Hutchins (2013)]. Below this uppermost layer, downwelling (negative vertical velocities) occurs, that reaches down into the OMZ layers (indicated by the red lines) and therefore allows for direct supply of waters from above. However, due to the upwelling in

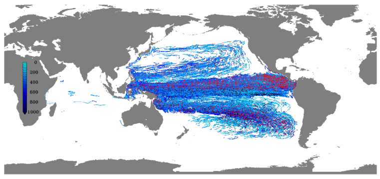

the uppermost 150 m, the direct ventilation from the surface is suppressed; waters located directly above the OMZs need to be transported there laterally for instance by the circulation in the subthermocline layer [Rabe et al. (2008)].

In the northern region downwelling persists throughout the rest of the upper 1000 m of the water column, whereas in the southern region it is restricted to a layer down to ∼480 m depth. Below this layer, the temporally and horizontally averaged vertical velocities are almost zero and therefore, in an averaged sense, no vertical motion occurs and, in both regions, there is no direct supply from below the OMZ layers.

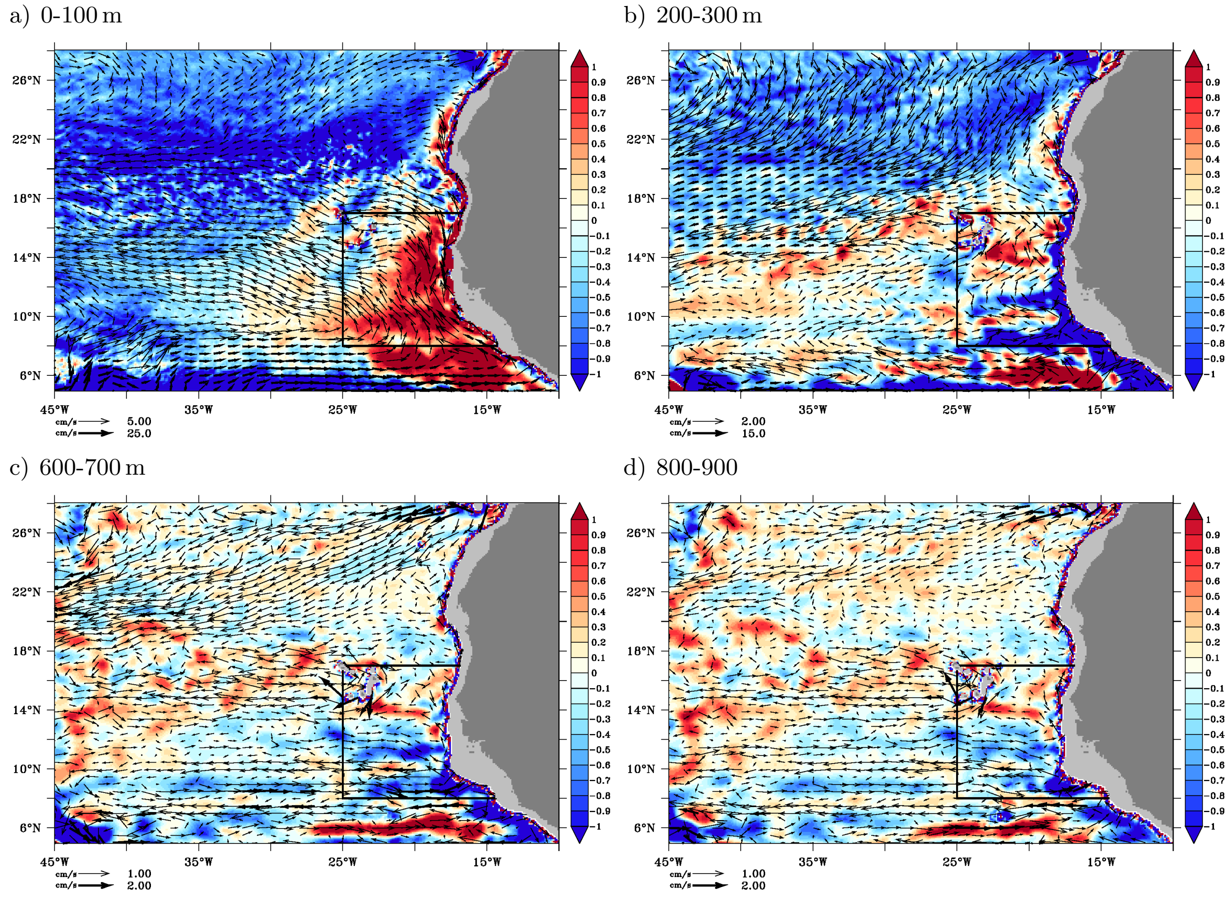
a) 0-100 m

b) 200-300 m

c) 600-700 m

d) 800-900

Figure 5.4.: Ten year mean vertical velocity (10^{-6} m/s shaded) in TRATL01 and horizontal velocities (vectors) averaged over 100 m of the water column between the surface and 100 m depth a), 200 m and 300 m depth b), 600 m and 700 m depth c) and 800 m and 900 m depth d)

The horizontal structure of the vertical velocities shows upwelling within the uppermost 100 m of the water column throughout the horizontal extent of the nOMZ (figure 5.4) and sOMZ (figure 5.5) with only the poleward western corner of the areas showing very weak and also negative velocities

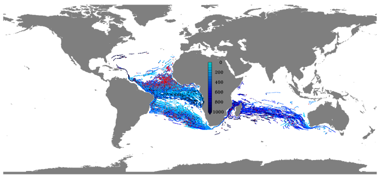

with values comparable to previous studies [e.g. Halliwell et al. (2003)]. At the upper boundary of the OMZs, at 300 m depth, the vertical velocity is horizontally inhomogeneous with negative values, most pronounced along the coast and in two zonal bands at 8° N and 11° N in the nOMZ and positive velocities south east of the Cape Verde Islands. This structure persists throughout the vertical extent of the OMZs ($\sim$700 m) and down to 900 m depth with decreasing amplitudes. Peña-Izquierdo et al. (2015) show annual mean vertical velocity fields from ECCO2 for the upper and lower Central Water layers, approximately corresponding to the 300 m layer and 700 m layer shown here, respectively, that agree with what is found here. In the sOMZ, downwelling takes place in the northern part and along the coast in 300 m depth, while in the south western part of the sOMZ upwelling occurs. Below, only very weak horizontally unstructured vertical velocities prevail, that, on average, are close to zero. The downwelling areas in both, the northern and southern OMZ, can partly be identified in the tracer fields (figures 4.15) as low AGE and high CONC values.

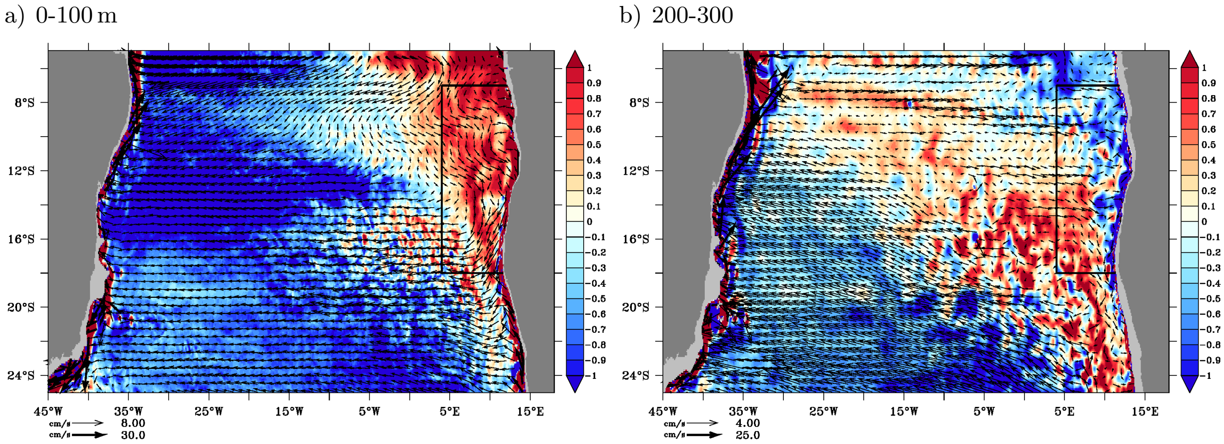
a) 0-100 m

b) 200-300

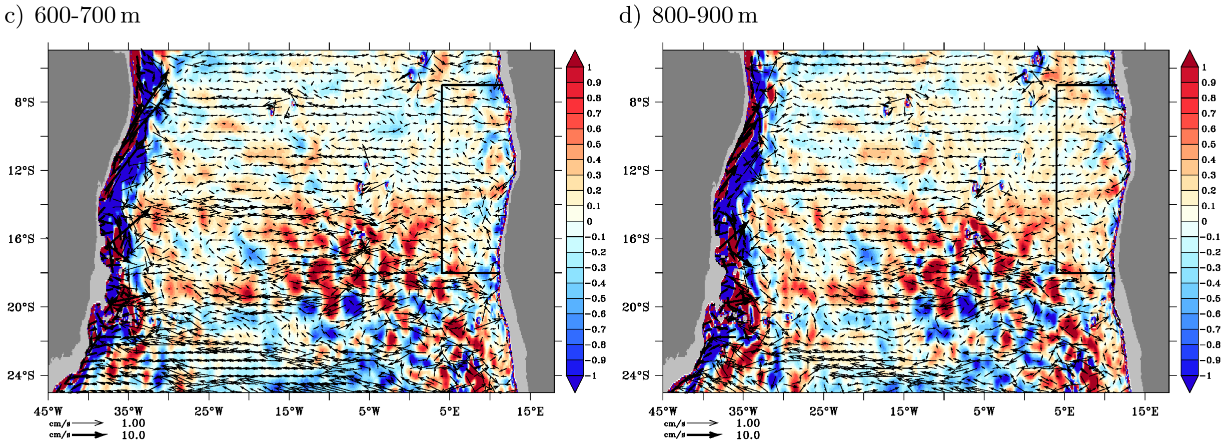
c) 600-700 m

d) 800-900 m

Figure 5.5.: Ten year mean vertical velocity (10^{-6} m/s shaded) in TRATL01 and horizontal velocities (vectors) averaged over 100 m of the water column between the surface and 100 m depth a), 200 m and 300 m depth b), 600 m and 700 m depth c) and 800 m and 900 m depth d)

The following Lagrangian experiments are built on the above described three dimensional velocities.

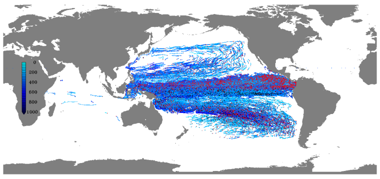

5.2. Ventilation pathways assessed by particle trajectories

Lagrangian trajectory experiments have been performed to identify pathways and timescales, waters take and need to enter the OMZs. Particles released within the OMZs (boxes in figure 5.2) have been traced backwards (see section 2.3) using velocity fields from TRATL01-IA and ORCA05-IA to also identify the effect of increased model resolution and thereby better representation of the equatorial and off-equatorial current system (see section 3.6) on these ventilation aspects.

Particles are seeded on a regular spatial pattern within the OMZs, defined as three dimensional boxes (see table 5.1 for definitions; these areas are marked in figures 5.2 to 5.5), at one point in time at the end of the integration period. Their locations are then traced backwards for 80 years using 5-daily averaged velocity fields. To generate these 80 years of velocity time series, the model output from 1960 to 2007 is used repeatedly. The resulting particle trajectories and derived populations (see section 2.3.4), are presented here.

The temporal evolution of particle populations within the release areas during the backward integration gives an integral measure for the time scales and processes within the different areas, referred to as OMZs. An exponential decline in this population occurs during the first decades with varying e-folding time scales for the different experiments (figure 5.6, left column).

In the Atlantic nOMZ the decline in ORCA05 is faster than in (but comparable to) TRATL01 with an e-folding time scale of 7 years (black curve) compared to 9 years (red curve). In both cases, a linear decrease can be identified for the last 50 and 40 years in ORCA05 and TRATL01 respectively, leading to almost identical fraction of remaining particles within the release area after the 80 year integration. In the Atlantic sOMZ, the comparison between the two experiments leads to the opposite result, with ORCA05 showing a slower initial decline on a 16 years time scale, losing its exponential character already after ∼13 years, than TRATL01 with 10 years time scale for the first 20 years. TRATL01 again shows a linear decrease within the last 50 years that is missing in ORCA05. The differences between the results from the experiments in TRATL01 and ORCA05 show, that for the Atlantic nOMZ the model resolution has a smaller impact on the local ventilation processes than for the sOMZ, supporting the finding by Duteil et al. (2014).

Particles that leave the nested area in TRATL01 cannot be analyzed beyond the nest-boundaries. To keep the results from the nested and the global simulations comparable only particles, within the nested area are taken into account for all experiments in the following analyses. All particles, that leave the nested area are from then on referred to as "lost" (figure 5.6, right column). For the particles released in the Atlantic nOMZ, the loss of particles starts earlier in ORCA05 than in TRATL01 and is well comparable between the two models for the particles released in the sOMZ. After the 80 years integration ∼60% remain within the nested area for the nOMZ experiment and ∼65% for the sOMZ experiment.

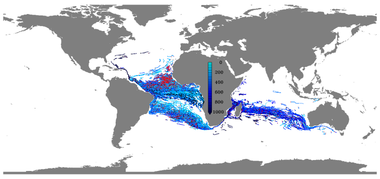

a) nOMZ - release area b) nOMZ - nest area

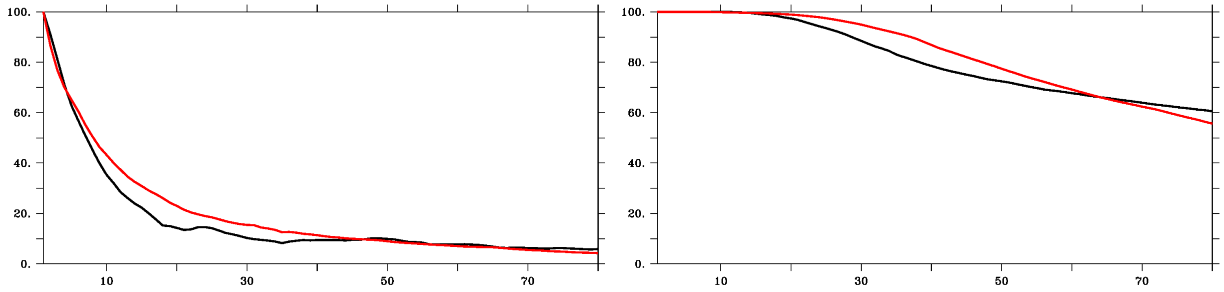

c) sOMZ - release area d) sOMZ - nest area

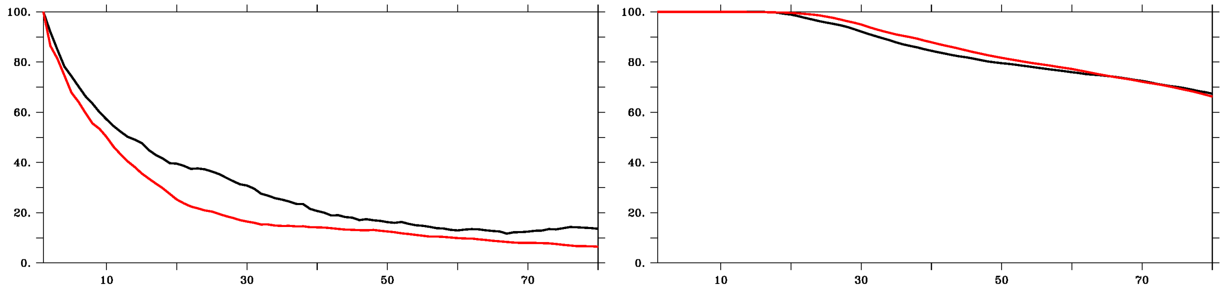

Figure 5.6.: Temporal evolution (year of the Lagrangian backward integration) of number of particles [yearly averages in %] still found in the release area (a and c) and the nested model domain of TRATL01 (b and d), for the releases in the northern (a and b) and southern (c and d) OMZs. The experiments in TRATL01 are marked by the red curves; curves from the ORCA05 experiments are in black.

The evolution of particle numbers within the OMZs only describe the behaviour close to these zones. For ventilation, the last contact of a particle with well oxygenated waters, before entering the OMZs is of importance. As a simple approximation for “well oxygenated waters”, the upper 50 m of the water column are taken. The fraction of particles entering (in a backward sense) this layer in a certain year of the integration, depending on their release depth shows that only a small fraction makes it into this layer within the 80 years (figures 5.7 and 5.8). The fraction entering the upper 50 m of the water column is referred to the total number of particles within the corresponding depth layers, irrespective of the lost particles over time.

The definitions of the release areas in TRATL01 and ORCA05 differ slightly in their vertical extent. When only taking into account for particles in the common range of release depths within the nOMZ, 6.4% reach the upper 50 m in TRATL01 and 14.7% in ORCA05. The deeper the release depth of the particles, the smaller the fraction of particles reaching the upper 50 m. More than 30% of the particles released within the upper 400 m of the water column reach the upper 50 m in ORCA05 for the nOMZ experiment, whereas it is only a fraction of 10% in TRATL01. For the deepest common part of the release area, the fraction of particles is higher in TRATL01 (3.1%) than in ORCA05 (1.3%). In the sOMZ less particles make it into the upper 50 m of the water column during the integration with 10.4% in ORCA05 and 3.9% in TRATL01. For the particles released above 500 m more particles make it into that layer in ORCA05 than in TRATL01 whereas, as for

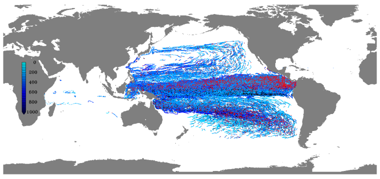

the nOMZ, the fraction of particles released in the deepest common depths reaching that layer is higher (1.4%) in TRATL01 than in ORCA05 (0.6%). The full statistics are given in table 5.2.

Experiment	total	common	200-300 m	300-400 m	400-500 m	500-600 m	600-700 m
Atlantic nOMZ 0.5°	18.0	14.7	37.2	30.2	12.5	1.3	-
Atlantic nOMZ 0.1°	5.2	6.4	-	10.2	5.7	3.1	1.6
Atlantic sOMZ 0.5°	10.4	10.4	24.3	13.2	3.5	0.6	-
Atlantic sOMZ 0.1°	3.2	3.9	9.5	5.3	2.3	1.4	0.6

Table 5.2.: Fraction of particles reaching the upper 50 m of the water column within the nested area in TRATL01 during the 80 year integration. Missing values mean, no particles have been released in the corresponding depth range. Total refers to all particles released in the corresponding experiment whereas common refers to the depths common between the TRATL01 and ORCA05 experiments with the same release area.

The temporal evolution of the number of particles reaching the upper 50 m of the water column (figure 5.7) shows, that for the shallowest common release depth range in the nOMZ (300-400 m, red curves) the particles in TRATL01 (upper panel) need about 25 years whereas in ORCA05 (lower panel) it takes more than 30 years. Note, that the lost particles are not taken into account, therefore the decrease in the number of particles entering the upper 50 m with time is rather an artefact than a signal. For the other depth ranges, the decline, that can be seen in TRATL01 for the uppermost part of the release area vanishes, meaning that less particles reach the nest boundaries within the 80 years of the integration. The plateau in particle numbers reaching the upper 50 m of the water column develops earlier in TRATL01 than in ORCA05, nevertheless, the fraction of particles reaching that layer is significantly smaller in TRATL01 than in ORCA05 except for the deepest particles (released below 500 m depth). This shows that the connection between the upper 50 m and the nOMZ is faster but weaker in TRATL01 than in ORCA05.

In the sOMZ the behaviour is similar to that in the nOMZ with ORCA05 showing longer timescales for the particles to reach the upper layer than in TRATL01 (figure 5.8). Again, the particles released within the uppermost depth range leave the nested region faster in TRATL01 than in ORCA05 leading to a drop in the numbers (purple curves). For the deeper layers it also takes longer for the particles in ORCA05 to reach the upper layer than in TRATL01. Comparing the full depth range (black curves), the timescales are similar for the two experiments, both reaching a plateau within about 30 years.

From this rough estimation of “well ventilated waters” as represented by the upper 50 m of the water column, one can state, that the coarser ORCA05 simulation provides a better connection to the OMZs than the nested solution. Most of this connection is attributed to the shallow particles.

For the OMZ area and the nested region in TRATL01 50 m is a good estimate for a mean mixed layer depth but it is non-uniform in space and time and, away from this restricted area, signifi-

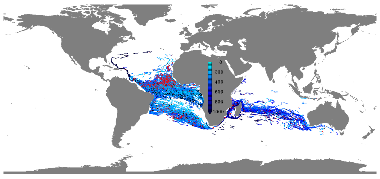

a) nOMZ TRATL01

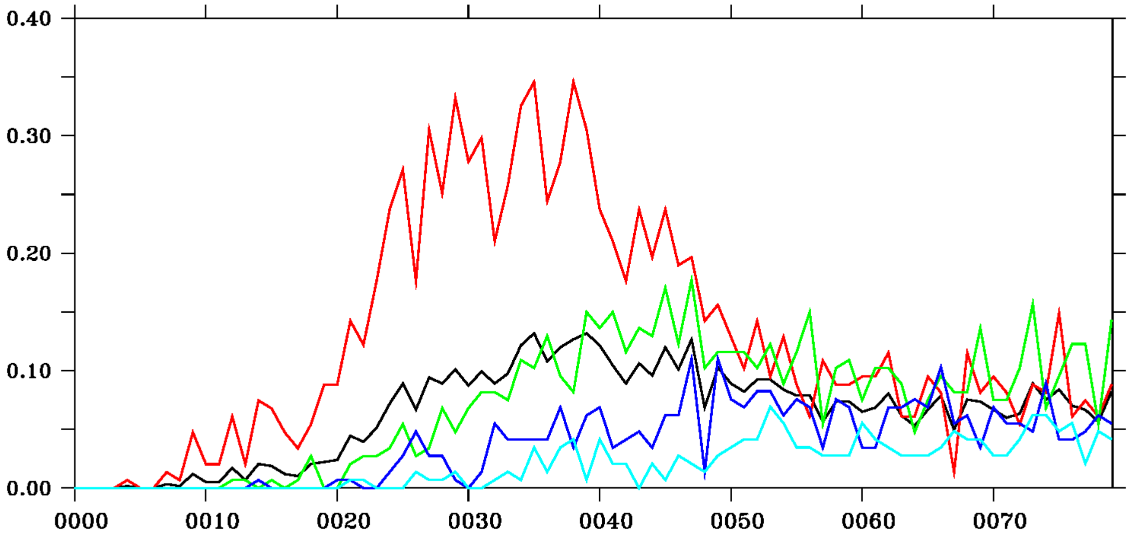

b) nOMZ ORCA05

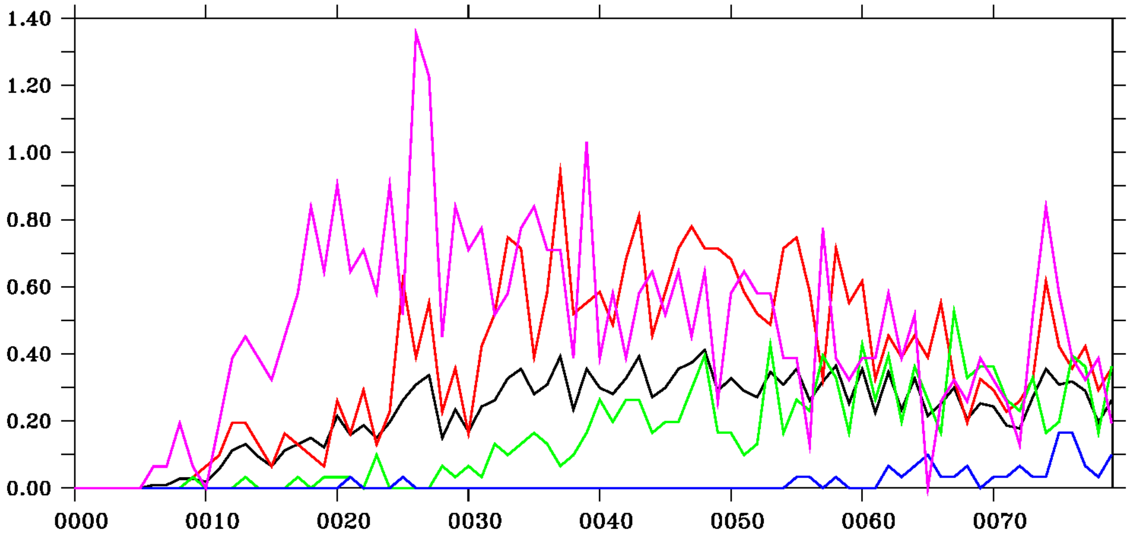

Figure 5.7.: Amount of particles [yearly averages in %] reaching the upper 50 m of the water column at a certain time after their release in the Atlantic nOMZ in certain depth ranges: 200 m to 300 m (purple), 300 m to 400 m (red), 400 m to 500 m (green), 500 m to 600 m (blue), 600 m to 700 m (light blue) and independent from the release depth (black) in TRATL01 a) and ORCA05 b). Note the different scales on the y-axis.

cantly deviates into both directions [de Boyer Montégut et al. (2004)]. Therefore the spatially and temporally varying mixed layer, as a more sensitive quantity for the ventilated area, is used in the following. A particle is defined to be within the mixed layer, when it is located at a depth, shallower than the temporally changing mixed layer depth at its instantaneous horizontal location. The fractions of particles and the averaged times between the last occurrence in the mixed layer and their final location within the OMZs are given in table 5.3 for the experiments in TRATL01

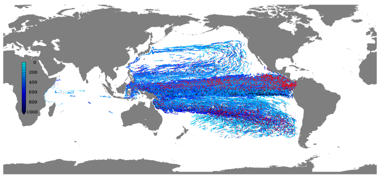

a) sOMZ TRATL01

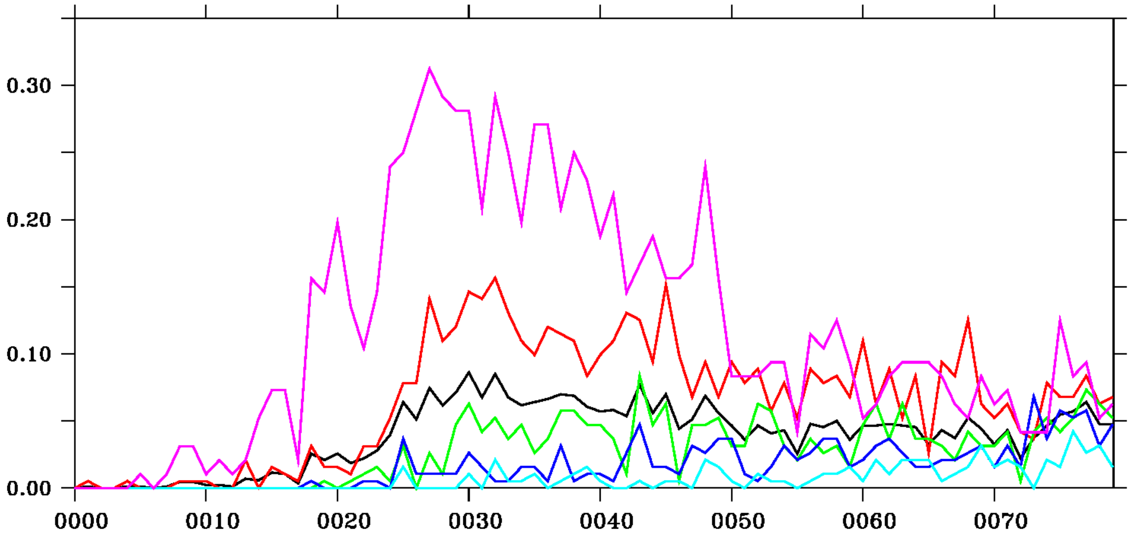

b) sOMZ ORCA05

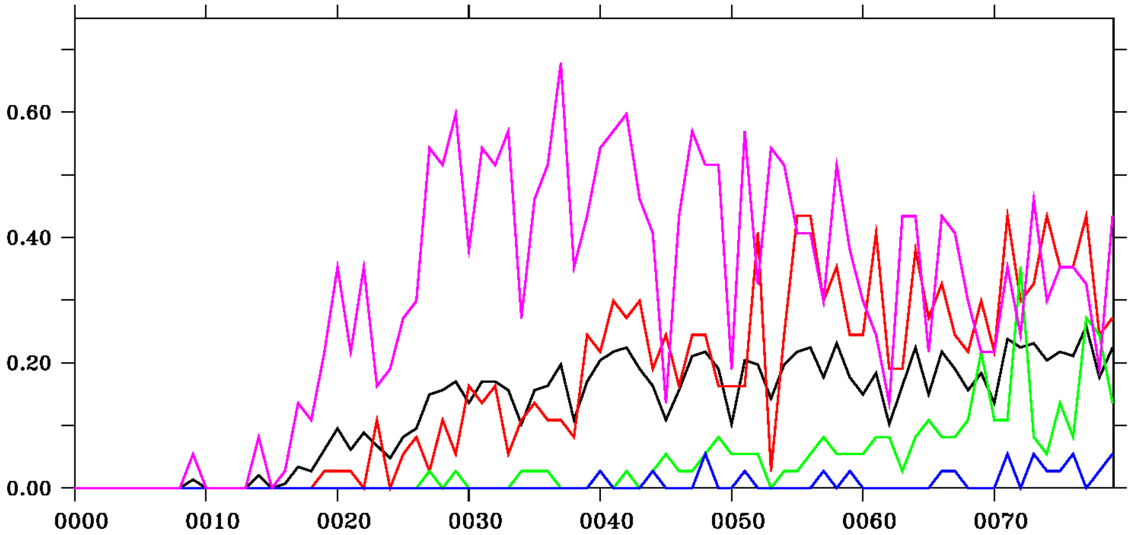

Figure 5.8.: Amount of particles [yearly averages in %] reaching the upper 50 m of the water column at a certain time after their release in the Atlantic sOMZ in certain depth ranges: 200 m to 300 m (purple), 300 m to 400 m (red), 400 m to 500 m (green), 500 m to 600 m (blue), 600 m to 700 m (light blue) and independent from the release depth (black) in TRATL01 a) and ORCA05 b). Note the different scales on the y-axis.

and ORCA05 with releases in the Atlantic nOMZ and sOMZ. Overall, only a small fraction of the particles analyzed here, was located within the mixed layer during the 80 years of integration. Within the nested region, 7% and 4% of the particles were located in the mixed layer before they enter the nOMZ and sOMZ respectively in ORCA05 whereas these numbers are only half as high for the experiments in TRATL01. In the ORCA05 experiments, where it is possible to identify particles that get ventilated outside the nested region, significantly more particles got in touch with

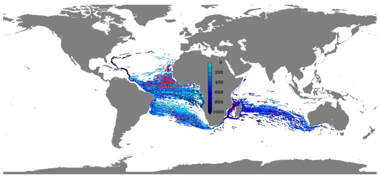

the mixed layer with 25% and 15% in the nOMZ and the sOMZ respectively. The averaged time particles need to enter the OMZs after they leave the mixed layer is roughly 45 years for both OMZs and both models. Note that these times are only averaged for those particles that actually got ventilated during the 80 year integration and are therefore biased towards shorter timescales.

Experiment	within nest [%]	global [%]	time [years]
Atlantic nOMZ ORCA05	7	25	44
Atlantic nOMZ TRATL01	4	-	45
Atlantic sOMZ ORCA05	4	15	48
Atlantic sOMZ TRATL01	2	-	46

Table 5.3.: Amount of ventilated particles (within the nested region and global for the ORCA05 experiment) and averaged ventilation time for the Lagrangian experiments in the Atlantic OMZs in the ORCA05 and nested TRATL01 models.

The temporal evolution of the number of particles reaching the mixed layer (figure 5.9) exhibits the persistence of the larger fraction in ORCA05 during the entire integration time. For the nOMZ experiment in ORCA05 a tendency to declining numbers after 50 years of integration indicate some saturation, that is however, not present in the TRATL01 experiment nor for the experiments in the sOMZ. Here, after ~30 years a plateau is reached, that persists throughout the 80 years long integration period of the Lagrangian particles, pointing to a prolonged time scale for ventilation, not covered by the present experiments.

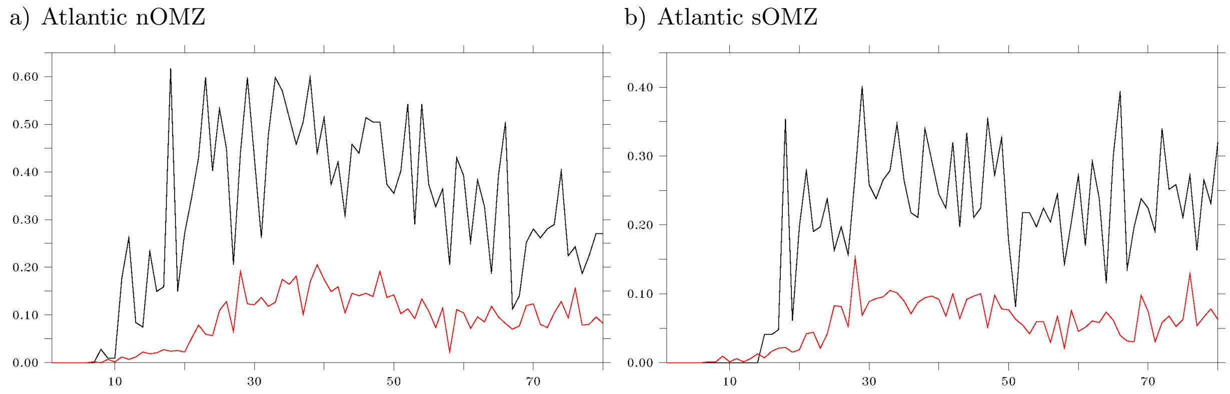
a) Atlantic nOMZ

b) Atlantic sOMZ

Figure 5.9.: Fraction of particles (in percent of released particles) entering the mixed layer (in a backward sense) in a certain year after release in the Atlantic nOMZ a) and sOMZ b). Black curves are from the experiments in ORCA05 and red curves are from the experiments in TRATL01.

The regions where the particles leave the mixed layer before they enter the OMZs (populated areas in figures 5.10 to 5.13) are mainly located in the subtropical Atlantic Ocean. In TRATL01, for both, the experiment for the nOMZ (figure 5.10) and the sOMZ (figure 5.12), two distinct regions, where particles get ventilated can be identified: in the north, between 20° N and 30° N, concentrated in

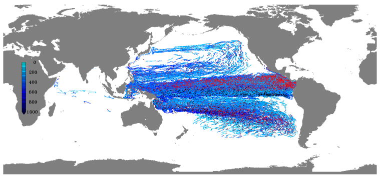

the eastern part of the Atlantic Ocean and in a southern region between 15° S and 30° S. In the latter, two areas can be described separately, one as a zonal band between 15° S and ~20° S and a second one south of 20° S where particles are clustered in the eastern part of the basin. In the experiment where the particles are released within the sOMZ, less particles get ventilated in the north, whereas in the experiment with the release in the nOMZ, the fraction that gets ventilated in the south are comparable to those in the sOMZ experiment.

a) # nOMZ TRATL01

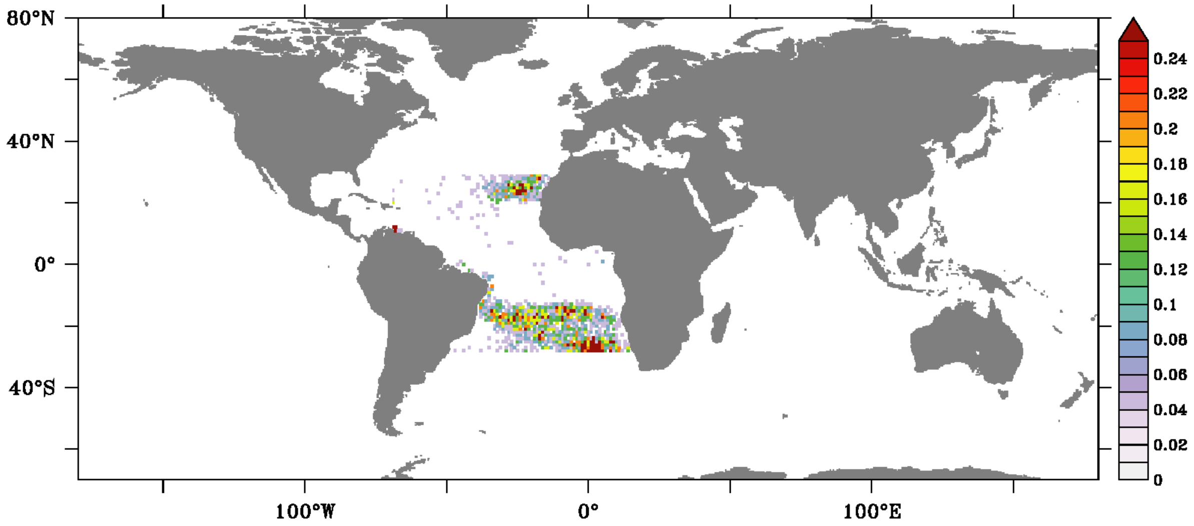

b) time nOMZ TRATL01

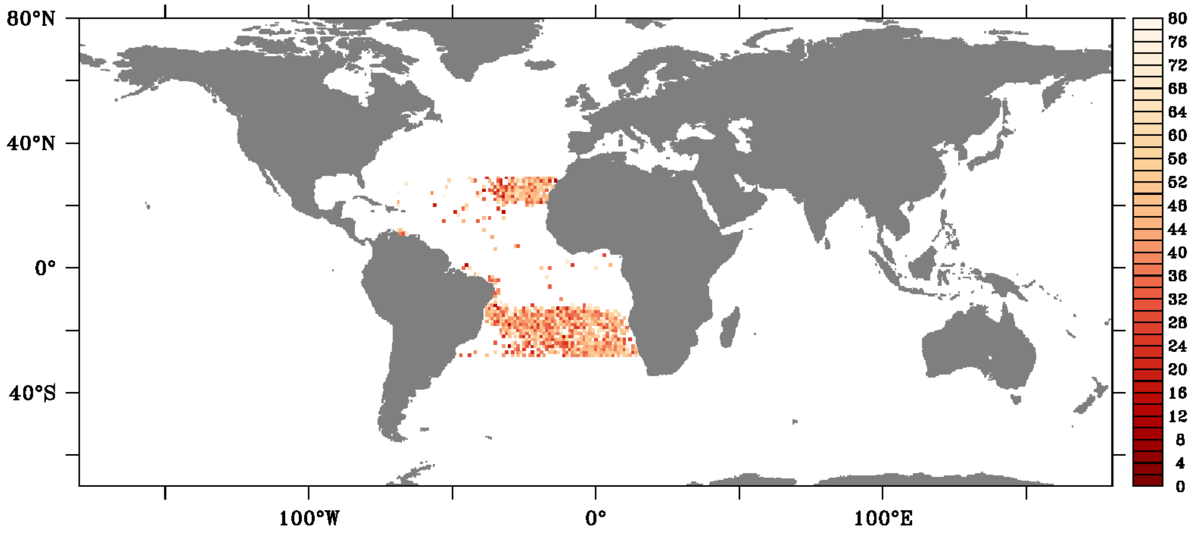

Figure 5.10.: nOMZ TRATL01: Number of particles that make it to the mixed layer [in % of released particles counted within 0.5° by 0.5° squares] a) and the averaged time they need to get there [in years] b).

In the ORCA05 experiments, additional to the ventilation regions in the Atlantic Ocean that extend

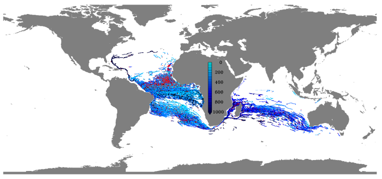

a) # nOMZ ORCA05

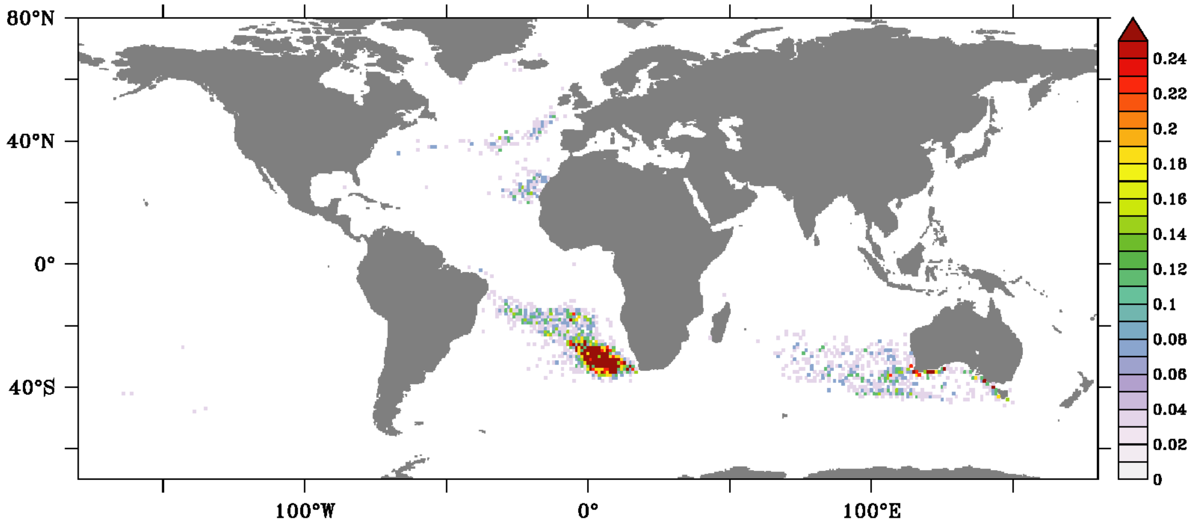

b) time nOMZ ORCA05

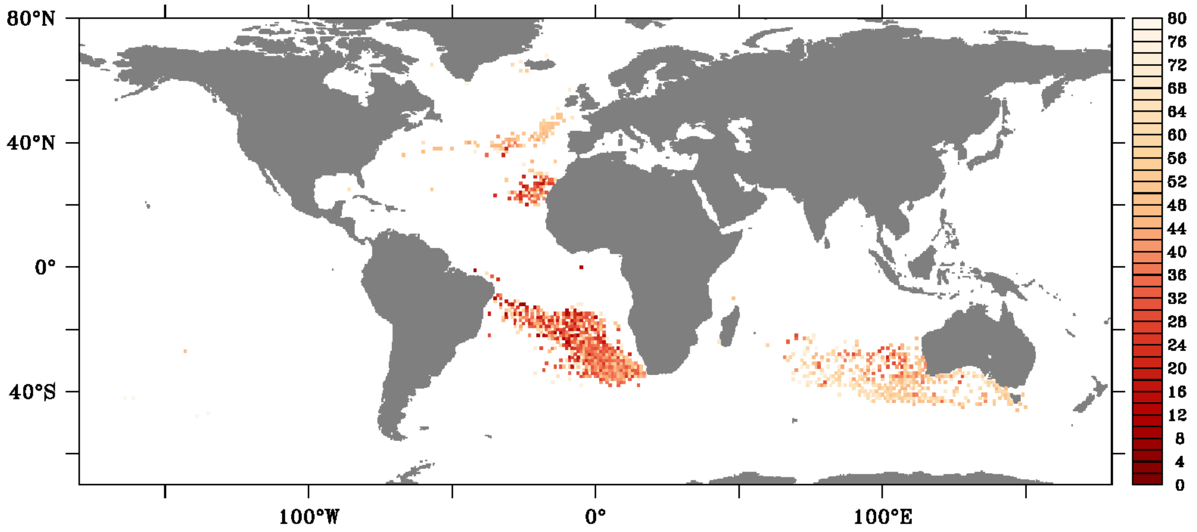

Figure 5.11.: nOMZ ORCA05: Number of particles that make it to the mixed layer [in % of released particles counted within 0.5° by 0.5° squares] a) and the averaged time they need to get there [in years] b).

further north and south beyond the nested region, particles get also ventilated within a band in the Indian Ocean between 20° S and 45° S including the Great Australian Bight. The ventilation areas are similar for the two experiments with the nOMZ experiment (figure 5.11) showing an additional ventilation region in the northern Atlantic that is missing in the sOMZ experiment (figure 5.13). In all four experiments, the most pronounced ventilation patch (red colours in the top panels of figures 5.10 to 5.13) is located in the southern Atlantic Ocean, concentrated in the eastern part, off South Africa.

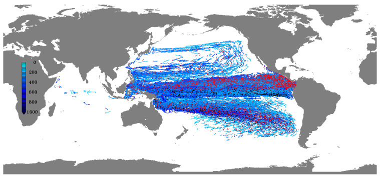

a) # sOMZ TRATL01

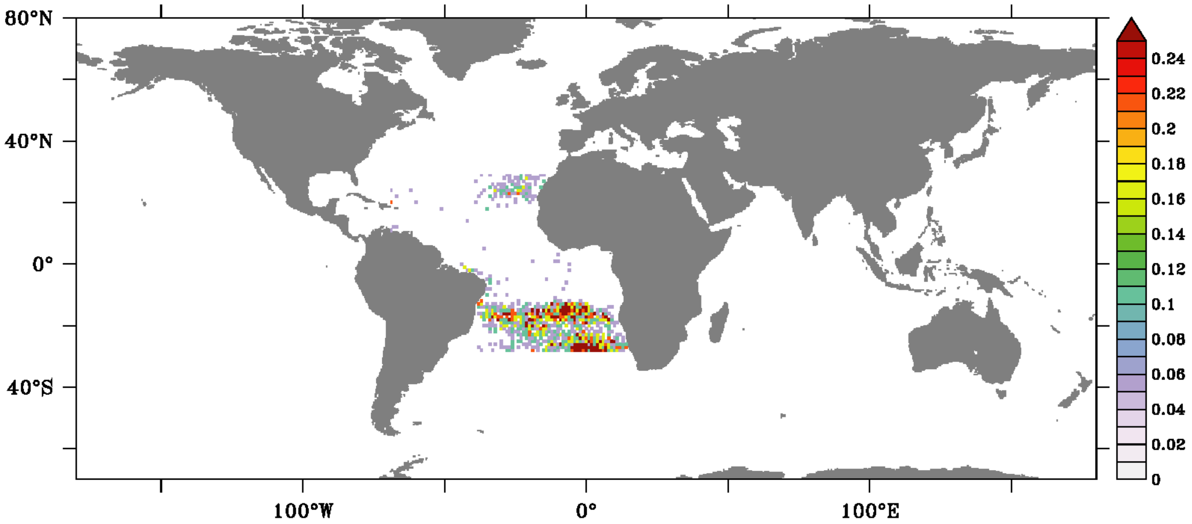

b) time sOMZ TRATL01

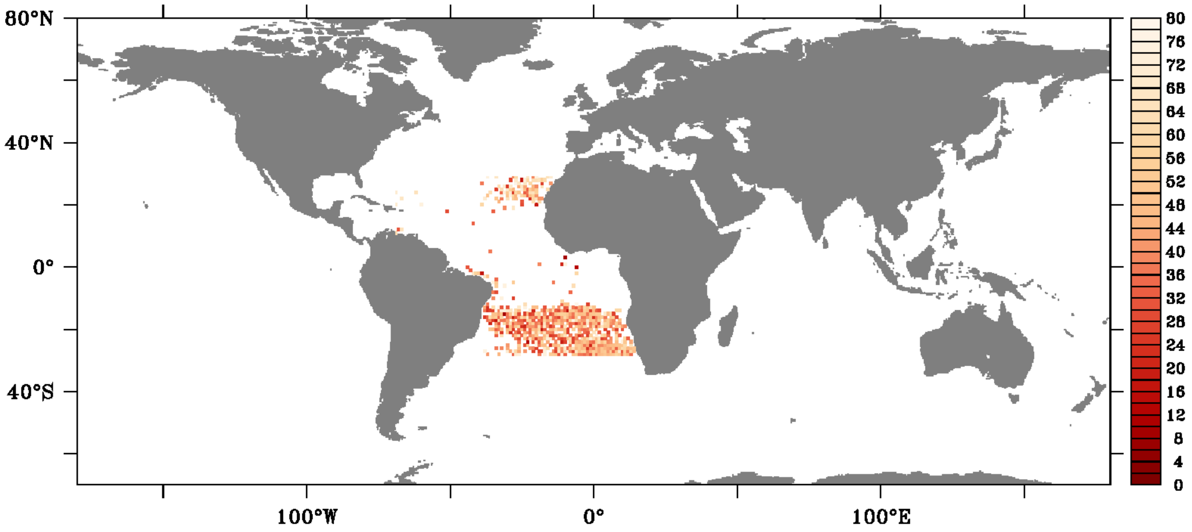

Figure 5.12.: sOMZ TRATL01: Number of particles that make it to the mixed layer [in % of released particles counted within 0.5° by 0.5° squares] a) and the averaged time they need to get there [in years] b).

Again, for the particles, that reach (in a backward sense) the mixed layer within the 80 years the averaged time they need to get there is ∼45 years for all the experiments (see table 5.3 for exact values). Depending on the location, where the particles get ventilated, this time ranges from ∼7 to 80 years. These times are only based on the fraction of particles reaching the mixed layer and therefore do not correspond to the age of the waters within the OMZs, namely the averaged time since the last surface contact of all water parcels contained in these zones. In all experiments, the fastest tracks into the OMZs are taken by particles ventilated in the western part of the southern Atlantic Ocean and some single particles spotted in the equatorial and northern subtropical Atlantic Ocean.

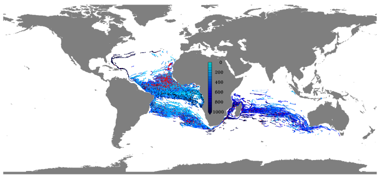

a) # sOMZ ORCA05

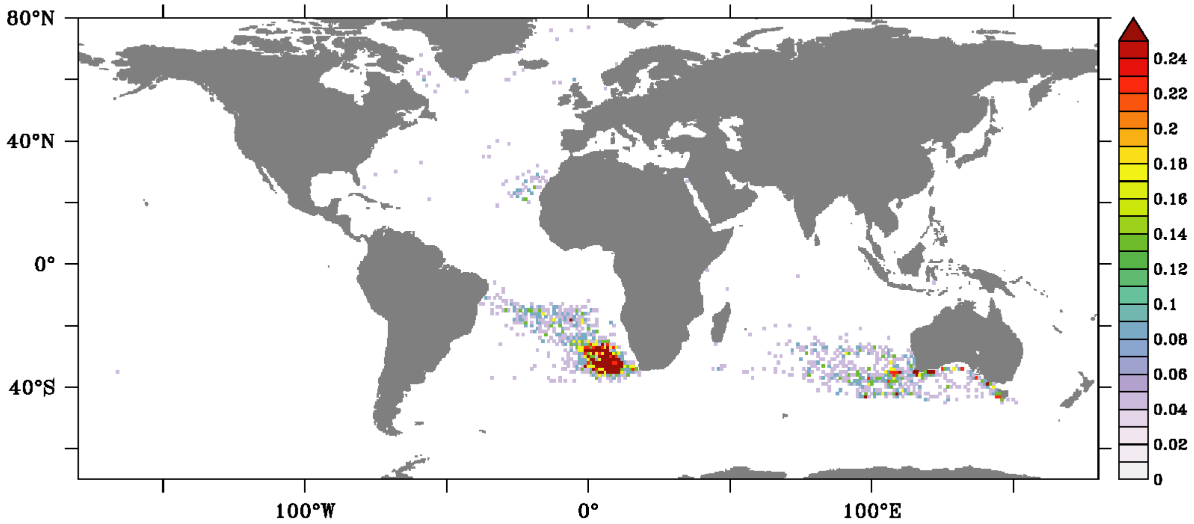

b) time sOMZ ORCA05

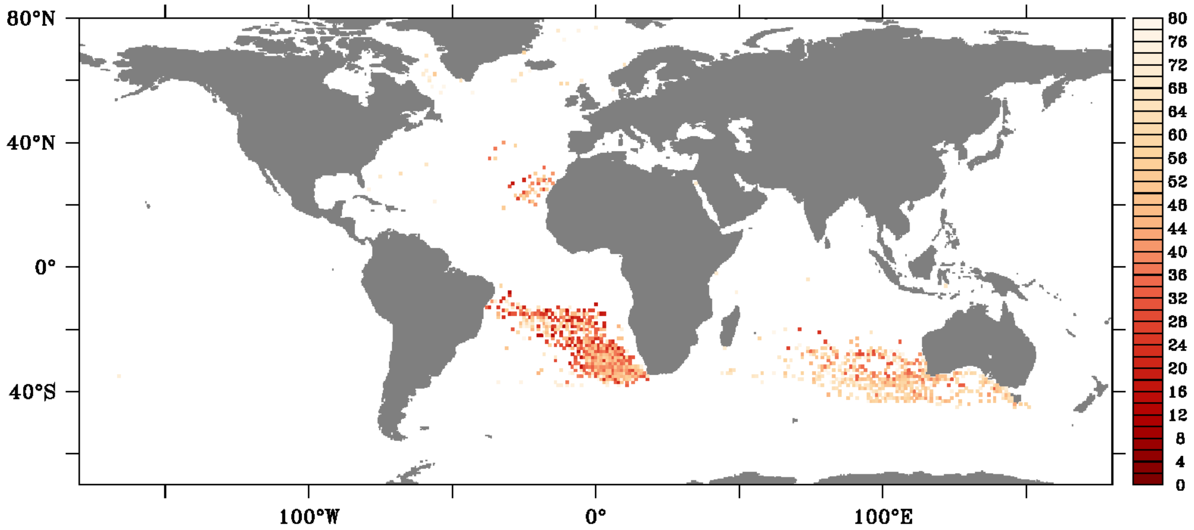

Figure 5.13.: sOMZ ORCA05: Number of particles that make it to the mixed layer [in % of released particles counted within 0.5° by 0.5° squares] a) and the averaged time they need to get there [in years] b).

The particles ventilated in the Indian Ocean in the ORCA05 experiments need 70 to 80 years. A longer integration time would probably show more regions where particles get ventilated; only the fastest are shown here.

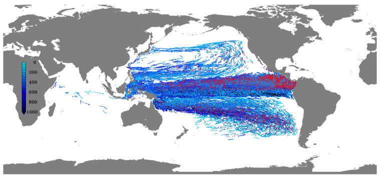

5.2.1. Pathways into the northern OMZ

In the following, the pathways of the released particles are given as depth integrated populations. Their temporal evolution during the first eight years (on a linear scale, figures 5.14 and 5.15) of the integration as well as the consecutive eight decades (as annual averages on a logarithmic scale, figures 5.16 and 5.17) show the main routes, waters take to enter the OMZs. Note, that the integration is not restricted to the time since the last contact with the mixed layer and therefore includes some movement before the actual subduction takes place. This is however a minor contribution, as only few particles actually get ventilated during the integration time (see section 5.2). To facilitate the wording, the description in this and the following sections will be given in a backward sense.

During the first year of the integration, in TRATL01 four distinct band-like structures along the western border of the nOMZ occur, transporting the particles westward (figure 5.14) at 9° N, 13° N, 16° N and 17.5° N. South of the nOMZ, at ∼5° N very few particles begin their way towards the American coast. Along this path, the first particles reach the American coast already during the first two years of the integration. At this point in time, the northernmost band begins to vanish and a more diffuse expansion of the particles' residence area towards the north evolves. The three remaining bands persist throughout the following four years, thereafter the two northern join and the band that started at 9° N is now located at 8° N, already reaching further than 40° W towards the west. The weak but present expansion towards the north keeps on and the fastest particles that already reached the American coast within two years, make their way into the South Atlantic and back east until 0° E after eight years. After those first eight years of the integration in TRATL01, highest populations dropped to 0.2% of the released amount of particles per 0.5° square and the area widened from 870 after the first year of integration to 5070 populated 0.5° times 0.5° boxes.

In ORCA05 from the beginning only one band evolves at ∼13° N, that persists throughout the first eight years (figure 5.15) but does not penetrate far towards the west, but rather forms a patch of higher populations with more that 0.3% of the released amount of particles per 0.5° square, that persists during the first decade of the integration. In the second and the following years, a path along the African coast transports the particles south to ∼4° N where they also start to move west. In the ORCA05 experiment, the first particle crosses the Atlantic basin towards the American coast in the fifth year of the integration. The area covered by the particles after the first year of the integration is 450 boxes and grows to 3110 after the eighth year.

The more diffusive character in the particle spread in TRATL01 compared to ORCA05 already appears within this first decade. Note, that the term "diffusive" merely indicates a more prominent role of small scale fluctuations in the velocity field which act to disperse the paths of particles that are subject to pure advection (see section 2.3). In ORCA05 the majority of particles stays closer together than in TRATL01. The trans-Atlantic connection is faster in TRATL01 than in ORCA05.

On time scales of decades, in TRATL01 the mainly diffusive behaviour manifests. On a linear scale

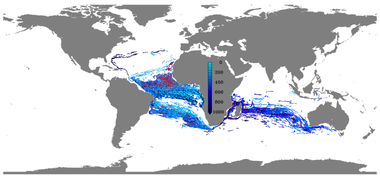

a) Population in year 1 b) Population in year 2

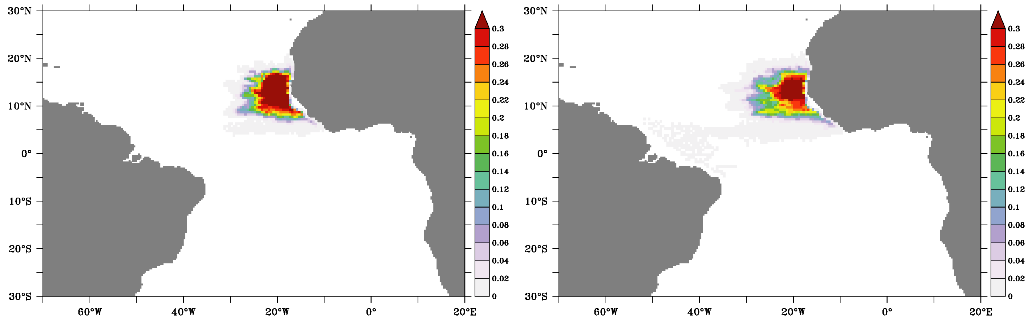

c) Population in year 5 d) Population in year 8

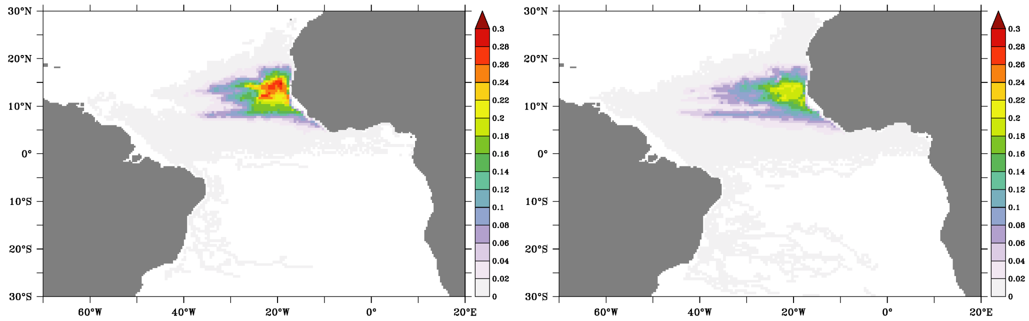

Figure 5.14.: Depth integrated particle population [in % of released particles per 0.5° square] in the first a), second b), fifth c) and eighth d) year after release in the nOMZ in TRATL01.

(this figure is deferred to the appendix; figure A.21) the nested area seems to fill up rather homogeneously with elevated populations only in the northern tropical Atlantic, that slowly decline. Therefore a logarithmic scale (figure 5.16) is used here, to illustrate the particle pathways. Highest populations stay within the northern tropical Atlantic throughout the entire integration. The path into the South Atlantic via the western side of the basin, that began during the first decade with single particles, persists and becomes the main path of the particles. It follows the off-equatorial zonal bands, turns south along the Brazilian coast and further off-coast towards the South East, following the subtropical cell circulation [Schott et al. (2004)], where the nested region in TRATL01 ends.

In ORCA05 (figure 5.17; the same figure using a linear scale is also deferred to the appendix; figure A.22) the main routes are similar to those in TRATL01 but less diffusive, showing more distinct paths. After ten years of integration (see figure A.22a), all particles are still within the nested region. Most particles are located in and close to the nOMZ. An equatorial and an off-equatorial band with higher populations form at ~8° N and particles also occur in a narrow band along the Brazilian coast and already within a north-west/south-east band, entering the South Atlantic basin. After 20 years, the particles begin to leave the nested region. A direct comparison between the two models cannot be done beyond those lines but the paths of the particles can further be analyzed in ORCA05 only.

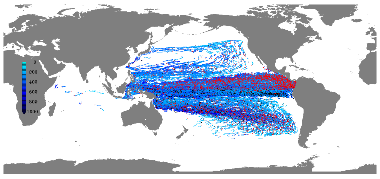

a) Population in year 1 b) Population in year 2

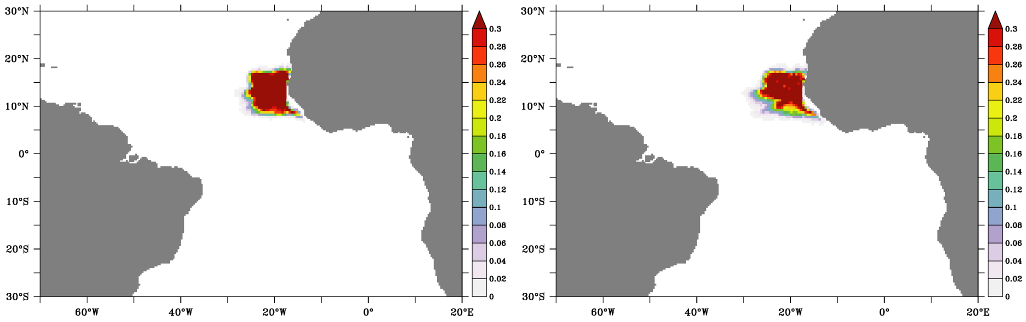

c) Population in year 5 d) Population in year 8

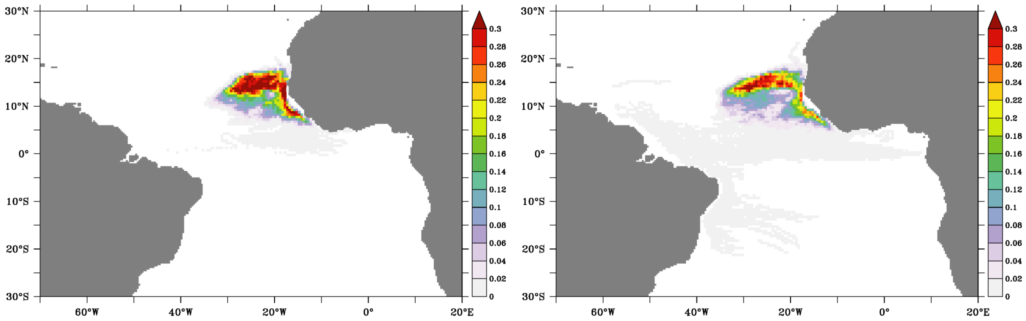

Figure 5.15.: Depth integrated particle population [in % of released particles per 0.5° square] in the first a), second b), fifth c) and eighth d) year after release in the nOMZ in ORCA05.

Throughout the 80 years of integration, the populations in the northern tropical Atlantic become more structured: a “hole” with lower populations forms at ∼15° N near the African coast, that moves westward over time. High concentrations form north and south as well as west of it, transporting the particles west. The off-equatorial band strengthens and high populations evolve along the African coast, slowly extending south to the equator. Already after 20 years, some particles entered the Indian Ocean, filling up the Mozambique channel. At that time, first particles also made their way into the Southern Ocean as well as into the North Atlantic. After 30 years (see figure A.22 in the appendix), the connection down to Australia is done and the part of the Indian Ocean, south of the equator becomes populated. Individual particles make it into the Pacific Ocean during that time. After 40 years of integration the particle distribution starts to stabilize while during the following decades only the levels increase: the Indian Ocean fills up with particles, more particles enter the Southern Ocean and the tropical Pacific, mainly through the Indonesian throughflow and some more particles get into the North Atlantic.

In forward sense, this means, that some particles surrounded Antarctica within the ACC and some were located in the Pacific Ocean before entering the main route, the particles take into the nOMZ from an origin in the South Atlantic or the Indian Ocean from where they enter the Atlantic basin

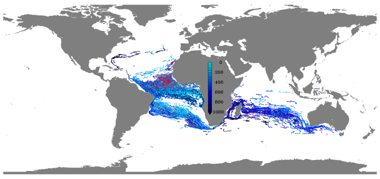

a) Population in year 20

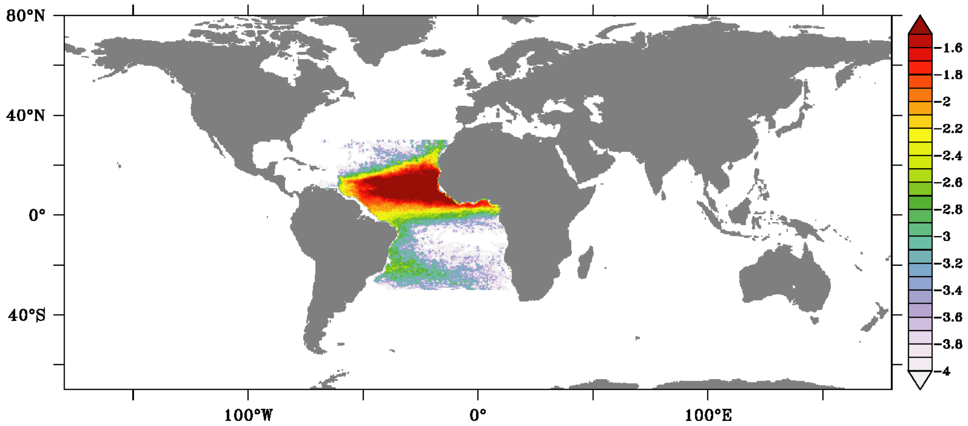

b) Population in year 40

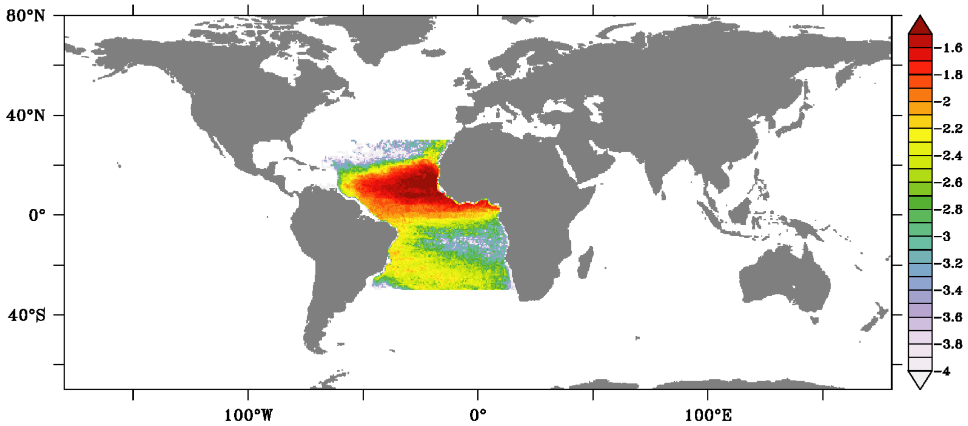

c) Population in year 80

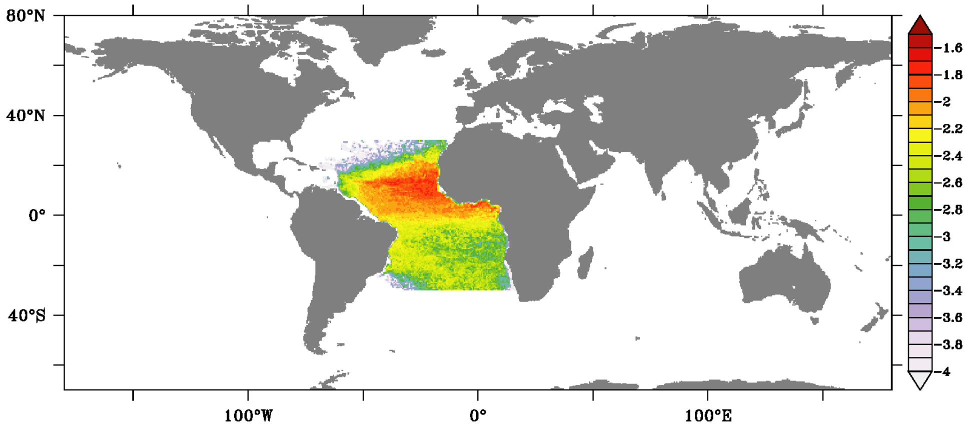

Figure 5.16.: Depth integrated particle population [in % of released particles per 0.5° square on a logarithmic scale] 20 a), 40 b) and 80 c) years after release in the nOMZ in TRATL01.

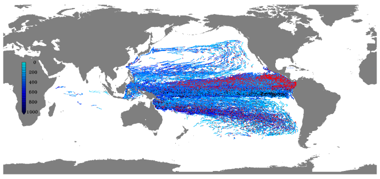

a) Population in year 20

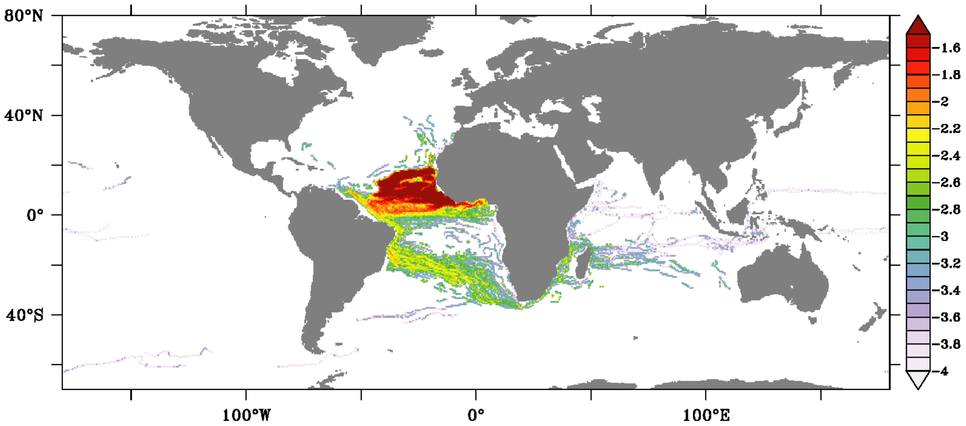

b) Population in year 40

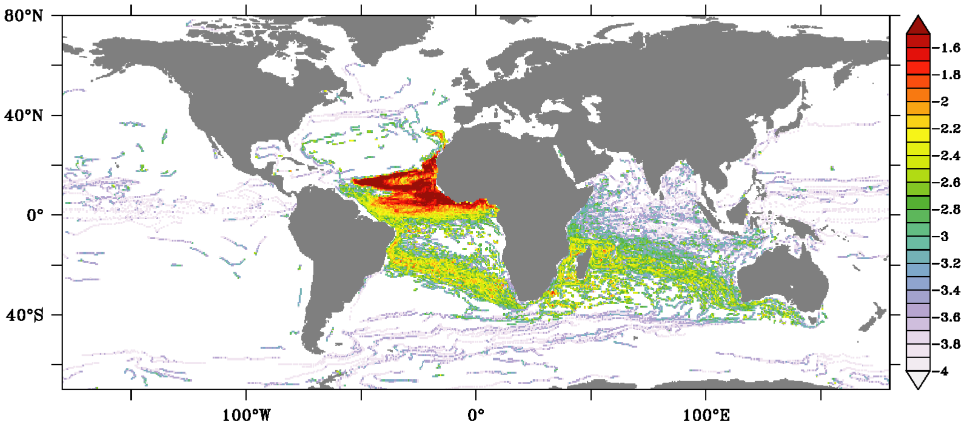

c) Population in year 80

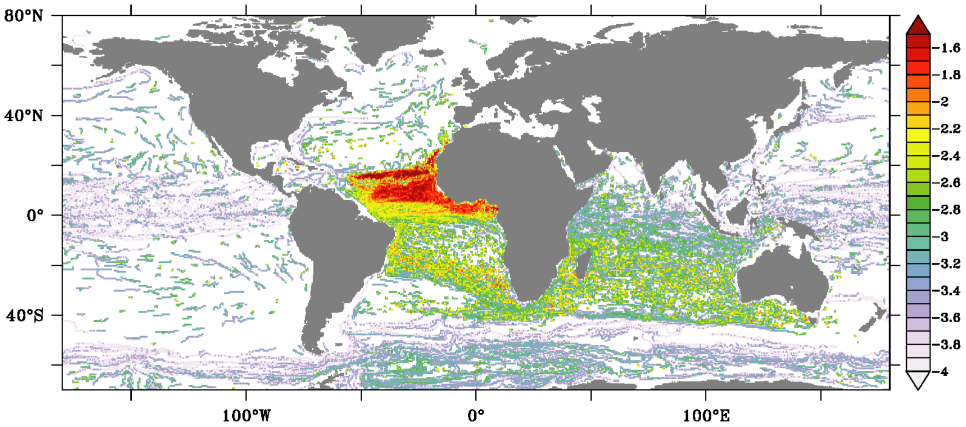

Figure 5.17.: Depth integrated particle population [in % of released particles per 0.5° square on a logarithmic scale] 20 a), 40 b) and 80 c) years after release in the nOMZ in ORCA05.

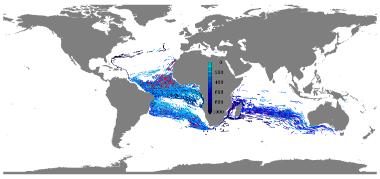

via the Agulhas system. Particles cross the South Atlantic with the SEC and move north along the Brazilian coast with the NBC into the northern Hemisphere where they reach into the nOMZ with the mid-depth off-equatorial zonal current bands (see figure 5.18) [Schott et al. (2004)]. A minor fraction of particles originates in the North Atlantic, partly entering the nOMZ area from the north along the African coast and also by crossing the Atlantic basin from the west, after getting transported into the tropical region along the north American continent. These paths (at least the comparable parts within the nested region) are similar in TRATL01 and ORCA05 with the main differences showing up in the degree of diffusive behaviour, that is elevated in TRATL01 and the final crossing of the Atlantic basin, that differs due to the different representation of the zonal currents within the two models.

The particle populations for the first ten years of the integration along a section at 35° W exhibit two cores in TRATL01 and one core in ORCA05 where particles get transported across the Atlantic basin towards the nOMZ. In ORCA05 this core is located between 300 m and 500 m depth in a meridional band between 8° N and 14° N, with highest populations at ~11° N in 300 m depth. This core co-occurs with the lower part of a slow eastward mean flow (contours in figure 5.18b). In TRATL01 the southern core is located at 8° N in 600 m depth below the northern NECC (nNECC) and the northern, shallower core is located between 300 m and 500 m depth and 11° N to 14° N. Both are co-located with weak eastward velocities that also appear in observations (compare to Brandt et al. (2010), figure 2a). Peña-Izquierdo et al. (2015) also find a main contruibution to the ventilation of the north Atlantic OMZ within the eastward flow around 14° N.

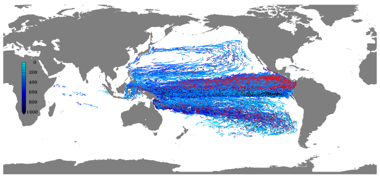

a) TRATL01

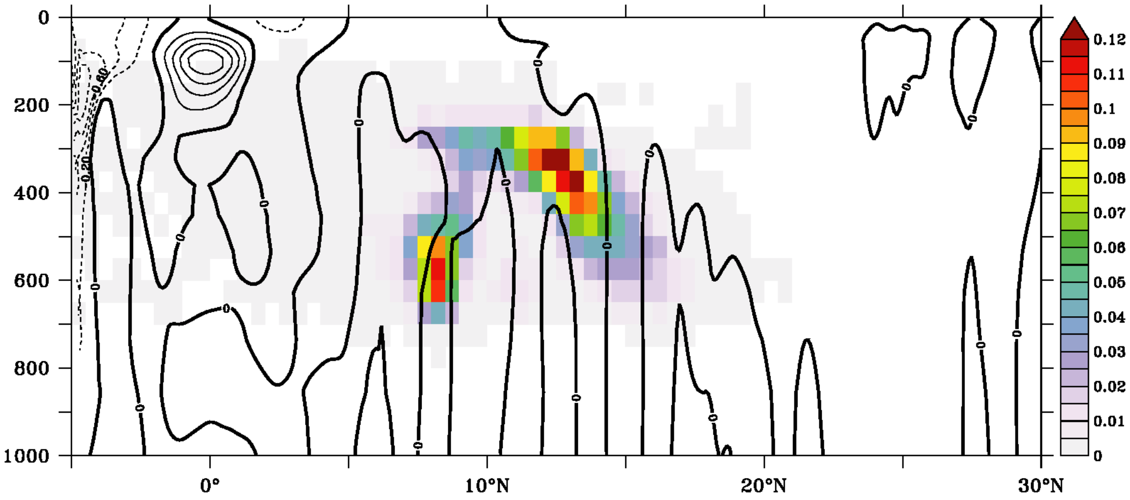

b) ORCA05

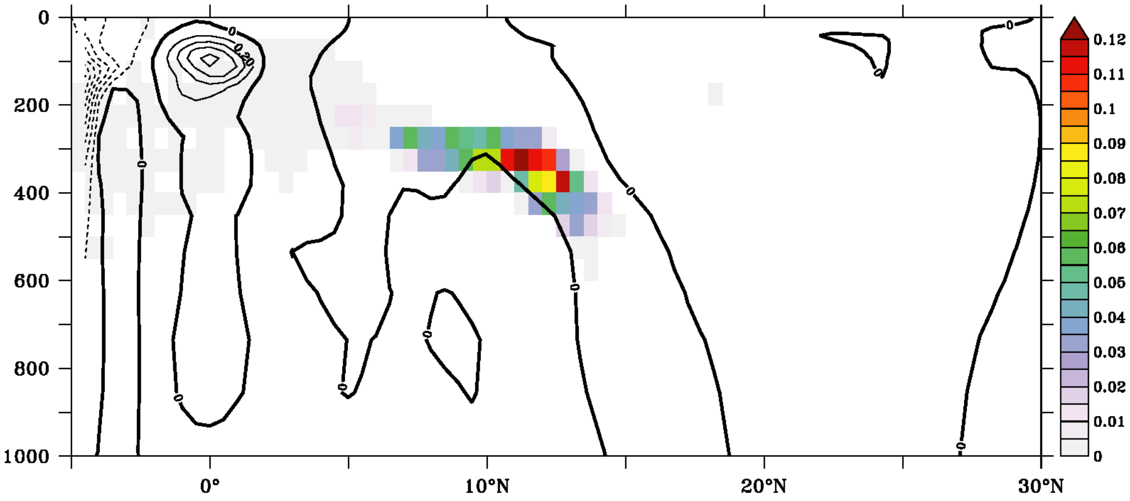

Figure 5.18.: Particle population within the first ten years of the integration (shading) and ten year averaged zonal velocity at 35° W (contours) from TRATL01 a) and ORCA05 b).

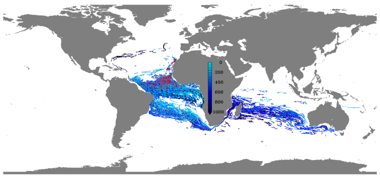

5.2.2. Pathways into the southern OMZ

Within the first years after release, particles originating (in a backward sense) from the sOMZ in TRATL01 show an equivalent behaviour to those released in the nOMZ: several bands evolve, that transport the particles west (figure 5.19). Here, the persisting bands are located at ~8° S and ~13° S. The first particle reaches the Brazilian coast within three years after the release. High populations rapidly decrease and start forming a triangular shape within the southern tropical Atlantic while the rest of this part of the Ocean fills up quite homogeneously depicting the diffusive behaviour in TRATL01. The area populated after the first year of the integration is 970 0.5° squares and grows with a factor of five to 4960 within the first eight years of the integration. On a logarithmic scale (figure A.23 in the appendix), the band-like structure appears to be more detailed and exhibits a tongue (that vanishes on the linear scale) of higher populations, that crosses the basin within seven to eight years located between 4° S an 7° S.

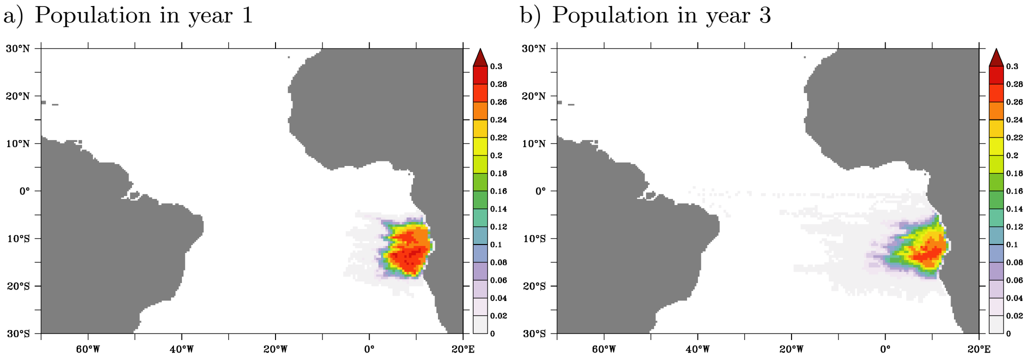
a) Population in year 1

b) Population in year 3

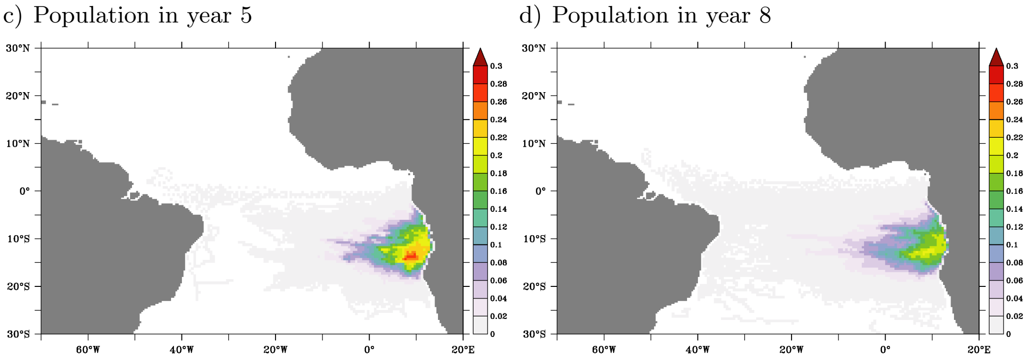
c) Population in year 5

d) Population in year 8

Figure 5.19.: Depth integrated particle population [in % of released particles per 0.5° square] in the first a), third b) fifth c) and eighth d) year after release in the sOMZ in TRATL01.

In ORCA05 the particles stay closer together, near the coast with the covered area only growing by a factor of less than three within the first eight years of the integration from 500 to 1400 0.5° squares. One prominent tongue towards the Brazilian coast forms during the first decade, that originates at ~12° S within the sOMZ and extends towards the North West, reaching 5° S at ~25° W. However this path does not make it to the coast within the first eight years of the integration. The structure

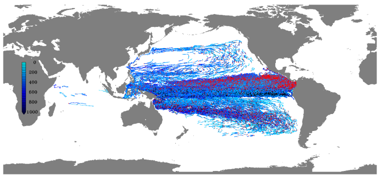

in this experiment appears similar on the logarithmic scale (see figure A.24 in the appendix).

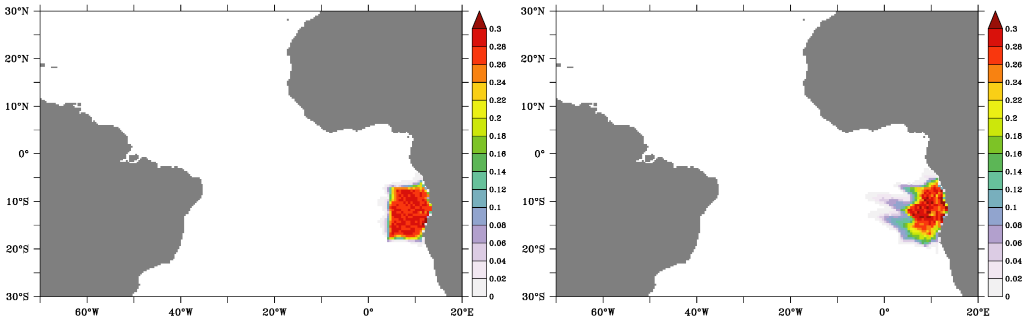
a) Population in year 1
b) Population in year 3

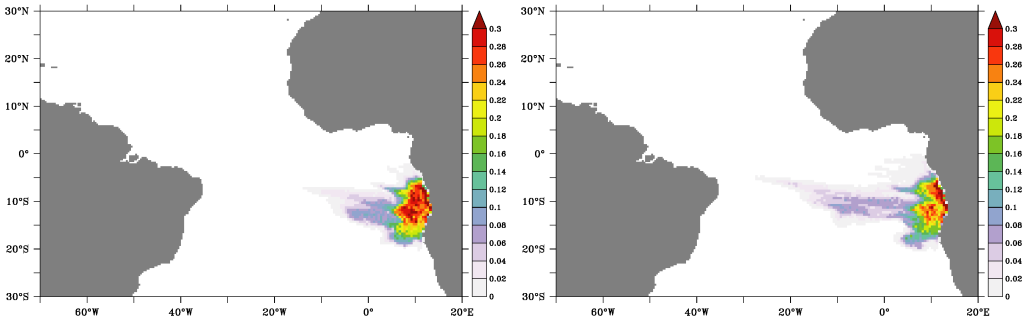
c) Population in year 5
d) Population in year 8

Figure 5.20.: Depth integrated particle population [in % of released particles per 0.5° square] in the first a), third b) fifth c) and eighth d) year after release in the sOMZ in ORCA05.

The comparison of TRATL01 and ORCA05 shows the same features for the sOMZ as for the nOMZ releases, with more diffusive behaviour that holds on during the upcoming decades, and a faster connection to the South American coast in TRATL01.

On decadal timescales, the southern tropical Atlantic seems to zonally fill up, with higher populations in the east than in the west and strongly decreasing towards the north and the south. Masked by this diffusive spreading of particles is the path they take towards the Brazilian coast and then back, southeast, where particles leave the nested region in a similar way as they do in the experiment where the nOMZ is the release area. Only very few particles find their way into the northern part of the Atlantic Ocean.

The experiment in ORCA05 however exhibits more clearly defined paths from decade to decade (figure 5.22). Within the first ten years (see figure 5.22 in the appendix), the particles cross the Atlantic Ocean. After 20 years, the particles move southward along the American coast where they turn east, back into the basin at ∼20° S. The first particles already reach the Mozambique Chanel at that time. After 30 years (see figure 5.22 in the appendix), the connection via the Indian Ocean

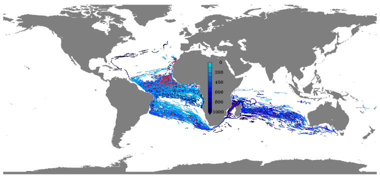

a) Population in year 20

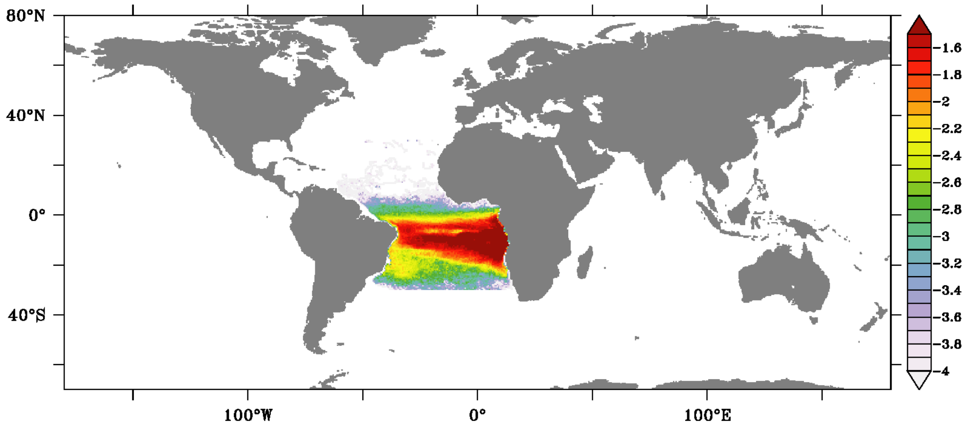

b) Population in year 40

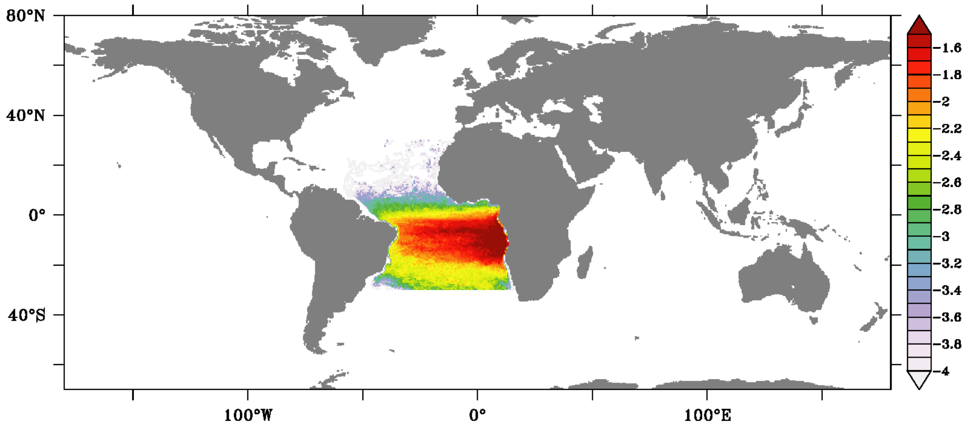

c) Population in year 80

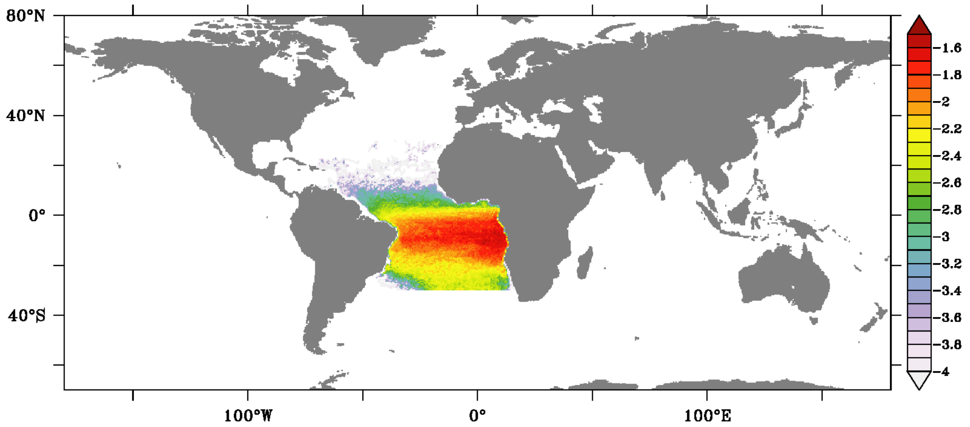

Figure 5.21.: Depth integrated particle population [in % of released particles per 0.5° square on a logarithmic scale] 20 a), 40 b) and 80 c) years after release in the sOMZ in TRATL01.

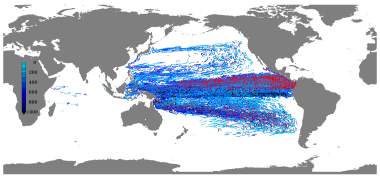

a) Population in year 20

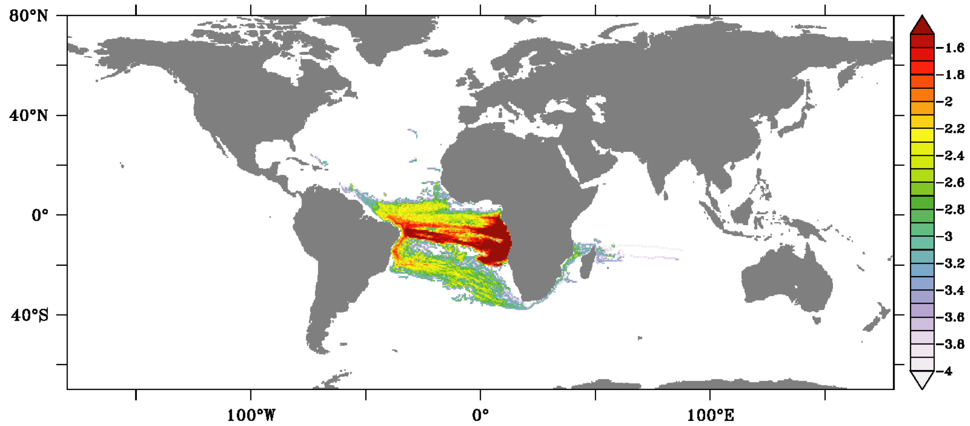

b) Population in year 40

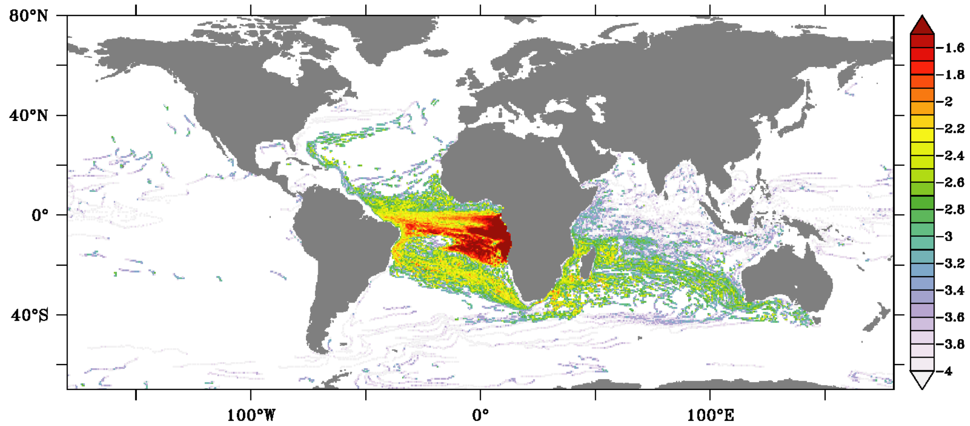

c) Population in year 80

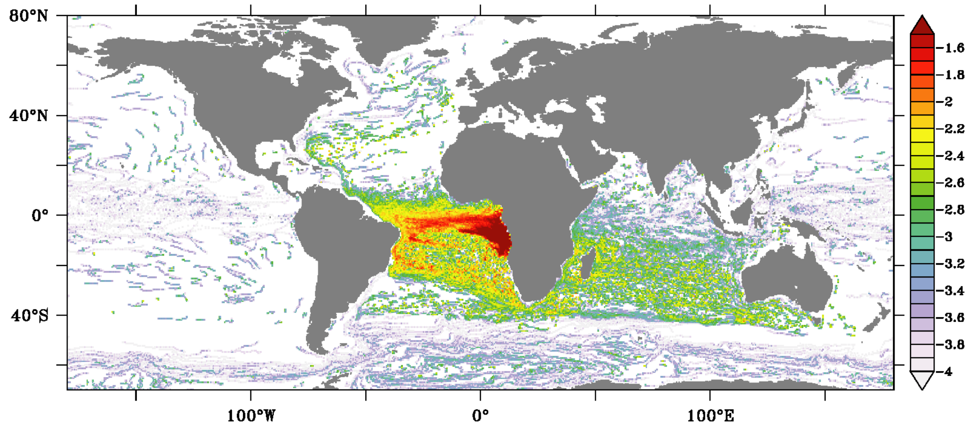

Figure 5.22.: Depth integrated particle population [in % of released particles per 0.5° square on a logarithmic scale] 20 a), 40 b) and 80 c) years after release in the sOMZ in ORCA05.

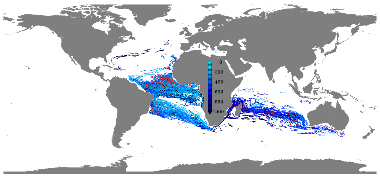

to the Australian coast is done and a path into the North Atlantic begins to form and strengthens during the following 10 years. From then on, the shape of the populations stays almost the same until the end of the integration with values decreasing in the southern tropical Atlantic and increasing and further spreading in the Indian Ocean. Some particles also reach the tropical Pacific Ocean and the Southern Ocean.

Except for the elevated populations within the release area and the corresponding part of the Atlantic basin, the population distribution is very similar to the one originating from the nOMZ experiments (compare figures 5.17 and 5.22). The forward ventilation pathways, that can be identified using the particle populations are the same as for the nOMZ except for the very last part of the path, where particles are crossing the Atlantic basin from west to east south of the equator. The particle populations within the first ten years of the experiments at 5° W (figure 5.23) show similar paths for the experiments in TRATL01 and ORCA05. Both show mainly one core, located between 200 m and 400 m depth and 10° S to 14° S, also co-occurring with very weak eastward mean velocities (contours), the SECC, that is more structured in TRATL01 than in ORCA05. Apart from this focus, two additional, weaker cores are present in TRATL01, that are not as clearly correlated with the mean flow, indicating the high variability within the velocity field.

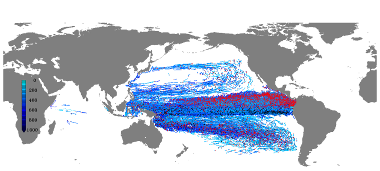

a) TRATL01

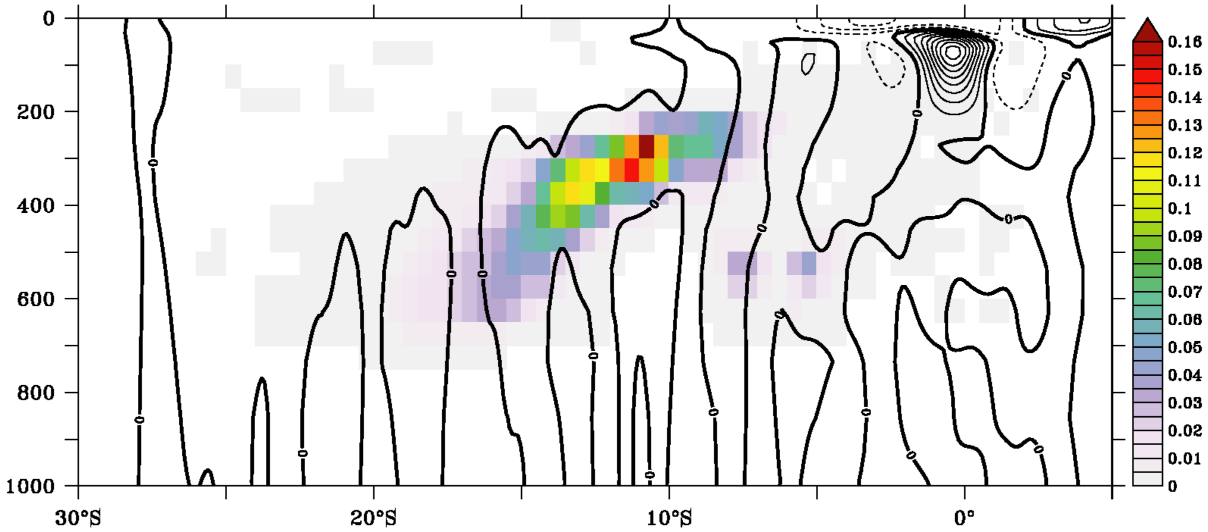

b) ORCA05

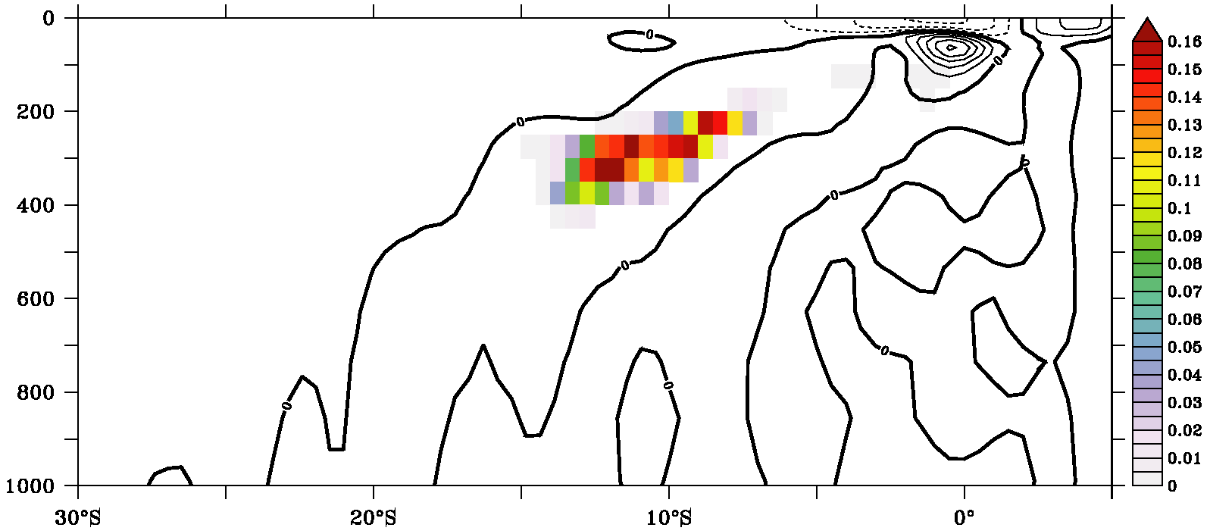

Figure 5.23.: Particle population within the first ten years of the integration (shading) and ten year averaged zonal velocity at 5° W (contours) from TRATL01 a) and ORCA05 b).

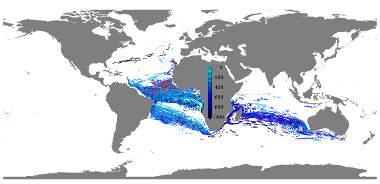

5.3. Temporally integrated Lagrangian pathways

In the previous sections, the temporal evolution of particle populations has been shown. Here the populations in a temporally integrated sense are used to reveal all the locations particles pass during the integration time. High values not only mark areas where many particles pass but also where particles reside for longer times. Similar analyses have been done with focus on the off-equatorial undercurrents in the Atlantic Ocean by Hüttl-Kabus and Böning (2008). Additional particle populations are derived as “first arrivals”, where only the first occurrence of a distinct particle within one box is counted. The first arrivals to some extent better exhibit narrow paths, without the blurring effect of mesoscale eddies and long residence times, nevertheless, these figures are deferred to the appendix (figures A.27 and A.28).

The main features in the full depth integrated particle populations (figure 5.24) in TRATL01 (left panel) are an approximately zonal band of high populations meridionally co-located with the corresponding OMZs and an area surrounding these bands where populations decrease laterally, exhibiting the diffusive character of the eddy advection, transporting the particles. Peña-Izquierdo et al. (2015) find similar populations, although their area of study is restricted to the zonal band between 5° S and 30° N. For the nOMZ experiments, additionally a path of elevated populations from the southern hemisphere is shown. The particle populations in the global ORCA05 model additionally exhibit the paths particles take into the respective tropical basins. For both experiments in the Atlantic Oceans these are the subtropical gyre circulation in the Indian Ocean, a strong path along the SEC and a weaker path from the North Atlantic.

The vertical distribution of these particle populations exhibits distinct currents transporting waters into the OMZs. Three different depth ranges are chosen to differentiate between the part of the particles that is basically transported at the OMZ's depth layer, between 200 m and 800 m depth, the particles that are transported above (surface to 200 m depth) and those that come from below (800 m depth to seafloor) (see figures 5.25 and 5.26). In both experiments, for the northern and southern OMZs in the Atlantic Ocean, more emphasized in those in the nested models, the particle populations integrated over the mid-depth range, at a first glance, reproduce the pattern in the particle population given by the full depth integrated populations. Closer inspection shows, that this is true especially for the highest values, in a zonal band, meridionally co-located with the different OMZs. This indicates, that the eastward transport of particles into the OMZs, dominated by mesoscale processes, takes place in the same depth range as the destination zone. In the ORCA05 experiments, some parts of the full depth population patterns are not reflected by the mid-depth range pattern. These are the northern flank of the ACC in the Atlantic sector, the path from the North Atlantic and the southern part of the path through the Indian Ocean, that consequently have to take place in a different depth layer.

Above and below the mid-depth range, only a minor fraction of particles is transported. However, the paths, particles describe in the surface and the deep layers, are clearly defined (top and bottom

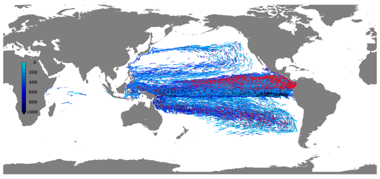

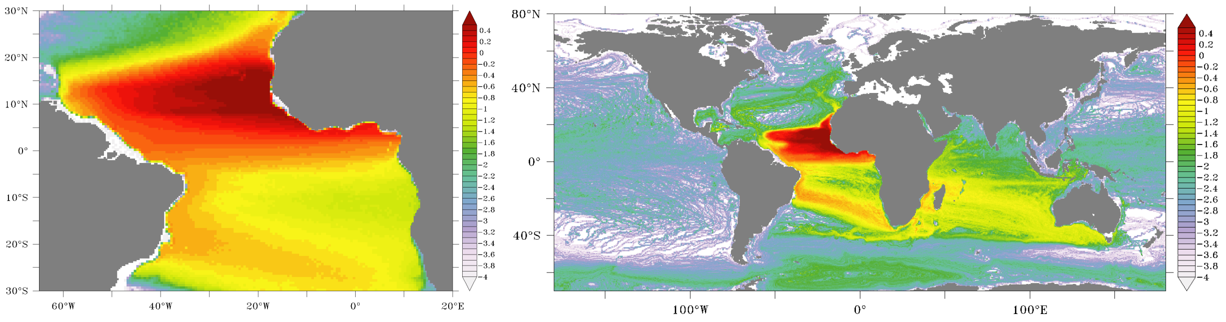
a) nOMZ TRATL01 b) nOMZ ORCA05

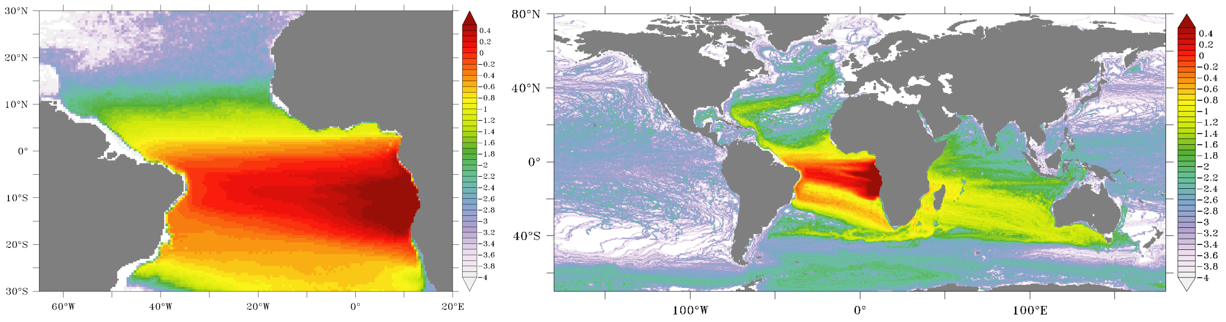
c) sOMZ TRATL01 d) sOMZ ORCA05

Figure 5.24.: Full depth integrated particle population [in % of released particles per 0.5° square on a logarithmic scale] temporally integrated over the full period of the Lagrangian experiments of 80 years for particles released in the Atlantic nOMZ (top) and sOMZ (bottom) in TRATL01 (left) and ORCA05 (right).

panels of figures 5.25 and 5.26). The particle populations in the near surface layer exhibit a zonal band of highest populations north and south of the equator for the nOMZ and sOMZ experiment respectively. These bands reach the horizontal location of the OMZs at their respective equatorward limits. In both experiments elevated populations are also found on the other side of the equator and in the eastern part of the southern tropical Atlantic. For the nOMZ experiments some particles are also found in the eastern part of the northern tropical Atlantic. In the experiments in ORCA05 the paths north and south of the equator show even higher populations that can most probably be attributed to slower circulation and longer residence times of the particles rather than more particles taking these paths (also confirmed by the populations derived as “first arrivals”; figures A.27 and A.28 in the appendix). In both experiments a strong path from the southern tip of Africa north west towards the Brazilian coast is present in this shallow layer, although the connection to the bands beside the equator takes place in another depth layer. In contrast to the nOMZ experiment in TRATL01, the band north of the equator enters the horizontal location of the nOMZ from the south, showing highest values along the African coast, probably entering the nOMZ from above. In the sOMZ experiment, highest values at this depth layer also occur along the African coast, here north of the sOMZ limits.

In the nOMZ experiment in ORCA05 a path in the eastern part of the basin from the North enters

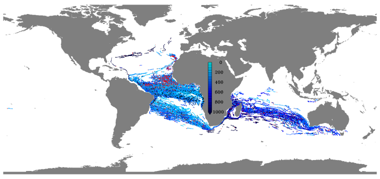

a) surface to 200 m TRATL01 b) surface to 200 m ORCA05

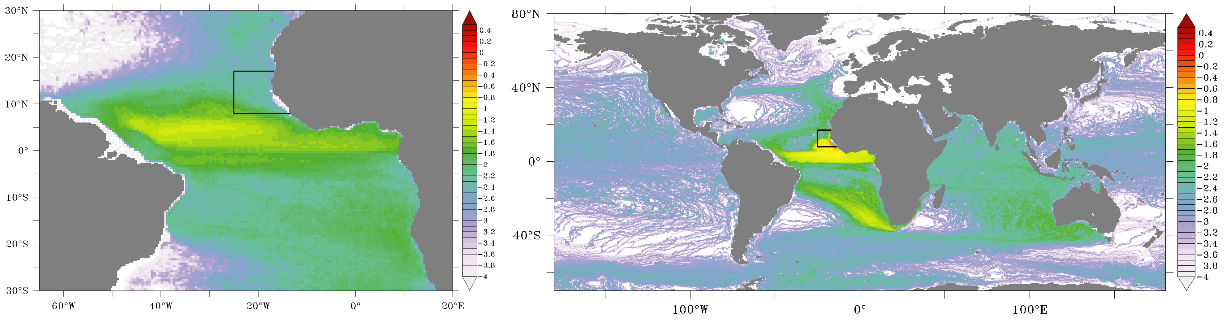

c) 200 m to 800 m TRATL01 d) 200 m to 800 m ORCA05

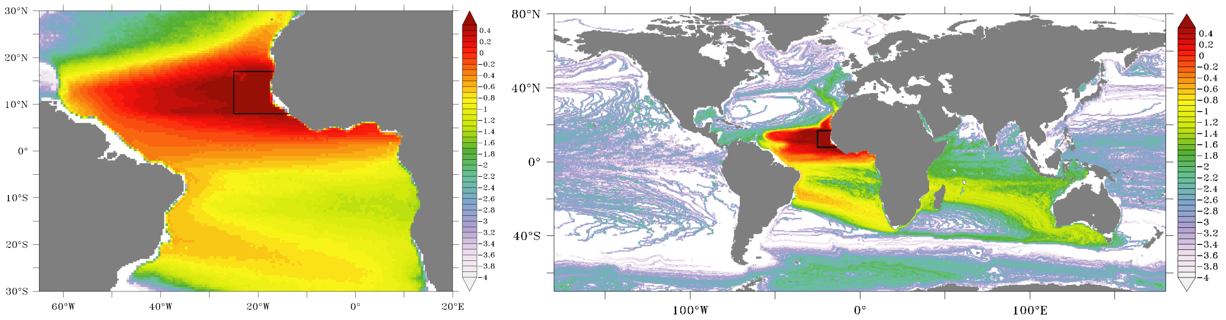

e) 800 m to bottom TRATL01 f) 800 m to bottom ORCA05

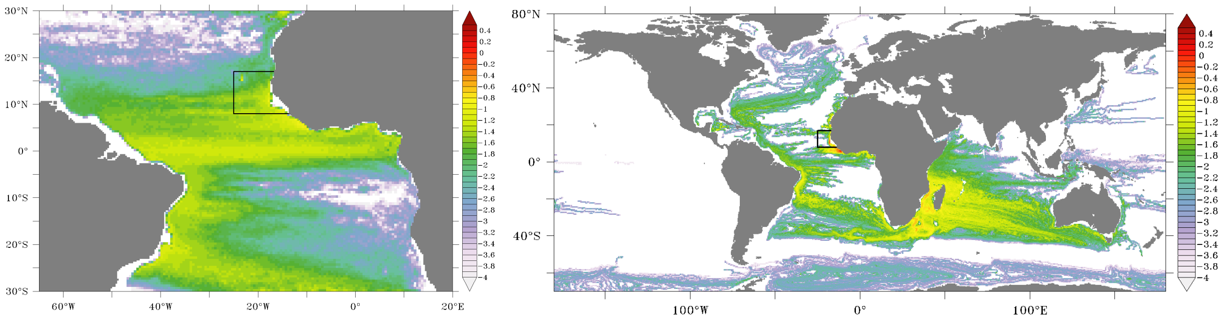

Figure 5.25.: Depth integrated particle population [in % of released particles per 0.5° square on a logarithmic scale] temporally integrated over the full period of the Lagrangian experiments of 80 years for particles released in the Atlantic nOMZ in TRATL01 (left) and ORCA05 (right) for the depth ranges 0 m to 200 m (top), 200 m to 800 m (middle panel) and 800 m to the seafloor (bottom).

the NEC transporting particles to the western boundary of the basin and some directly into the nOMZ area, although at shallower depths. These could directly contribute to the supply of the nOMZ, by the prevailing downwelling above the OMZ layer (see figure 5.3). Most of the movement of the particles in the northern Indian Ocean, the Pacific basin and in the ACC takes place in this uppermost layer. West of Australia elevated populations are found in this layer, where particles get subducted (see section 5.2). Except for the less pronounced path from the North Atlantic, the particle population pattern in the near surface layer in the sOMZ experiment is very similar to the pattern from the nOMZ experiment.

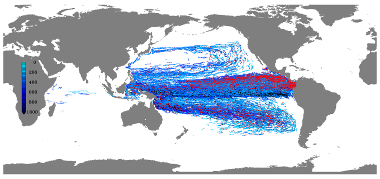

a) surface to 200 m TRATL01 b) surface to 200 m ORCA05

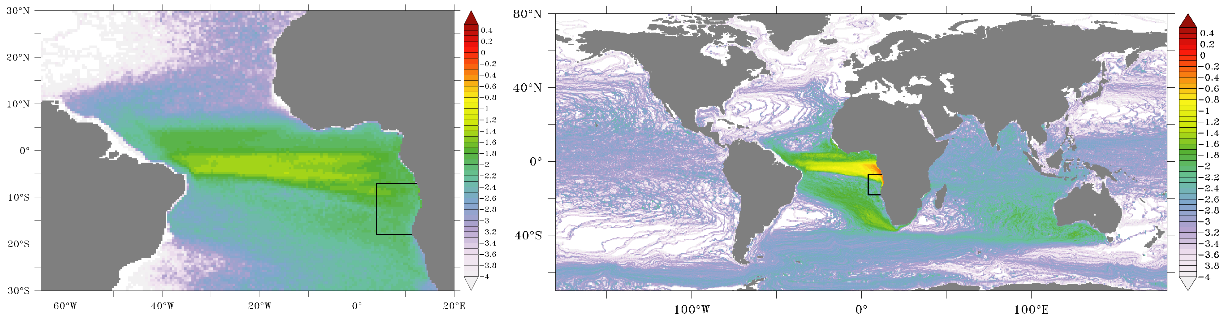

c) 200 m to 800 m TRATL01 d) 200 m to 800 m ORCA05

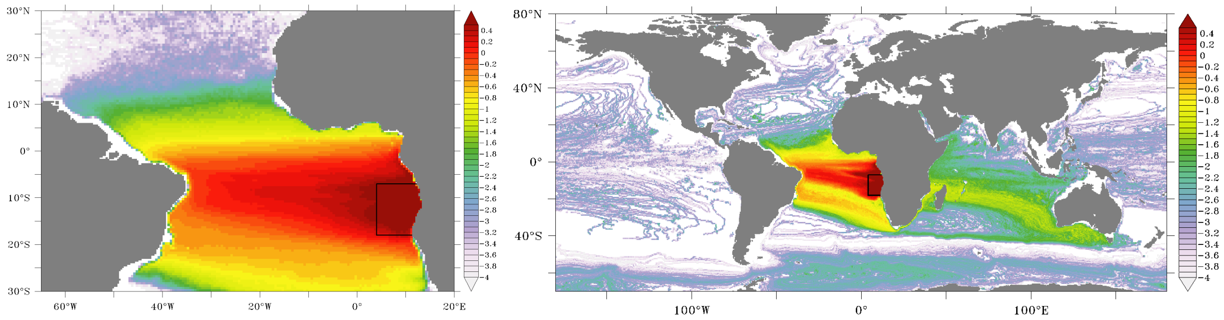

e) 800 m to bottom TRATL01 f) 800 m to bottom ORCA05

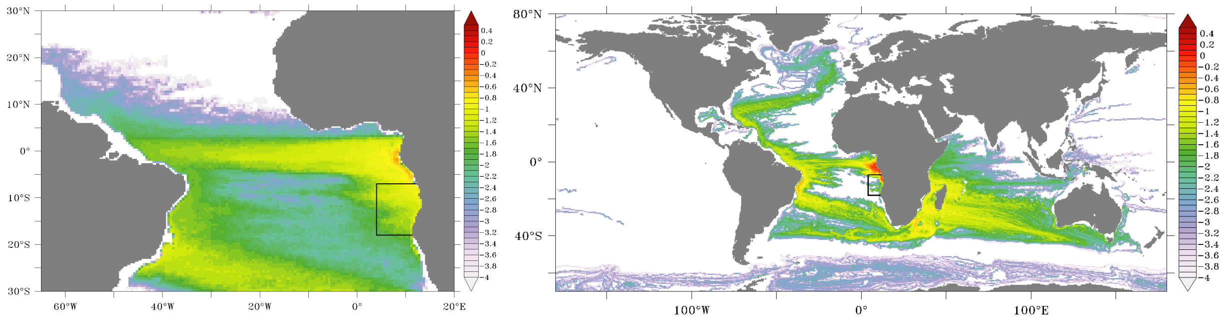

Figure 5.26.: Depth integrated particle population [in % of released particles per 0.5° square on a logarithmic scale] temporally integrated over the full period of the Lagrangian experiments of 80 years for particles released in the Atlantic sOMZ in TRATL01 (left) and ORCA05 (right) for the depth ranges 0 m to 200 m (top), 200 m to 800 m (middle panel) and 800 m to the seafloor (bottom).

In the layer below the OMZs, the populations in TRATL01 for both, the nOMZ and the sOMZ experiment, show a path from the centre of the basin along the southern boundary of the nested region towards the south American coast. This path then continues northward along the coast and turns east towards the African coast along the equator. In the nOMZ experiment elevated populations are also found north of the equator to ∼15° N. In the populations resulting from the sOMZ experiment below the sOMZ elevated values occur, whereas here as well as resulting from the

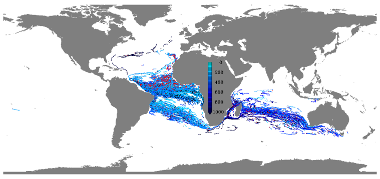

nOMZ experiment the centre of the South Atlantic is almost empty. This hole in the centre of the South Atlantic is even more pronounced in the populations from the experiments in ORCA05. In the deeper layer a path along the northern flank of the ACC in the Atlantic sector is shown to feed into the path, crossing the South Atlantic from the east towards the Brazilian coast. In addition to the populations in the mid-depth range, a path crossing the southern Indian Ocean, south of Madagascar complements the path north of this island. At the equatorward limits of the Atlantic OMZs highest populations occur. This points to a feeding of the OMZs from the equatorward flanks. The equatorial band is more pronounced in the sOMZ experiment when compared to the nOMZ. This also holds for the high particle populations along the deep western boundary current that exhibits a clear path from the North Atlantic. The paths, waters take to enter the Atlantic nOMZ and sOMZ are very similar, especially in the deep layer, and they diverge only in the last part, where the particles cross the Atlantic Ocean from the West and enter the OMZs in the East.

The Lagrangian experiments described above exhibit sources and pathways of waters, ending up in the northern and southern OMZs in the Atlantic Ocean. Within a limited time frame of 80 years only a small fraction of waters actually gets ventilated (table 5.3). The experiments using the velocity fields from the coarser ORCA05 simulation result in a doubled fraction (7% and 4% for the nOMZ and sOMZ respectively) of waters getting ventilated within the tropical-subtropical Atlantic when compared to the experiments using the high-resolution velocity fields from TRATL01 (4% and 2%). Taking into account the areas outside the nested region, that are not covered by the high-resolution experiments, the ventilated fractions increase to 25% and 15% for the nOMZ and sOMZ respectively. The differences in the total numbers for the nOMZ and the sOMZ reflects, that the sOMZ ventilation is weaker and therefore also more pronounced in terms of lower oxygen concentrations than the nOMZ [e.g. Karstensen et al. (2008)].

The main source regions of OMZ waters were found to be located in the south Indian Ocean with ventilation time scales in the range of the integration period and along the SEC path in the South Atlantic [Schott et al. (2004)], from where only ∼40 years are enough to reach the OMZs. A minor fraction was shown to originate from the northern Atlantic Ocean, leaving the mixed layer along the NEC path and between 20° N and 30° N off the African coast. Except for these northern source regions, that are more pronounced in the nOMZ experiments, the two Atlantic OMZs receive their waters from the same origins and also the remote pathways towards two different OMZs are very similar. After surrounding Antarctica and some circulation in the Pacific Ocean, the simulated particles, that originate from the South either cross the Indian Ocean below the thermocline or get subducted there, before they enter the Atlantic Ocean via the Agulhas current system [Lutjeharms (2006)]. The particles then get transported across the Atlantic Basin via the SEC [Schott et al. (2004)] and then follow the South American coast northward, through the NBC [Johns et al. (1998)], that forms a constriction along this route. In deeper layers, below the OMZ layers, a distinct path bringing waters from the North Atlantic into the equatorial region along the deep western boundary current [e.g. Bower et al. (2009)] could be identified. A shallow route via the NEC is present in both cases, whereas it is more pronounced for the nOMZ ventilation. Only the last part of the pathways into the OMZs, the final crossing of the Atlantic basin, is different for the nOMZ and sOMZ, taking

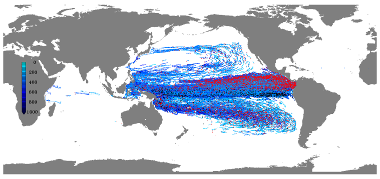

place north and south of the equator respectively, within zonal bands between ∼7° and ∼18° off the equator.

TRATL01 is more diffusive and variable than ORCA05. This diffusive behaviour partly masks the most prominent pathways, that are, however, found to be similar in TRATL01 and ORCA05 on decadal time scales. The impact of the enhanced mesoscale in the higher resolution experiments is stronger for the sOMZ than for the nOMZ, which is in agreement with the findings by Duteil et al. (2014).

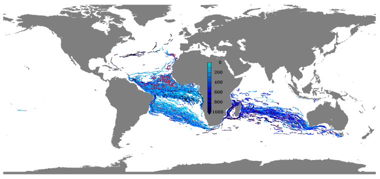

6. Ventilation of the eastern tropical Pacific

Similar to the Atlantic Ocean, OMZs are found at mid-depth in the eastern tropical Pacific Ocean. The northern and southern OMZs in the Pacific Ocean are much stronger in terms of extent and oxygen depletion compared to those in the Atlantic Ocean. The Pacific nOMZ and sOMZ regions will be analyzed within this chapter using the hindcast experiments in TROPAC01 and ORCA05 analogous to what is done for the Atlantic OMZs in chapter 5.

Contents

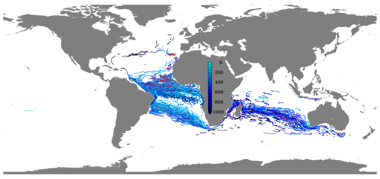

6.1. Mean circulation in the eastern tropical Pacific

The mean circulation, given as ten year averaged velocities in TROPAC01, is described within this section (see figure 6.1). Enlarged versions of these figures, directly juxtaposed to the circulations simulated in ORCA05 are reproduced in the appendix (figures A.29 to A.46).

The surface circulation is dominated by the broad south-westward flowing wind driven southern branch of the SEC south of the equator and its north-westward northern branch north of the equator. The nSEC is narrower compared to the sSEC and is more concentrated to the eastern part of the basin. The NECC flows eastward and is confined to the eastern half of the Pacific Ocean basin at ∼5° N. A broad band of north-westward velocities centered at ∼10° N more pronounced in the western part of the basin marks the NEC [see Schott et al. (2004) for a detailed description of these currents]. Strong currents along the coasts of the Maritime Continent transport Pacific waters into the Indian Ocean [Lukas et al. (1996)]. The East Australian Current (EAC) [Ridgway and Hill (2009)] and the Kuroshio Current (KC) [Barkley (1970)] transport waters poleward along the western boundary of the Pacific Ocean and the Peru Current (PC), also referred to as the Humboldt Current [Chaigneau et al. (2013)], is directed towards the north along the South American coast.

At 50 m depth, where the SEC and its branches and the NEC are still present, the uppermost part of the EUC dominates the current structure along the equator, most pronounced in the eastern part of the basin and bifurcates when it impinges on the Galapagos Islands [Lukas (1986)]. In the westernmost portion, the Equatorial Counter Current (ECC) is fed from the South by the New Guinea Coast Current (NGCC) [Goodman et al. (2005)]. North of the nSEC at ∼5° N the NECC flows eastward. At 100 m depth the EUC reaches its maximal velocities with more than 1 m/s in the centre of the basin. Due to its vertically tilted structure (shoaling towards the east) the basin wide extent of the EUC only becomes visible at this depth [Johnson et al. (2002)], whereas it has already vanished at 200 m depth. In this depth range and below, the NEC is directed towards the South West. At 200 m depth, north and south of the equator at ∼3° N and ∼3° S the Northern and Southern Subsurface Counter Currents (NSCC and SSCC) transport waters towards the east [McPhaden (1984); Johnson et al. (2002)].

The dominating structure at 400 m depth is the westward flowing EIC [Delcroix and Henin (1988); Marin et al. (2010)] at the equator that is embraced by the eastward off-equatorial lowermost portions of the NSCC and SSCC. Note the stretched colour scale that exposes the coastal currents at that depth as well as the topographic currents around sea mounts. At 600 m depth the only remarkable currents are the eastward flowing equatorial band below the EIC in the centre of the basin and the westward currents north as well as a weak westward current south of it. The NEC and SEC are still present but only very weak.

At deeper depth, below 1000 m, the overall current strength is reduced. Mainly weak zonal bands and topographic currents dominate the circulation [Qiu et al. (2013)]. The dominance of the al-

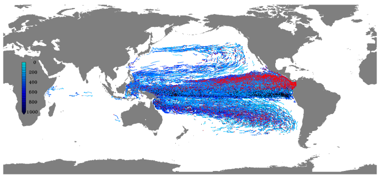

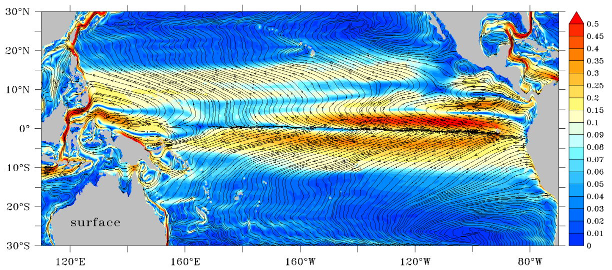
a) Surface b) 50 m depth

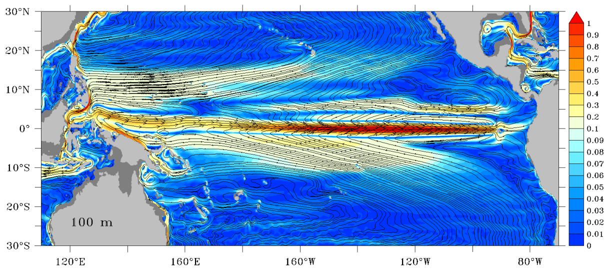
c) 100 m depth d) 200 m depth

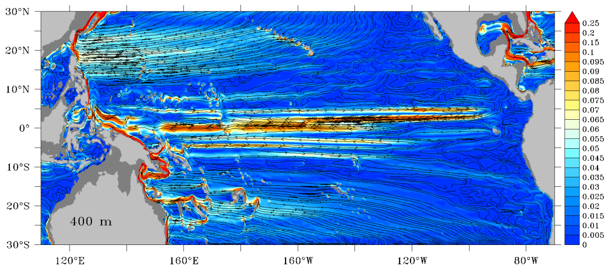
e) 400 m depth f) 600 m depth

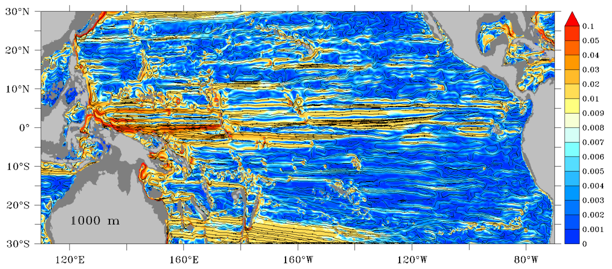
g) 1000 m depth h) 1500 m depth

Figure 6.1.: Ten year averaged (2000 to 2009) circulation at different depths in TROPAC01: shaded is speed [m/s] with streamlines overlaid. Note the different scales. See Appendix for enlarged versions.

ternating zonal structure at 1000 m depth is also observed by Argo Floats [Cravatte et al. (2012); Ollitrault and Colin de Verdière (2014)].

The circulation in ORCA05 (see figures A.29 to A.46 in the appendix) depicts a very similar struc-

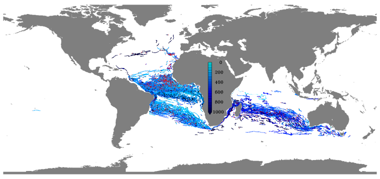

ture when compared to the TROPAC01 circulation within the upper 200 m of the water column. This is due to the application of the same wind forcing onto both models, although the currents are stronger in TROPAC01, especially the EUC reaches further into the eastern part of the basin and its bifurcating structure at the Galapagos Islands is more pronounced in TROPAC01 when compared to ORCA05. Below these uppermost layers, the most prominent currents are weaker in ORCA05 and the weaker currents are not present in the coarse resolution simulation.

The northern and southern OMZs (nOMZ and sOMZ) in the Pacific Ocean, that are subject to further investigations within this chapter, are defined as areas containing the regions where lowest oxygen concentrations are observed, off the American coast at mid depth [Karstensen et al. (2008)], marked by the red and green boxes in figure 6.2 (see table 6.1 for details of the definitions). Both regions only show very weak velocities. Within the nOMZ (red box) in TROPAC01 weak zonal current bands are simulated, whereas in ORCA05 only two remarkable currents can be seen at ∼10° N and ∼13° N with velocities of ∼1 cm/s. Within the sOMZ (green box), mean velocities are almost zero in both, TROPAC01 and ORCA05.

OMZ	Longitude	Latitude	Depth
Pacific nOMZ	120° W to American coast	8° N to 20° N	275 m to 650 m
Pacific sOMZ	90° W to American coast	15° S to 5° S	320 m to 650 m

Table 6.1.: OMZ definitions

6.1.1. Vertical velocities in TROPAC01

Profiles of ten year averaged vertical velocities in TROPAC01 for the horizontal extent of the OMZs show upwelling in the uppermost 130 m and 300 m depth in the northern and southern OMZ respectively (figure 6.3). Below this layer, downwelling prevails down to 1000 m and below. In the nOMZ the upwelling is weak compared to the sOMZ whereas the downwelling in the upper part of the OMZ layer (indicated by the red lines) is stronger than in the sOMZ. The depth of the change between positive (upward) and negative (downward) velocities in the sOMZ co-occurs with its upper limit and therefore in a horizontal and temporal mean sense, no direct ventilation from above takes place. In the nOMZ, waters layered between 160 m depth and the upper limit of the nOMZ at 275 m depth can, even in such a mean sense, be directly subducted into this OMZ from above.

The horizontal patterns of vertical velocities in the northern (figure 6.4) and southern (figure 6.5) OMZ expose parts of the OMZs beeing subject to up- or downwelling at all depths. In a narrow band along the coast, upwelling prevails in the upper 100 m of the water column and downwelling dominates below, except for the coastal area in the southern half of the sOMZ, where upwelling patches persist throughout the upper 1000 m. The velocities decrease from the surface downwards

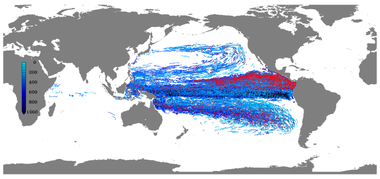

a) TROPAC01

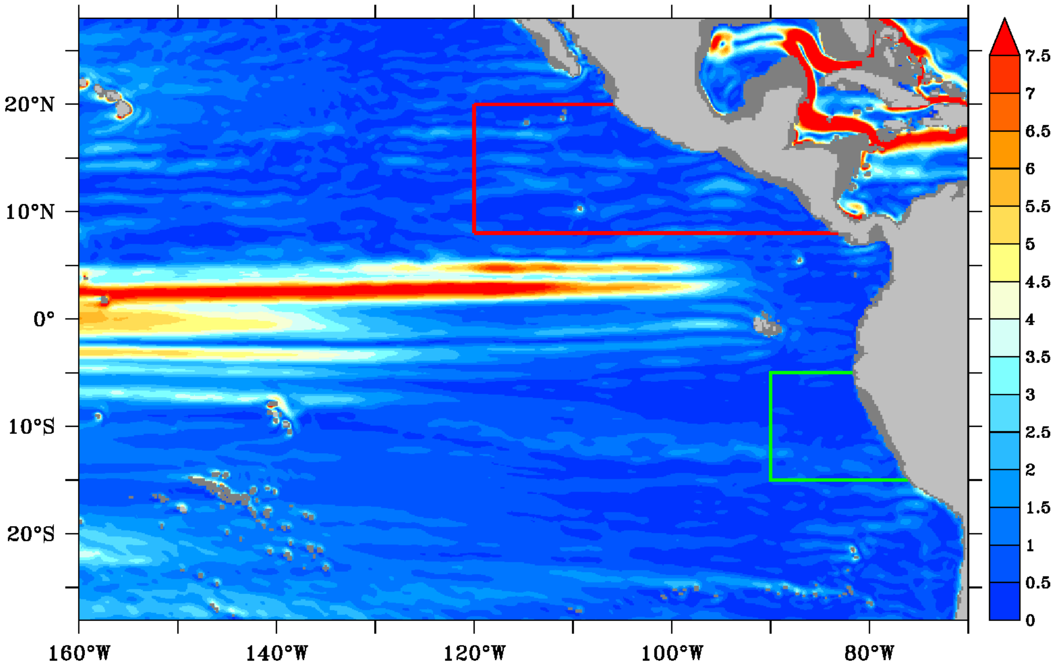

b) ORCA05

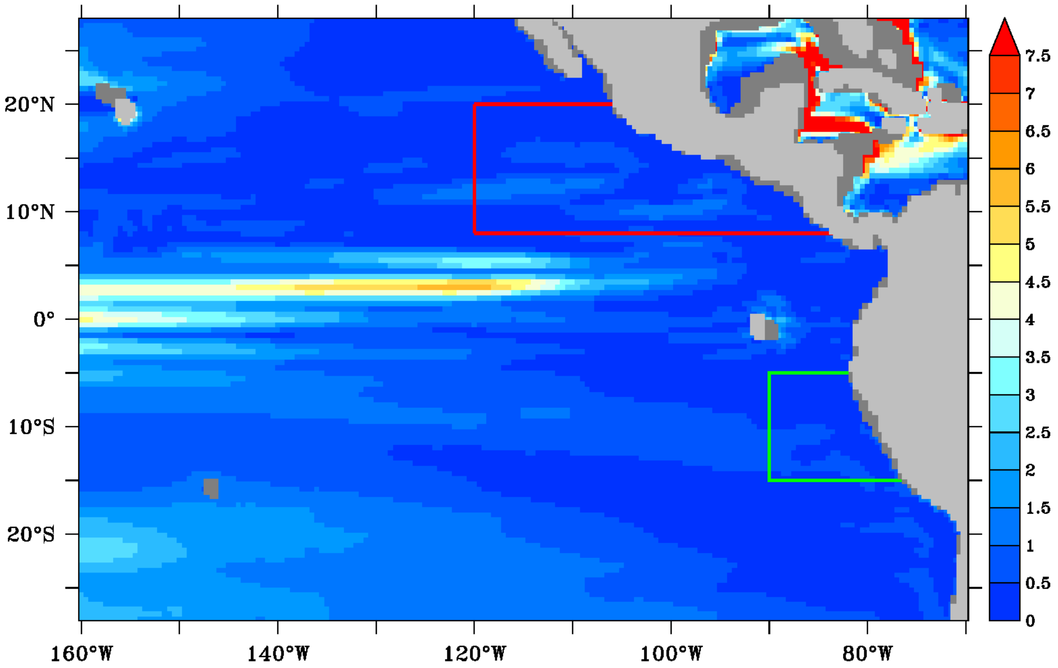

Figure 6.2.: Averaged (2000 to 2009) speed [cm/s] in the OMZ depth layer between 300 m and 650 m in TROPAC01 a) and ORCA05 b). The boxes indicate the regions referred to as nOMZ (red) and sOMZ (green)

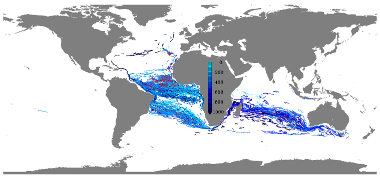

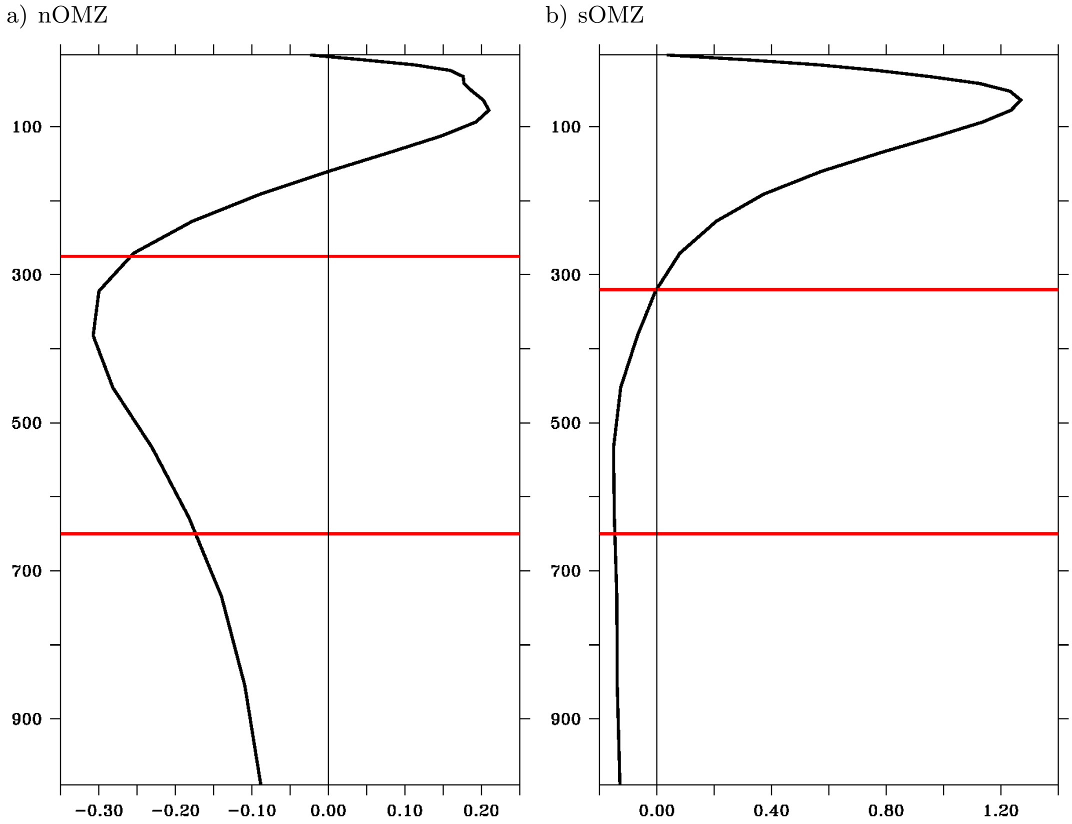

Figure 6.3.: Ten year mean vertical velocity (10^{-6} m/s) profile in TROPAC01 horizontally averaged over the nOMZ a) and sOMZ b). The red lines indicate the upper and lower limits of the OMZs respectively.

and the patterns split up in rather small patches of up- and downward velocities. A similar pattern is found by Hansen and Paul (1987), analyzing drifter data in the eastern tropical Pacific Ocean.

At the southern boundary of the nOMZ, a patch of positive vertical velocities is present throughout the upper 1000 m, shrinking and weakening with increasing depth. Two patches of negative velocities north and east of this upwelling area behave similarly. Around 14° N, in the range between 200 m and 300 m depth, downwelling co-occurs with the location, where the horizontal circulation transports waters from the West towards the OMZs (horizontal velocities are indicated by the arrows in figure 6.4). This indicates a possible region for direct ventilation from above. The rest of the nOMZ area is characterized by weak inhomogeneous positive and negative vertical velocities.

Except for the coastal upwelling band in the upper 100 m of the water column in the sOMZ, downwelling occurs away from the coast. Below this uppermost layer, a downwelling band at the northern boundary of the sOMZ and alternating areas of negative and positive velocities along the coast occur with only weak vertical velocities away from the coast.

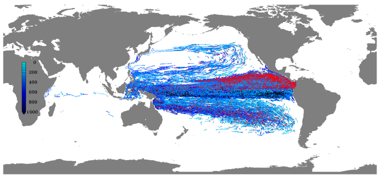

a) 0-100 m

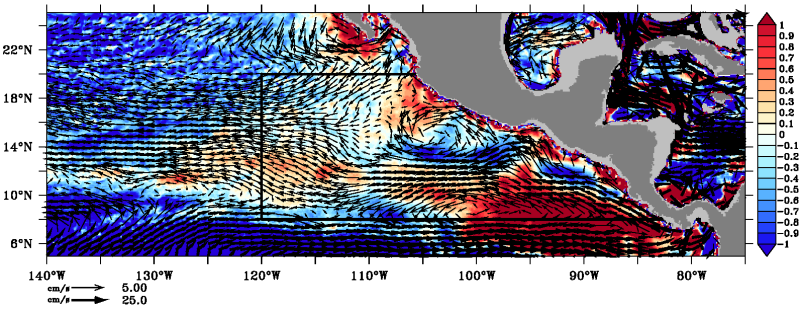

b) 200-300 m

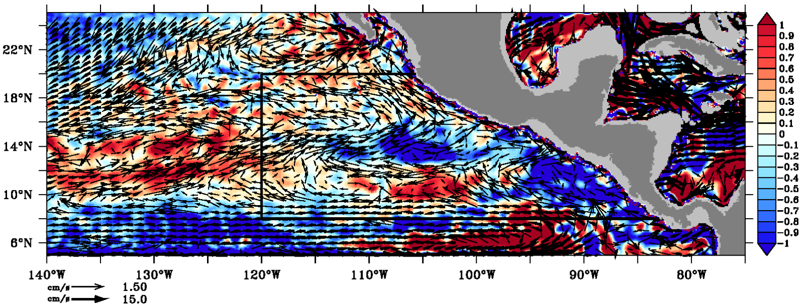

c) 600-700 m

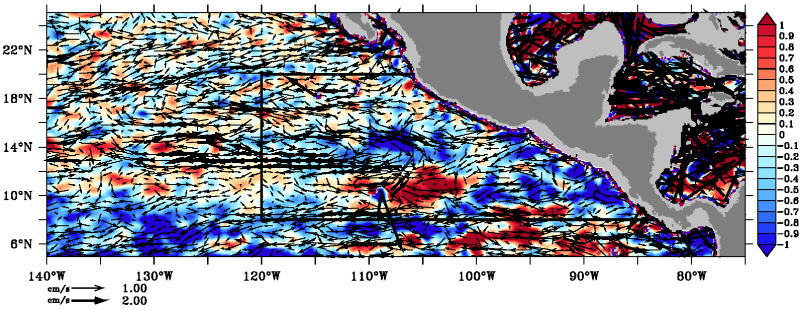

d) 800-900 m

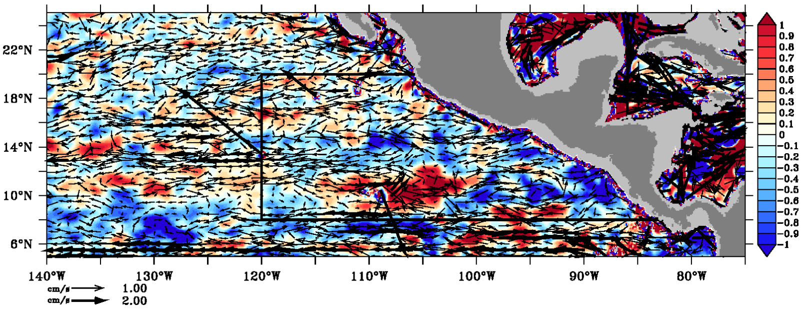

Figure 6.4.: Ten year mean vertical velocity (10^{-6} m/s shaded) in TROPAC01 and horizontal velocities (vectors) averaged over 100 m of the water column between the surface and 100 m depth a), 200 m and 300 m depth b), 600 m and 700 m depth c) and 800 m and 900 m depth d).

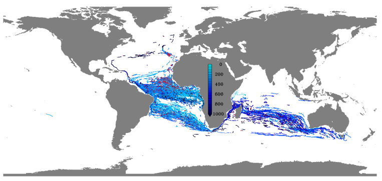

a) 0-100 m

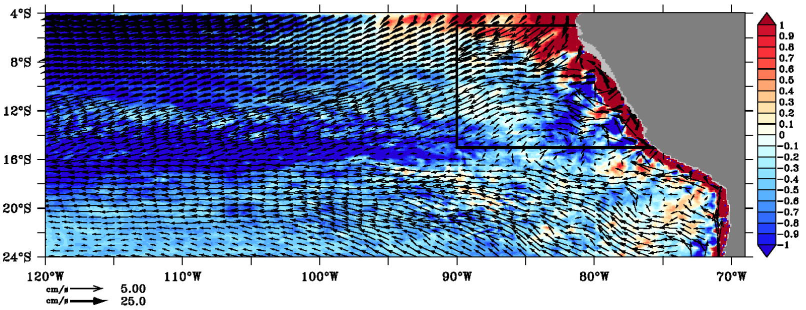

b) 200-300 m

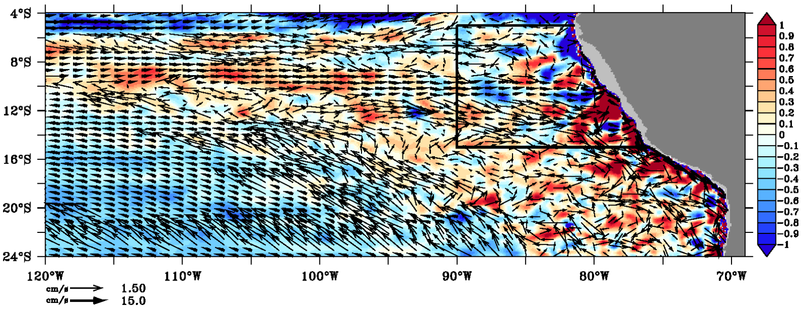

c) 600-700 m

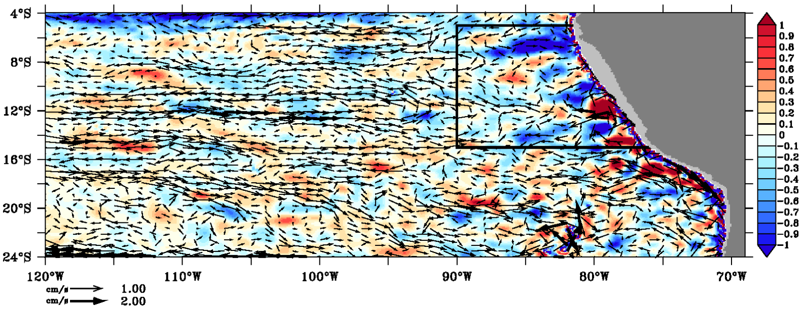

d) 800-900 m

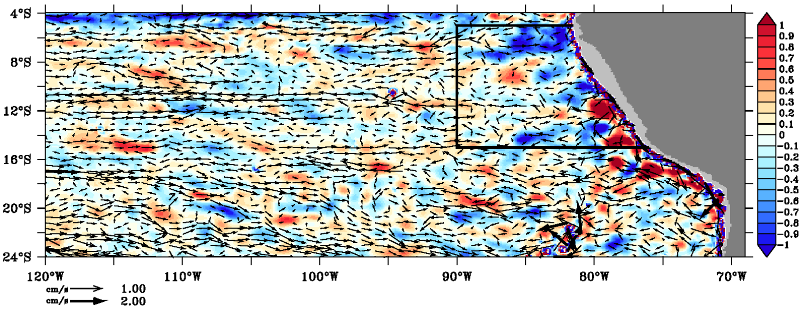

Figure 6.5.: Ten year mean vertical velocity (10^{-6} m/s shaded) in TROPAC01 and horizontal velocities (vectors) averaged over 100 m of the water column between the surface and 100 m depth a), 200 m and 300 m depth b), 600 m and 700 m depth c) and 800 m and 900 m depth d).

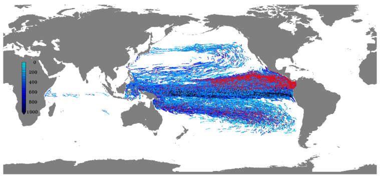

6.2. Ventilation pathways assessed by particle trajectories

The origins of waters within the Pacific nOMZ and sOMZ are analyzed here, using Lagrangian experiments, tracking particles, released within these zones (see table 6.1 for definitions; these areas are marked in figures 6.2 to 6.5) backwards for 80 years in TROPAC01-IA and ORCA05-IA. Except for the release areas, the setup of the experiments is identical to that for the Atlantic Ocean experiments (see section 5.2).

The temporal evolution of the number of particles within the release areas (figure 6.6a and c) shows a strong decline in the beginning of the integration and a slowdown later on. In the nOMZ (figure 6.6a), the decline is faster in TROPAC01 (red curve) with an e-folding time-scale of 14 years than in ORCA05 (black curve) with more than 20 years. Within the last ∼30 years of the integration a linear decline of particles within the release area is simulated in ORCA05 as well as TROPAC01, resulting in ∼15% of the particles remaining in the nOMZ in ORCA05 and only less than 10% in TROPAC01 at the end of the 80 years integration. In the sOMZ experiment, the exponential decline is faster when compared to the nOMZ experiment with e-folding times of only 6 years in TROPAC01 and 8 years in ORCA05. After ∼20 years of integration, 75% of the particles left the sOMZ in both experiments. The decline beyond that point is slower in TROPAC01 than in ORCA05, where almost all particles left the sOMZ after 70 years whereas a remainder of 5% stay within the release area in TROPAC01 throughout the entire integration period.

Again, as for the experiments in the Atlantic Ocean, this only gives the behaviour close to the Pacific OMZs and does not give a direct measure for ventilation time scales. To investigate the latter in a first approximation, the focus is set to the temporal evolution of the number of particles reaching (in a backward sense) the upper 50 m of the water column (see figures 6.7 and 6.8) depending on their release depths (given as different colours). These numbers are only based on the particles, that are located within the nested area of TROPAC01. Due to the larger extent of the nested area in TROPAC01, when compared to TRATL01 and the larger basin width, the number of "lost particles" (figure 6.6b and d) is lower here, with more than 80% of the particles staying within the nested area throughout the entire integration period in the four experiments, whereas the loss of particles is approximately twice as high in TROPAC01 as in ORCA05. The loss of particles starts after 20 years for the nOMZ experiments and 30 years for the sOMZ experiments.

Accumulated over time, the fractions of particles entering the upper 50 m of the water column are comparable in TROPAC01 and ORCA05 for both, the release in the nOMZ with 13.0% in ORCA05 and 12.4% in TROPAC01 and the sOMZ with 11.3% in ORCA05 and slightly more (13.8%) in TROPAC01. For all experiments, the fraction of particles reaching the upper 50 m of the water column declines with increasing release depths with overall comparable numbers between TROPAC01 and ORCA05. Almost 1/3 of the particles released in the nOMZ above 300 m depth reach the upper 50 m when integrated in ORCA05 whereas only 1/4 find their way up there when integrated in TROPAC01. For the layers below, the fractions of particles reaching the upper 50 m is higher in

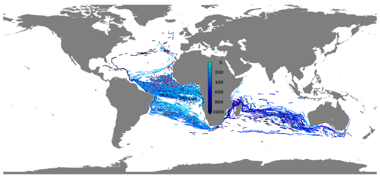

a) nOMZ - release area

b) nOMZ - nest area

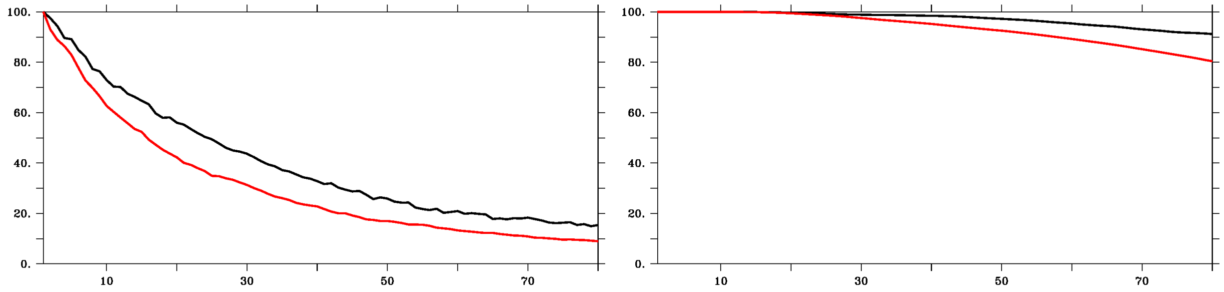

c) sOMZ - release area

d) sOMZ - nest area

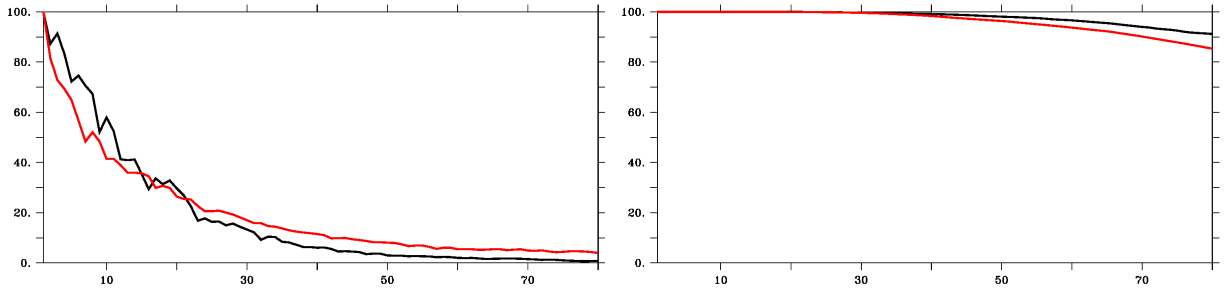

Figure 6.6.: Temporal evolution of particles released within the northern a) and southern c) OMZ in the tropical Atlantic Ocean within the release area [yearly averages in %] for an integration in TROPAC01 (red curves) and ORCA05 (black curves). The number of particles within the nested area of TROPAC01 over time for the nOMZ experiment is given in b) and for the sOMZ in d).

TROPAC01 than in ORCA05. In the sOMZ the numbers are even closer with the largest difference in the layer between 300 m and 400 m depth where the fraction is 5% higher in TROPAC01 than in ORCA05. See table 6.2 for the full statistics.

Experiment	total	common	200-300 m	300-400 m	400-500 m	500-600 m	600-700 m
Pacific nOMZ 0.5°	13.0	13.0	31.8	15.2	3.7	1.3	-
Pacific nOMZ 0.1°	9.9	12.4	23.8	18.3	9.5	3.4	1.4
Pacific sOMZ 0.5°	12.6	11.3	20.4	17.1	11.4	5.4	-
Pacific sOMZ 0.1°	11.0	13.8	-	22.4	12.9	5.9	2.5

Table 6.2.: Fraction of particles reaching the upper 50 m of the water column within the nested area in TROPAC01 during the 80 year integration. Missing values mean, no particles have been released in the corresponding depth range. Total refers to all particles released in the corresponding experiment whereas common refers to the depths common between the TROPAC01 and ORCA05 experiments with the same release area.

In the Pacific nOMZ, the particles released between 200 m and 300 m depth start to reach the upper 50 m of the water column in a sizeable amount between the years 20 and 45 of the integration in TROPAC01 (figure 6.7a). In ORCA05 (figure 6.7b) the amount slowly increases over the first 40 years whereupon, except for a peak in year 55 of the integration, the amount only slightly changes

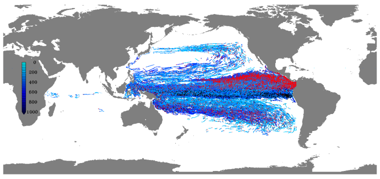

a) nOMZ TROPAC01

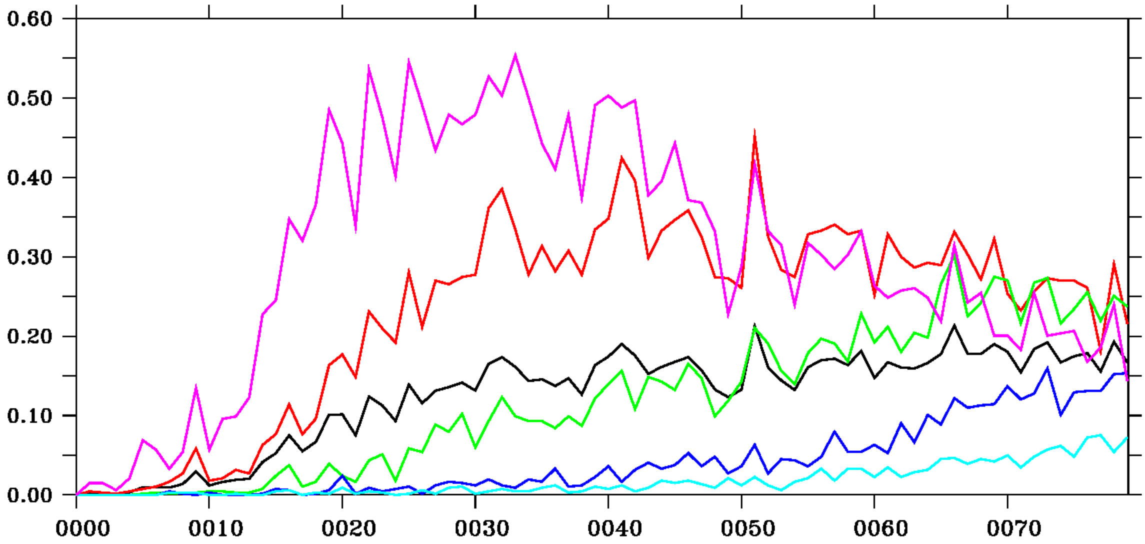

b) nOMZ ORCA05

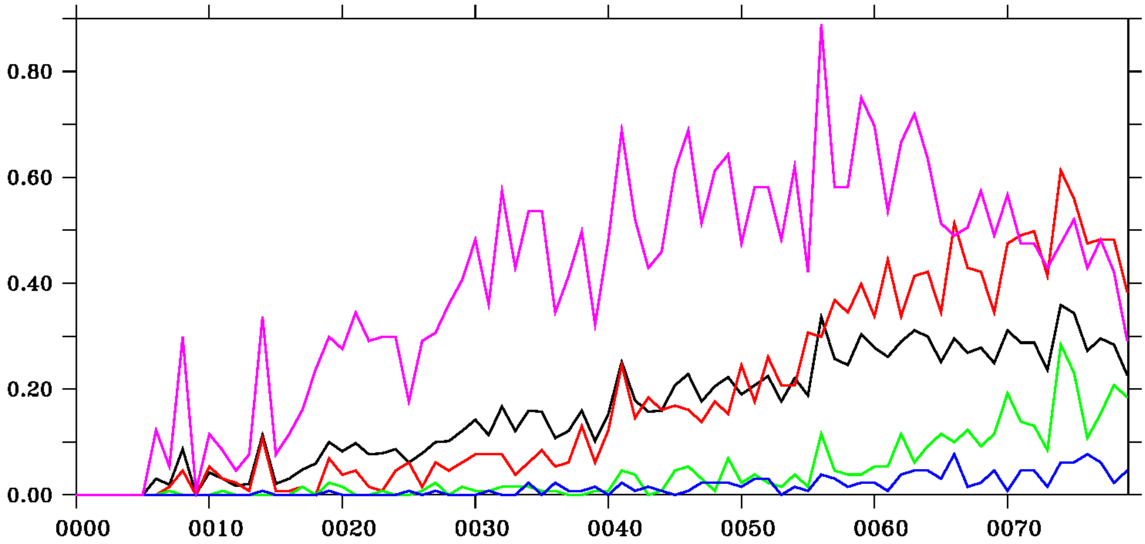

Figure 6.7.: Amount of particles [yearly averages in %] reaching the upper 50 m of the water column at a certain time after their release in the Pacific nOMZ in certain depth ranges: 200 m to 300 m (purple), 300 m to 400 m (red), 400 m to 500 m (green), 500 m to 600 m (blue), 600 m to 700 m (light blue) and independent from the release depth (black) in TROPAC01 a) and ORCA05 b). Note the different scales on the y-axis.

and particles constantly enter the uppermost layer. After 45 years of the integration in TROPAC01, the amount of particles within the upper 50 m that were released between 300 m and 400 m depth reaches the same level as those released above. In ORCA05 this only happens after 70 years. Particles released deeper down the water column need longer to get up in both, the TROPAC01 and ORCA05 experiments. The ventilation timescales are longer in ORCA05 compared to TROPAC01,

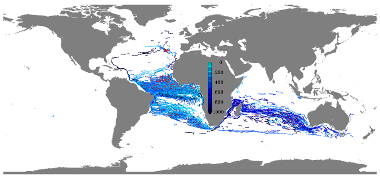

whereas the total amount is larger in ORCA05.

The temporal evolution of particles reaching the upper 50 m of the water column in the Pacific sOMZ experiments (figure 6.8) shows larger differences between TROPAC01 and ORCA05 when compared to the nOMZ experiments. The number of particles released within the uppermost layer of the sOMZ, reaching the upper 50 m of the water column increases fast during the first 30 years of the integration with only a slow decline after $\sim$40 years. At all other depths, a slight increase over the integration period can be seen with a plateau reached after 50 years. In ORCA05, for all depths the amount increases within the first 50 years and stays at this level for the rest of the integration period, with higher values, when compared to the TROPAC01 experiment.

For the nOMZ this means that the ventilation in ORCA05 is slower but stronger than in TROPAC01, whereas for the sOMZ the ventilation is weaker and slower in ORCA05 than in TROPAC01. However, the first (in a backward sense) crossing of the 50 m isobath is only a rough measure for ventilation. In a further step, like for the experiments in the Atlantic Ocean, the time and location when and where the particles enter (still in backward sense) the temporally and spatially varying mixed layer are analyzed in the following.

For at least 70 years of integration, the number of particles entering the mixed layer increases throughout the four experiments (figure 6.9). This emphasizes, that the integration period of 80 years is not long enough to cover all ventilation time scales for the OMZs in the Pacific Ocean.

13% of the particles released in the Pacific nOMZ in TROPAC01 are ventilated within the nested area during the 80 years integration (table 6.3). The locations where most of these particles reach the mixed layer can be separated into four regions (figure 6.10a). The majority gets ventilated east of New Zealand in a $\sim$20° wide zonal band between the southern boundary of the nest and 30° S, reaching towards 140° W. Two zonally extended areas in the eastern part of the southern Pacific at 15° S and 40° S as well as at the northern boundary of the nest between 20° N and 30° N centered at 130° E are weaker smaller areas, where particles get ventilated. In the three areas in the southern hemisphere, the particles need more than 60 years to reach the mixed layer, whereas the averaged time, particles need to reach the mixed layer in the region at the northern boundary of the nest is shorter with $\sim$50 years (figure 6.10b).

In the equatorial band between $\sim$15° S and 20° N only very few particles get ventilated but this path into the mixed layer is fast, with only 20 years or less. Averaged over all particles that find their way into the mixed layer, the time they need to get there is 51 years in TROPAC01. Note, that this time is only an average of the particles that make their way into the mixed layer within the integration period of 80 years (13% of the released particles) and does therefore not reflect the age of waters within the Pacific nOMZ, that is consequently higher than the 51 years found here.

Within the nested area, the same fraction of particles released in the nOMZ reach the mixed layer

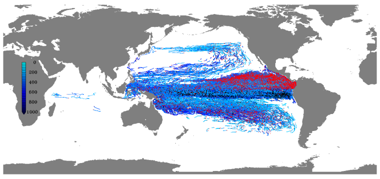

a) sOMZ TROPAC01

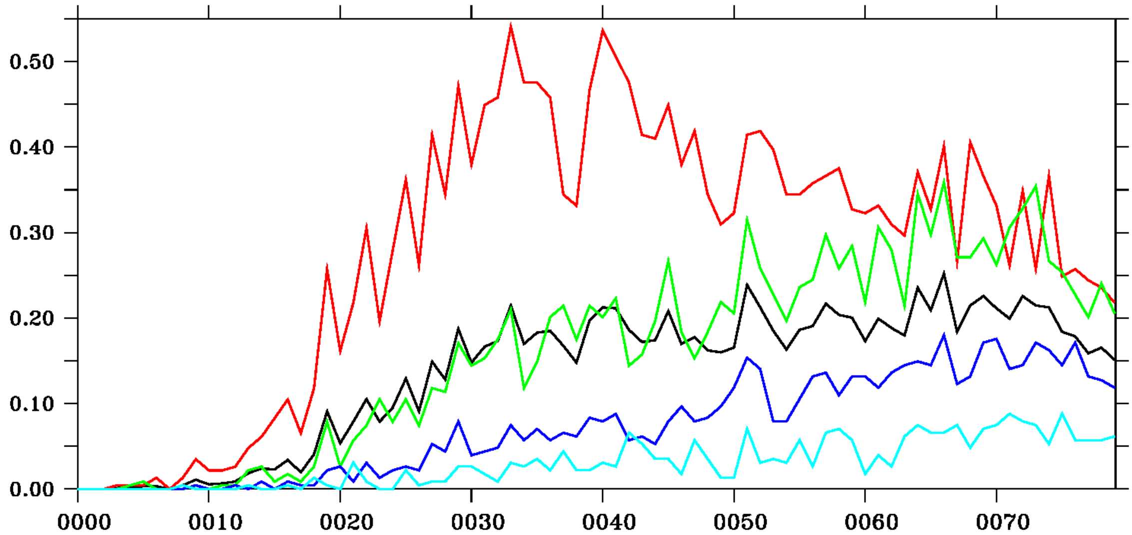

b) sOMZ ORCA05

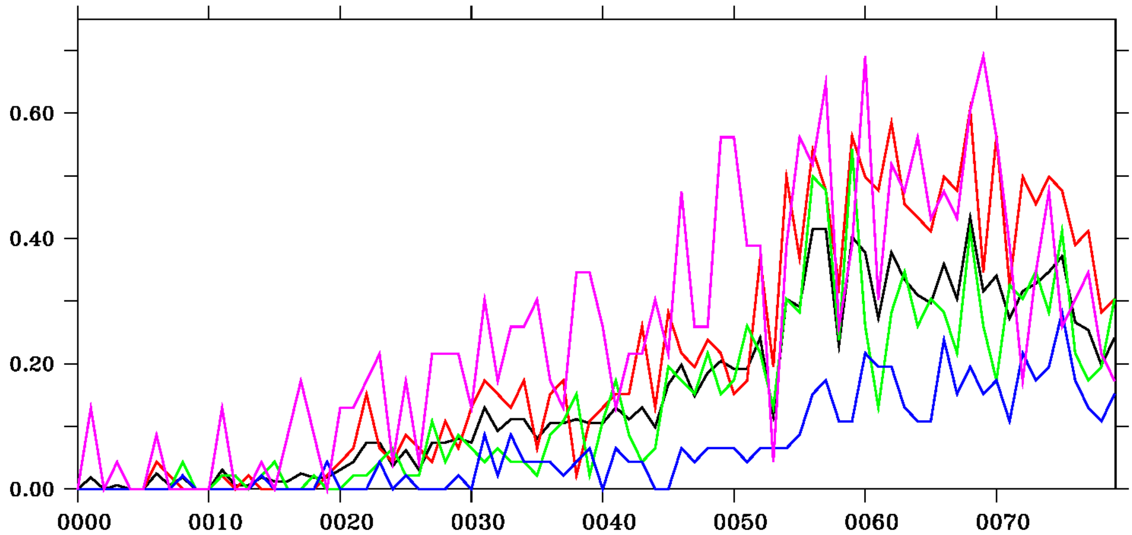

Figure 6.8.: Amount of particles [yearly averages in %] reaching the upper 50 m of the water column at a certain time after their release in the Pacific sOMZ in certain depth ranges: 200 m to 300 m (purple), 300 m to 400 m (red), 400 m to 500 m (green), 500 m to 600 m (blue), 600 m to 700 m (light blue) and independent from the release depth (black) in TROPAC01 a) and ORCA05 b). Note the different scales on the y-axis.

in ORCA05 as in TROPAC01 in an averaged time of 55 years, whereas an additional 6% get ventilated outside the nested area (table 6.3). The regions where most of the ventilation takes place in ORCA05 (figure 6.11) are in a zonal band at ∼40° N along the Kuroshio extension, which is in alignment with the results from the tracer experiments (section 4), almost all over the North Pacific except for a band of ∼10° off the coasts, and in the South Pacific between 20° S and 50° S, again also spanning almost the entire zonal extend of the basin. The time, the particles need to enter

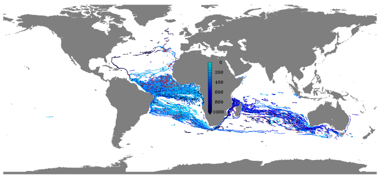

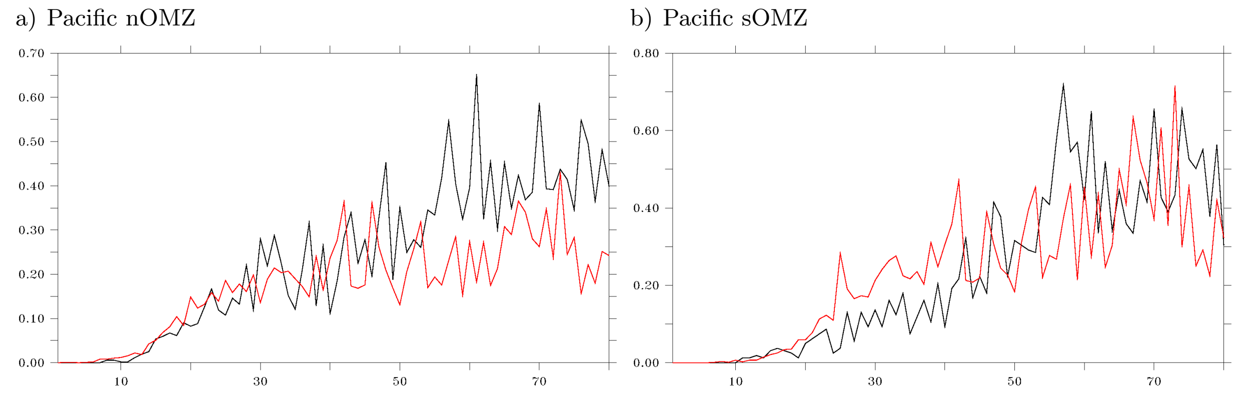

Figure 6.9.: Fraction of particles (in percent of released particles) entering the mixed layer (in a backward sense) in a certain year after release in the Pacific nOMZ a) and sOMZ b). Black curves are from the experiments in ORCA05 and red curves are from the experiments in TROPAC01.

Experiment	within nest [%]	global [%]	time [years]
Pacific nOMZ ORCA05	13	19	55
Pacific nOMZ TROPAC01	13	-	51
Pacific sOMZ ORCA05	16	19	58
Pacific sOMZ TROPAC01	18	-	54

Table 6.3.: Amount of ventilated particles (within the nested region and global for the ORCA05 experiment) and averaged ventilation time for the Lagrangian experiments in the Pacific OMZs in the ORCA05 and nested TROPAC01 models.

the mixed layer is rather homogeneous with 55 years and only single 0.5° by 0.5° boxes show faster connections. Within 80 years only very few particles reach the mixed layer in the Indian Ocean and none in the Atlantic basin.

Overall, the ventilation of particles, that end up in the Pacific nOMZ (in a forward sense), is very similar in TROPAC01 when compared to ORCA05. The path from the equatorial band, that is present in TROPAC01 (figure 6.10), is absent in ORCA05 (figure 6.11) and the areas, where ventilation takes place, show clearer borders in TROPAC01. The areas, where particles are ventilated outside the nested area of TROPAC01 are not simulated in the experiment in the nested model and therefore can only be analyzed in the coarser resolution simulation.

For the experiments where particles are released in the Pacific sOMZ, the fractions of particles that reach the mixed layer within the nested area are slightly higher than those for the nOMZ with 18% for the experiment in TROPAC01 and 16% in ORCA05 whereas in the latter experiment 19% get ventilated globally within the 80 years integration, in agreement with the nOMZ experiments. The times particles need to reach (in a backward sense) the mixed layer are slightly higher for the sOMZ

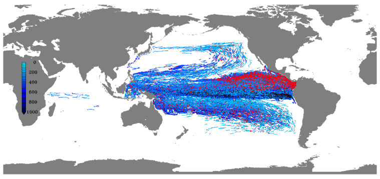

a) # nOMZ TROPAC01

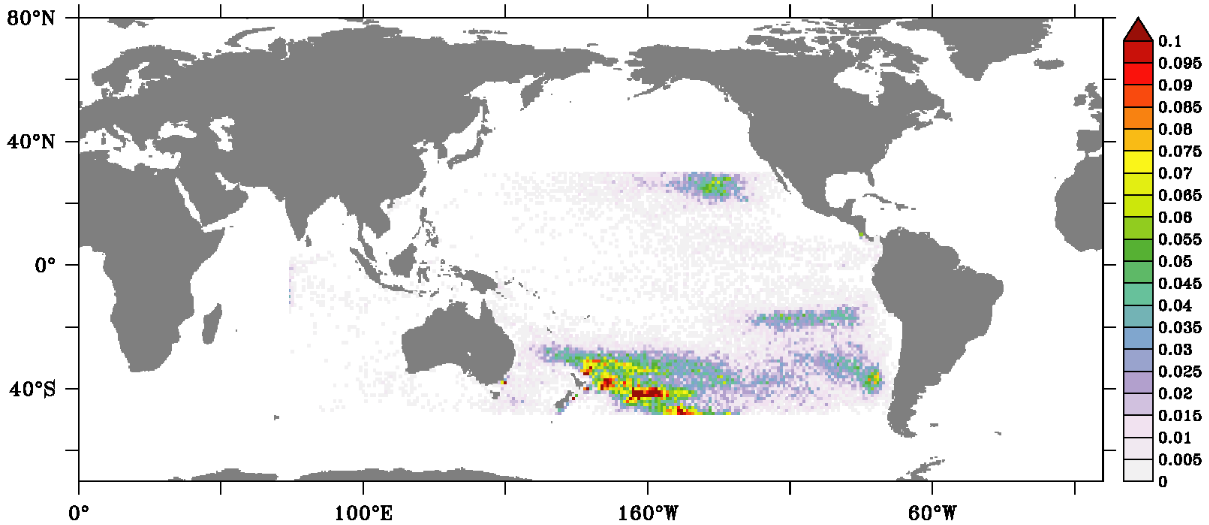

b) time nOMZ TROPAC01

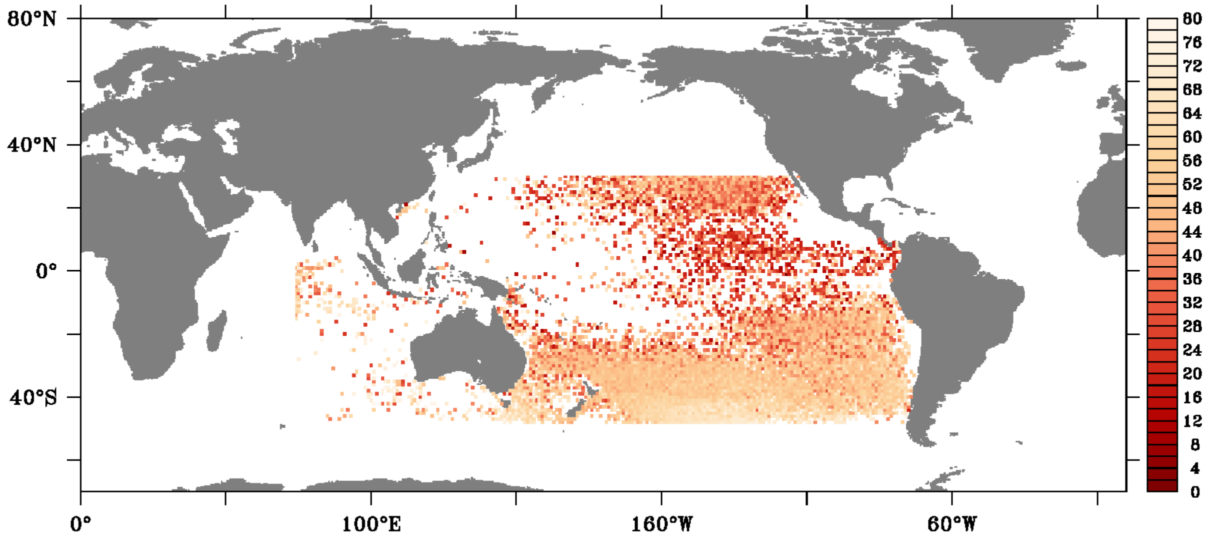

Figure 6.10.: nOMZ TROPAC01: Number of particles that make it to the mixed layer [in % of released particles counted within 0.5° by 0.5° squares] a) and the averaged time they need to get there [in years] b).

experiments with 54 years and 58 years in TROPAC01 and ORCA05, respectively. The results from the experiments in the two different models, however, are again comparable.

The spatial distribution of ventilation areas in TROPAC01 (figure 6.12) is very similar between the experiments where particles are released within the nOMZ and the sOMZ with the latter only lacking the ventilation patch in the northern Pacific and in the equatorial band, and showing a broader band of ventilation south of 20° S. The most pronounced area where particles reach the mixed layer

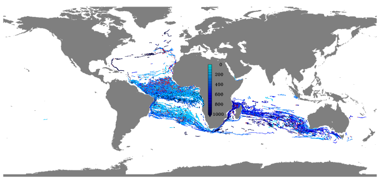

a) # nOMZ ORCA05

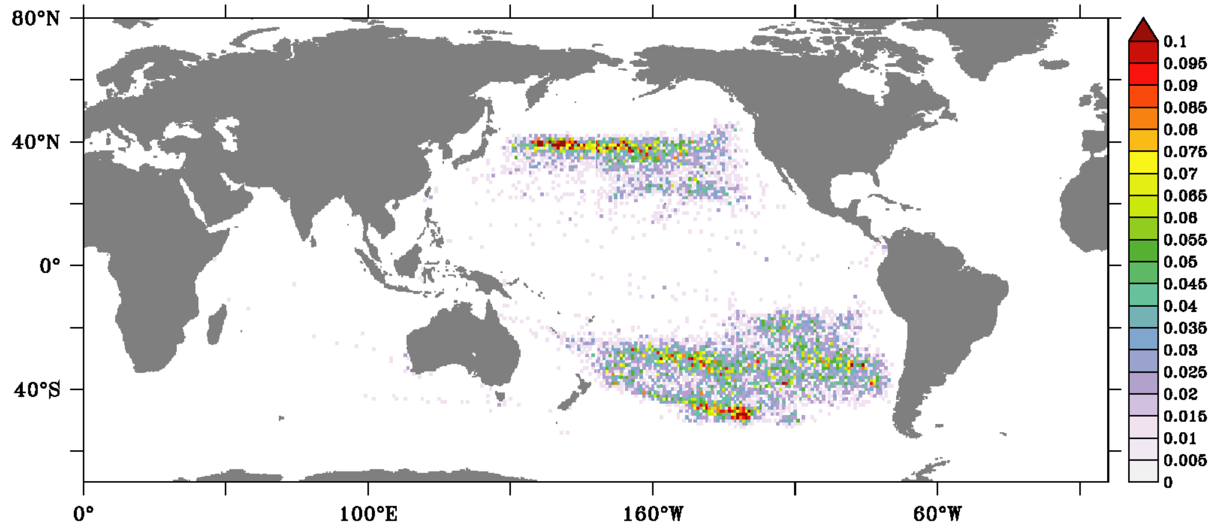

b) time nOMZ ORCA05

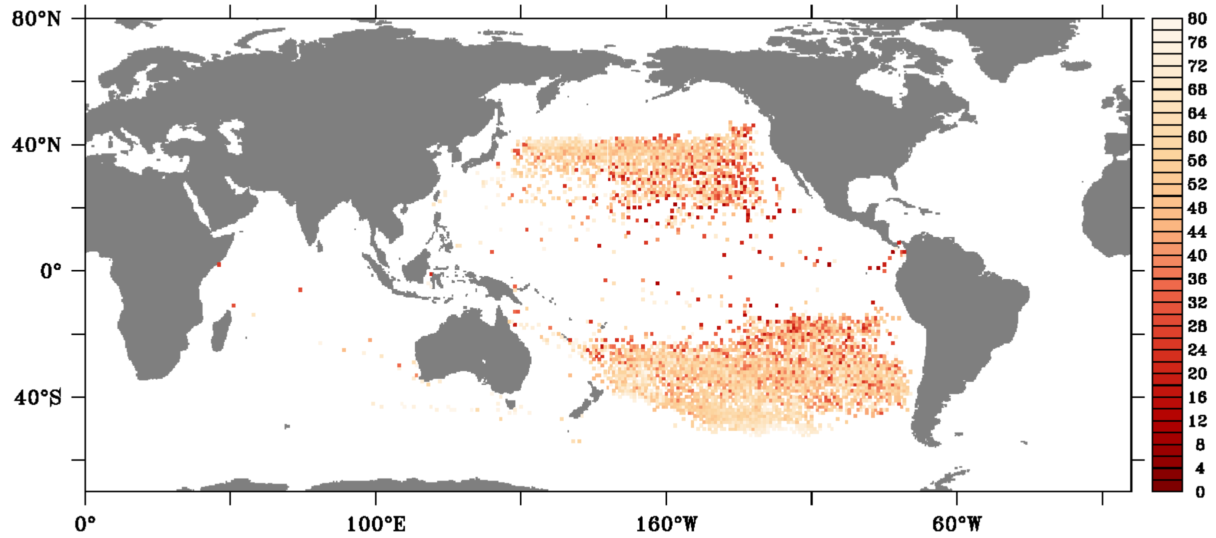

Figure 6.11.: nOMZ ORCA05: Number of particles that make it to the mixed layer [in % of released particles counted within 0.5° by 0.5° squares] a) and the averaged time they need to get there [in years] b).

is again east of New Zealand, here south of 40° S, where the time, particles need to reach the mixed layer, is highest with values of more than 70 years. The particles reaching the mixed layer in the eastern part of the basin and north of the equator only need between 30 years and 60 years.

In ORCA05 (figure 6.13) the locations where particles reach the mixed layer when released within the Pacific sOMZ are almost the same as in TROPAC01 and also the time they need to get there is similar with a tendency to slightly longer timescales. Only an additional zonal band at 40° N

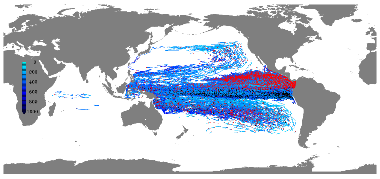

a) # sOMZ TROPAC01

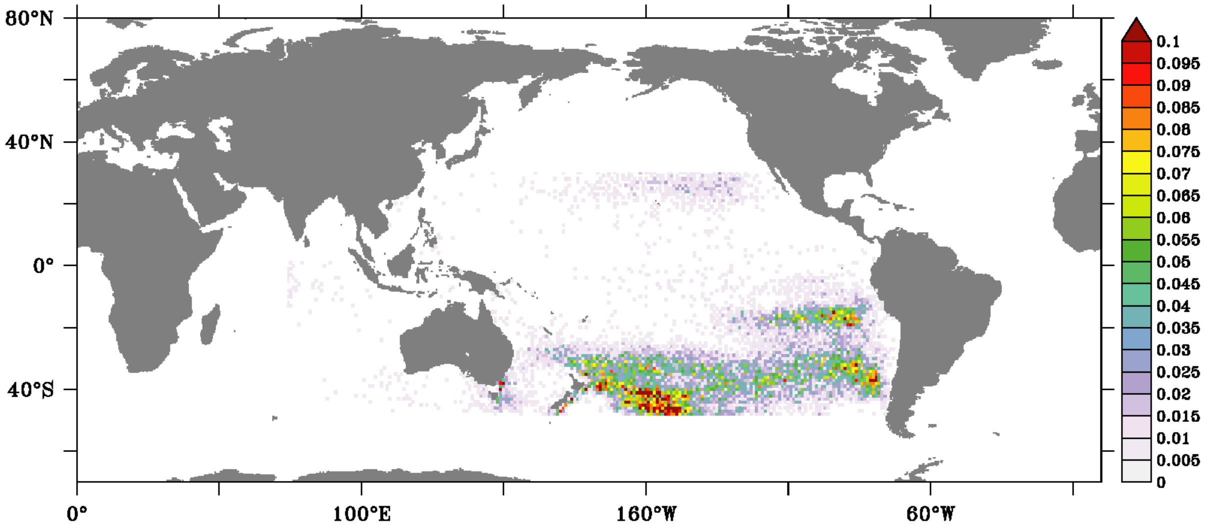

b) time sOMZ TROPAC01

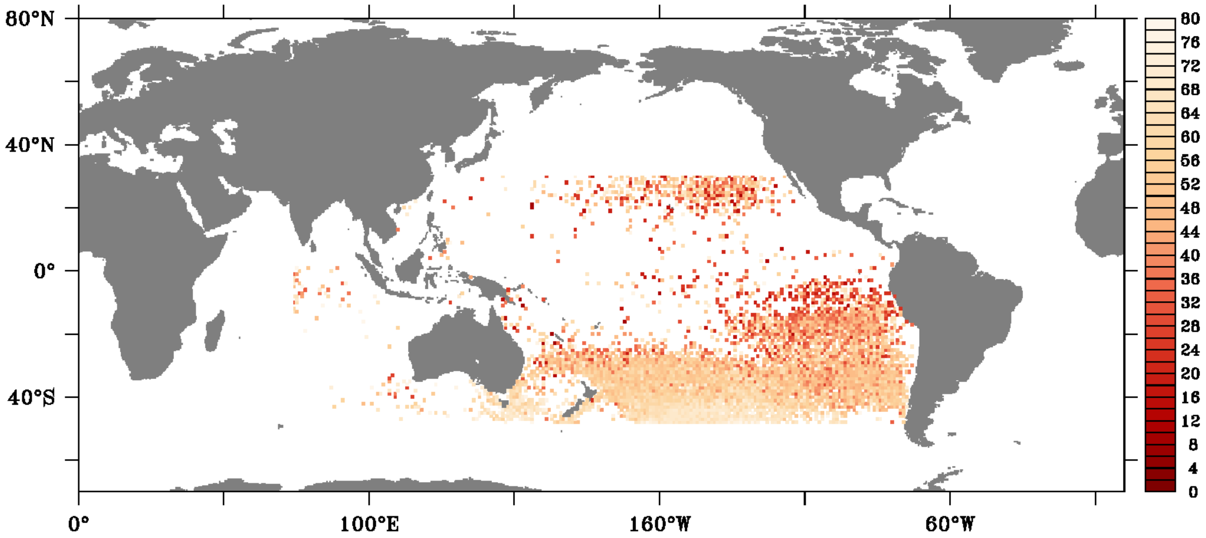

Figure 6.12.: sOMZ TROPAC01: Number of particles that make it to the mixed layer [in % of released particles counted within 0.5° by 0.5° squares] a) and the averaged time they need to get there [in years] b).

where particles reach the mixed layer appears in the ORCA05 experiments, that is not simulated in TROPAC01 due to the nest limitations.

In a forward sense this means, that particles, that end up in the OMZs in the Pacific Ocean within an 80 years integration, get subducted within the Pacific Ocean, independent from the model resolution or whether they end up in the sOMZ or the nOMZ, mainly in an area east of New Zealand centered at ~40° S. Particles reaching the nOMZ show an additional source region in the northern

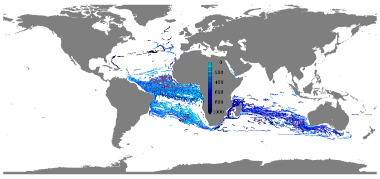

a) # sOMZ ORCA05

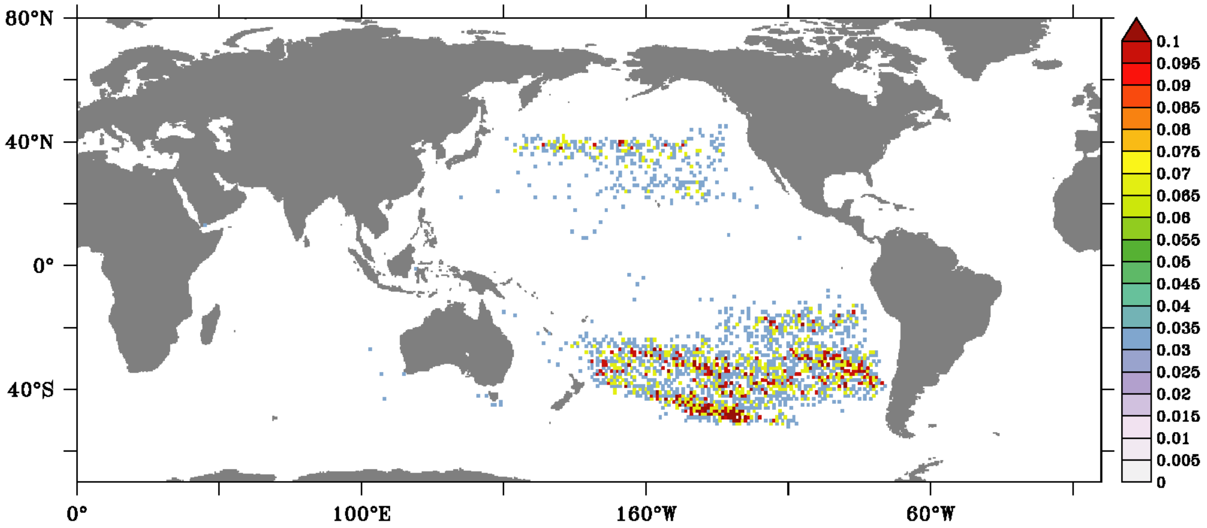

b) time sOMZ ORCA05

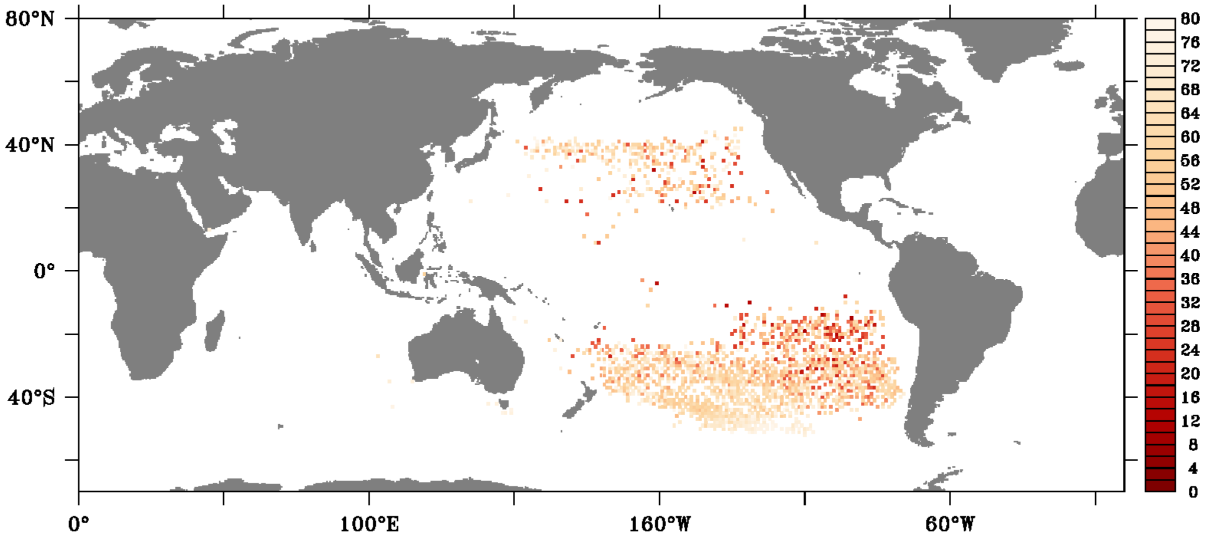

Figure 6.13.: sOMZ ORCA05: Number of particles that make it to the mixed layer [in % of released particles counted within 0.5° by 0.5° squares] a) and the averaged time they need to get there [in years] b).

part of the Pacific basin, that is only very weak for particles ending up in the sOMZ. The difference between the two models is not as prominent in the Pacific as it is in the Atlantic and the fraction of particles ventilated outside the nested area, or even in a diffrent ocean basin, is negligible for the sOMZ experiments, at least in an 80 years framework.

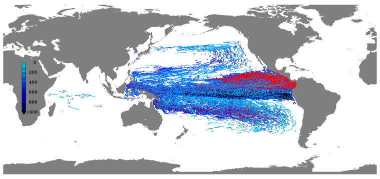

6.2.1. Pathways into the northern OMZ

The pathways of the particles released in the Pacific nOMZ are described in the following section. The temporal evolution of the vertically integrated particle populations is given on a linear scale for the first eight years of the integration in TROPAC01-IA (figure 6.14) and ORCA05-IA (figure 6.15) and on a logarithmic scale for the consecutive decades (figures 6.16 and 6.17) to show the long term particle spread. These particle populations are repeated in the appendix on a logarithmic scale for the short term and on a linear scale for the long term evolution (figures A.47 to A.50). Note that, like in sections 5.2.1 and 5.2.2, the wording is chosen in a temporally backward sense.

In TROPAC01, during the first year of the integration (figure 6.14) along the western boundary of the release area some weak, band-like structures evolve, transporting particles slightly westwards. At the northern boundary in a small area at ∼110° W some particles move northward. Centered at 4° N first single particles start their way west, already reach 150° W within this first year of the integration and even the western boundary of the Pacific basin within the second year. At that time, the populations weaken in the region of the release, already exposing the diffusive character of the particle spread. After three years (see figure A.47 in the appendix), three main routes, particles take towards the west, can be identified at ∼9° N, ∼14° N and ∼17° N, that persist for another three years. Afterwards, the band-like structure weakens and the particle distribution rather shows a wide zonal band, where particles are transported between 5° N and 20° N. Some of the fast particles already make their ways into the center of the southern and northern basin via the western boundary of the Pacific Ocean during these first eight years of the integration period. It appears that more particles enter the northern part of the Pacific when compared to the populations in the southern part, which is at least visible on a logarithmic scale (see figure A.47). While after the first year, the number of boxes on the sampling grid (0.5° times 0.5° squares) that are populated by particles at any depth is 3,500, after eight years this area widened by a factor of more than six to 22,000.

In ORCA05 during the first three years of the integration, a shape resembling the release area is almost unaltered, with sharp gradients in the particle populations along all boundaries (figure 6.15). During that time, as in TROPAC01, first single particles start their way along ∼4° N towards the west but only reach the coast within the fourth year. The structure of the particle population starts to significantly change after five years (see figure A.48 in the appendix), when between 14° N and 19° N particles begin their way towards the west, but south of this area, the most prominent zonal front moves east throughout the rest of the first eight years of the integration. Significant numbers of particles get transported south east along the American coast. A small, but non-negligible number of particles makes its way back into the centre of the basin via the western boundary, like in TROPAC01, but slower. The original area of 1,825 grid boxes, that were covered by particles after one year of the integration grew to 13,160 after eight years.

On decadal time scales in TROPAC01 the particle populations exhibit a strongly diffusive behaviour (figure 6.16). After ten years (see figure A.49 in the appendix) of the integration the particle distribution displays a triangular shape of high populations in and around the release area with a swath

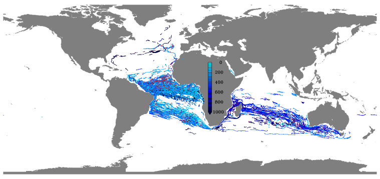

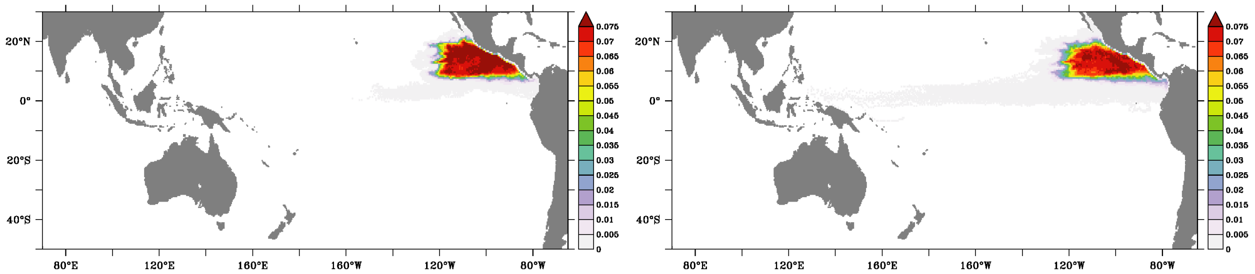

a) Population in year 1

b) Population in year 2

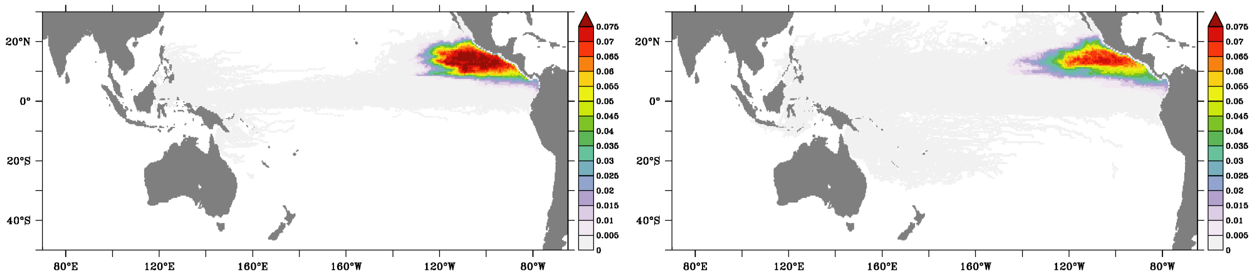

c) Population in year 4

d) Population in year 8

Figure 6.14.: Depth integrated particle population [in % of released particles per 0.5° square] in the first a), second b), fourth c) and eighth d) year after release in the nOMZ in TROPAC01.

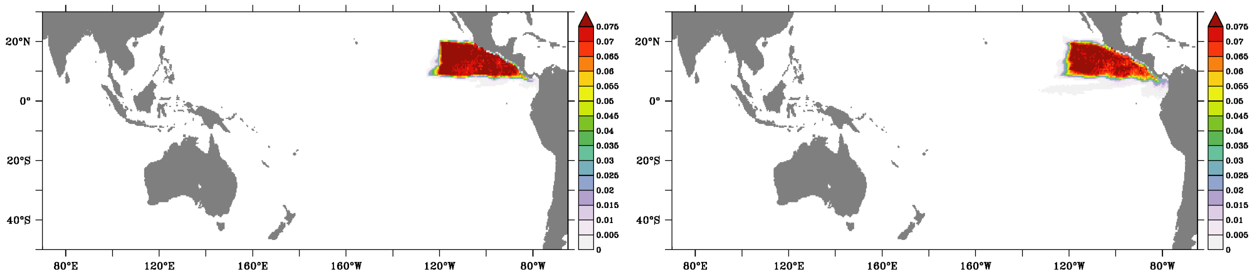

a) Population in year 1

b) Population in year 2

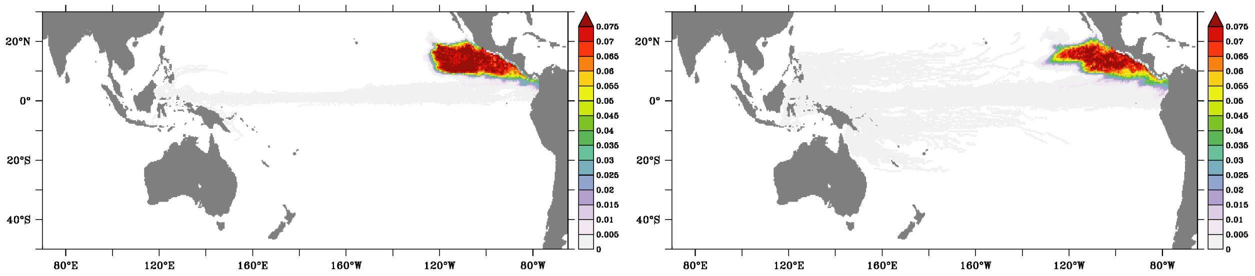

c) Population in year 4

d) Population in year 8

Figure 6.15.: Depth integrated particle population [in % of released particles per 0.5° square] in the first a), second b), fourth c) and eighth d) year after release in the nOMZ in ORCA05.

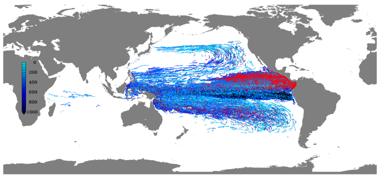

of particles moving westward. Along 4° N an additional band of elevated populations shows a connection to the western boundary of the basin, from where particles move back into the centre of the basin north and south of the equator, where in the northern hemisphere this happens at ∼10° N, in the southern hemisphere the particles move further south along the Australian coast and back into the basin south of 20° S. After 20 years, while a significant number of particles reaches the northern boundary of the nested region, the western tip of the triangle already crosses the date line and connects with the patch of particle populations coming back from the west. This connection leads to elevated populations in a zonal band, spanning the entire basin centered at 10° N throughout the rest of the integration. After 50 years, sizeable amounts of particles start to leave the nested area across the southern boundary and the subtropical south Pacific fills up with particles towards the end of the 80 years integration. A tongue of particles enters the Indian Ocean via the Indonesian passages from year 20 onwards.

In ORCA05, particle populations in their decadal evolution (figure 6.17) show a similar behaviour to those in TROPAC01 within the nested area. The main difference is the absence of the diffusive character in the coarser ORCA05 experiment. Distinct paths dominate the particle populations in ORCA05. The connections are slower when compared to TROPAC01 and the path into the Indian Ocean via the Indonesian passages is, except for single particles, not present. A direct path from the northern boundary of the nOMZ towards the north shows up after ten years (see figure A.50 in the appendix) weakening and vanishing during the following decades. This path cannot be identified in TROPAC01 due to the horizontal limitations of the nested area. The westward spread of particles is confined to relatively narrow bands, not only at 4° N where the fastest particles cross the basin but also within the region, that was marked by the triangularly shaped particle population pattern in TROPAC01. Particles move south along the American coast, from where they turn into the Pacific basin, forming these narrow zonal bands. The northernmost edge of high populations is a northeast to southwest tilted band from 15° N at 120° W to 5° N at 180° W. It persists, with small local deviations until the end of the integration period. Another zonal band at ∼10° N evolves after 30 years and is present till the end of the 80 years.

Already after 20 years of the integration particles start to leave the nested area towards the North, where a zonal structure, spanning the entire Pacific basin at ∼40° N, evolves, that persists throughout the entire integration. After 40 years (see figure A.50 in the appendix), particles also start to leave the nested area of TROPAC01 south, via the Tasman Sea and across the Pacific basin, entering and slowly covering the Southern Ocean.

In a forward sense, to answer how waters find their way into the Pacific nOMZ, this means, that some fraction circulates with the ACC around Antarctica before the waters enter the Pacific Ocean, mainly in the eastern part of the basin but also through the Tasman Sea. With the SEC, waters get transported northwest towards the western boundary of the Pacific Ocean, where they get transported north, and along the New Guinea coast with the NGCC across the equator, where they enter the current band at 4° N, the NSCC or by meridional displacement one of the other bands, that transport the waters east and into the nOMZ. From the North, waters cross the Pacific Ocean

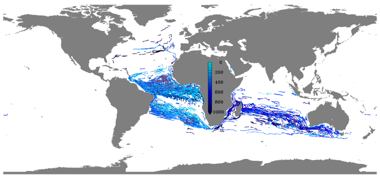

a) Population in year 20

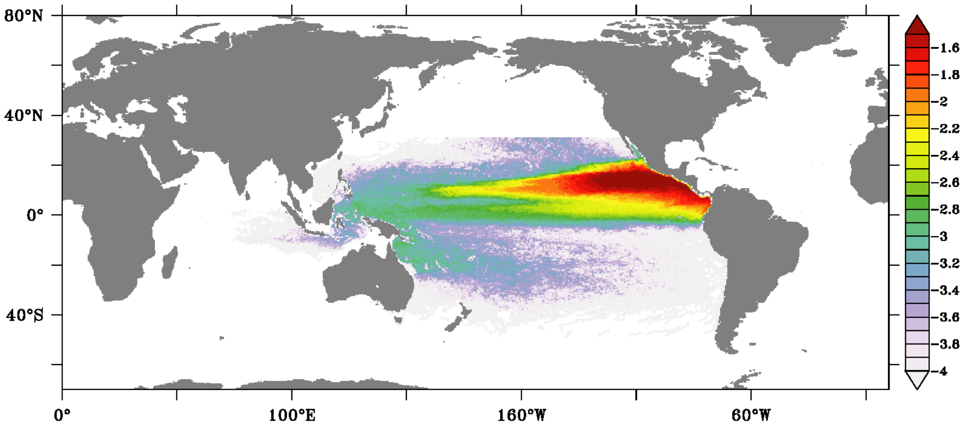

b) Population in year 50

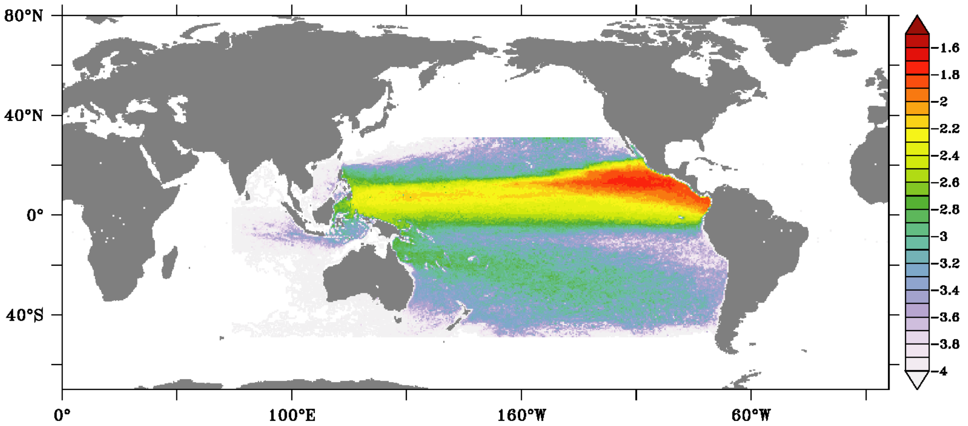

c) Population in year 80

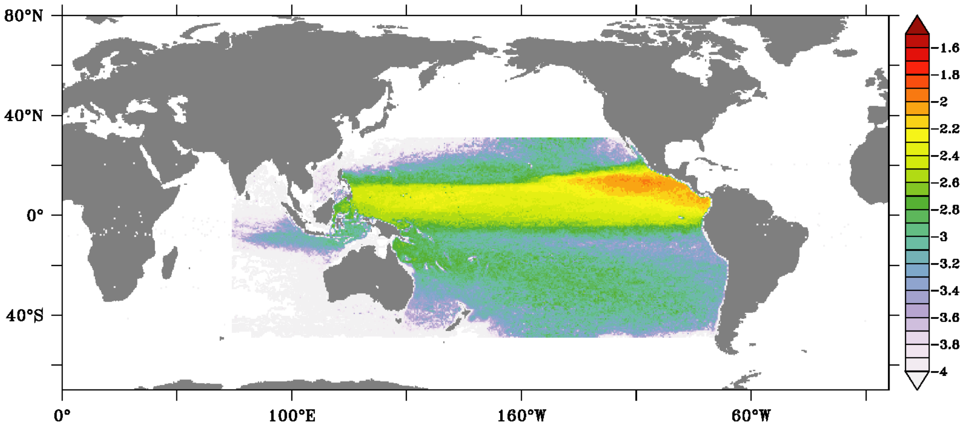

Figure 6.16.: Depth integrated particle population [in % of released particles per 0.5° square on a logarithmic scale] 20 a), 50 b) and 80 c) years after release in the nOMZ in TROPAC01.

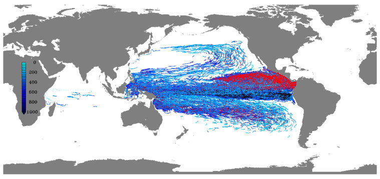

a) Population in year 20

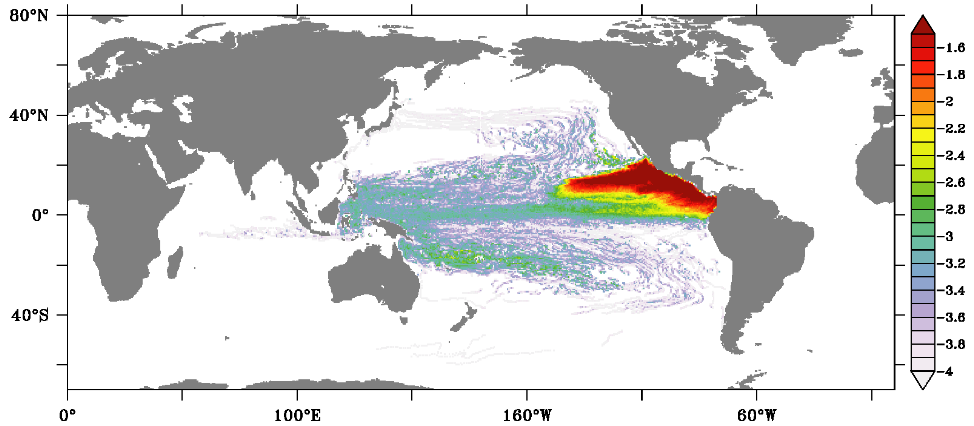

b) Population in year 50

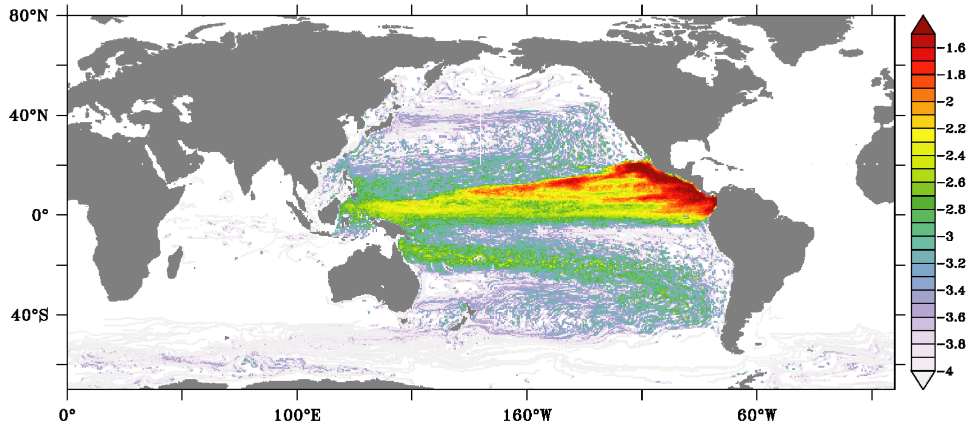

c) Population in year 80

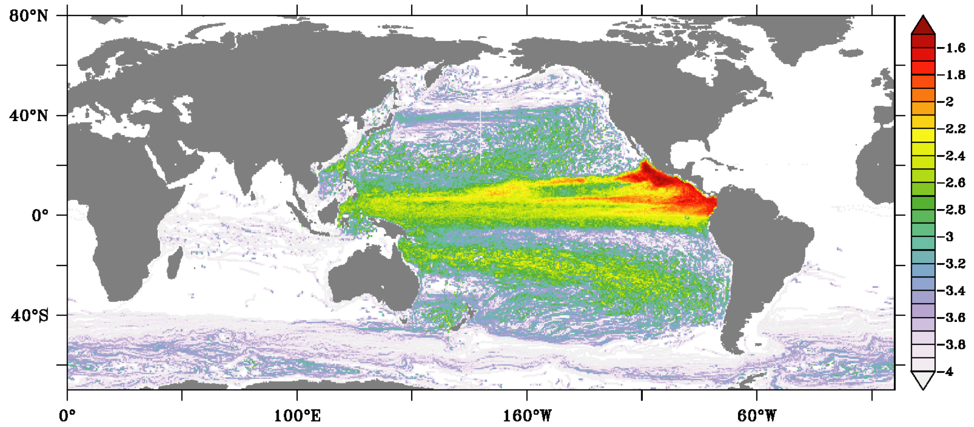

Figure 6.17.: Depth integrated particle population [in % of released particles per 0.5° square on a logarithmic scale] 20 a), 50 b) and 80 c) years after release in the nOMZ in ORCA05.

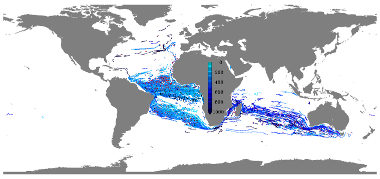

with the Kuroshio extension from west to east and turn into the NEC, that transports them back towards the West or directly enter the nOMZ via its northern boundary. Waters that make their way back to the West enter one of the zonal bands flowing back east, entering the nOMZ mainly via its western boundary.

The last part of the waters' way into the nOMZ is taken between 200 m and 600 m depth, between 10° N and 15° N co-occurring with very weak eastward velocities in TROPAC01 (see figure 6.18). This is shown in the particle populations at 130° W, 10° west of the western boundary of the nOMZ, integrated over the first ten years of the integration and therefore the last ten years before all particles are located within the nOMZ (shading in figure 6.18) and the overlaid ten year averaged velocities (contours). In ORCA05 there is also a small core of higher particle populations, co-occurring with eastward velocities centered at ∼14° N, that however is very weak when compared to the TROPAC01 populations. The concentrated pathways of the particles crossing a section can not readily be inferred from the Eulerian mean flow, meaning that the determination and measurement of a mean flow at a single section is not enough for unraveling water pathways.

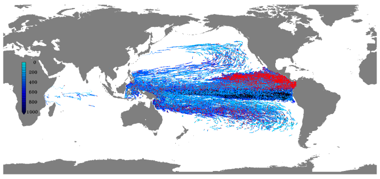

a) TROPAC01

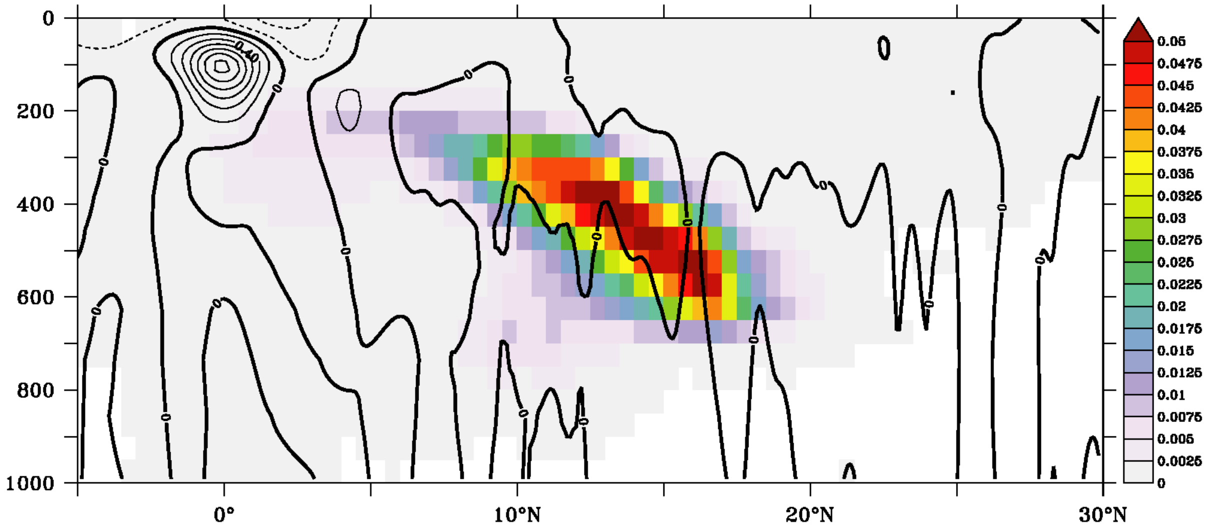

b) ORCA05

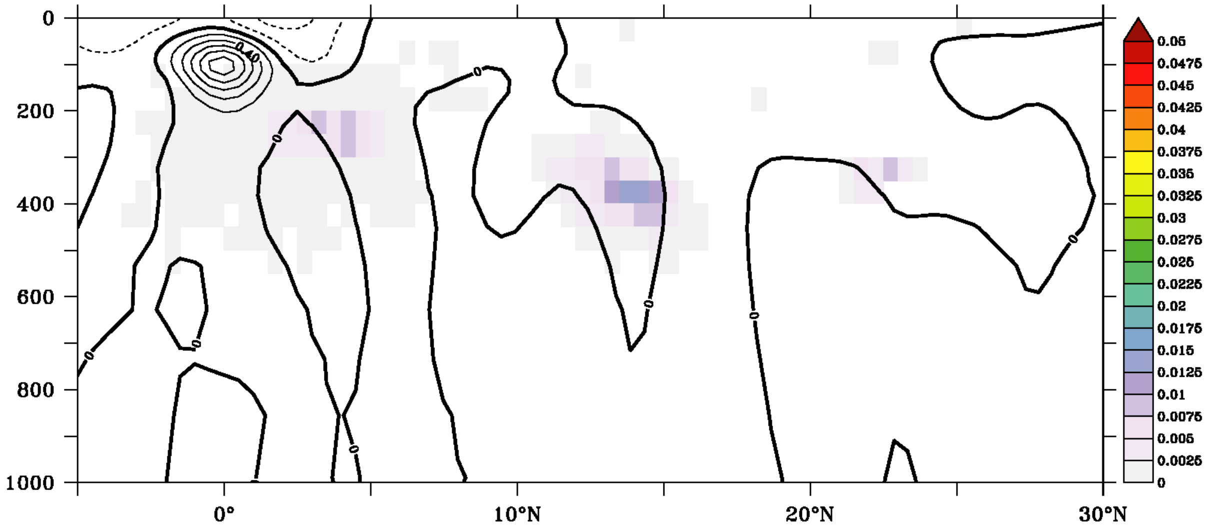

Figure 6.18.: Particle population within the first ten years of the integration (shading) and ten year averaged zonal velocity at 130° W (contours) from TROPAC01 a) and ORCA05 b).

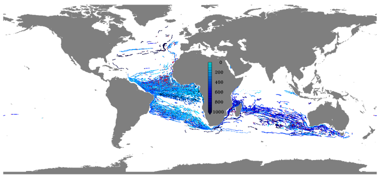

6.2.2. Pathways into the southern OMZ

The temporal evolution of particle populations originating from the Pacific sOMZ experiments in TROPAC01-IA and ORCA05-IA is given on a linear scale for the first eight years of the integration (figure 6.19 and 6.20) and on a logarithmic scale for the following decades (figures 6.21 and 6.22). The description of these evolutions will again be given in a backward sense.

In TROPAC01 in the first year of the integration the particle population (figure 6.19) exhibits three bands at the western boundary of the release area, showing elevated values at the northern and the southern boundary of the sOMZ as well as right in the middle at 10° S. Between those bands, two areas of lower populations occur, that shift the location of the strongest gradient in populations eastward into the sOMZ. After the second year of the integration, the southern band begins to merge with the central one, whereas a patch of low population values strengthens between the two northern bands of high populations. This mirrored c-shape persists for the first five years, after which the southern band starts to extend westward, whereas the northern band narrows, also extending west, but comparably slow. In the surroundings of the sOMZ, the diffusive character of the particle spread appears by reducing the populations, weakening gradients between high and low population values and widening the area, where particles are present, from 790 to 4,200 grid boxes (0.5° times 0.5° squares) after the first eight years of the integration.

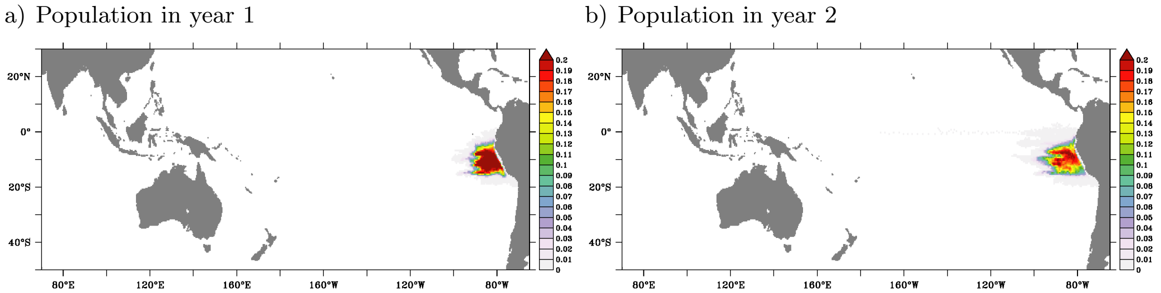
a) Population in year 1

b) Population in year 2

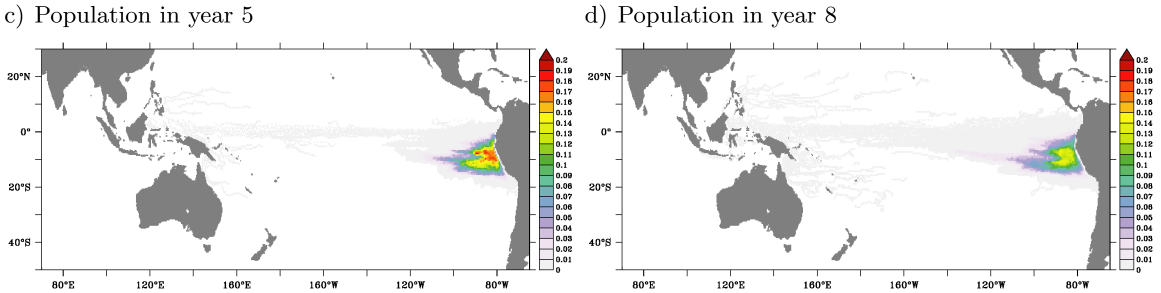
c) Population in year 5

d) Population in year 8

Figure 6.19.: Depth integrated particle population [in % of released particles per 0.5° square] in the first a), second b), fifth c) and eighth d) year after release in the sOMZ in TROPAC01.

In this experiment, the first particle makes its way to the western boundary of the basin within three years, along 3° S. By then, particles also cross the equator in the eastern part of the basin.

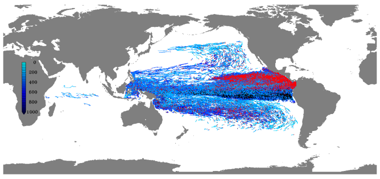

Within the rest of the first decade of integration, more, but overall very few, particles find their way via the western boundary back eastward into the northern and southern part of the Pacific basin. Some particles also seem to take a direct route from the vicinity of the release area into the centre of the southern part of the Pacific basin.

In ORCA05, the three bands occurring after the first year of integration in TROPAC01 develop after three years. Only one year later, the first single particle reaches the western boundary (figure 6.20). The southernmost band persists during the first eight years of the integration and the overall shape of particle populations looks very similar to that in TROPAC01 except for the fact, that in ORCA05 the patterns are less diffusive. Within these years, the populated area grows by a factor of 7 from 1,250 to 9,590 populated boxes on the sampling grid.

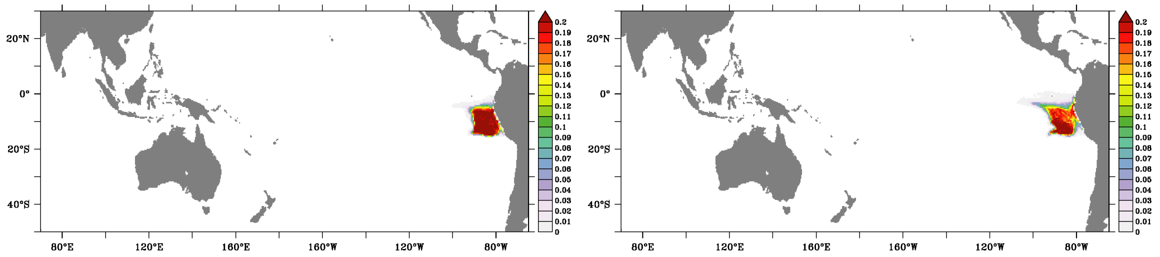
a) Population in year 1
b) Population in year 2

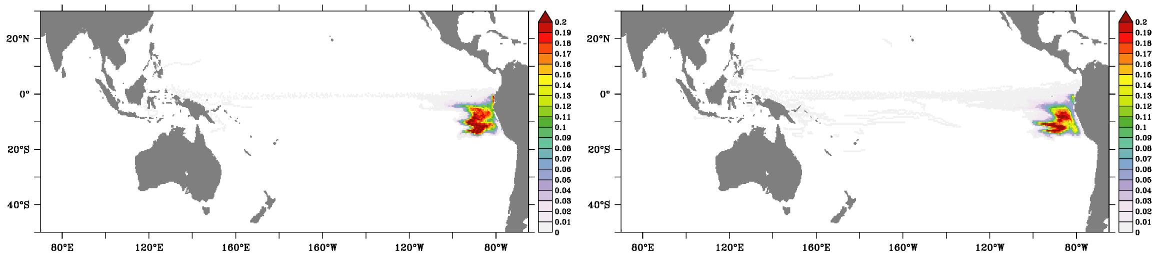
c) Population in year 5
d) Population in year 8

Figure 6.20.: Depth integrated particle population [in % of released particles per 0.5° square] in the first a), second b), fifth c) and eighth d) year after release in the sOMZ in ORCA05.

After the first and second decade of the integration, the particle population in TROPAC01 still exhibits the two bands penetrating westward (figure 6.21), with the southern one of them being slightly tilted from the southeast to the northwest. Overall, the diffusive character of the particle spread dominates the shape of the particle population. After twenty years, a remarkable amount of particles starts to enter the southern part of the Pacific via the western boundary, whereas only a very small fraction enters the northern hemisphere. After three decades, except for a distinct band at the southern boundary of the patch of elevated population values, a triangularly shaped area of high populations with its core located at the sOMZ, dominates the population structure. This structure prevails throughout the rest of the integration period although the values weaken with time. The amount of particles within the southern subtropical Pacific Ocean grows, not only via the western boundary but also on shorter paths in the inner part of the basin.

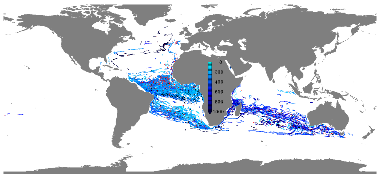

a) Population in year 20

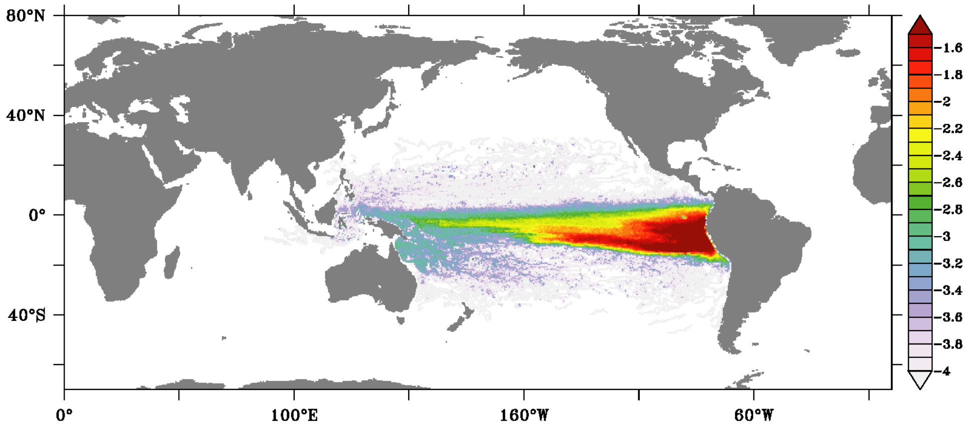

b) Population in year 40

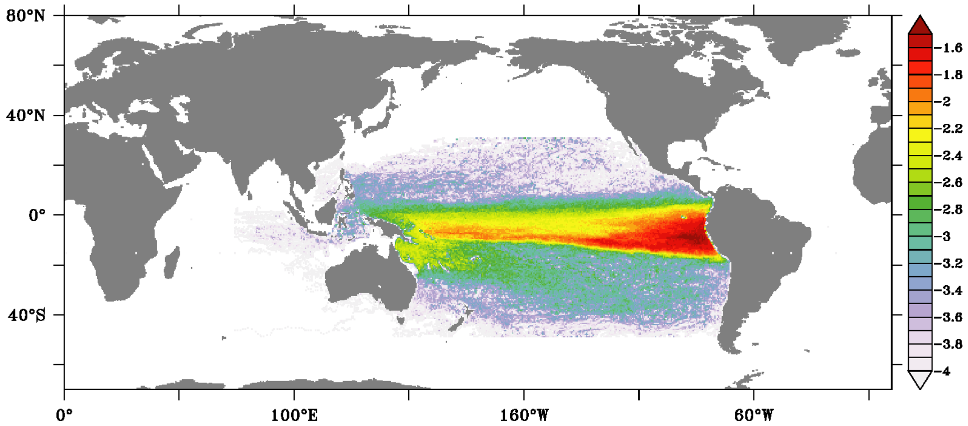

c) Population in year 80

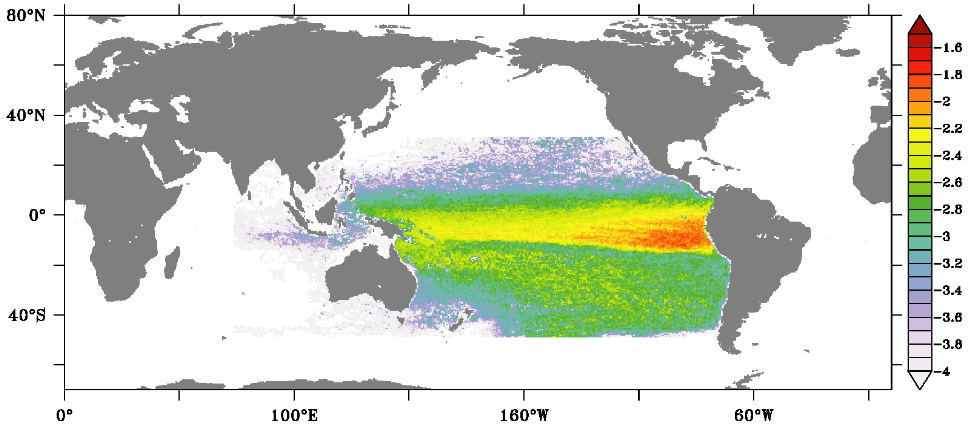

Figure 6.21.: Depth integrated particle population [in % of released particles per 0.5° square on a logarithmic scale] 20 a), 40 b) and 80 c) years after release in the sOMZ in TROPAC01.

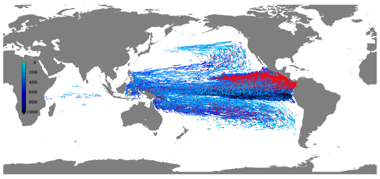

In ORCA05 (figure 6.22), after one decade of integration, a pronounced tongue at the northern boundary of the sOMZ evolves and moves particles towards the west. One decade later, a path in the South evolves, that overtakes the northern part and becomes the dominating structure within the third decade. From then on, except for the lack of the particle diffusion, the main structure of the evolution of particle populations within the nested area is similar to the one simulated in TROPAC01. The particles move across the Pacific Ocean, westward in a band between the equator and ~15° S and return back into the southern subtropical basin mainly via the western boundary. Some particles also find their way directly from the release area into the southern part of the basin. In the global ORCA05 experiment a small fraction of particles also spreads into the North Pacific and the Southern Ocean.

In a temporally forward sense, this means, that particles ending up in the Pacific sOMZ partly come from the Southern Ocean, where they circulate around Antarctica within the ACC, before they enter the Pacific basin, partly via the Tasman Sea, get transported to the western boundary of the basin with the SEC and along the coast, with the NGCC into the SSCC and eastward towards the sOMZ. Some particles originate from the North Pacific, circulate with the subtropical gyre, and also enter the off-equatorial eastward currents via the western boundary of the basin.

The depth structure of the particle populations within the first ten years of the integration 10° west of the western boundary of the sOMZ (figure 6.23) shows highest populations between 300 m and 500 m depth, between 14° S and 9° S in TROPAC01 co-occurring with eastward velocities (contours), as well as another weaker and smaller core at ~7° S, between 500 m and 600 m depth. In ORCA05 the populations at 100° W are weaker when compared to those in TROPAC01 and two cores are located, co-occurring with eastward velocities at 3° S and 11° S.

In the Pacific Ocean, both, the northern and the southern OMZs, are mainly ventilated via a pathway from the southern subtropical Pacific by a route via the western boundary of the basin. The main difference between the ventilation of the nOMZ and the sOMZ is the presence of a remarkable source in the North Pacific, that is only very weak for the sOMZ. The strong particle diffusion in TROPAC01, that is missing in ORCA05 is the main difference between the two model configurations, while the paths are comparable.

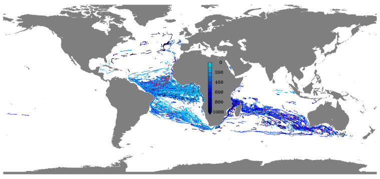

a) Population in year 20

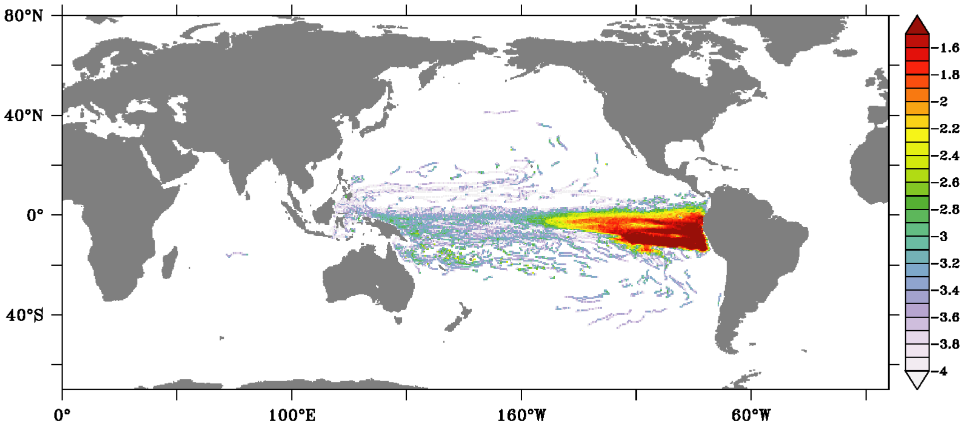

b) Population in year 40

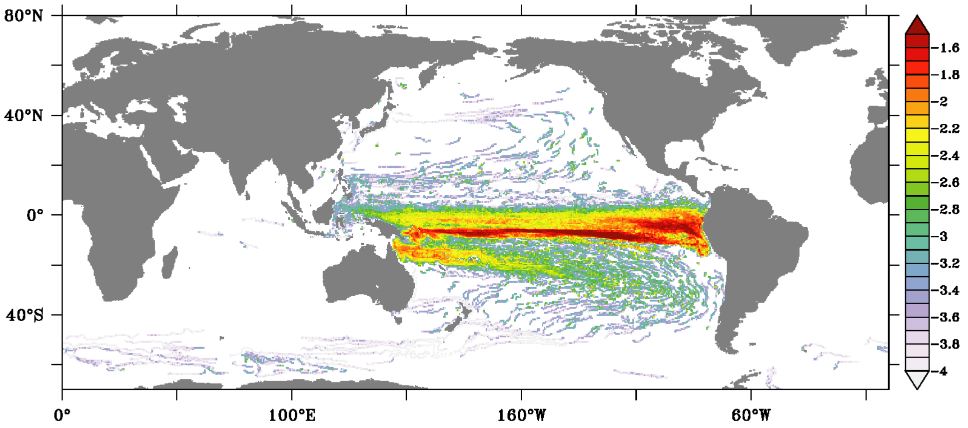

c) Population in year 80

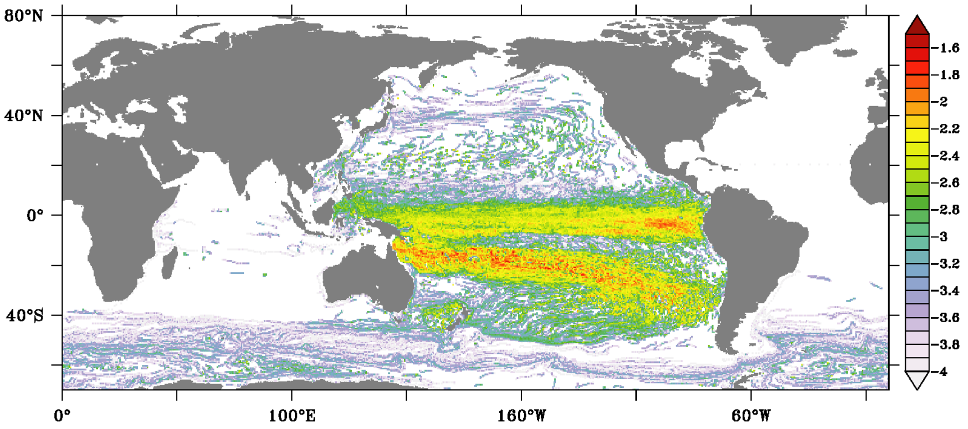

Figure 6.22.: Depth integrated particle population [in % of released particles per 0.5° square on a logarithmic scale] 20 a), 40 b) and 80 c) years after release in the sOMZ in ORCA05.

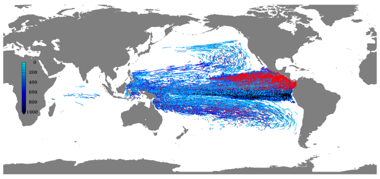

a) TROPAC01

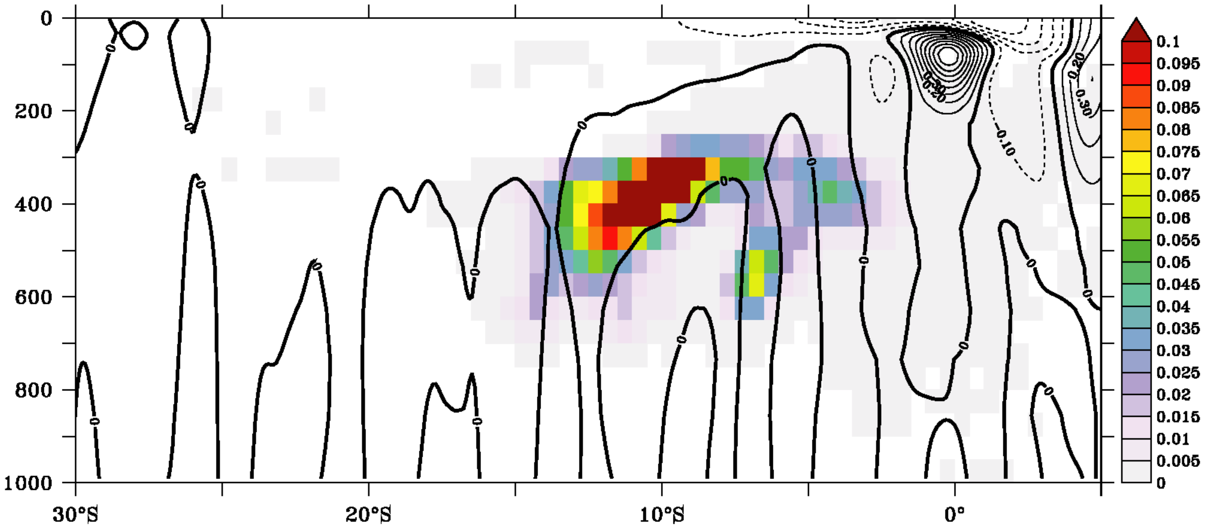

b) ORCA05

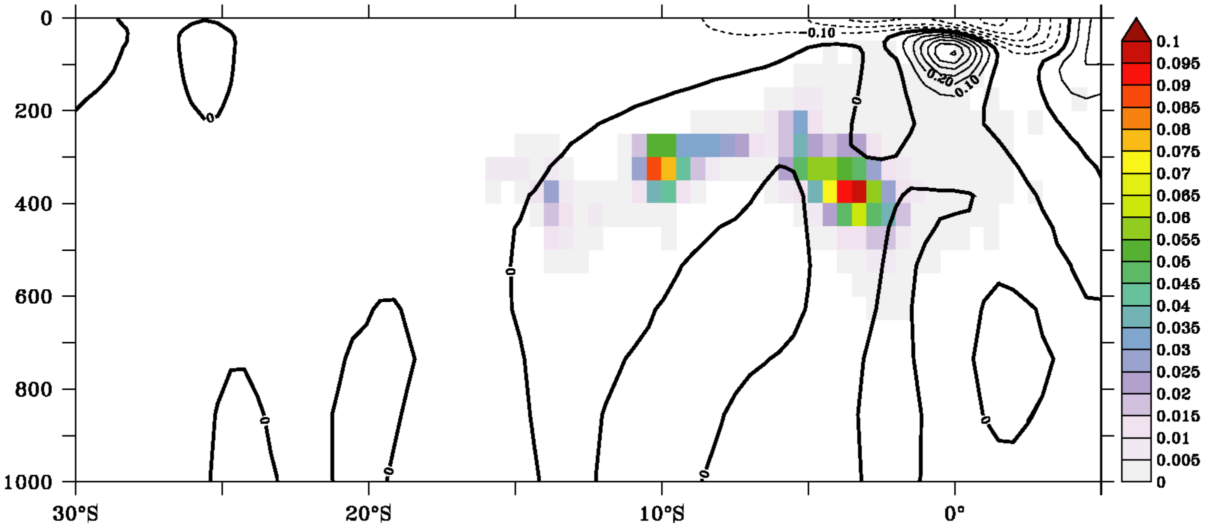

Figure 6.23.: Particle population within the first ten years of the integration (shading) and ten year averaged zonal velocity at 100° W (contours) from TROPAC01 a) and ORCA05 b).

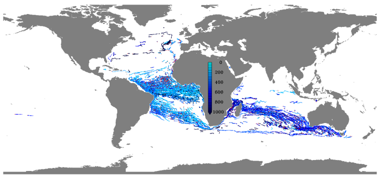

6.3. Temporally integrated Lagrangian pathways

Like in the experiments in the Atlantic Ocean, the temporally integrated particle populations are shown here for the experiments in the Pacific Ocean. The figures showing the first arrivals are again deferred to the appendix (figures A.55 and A.56).

In the full depth integrated particle populations (figure 6.24) in TROPAC01 (left panel), like in TRATL01, the main features are approximately zonal bands of high populations, transporting the particles. For the nOMZ experiments, an additional path of elevated populations from the southern hemisphere exists. In the simulation in the global ORCA05 model, pronounced paths from the northern and southern subtropical Pacific dominate the pattern, where for the nOMZ experiment the path from the North is stronger than for the sOMZ experiment, where the path from the South is most prominent.

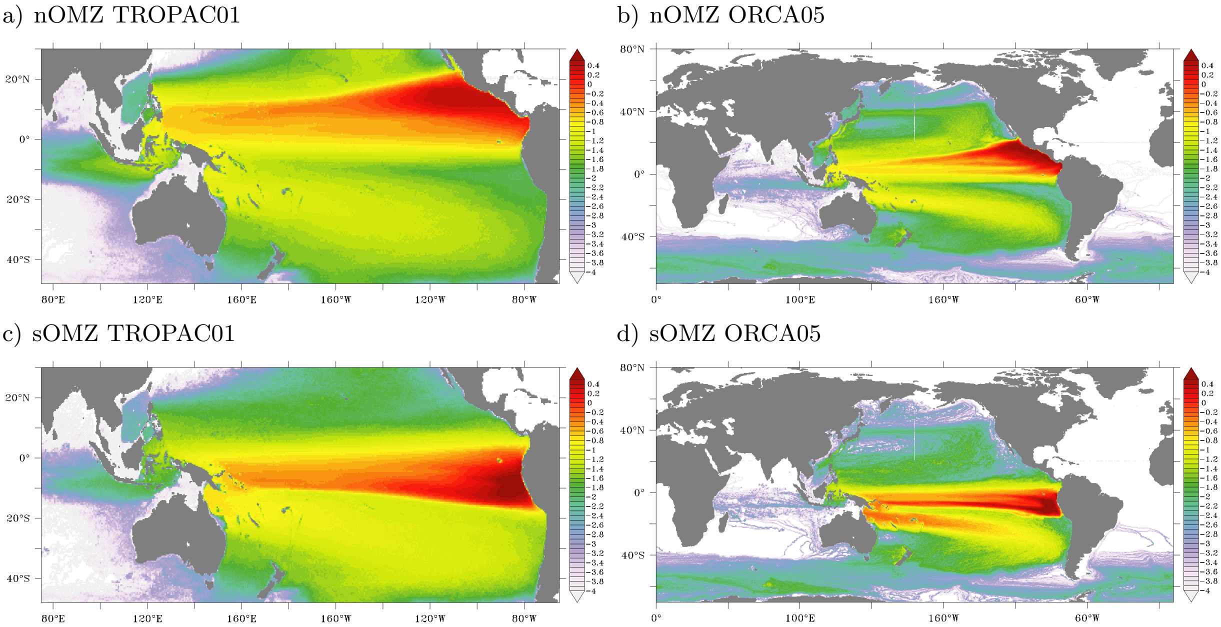
a) nOMZ TROPAC01

b) nOMZ ORCA05

c) sOMZ TROPAC01

d) sOMZ ORCA05

Figure 6.24.: Full depth integrated particle population [in % of released particles per 0.5° square on a logarithmic scale] temporally integrated over the full period of the Lagrangian experiments of 80 years for particles released in the Pacific nOMZ (top) and sOMZ (bottom) in TROPAC01 (left) and ORCA05 (right).

Separating the populations in three different depth ranges, an upper (surface to 200 m depth), a mid-depth (200 m to 800 m) and a deep (below 800 m depth) layer (figure 6.26) shows the vertical distribution of the particles and exhibits distinct paths that are masked in the full depth integrated view. Similar to the experiments in the Atlantic Ocean, the mid-depth populations broadly reproduce the full-depth structure in all experiments in the Pacific and only a minor fraction of the particles gets transported in the shallow and the deep layers.

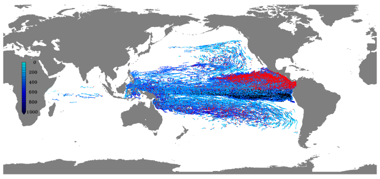

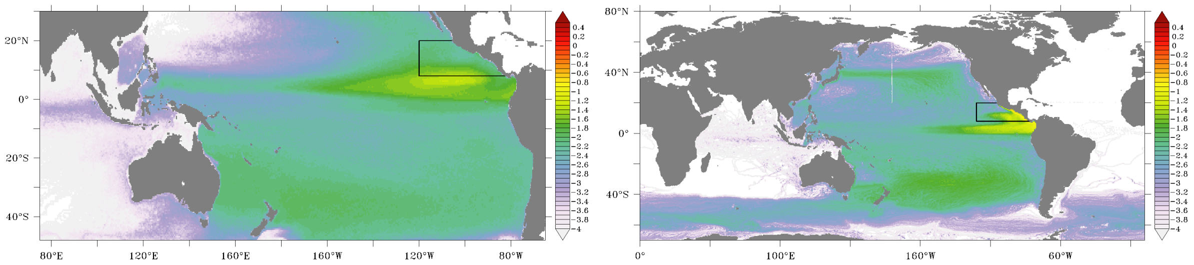

a) surface to 200 m TROPAC01

b) surface to 200 m ORCA05

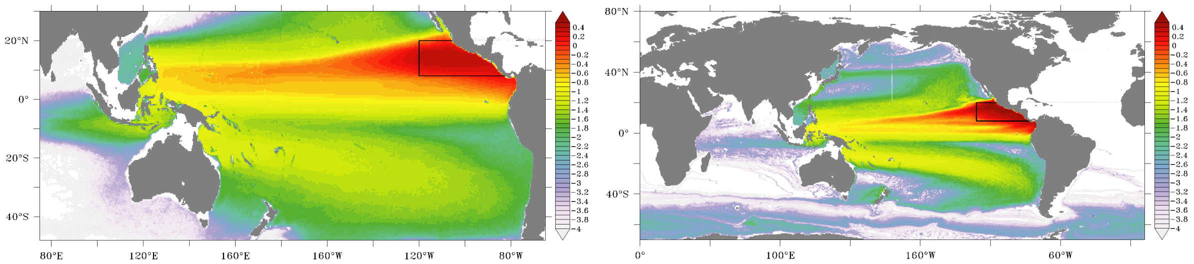

c) 200 m to 800 m TROPAC01

d) 200 m to 800 m ORCA05

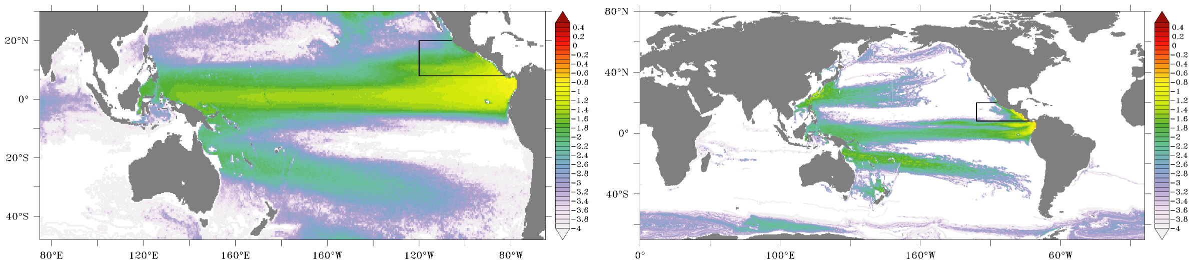

e) 800 m to bottom TROPAC01

f) 800 m to bottom ORCA05

Figure 6.25.: Depth integrated particle population [in % of released particles per 0.5° square on a logarithmic scale] temporally integrated over the full period of the Lagrangian experiments of 80 years for particles released in the Pacific nOMZ in TROPAC01 (left) and ORCA05 (right) for the depth ranges 0 m to 200 m (top), 200 m to 800 m (middle panel) and 800 m to the seafloor (bottom).

In the shallow layer, above 200 m depth, highest populations are found north and south of the equator for the nOMZ and sOMZ experiments respectively, restricted to the eastern half of the basin. A broad path in the upper layer from the southern part of the South Pacific via the eastern boundary of the basin towards the North feeds waters into both, the sOMZ and, although weaker, the nOMZ. The nOMZ is additionally supplied from the North. Below the OMZ layer a path from the centre of the southern basin towards the western boundary and further on east within a ~10° wide equatorial band is present for both experiments.

The populations resulting from the experiments in ORCA05 also show the highest values in the mid-depth range. In the shallow layer the populations basically show the same structure as in the nested experiments, with additional paths along the ACC and the Kuroshio extension with the

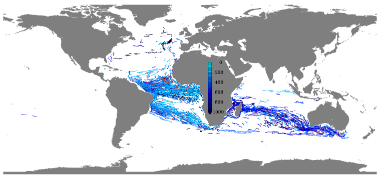

a) surface to 200 m TROPAC01 b) surface to 200 m ORCA05

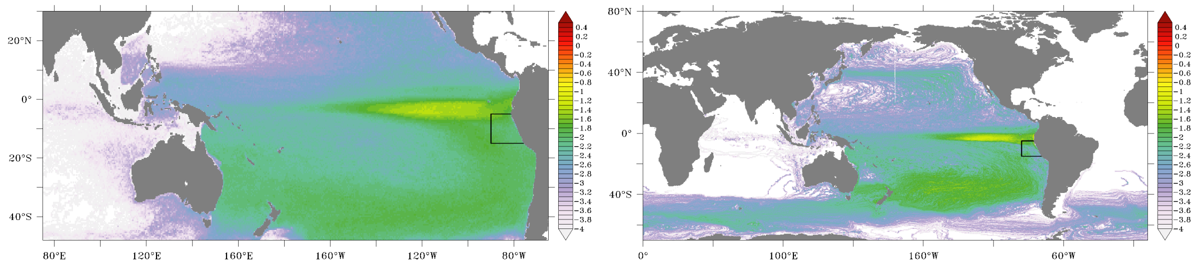

c) 200 m to 800 m TROPAC01 d) 200 m to 800 m ORCA05

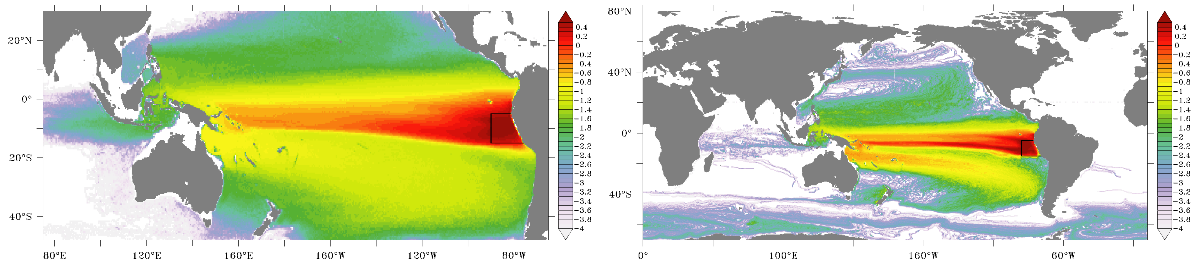

e) 800 m to bottom TROPAC01 f) 800 m to bottom ORCA05

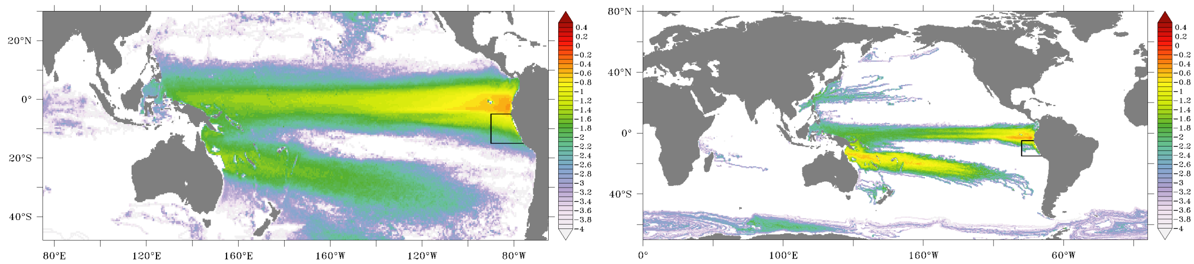

Figure 6.26.: Depth integrated particle population [in % of released particles per 0.5° square on a logarithmic scale] temporally integrated over the full period of the Lagrangian experiments of 80 years for particles released in the Pacific sOMZ in TROPAC01 (left) and ORCA05 (right) for the depth ranges 0 m to 200 m (top), 200 m to 800 m (middle panel) and 800 m to the seafloor (bottom).

latter being more emphasized for the nOMZ experiment. The most prominent paths in this layer, equatorward of the OMZs, are however shifted further away from the OMZs when compared to the experiments in TROPAC01. For the deep layer, only the equatorial band and the path from the North and the South Pacific via the western boundary of the basin is populated with the latter two only reaching back into the center of the basins during the 80 years of integration. The path from the North is more pronounced for the nOMZ experiment, whereas the path from the South is more pronounced for the sOMZ experiment. The populations within the Southern Ocean decrease with increasing depth.

The Lagrangian experiments exhibit the advective pathways and sources of waters ending up in the northern and southern OMZ in the eastern tropical Pacific within an 80 years time frame. The average ventilation timescale (table 6.3) for the sOMZ with 54 years for the nested and 58 years for

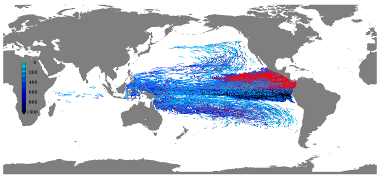

the coarser experiment is slightly longer when compared to the nOMZ with 51 years and 55 years respectively. Integrated in TROPAC01 within 80 years only 13% of the particles analyzed for the nOMZ and 16% for the sOMZ actually get ventilated, whereas for both OMZs the fraction of ventilated particles is 19% in the ORCA05 experiments. The source regions of OMZ waters are found to be largely independent from the model resolution. Furthermore, they are very similar for both OMZs (compare figures 6.10 to 6.13).

It could be shown, that the waters ending up in the nOMZ and the sOMZ share a large faction of their ventilation paths. The most prominent route was identified to lead from the South Pacific with the SEC [Schott et al. (2004)] towards the westernmost part of the tropical Pacific and via the NGCC [Goodman et al. (2005)] into the NSCC and SSCC [McPhaden (1984); Johnson et al. (2002)] as well as other eastward bands towards the nOMZ and sOMZ, respectively. The largest fraction of waters is transported across the Pacific basin within zonal off-equatorial bands in the depth range of the OMZs. These currents are more variable in TROPAC01 than in ORCA05. The sOMZ additionally is fed via a shortcut along a shallow path from the interior South Pacific via the eastern boundary. It is remarkable, that besides this shortcut, the main routes into the Pacific OMZs as governed by the experiments in TROPAC01 are basically analogous to those into the Atlantic OMZs in TRATL01.

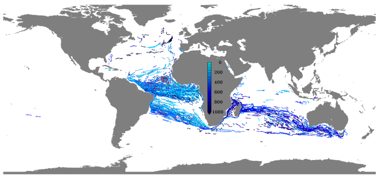

7. Summary and conclusions

The main subject of this study is the ventilation of the Oxygen Minimum Zones in the eastern tropical Atlantic and Pacific Oceans. To investigate the physical processes affecting these zones, high resolution ocean circulation models have been developed, evaluated and analyzed. Two methods to identify ventilation pathways have been applied: a Lagrangian approach and the implementation of passive tracers. This closing chapter will summarize the findings and draw conclusions from these model experiments.

Contents

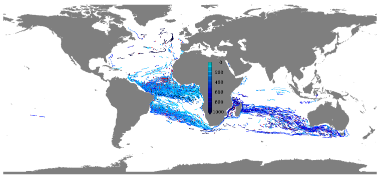

7.1. Methodological aspects

Within the NEMO [Madec (2008)] framework a global ORCA05 configuration at 0.5° horizontal resolution is used as a base for the development of model configurations with regionally high resolution (0.1°) and to complement those (section 2.1.5). The high resolution is achieved by embedding two-way AGRIF nests [Debreu et al. (2008)] in the tropical Atlantic (TRATL01) and Pacific (TROPAC01) Ocean, respectively. The nesting approach used here provides high flexibility in the determination of the high resolution regions. During this study, it has been established as a method to relatively fast develop a new configuration: a third configuration covering the North Pacific has been developed to analyze the fate of radioactively contaminated waters released off Fukushima [Behrens et al. (2012)]. Hindcast and climatologically forced [Large and Yeager (2009)] experiments in ORCA05, TRATL01 and TROPAC01 have been performed (section 2.1.5). Two passive tracers, AGE and CONC [comparable to those used by England (1995)] have been implemented in these experiments to trace waters entering the Oceans from the surface over a time of 140 years (section 2.1.7). The implementation of tracers also allows for dedicated experiments, as done here by the reproduction of the Guinea Upwelling Tracer Release Experiment (GUTRE, section 3.4) [Banyte et al. (2012)]. Lagrangian trajectories [Blanke and Grima (2008)] have been integrated using the model velocity fields to trace back waters that enter the OMZs within an 80 years framework (section2.3).

ORCA05 has been evaluated against observed sea level data and shows good capability to reproduce observed regional sea surface height variations, especially on interannual timescales (section 3.1). In a sensitivity study, ORCA05 simulations exhibit the influence of Pacific winds on Indian Ocean heat content variations [Schwarzkopf and Böning (2011), reproduced in section 3.2]. The comparison between ORCA05 and the nested experiments shows improvements in the simulation of the circulation when going to higher resolution (section 3.6). The nested configurations TRATL01 and TROPAC01 show high fidelity in simulating the strongly variable current fields in the tropical Atlantic and Pacific Oceans, respectively. TRATL01 and TROPAC01 were validated against observations at 23° W [e.g. Brandt et al. (2010)] in the Atlantic and 86° W in the Pacific Ocean [Czeschel et al. (2011)] and exhibit their strength in these regions (sections 3.3 and 3.5).

The evolution of two tracers, CONC and AGE, in ORCA05 initialized with zero everywhere, reveals the regions where surface waters enter the interior Ocean and then spread on a global scale (see section 2.1.7 and chapter 4 for details). Convection areas [Killworth (1983); Marshall and Schott (1999)] as well as shadow zones [Luyten et al. (1983)] and their formation are exhibited. CONC better represents the fast processes whereas AGE keeps spatial patterns, that in CONC vanish with time. The major structures of the oxygen distribution down to mid-depth, as provided by the World Ocean Atlas [Garcia et al. (2006)] are partly reproduced by AGE and CONC at different times during the integration period (section 4.2.3). In the nested simulations, the tracers show the effect of vigorous mesoscale features diffusing the tracers, especially at locations where in the coarser tracer distribution sharp gradients persist. The tracers in the nested simulations have been initialized with the AGE and CONC fields at the end of an 80 years long spin-up in ORCA05 (see section 4.3). Therefore, the nested simulations have only been used to analyze the tracer distribution at the end

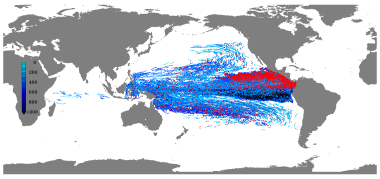

of the integration period, rather than their temporal evolution.

Lagrangian experiments (chapters 5 and 6) in which particles ending up in the Atlantic and Pacific northern and southern OMZs are traced backwards in time for 80 years and exhibit the pathways waters take to reach these zones and partly also show, where the particles leave the mixed layer. In some features, the paths show an agreement, when comparing experiments in the nested configurations to those in the global model. The latter also allows to analyze the paths beyond the boundaries of the nested areas, however, the tropical circulation in the coarser global model is not represented as good as in the high resolution models.

7.2. Representation of circulation features in the models

In the Atlantic Ocean at 23° W where, due to the presence of several moorings and repeated ship sections [Brandt et al. (2006, 2010)], the coverage of observational data is good compared to other regions in the tropical Atlantic, modelled velocity structures and variability have been compared to the observed fields (section 3.3). The strongest temporally averaged circulation features match the observed [Brandt et al. (2010)] structures very well, especially when not only a mean field but also the effect of the spatial and temporal availability of the observations is taken into account. The application and variation of spatio-temporal sub-sampling of the modelled velocity fields exhibit a strong effect of the variability on different time-scales onto the modelled mean fields (figure 3.16). This emphasizes the importance of continuous velocity measurements for the observational estimation of mean current fields and points to the need of more continuous observations to actually capture the variability in the equatorial current system in the real Ocean (section 3.3.1).

The variability in zonal currents, as measured by moorings [Brandt et al. (2014)], at and close to the equator is well reproduced in TRATL01 with most skill directly on the equator (section 3.3.2). The off-equatorial NICC in the model is weaker, non-continuous and spatially shifted when compared to the observations. The complete spatio-temporal coverage of the model leads to its capability to give insights in variability beyond directly observed fields and underlines the importance of this variability for the interpretation of observed time series from mooring sites.

The release of a passive dye in TRATL01, similar to the procedure that was followed in reality during GUTRE (section 3.4) [Banyte et al. (2012)] reproduces the two main findings, that were possible to assess with TRATL01: in the eastern tropical north Atlantic, zonal mixing is approximately twice as strong as meridional mixing and a tendency to upward mixing is visible, although masked by the limited vertical resolution of the model.

Comparing an observed velocity section at ∼86° W, east of the Galapagos islands, in the tropical Pacific Ocean in 2009 [Czeschel et al. (2011)] to modelled zonal velocities at the same time within the

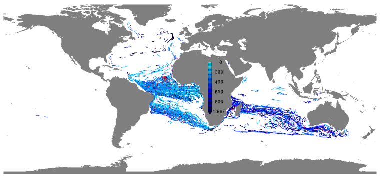

forcing period exhibits the capability of TROPAC01 to reproduce the observed field (section 3.5). This was partly disgraded in Czeschel et al. (2011), where observations were compared to modelled velocity fields at a different time. The good agreement between the observed and modelled velocity section in 2009 and the good agreement of the velocity section from an assimilation model (SODA) and TROPAC01 in 2002 points to a major dependency on the temporally varying forcing. The difference between the two modelled sections already exhibits strong interannual variability, especially in the equatorial region east of the Galapagos islands. Time series of zonal velocity sections west and east of these islands at different depths emphasize their influence on the circulation [Eden and Timmermann (2004)] on all time scales east of them, while west of Galapagos the seasonal cycle is the dominating period of variability. For the section in 2009 the modelled velocity time series shows, that the observed current structure might have only been lasting for one month (see figures 3.27 and 3.29).

The imprint of the circulation onto the SSH pattern also exhibits the capability of TROPAC01 to simulate large scale patterns as well as smaller meso-scale features like eddies, that are important for local biogeochemical processes [Stramma et al. (2013)], in the observed spatial dimension and strength (figure 3.30). Due to their stochastic nature these eddies are not necessarily located at the exact instantaneous positions where they are observed. For the eastern tropical south Pacific, it has been shown, that eddies and their propagation dominate and mask the mean currents (section 3.5.3). Hence, it cannot be expected to identify features of the mean circulation in instantaneous observations.

Both nested models, TRATL01 and TROPAC01 have been shown to help to embed temporally and spatially rare observations into variable circulation fields and better reproduce observed circulation features when compared to the coarser ORCA05 simulation (section 3.6). The EUC is simulated more realistically in its eastward penetration, vertical location and strength in the Atlantic Ocean. Observed depth-alternating jets [e.g. Eden and Dengler (2008)] that are absent in ORCA05 can be reproduced in TRATL01. The narrow off-equatorial zonal current bands in TRATL01 as well as TROPAC01 are not resolved in ORCA05 but simulated as weak, wide currents. The eddy dominated meridional currents in TROPAC01 show the same behaviour. Directly forcing dependent features have been shown to already be captured in the coarser model configuration.

7.3. Ventilation of the OMZs

The ventilation areas, where surface waters enter the interior ocean in the ORCA05 model simulation have been identified to be located in the Southern Ocean and the Nordic Seas (chapter 4). Here convection into the deep Ocean takes place [Marshall and Schott (1999)]. The mid-depth Ocean is additionally ventilated from the subtropical gyre regions. The shadow zones in the tropical Oceans [Luyten et al. (1983)], where the OMZs are located [e.g. Karstensen et al. (2008)] appear as rather wide areas of poorly ventilated waters in the eastern part of the Atlantic and Pacific Oceans as well as the northern part of the Indian Ocean.

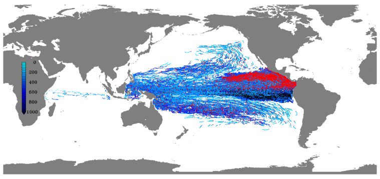

In ORCA05 as well as in TRATL01, the tracer integrations exhibit the least ventilated regions in the tropical Atlantic Ocean to be located off coast, and thereby differently from where the observed Oxygen Minimum Zones are located in the real Ocean and the sOMZ and nOMZ in the models are defined. However, observed and defined OMZs are included in the poorly ventilated areas, simulated by the two passive tracers. In the Pacific Ocean, the OMZs (observed as well as defined for this study) are co-located with the least ventilated areas as given by the tracer integrations in ORCA05 and TROPAC01.

Only a fraction of 4% of the waters, entering the nOMZ in the Atlantic Ocean within an 80 years time frame were ventilated in an averaged time of 45 years within the nested area of TRATL01, twice as much as for the sOMZ in a comparable averaged time (chapter 5). The OMZ in the southern part of the eastern tropical Atlantic is observed to be stronger (lower oxygen concentrations) when compared to the northern OMZ [Karstensen et al. (2008)]. This can, at least partly, be ascribed to the weaker ventilation that is also shown here. The areas where these waters get ventilated are located in the northern and southern tropical Atlantic with a larger contribution from the South. Taking into account ventilation outside the nested area but only applying the coarse velocity fields as given by the ORCA05 simulation increases these fractions to 25% for the nOMZ and 15% for the sOMZ. Additional ventilation areas south of Australia, in the Indian Ocean and in the North Atlantic are exhibited in the ORCA05 simulation.

A large majority of waters take a path from their ventilation sites into the Atlantic OMZs via the western boundary of the basin. This is also true for waters, that need longer than 80 years to make their way from their ventilation area into the OMZs. It has been shown that only a very small fraction is transported in the upper 200 m of the water column (section 5.3). Most waters make their way in a mid-depth range between 200 m and 800 m depth and in the nested configurations, their pathways are dominated by diffusive characteristics. Below this layer, defined paths occur along which substantial fractions of waters flow before they enter the OMZs. The most prominent parts of these deep paths are the SEC [Schott et al. (2004)] feeding the NBC [Johns et al. (1998)] from the South and the deep western boundary current from the North [e.g. Bower et al. (2009)], that is contributing to both, the nOMZ and sOMZ waters. The last part of the paths into the OMZs is taken at mid depth with the northern off-equatorial currents into the nOMZ, that has also been found by Peña-Izquierdo et al. (2015), and the southern off-equatorial currents into the sOMZ.

In the tropical Pacific Ocean, within an 80 years time frame, the averaged time for waters to enter the nOMZ is 51 years and only a few years longer, 54 years, for the sOMZ (chapter 6). The fraction of waters, ventilated within the nested area of TROPAC01 during this time is 13% for the nOMZ and 18% for the sOMZ. These numbers both increase to 19% when including the remainder of the global Ocean in the ORCA05 simulation and averaged ventilation times increase by 4 years each. It is clear, that these numbers are biased low because of the experimental design: the average time to ventilate the OMZs in the real ocean is longer. The waters in the nOMZ and sOMZ get venti-

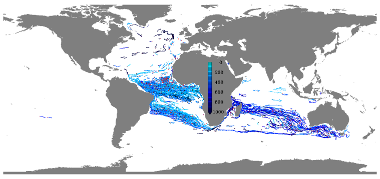

lated in very similar areas and their origin, within the nested area, is independent from the model configuration (ORCA05 or TROPAC01). These source regions are in the western south Pacific, in two areas in the eastern south Pacific, and additionally north of the nested area of TROPAC01, along the Kuroshio extension [Qiu (2002)], appearing in the ORCA05 simulation. A remarkably fast ventilation from the eastern tropical Pacific into the nOMZ has been shown in TROPAC01, that however, only contributed to an almost negligible fraction of nOMZ waters.

In the Pacific Ocean, waters find their ways into the nOMZ via the western boundary of the basin and then by following the northern off-equatorial currents. The majority of waters travel at mid-depth, whereas below, the paths are very similar but weaker. Waters ending up in the sOMZ describe similar paths except for the waters crossing the basin with the off-equatorial currents in the south. An additional path in the shallow layer that directly connects the eastern tropical Pacific with the sOMZ occurs with a stronger imprint in the simulation in TROPAC01 when compared to ORCA05.

7.4. Connection of tracers and trajectories

In chapter 4 two passive tracers and their temporal evolution have been used to show how surface waters enter the Ocean and spread on time scales covered by the integration period of the models. The distribution of the the two tracers, and especially of AGE, at the end of the integration period highlights the first part of the ventilation pathways and reveals the location of poorly ventilated regions. The Lagrangian experiments in chapters 5 and 6 are designed to exhibit the other end of the paths into these regions where the OMZs are located. The results from the two methods can be understood as the two ends of one path and can, to some degree, be connected here.

A small fraction of the particles that end up in the OMZs after an 80 years long integration was located within the mixed layer during that time (see tables 5.3 and 6.3). For these particles, the Lagrangian approach covers the full ventilation paths. These particles, however, only represent a minority; most particles ending up in the OMZs have not been in contact with the mixed layer for at least 80 years. A weaker, but still valid, measure for probable ventilation pathways is the occurrence of particles in areas of high CONC or low AGE values, indicating better ventilated regions.

For both OMZs in the Atlantic Ocean a deep path from the North Atlantic is simulated in the Lagrangian experiments (see figures 5.25f and 5.26f). This path begins close to an area in the northeastern North Atlantic where convection takes place (see figures 4.4 and 4.8). In these convective regions, tracer gets subducted and then transported south in deeper layers (figure 4.6). Thus, this deep path might largely contribute to the ventilation of the Atlantic OMZs. The deep path from the South is also connected to well ventilated regions in the Indian Ocean via the Agulhas current. On shorter timescales, the Indian Ocean gets ventilated by waters, that are entrained in the Ocean along the southern coast of Australia (see figures 4.4 and 4.5), closing that way between the

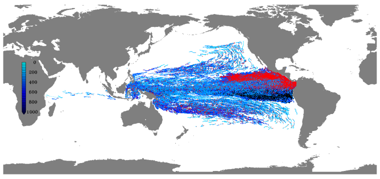

surface and the Atlantic OMZs. A third area, where this connection can be made is the Weddell Sea, where deep convection takes place and particles make their way via the ACC into the Atlantic OMZs.

The analyses shown here do not allow for a quantification of the contribution of these paths to the ventilation of the OMZs. There are trajectories in an 80 years framework which are found to start in an area where in a separate 140 years tracer integration a region with well ventilated waters evolves. The strength of the ventilation cannot be directly quantified based on these two measures but the co-occurrence suggests that particles taking these paths might contribute to the ventilation of the OMZs.

A direct connection between the convection area in the Weddell Sea and the OMZs in the Pacific Ocean cannot be found within the integration periods for the tracers and the particles used here. At mid-depth, the points where the 80 year long paths from the North and the South Pacific begin are located in areas at the outer boundaries of the well ventilated areas, the subtropical gyres. Here, only very few particles cross areas where tracer values are high. The only region, where the starting points of the particle trajectories are located in high CONC and low AGE areas is the shallow subtropical South Pacific, from where a direct path via the eastern boundary of the Pacific Ocean into the OMZs exists. An end-to-end connection exists for some parts of the OMZ waters, but mostly, the paths of well ventilated waters identified by the tracers and the paths into the Pacific OMZs as given by the particle trajectories are not connected within the two integration periods that, in sum, last for 220 years. This leads to the conclusion, that a substantial fraction of the water ventilating the OMZs is older than these 220 years.

7.5. Comparison between Atlantic and Pacific

The OMZs in the Atlantic and Pacific Oceans differ fundamentally with respect to the absolute values of oxygen concentrations [Karstensen et al. (2008)]. Where in the Pacific Ocean even anoxic areas persist, the Atlantic OMZs are still marked by oxygen concentrations of up to 1 ml/l (see figure 4.12a). This behaviour is partly mirrored in the CONC fields. The Atlantic nOMZ is marked by high CONC values of up to 0.8, whereas in the Pacific nOMZ, the lowest values are less than 0.5 after 140 years of integration. The sOMZs, however, show even lower CONC values in the Atlantic than in the Pacific Ocean. This characteristic is also reflected by the AGE fields, although less pronounced.

In the Pacific, tracer enters the eastern part of the basin in a broad band along the equator, whereas in the Atlantic the transport from the west only takes place in a narrower band north of the equator. Elevated CONC values along the coasts in the northern tropical Atlantic and the northern as well as southern tropical Pacific can additionally be attributed to direct ventilation from above, that is supported by the negative (downward) temporally averaged velocities occurring at the upper boundary of the OMZs (see figures 5.4 as well as 6.4 and 6.5). The elevated CONC values and lower

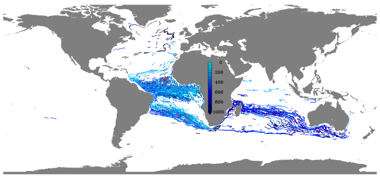

AGE values in the Atlantic sOMZ, when compared to the Pacific sOMZ, could be attributed to the lack of that direct path from above.

For the tracer fields within the nOMZs, the main difference is the presence of a convection area in the North Atlantic, that is missing in the Pacific Ocean. Due to this additional source, CONC at mid-depth in the northern Atlantic Ocean increases faster during the integration time than in the North Pacific. The lower CONC and higher AGE values in the Atlantic sOMZ compared to the Pacific sOMZ can be attributed to shallower mixed layer depths in the Atlantic [de Boyer Montégut et al. (2004)], suppressing deeper tracer entrainment from above and inhibiting CONC from increasing and AGE from decreasing through mixing.

Along the southern and northern limits of the poorly ventilated areas in the Pacific Ocean and to a weaker extent in the Atlantic, plumes of higher CONC values enter the low CONC areas. This spatial pattern of the tracer plumes is weaker but still identifiable even in an annual mean (compare figure 4.13b to 4.17b), indicating that these filaments evolve on time scales longer than a year. The spatial distribution of oxygen at the boundaries of the poorly ventilated regions could be characterized by similar structures. These are however not represented in the climatologies of observed oxygen, most probable due to the low spatial resolution of the measurements and due to the long temporal averages that the climatological fields correspond to [Garcia et al. (2006)].

From the passive tracers, the purely physical ventilation of the sOMZs seems to be stronger in the Pacific than in the Atlantic Ocean. The difference in the spatial patterns of CONC in TRATL01 and TROPAC01 and the observed oxygen concentrations, especially the higher CONC values in the Pacific sOMZ when compared to the Atlantic sOMZ could either be a hint for an imbalance between vertical and horizontal mixing processes or for a major role of biological processes consuming oxygen along the larger horizontal scales in the Pacific.

7.6. Final remarks

The simulations with the high-resolution model configurations developed within this study show a remarkable skill in reproducing observed equatorial circulation features. This lends confidence to model estimates of variability that goes beyond the spatial and temporal coverage of the observational data. These models are useful tools to support observational data and to embed them into a broader context.

The flexibility of the nesting technique including the possible implementation of passive tracers allow for dedicated regionally highly resolved simulations, without losing the global context.

From the experiences with this study, the ideal way to assess the physical ventilation processes of

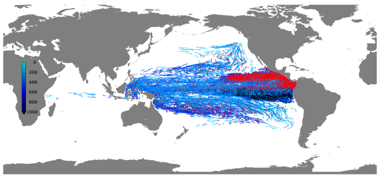

poorly ventilated regions like the OMZs, would be an integration of tracers like AGE in a global high resolution model for much longer time scales than the 220 years that have been indirectly covered here. These, complemented by hundreds of years long Lagrangian experiments would be able to exhibit the full ventilation paths into such zones.

The ventilation of the Atlantic and Pacific OMZs has been found to be mainly governed by pathways via the western boundaries of the basins and highly affected by the off-equatorial currents. In this study, it has been revealed, that distinct paths in layers deeper than the upper 1000 m of the water column are likely to have a large impact on the ventilation. The differences between the coarse and the high resolution experiments confirm observational studies indicating, that mesoscale features play a role in the ventilation of the OMZs via shortcuts across strong gradients, that persist without the mesoscale.

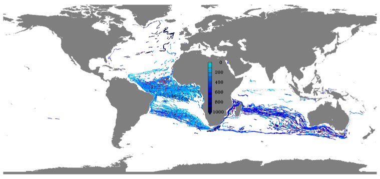

Bibliography

Alory, G. and G. Meyers, 2009: Warming of the upper equatorial Indian Ocean and change in the heat budget (1960-99). *Journal of Climate*, **22**, 93–113.

Alory, G., S. Wijffels, and G. Meyers, 2007: Observed temperature trends in the Indian Ocean over 1960-1999 and associated mechanisms. *Geophysical Research Letters*, **34 (L02606)**.

Arakawa, A. and V. Lamb, 1977: Computational design of the basic dynamical processes of the UCLA general circulation model. *Methods in Computational Physics*, **17**, 174–267.

Arévalo-Martínez, D., A. Kock, C. Löscher, R. Schmitz, and H. W. Bange, 2015: Massive nitrous oxide emissions from the tropical South Pacific Ocean. *Nature Geosciences*, **8**, 530–535.

Ascani, F., 2008: Wave-induced deep equatorial ocean circulation. *A dissertation submitted to the graduate division of the University of Hawaii*, 158.

Banyte, D., T. Tanhua, M. Visbeck, D. E. R. Wallace, J. Karstensen, G. Krahmann, A. Schneider, and L. Stramma, 2012: Diapycnal diffusivity at the upper boundary of the tropical North Atlantic oxygen minimum zone. *Journal of Geophysical Research*, **117 (C09016)**.

Barkley, R. A., 1970: The Kuroshio Current. *Sience Journal*, 54–60.

Barnier, B., L. Brodeau, J. L. Sommer, J.-M. Molines, T. Penduff, S. Theetten, A.-M. Treguier, G. Madec, A. Biastoch, C. W. Böning, J. Dengg, S. Gulev, R. Bourdallé-Badie, J. Chanut, G. Garric, S. Alderson, A. Coward, B. de Cuevas, A. New, K. Haines, G. Smith, S. Drijfhout, W. Hazeleger, C. Severijns, and P. Myers, 2007: Eddy-permitting ocean circulation hindcasts of past decades. *CLIVAR Exchanges*, **12 (3)**, 8–10.

Behera, S. and T. Yamagata, 2010: Imprint of the El Niño Modoki on decadal sea level changes. *Geophysical Research Letters*, **37 (L23702)**.

Behrens, E., A. Biastoch, and C. W. Böning, 2013: Spurious AMOC trends in global ocean sea-ice models related to subarctic freshwater forcing. *Ocean Modelling*, **69 (0)**, 39 – 49.

Behrens, E., F. U. Schwarzkopf, J. F. Lübbecke, and C. W. Böning, 2012: Model simulations on the long-term dispersal of ^{137}Cs released into the Pacific Ocean off Fukushima. *Environmental Research Letters*, **7 (034004)**.

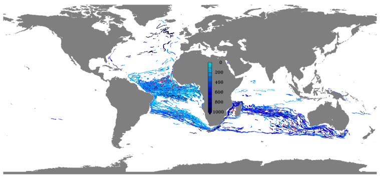

Biastoch, A., 2008: The Agulhas Leakage: Role of Mesoscale Processes and Impact on the Atlantic Meridional Overturning Circulation. *(Professorial dissertation), Christian-Albrechts-Universität, Kiel*, 66.

Biastoch, A., C. W. Böning, and J. R. E. Lutjeharms, 2008: Agulhas leakage dynamics affects decadal variability in Atlantic overturning circulation. *Nature*, **456**, 489–492.

Blanke, B. and N. Grima, 2008: Tutorial : first steps with ARIANE, sequential version (version 2.x.x). URL `stockage.univ-brest.fr/∼grima/Ariane/ariane_tutorial_2.x.x_sep08.pdf`.

Blanke, B. and S. Raynaud, 1997: Kinematics of the Pacific Equatorial Undercurrent: An Eulerian and Lagrangian Approach from GCM Results. *Journal of Physical Oceanography*, **27**, 1038–1053.

Blanke, B., S. Speich, G. Madec, and R. Maugé, 2002: A global diagnostic of interior ocean ventilation. *Geophysical Research Letters*, **29 (8)**.

Blayo, E. and L. Debreu, 2006: Nesting ocean models. *An Integrated View of Oceanography: Ocean Weather Forecasting in the 21st Century*, Chassignet, E. and J. Verron, Eds., Kluwer.

Bopp, L., C. Le Quéré, M. Heinmann, and A. C. Manning, 2002: Climate-induced oceanic oxygen fluxes: Implications for the contemporary carbon budget. *Global Biogeochemical Cycles*, **16 (2)**.

Bougeault, P. and P. Lacarrere, 1989: Parameterization of orography-induced turbulence in a mesobetascale model. *Monthly Weather Review*, **117 (8)**, 1872–1890.

Bower, A. S., M. S. Lozier, S. F. Gary, and C. W. Böning, 2009: Interior pathways of the North Atlantic meridional overturning circulation. *Nature*, **459**, 243–247.

Brandt, P., H. W. Bange, D. Banyte, M. Dengler, S.-H. Didwischus, T. Fischer, R. J. Greatbatch, J. Hahn, T. Kanzow, J. Karstensen, A. Körtzinger, G. Krahmann, S. Schmidtko, L. Stramma, T. Tanhua, and M. Visbeck, 2015: On the role of circulation and mixing in the ventilation of the oxygen minimum zones with a focus on the eastern tropical North Atlantic. *Biogeosciences*, **12**, 489–512.

Brandt, P., A. Funk, V. Hormann, M. Dengler, R. J. Greatbatch, and J. M. Toole, 2011: Interannual atmospheric variability forced by the deep equatorial Atlantic Ocean. *Nature*, **473**, 497–500.

Brandt, P., A. Funk, A. Tantet, W. E. Johns, and J. Fischer, 2014: The Equatorial Undercurrent in the central Atlantic and its relation to tropical Atlantic variability. *Climate Dynamics*, **43 (11)**, 2985–2997.

Brandt, P., R. J. Greatbatch, M. Claus, S.-H. Didwischus, V. Hormann, A. Funk, J. Hahn, G. Krahmann, J. Fischer, and A. Körtzinger, 2012: Ventilation of the equatorial Atlantic by the equatorial deep jets. *Journal of Geophysical Research*, **117 (C12015)**.

Brandt, P., V. Hormann, B. Bourlès, J. Fischer, F. A. Schott, L. Stramma, and M. Dengler, 2008: Oxygen tongues and zonal currents in the equatorial Atlantic. *Journal of Geophysical Research*, **113 (C04012)**.

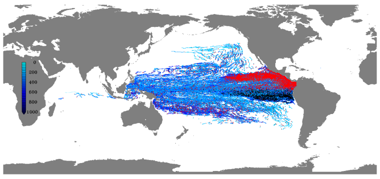

Brandt, P., V. Hormann, A. Körtzinger, M. Visbeck, G. Krahmann, L. Stramma, R. Lumpkin, and C. Schmid, 2010: Changes in the Ventilation of the Oxygen Minimum Zone of the Tropical North Atlantic. *Journal of Physical Oceanography*, **40 (8)**, 1784–1801.

Brandt, P., F. A. Schott, C. Provost, A. Kartavtseff, V. Hormann, B. Bourlès, and J. Fischer, 2006: Circulation in the central equatorial Atlantic: Mean and intraseasonal to seasonal variability. *Geophysical Research Letters*, **33 (L07609)**.

Brewer, P. G. and E. T. Peltzer, 2009: Limits to Marine Life. *Science*, **324**, 347–348.

Bryan, F. O., G. Danabasoglu, O. R. Gent, and K. Lindsay, 2006: Changes in ocean ventilation during the 21st Century in the CCSM3. *Ocean Modelling*, **15**, 141–156.

Cai, W., G. Meyers, and G. Shi, 2005: Transmission of ENSO signal to the Indian Ocean. *Geophysical Research Letters*, **32 (L05616)**.

Cai, W., A. Sullivan, and T. Cowan, 2008: Shoaling of the off-equatorial south Indian Ocean thermocline: Is it driven by anthropogenic forcing? *Geophysical Research Letters*, **35 (L12711)**.

Capone, D. G. and D. A. Hutchins, 2013: Microbial biogeochemistry of coastal upwelling regimes in a changing ocean. *Nature Geosciences*, **6**, 711–717.

Carr, M.-E. and H. T. Rossby, 2001: Pathways of the North Atlantic Current from surface drifters and subsurface floats. *Journal of Geophysical Research*, **106 (C3)**, 4405–4419.

Carton, J. A. and B. S. Giese, 2008: A Reanalysis of Ocean Climate Using Simple Ocean Data Assimilation (SODA). *Monthly Weather Review*, **136**, 2999–3017.

Cazenave, A. and R. S. Nerem, 2004: Present-day sea level change: observations and causes. *Reviews of Geophysics*, **42 (RG3001)**.

Chaigneau, A., N. Dominguez, G. Eldin, L. Vasquez, R. Flores, C. Grados, and V. Echevin, 2013: Near-coastal circulation in the Northern Humboldt Current System from shipboard ADCP data. *Journal of Geophysical Research*, **118 (10)**, 5251–5266.

Chanut, J., B. Barnier, W. Large, L. Debreu, T. Penduff, J. M. Molines, and P. Mathiot, 2008: Mesoscale Eddies in the Labrador Sea and their Contribution to Convection and Restratification. *Journal of Physical Oceanography*, **38**, 1617–1643.

Collins, M., S.-I. An, W. Cai, A. Ganachaud, E. Guilyardi, F.-F. Jin, M. Jochum, M. Lengaigne, S. Power, A. Timmermann, G. Vecchi, and A. Wittenberg, 2010: The impact of global warming on the tropical Pacific Ocean and El Niño. *Nature Geosciences*, **3**, 391–397.

Cox, P. M., R. A. Betts, C. D. Jones, S. A. Spall, and I. J. Totterdell, 2000: Acceleration of global warming due to carbon-cycle feedbacks in a coupled climate model. *Nature*, **408**, 184–187.

Craig, H., 1971: The Deep Metabolism: Oxygen Consumption in Abyssal Ocean Water. *Journal of Geophysical Research*, **76 (21)**, 5078–5086.

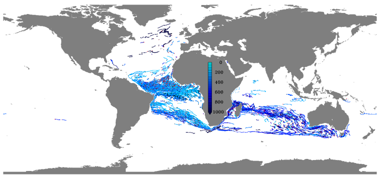

Cravatte, S., W. S. Kessler, and F. Marin, 2012: Intermediate Zonal Jets in the Tropical Pacific Ocean Observed by Argo Floats. *Journal of Physical Oceanography*, **42**, 1475–1485.

Czeschel, R., L. Stramma, F. U. Schwarzkopf, B. S. Giese, A. Funk, and J. Karstensen, 2011: Middepth circulation of the eastern tropical South Pacific and its link to the oxygen minimum zone. *Journal of Geophysical Research*, **116 (C01015)**.

da Silveira, I., L. de Miranda, and W. Brown, 1994: On the origins of the North Brazil Current. *Journal of Geophysical Research*, **99 (C11)**.

de Boyer Montégut, C., G. Madec, A. S. Fischer, A. Lazar, and D. Iudicone, 2004: Mixed layer depth over the global ocean: An examination of profile data and a profile-based climatology. *Journal of Geophysical Research*, **109 (C12003)**.

de Brauwere, A., S. H. M. Jacquet, F. De Ridder, F. Dehairs, R. Pintelon, J. Schoukens, and W. Baeyens, 2007: Water mass distributions in the Southern Ocean derived from a parametric analysis of mixing water masses. *Journal of Geophysical Research*, **112 (C02021)**.

Debreu, L., 2006: AGRIF Adaptive grid refinement in Fortran, User's Guide Version 1.3 (27 November 2006). http://www-ljk.imag.fr/MOISE/AGRIF/documentation.html.

Debreu, L., C. Vouland, and E. Blayo, 2008: AGRIF: Adaptive grid refinement in Fortran. *Computer & Geosciences*, **34**, 8–13.

Delcroix, T. and C. Henin, 1988: Observations of the Equatorial Intermediate Current in the Western Pacific Ocean (165° E). *Journal of Physical Oceanography*, **18 (2)**, 363–366.

Denman, K. L., G. Brasseur, A. Chidthaisong, P. Ciais, P. Cox, R. Dickinson, D. Hauglustaine, C. Heinze, E. Holland, D. Jacob, U. Lohmann, S. Ramachandran, P. da Silva Dias, S. Wofsy, and X. Zhang, 2007: Couplings Between Changes in the Climate System and Biogeochemistry. *Climate Change 2007: The Physical Science Basis. Contribution of Working Group I to the Fourth Assessment Report of the Intergovernmental Panel on Climate Change*, Solomon, S., D. Qin, M. Manning, Z. Chen, M. Marquis, K. Averyt, M.Tignor, and H. Miller, Eds., Cambridge University Press, Cambridge, United Kingdom and New York, NY, USA, chap. 7.3.

Deutsch, C., H. Brix, T. Ito, H. Frenzel, and L. Thompson, 2011: Climate-Forced Variability of Ocean Hypoxia. *Science*, **333**, 336–339.

Djath, B., J. Verron, A. Melet, L. Gourdeau, B. Barnier, and J. M. Molines, 2014: Multiscale dynamical analysis of a high-resolution numerical model simulation of the Solomon Sea circulation. *Journal of Geophysical Research*, **119**, 6286–6304.

Domingues, C. M., J. A. Church, N. J. White, P. J. Gleckler, S. E. Wijffels, P. M. Barker, and J. R. Dunn, 2008: Improved estimates of upper-ocean warming and multi-decadal sea-level rise. *Nature*, **453**, 1090–1093.

Doney, S. C., S. Yeager, G. Danabasoglu, W. G. Large, and J. C. McWilliams, 2007: Mechanisms governing interannual variability of upper-ocean temperature in a global ocean hindcast simulation. *Journal of Physical Oceanography*, **37**, 1918–1938.

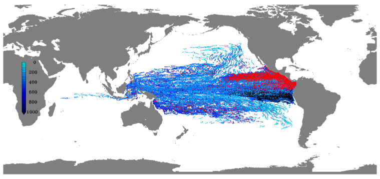

Duteil, O., F. U. Schwarzkopf, C. W. Böning, and A. Oschlies, 2014: Major role of the equatorial current system in setting oxygen levels in the eastern tropical Atlantic Ocean: A high-resolution model study. *Geophysical Research Letters*, **41**, 2033–2040.

Eden, C. and M. Dengler, 2008: Stacked jets in the deep equatorial Atlantic Ocean. *Journal of Geophysical Research*, **113 (C04003)**.

Eden, C. and A. Timmermann, 2004: The influence of the Galapagos Islands on tropical temperatures, currents and the generation of tropical instability waves. *Geophysical Research Letters*, **31 (L15308)**.

Elkins, J. W., S. C. Wofsy, M. B. McElroy, C. E. Kolb, and W. A. Kaplan, 1978: Aquatic sources and sinks for nitrous oxide. *Nature*, **257**, 602–606.

England, M. H., 1995: The Age of Water and Ventilation Timescales in a Global Ocean Model. *Journal of Physical Oceanography*, **25**.

England, M. H., C. C. Ummenhofer, and A. Santoso, 2006: Interannual rainfall extremes over southwest western Australia linked to Indian Ocean climate variability. *Journal of Climate*, **19**, 1948–1969.

Fahrbach, E., G. Rohardt, N. Scheele, M. M. Schröder, V. Strass, and A. Wisotzki, 1995: Formation and discharge of deep and bottom water in the northwestern Weddell Sea. *Journal of Marine Research*, **53 (4)**, 515–538.

Feng, M., C. W. Böning, A. Biastoch, E. Behrens, E. Weller, and Y. Masumoto, 2011: The reversal of the multi-decadal trends of the equatorial Pacific easterly winds, and the Indonesian Throughflow and Leeuwin Current transports. *Geophysical Research Letters*, **38 (L11604)**.

Feng, M., Y. Li, and G. Meyers, 2004: Multidecadal variations of Fremantle sea level: Footprint of climate variability in the tropical Pacific. *Geophysical Research Letters*, **31 (L16302)**.

Fichefet, T. and M. M. Maqueda, 1997: Sensitivity of a global sea ice model to the treatment of ice thermodynamics and dynamics. *Journal of Geophysical Research*, **102 (C6)**, 12 609–12 646.

Fiedler, P. and L. Talley, 2006: Hydrography of the eastern tropical Pacific: a review. *Progress in Oceanography*, **69**, 134–180.

Fischer, J., J. Karstensen, R. Zantopp, M. Visbeck, A. Biastoch, E. Behrens, C. W. Böning, D. Quadfasel, K. Jochumsen, H. Valdimarsson, S. Jónsson, S. Bacon, N. O. Holliday, S. Dye, M. Rhein, and C. Mertens, 2015: Intra-seasonal variability of the DWBC in the western subpolar North Atlantic. *Progress in Oceanography*, **132**, 233–249.

Fischer, T., D. Banyte, P. Brandt, M. Dengler, G. Krahmann, T. Tanhua, and M. Visbeck, 2013: Diapycnal oxygen supply to the tropical North Atlantic oxygen minimum zone. *Biogeosciences*, **10**, 5079–5093.

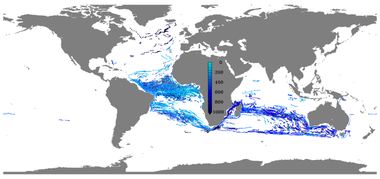

Garcia, H. E., R. A. Locarnini, T. P. Boyer, and J. I. Antonov, 2006: World Ocean Atlas 2005, Volume 3: Dissolved Oxygen, Apparent Oxygen Utilization, and Oxygen Saturation. *NOAA Atlas NESDIS 63, U.S. Government Printing Office, Washington, D.C.*

Garraffo, Z. D., W. E. Johns, W. P. Chassignet, and G. J. Goni, 2003: North Brazil Current rings and transport of southern waters in a high resolution numerical simulation of the North Atlantic. *Interhemispheric Water Exchange in the Atlantic Ocean*, Goni, G. J. and P. Malanotte-Rizzoli, Eds., Elsevier B. V.

Gary, S. F., M. S. Lozier, C. W. Böning, and A. Biastoch, 2011: Deciphering the pathways for the deep limb of the Meridional Overturning Circulation. *Deep Sea Research II*, **58**, 1781–1797.

Gent, P. R. and J. McWilliams, 1990: Isopycnal Mixing in Ocean Circulation Models. *Journal of Physical Oceanography*, **20 (1)**, 150–155.

Gill, A. E. and P. P. Niiler, 1973: The theory of the seasonal variability in the ocean. *Deep Sea Research*, **20 (2)**, 141–177.

Gleßmer, M. S., W. Park, and A. Oschlies, 2011: Simulated reduction in upwelling of tropical oxygen minimum waters in a warmer climate. *Environmental Research Letters*, **6 (045001)**.

Gnanadesikan, A., D. Bianchi, and M.-A. Pradal, 2013: Critical role for mesoscale eddy diffusion on supplying oxygen to hypoxic ocean waters. *Geophysical Research Letters*, **40**, 5194–5198.

Gnanadesikan, A., J. L. Russell, and F. Zeng, 2007: How does ocean ventilation change under global warming? *Ocean Science*, **3 (1)**, 43–53.

Goodman, P. J., W. Hazeleger, P. de Vries, and M. Cane, 2005: Pathways into the Pacific Equatorial Undercurrent: A Trajectory Analysis. *Journal of Physical Oceanography*, **35 (11)**, 2134–2151.

Gordon, A. L., 2001: Bottom water formation. *Encyclopedia of Ocean Sciences*, Steele, J. H., K. K. Turekiana, and S. A. Thorpe, Eds., Academic Press, 334340.

Griffies, S. M., A. Biastoch, C. W. Böning, F. Bryan, G. Danabasoglu, E. P. Chassignet, M. H. England, R. Gerdes, H. Haak, R. W. Hallberg, W. Hazeleger, J. Jungclaus, W. G. Large, G. Madec, A. Pirani, B. L. Samuels, M. Scheinert, A. Sen Guptay, C. A. Severijns, H. L. Simmons, A.-M. Treguier, M. Winton, S. Yeager, and J. Yin, 2009: Coordinated Ocean-Ice Reference Experiments (COREs). *Ocean Modelling*, **26**, 1–46.

Grodsky, S. A. and J. A. Carton, 2002: Surface drifter pathways originating in the equatorial Atlantic cold tongue. *Geophysical Research Letters*, **29 (23)**.

Gruber, N., M. Gloor, S. E. Mikaloff Fletcher, S. C. Doney, S. Dutkiewicz, M. J. Follows, M. Gerber, A. R. Jocobson, F. Joos, K. Lindsey, D. Menemenlis, A. Mouchet, S. A. Müller, J. L. Sarmiento, and T. Takahashi, 2009: Oceanic sources, sinks, and transport of atmospheric CO_2. *Global Biogeochemical Cycles*, **23 (GB1005)**.

Haertel, P. and A. Fedorov, 2012: The Ventilated Ocean. *Journal of Physical Oceanography*, **42**, 141–164.

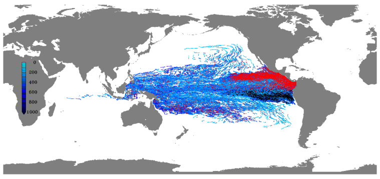

Hahn, J., P. Brandt, R. J. Greatbatch, G. Krahmann, and A. Körtzinger, 2014: Oxygen variance and meridional oxygen supply in the Tropical North East Atlantic oxygen minimum zone. *Climate Dynamics*, **43 (11)**, 2999–3024.

Halliwell, G. R., R. H. Weisberg, and D. A. Mayer, 2003: A synthetic float analysis of upper-limb meridional overturning circulation interior ocean pathways in the tropical/subtropical Atlantic. *Interhemispheric Water Exchange in the Atlantic Ocean*, Goni, G. J. and P. Malanotte-Rizzoli, Eds., Elsevier B. V.

Han, W., G. A. Meehl, and A. Hu, 2006: Interpretation of tropical thermocline cooling in the Indian and Pacific oceans during recent decades. *Geophysical Research Letters*, **33 (L23615)**.

Han, W., G. A. Meehl, B. Rajagopalan, J. T. Fasullo, A. Hu, J. Lin, W. G. Large, J.-W. Wang, X.-W. Quan, L. L. Trenary, A. Wallcraft, T. Shinoda, and S. Yeager, 2010: Patterns of Indian Ocean sea-level change in a warming climate. *Nature Geosciences*, **3**, 546–550.

Hansen, D. V. and C. A. Paul, 1987: Vertical motion in the eastern equatorial Pacific, inferred from drifting buoys. *Oceanologica Acta*, **Special Volume**, 27–32.

Helly, J. J. and L. A. Levin, 2004: Global distribution of naturally occurring marine hypoxia on continental margins. *Deep Sea Research I*, **51**, 1159–1168.

Holgate, S. J., A. Matthews, P. L. Woodworth, L. J. Rickards, M. E. Tamisiea, E. Bradshaw, P. R. Foden, K. M. Gordon, S. Jevrejeva, and J. Pugh, 2013: New Data Systems and Products at the Permanent Service for Mean Sea Level. *Journal of Coastal Research*, **29 (3)**, 493–504.

Holzer, M. and T. M. Hall, 2000: Transit-Time and Tracer-Age Distributions in Geophysical Flows. *Journal of the Atmospheric Sciences*, **57**, 3539–3558.

Houry, S., E. Dombrowsky, P. De Mey, and J.-F. Minster, 1987: Brunt-Väisälä Frequency and Rossby Radii in the South Atlantic. *Journal of Physical Oceanography*, **17**, 1619–1626.

Hüttl, S. and C. W. Böning, 2006: Mechanisms of decadal variability in the shallow subtropical-tropical circulation of the Atlantic Ocean: A model study. *Journal of Geophysical Research*, **111 (C07011)**.

Hüttl-Kabus, S. and C. W. Böning, 2008: Pathways and variability of the off-equatorial undercurrents in the Atlantic Ocean. *Journal of Geophysical Research*, **113 (C10018)**.

Johns, W. E., T. N. Lee, R. C. Beardsley, J. Candela, R. Limeburner, and B. Castro, 1998: Annual Cycle and Variability of the North Brazil Current. *Journal of Physical Oceanography*, **28 (1)**, 103–128.

Johnson, G. C., 2008: Quantifying Antarctic Bottom Water and North Atlantic Deep Water volumes. *Journal of Geophysical Research*, **113 (C05027)**.

Johnson, G. C., B. M. Sloyan, W. S. Kessler, and K. W. McTaggart, 2002: Direct measurements of upper ocean currents and water properties across the tropical Pacific during the 1990s. *Progress in Oceanography*, **52**, 31–61.

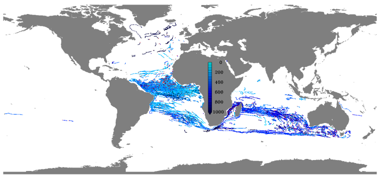

Jones, P. W., 1998: A User's Guide for SCRIP: A Spherical Coordinate Remapping and Interpolation Package, version 1.4. http://climate.lanl.gov/Software/SCRIP/.

Joos, F., G.-K. Plattner, T. F. Stocker, A. Körtzinger, and D. W. R. Wallace, 2003: Trends in marine dissolved oxygen: Implications for ocean circulation changes and the carbon budget. *Eos, Transctions, AGU*, **84 (21)**, 197–201.

Kantha, L. and C. Clayson, 2000: Numerical Models of Oceans and Oceanic Processes. *Academic Press*, 750pp.

Karstensen, J., L. Stramma, and M. Visbeck, 2008: Oxygen minimum zones in the eastern tropical Atlantic and Pacific oceans. *Progress in Oceanography*, **77 (4)**, 331–350.

Keeling, R. and H. Garcia, 2002: The change in oceanic O_2 inventory associated with recent global warming. *Proceedings of the National Academy of Sciences of the United States of America*, **99 (12)**, 7848–7853.

Khatiwala, S., F. Primeau, and M. Holzer, 2012: Ventilation of the deep ocean constrained with tracer observations and implications for radiocarbon estimates of ideal mean age. *Earth and Planetary Science Letters*, **325-326**, 116–125.

Killworth, P., 1983: Deep convection in the World Ocean. *Reviews of Geophysics*, **21 (1)**, 1–26.

Krauss, W., 1986: The North Atlantic Current. *Journal of Geophysical Research*, **91 (C4)**, 50615074.

Kuhlbrodt, T., A. Griesel, M. Montoya, A. Levermann, M. Hofmann, and S. Rahmstorf, 2007: On the driving processes of the Atlantic meridional overturning circulation. *Reviews of Geophysics*, **45 (RG2001)**.

Large, W. and S. Yeager, 2004: Diurnal to decadal global forcing for ocean and sea-ice models: the data sets and flux climatologies. *NCAR Technical Note*, **460+STR**.

Large, W. G. and S. G. Yeager, 2009: The global climatology of an interannually varying air-sea flux data set. *Climate Dynamics*, **33 (2-3)**, 341–364.

Lee, T. and M. J. McPhaden, 2008: Decadal phase changes in large-scale sea level and winds in the Indo-Pacific region at the end of the 20th century. *Geophysical Research Letters*, **35 (L01605)**.

Lemarié, F., 2006: NEMO/AGRIF Nesting tools, User's Guide (30 January 2006). http://www.atmos.ucla.edu/˜florian/NEMO_AGRIF/.

Levitus, S., T. P. Boyer, M. E. Conkright, T. O. Brien, J. Antonov, C. Stephens, L. Stathoplos, D. Johnson, and R. Gelfeld, 1998: NOAA Atlas NESDIS 18,World Ocean Database 1998: Volume 1: Introduction. 346pp.

Liss, P. S. and L. Merlivat, 1986: Air-Sea Gas Exchange Rates: Introduction and Synthesis. *The Role of Air-Sea Exchange in Geochemical Cycling*, Buat-Ménard, P., Ed., Springer Netherlands, Vol. 185, 113–127.

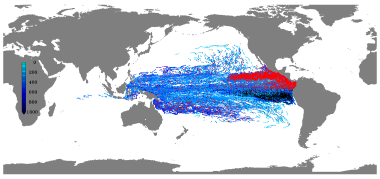

Löscher, C. R., H. W. Bange, R. A. Schmitz, C. M. Callbeck, A. Engel, H. Hauss, T. Kanzow, R. Kiko, G. Lavik, A. Loginova, F. Melzner, S. C. Neulinger, M. Pahlow, U. Riebesell, H. Schunck, S. Thomsen, and H. Wagner, 2015: Water column biogeochemistry of oxygen minimum zones in the eastern tropical North Atlantic and eastern tropical South Pacific Oceans. *Biogeosciences Discussions*, **12**, 4495–4556.

Lukas, R., 1986: The termination of the Equatorial Undercurrent in the eastern Pacific. *Progress in Oceanography*, **16 (2)**, 63–90.

Lukas, R., T. Yamagata, and J. P. McCreary, 1996: Pacific low-latitude western boundary currents and the Indonesian throughflow. *Journal of Geophysical Research*, **101 (C5)**, 12 209–12 216.

Lutjeharms, J. R. E., 2006: The Agulhas Current. *Springer*, 329pp.

Luyten, J. R., J. Pedlosky, and H. Stommel, 1983: The Ventilated Thermocline. *Journal of Physical Oceanography*, **13**, 292–309.

Lynn, R. J. and J. Reid, 1968: Characteristics and circulation of deep and abyssal waters. *Deep Sea Research*, **15 (5)**, 577–598.

Madec, G., 2008: NEMO ocean engine - version 3.1. *Note du Pole de modélisation, Institut Pierre-Simon Laplace (IPSL)*, **27**.

Madec, G., P. Delecluse, M. Imbard, and C. Levy, 1998: Opa 8 ocean general circulation model - reference manual. *Note du Pole de modélisation, Institut Pierre-Simon Laplace (IPSL)*, **11**.

Marin, F., E. Kestenare, T. Delcroix, F. Durand, S. Cravatte, G. Eldin, and R. Bourdallé-Badie, 2010: Annual Reversal of the Equatorial Intermediate Current in the Pacific: Observations and Model Diagnostics. *Journal of Physical Oceanography*, **40 (5)**, 915–933.

Marshall, J. and F. Schott, 1999: Open-ocean convection: Observations, theory, and models. *Reviews of Geophysics*, **37 (1)**, 1–64.

Marshall, J. and K. Speer, 2012: Closure of the meridional overturning circulation through Southern Ocean upwelling. *Nature Geosciences*, **35**, 171–180.

McCulloch, A., P. M. Midgley, and P. Ashford, 2003: Releases of refrigerant gases (CFC-12, HCFC-22 and HFC-134a) to the atmosphere. *Atmospheric Environment*, **37**, 889–902.

McPhaden, M. J., 1984: On the Dynamics of Equatorial Subsurface Countercurrents. *Journal of Physical Oceanography*, **14 (7)**, 1216–1225.

Mesinger, F. and A. Arakawa, 1976: Numerical methods used in Atmospheric models. *GARP Publication Series*, **17**.

Metcalf, W. G. and M. C. Stalcup, 1967: Origin of the Atlantic Equatorial Undercurrent. *Journal of Geophysical Research*, **72 (20)**, 4959–4975.

Meyers, G., 1996: Variation of Indonesian Throughflow and the El Niño-Southern Oscillation. *Journal of Geophysical Research*, **101**, 12,255–12,263.

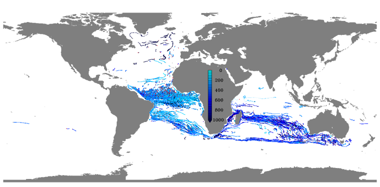

Molinari, R., 1982: Observations of eastward currents in the tropical South Atlantic Ocean: 1978-1980. *Journal of Geophysical Research*, **87**, 9707–9714.

Munk, W. H., 1950: On the wind-driven ocean circulation. *Journal of Meteorology*, **7 (2)**, 79–93.

Nowlin Jr., W. and J. M. Klinck, 1986: The physics of the Antarctic Circumpolar Current. *Reviews of Geophysics*, **24 (2)**, 469–491.

Ollitrault, M. and A. Colin de Verdière, 2014: The Ocean General Circulation near 1000-m Depth. *Journal of Physical Oceanography*, **44**, 384–409.

Ollitrault, M., M. Lankhorst, D. Fratantoni, P. Richardson, and W. Zenk, 2006: Zonal intermediate currents in the equatorial Atlantic Ocean. *Geophysical Research Letters*, **33 (L05605)**.

Pacanowski, R. C. and A. Gnanadesikan, 1998: Transient Response in a Z-Level Ocean Model that Resolves Topography with Partial Cells. *Monthly Weather Review*, **126**, 3248–3270.

Paulmier, A. and D. Ruiz-Pino, 2009: Oxygen minimum zones (OMZs) in the modern ocean. *Progress in Oceanography*, **80**, 113–128.

Peña-Izquierdo, J., E. van Sebille, J. L. Pelegrí, J. Sprintall, E. Mason, P. J. Llanillo, and F. Machin, 2015: Water mass pathways to the North Atlantic oxygen minimum zone. *Journal of Geophysical Research*, **120 (5)**.

Phillips, L. F., 1994: The Theory of Air-Sea Gas Exchange. *Accounts of Chemical Research*, **27 (8)**, 217–223.

Pickart, R. S., K. Våge, G. W. K. Moore, I. A. Renfrew, M. H. Ribergaard, and H. C. Davies, 2008: Arctic–Subarctic Ocean Fluxes: Defining the Role of the Northern Seas in Climate. Springer Netherlands, chap. Convection in the Western North Atlantic Sub-Polar Gyre: Do Small-Scale Wind Events Matter?, 629–652.

Qiu, B., 2002: The Kuroshio Extension System: Its Large-Scale Variability and Role in the Mid-latitude Ocean-Atmosphere Interaction. *Journal of Oceanography*, **58**, 57–75–223.

Qiu, B., D. L. Rudnick, S. Chen, and Y. Kashino, 2013: Quasi-stationary North Equatorial Undercurrent jets across the tropical North Pacific Ocean. *Geophysical Research Letters*, **40 (10)**, 2183–2187.

Rabe, B., F. A. Schott, and A. Köhl, 2008: Mean Circulation and Variability of the Tropical Atlantic during 1952-2001 in the GECCO Assimilation Fields. *Journal of Physical Oceanography*, **38 (1)**, 177–192.

Reason, C. J. C., R. J. Allan, and J. A. Lindesay, 1996: Evidence for the influence of remote forcing on interdecadal variability in the southern Indian Ocean. *Journal of Geophysical Research*, **101**, 11,867–11,882.

Ridder, N. N. and M. H. England, 2014: Sensitivity of ocean oxygenation to variations in tropical zonal wind stress magnitude. *Global Biogeochemical Cycles*, **28**.

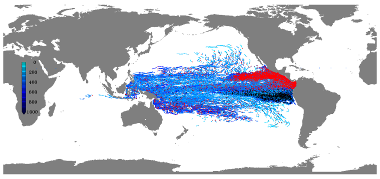

Ridgway, K. and K. Hill, 2009: A Marine Climate Change Impacts and Adaptation Report Card for Australia. NCCARF Publication, chap. The East Australian Current.

Ridgway, K. R. and J. R. Dunn, 2007: Observational evidence for a Southern Hemisphere oceanic supergyre. *Geophysical Research Letters*, **34 (L13612)**.

Rosell-Fieschi, M., J. Pelegrí, and J. Gourrion, 2015: Zonal jets in the equatorial Atlantic Ocean. *Progress in Oceanography*, **130**, 1–18.

Roullet, G. and G. Madec, 2000: Salt conservation, free surface and varying levels: a new formulation for ocean general circulation models. *Journal of Geophysical Research*, **105 (C10)**, 23 927–23 942.

Sallée, J.-B., K. Speer, S. Rintoul, and S. Wijffels, 2010: Southern Ocean Thermocline Ventilation. *Journal of Physical Oceanography*, **40 (3)**, 509–529.

Sarmiento, J. and C. L. Quéré, 1996: Oceanic Carbon Dioxide Uptake in a Model of Century-Scale Global Warming. *Science*, **274**, 1346–1350.

Schott, F., S.-P. Xie, and J. McCreary Jr., 2009: Indian Ocean circulation and climate variability. *Reviews of Geophysics*, **47**.

Schott, F. A., P. Brandt, M. Hamann, J. Fischer, and L. Stramma, 2002: On the boundary flow off Brazil at 5 - 10° S and its connection to the interior tropical Atlantic. *Geophysical Research Letters*, **29 (17)**.

Schott, F. A., J. P. McCreary, and G. C. Johnson, 2004: Shallow Overturning Circulations of the Tropical-Subtropical Oceans. *Earth's Climate*, C. Wang, S. X. and J. Carton, Eds., American Geophysical Union, Washington, D. C.

Schwarzkopf, F. U. and C. W. Böning, 2011: Contribution of Pacific wind stress to multi-decadal variations in upper-ocean heat content and sea level in the tropical south Indian Ocean. *Geophysical Research Letters*, **38 (L12602)**.

Sonnerup, R. E., 2001: On the relations among CFC derived water mass ages. *Geophysical Research Letters*, **28 (9)**, 1739–1742.

Steele, M., R. Morley, and W. Ermold, 2001: PHC: A Global Ocean Hydrography with a High-Quality Arctic Ocean. *Journal of Climate*, **14 (9)**, 2079–2087.

Stewart, R. H., 2008: Introduction To Physical Oceanography. *Department of Oceanography, Texas A & M University.*

Stommel, H., 1948: The westward intensification of wind-driven ocean currents. *Transactions, American Geophysical Union*, **29 (2)**, 202–206.

Stramma, L., H. W. Bange, R. Czeschel, A. Lorenzo, and M. Frank, 2013: On the role of mesoscale eddies for the biological productivity and biogeochemistry in the eastern tropical Pacific Ocean off Peru. *Biogeosciences*, **10**, 7293–7306.

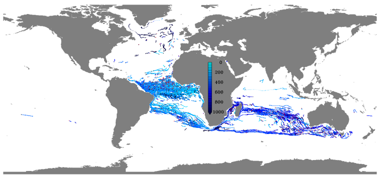

Stramma, L., G. C. Johnson, J. Sprintall, and V. Mohrholz, 2008: Expanding Oxygen-Minimum Zones in the Tropical Oceans. *Science*, **320 (5876)**, 655–658.

Stramma, L., E. D. Prince, S. Schmidtko, J. Luo, J. P. Hoolihan, M. Visbeck, D. W. R. Wallace, P. Brandt, and A. Körtzinger, 2012: Expansion of oxygen minimum zones may reduce available habitat for tropical pelagic fishes. *Nature Climate Change*, **2**, 33–37.

Stramma, L., S. Schmidtko, L. A. Levin, and G. C. Johnson, 2010: Ocean oxygen minima expansions and their biological impacts. *Deep Sea Research I*, **57**, 587–595.

Stramma, L. and F. Schott, 1999: The mean flow field of the tropical Atlantic Ocean. *Deep Sea Research II*, **46**, 279–303.

Sverdrup, H. U., 1947: Wind-Driven Currents in a Baroclinic Ocean; with Application to the Equatorial Currents of the Eastern Pacific. *Proceedings of the National Academy of Sciences of the United States of America*, **33 (11)**, 318–326.

Takahashi, T., S. C. Sutherland, C. Sweeney, A. Poisson, N. Metzl, B. Tilbrook, N. Bates, R. Wanninkhof, R. A. Feely, C. Sabine, J. Olafsson, and Y. Nojiri, 2002: Global sea-air CO_2 flux based on climatological surface ocean pCO_2, and seasonal biological and temperature effects. *Deep Sea Research II*, **49**, 1601–1622.

Takahashi, T., C. Sweeney, B. Hales, D. W. Chipman, T. Newberger, J. G. Goddard, R. A. Oannuzzi, and S. C. Sutherlans, 2012: The changing carbon cycle in the Southern Ocean. *Oceanography*, **25 (3)**, 26–37.

Talley, L., G. Rickard, W. Emery, and J. Swift, 2011: Descriptive Physical Oceanography. *Elsevier Academic Press.*

Timmermann, A., S. McGregor, and F.-F. Jin, 2010: Wind effects on past and future regional sea level trends in the southern Indo-Pacific. *Journal of Climate*, **23**, 4429–4437.

Trenary, L. L. and W. Han, 2008: Causes of decadal subsurface cooling in the tropical Indian Ocean during 1961-2000. *Geophysical Research Letters*, **35 (L17602)**.

Ummenhofer, C. C., F. U. Schwarzkopf, G. Meyers, E. Behrens, A. Biastoch, and C. W. Böning, 2013: Pacific Ocean Contribution to the Asymmetry in Eastern Indian Ocean Variability. *Journal of Climate*, **26**, 1152–1171.

Ummenhofer, C. C., A. Sen Gupta, M. H. England, and C. J. C. Reason, 2009: Contributions of Indian Ocean sea surface temperatures to enhanced east African rainfall. *Journal of Climate*, **22**, 993–1013.

U.S. Department of Commerce, N. O. and N. G. D. C. Atmospheric Administration, 2006: 2-minute Gridded Global Relief Data (ETOPO2v2). URL `http://www.ngdc.noaa.gov/mgg/fliers/06mgg01.html`.

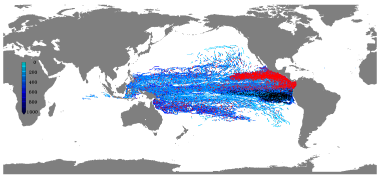

Vecchi, G. A., B. J. Soden, A. T. Wittenberg, I. M. Held, A. Leetmaa, and M. J. Harrison, 2006: Weakening of tropical Pacific atmospheric circulation due to anthropogenic forcing. *Nature*, **441**, 73–76.

Wainwright, L., G. Meyers, S. Wijffels, and L. Pigot, 2008: Change in the Indonesian Throughflow with the climatic shift of 1976/1977. *Geophysical Research Letters*, **35 (L03604)**.

Walker, S. J., R. F. Weiss, and P. K. Salameh, 2000: Reconstructed histories of the annual mean atmospheric mole fractions for the halocarbons CFC-11 CFC-12, CFC-113, and carbon tetrachloride. *Journal of Geophysical Research*, **105 (C6)**, 14 285–14 296.

Wijffels, S. and G. Meyers, 2004: An intersection of oceanic waveguides: variability in the Indonesian Throughflow region. *Journal of Physical Oceanography*, **34**, 1232–1253.

Williams, B. and A. G. Grottoli, 2010: Recent shoaling of the nutricline and thermocline in the western topical Pacific. *Geophysical Research Letters*, **37 (L22601)**.

Williams, R. G. and M. J. Follows, 2003: Ocean Biogeochemistry: The role of the ocean carbon cycle in global change. Springer, chap. Physical transport of nutrients and the maintenance of biological production, 19–51.

Wunsch, C., R. M. Ponte, and P. Heimbach, 2007: Decadal trends in sea level patterns: 1993-2004. *Journal of Climate*, **20**, 5889–5911.

Yamamoto, A., A. Abe-Ouchi, M. Shigemitsu, A. Oka, K. Takahashi, R. Ohgaito, and Y. Yamanaka, 2015: Global deep ocean oxygenation by enhanced ventilation in the Southern Ocean under long-term global warming. *Global Biogeochemical Cycles*, **29 (10)**, 1801–1815.

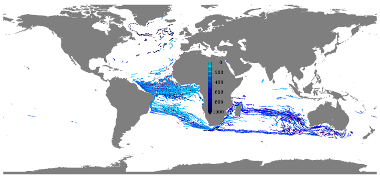

A. Appendix

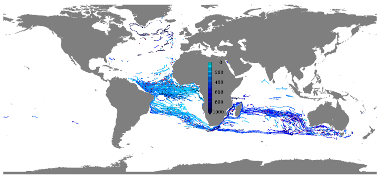

a) Surface TRATL01

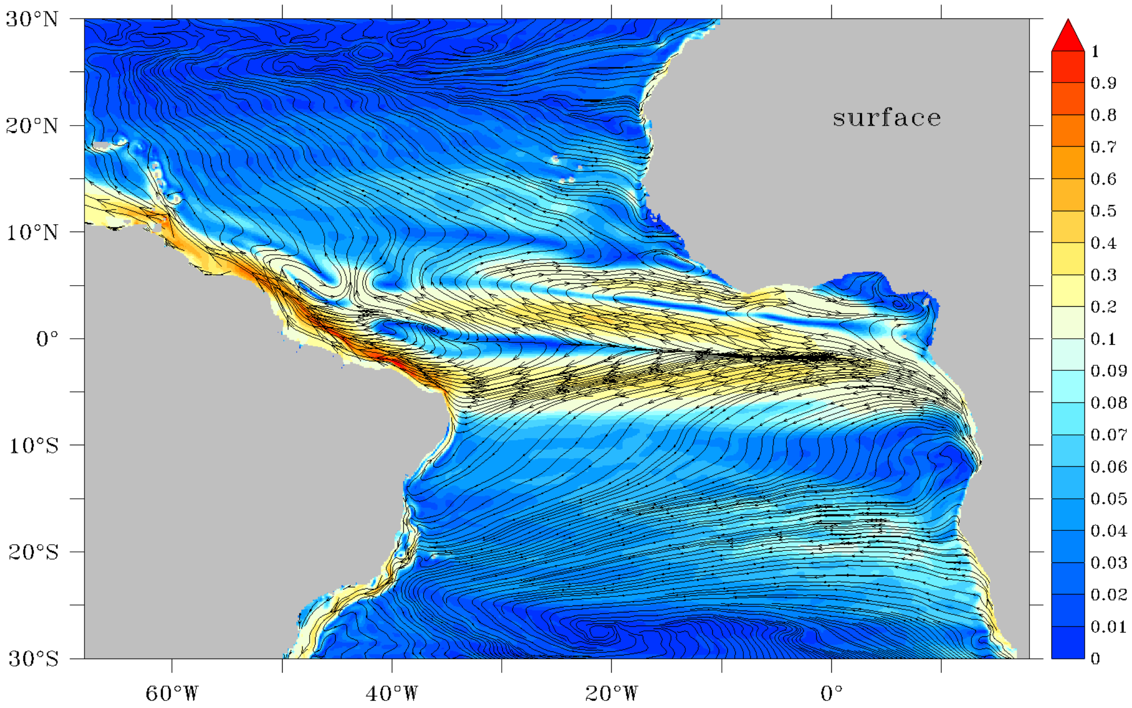

b) Surface ORCA05

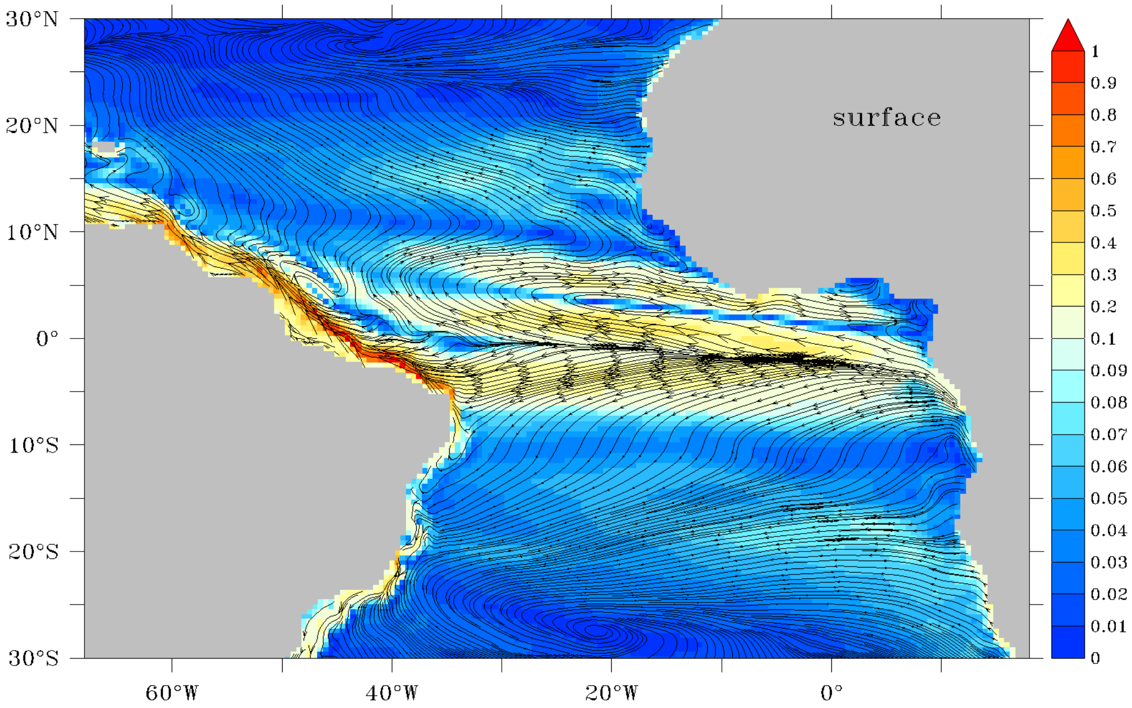

Figure A.1.: Ten year averaged (2000 to 2009) circulation: shaded is speed [m/s] with velocity vectors overlaid.

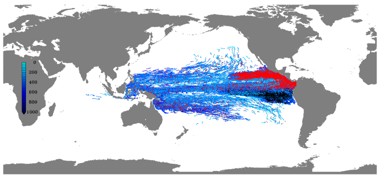

a) 25 m depth TRATL01

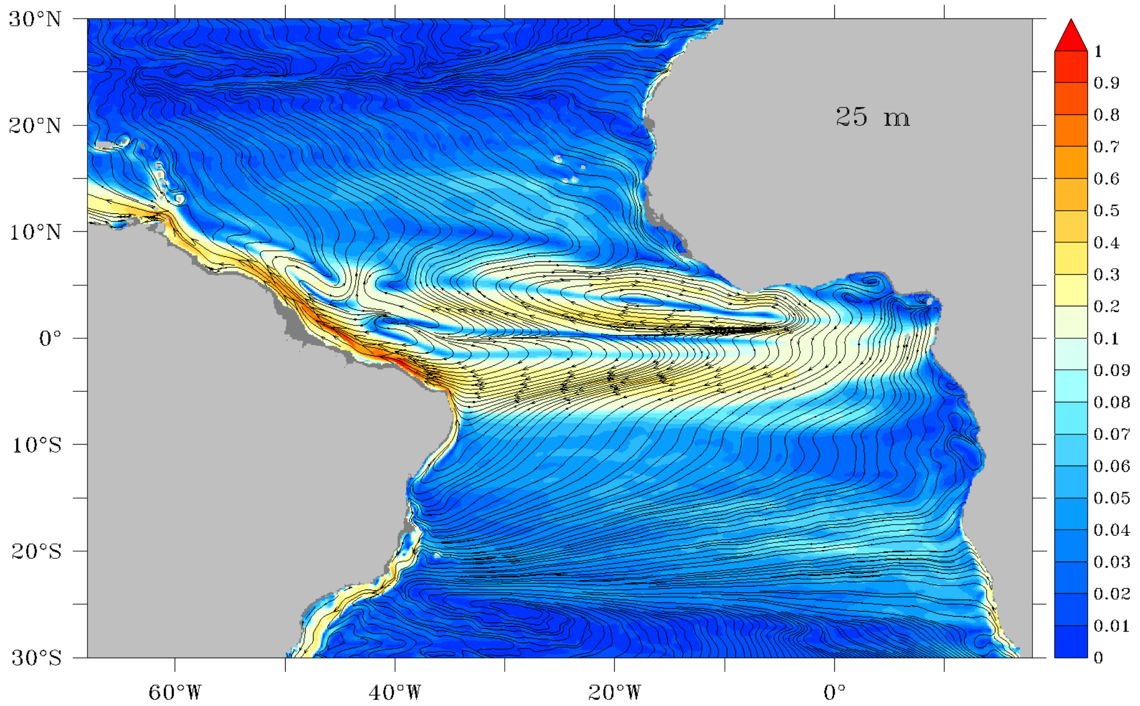

b) 25 m depth ORCA05

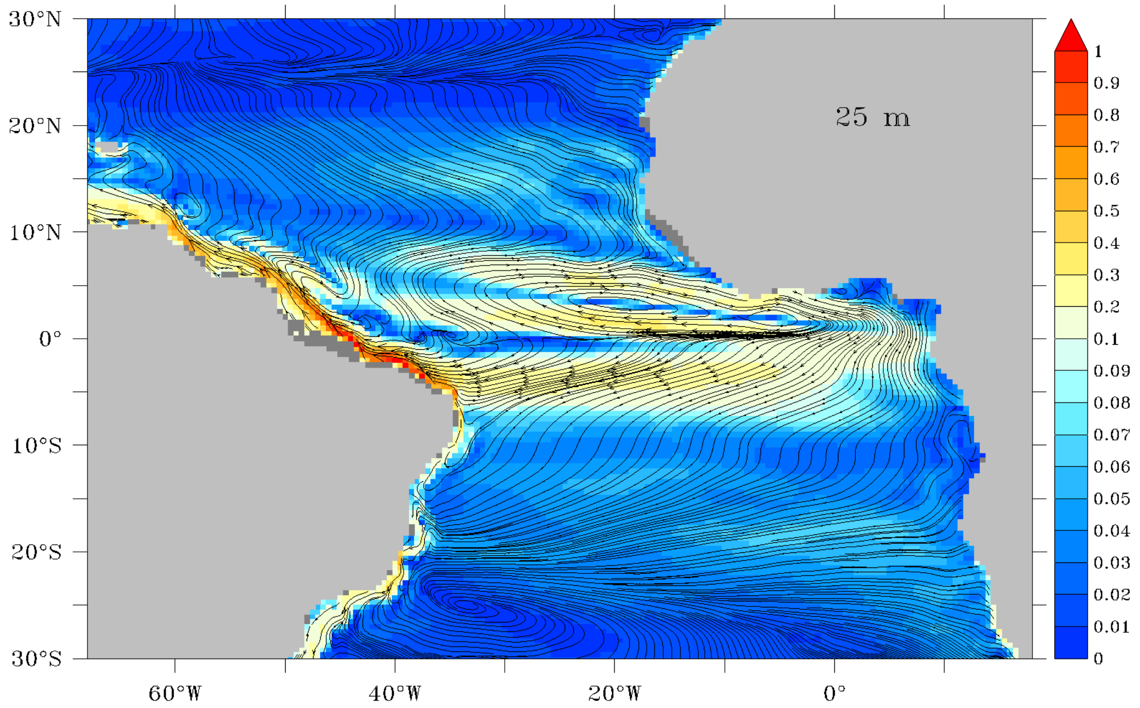

Figure A.2.: Ten year averaged (2000 to 2009) circulation: shaded is speed [m/s] with velocity vectors overlaid.

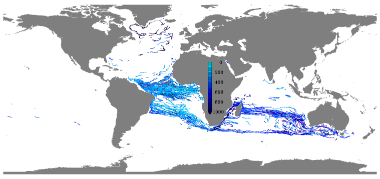

a) 50 m depth TRATL01

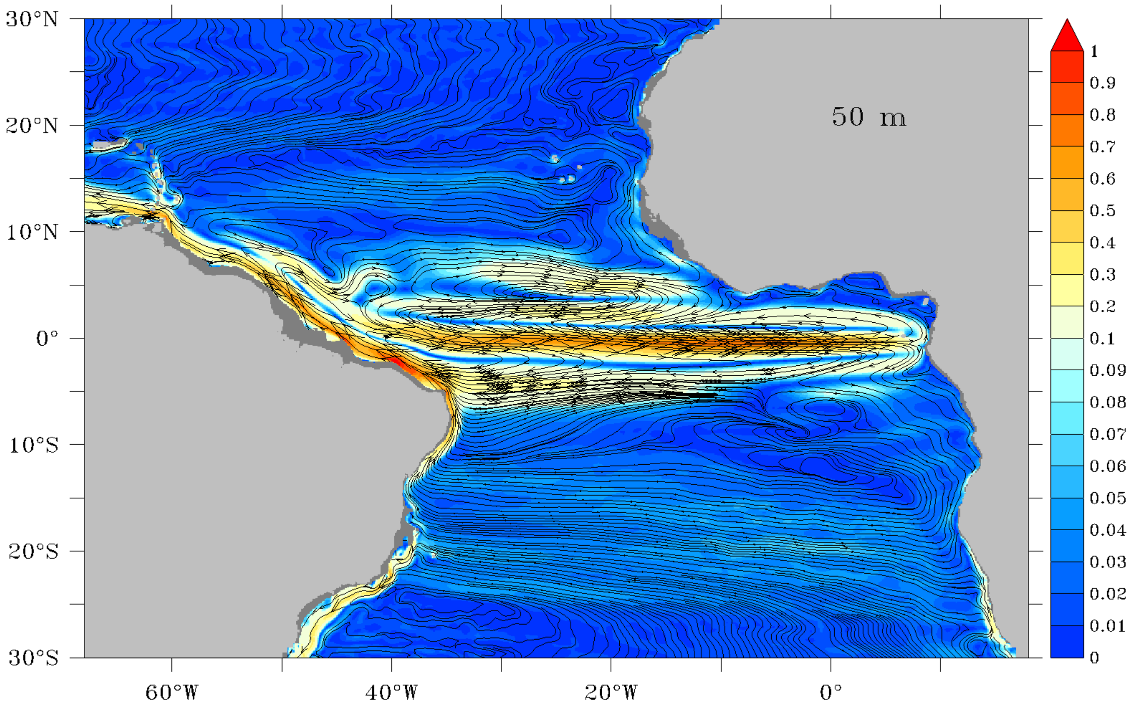

b) 50 m depth ORCA05

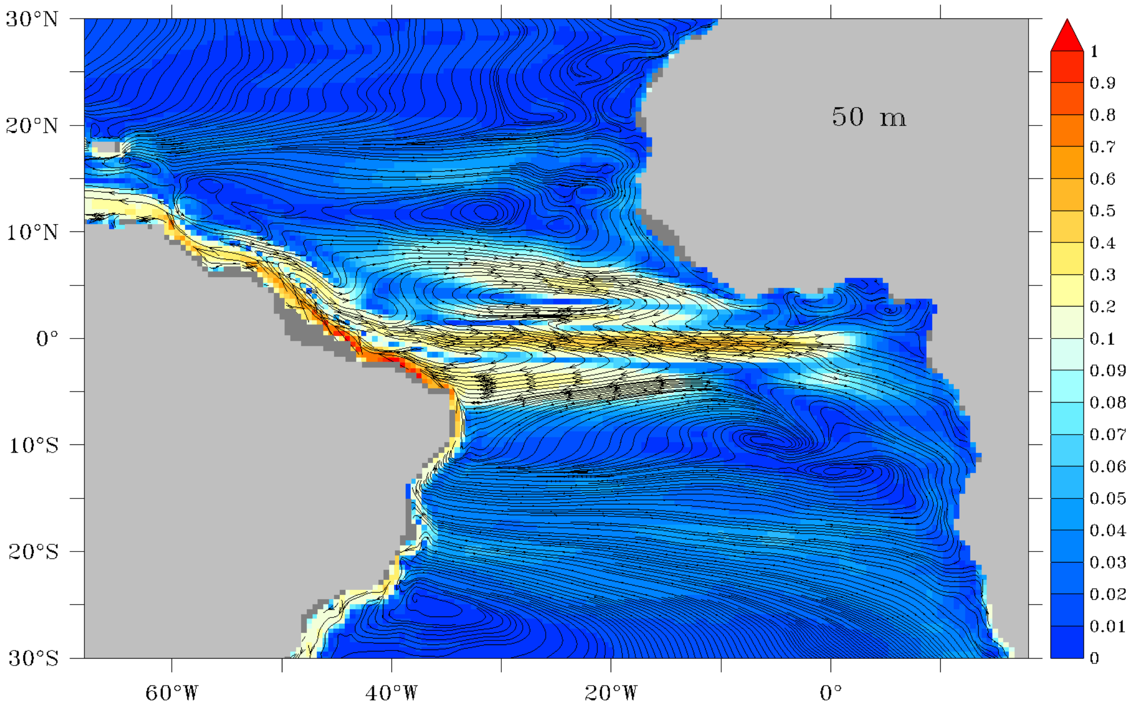

Figure A.3.: Ten year averaged (2000 to 2009) circulation: shaded is speed [m/s] with velocity vectors overlaid.

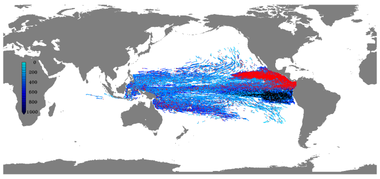

a) 100 m depth TRATL01

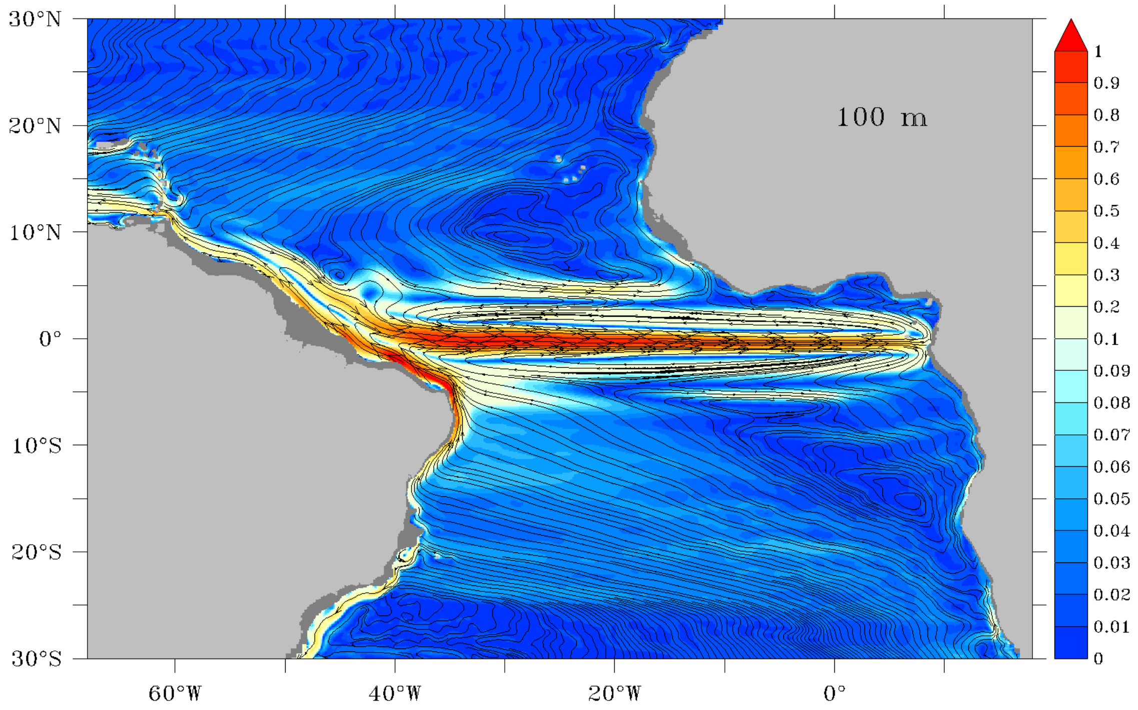

b) 100 m depth ORCA05

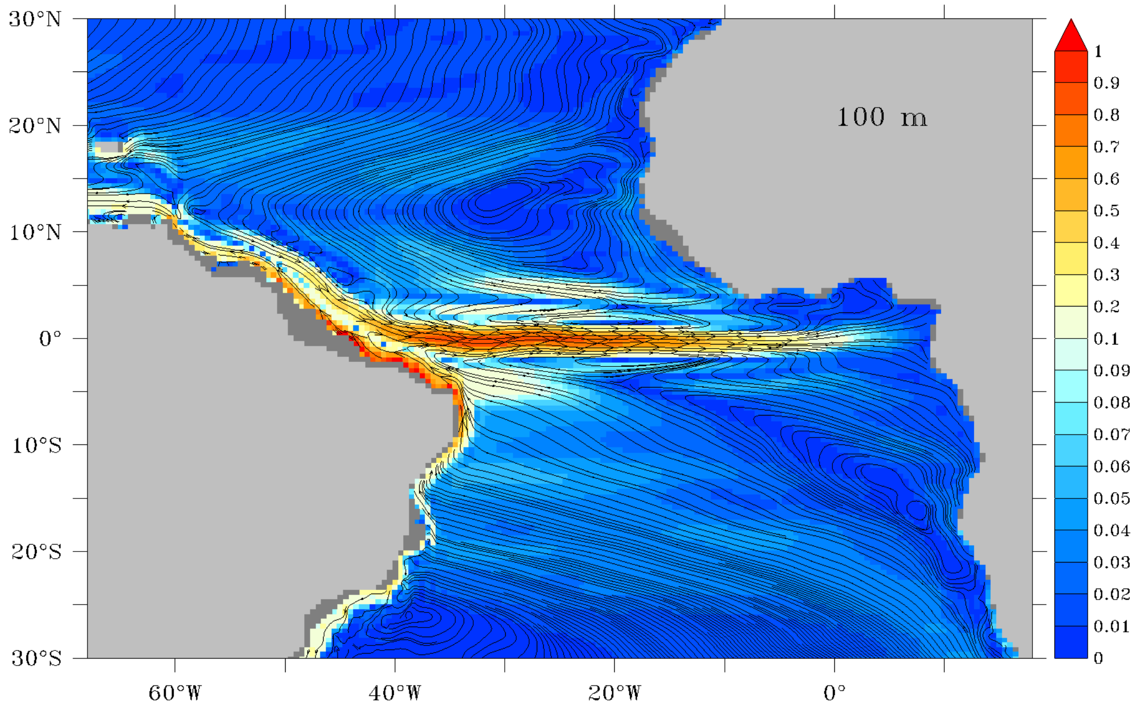

Figure A.4.: Ten year averaged (2000 to 2009) circulation: shaded is speed [m/s] with velocity vectors overlaid.

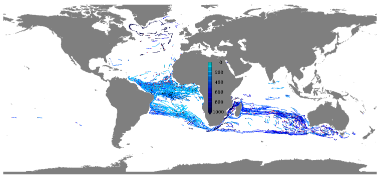

a) 200 m depth TRATL01

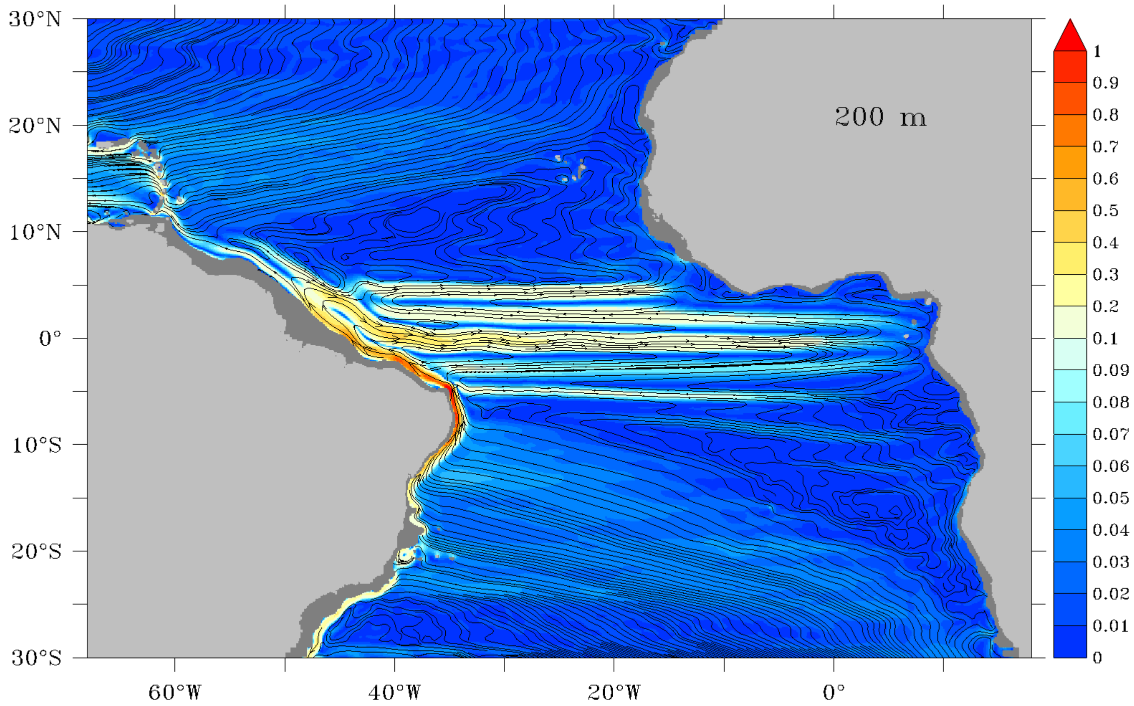

b) 200 m depth ORCA05

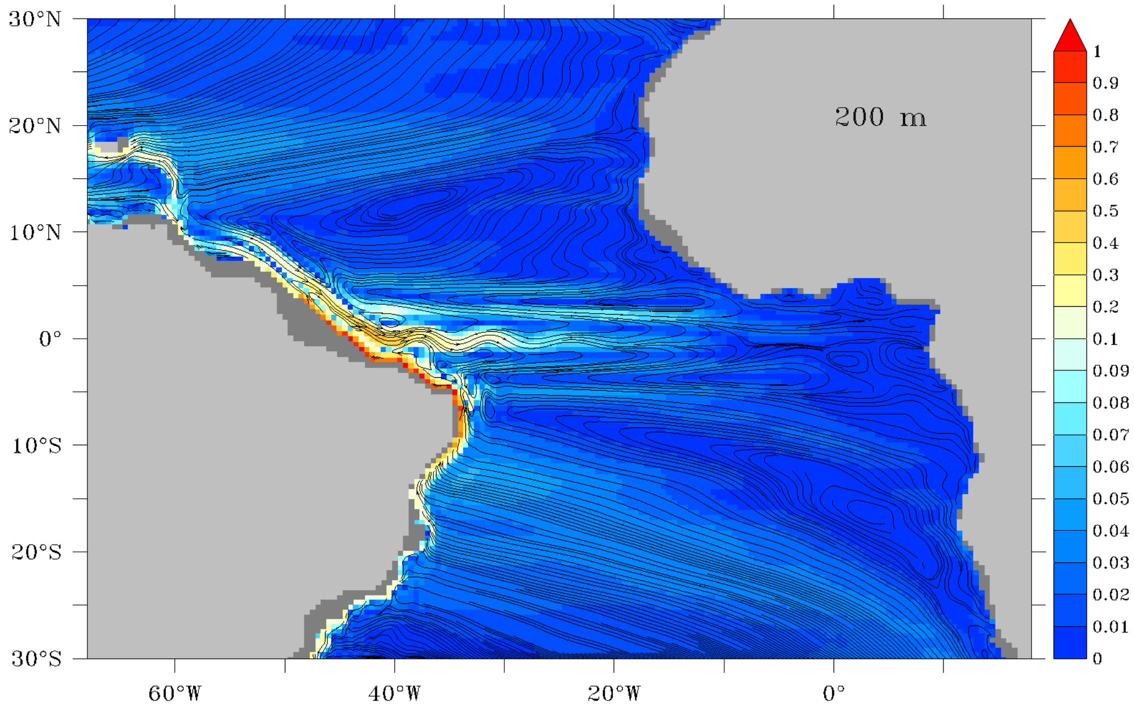

Figure A.5.: Ten year averaged (2000 to 2009) circulation: shaded is speed [m/s] with velocity vectors overlaid.

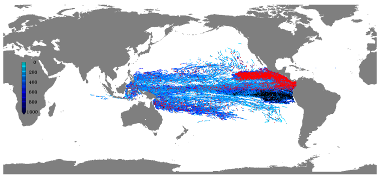

a) 300 m depth TRATL01

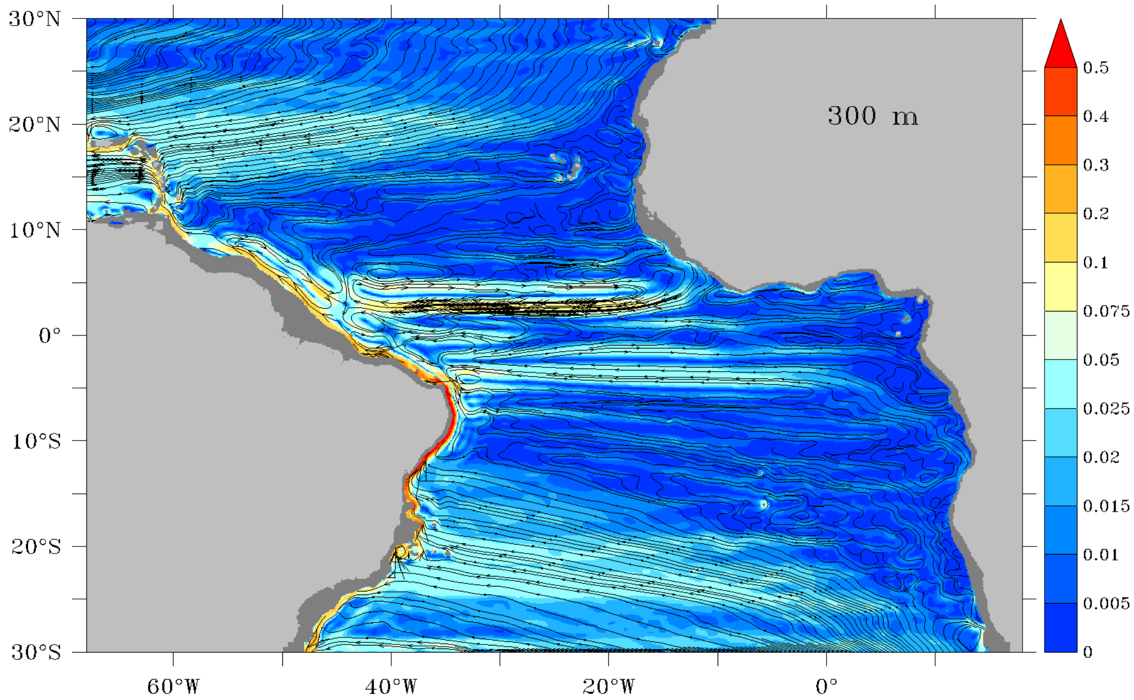

b) 300 m depth ORCA05

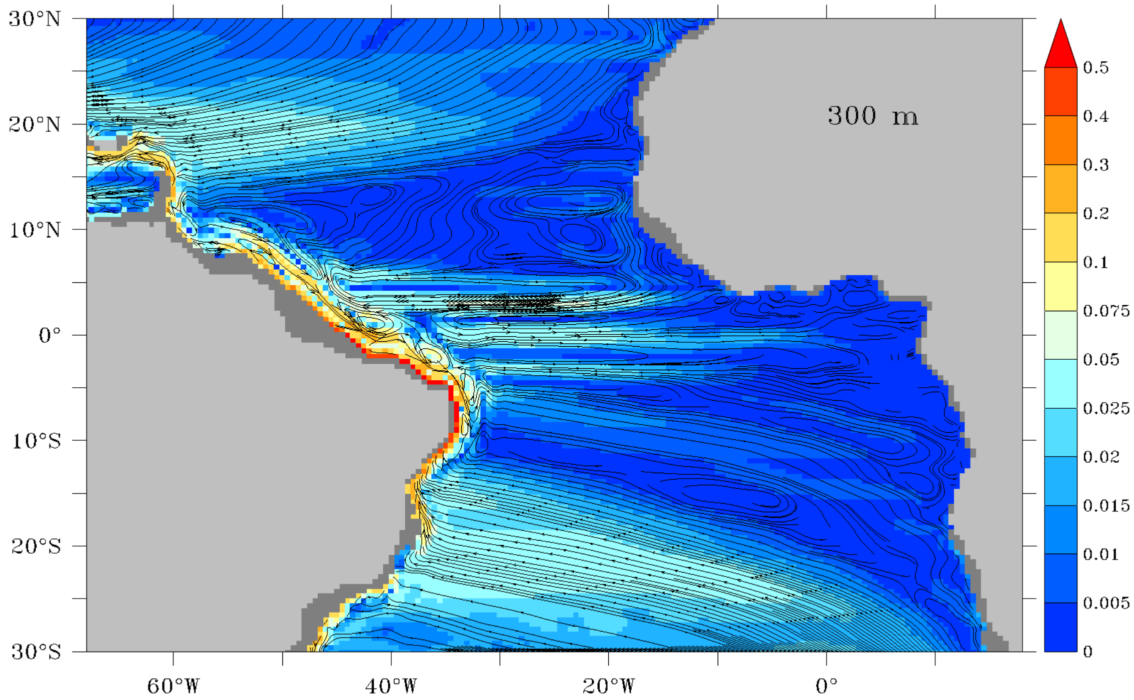

Figure A.6.: Ten year averaged (2000 to 2009) circulation: shaded is speed [m/s] with velocity vectors overlaid.

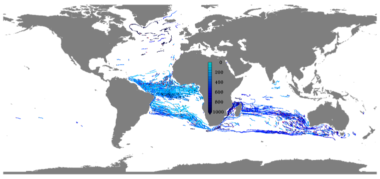

a) 400 m depth TRATL01

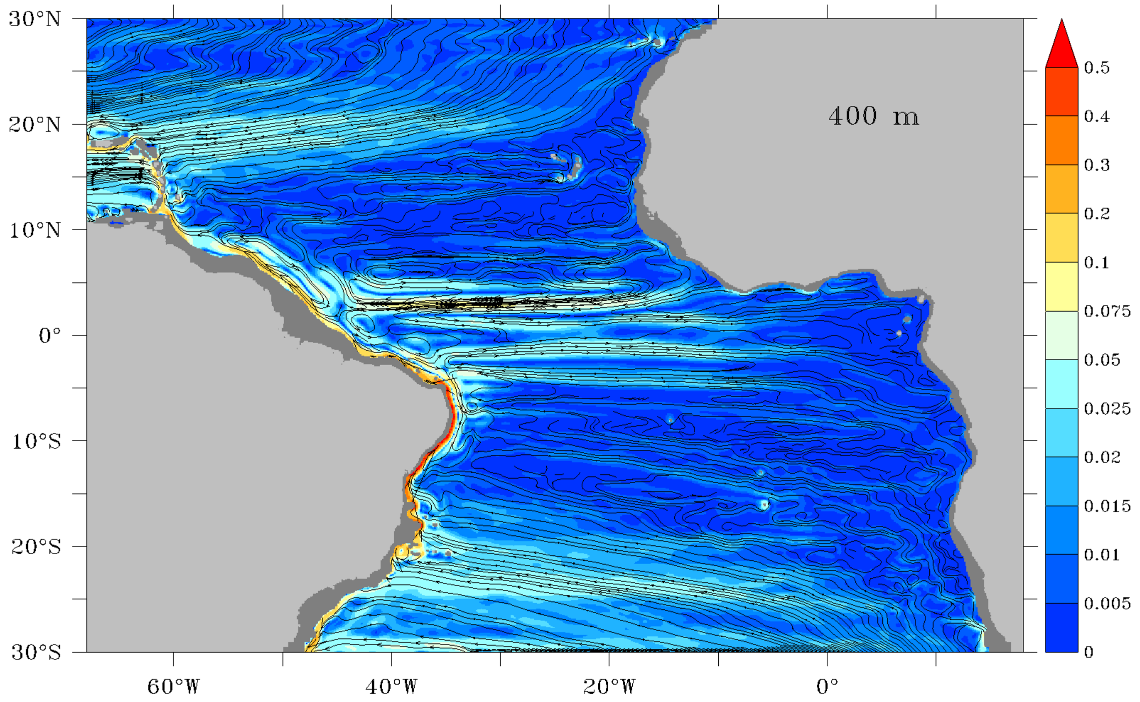

b) 400 m depth ORCA05

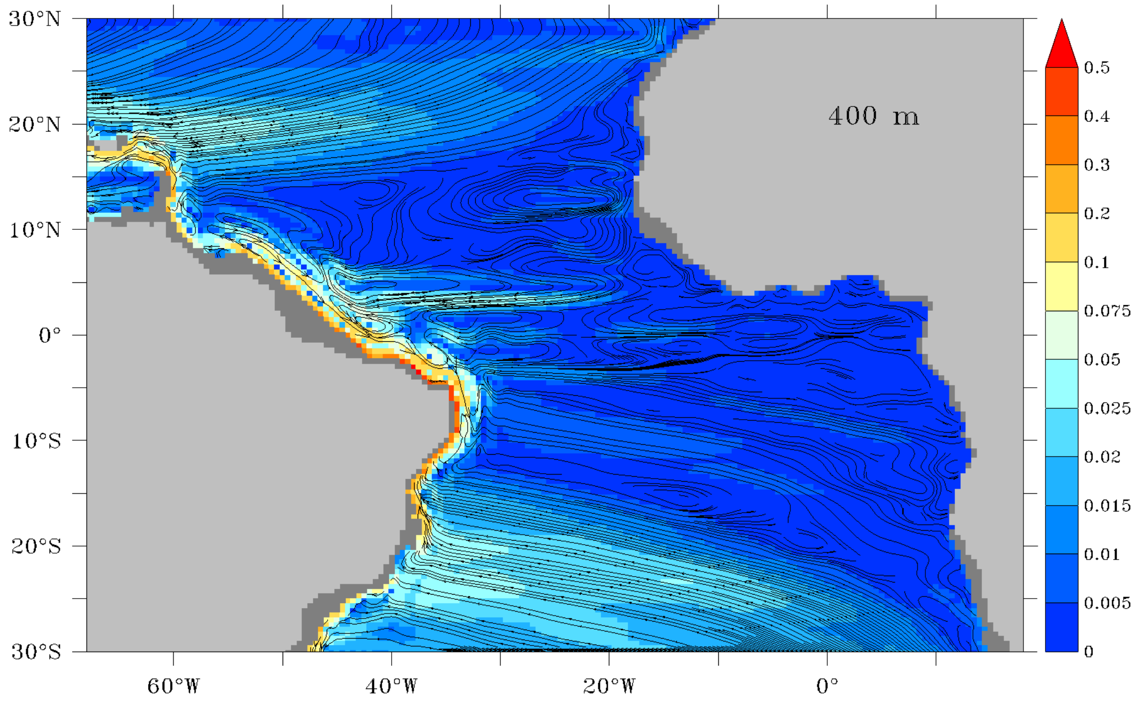

Figure A.7.: Ten year averaged (2000 to 2009) circulation: shaded is speed [m/s] with velocity vectors overlaid.

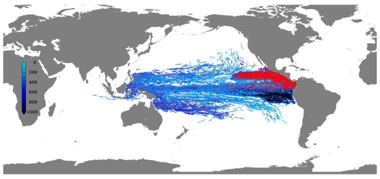

a) 500 m depth TRATL01

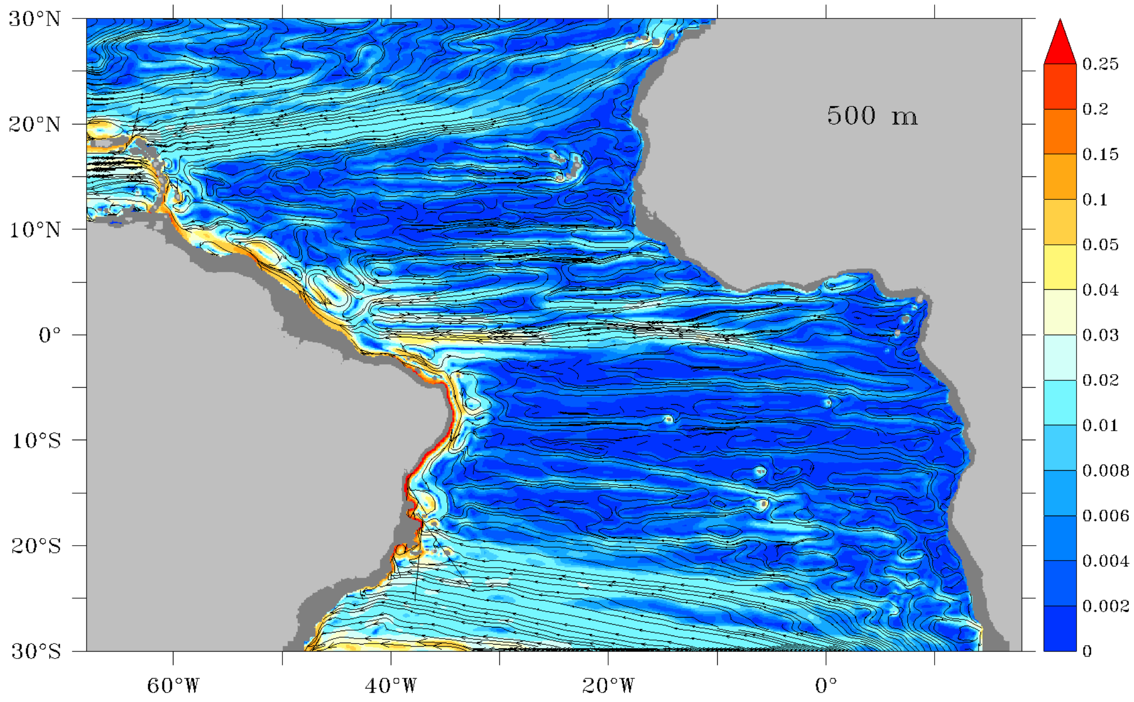

b) 500 m depth ORCA05

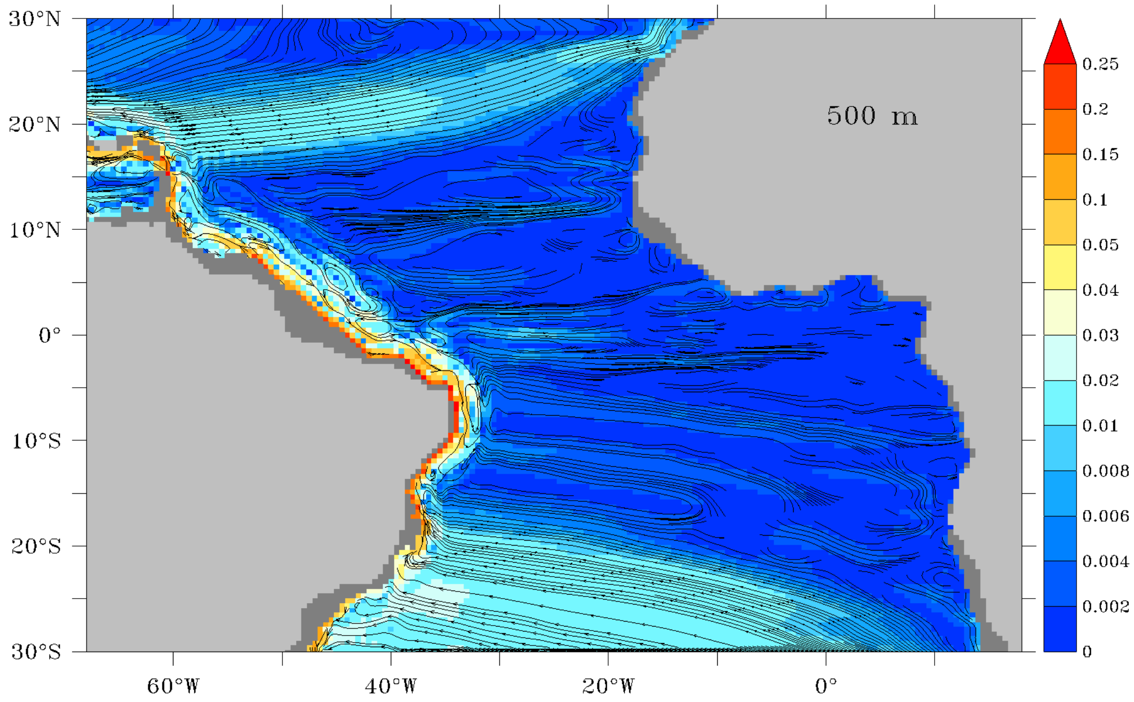

Figure A.8.: Ten year averaged (2000 to 2009) circulation: shaded is speed [m/s] with velocity vectors overlaid.

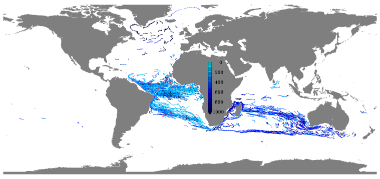

a) 600 m depth TRATL01

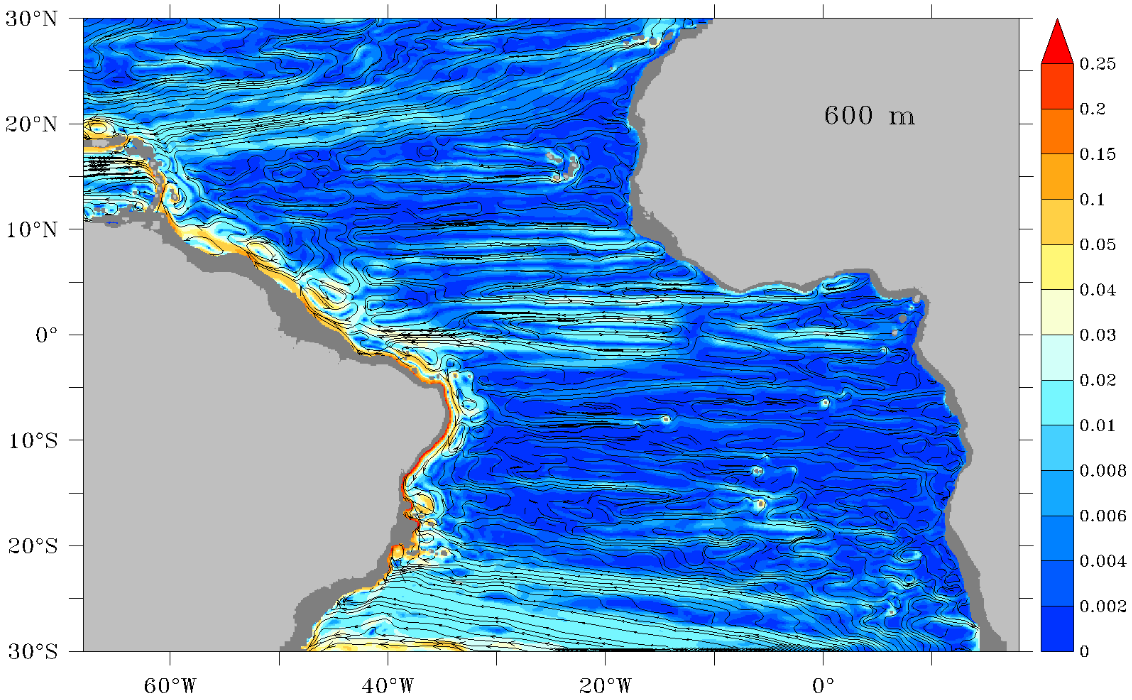

b) 600 m depth ORCA05

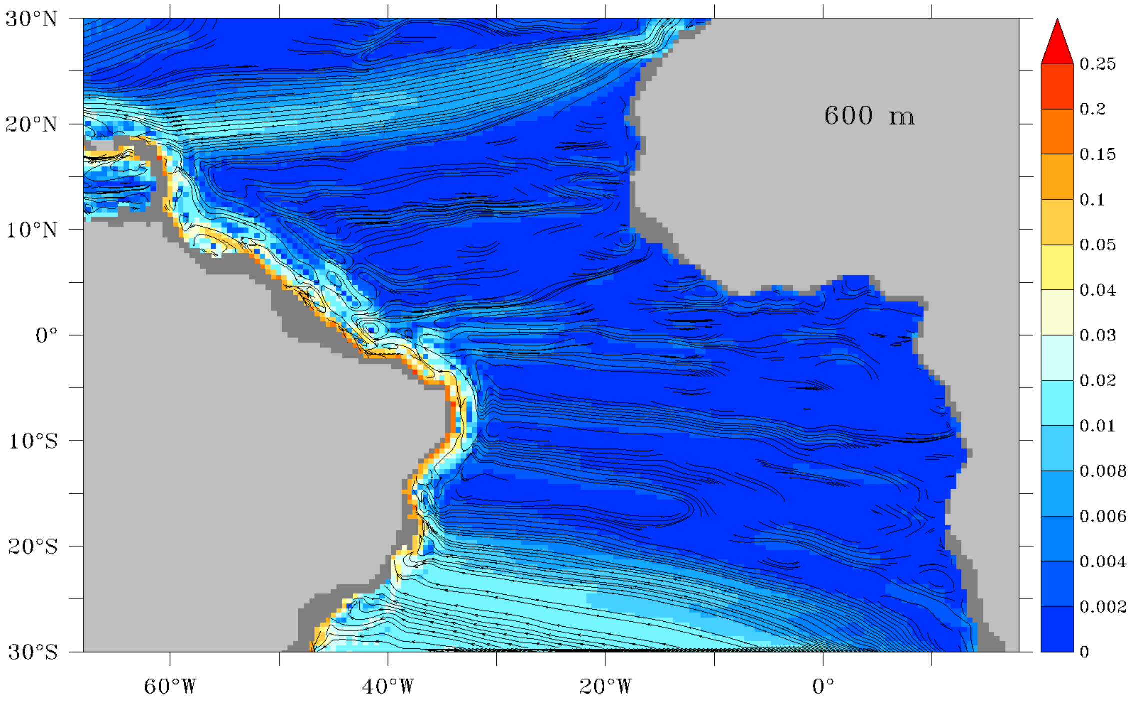

Figure A.9.: Ten year averaged (2000 to 2009) circulation: shaded is speed [m/s] with velocity vectors overlaid.

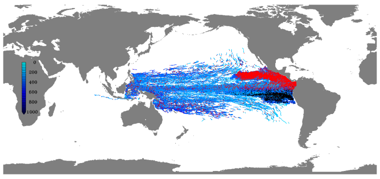

a) 700 m depth TRATL01

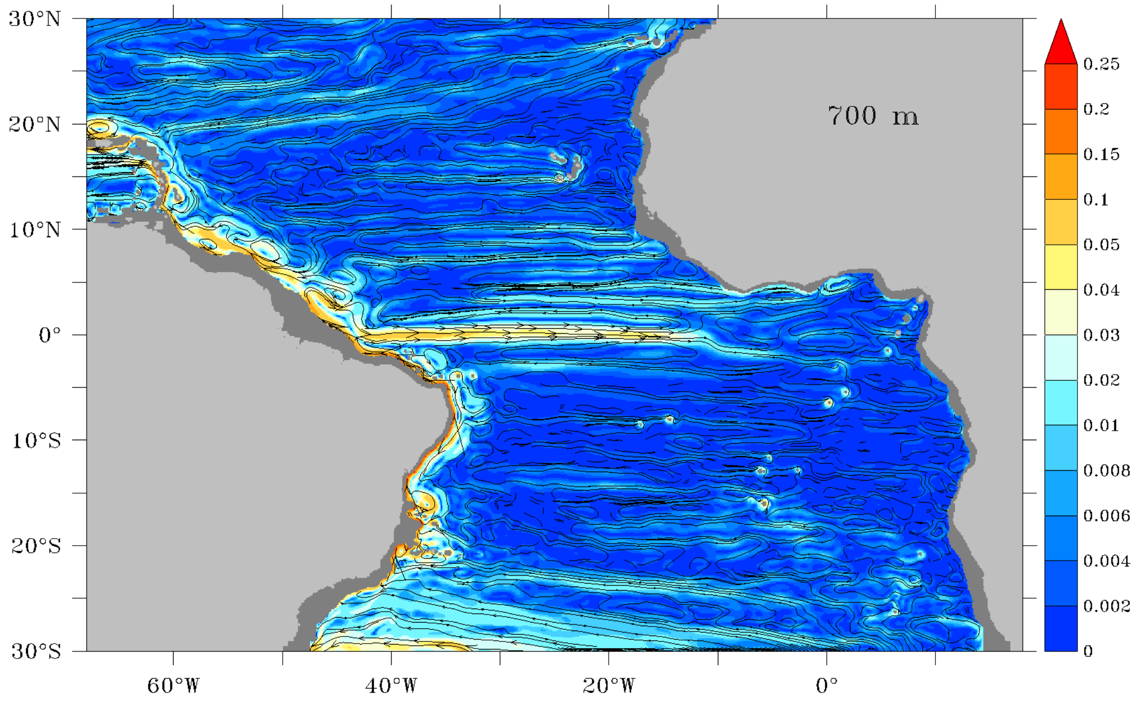

b) 700 m depth ORCA05

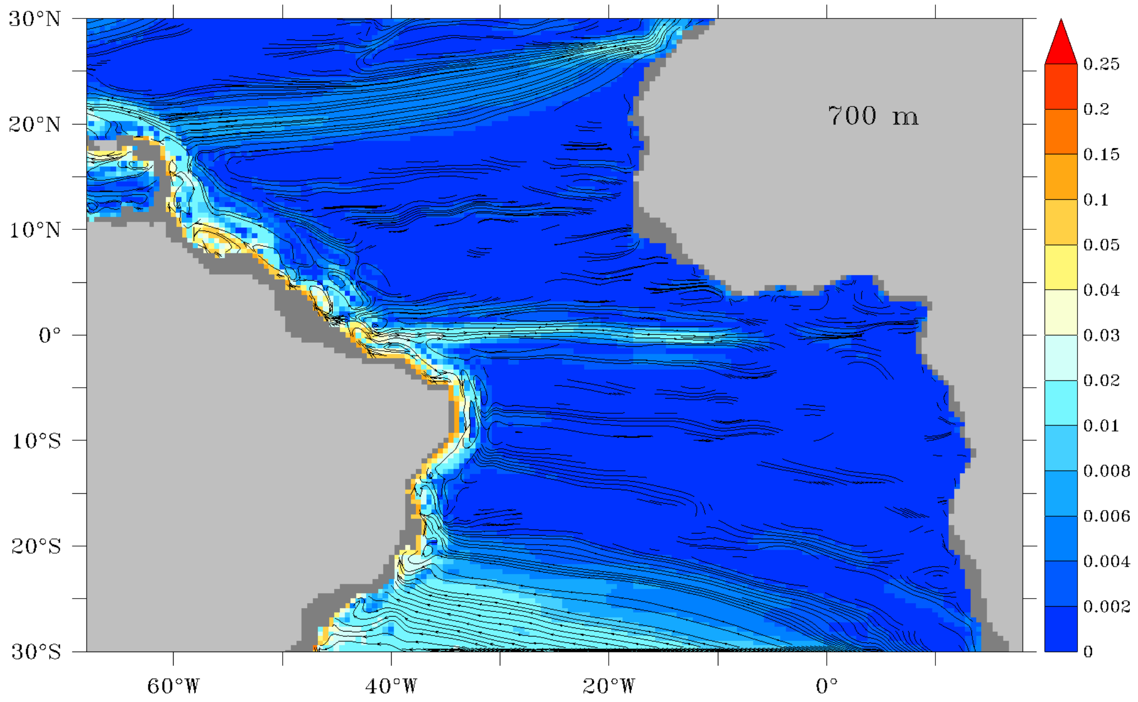

Figure A.10.: Ten year averaged (2000 to 2009) circulation: shaded is speed [m/s] with velocity vectors overlaid.

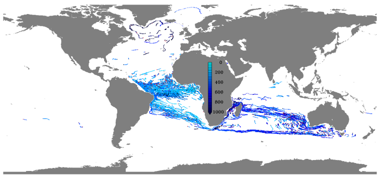

a) 850 m depth TRATL01

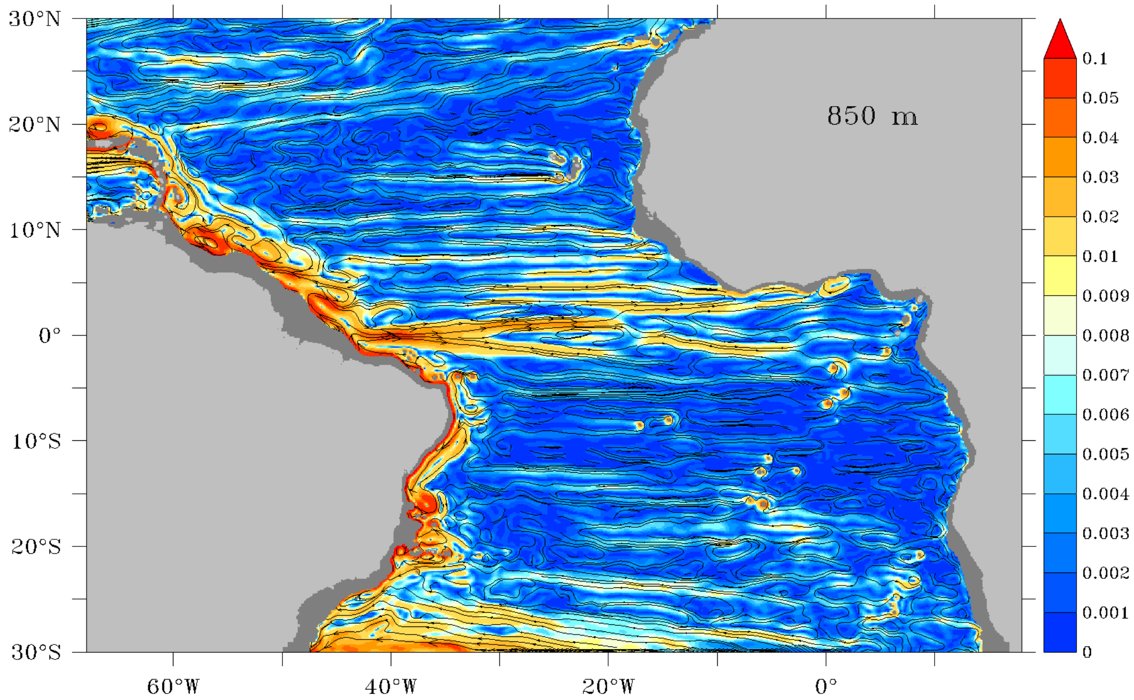

b) 850 m depth ORCA05

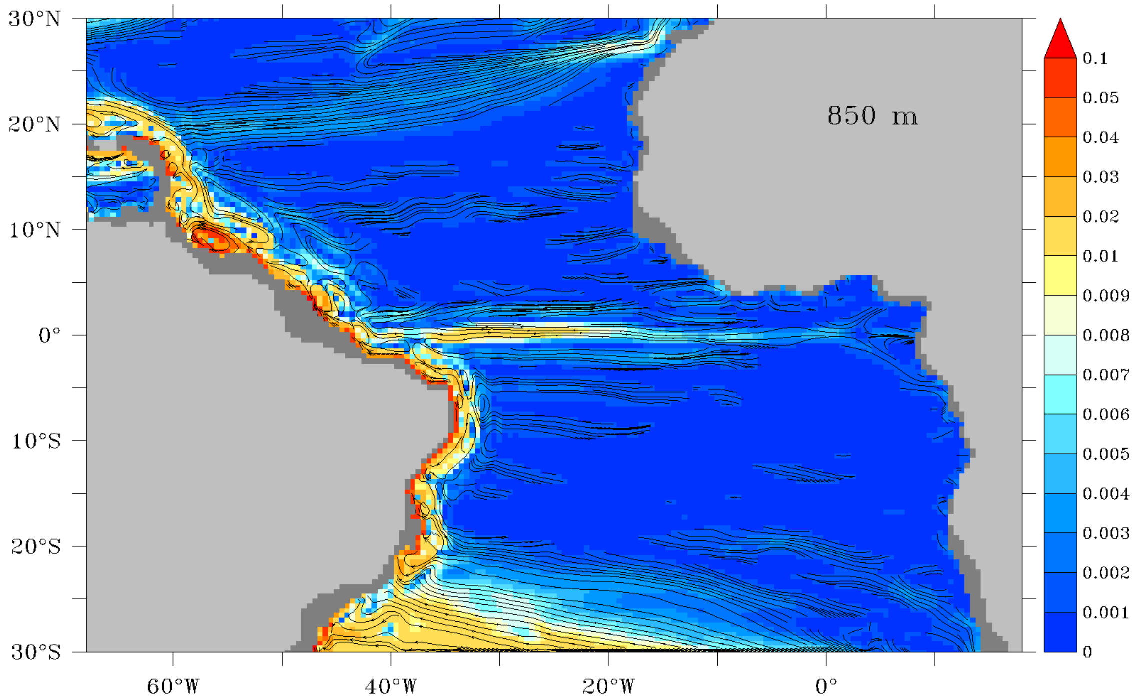

Figure A.11.: Ten year averaged (2000 to 2009) circulation: shaded is speed [m/s] with velocity vectors overlaid.

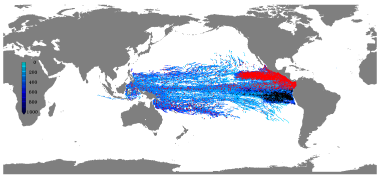

a) 1000 m depth TRATL01

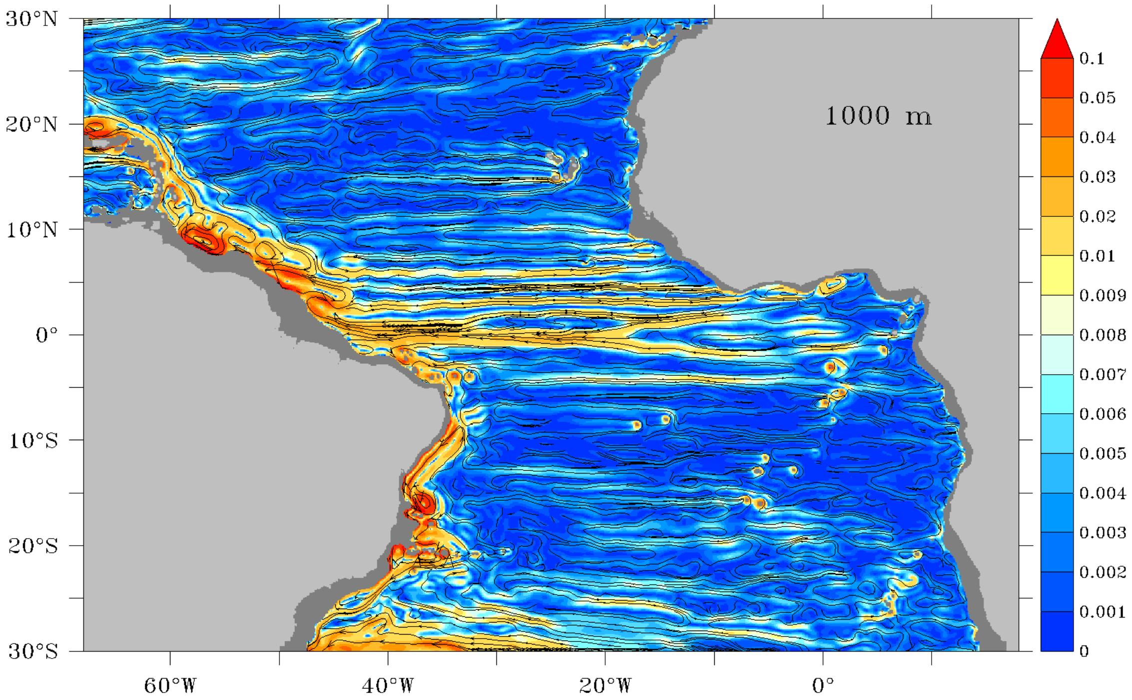

b) 1000 m depth ORCA05

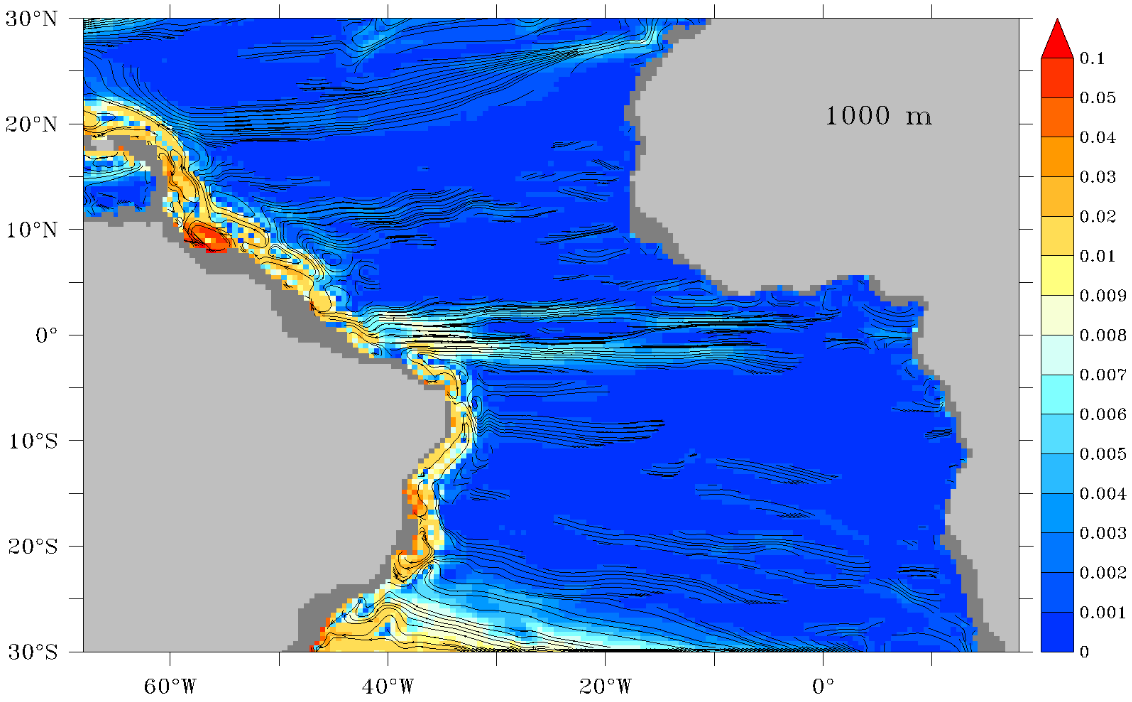

Figure A.12.: Ten year averaged (2000 to 2009) circulation: shaded is speed [m/s] with velocity vectors overlaid.

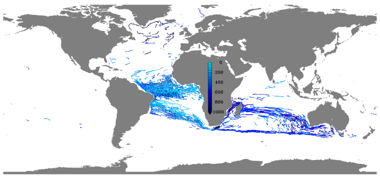

a) 1100 m depth TRATL01

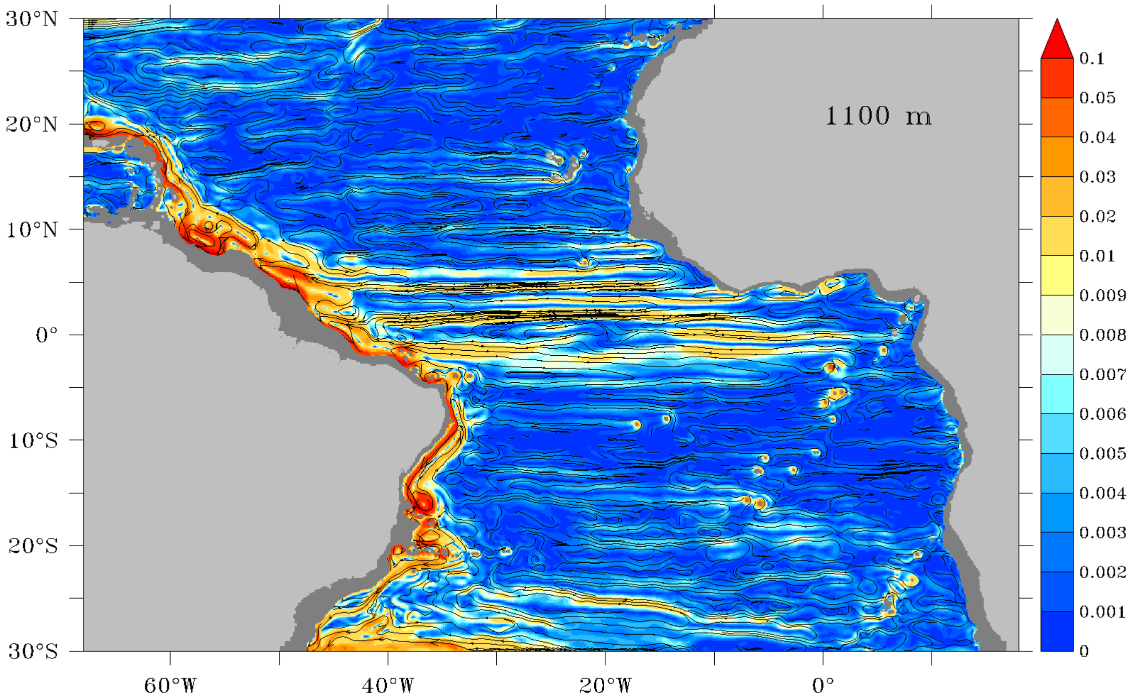

b) 1100 m depth ORCA05

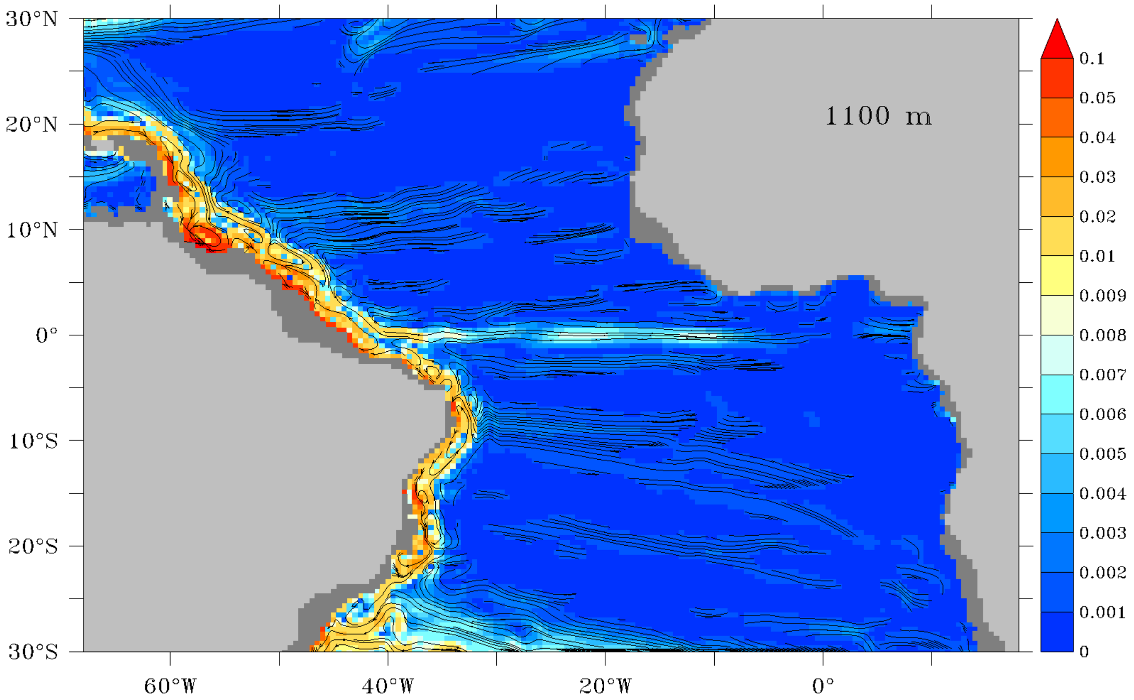

Figure A.13.: Ten year averaged (2000 to 2009) circulation: shaded is speed [m/s] with velocity vectors overlaid.

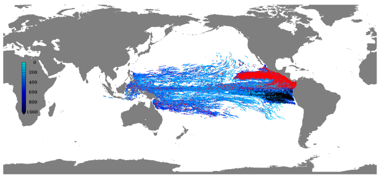

a) 1300 m depth TRATL01

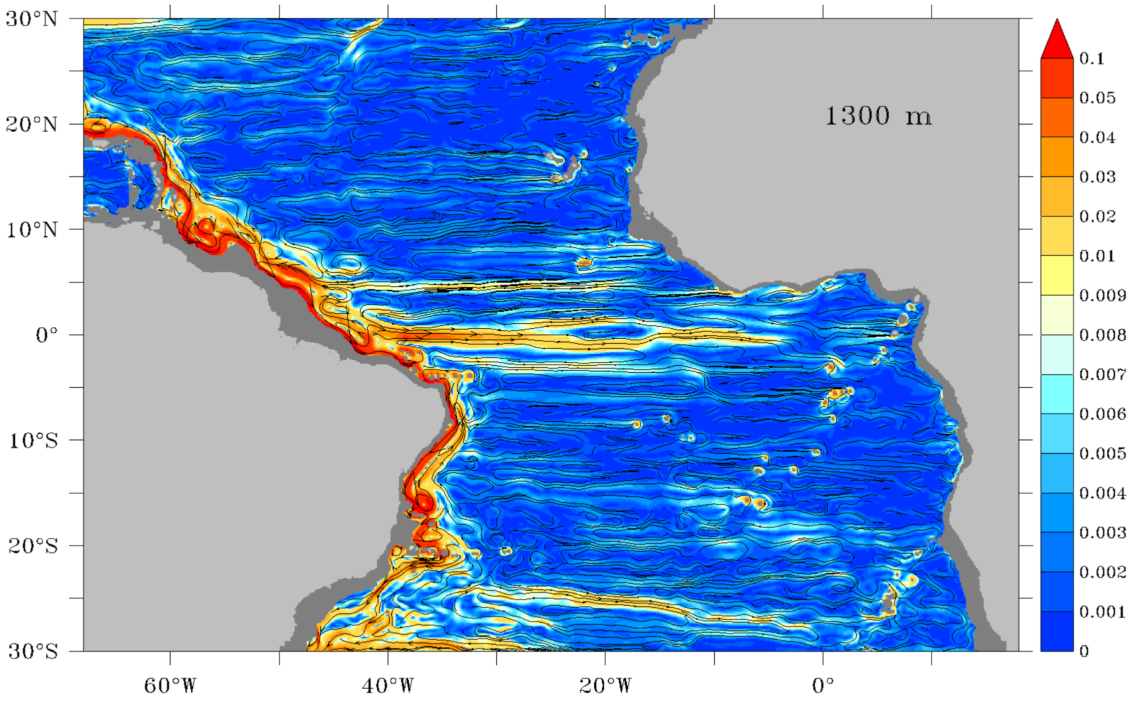

b) 1300 m depth ORCA05

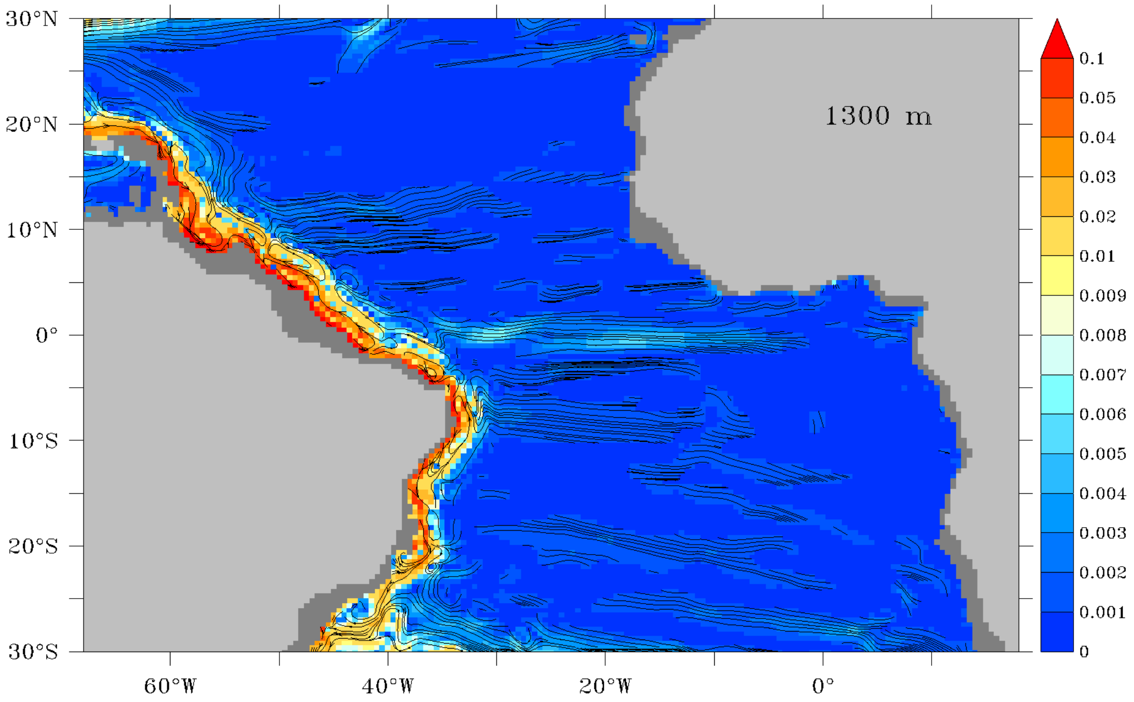

Figure A.14.: Ten year averaged (2000 to 2009) circulation: shaded is speed [m/s] with velocity vectors overlaid.

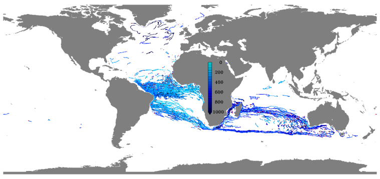

a) 1500 m depth TRATL01

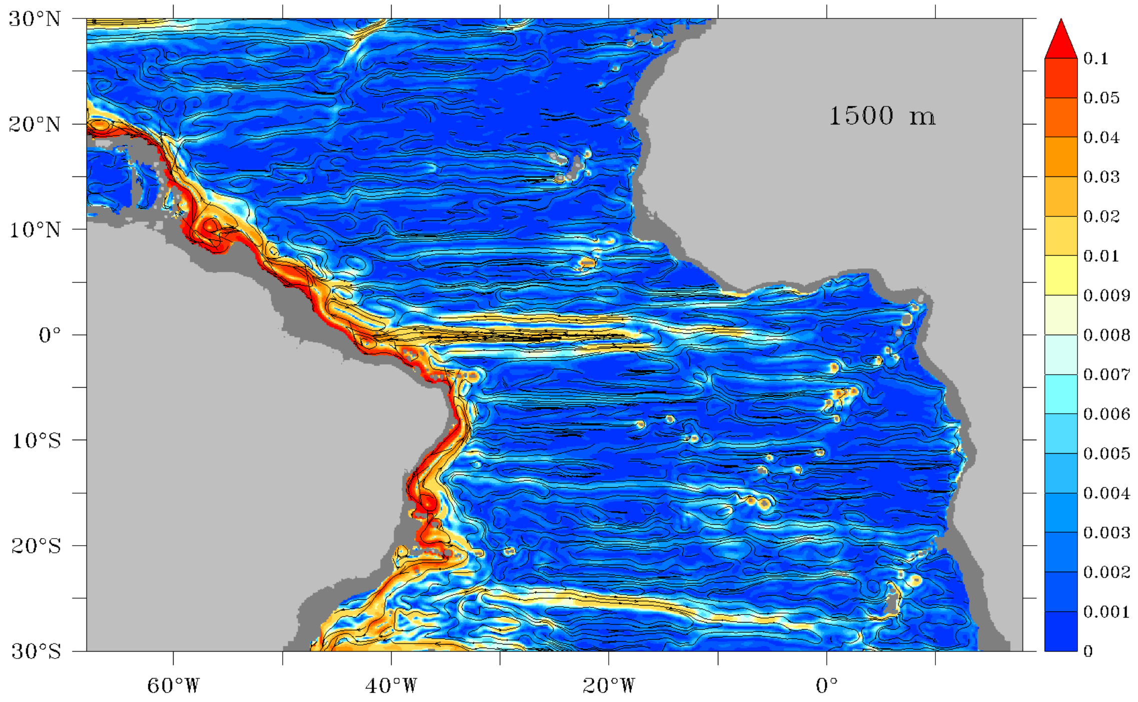

b) 1500 m depth ORCA05

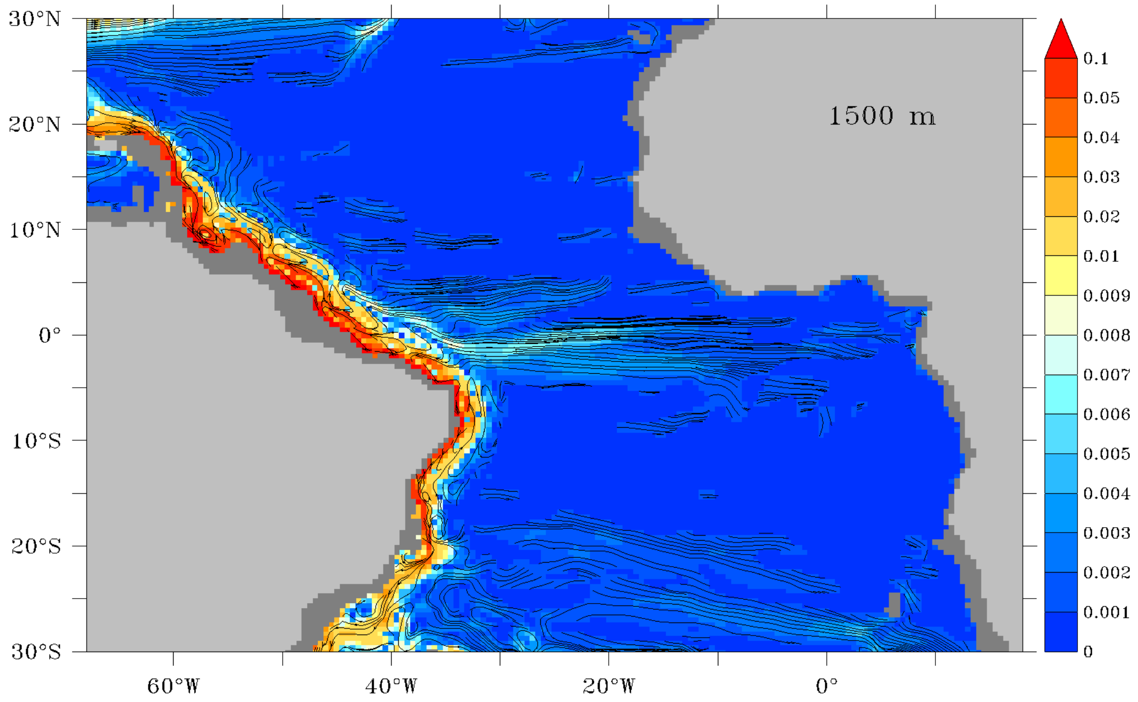

Figure A.15.: Ten year averaged (2000 to 2009) circulation: shaded is speed [m/s] with velocity vectors overlaid.

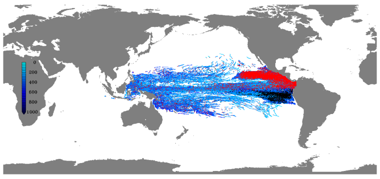

a) 1650 m depth TRATL01

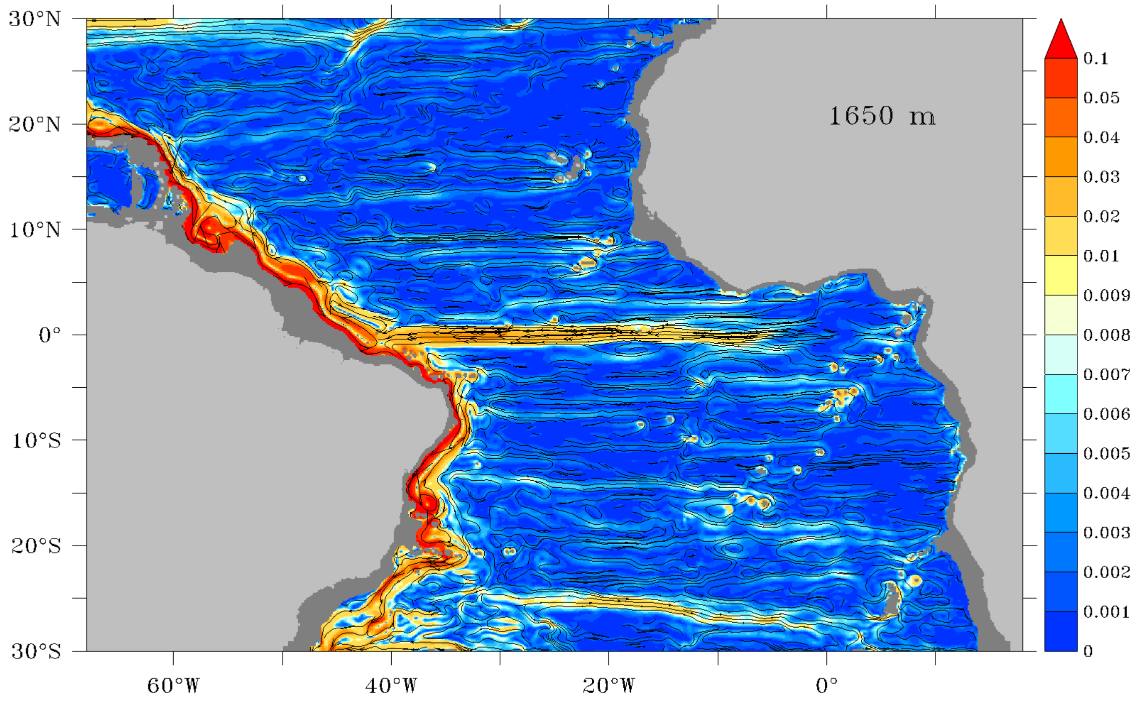

b) 1650 m depth ORCA05

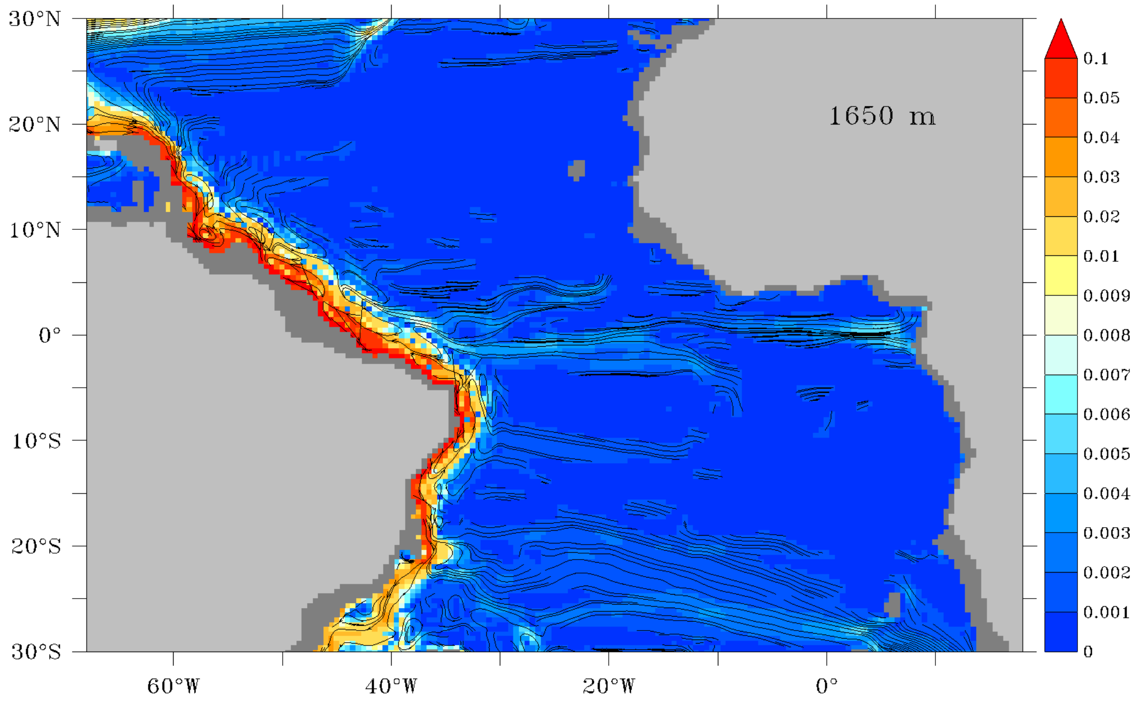

Figure A.16.: Ten year averaged (2000 to 2009) circulation: shaded is speed [m/s] with velocity vectors overlaid.

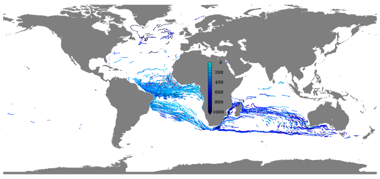

a) 1850 m depth TRATL01

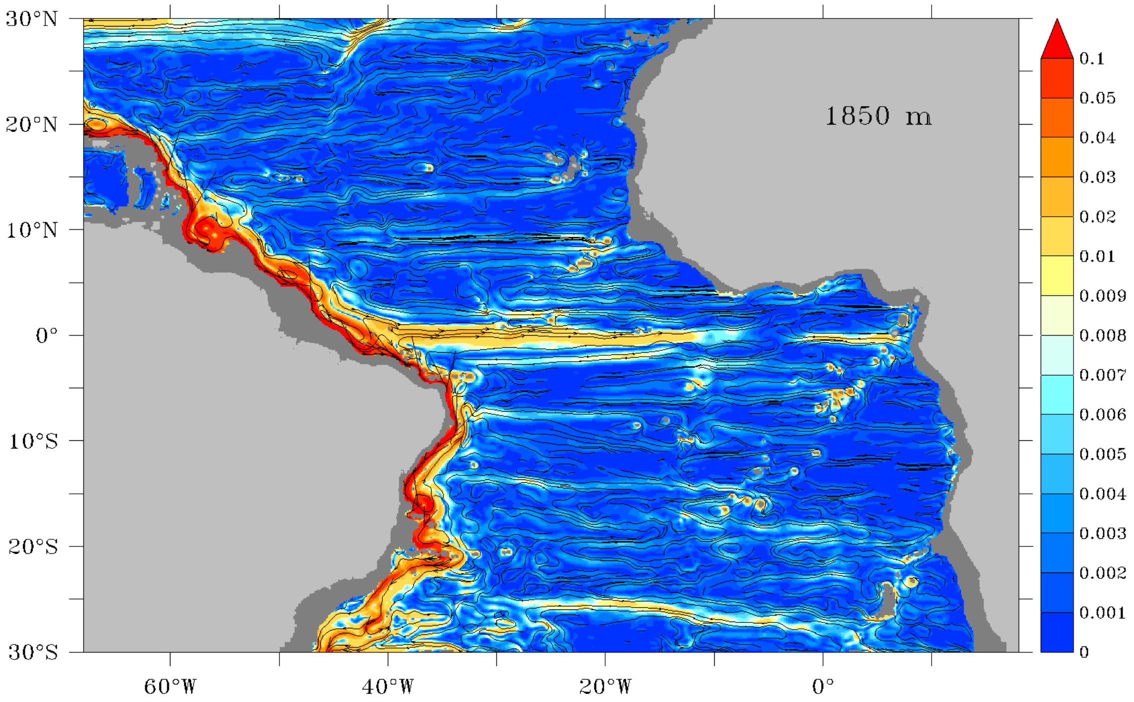

b) 1850 m depth ORCA05

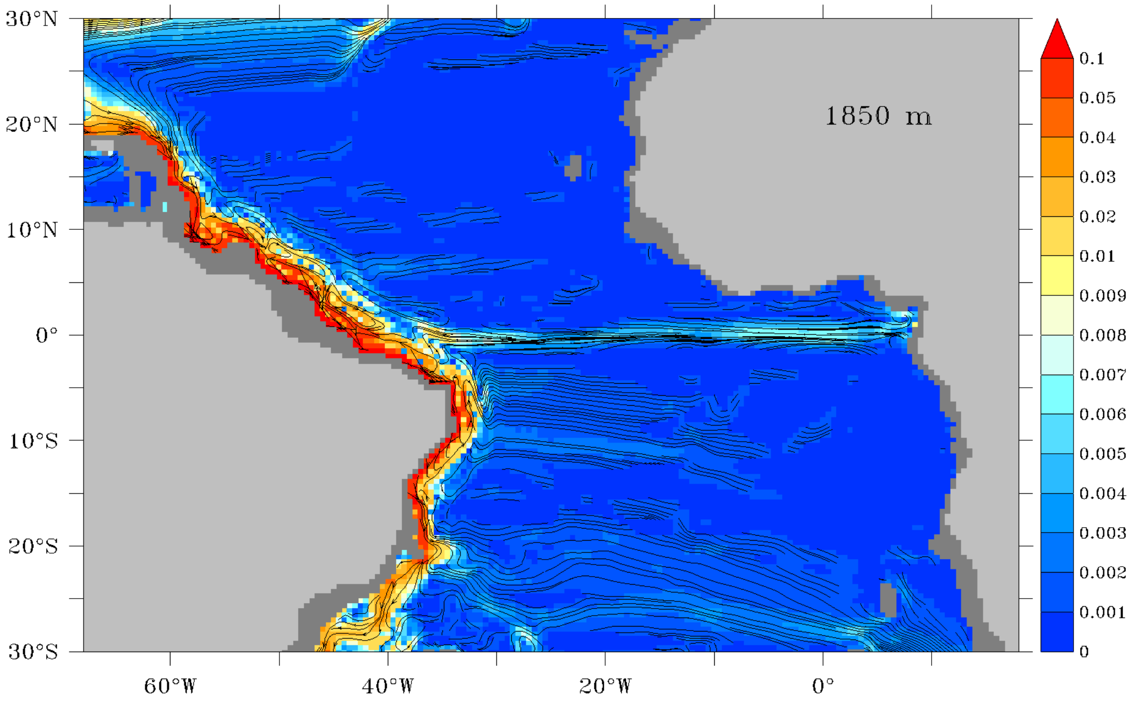

Figure A.17.: Ten year averaged (2000 to 2009) circulation: shaded is speed [m/s] with velocity vectors overlaid.

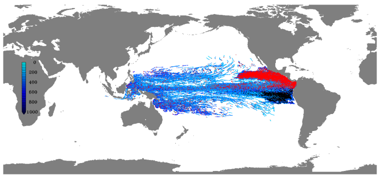

a) 2050 m depth TRATL01

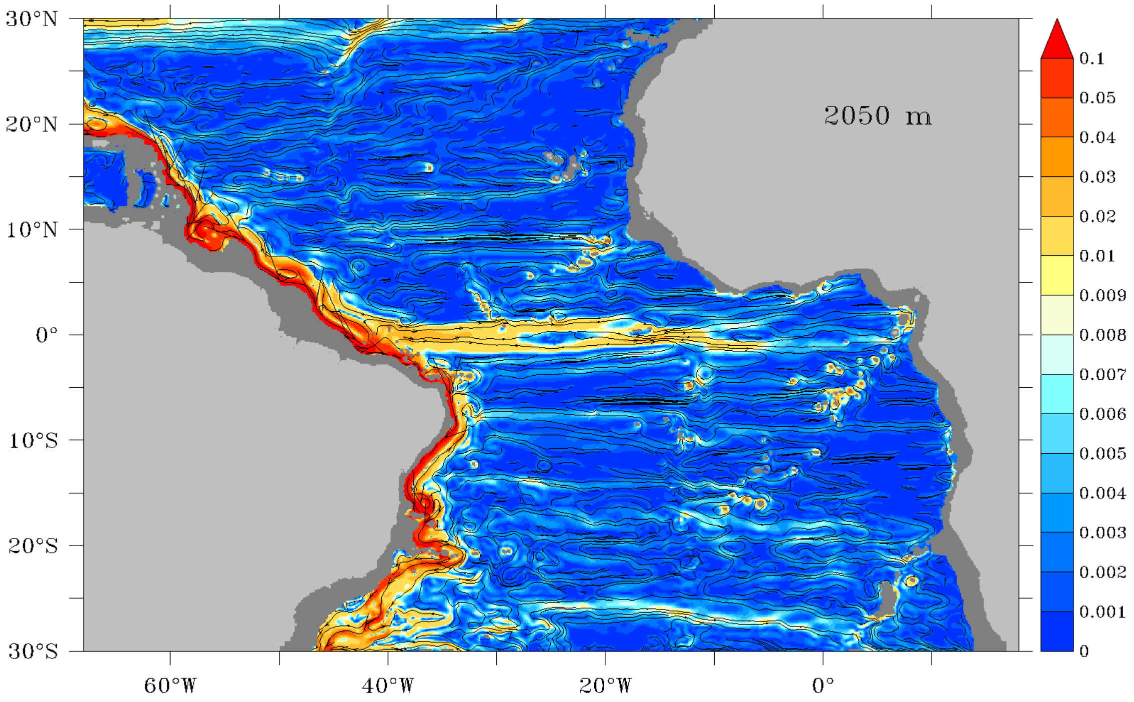

b) 2050 m depth ORCA05

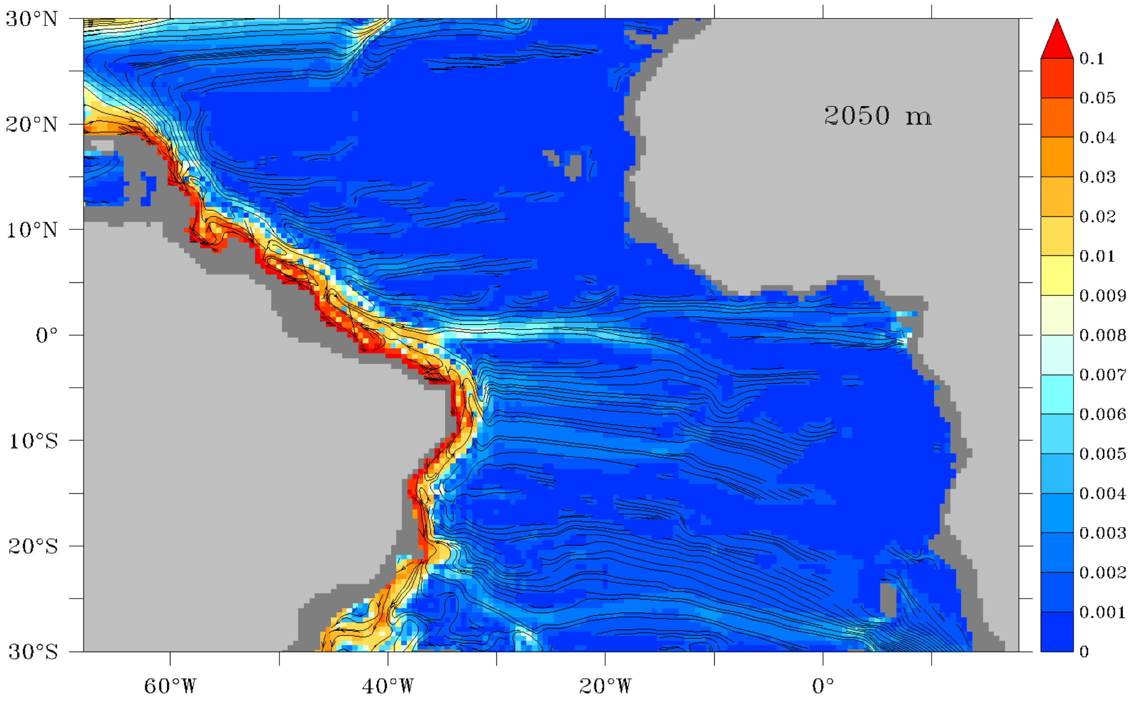

Figure A.18.: Ten year averaged (2000 to 2009) circulation: shaded is speed [m/s] with velocity vectors overlaid.

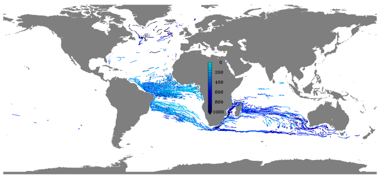

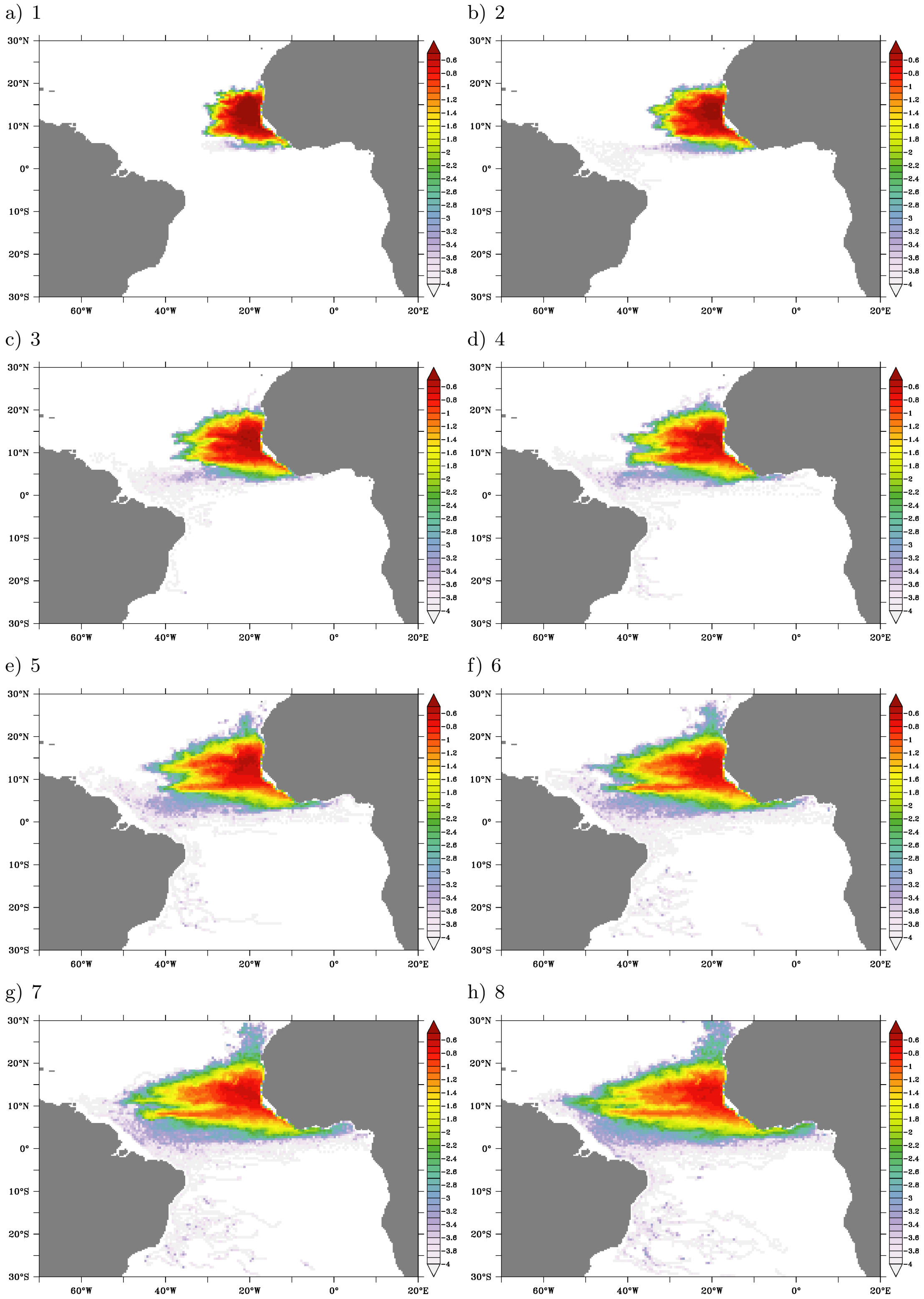

Figure A.19.: Depth integrated particle population [in % of released particles per 0.5° square on a logarithmic scale] in the first to eighth (a to h) year after release in the nOMZ in TRATL01.

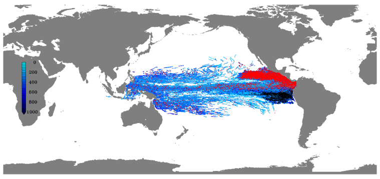

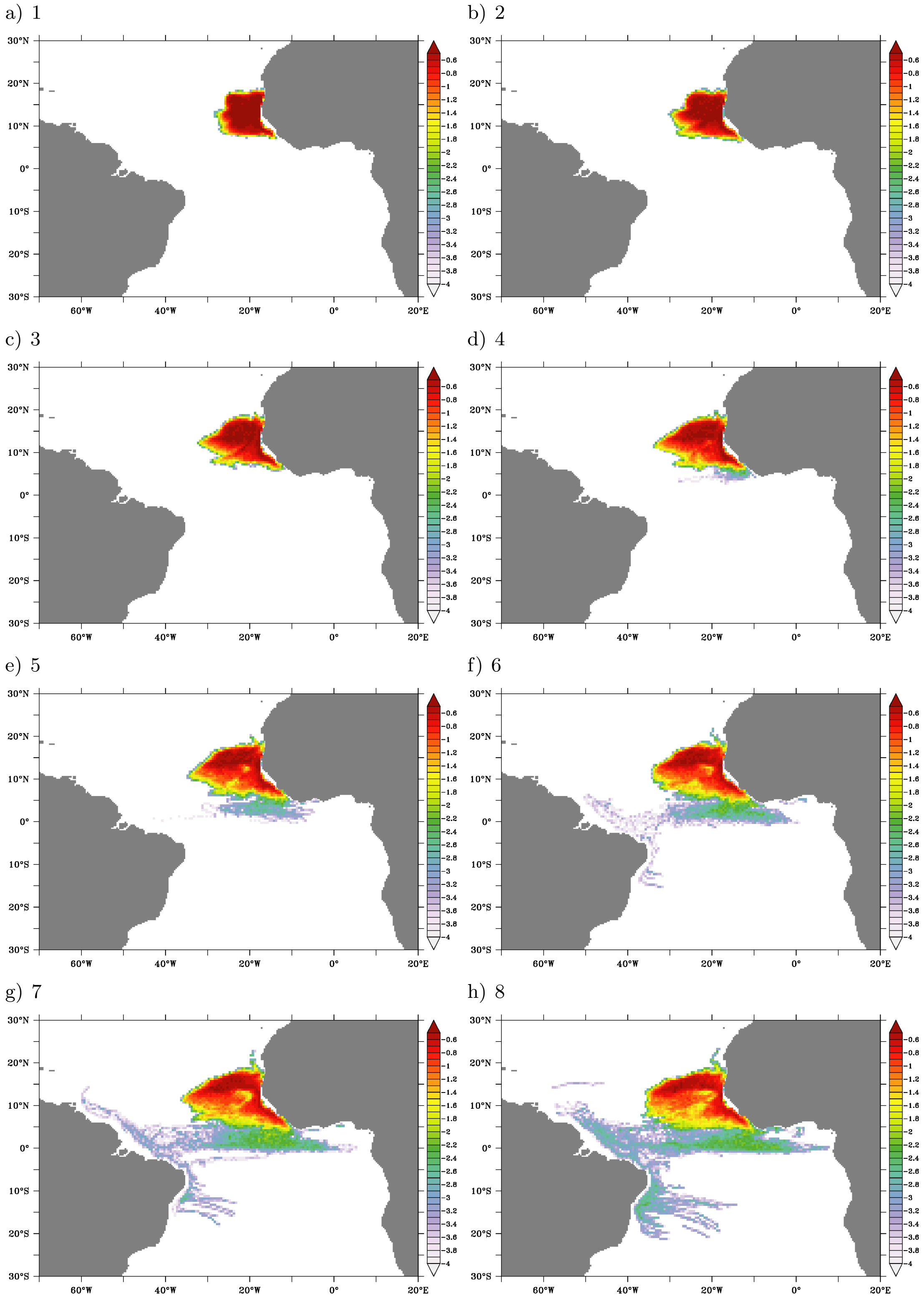

Figure A.20.: Depth integrated particle population [in % of released particles per 0.5° square on a logarithmic scale] in the first to eighth (a to h) year after release in the nOMZ in ORCA05.

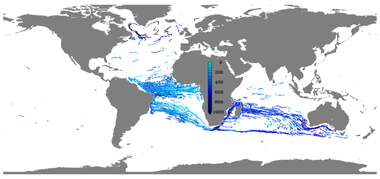

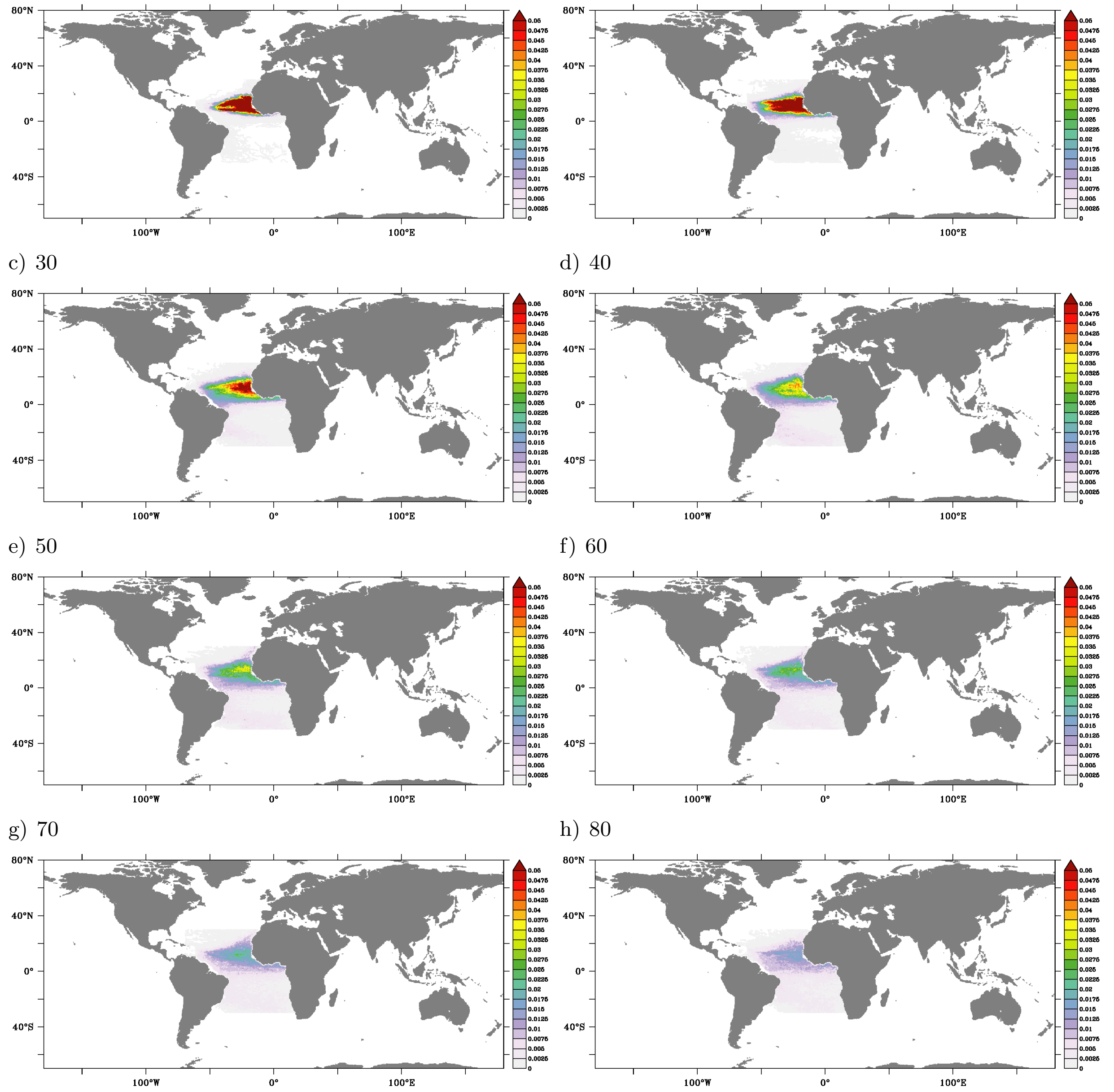
a) 10

b) 20

c) 30

d) 40

e) 50

f) 60

g) 70

h) 80

Figure A.21.: Depth integrated particle population [in % of released particles per 0.5° square] 10 a), 20 b), 30 c), 40 d), 50 e), 60 f), 70 g) and 80 h) years after release in the nOMZ in TRATL01.

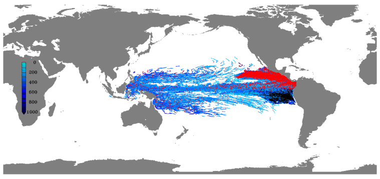

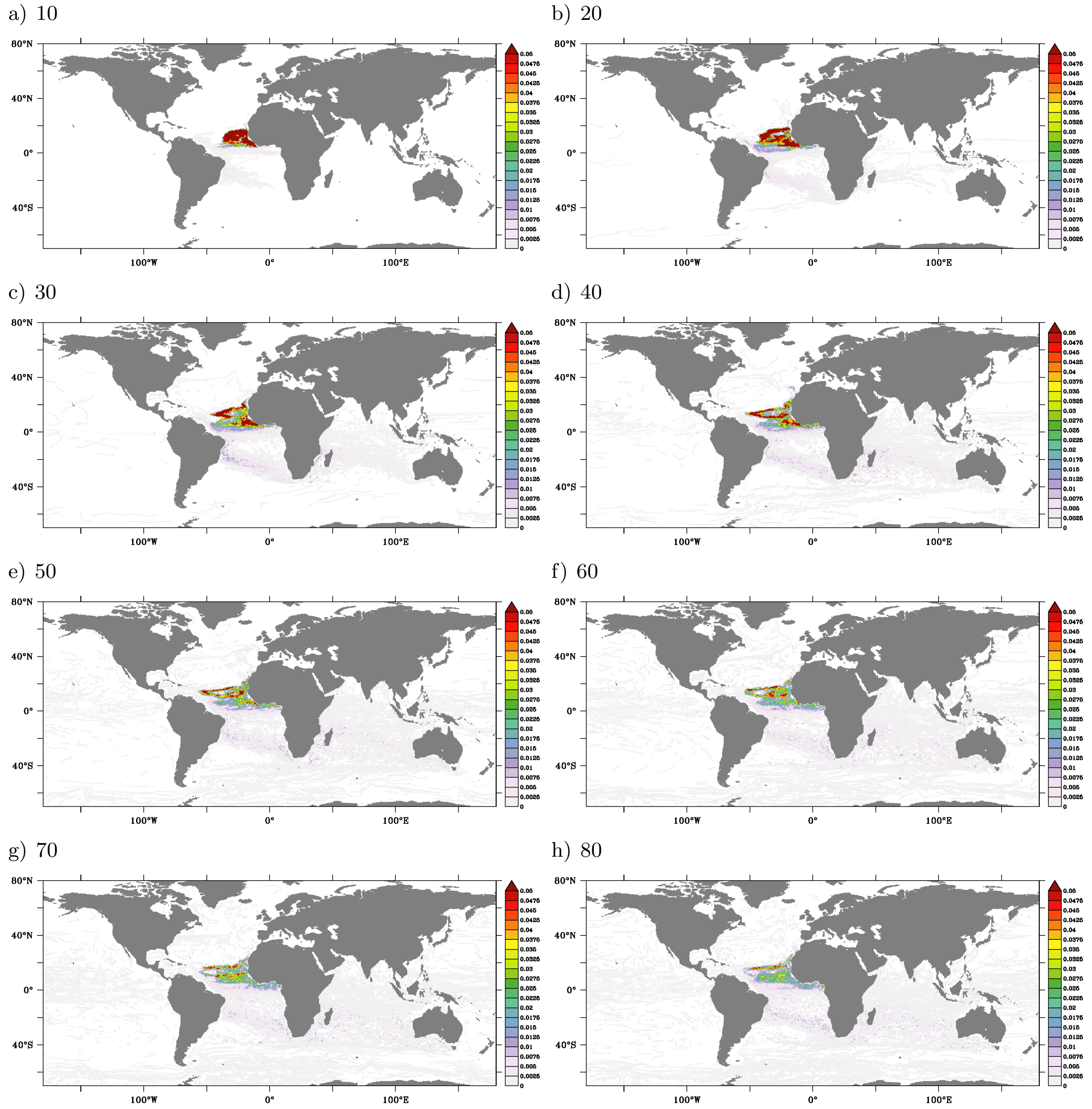
a) 10 b) 20 c) 30 d) 40 e) 50 f) 60 g) 70 h) 80

Figure A.22.: Depth integrated particle population [in % of released particles per 0.5° square] 10 a), 20 b), 30 c), 40 d), 50 e), 60 f), 70 g) and 80 h) years after release in the nOMZ in ORCA05.

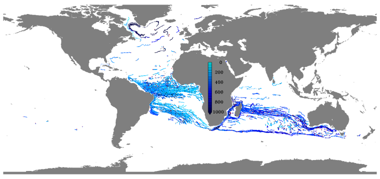

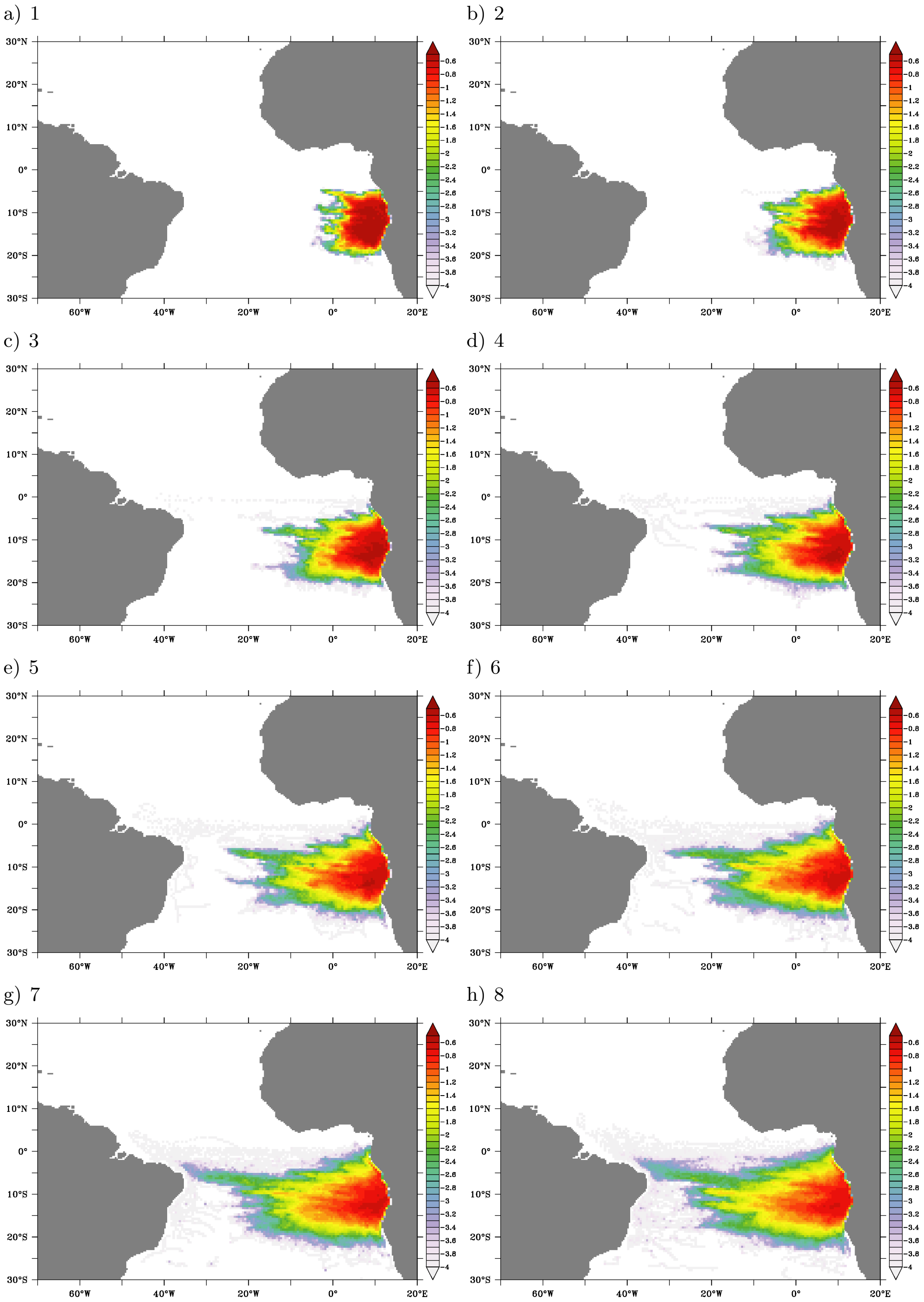

Figure A.23.: Depth integrated particle population [in % of released particles per 0.5° square on a logarithmic scale] in the first to eighth (a to h) year after release in the sOMZ in TRATL01.

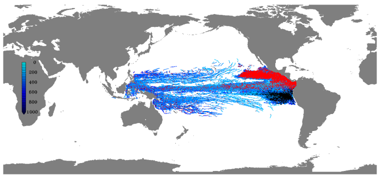

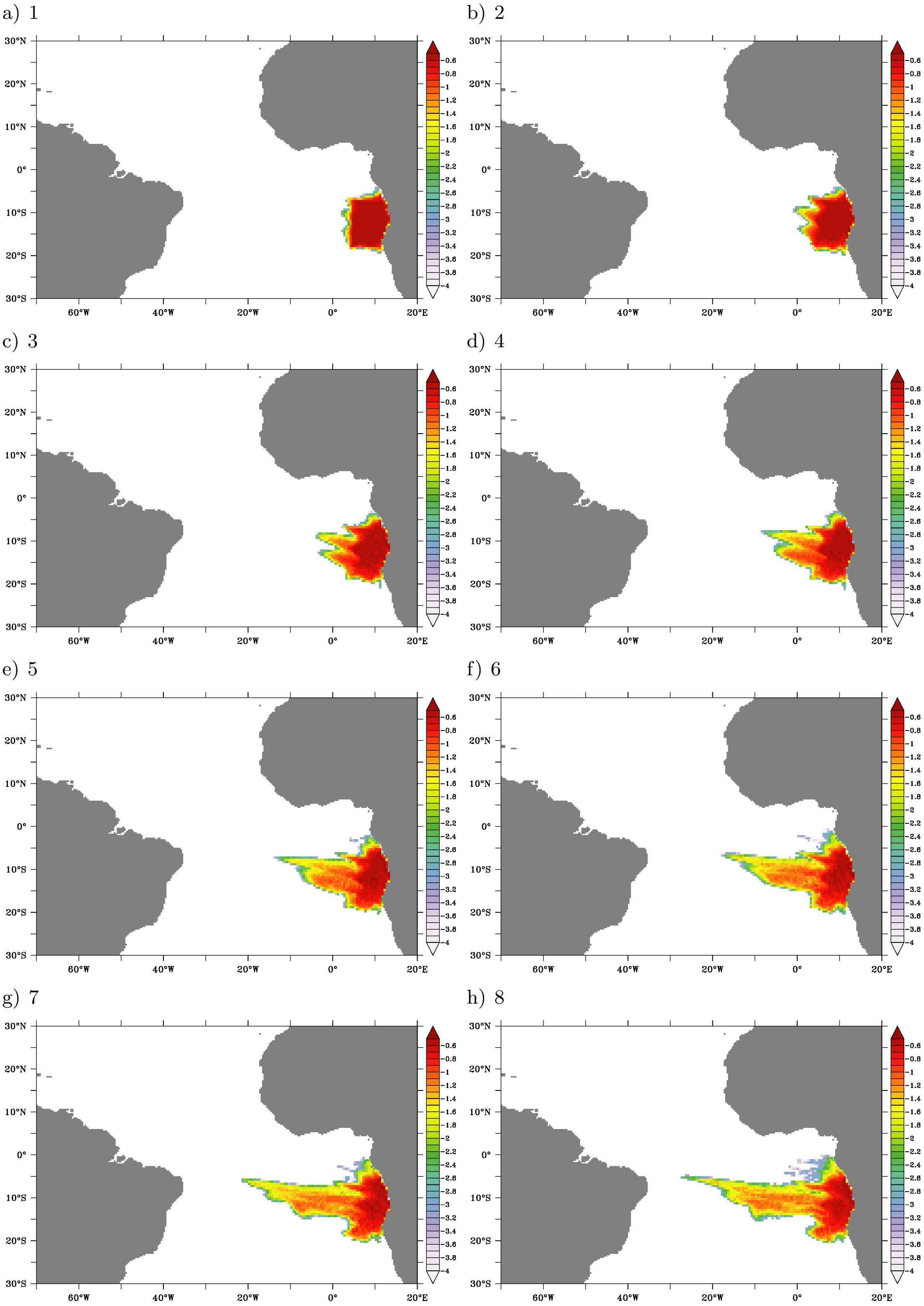
a) 1
b) 2
c) 3
d) 4
e) 5
f) 6
g) 7
h) 8

Figure A.24.: Depth integrated particle population [in % of released particles per 0.5° square on a logarithmic scale] in the first to eighth (a to h) year after release in the sOMZ in ORCA05.

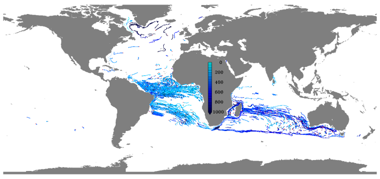

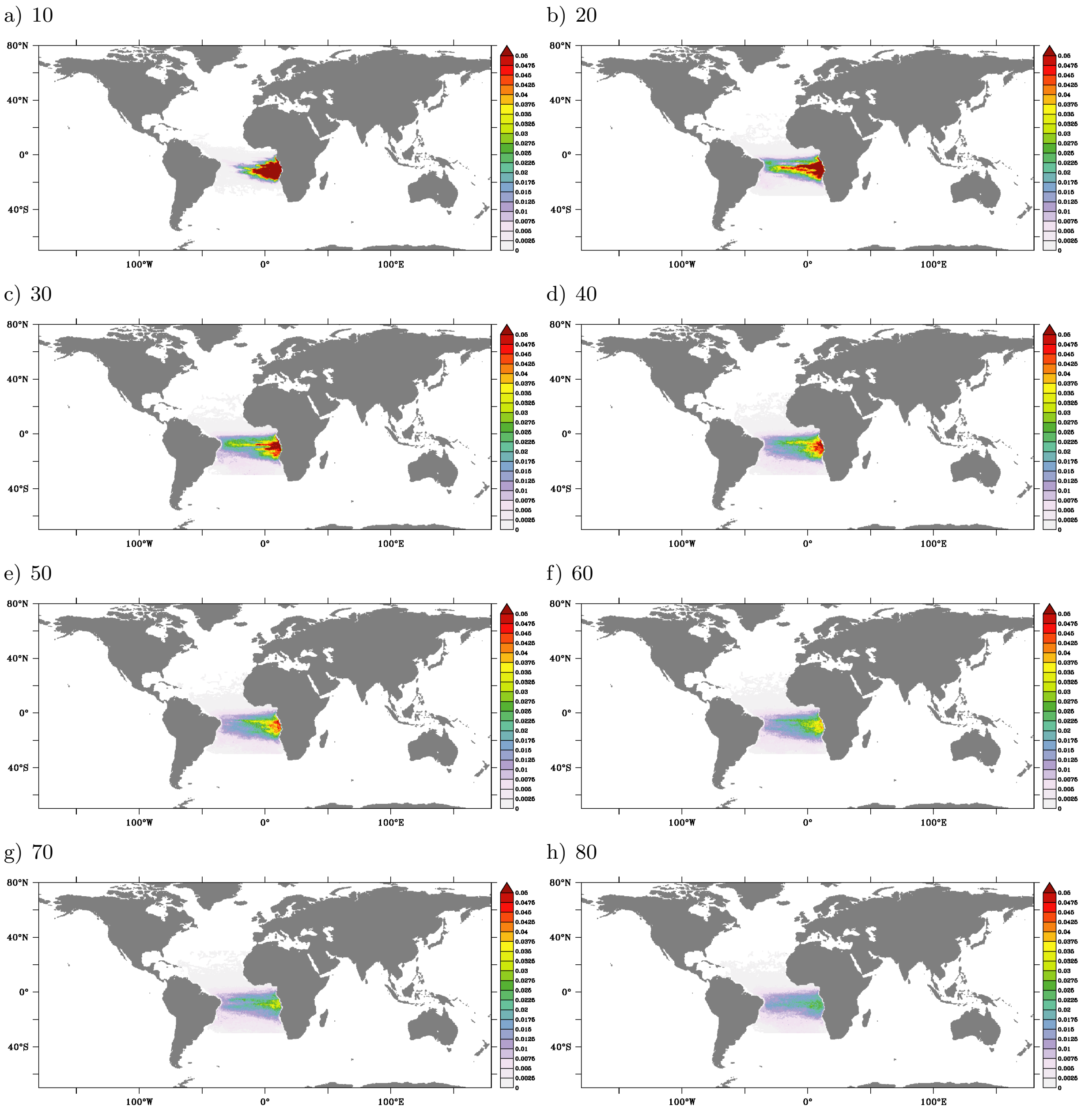

Figure A.25.: Depth integrated particle population [in % of released particles per 0.5° square] 10 a), 20 b), 30 c), 40 d), 50 e), 60 f), 70 g) and 80 h) years after release in the sOMZ in TRATL01.

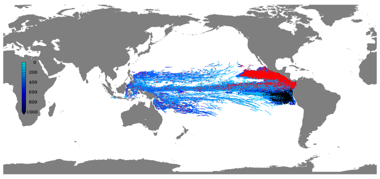

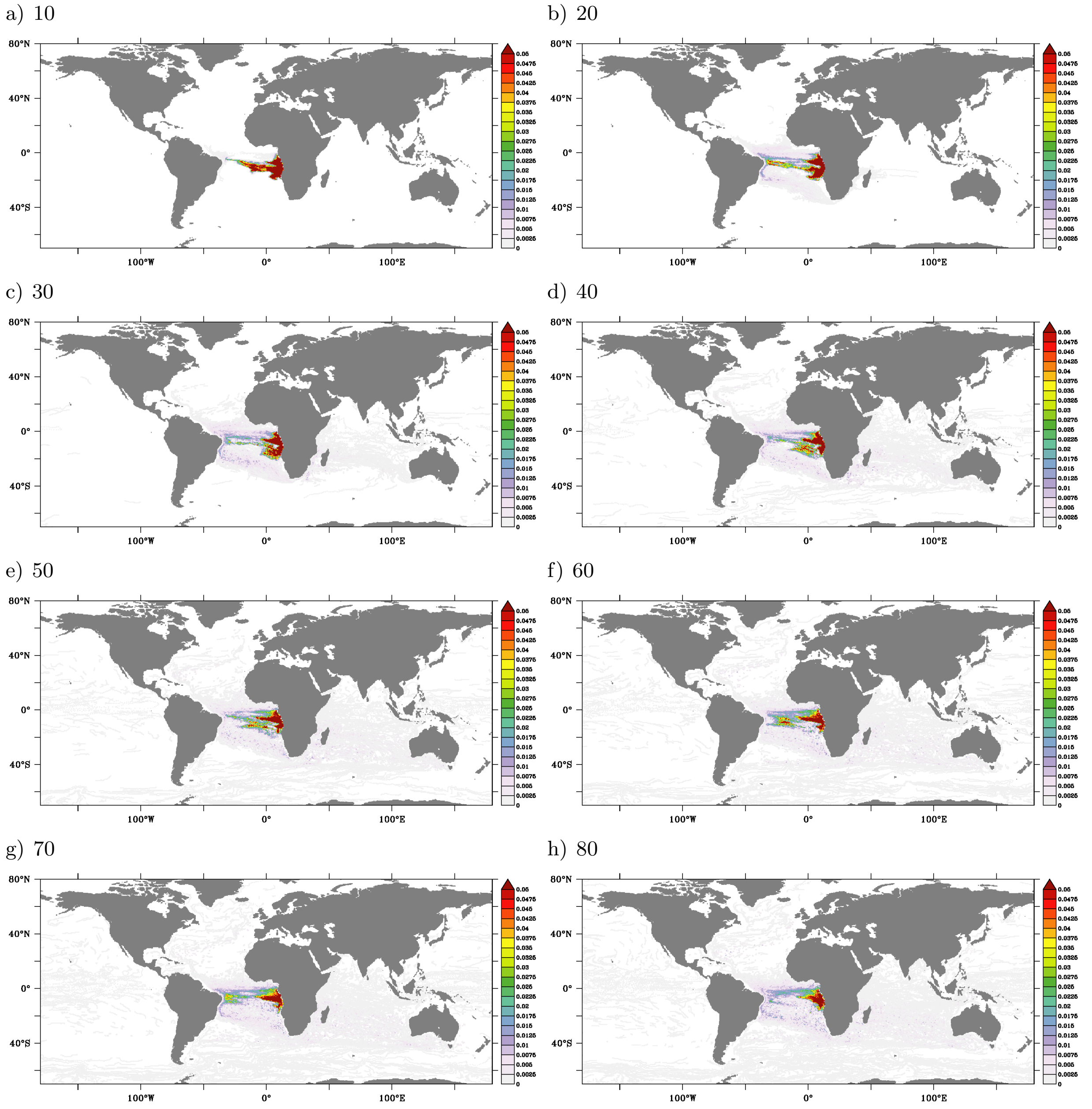

Figure A.26.: Depth integrated particle population [in % of released particles per 0.5° square] 10 a), 20 b), 30 c), 40 d), 50 e), 60 f), 70 g) and 80 h) years after release in the sOMZ in ORCA05.

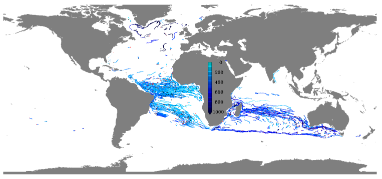

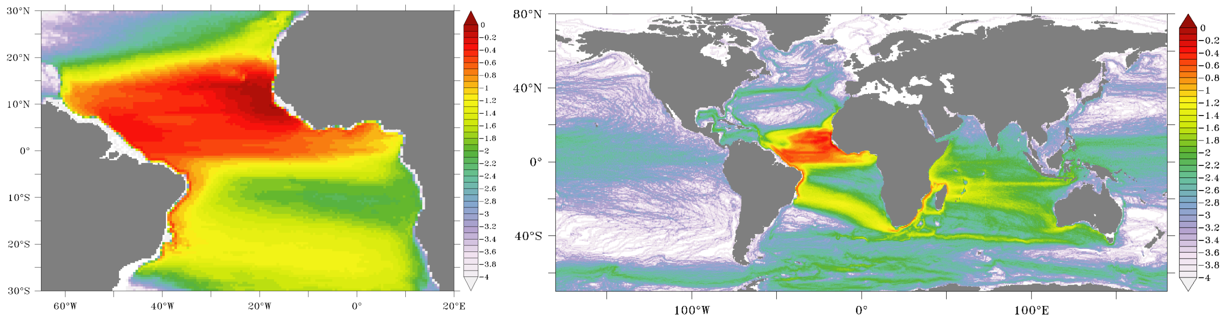
a) nOMZ TRATL01 first arrivals

b) nOMZ ORCA05 first arrivals

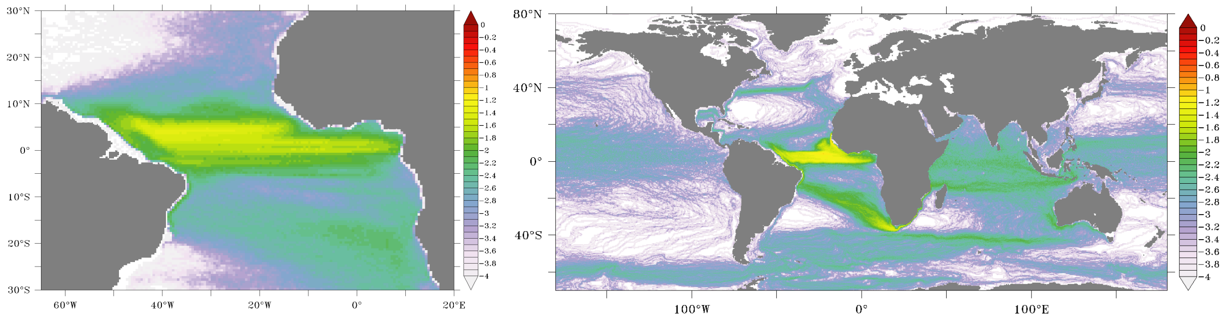
c) surface to 200 m

d) surface to 200 m

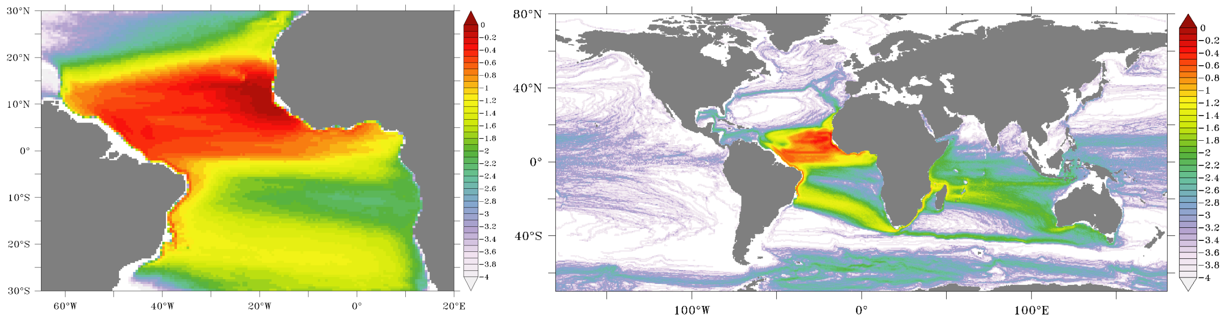
e) 200 m to 800 m

f) 200 m to 800 m

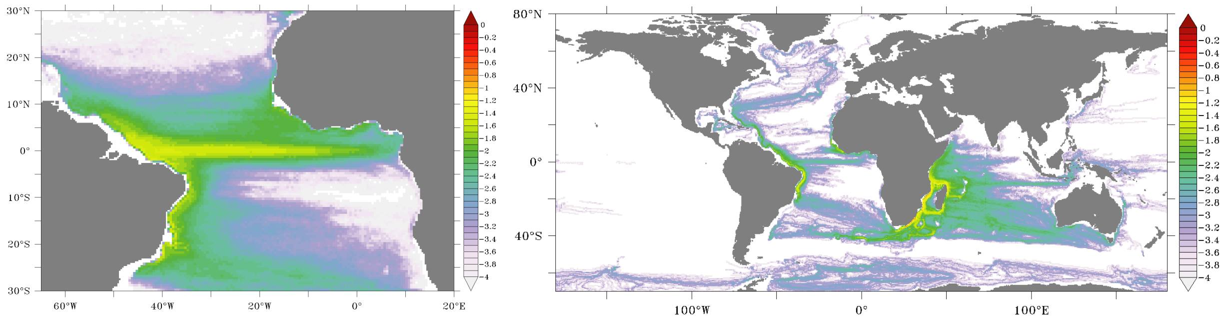
g) 800 m to bottom

h) 800 m to bottom

Figure A.27.: Depth integrated particle population derived as "first arrivals" [in % of released particles per 0.5° square on a logarithmic scale] temporally integrated over the full period of the Lagrangian experiments of 80 years for particles released in the Atlantic nOMZ in TRATL01 (left) and ORCA05 (right) for the full depth (a and b), the uppermost 200 m of the water column (c and d), 200 m to 800 m depth (e and f) and 800 m depth to the seafloor (g and h).

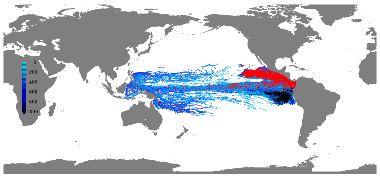

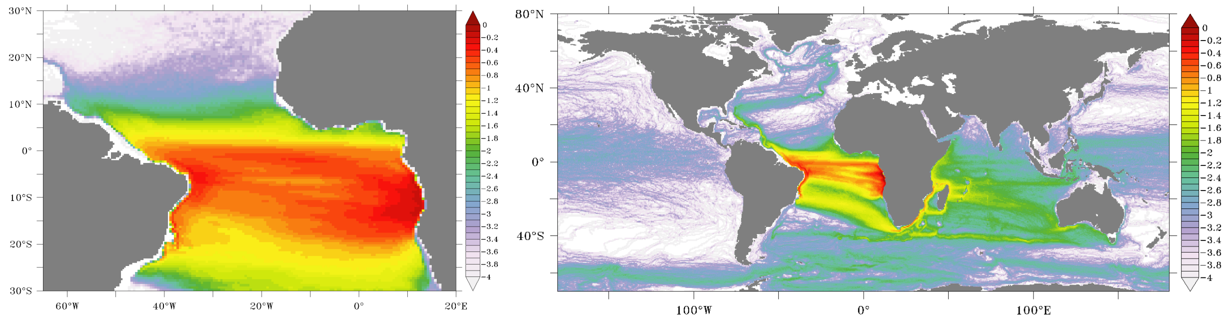
a) sOMZ TRATL01 first arrivals

b) sOMZ ORCA05 first arrivals

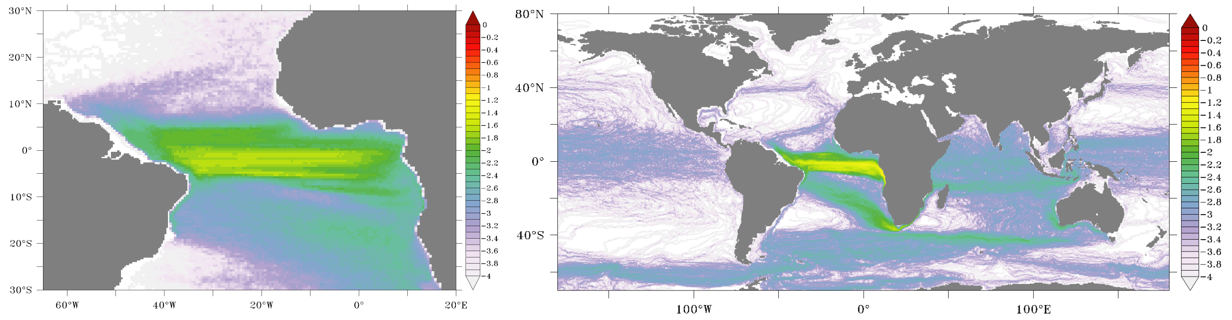
c) surface to 200 m

d) surface to 200 m

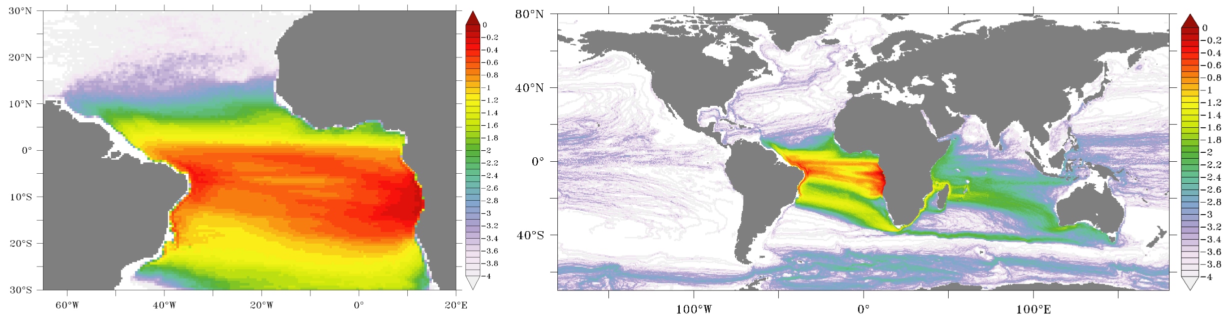
e) 200 m to 800 m

f) 200 m to 800 m

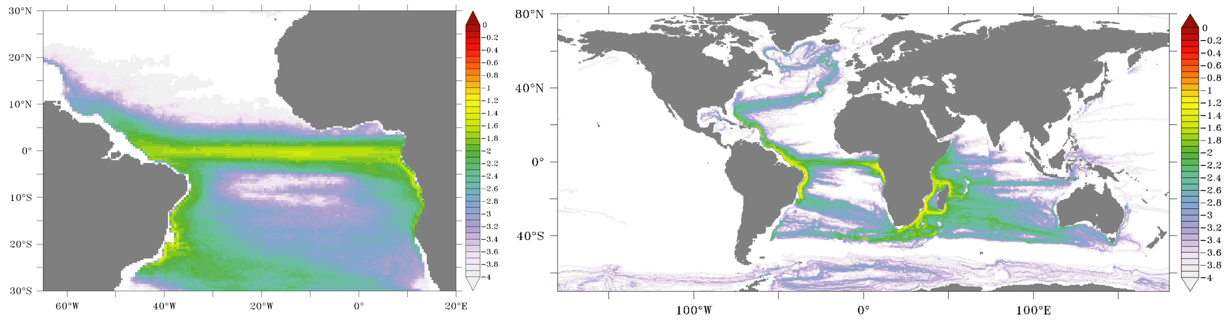
g) 800 m to bottom

h) 800 m to bottom

Figure A.28.: Depth integrated particle population derived as "first arrivals" [in % of released particles per 0.5° square on a logarithmic scale] temporally integrated over the full period of the Lagrangian experiments of 80 years for particles released in the Atlantic sOMZ in TRATL01 (left) and ORCA05 (right) for the full depth (a and b), the uppermost 200 m of the water column (c and d), 200 m to 800 m depth (e and f) and 800 m depth to the seafloor (g and h).

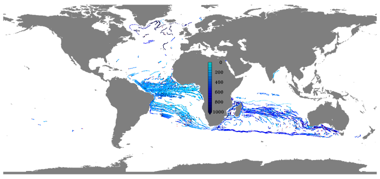

a) Surface TROPAC01

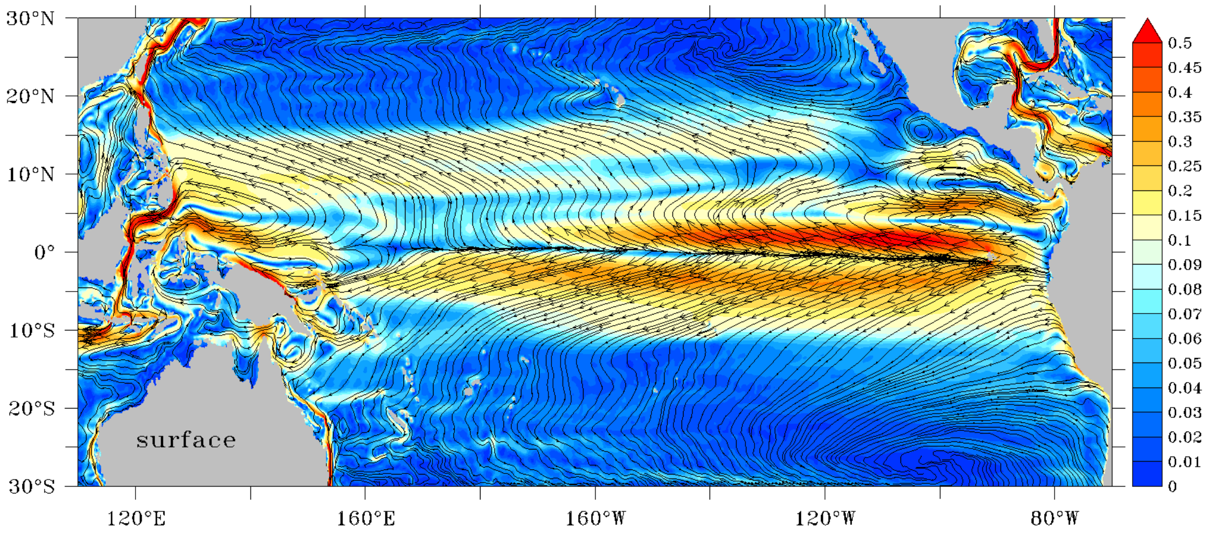

b) Surface ORCA05

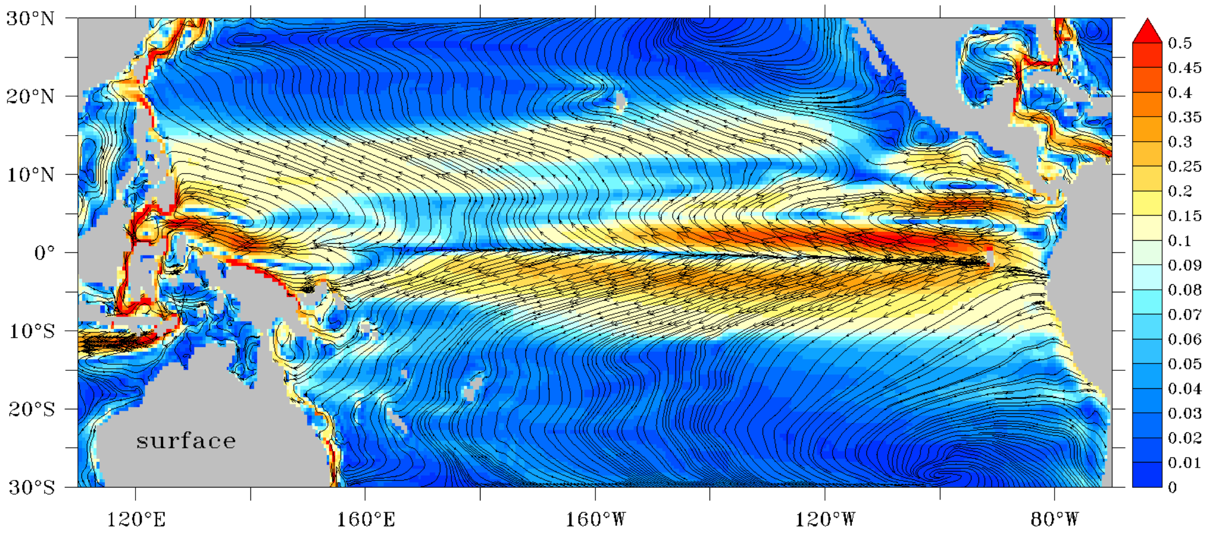

Figure A.29.: Ten year averaged (2000 to 2009) circulation: shaded is speed [m/s] with velocity vectors overlaid.

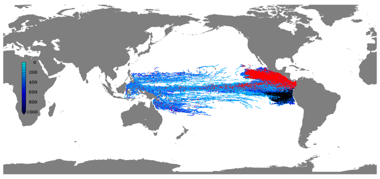

a) 25 m depth TROPAC01

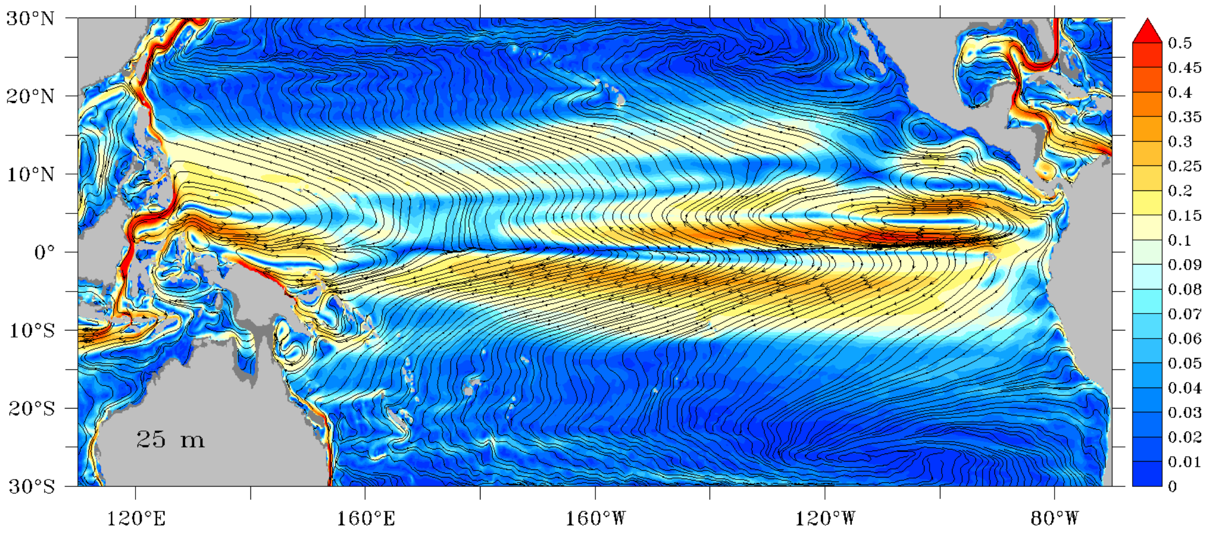

b) 25 m depth ORCA05

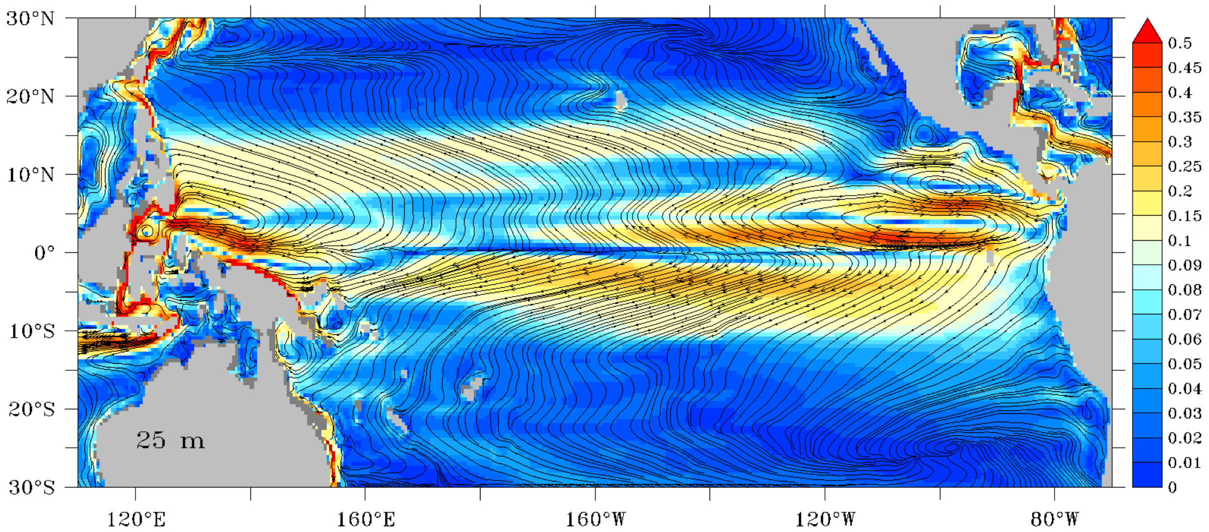

Figure A.30.: Ten year averaged (2000 to 2009) circulation: shaded is speed [m/s] with velocity vectors overlaid.

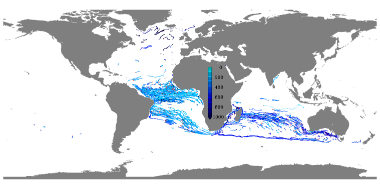

a) 50 m depth TROPAC01

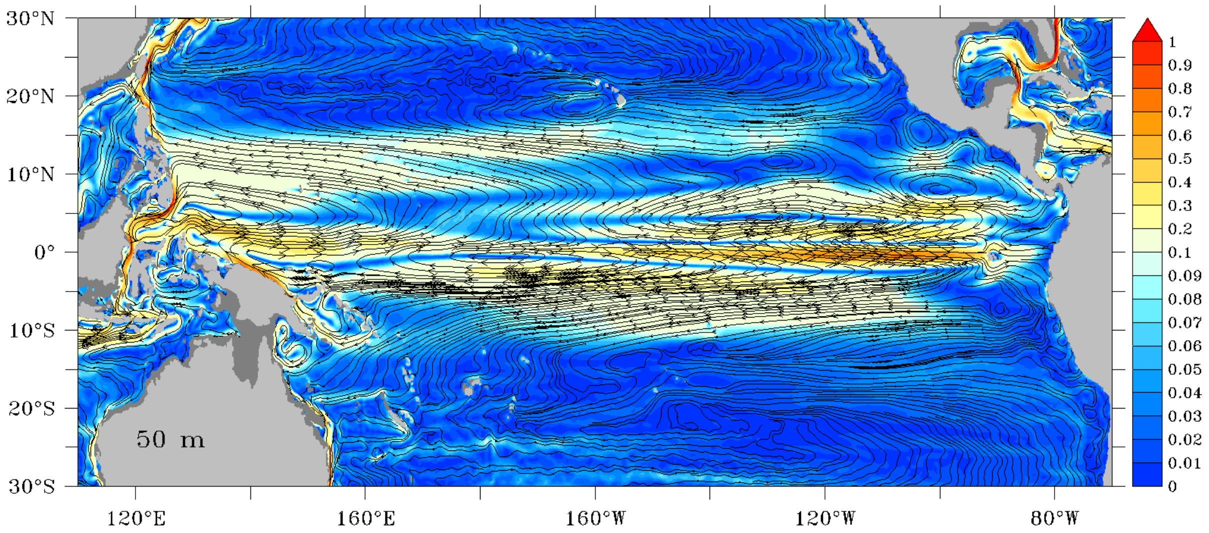

b) 50 m depth ORCA05

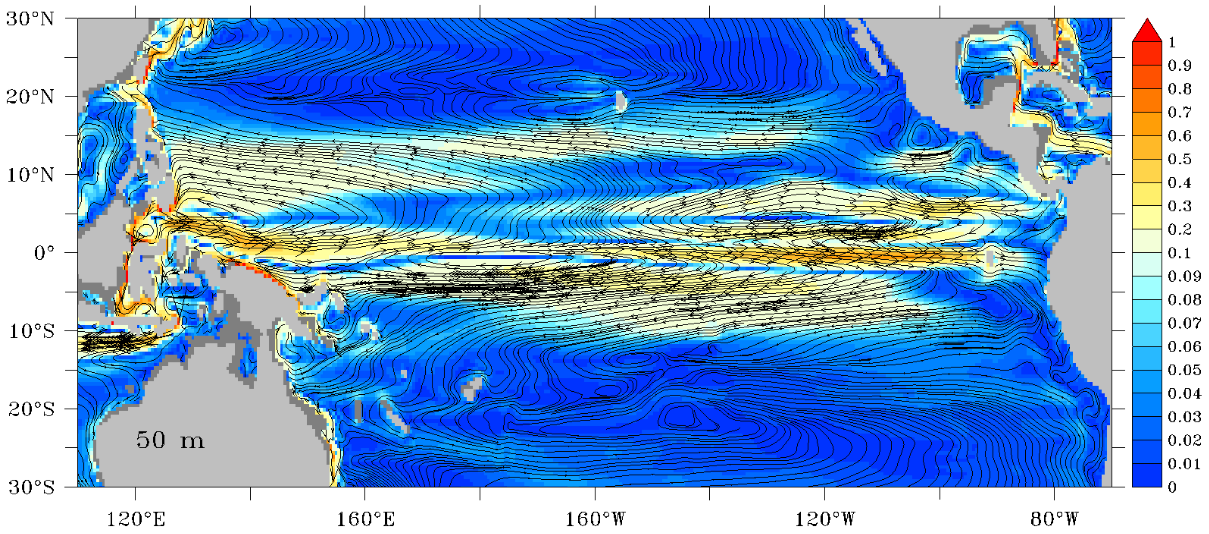

Figure A.31.: Ten year averaged (2000 to 2009) circulation: shaded is speed [m/s] with velocity vectors overlaid.

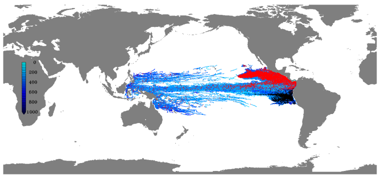

a) 100 m depth TROPAC01

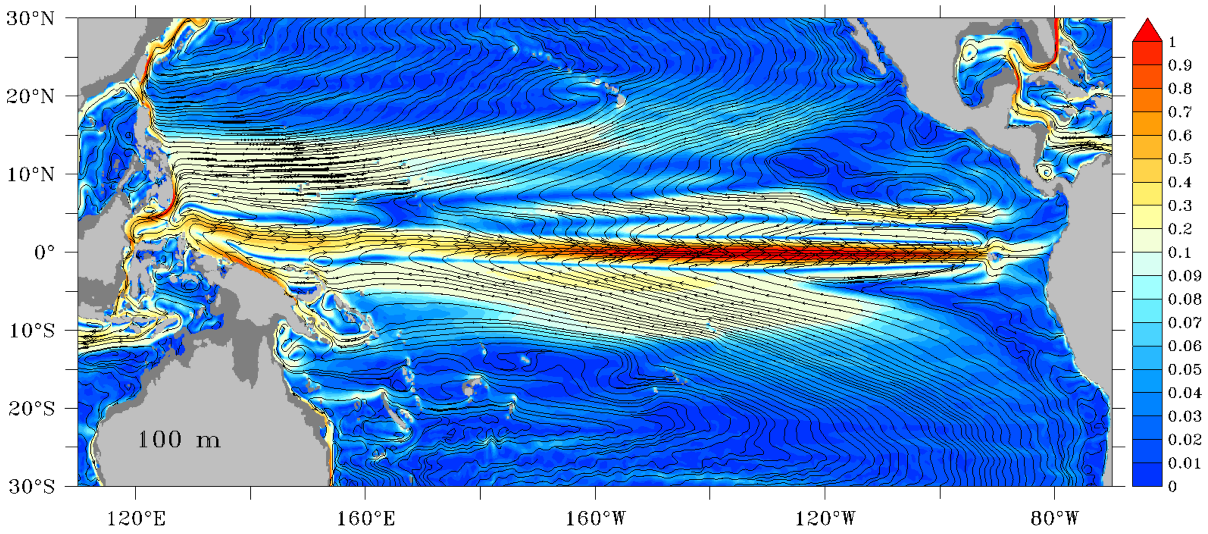

b) 100 m depth ORCA05

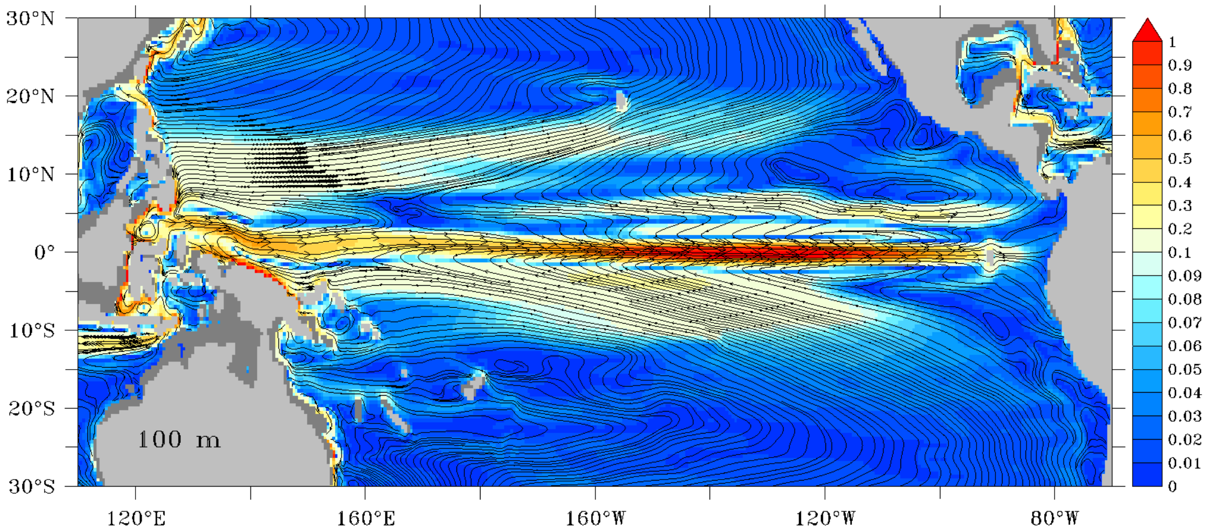

Figure A.32.: Ten year averaged (2000 to 2009) circulation: shaded is speed [m/s] with velocity vectors overlaid.

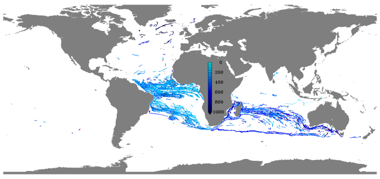

a) 200 m depth TROPAC01

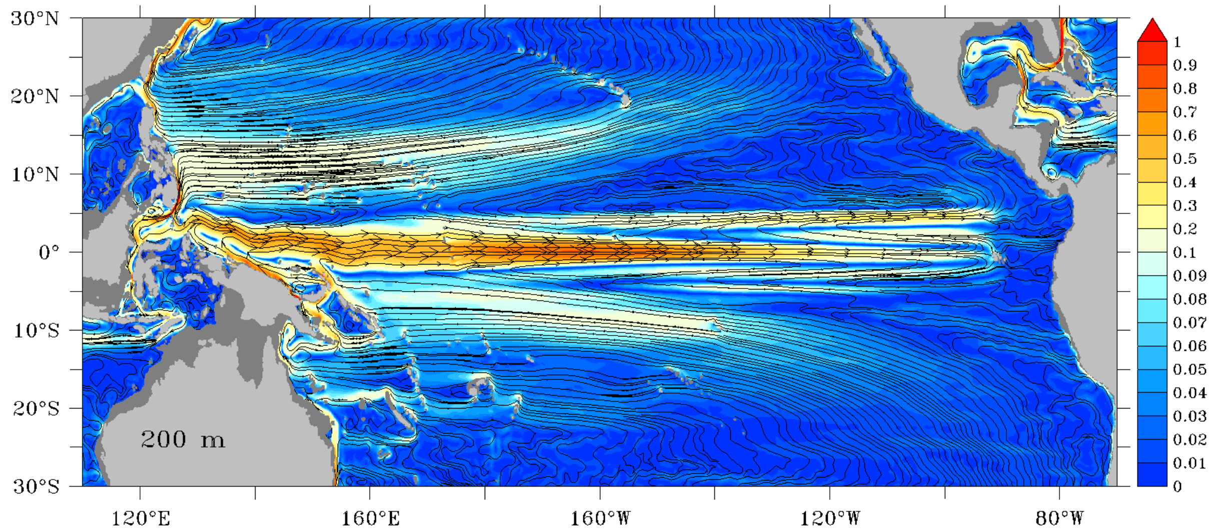

b) 200 m depth ORCA05

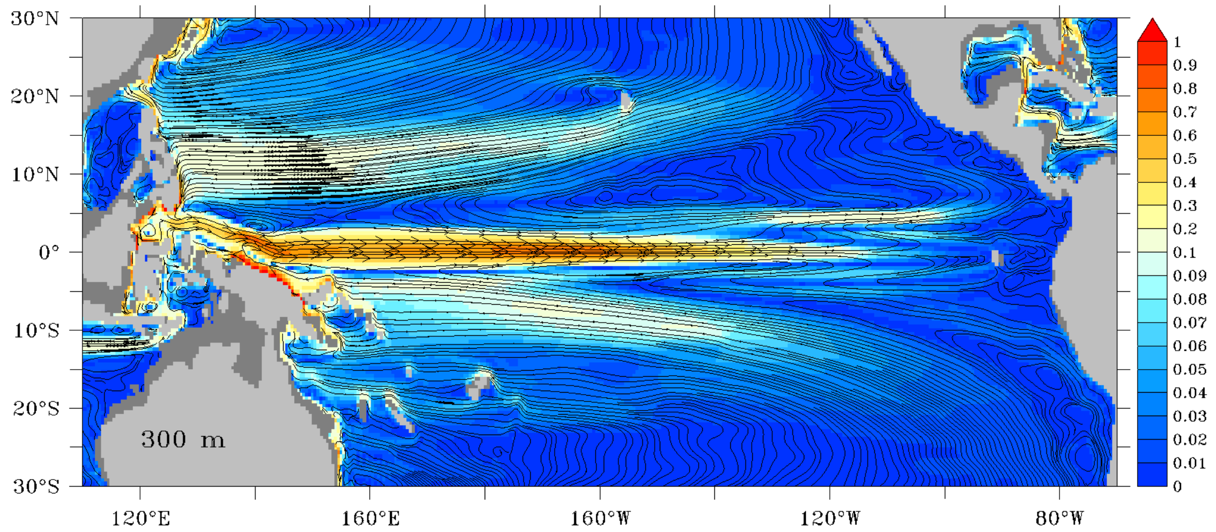

Figure A.33.: Ten year averaged (2000 to 2009) circulation: shaded is speed [m/s] with velocity vectors overlaid.

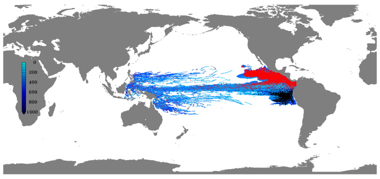

a) 300 m depth TROPAC01

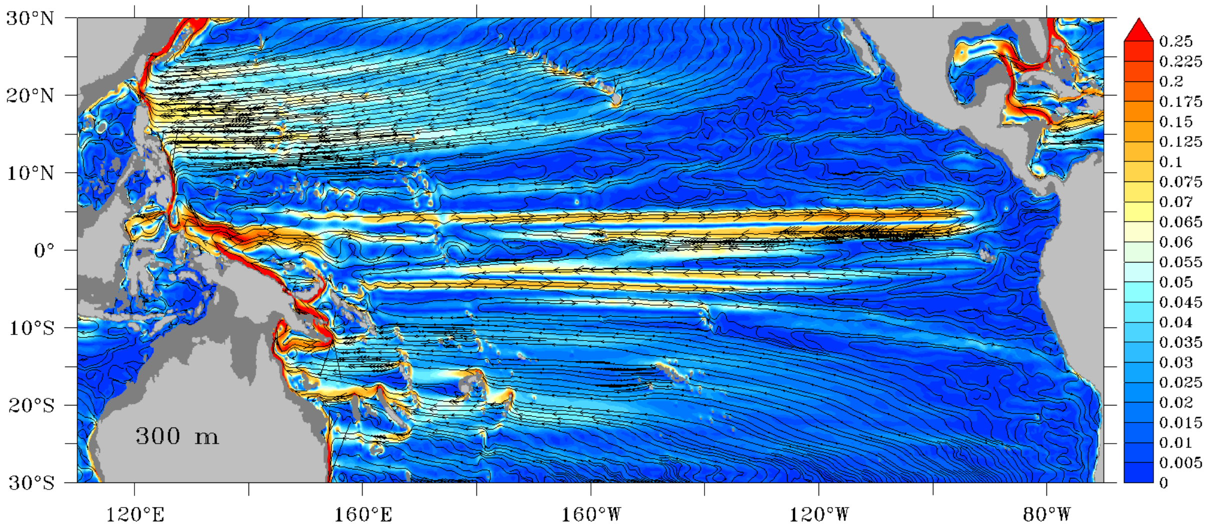

b) 300 m depth ORCA05

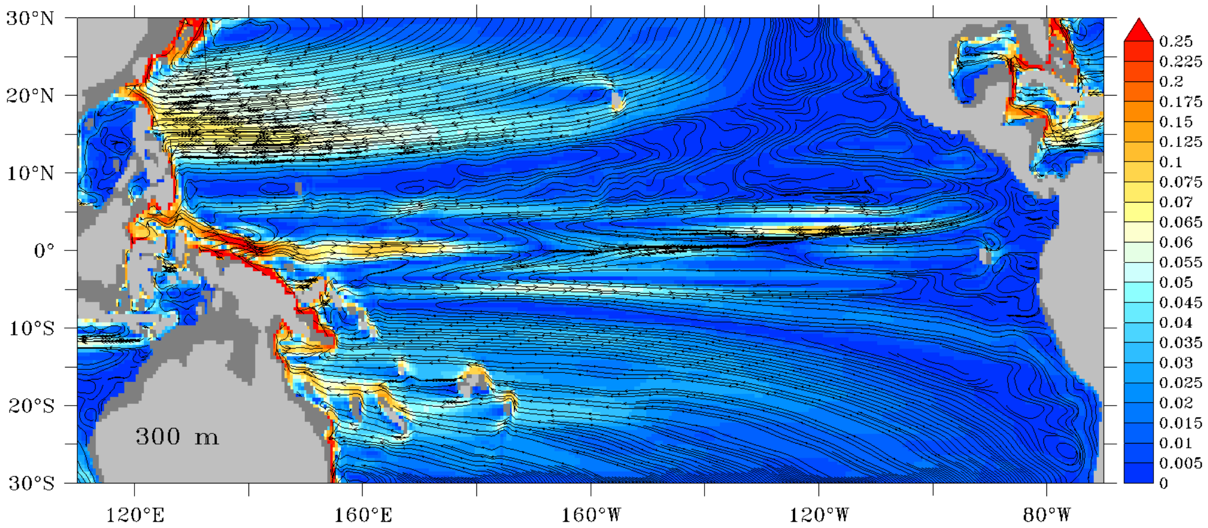

Figure A.34.: Ten year averaged (2000 to 2009) circulation: shaded is speed [m/s] with velocity vectors overlaid.

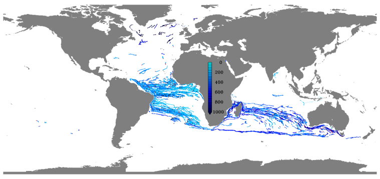

a) 400 m depth TROPAC01

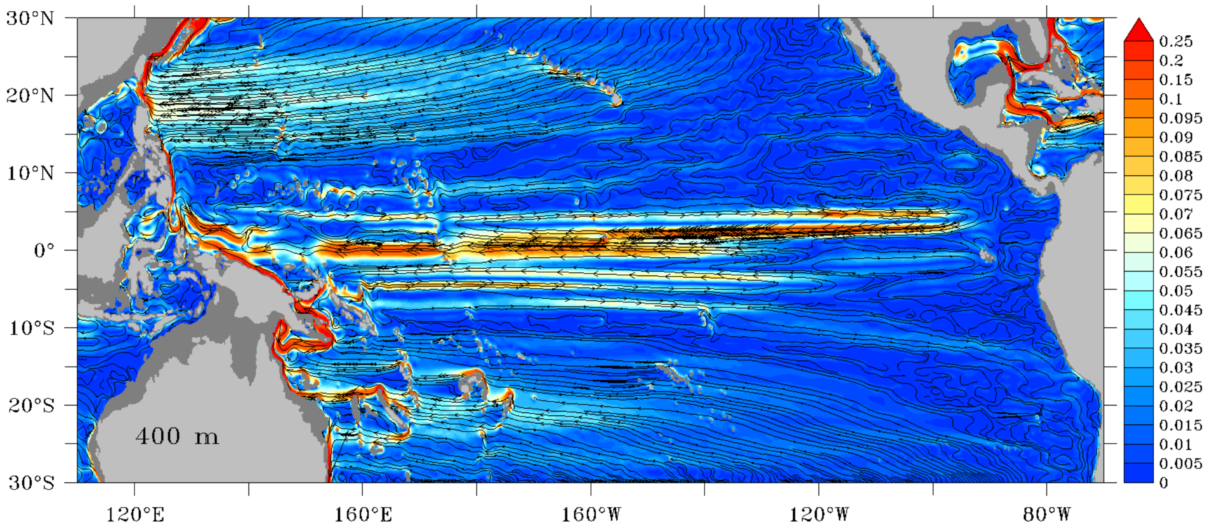

b) 400 m depth ORCA05

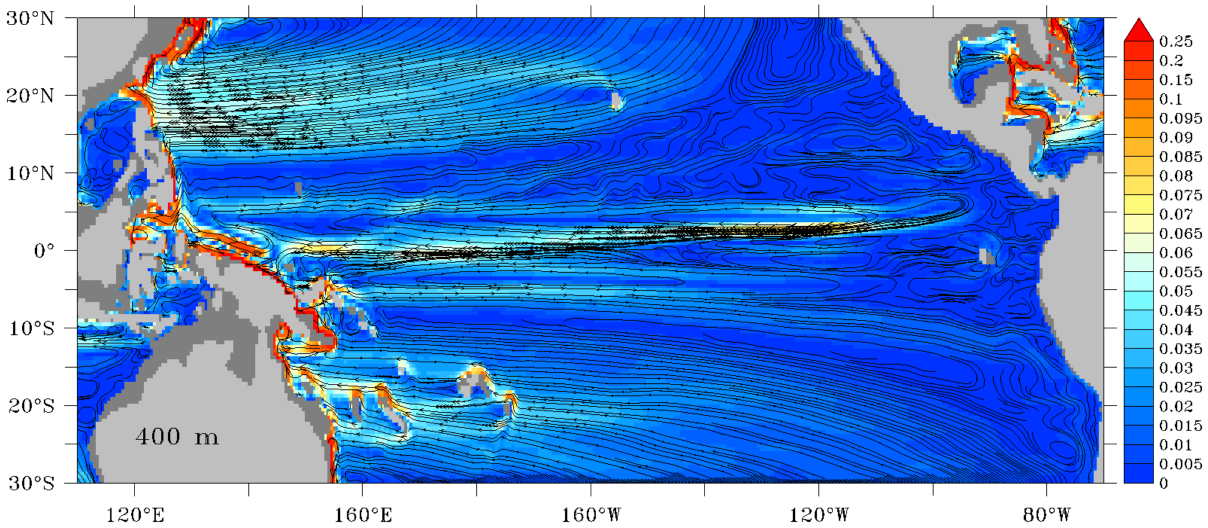

Figure A.35.: Ten year averaged (2000 to 2009) circulation: shaded is speed [m/s] with velocity vectors overlaid.

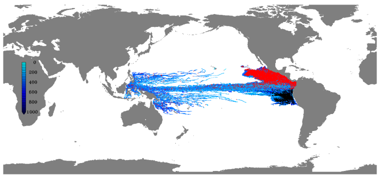

a) 500 m depth TROPAC01

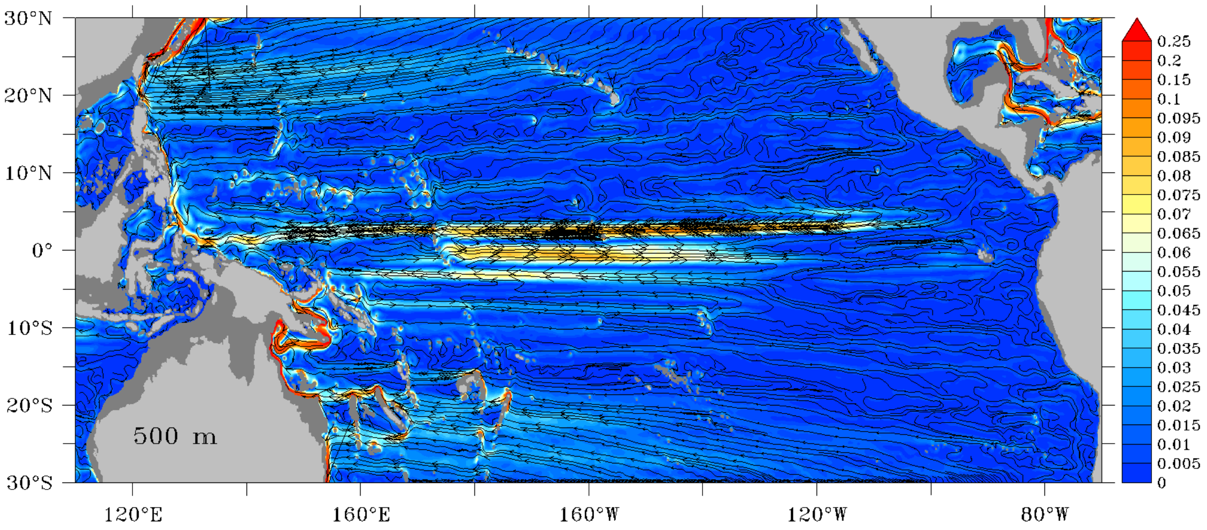

b) 500 m depth ORCA05

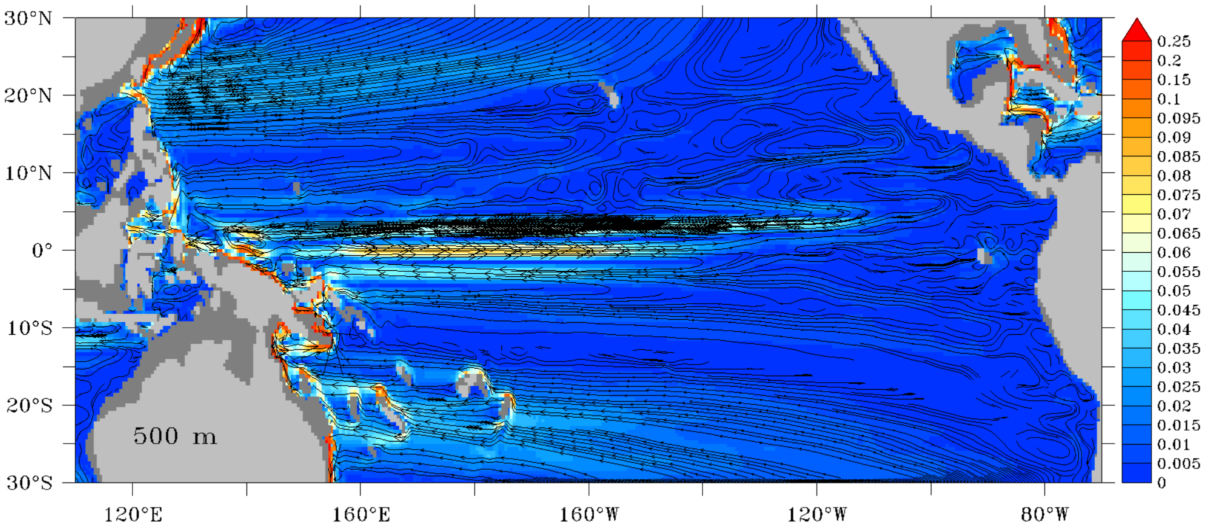

Figure A.36.: Ten year averaged (2000 to 2009) circulation: shaded is speed [m/s] with velocity vectors overlaid.

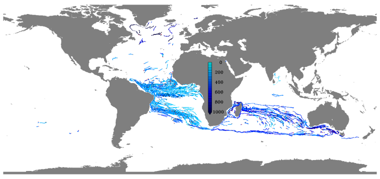

a) 600 m depth TROPAC01

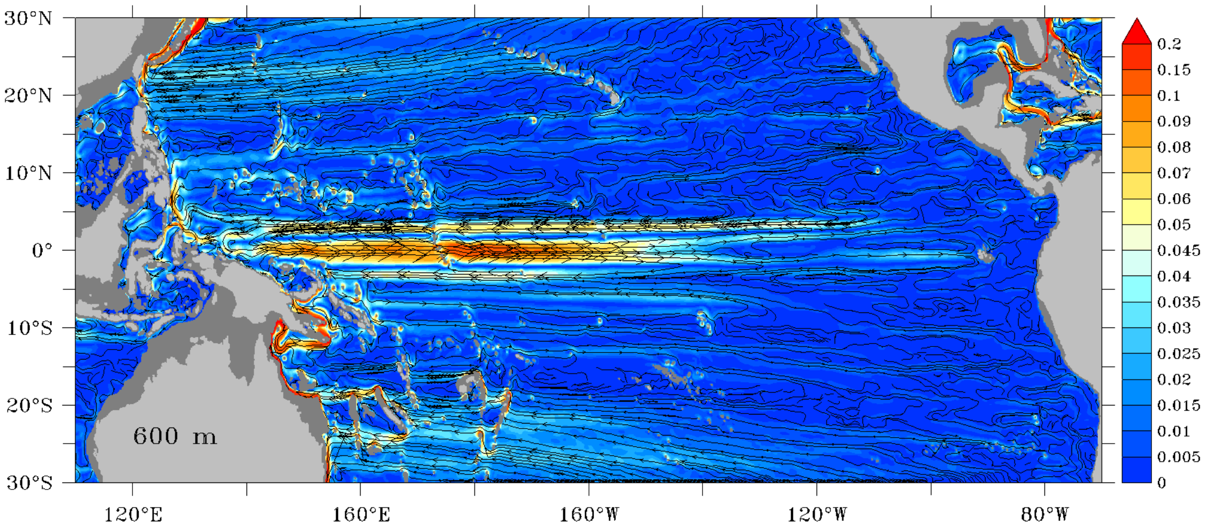

b) 600 m depth ORCA05

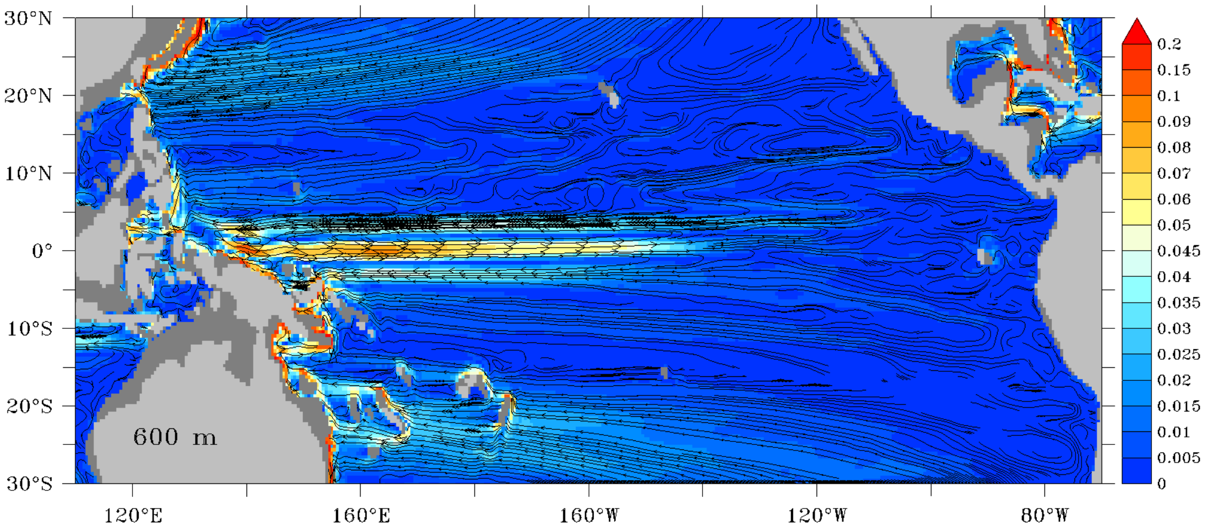

Figure A.37.: Ten year averaged (2000 to 2009) circulation: shaded is speed [m/s] with velocity vectors overlaid.

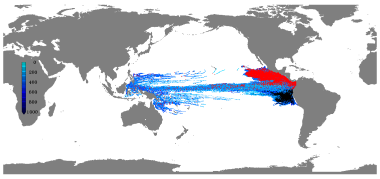

a) 700 m depth TROPAC01

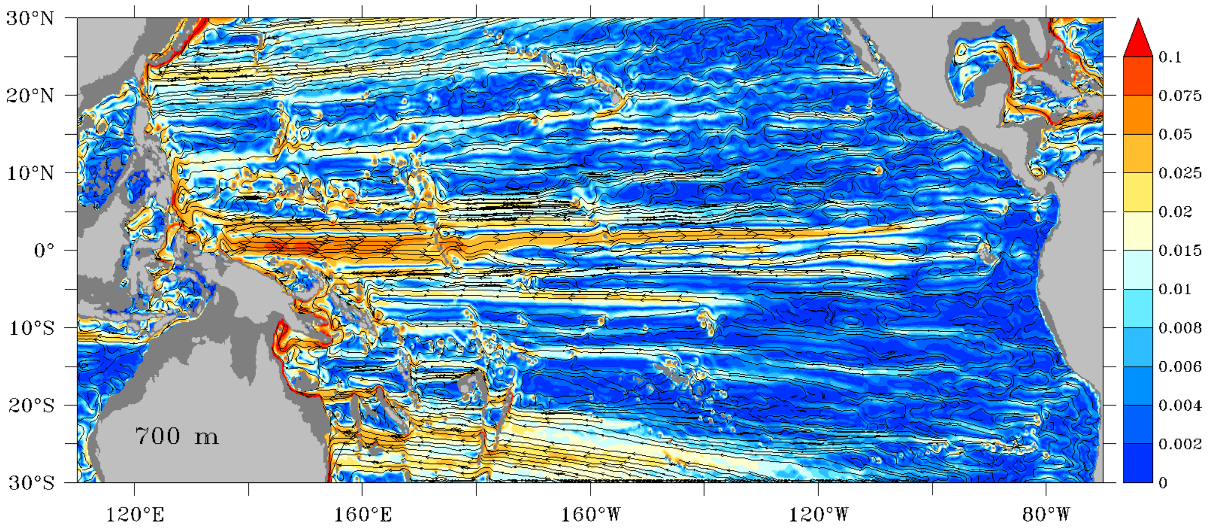

b) 700 m depth ORCA05

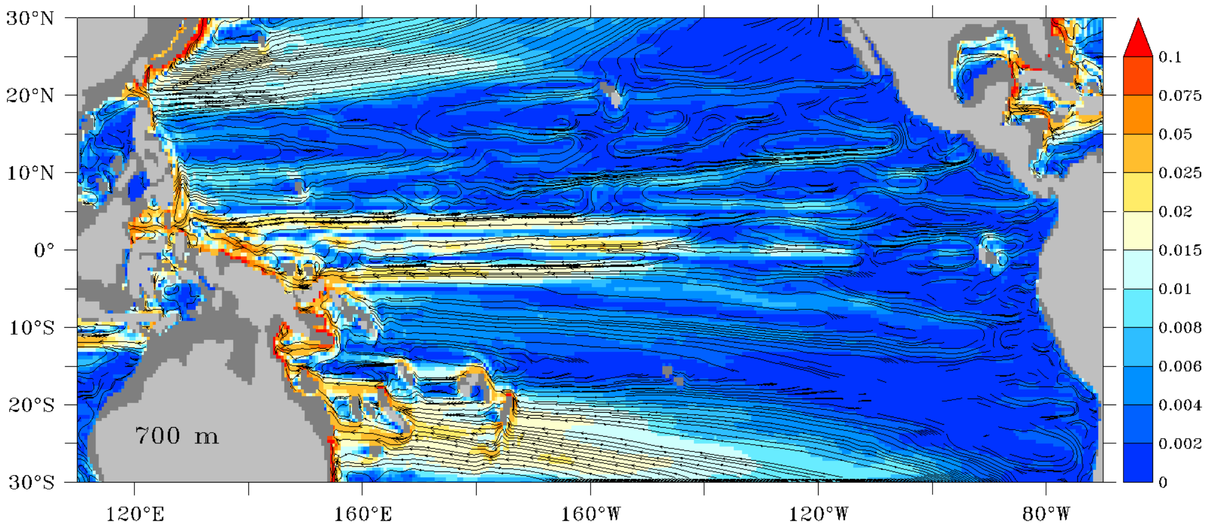

Figure A.38.: Ten year averaged (2000 to 2009) circulation: shaded is speed [m/s] with velocity vectors overlaid.

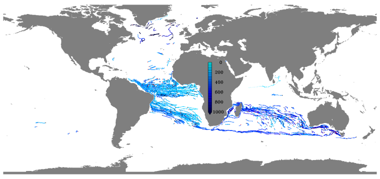

a) 850 m depth TROPAC01

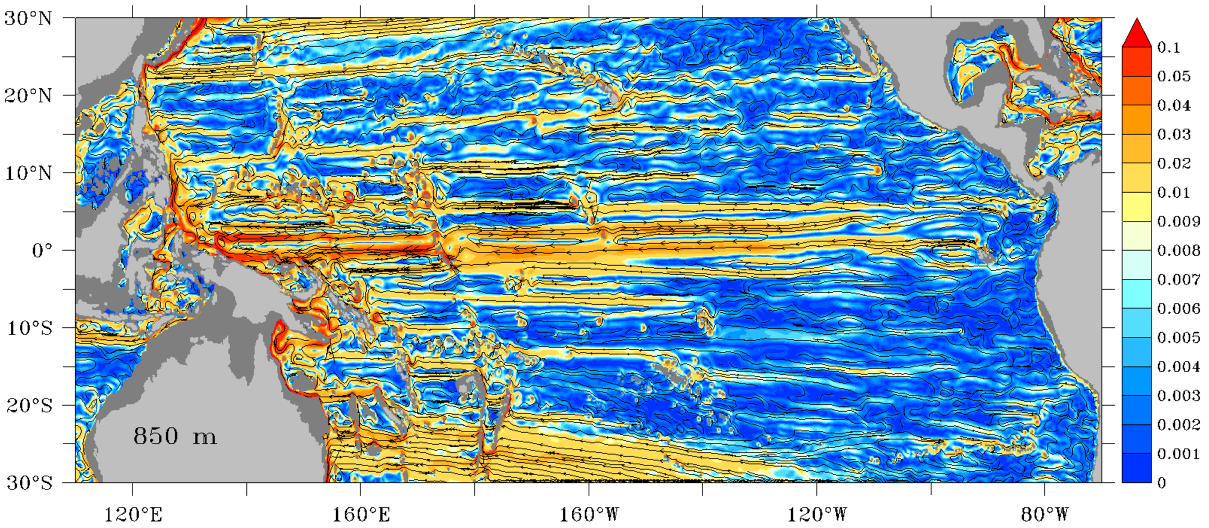

b) 850 m depth ORCA05

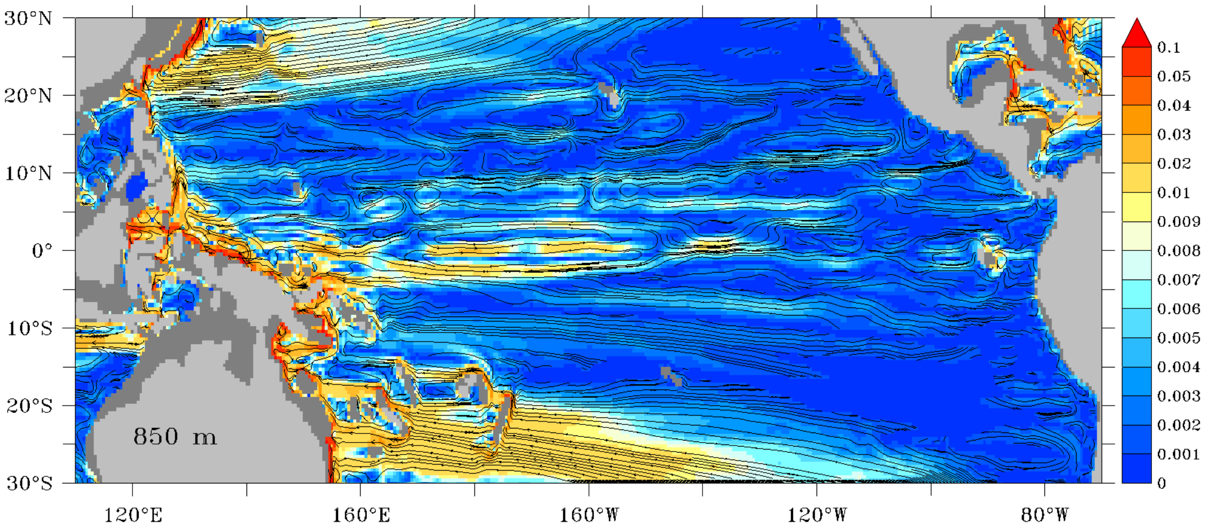

Figure A.39.: Ten year averaged (2000 to 2009) circulation: shaded is speed [m/s] with velocity vectors overlaid.

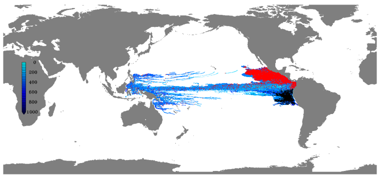

a) 1000 m depth TROPAC01

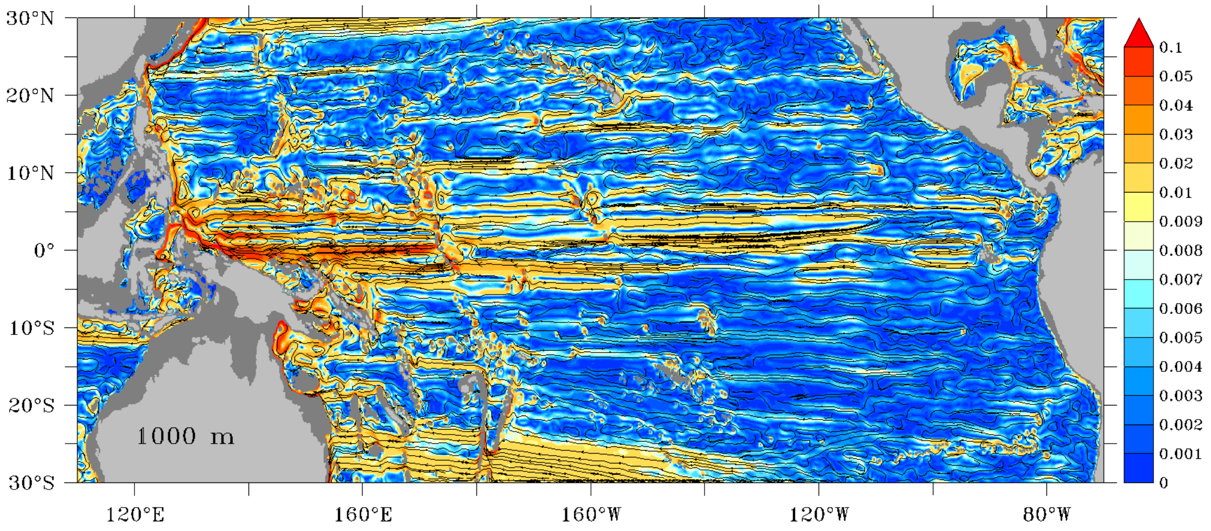

b) 1000 m depth ORCA05

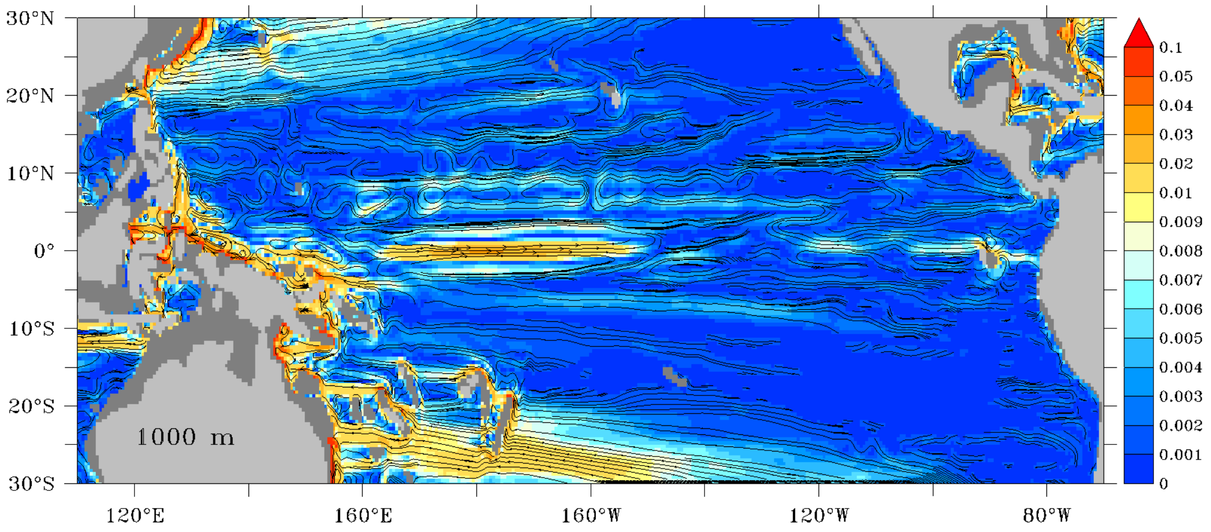

Figure A.40.: Ten year averaged (2000 to 2009) circulation: shaded is speed [m/s] with velocity vectors overlaid.

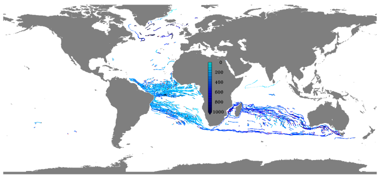

a) 1100 m depth TROPAC01

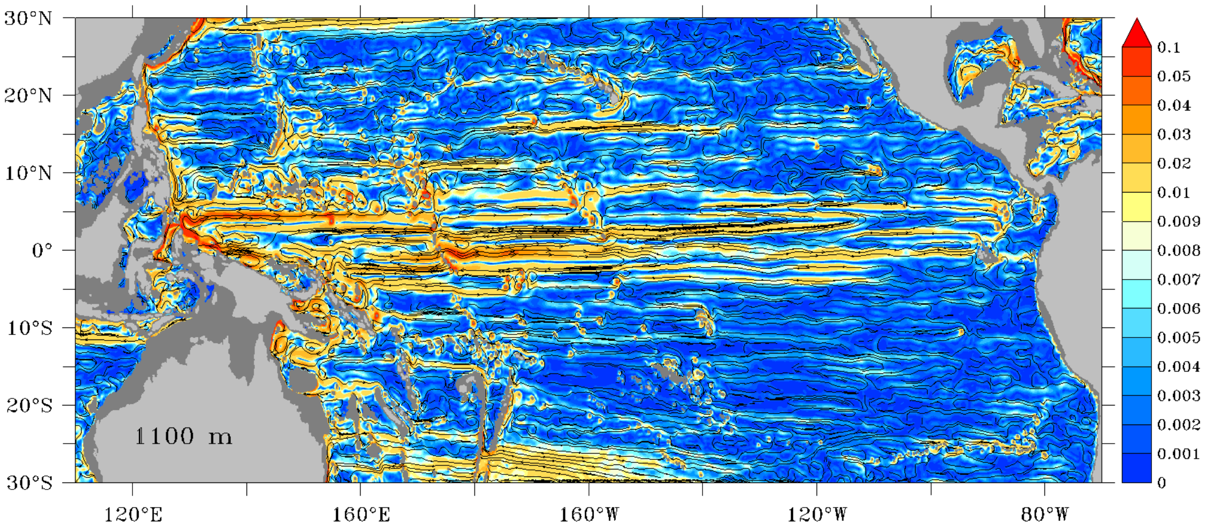

b) 1100 m depth ORCA05

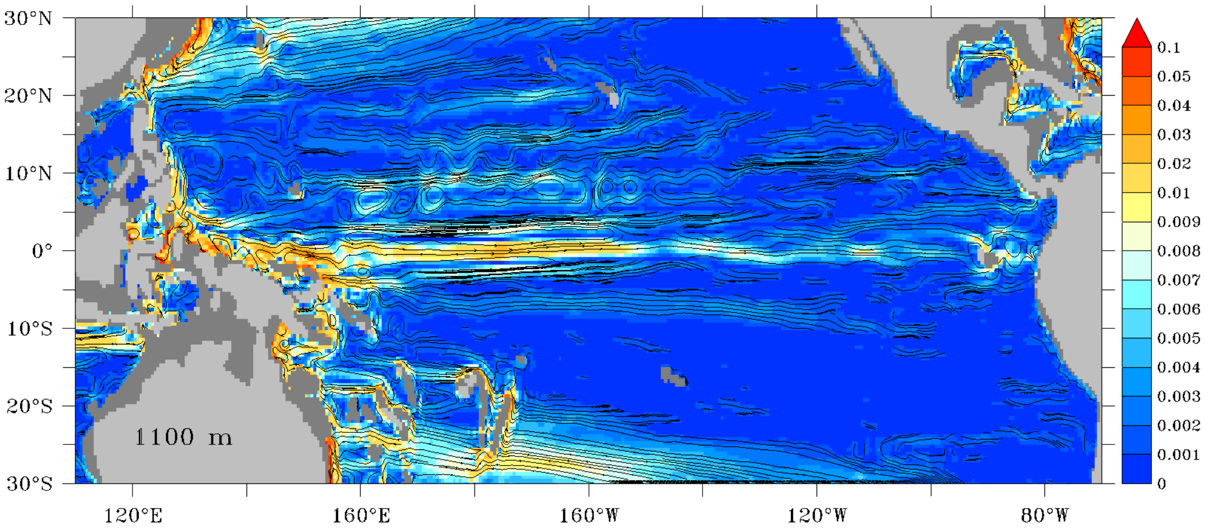

Figure A.41.: Ten year averaged (2000 to 2009) circulation: shaded is speed [m/s] with velocity vectors overlaid.

a) 1300 m depth TROPAC01

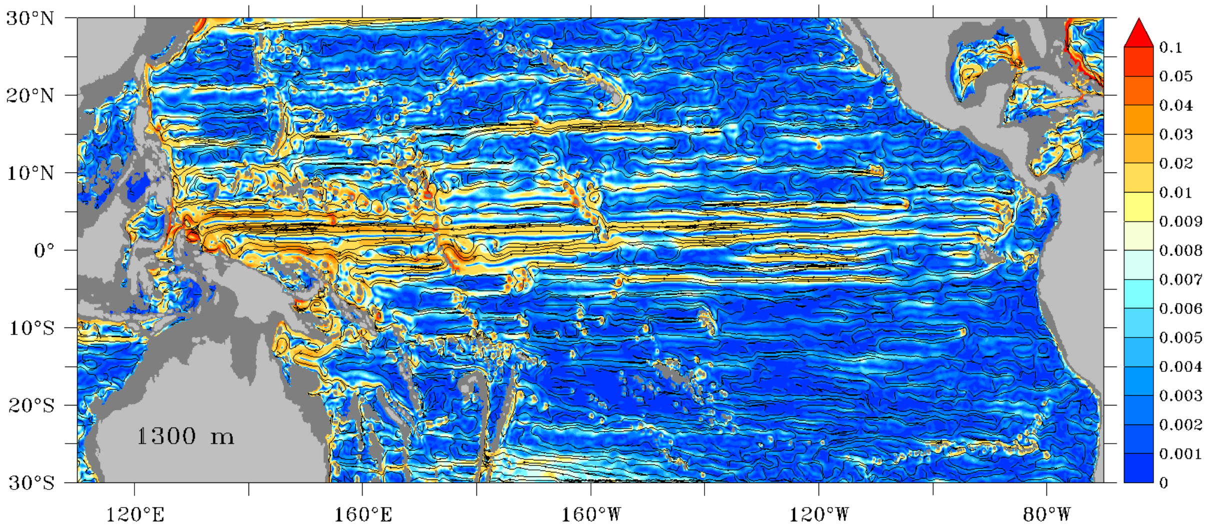

b) 1300 m depth ORCA05

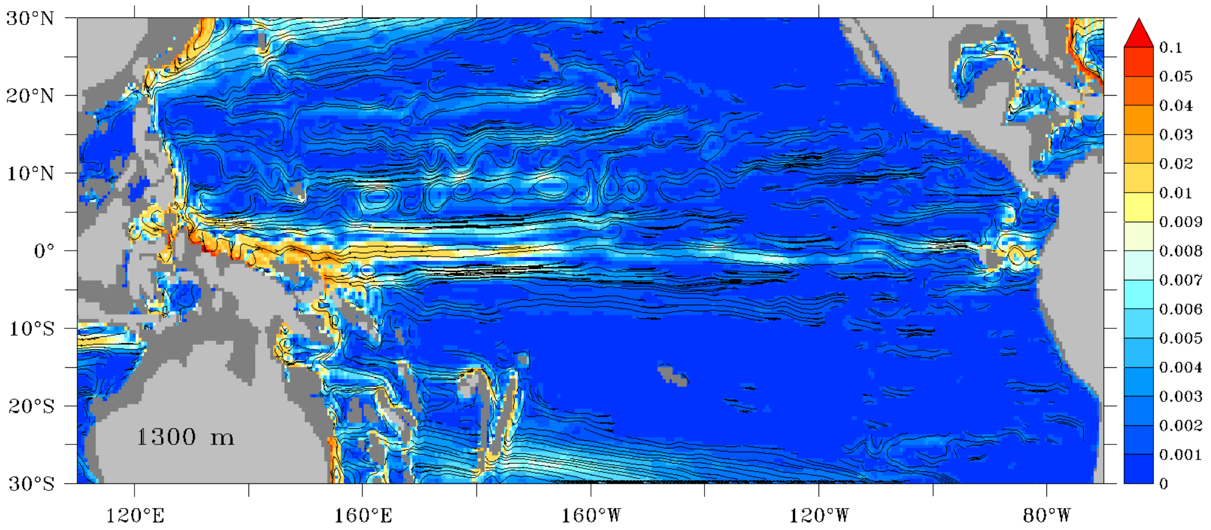

Figure A.42.: Ten year averaged (2000 to 2009) circulation: shaded is speed [m/s] with velocity vectors overlaid.

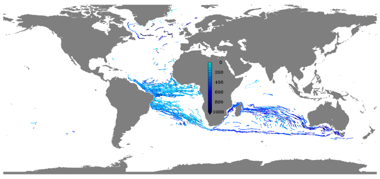

a) 1500 m depth TROPAC01

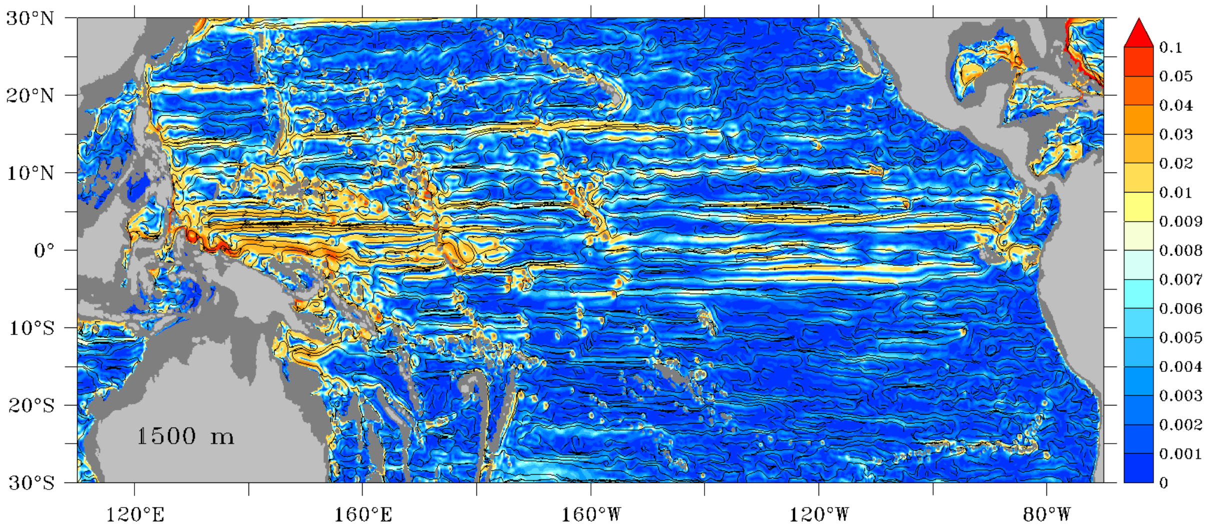

b) 1500 m depth ORCA05

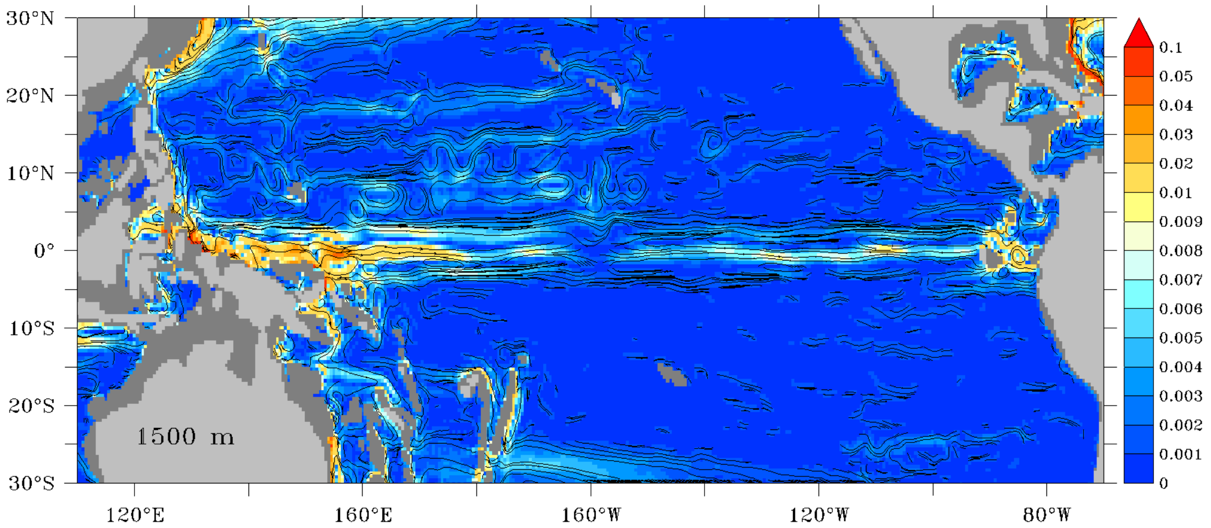

Figure A.43.: Ten year averaged (2000 to 2009) circulation: shaded is speed [m/s] with velocity vectors overlaid.

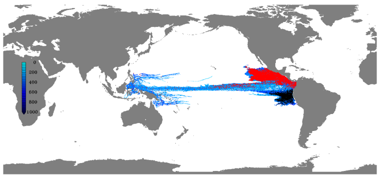

a) 1650 m depth TROPAC01

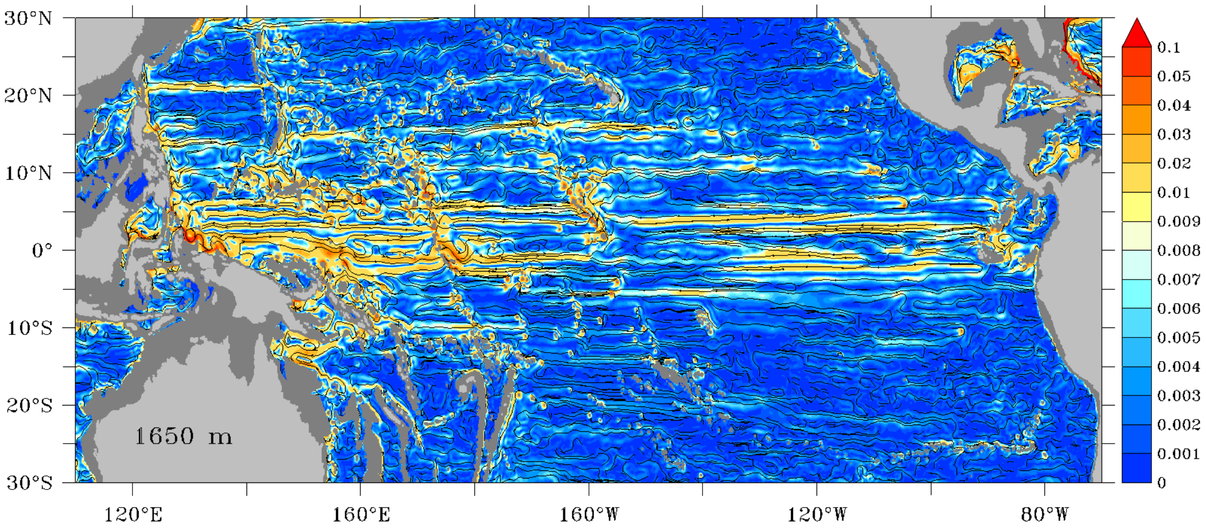

b) 1650 m depth ORCA05

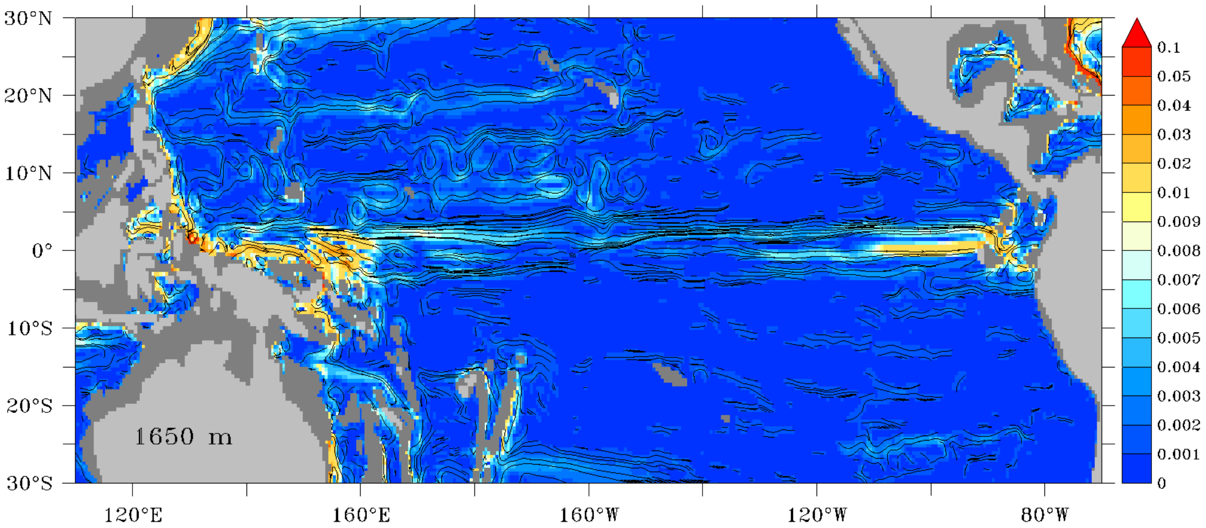

Figure A.44.: Ten year averaged (2000 to 2009) circulation: shaded is speed [m/s] with velocity vectors overlaid.

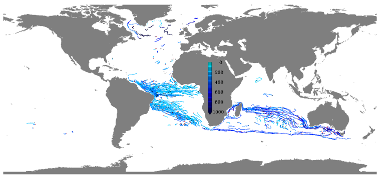

a) 1850 m depth TROPAC01

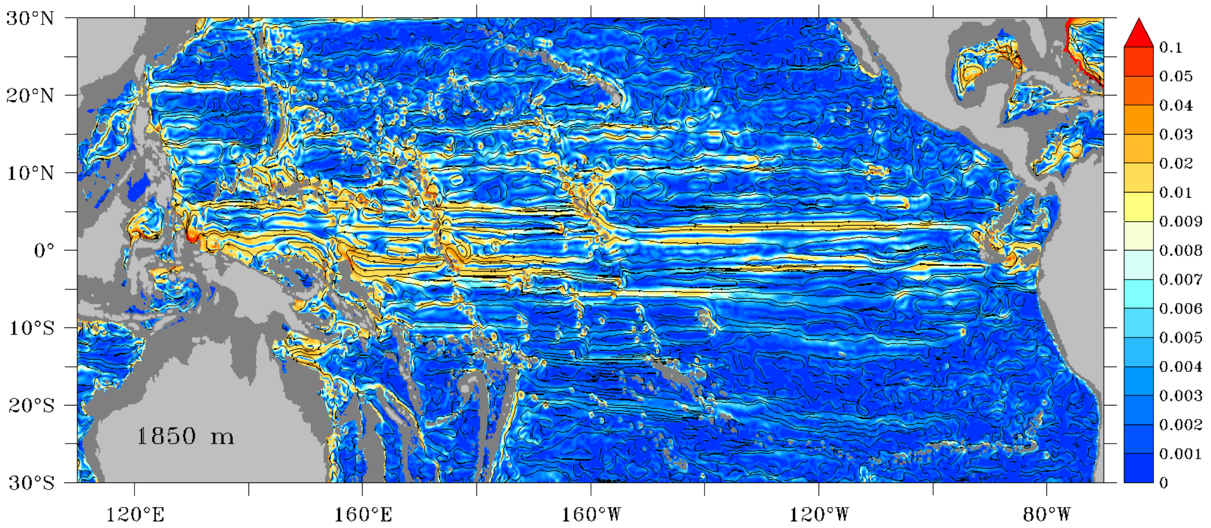

b) 1850 m depth ORCA05

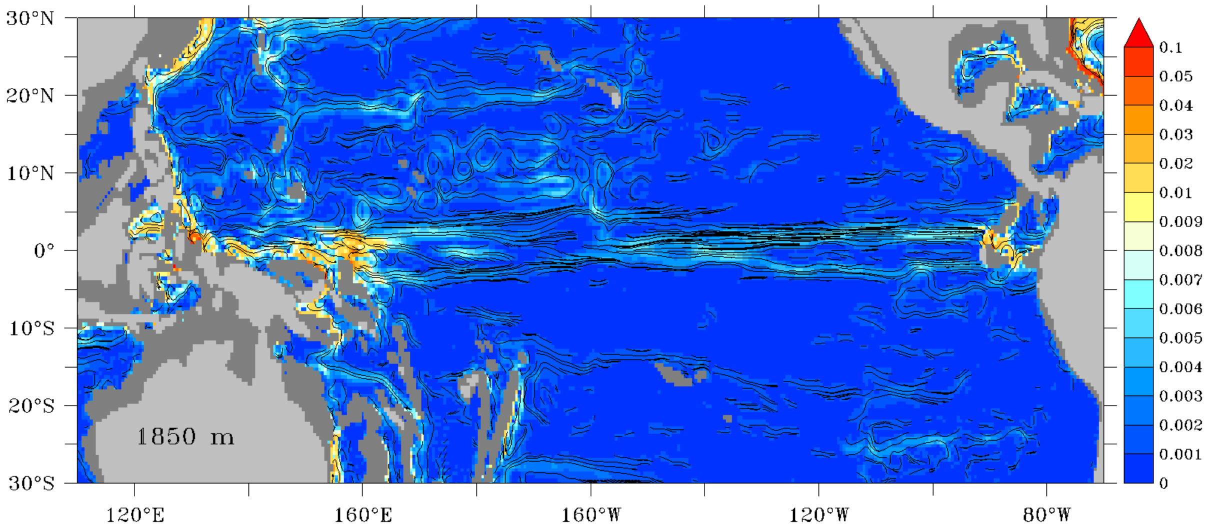

Figure A.45.: Ten year averaged (2000 to 2009) circulation: shaded is speed [m/s] with velocity vectors overlaid.

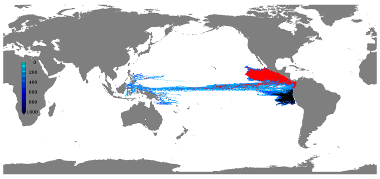

a) 2050 m depth TROPAC01

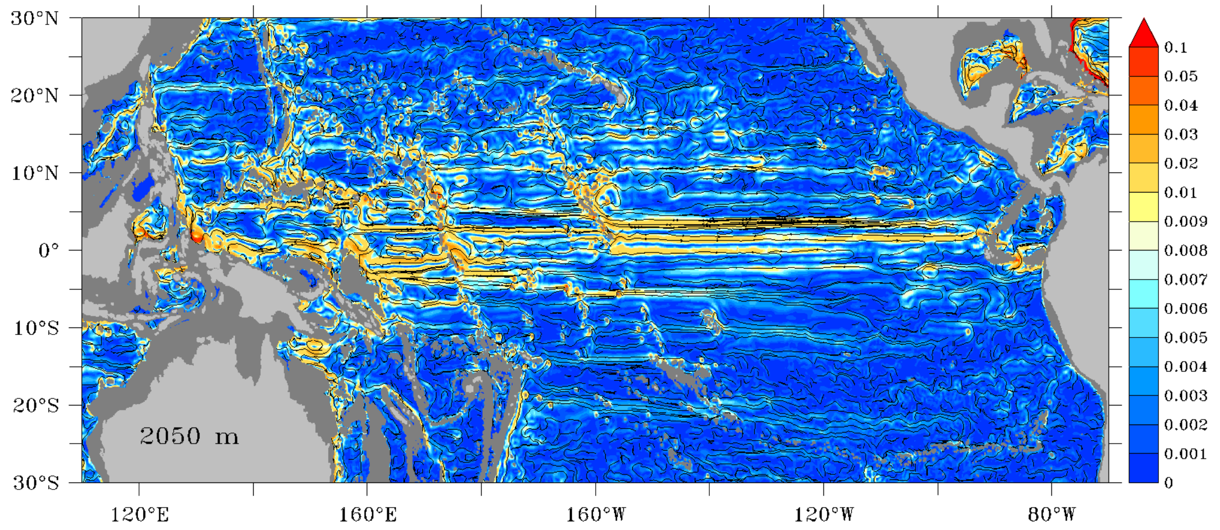

b) 2050 m depth ORCA05

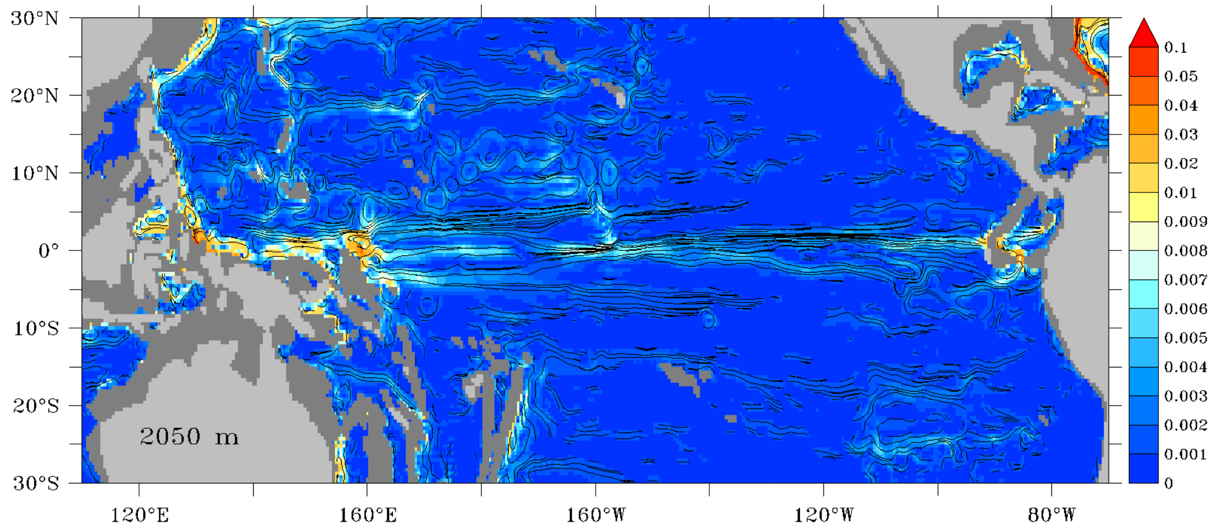

Figure A.46.: Ten year averaged (2000 to 2009) circulation: shaded is speed [m/s] with velocity vectors overlaid.

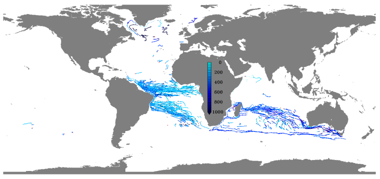

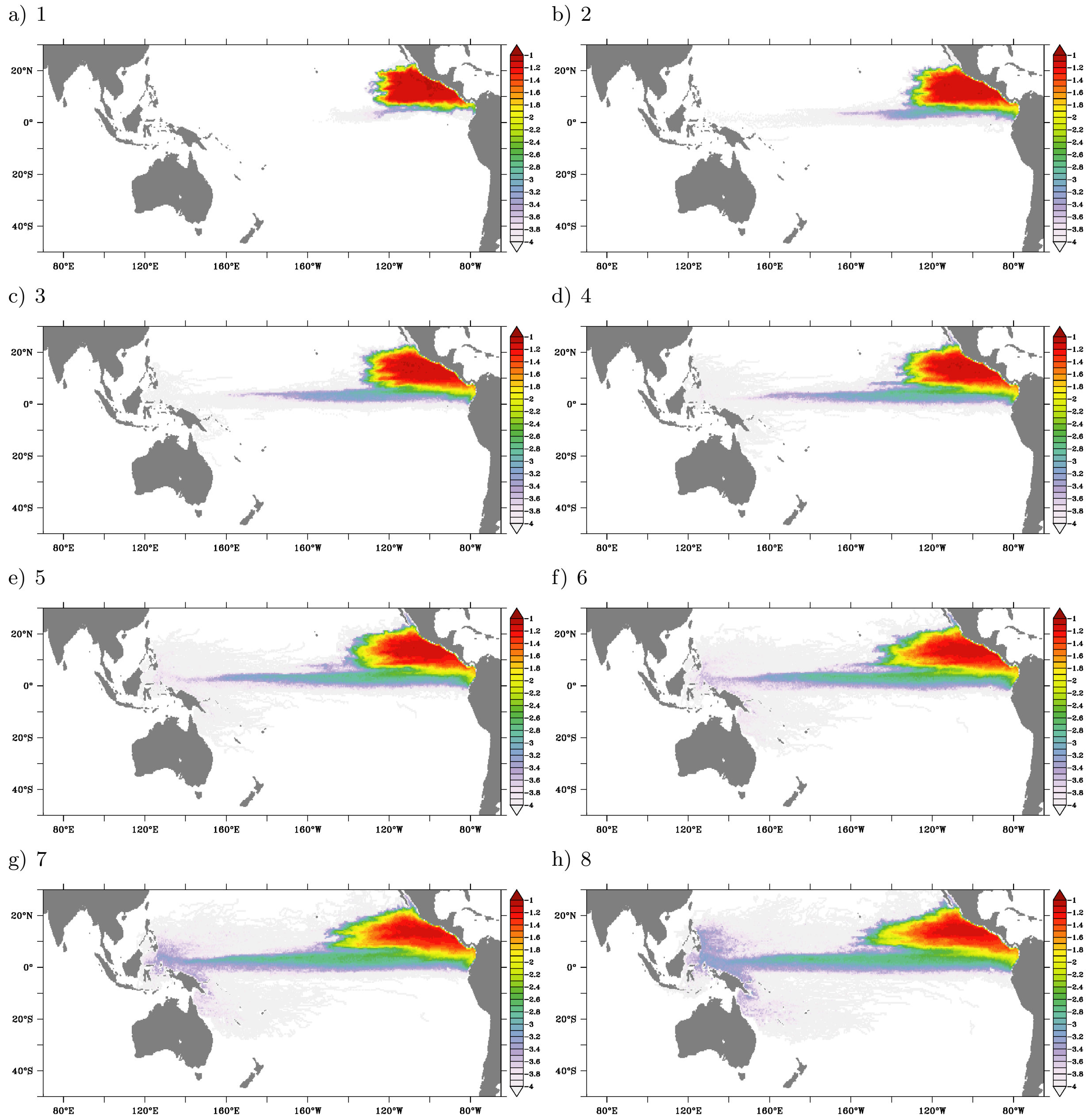

a) 1 b) 2 c) 3 d) 4 e) 5 f) 6 g) 7 h) 8

Figure A.47.: Depth integrated particle population [in % of released particles per 0.5° square on a logarithmic scale] in the first to eighth (a to h) year after release in the nOMZ in TROPAC01.

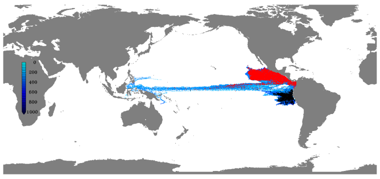

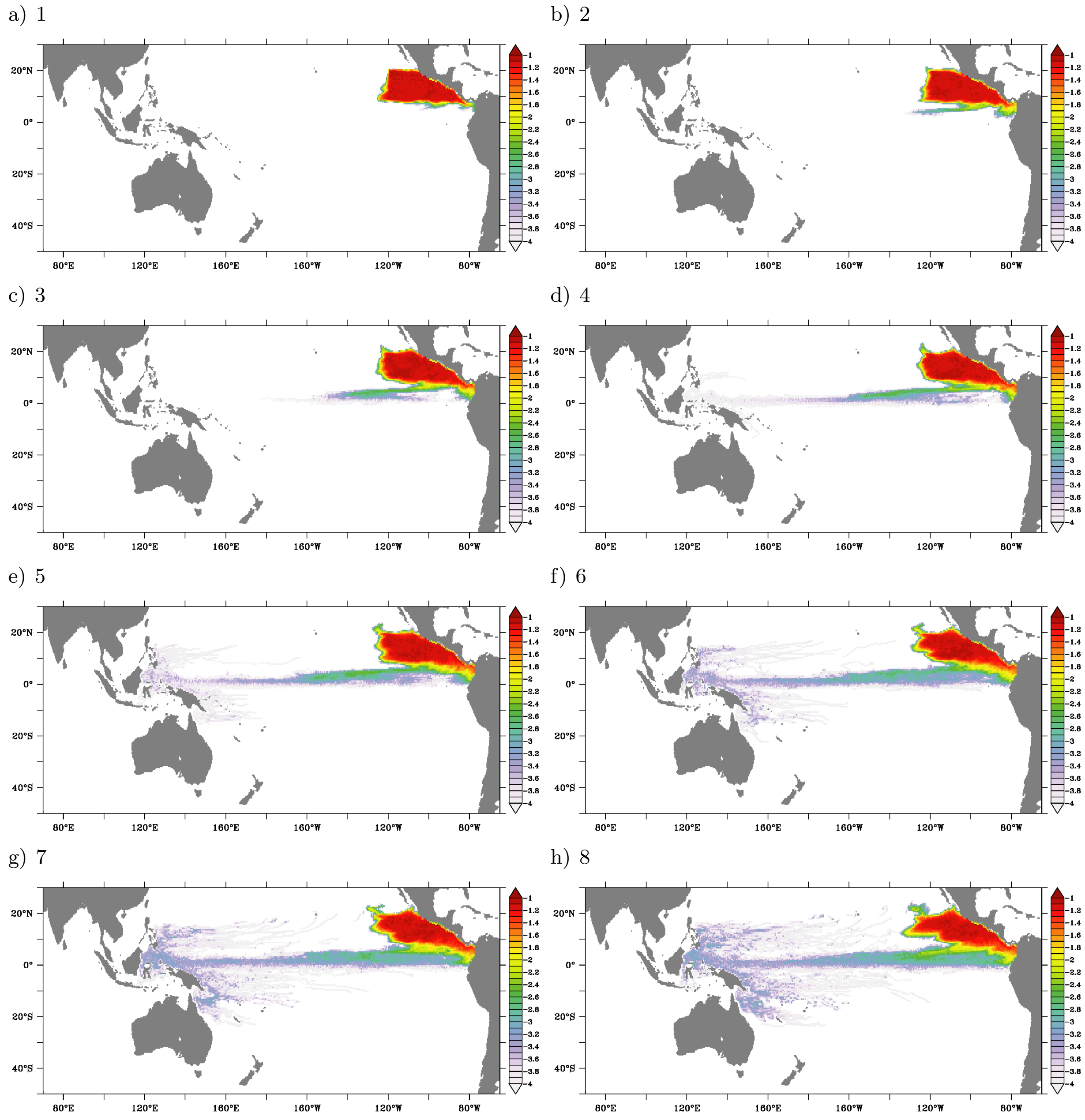

Figure A.48.: Depth integrated particle population [in % of released particles per 0.5° square on a logarithmic scale] in the first to eighth (a to h) year after release in the nOMZ in ORCA05.

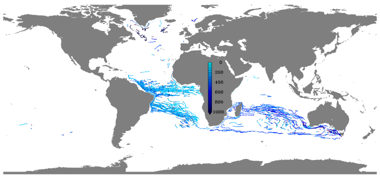

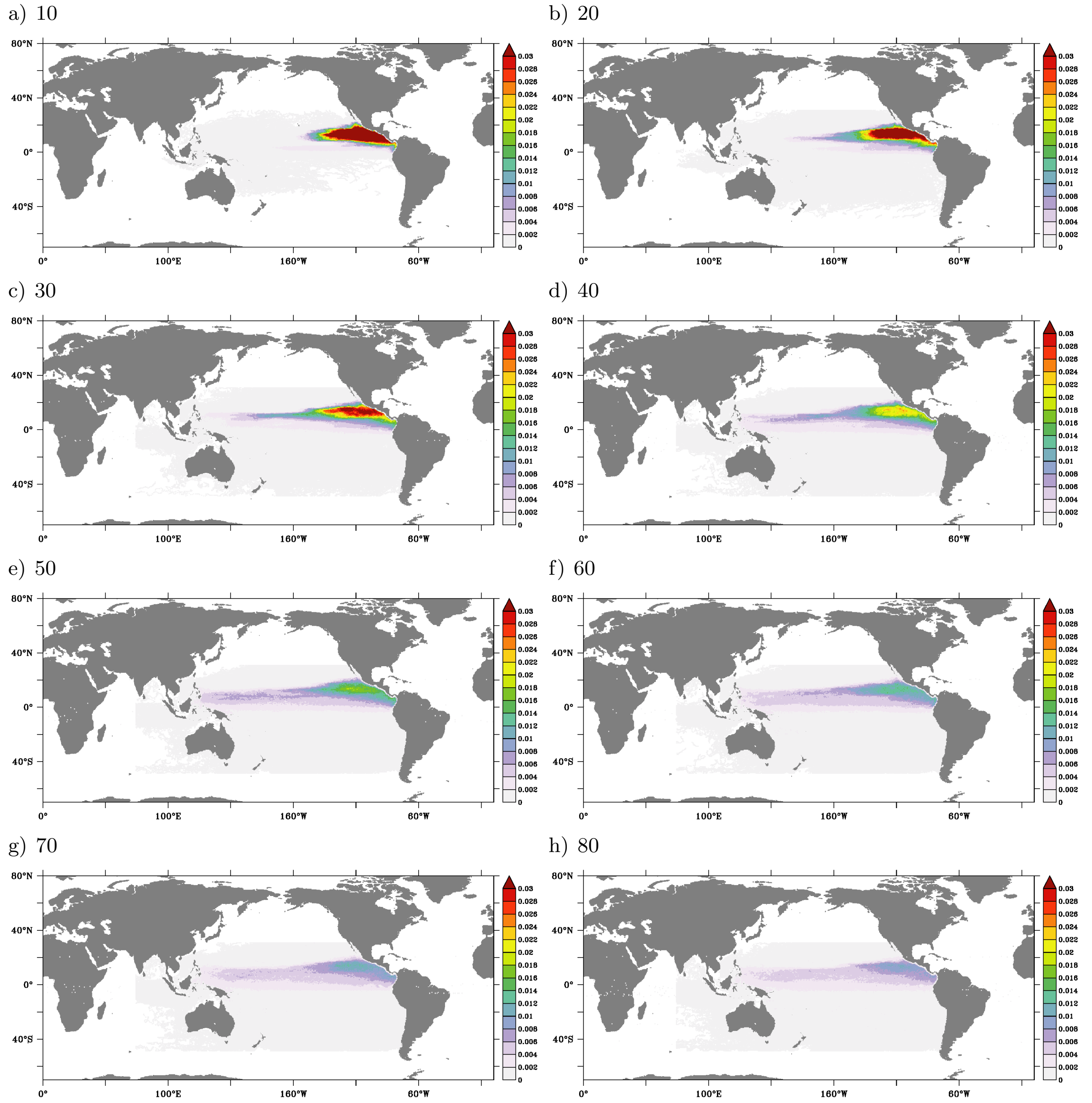
a) 10

b) 20

c) 30

d) 40

e) 50

f) 60

g) 70

h) 80

Figure A.49.: Depth integrated particle population [in % of released particles per 0.5° square] 10 a), 20 b), 30 c), 40 d), 50 e), 60 f), 70 g) and 80 h) years after release in the nOMZ in TROPAC01.

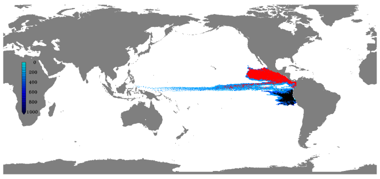

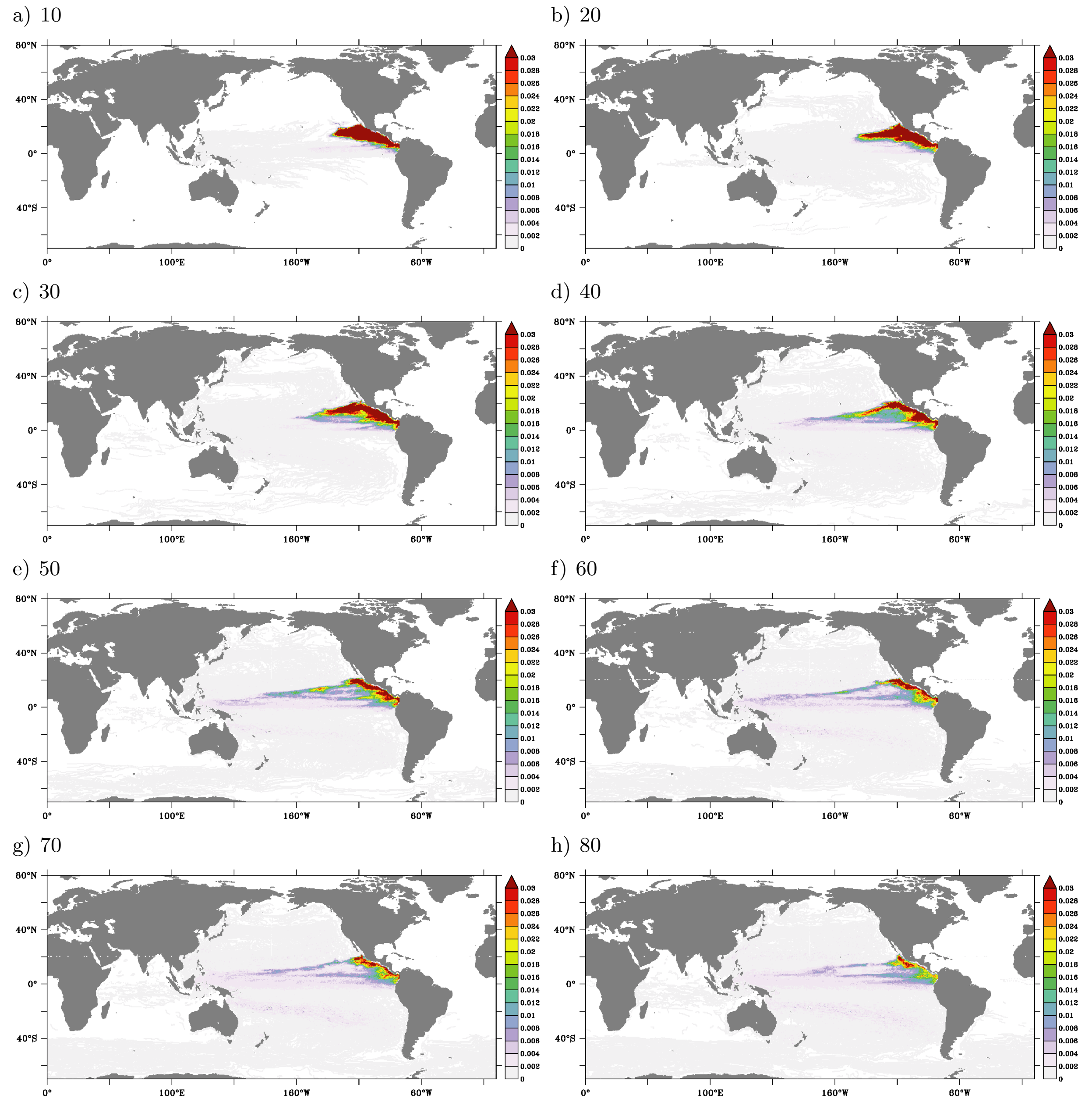

Figure A.50.: Depth integrated particle population [in % of released particles per 0.5° square] 10 a), 20 b), 30 c), 40 d), 50 e), 60 f), 70 g) and 80 h) years after release in the nOMZ in ORCA05.

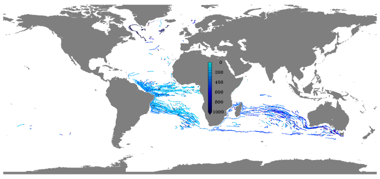

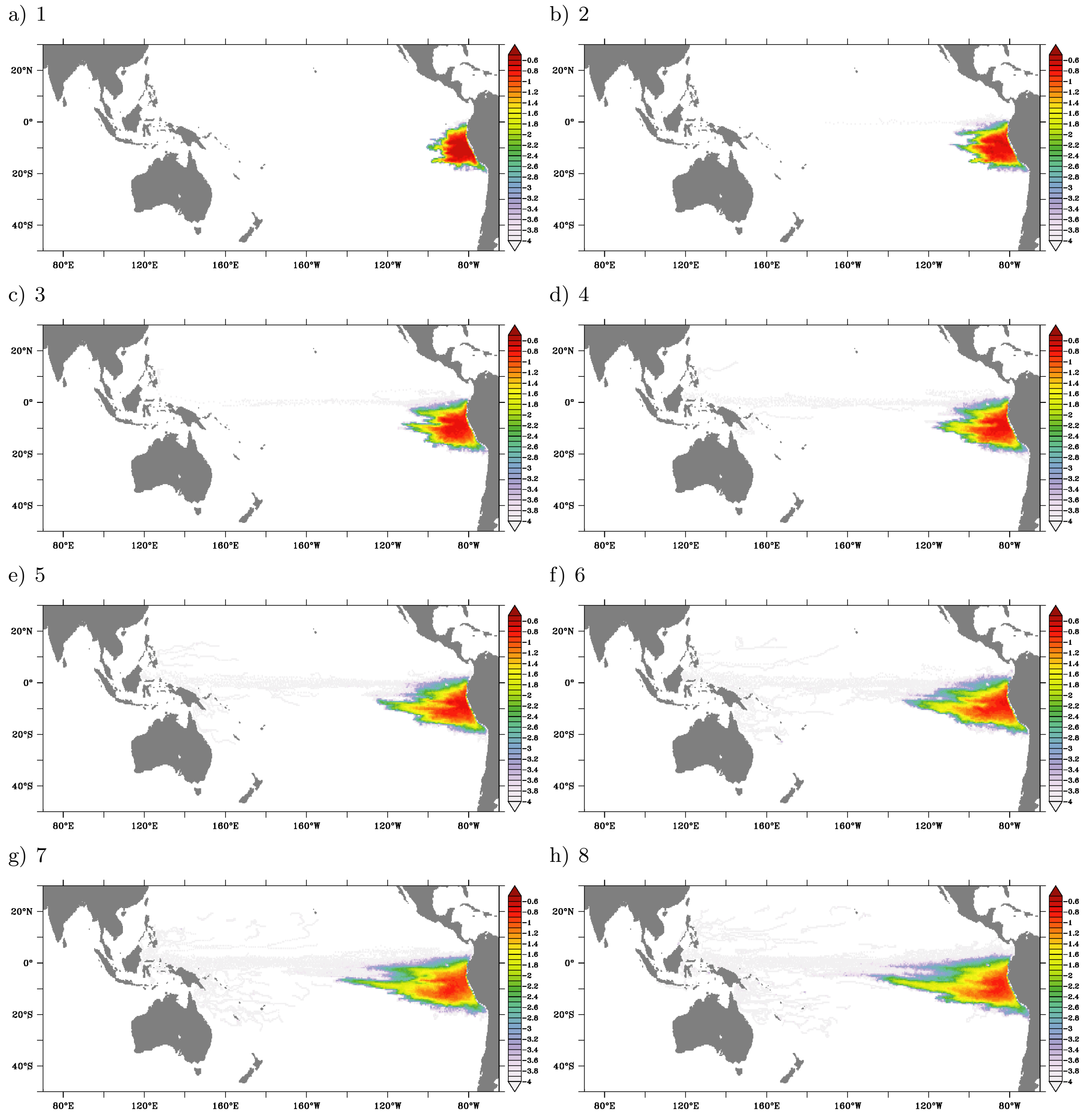

Figure A.51.: Depth integrated particle population [in % of released particles per 0.5° square on a logarithmic scale] in the first to eighth (a to h) year after release in the sOMZ in TROPAC01.

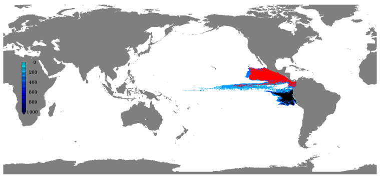

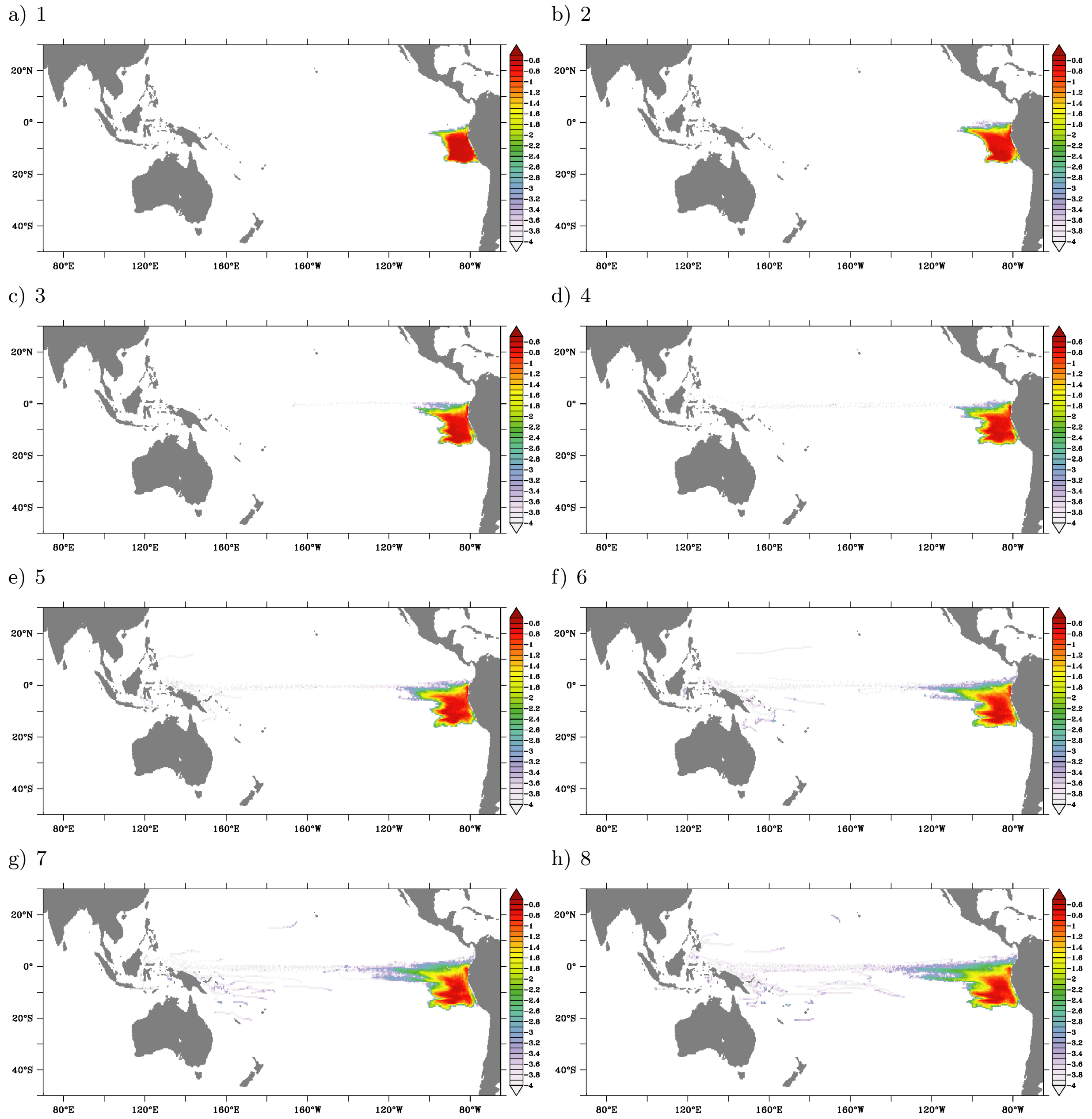
a) 1

b) 2

c) 3

d) 4

e) 5

f) 6

g) 7

h) 8

Figure A.52.: Depth integrated particle population [in % of released particles per 0.5° square on a logarithmic scale] in the first to eighth (a to h) year after release in the sOMZ in ORCA05.

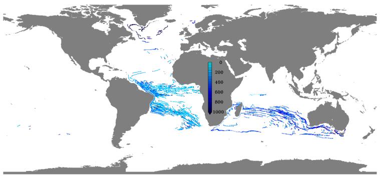

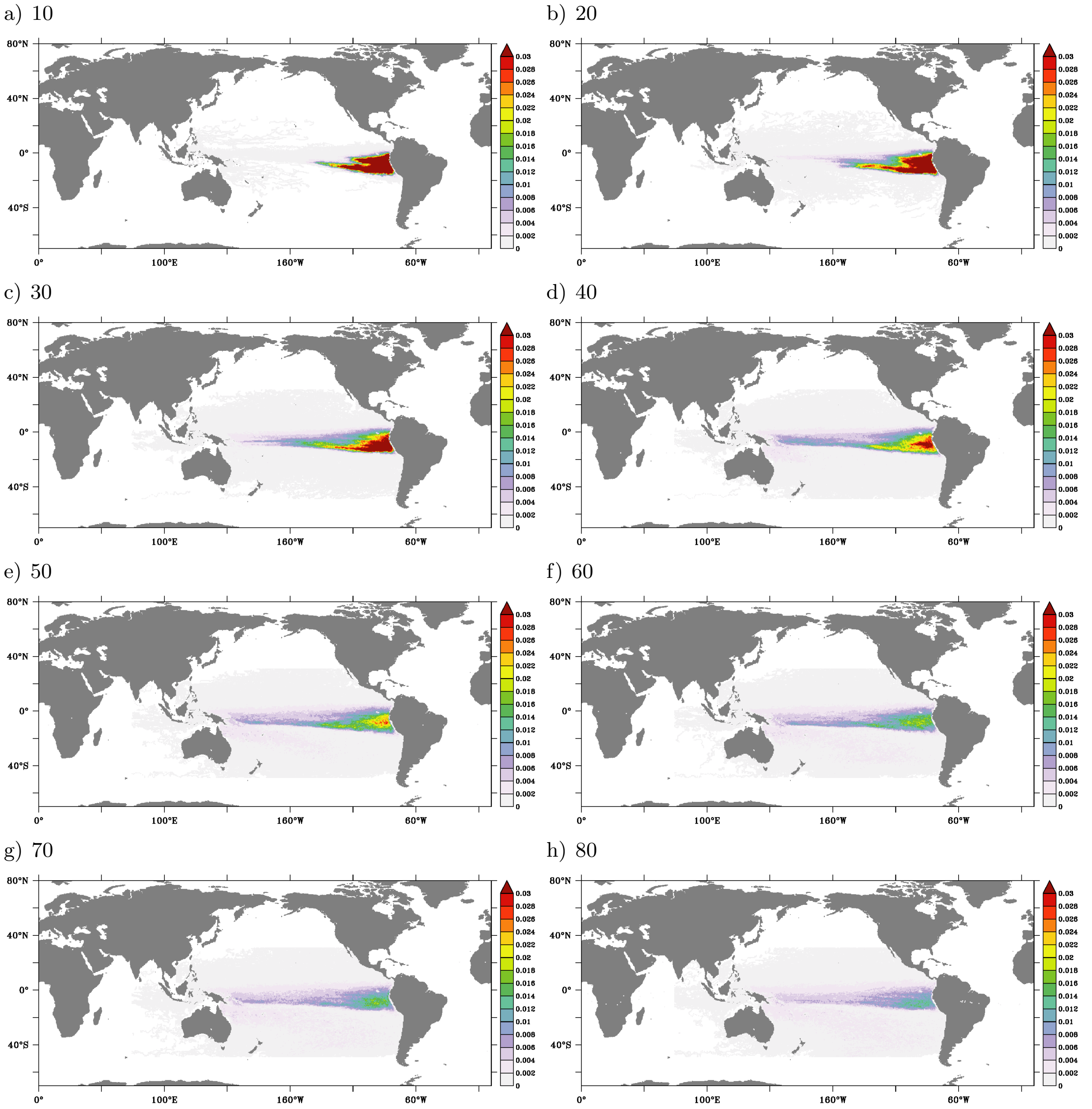

a) 10

b) 20

c) 30

d) 40

e) 50

f) 60

g) 70

h) 80

Figure A.53.: Depth integrated particle population [in % of released particles per 0.5° square] 10 a), 20 b), 30 c), 40 d), 50 e), 60 f), 70 g) and 80 h) years after release in the sOMZ in TROPAC01.

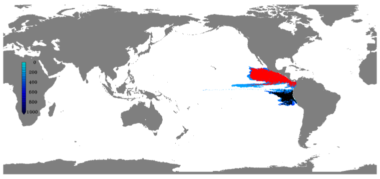

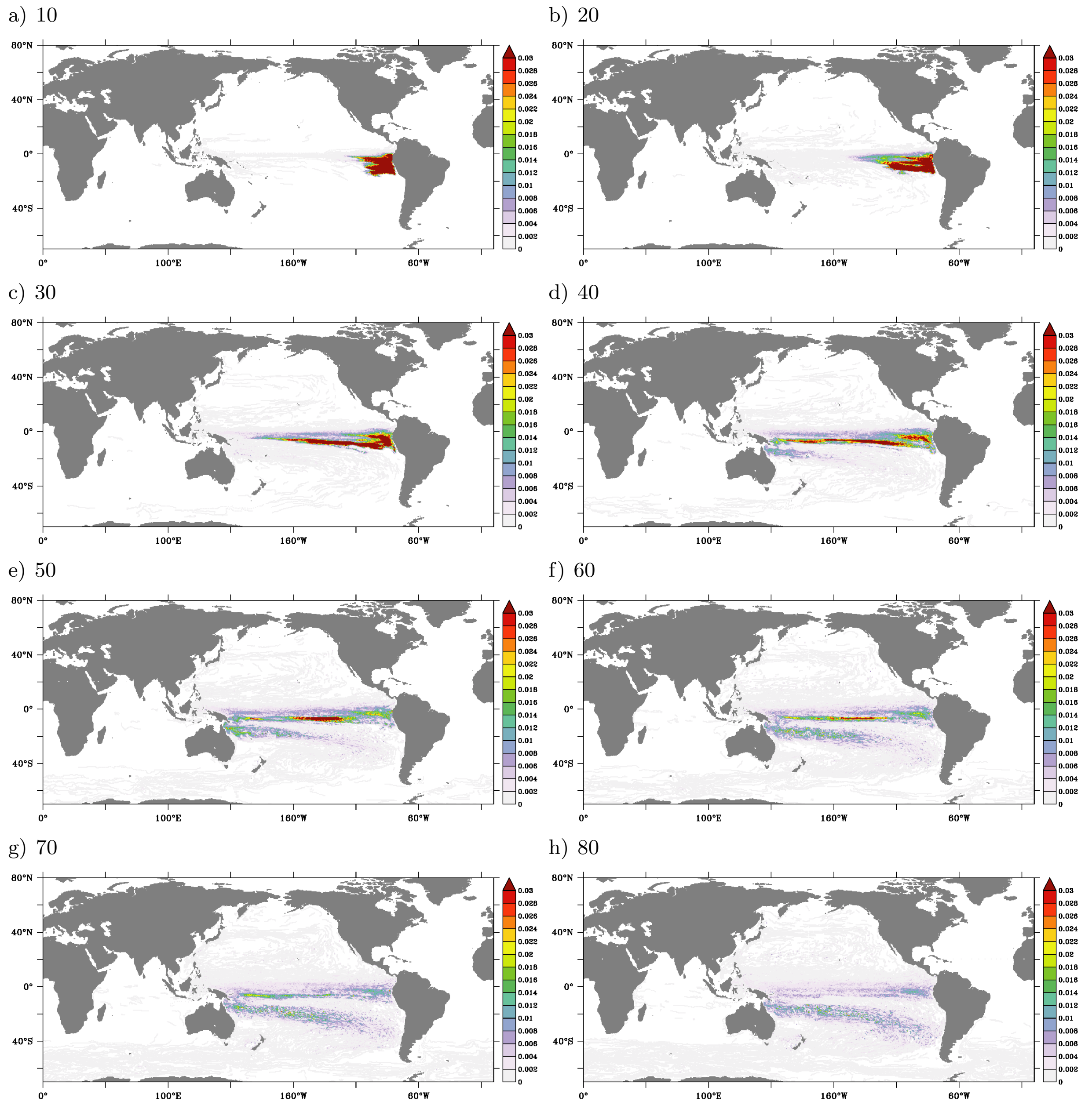
a) 10
b) 20
c) 30
d) 40
e) 50
f) 60
g) 70
h) 80

Figure A.54.: Depth integrated particle population [in % of released particles per 0.5° square] 10 a), 20 b), 30 c), 40 d), 50 e), 60 f), 70 g) and 80 h) years after release in the sOMZ in ORCA05.

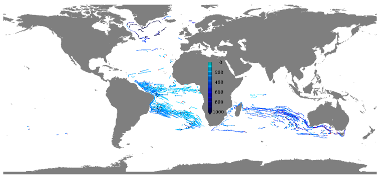

a) nOMZ TROPAC01 first arrivals

b) nOMZ ORCA05 first arrivals

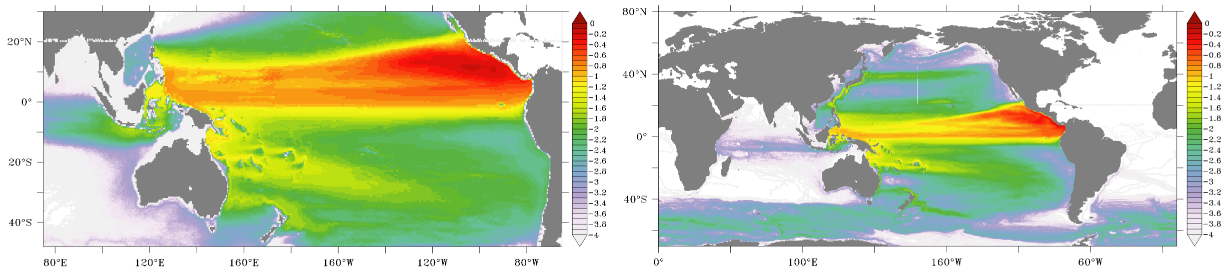

c) surface to 200 m

d) surface to 200 m

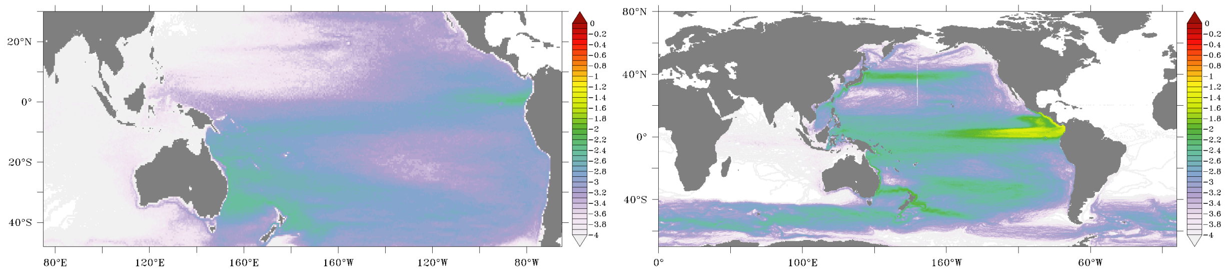

e) 200 m to 800 m

f) 200 m to 800 m

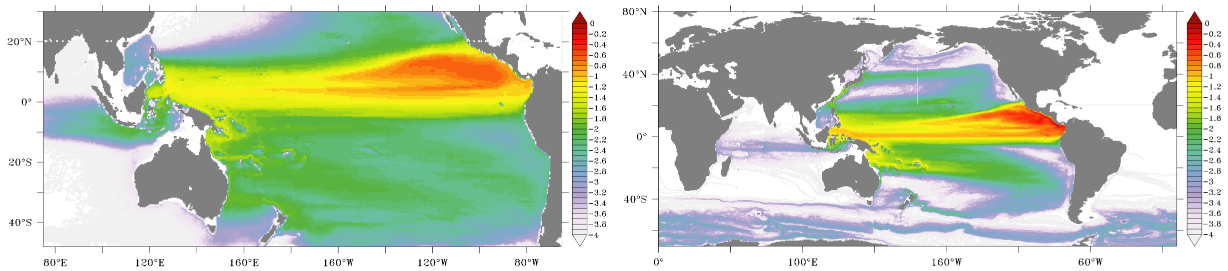

g) 800 m to bottom

h) 800 m to bottom

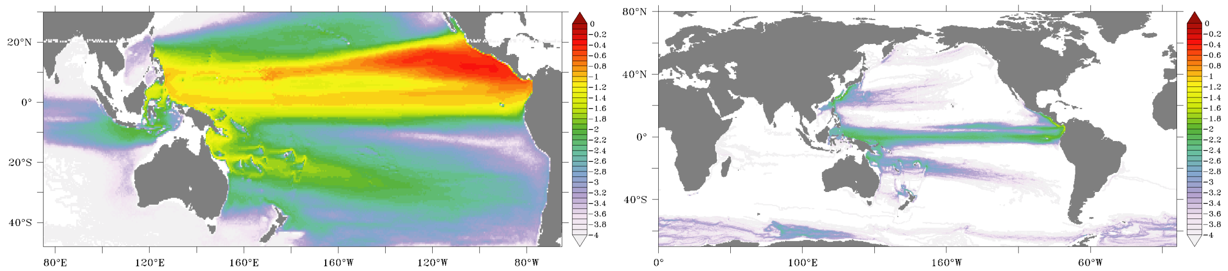

Figure A.55.: Depth integrated particle population derived as "first arrivals" [in % of released particles per 0.5° square on a logarithmic scale] temporally integrated over the full period of the Lagrangian experiments of 80 years for particles released in the Pacific nOMZ in TROPAC01 (left) and ORCA05 (right) for the full depth (a and b), the uppermost 200 m of the water column (c and d), 200 m to 800 m depth (e and f) and 800 m depth to the seafloor (g and h).

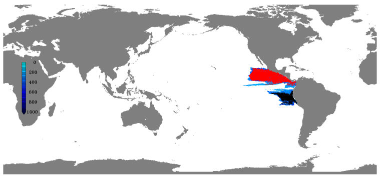

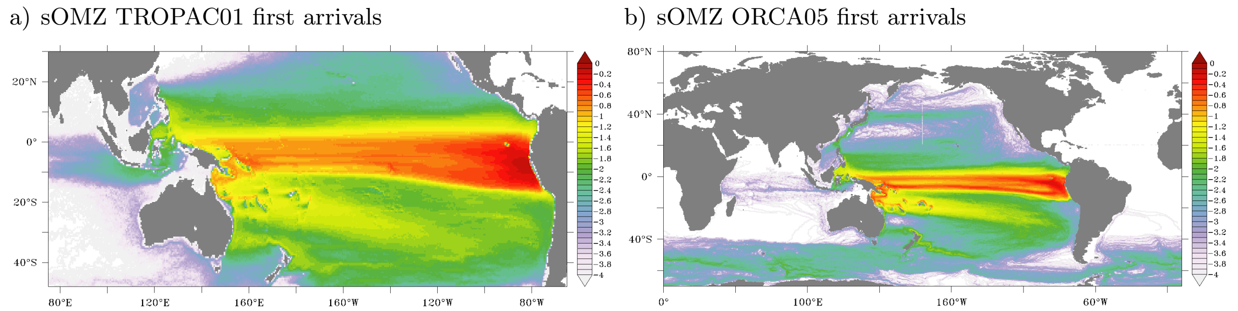

a) sOMZ TROPAC01 first arrivals

b) sOMZ ORCA05 first arrivals

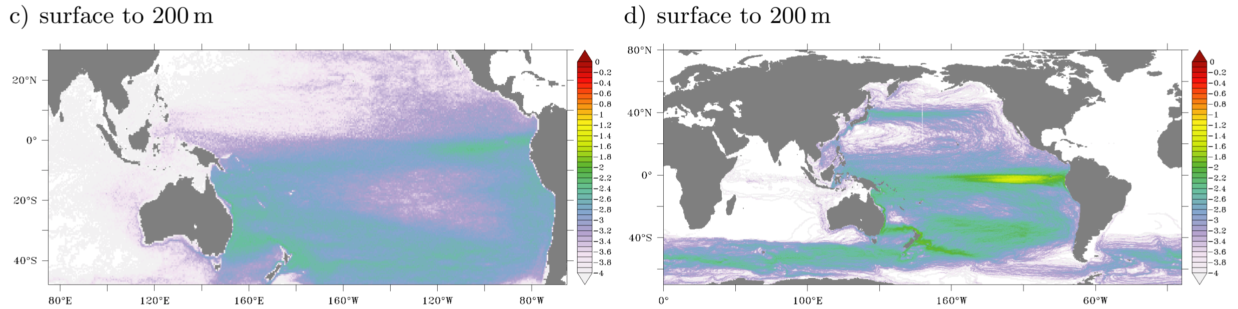

c) surface to 200 m

d) surface to 200 m

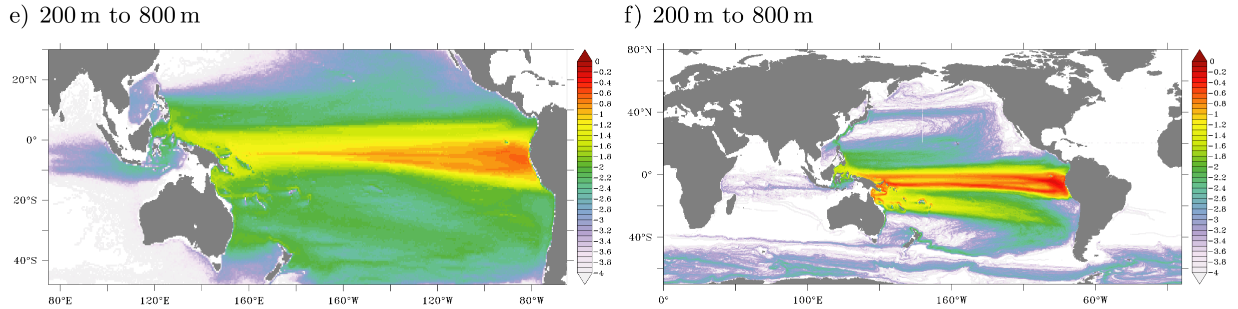

e) 200 m to 800 m

f) 200 m to 800 m

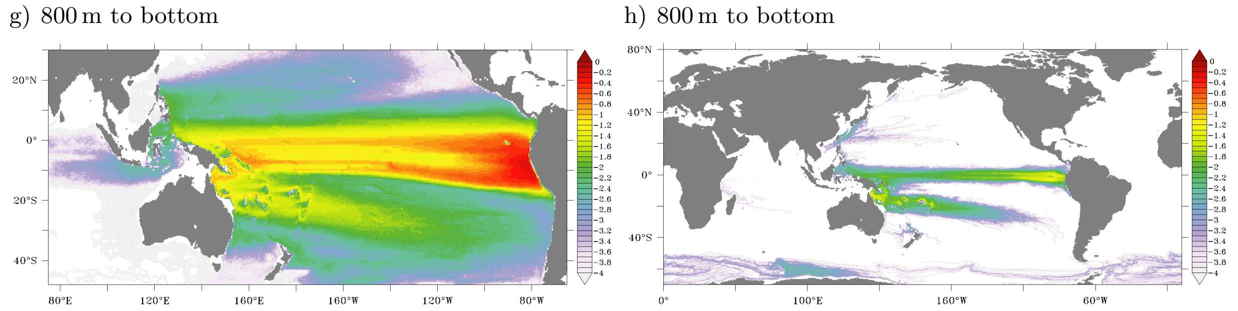

g) 800 m to bottom

h) 800 m to bottom

Figure A.56.: Depth integrated particle population derived as “first arrivals” [in % of released particles per 0.5° square on a logarithmic scale] temporally integrated over the full period of the Lagrangian experiments of 80 years for particles released in the Pacific sOMZ in TROPAC01 (left) and ORCA05 (right) for the full depth (a and b), the uppermost 200 m of the water column (c and d), 200 m to 800 m depth (e and f) and 800 m depth to the seafloor (g and h).

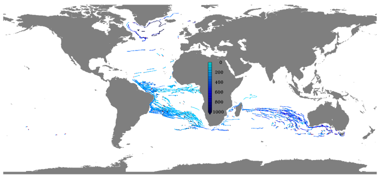

Erklärung

Hiermit erkläre ich, dass die vorliegende Dissertation, abgesehen von der Beratung durch den Betreuer, nach Inhalt und Form meine eigene Arbeit ist.
Kapitel 3.2 dieser Arbeit wurde 2011 im Fachblatt Geophysical Research Letters veröffentlicht und entstand in Zusammenarbeit mit meinem Koautor und Betreuer Claus W. Böning.
Ich erkläre, dass diese Arbeit weder ganz noch in Teilen an einer anderen Stelle im Rahmen eines Prüfungsverfahrens vorgelegen hat.
Die vorliegende Arbeit ist unter Einhaltung der Regeln guter wissenschaftlicher Praxis der Deutschen Forschungsgemeinschaft entstanden.

Kiel, April 2016 (Franziska Ulrike Schwarzkopf)